THE UNIVERSITY of ADELAIDE

## Department of Physics

# On the Structure of Nucleon Excited States in Lattice QCD

by

Finn Stokes

Supervisors:

Waseem Kamleh
Derek Leinweber

A thesis submitted towards the degree of
Doctor of Philosophy
at
The Faculty of Sciences
The University of Adelaide

June 2018

# Abstract

The structure of the nucleon and its excited states is governed by Quantum Chromodynamics (QCD), the theory of the strong force that binds constituent particles known as quarks into hadrons. The vacuum of QCD is non-trivial, and contains complicated, topologically non-trivial structures such as centre clusters. As a result, QCD cannot be solved by standard perturbative methods. Instead we formulate the theory on a discrete space-time lattice and evaluate expectation values computationally.

Centre clusters are localised spatial regions which play an important role in the confinement of quarks into hadrons. By visualising these centre clusters, we investigate their structure and observe the way they evolve under the algorithms used to solve QCD on the lattice. This gives insight into the role they play in confinement and hence how they underpin hadronic structure.

Moving on to the hadrons themselves, we develop the novel PEVA technique, which allows for the isolation of the nucleon, its excitations, and other baryons at finite momentum on the lattice. We then extend this technique to the calculation of form factors of baryons. Utilising this technique, we extract the Sachs electric and magnetic form factors for the ground stat nucleon, and demonstrate the necessity of PEVA for precision calculations of such form factors.

Finally, we turn our attention to the excitations of the nucleon. We present world first calculations of the Sachs electric and magnetic form factors of three localised excitations of the nucleon on the lattice. These results give fascinating insight into the structure of these states and pave the way for future effective field theory studies of the $N^*(1535)$ and $N^*(1650)$ resonances. These results would not have been possible without first developing the PEVA technique. Now that it has been developed, it will become a staple for investigations of baryon excited states.

# Acknowledgements

These past five years have been a journey, and I have only been able to travel as far as I have thanks to the support of a number of people.

Firstly, I would like to say a big thankyou to my supervisors, Derek Leinweber and Waseem Kamleh. Your advice and support has been invaluable throughout this process. Your guidance starting as early as my first undergraduate year, and continuing for the following decade, has been a critical part of me becoming the researcher I am today. I would also like to thank James Zanotti and Ross Young for offering additional advice when I needed it.

Throughout the five years of my PhD, I have had the pleasure of working alongside some great people. I would like to thank my office-mates, from the initial group of Sam, Jack, Daniel, Adrian and both Bens, to the later crowd of Dylan, Jacob, Ryan, Kim, Josh, Louis, and both spin-up and spin-down Alexes. I would particularly like to thank Ben Owen for helping me get started on my research, and Alex Chambers for the company as we both wrote up our theses.

Towards the end of my project, through the dedicated work of Alex Chambers and Kimmy Cushman, the lattice and S4S student groups were formed. I would like to thank all of the members of these two groups, and the current organisers Alex Westin, Ryan Bignell and Robert Perry, for all the stimulating discussions and fascinating talks that our meetings have contained.

I would also like to thank my parents Vikki and Martin, and my brothers Rory and Michael, for all their love and support. Mum and Dad, your encouragement of my interest in science from a young age has nurtured a curiosity and inquiring spirit that I value dearly. Your ongoing support and the availability of a place in the country to retreat from the stresses of day-to-day life has been so important to me.

Finally, I want to thank Sophie for all their support and encouragement, both academically and personally. I don't know how I would have made it to where I am now without your help. Our partnership means the world to me, and I look forward to our future adventures together as we head overseas to seek our careers in academia.

# Thesis Declaration

I certify that this work contains no material which has been accepted for the award of any other degree or diploma in my name in any university or other tertiary institution and, to the best of my knowledge and belief, contains no material previously published or written by another person, except where due reference has been made in the text. In addition, I certify that no part of this work will, in the future, be used in a submission in my name for any other degree or diploma in any university or other tertiary institution without the prior approval of the University of Adelaide and where applicable, any partner institution responsible for the joint award of this degree. I give permission for the digital version of my thesis to be made available on the web, via the University's digital research repository, the Library Search and also through web search engines, unless permission has been granted by the University to restrict access for a period of time.

I acknowledge the support I have received for my research through the provision of an Australian Government Research Training Program Scholarship.

02/02/2018

# Contents

# Chapter 1

# Introduction

Quantum chromodynamics (QCD) is the theory of the strong force, one of the four fundamental forces of nature. The strong force is responsible for the existence of hadronic matter. It binds fundamental particles known as quarks together into protons, neutrons, and other hadrons. When quarks interact in QCD, they do so by exchanging force carrying particles known as gluons. Gluons play a similar role in QCD to photons in quantum electrodynamics, and couple to quarks via a “colour” charge which is analogous to the electric charge. However, unlike photons which are electrically neutral and do not interact with one another directly, gluons themselves carry colour charge and hence are self-interacting. In Chapter 2, we will summarise the mathematics underlying QCD, and how we can study its consequences using lattice QCD.

The self-interactions of gluons in QCD lead to a non-trivial vacuum, which contains complicated topological structures, including instantons [1–3], centre vortices [4–6], and centre clusters [7–10]. Centre clusters are localised spatial regions within the QCD vacuum which play an important role in confinement, leading to the formation of hadrons such as protons and neutrons. Centre clusters will be discussed in detail in Chapter 3, which focuses on their behaviour and physical significance.

The confined hadrons resulting from this vacuum structure can be studied in lattice QCD by computing their two point correlation functions, which give us access to the energies of these states. The full ground-state energy spectrum of QCD has been successfully extracted from such correlation functions in multiple studies. These extractions have advanced to the point where they agree well with the physical spectrum [11]. This result is important, and demonstrates the effectiveness of lattice QCD at describing the physical world. However, lattice QCD gives us access to a lot more than just the ground-state spectrum: the states accessible on the lattice also include the full spectrum of excited hadron states.

This excited-state spectrum can provide valuable insights into the nature of the strong force and the resonances we observe in nature. Of particular interest are both resonances that have been observed in experiment but do not match simple theoretical models, and those that are predicted by QCD but have yet to be observed.

Accessing the excited-state spectrum on the lattice has been the focus of much research, which has led to the adoption of variational analysis techniques [12,13]. These techniques are a powerful tool that have allowed for the extraction of the excited-state spectrum of many hadrons. Our focus in this thesis is on the baryon sector, and the literature shows that much progress has been made in this area [14–23]. However, these techniques are only able to robustly isolate baryonic states when such states are at rest. Isolating these states when they are boosted to nontrivial momentum is important to enable investigations into their structure. A new variational analysis technique that overcomes this limitation is presented in Chapter 4.

Having isolated a spectrum of states at a range of momenta, the next step is to investigate their structure through the calculation of form factors. For example, the structure of the proton and neutron can be understood in terms of the Sachs electric and magnetic form factors. To calculate such form factors, we must extend the new variational analysis technique to deal with three point correlation functions. This extension and its application to the calculation of the Sachs form factors of the ground-state proton and neutron is presented in Chapter 5. Having demonstrated the functionality of this extension in the simplest case of the ground state, we can then apply it to the excited-state spectrum, as presented in Chapter 6. The development of these new variational analysis techniques allows us to investigate the structure of these states on the lattice for the first time, giving us new insight into the nature of QCD.

# Chapter 2

# Background

In this chapter we will introduce the formalism of lattice QCD upon which this thesis is based. While the underlying theory remains the same throughout, the implementation details vary from chapter to chapter. As such, we only provide a generalised overview here, and specify the implementation details where they are relevant.

## 2.1 Quantum Chromodynamics (QCD)

QCD is the gauge field theory describing the interactions of quarks. Quarks are the constituent particles making up all hadrons, including baryons such as the proton and neutron. In QCD, the strong interaction is mediated by a gauge boson known as the gluon. The gluon interacts via a "colour" charge, which is analogous to the electric charge in quantum electrodynamics (QED). The gluon itself carries a colour charge, leading to self-interactions between gluons. These interactions give rise to a non-trivial vacuum structure. This is in stark contrast to other gauge field theories such as QED, where the photon is electrically neutral and the vacuum structure is trivial. In this section we will summarise the mathematics underlying QCD, and how these self-interactions arise.

### 2.1.1 Quarks

In QCD the quarks are represented by fermion fields $\psi_i^a(x)$. The quarks have anti-particle partners known as anti-quarks, which are represented by similar fields $\overline{\psi}_i^a(x)$. Both states are fermions, and hence satisfy Fermi-Dirac statistics, so the fields must behave as Grassmann variables [24]. The quarks and anti-quarks carry a colour charge, and so exist in colour space, represented here by the index $a$. There are three colour charges (and three anti-colour charges), so this colour space is three dimensional. Since the quarks are spin-½ particles, they also exist in four-dimensional Dirac spin space, represented here by the indices $i, j \in \{1, 2, 3, 4\}$. In this thesis, we use the Pauli representation for the Dirac matrices, as outlined in Appendix C. We use a Euclidean metric ($\delta^{\mu\nu}$), and restore Minkowski space-time by including a factor of $i$ in the temporal component of the four-vectors ($a^4 = i\,a^0$). Hence, there is no need to distinguish between contravariant and covariant indices.

If the quarks were free particles, their Lagrangian density would be

$$\mathcal{L}_{\mathrm{F}}^{(0)}(x) = \overline{\psi}{}_i^a(x)\ \left(\not{\partial}_{ij} + m\,\delta_{ij}\right)\ \psi_j^a(x)\,, \tag{2.1}$$

where $\not{\partial}_{ij} \equiv \gamma_{ij}^{\mu}\partial^{\mu}$, and $m$ is the mass of the quark.

The quark fields transform in colour space under the fundamental representation of the non-Abelian gauge group SU(3). This is the group of all $3 \times 3$ unitary matrices with a determinant of 1. For example, under a global SU(3) transformation

$$\psi_i^a(x) \xrightarrow{\Omega} \Omega^{ab}\,\psi_i^b(x)\,, \tag{2.2a}$$

$$\overline{\psi}{}_i^a(x) \xrightarrow{\Omega} \overline{\psi}{}_i^b(x)\,\Omega^{\dagger\,ba}\,, \tag{2.2b}$$

where $\Omega \equiv \exp\left(i\,\theta_r\,\lambda_r/2\right) \in \mathrm{SU}(3)$ can be expressed in terms of a set of constant phases $\theta_r$ and the generators of SU(3), the Gell-Mann matrices $\lambda_r^{ab}/2$. Since all elements of SU(3) are unitary, under such a transformation the Lagrangian remains invariant.

However, in formulating a gauge field theory such as QCD, we seek a Lagrangian which is not only invariant under global gauge transformations, but also under local gauge transformations. In a local gauge transformation, instead of performing the same transformation at each point in space-time, we allow our phases $\theta_r(x)$ to vary across space-time, generating the transformation $\Omega(x) \equiv \exp\left(i\,\theta_r(x)\,\lambda_r/2\right) \in \mathrm{SU}(3)$. Under this transformation

$$\begin{aligned}\mathcal{L}_{\mathrm{F}}^{(0)}(x) \xrightarrow{\Omega(x)} &\overline{\psi}{}_i^b(x)\,\Omega^{\dagger\,ba}(x)\,\left(\not{\partial}_{ij} + m\,\delta_{ij}\right)\Omega^{ac}(x)\,\psi_j^c(x)\\ = &\overline{\psi}{}_i^b(x)\,\delta^{bc}\ \left(\not{\partial}_{ij} + m\,\delta_{ij}\right)\ \psi_j^c(x)\\ &+ \overline{\psi}{}_i^b(x)\,\left(\Omega^{\dagger\,ba}(x)\,\not{\partial}_{ij}\,\Omega^{ac}(x)\right)\psi_j^c(x)\\ \neq &\,\mathcal{L}_{\mathrm{F}}^{(0)}(x)\,,\end{aligned} \tag{2.3}$$

so this Lagrangian is not invariant under *local* gauge transformations. This results from the interaction of the derivative $\not{\partial}_{ij}$ with the space-time dependence of the local gauge transformation.

### 2.1.2 Gluons

In order to formulate a Lagrangian that is invariant under local gauge transformations, we seek a replacement derivative $\not{D}_{ij}^{ab}(x) \equiv \gamma_{ij}^{\mu} D^{ab\,\mu}(x)$, which we call the covariant derivative. For this derivative, we require that

$$\not{D}_{ij}^{ab}(x)\,\overline{\psi}_j^{b}(x) \xrightarrow{\Omega(x)} \Omega^{ac}(x)\,\not{D}_{ij}^{cb}(x)\,\psi_j^{b}(x)\,, \tag{2.4}$$

which means that the covariant derivative of a fermion field transforms in the same way as the fermion field itself.

Obtaining this transformation property requires adding a gauge field $\not{A}_{ij}^{ab}(x) \equiv \gamma_{ij}^{\mu} A^{ab\,\mu}(x)$ to the derivative

$$\not{D}_{ij}^{ab}(x) = \delta^{ab}\,\not{\partial}_{ij} - i\,g\,\not{A}_{ij}^{ab}(x)\,, \tag{2.5}$$

where $\not{A}_{ij}^{ab}(x)$ transforms in colour space under the adjoint representation of SU(3) as

$$\not{A}_{ij}^{ab}(x) \xrightarrow{\Omega(x)} \Omega^{ac}(x)\left[\not{A}_{ij}^{cd}(x) + \frac{1}{i\,g}\left(\Omega^{\dagger\,ce}(x)\,\not{\partial}_{ij}\,\Omega^{ed}(x)\right)\right]\Omega^{\dagger\,db}(x)\,. \tag{2.6}$$

This gauge field represents the gluons in QCD. Since $\not{A}_{ij}^{ab}(x)$ transforms under the adjoint representation of SU(3), it can be expressed in terms of the SU(3) generators

$$\not{A}_{ij}^{ab}(x) = \gamma_{ij}^{\mu}\,A_r^{\mu}(x)\,\frac{\lambda_r^{ab}}{2}\,, \tag{2.7}$$

where $\lambda_r$ are the Gell-Mann matrices.

Now that we have defined the covariant derivative, we can replace the derivative in Eq. (2.1), arriving at a gauge invariant Lagrangian

$$\mathcal{L}_{\mathrm{F}}(x) = \overline{\psi}_i^{a}(x)\,\left(\not{D}_{ij}^{ab}(x) + m\,\delta_{ij}\,\delta^{ab}\right)\,\psi_j^{b}(x)\,. \tag{2.8}$$

While this Lagrangian encodes the dynamics of the quarks in a gauge invariant manner, we have no kinematic terms for the gluons. Since $A^{ab\,\mu}(x)$ is a vector field, the kinematics can be expressed via the field strength tensor

$$G^{\mu\nu}(x) = \frac{1}{i\,g}\left[D^{\mu}(x), D^{\nu}(x)\right]\,. \tag{2.9}$$

The kinematic term we seek is then $\frac{1}{2}G^{ab\,\mu\nu}(x)G^{ba\,\mu\nu}(x)$. Using Eq. (2.4), we can show that this term is gauge invariant. In fact, unless we introduce new fields, this is the only term we can add to our Lagrangian that simultaneously satisfies gauge invariance, renormalisability, and an experimentally-observed symmetry of the strong interaction known as CP symmetry.

Thus, the full QCD Lagrangian is

$$\mathcal{L}_{\mathrm{QCD}}(x) = \overline{\psi}_i^{a}(x)\,\left(\not{D}_{ij}^{ab}(x) + m\,\delta_{ij}\,\delta^{ab}\right)\,\psi_j^{b}(x) - \frac{1}{2}G^{ab\,\mu\nu}(x)\,G^{ba\,\mu\nu}(x)\,. \tag{2.10}$$

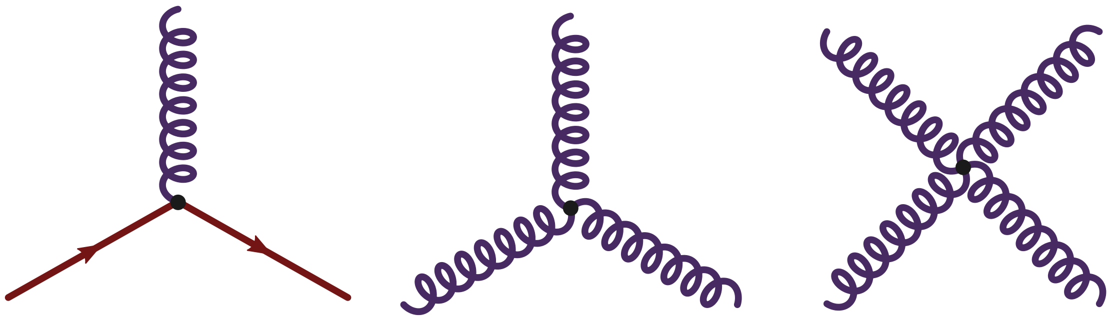

(a) The quark-gluon vertex (b) The three-gluon vertex (c) The four-gluon vertex

Figure 2.1: The three QCD interaction vertices arising from the interaction terms of the Lagrangian. The straight and coiled lines represent quarks and gluons respectively.

### 2.1.3 QCD interactions

The QCD Lagrangian has several interactions encoded into it that are not apparent at first glance. To better understand these interactions, we decompose the Lagrangian into non-interacting and interacting terms

$$\mathcal{L}_{\mathrm{QCD}}(x) = \mathcal{L}_{\mathrm{F}}^{(0)}(x) + \mathcal{L}_{\mathrm{G}}^{(0)}(x) + \mathcal{L}_{\mathrm{I}}(x)\,, \tag{2.11}$$

where $\mathcal{L}_{\mathrm{F}}^{(0)}(x)$ encodes the non-interacting quark dynamics, $\mathcal{L}_{\mathrm{G}}^{(0)}(x)$ encodes the non-interacting gluon dynamics, and $\mathcal{L}_{\mathrm{I}}(x)$ encodes the interactions between quarks and gluons.

To perform this decomposition, we first substitute the form of the covariant derivative into the field strength tensor from Eq. (2.9), giving the explicit form

$$\begin{aligned} G^{ab\,\mu\nu}(x) &= \left(\partial^\mu A_r^\nu(x) - \partial^\nu A_r^\mu(x) - g\, f_{rst} A_s^\mu(x)\, A_t^\nu(x)\right) \frac{\lambda_r^{ab}}{2} \\ &= \left(G_r^{(0)\,\mu\nu}(x) - g\, f_{rst} A_s^\mu(x)\, A_t^\nu(x)\right) \frac{\lambda_r^{ab}}{2}\,. \end{aligned} \tag{2.12}$$

This contains the kinematic term $G_r^{(0)\,\mu\nu}(x) \equiv \partial^\mu A_r^\nu(x) - \partial^\nu A_r^\mu(x)$. However, due to the non-Abelian nature of SU(3) we also obtain quadratic terms which depend on the SU(3) structure constants $f_{rst}$. These structure constants arise from the commutator

$$\left[\frac{\lambda_r}{2}, \frac{\lambda_s}{2}\right] = i\, f_{rst} \frac{\lambda_t}{2}\,. \tag{2.13}$$

Substituting both this expanded field strength tensor and the expanded form of the covariant derivative into the Lagrangian, we obtain the free field terms,

$$\mathcal{L}_{\mathrm{F}}^{(0)}(x) = \overline{\psi}^a_i(x)\,\left(\partial\!\!\!/_{ij} + m\,\delta_{ij}\right)\,\psi^a_j(x)\,, \text{ and} \tag{2.14}$$

$$\mathcal{L}_{\mathrm{G}}^{(0)}(x) = -\frac{1}{2}G^{(0)\,ab\,\mu\nu}G^{(0)\,ba\,\mu\nu}\,, \tag{2.15}$$

which encode the dynamics for a free quark field, and a massless vector boson respectively, as well as the interaction term

$$\mathcal{L}_{\mathrm{I}}(x) = i\,g\,\overline{\psi}^a_i(x)\,A\!\!\!/^{ab}_{ij}\,\psi^b_j(x) + g\,f_{rst}\partial^\mu A^\nu_r\,A^\mu_s A^\nu_t + \frac{g^2}{4}f_{rst}f_{ruv}A^\mu_s\,A^\nu_t\,A^\mu_u A^\nu_v\,. \tag{2.16}$$

This gives us the three interaction vertices, which are illustrated in Fig. 2.1. From left to right in Eq. (2.16), we have the quark-gluon vertex through which quarks can interact with gluons, and the three-gluon and four-gluon vertices through which gluons can interact with other gluons.

We note that the latter two of these vertices are both self-interactions between gluons. This corresponds to gluons themselves carrying colour charge. This is markedly different to QED, where the photons are neutral and do not interact with one another directly. These gluonic self-interactions are what makes QCD such a complicated field theory. They lead to three of the most interesting features of QCD:

1. **Non-trivial vacuum structure**
   The vacuum state of a quantum theory is the state with the lowest possible energy. The QCD vacuum state is non-empty, containing complicated topologically non-trivial structures made up of interacting gluons.

2. **Confinement**
   In low-energy QCD, quarks are bound within colour singlet states, and cannot occur in combinations with a net colour charge. We call this phenomenon confinement. Confinement is clearly produced by some mechanism within QCD, but the nature of this mechanism is poorly understood.

3. **Dynamical chiral symmetry breaking**
   Chiral symmetry is a symmetry of the QCD Lagrangian in the $m \to 0$ limit. At low energy scales this symmetry is spontaneously broken. This symmetry breaking effectively generates mass and is responsible for the majority of the mass of the proton and the neutron. Similar to confinement, the mechanism for dynamical chiral symmetry breaking is not yet well understood.

The conventional approach to solving a quantum field theory such as QCD is to treat the field dynamics as perturbations from free fields in an empty vacuum. This approach is known as perturbation theory. However, the QCD vacuum is non-empty and at low energies confinement requires that quarks are always bound into multi-particle states. Hence, the underlying assumptions of perturbation theory are invalid in low-energy QCD. Such techniques will only be valid at sufficiently high energy scales. To study low-energy QCD, a fundamentally non-perturbative calculation is required. The only *ab-initio* approach we currently have available to solve this problem is lattice QCD.

## 2.2 Lattice QCD

Lattice QCD was first proposed in 1974 by Kenneth Wilson as a means to demonstrate the confining nature of QCD [25]. He formulated QCD on a finite, discretised region of Euclidean space-time, known as a lattice. This formulation allows the vacuum expectation values to be interpreted by analogy to statistical mechanics over a finite phase space. It is thus possible to calculate the expectation values of operators using well-established Monte-Carlo techniques. In this section we will give an overview of this formulation and how it can be applied to computational calculations of hadronic observables.

### 2.2.1 Euclidean space-time

In a quantum field theory like QCD, observables are calculated by computing the vacuum expectation values of relevant operators using the Feynman path integral formalism. In QCD, such an expectation value for some operator $\mathcal{O}[\psi,\overline{\psi},A^\mu]$ is given by

$$\langle\Omega|\mathcal{O}[\psi,\overline{\psi},A^\mu]\,|\Omega\rangle = \frac{1}{\mathcal{Z}}\int \mathcal{D}\psi\,\mathcal{D}\overline{\psi}\,\mathcal{D}A^\mu\;\mathcal{O}[\psi,\overline{\psi},A^\mu]\,\exp\bigl(i\,\mathcal{S}_{\mathrm{QCD}}[\psi,\overline{\psi},A^\mu]\bigr)\,, \tag{2.17}$$

where the integral is over all possible field values for the quark, anti-quark and gluon fields at all possible points in space-time. Here, $|\Omega\rangle$ denotes the vacuum state. The action, $\mathcal{S}_{\mathrm{QCD}}$, is the integral of the Lagrangian over space-time

$$\mathcal{S}_{\mathrm{QCD}}[\psi,\overline{\psi},A^\mu] \equiv \int \mathrm{d}^4x\,\mathcal{L}_{\mathrm{QCD}}(x)\,, \tag{2.18}$$

and the generating functional $\mathcal{Z}$ is

$$\mathcal{Z} \equiv \int \mathcal{D}\psi\,\mathcal{D}\overline{\psi}\,\mathcal{D}A^\mu\;\exp\bigl(i\,\mathcal{S}_{\mathrm{QCD}}[\psi,\overline{\psi},A^\mu]\bigr)\,. \tag{2.19}$$

The form of this generating functional is reminiscent of the partition function from statistical mechanics. However the exponent is imaginary rather than real. If we reexpress the theory in Euclidean space-time by performing a Wick rotation

$$t \to -i\,t\,, \tag{2.20a}$$

$$A^4 \to +i\,A^4\,, \tag{2.20b}$$

$$\mathcal{S}_{\mathrm{QCD}} \to +i\,\mathcal{S}_{\mathrm{QCD}}^{Eucl}\,, \tag{2.20c}$$

then the generating functional takes the correct form for a partition function

$$Z = \int \mathcal{D}\psi\,\mathcal{D}\overline{\psi}\,\mathcal{D}A^\mu\,\exp\!\left(-\mathcal{S}_{\mathrm{QCD}}^{Eucl}[\psi,\overline{\psi},A^\mu]\right)\,. \tag{2.21}$$

This allows us to interpret the vacuum expectation value from Eq. (2.17) as the weighted average of the operator across the ensemble of all possible field configurations. Expectation values can then be approximated by generating a sub-ensemble of field configurations distributed according to the probability factor

$$P\big[\psi^i,\overline{\psi}^i,A^{\mu\,i}\big] = \exp\left(-\mathcal{S}_{\mathrm{QCD}}^{Eucl}\big[\psi^i,\overline{\psi}^i,A^{\mu\,i}\big]\right)\,, \tag{2.22}$$

and then calculating the average value of the operator across this sub-ensemble

$$\langle\Omega|\mathcal{O}[\psi,\overline{\psi},A^\mu]\,|\Omega\rangle \approx \frac{1}{N}\sum_{i=1}^{N}\mathcal{O}\big[\psi^i,\overline{\psi}^i,A^{\mu\,i}\big]\,. \tag{2.23}$$

In the case of position four-vectors, the Wick rotation cancels out the factor of $i$ introduced into the temporal component at the start of this chapter,

$$x^4 = i\,x^0 = i\,t \to i\,(-i\,t) = t\,. \tag{2.24}$$

As a result, our position vectors in Euclidean space-time are purely real. For the rest of this thesis, expressions are in Euclidean space-time unless otherwise stated.

### 2.2.2 Discretisation

Generating a sub-ensemble of field configurations distributed according to the action is a highly nontrivial problem to which we seek a computational solution. To do this, the infinite dimensional integrals of QCD are evaluated by approximating continuous space-time with a discrete four dimensional grid, or lattice. This corresponds to the transformation

$$x^\mu \to a\,n^\mu\,, \tag{2.25}$$

where $a$ is the spacing between lattice sites and $n^\mu \in \mathbb{Z}^4$ are integer valued coordinates that enumerate the vertices of the lattice. This lattice can then be restricted to a finite subset $\mathbb{L} \subset \mathbb{Z}^4$, describing a finite volume of space-time $V = {L_s}^3 \times L_t = (N_s\, a)^3 \times (N_t\, a)$, where $N_s$ is the number of lattice sites in each spatial dimension, and $N_t$ is the number of lattice sites in the time dimension. This reduces the phase space of gauge fields from an infinite dimensional space to finite dimensions, rendering the problem of generating sub-ensembles computationally tractable. An important additional benefit arising from the discretisation described here is that the lattice acts as a regulator for the theory, allowing us to calculate quantities free from ultraviolet divergences.

In constraining our fields to a finite volume we must choose the boundary conditions they obey; when generating gauge field configurations, the most common choice is to use periodic boundary conditions. This means taking the values of the field just beyond one edge of the lattice to be equal to the values on the opposite edge of the lattice. Periodic boundary conditions were used in all four dimensions when generating all gauge field configurations considered in this thesis.

In the formulation of lattice QCD, the fermion fields representing the quarks and anti-quarks take values on the lattice sites. The integrals over space-time are replaced by sums

$$\int \mathrm{d}^4x \to a^4 \sum_{x \in \mathbb{L}} , \tag{2.26}$$

and the derivatives are replaced by finite differences

$$\partial^\mu f(x) \to \delta^\mu f(x) \equiv \frac{1}{2a} \left( f\left(x + a e^\mu\right) - f\left(x - a e^\mu\right)\right) , \tag{2.27}$$

where $e^\mu$ is the unit four vector in the space-time direction specified by $\mu$. The finite difference of the fermion field transforms under a local gauge transformation $\Omega(x)$ as

$$\delta^\mu \psi_i^a(x) \xrightarrow{\Omega(x)} \frac{1}{2a} \left( \Omega^{ab}\left(x + a e^\mu\right) \psi_i^b\left(x + a e^\mu\right) - \Omega^{ab}\left(x - a e^\mu\right) \psi_i^b\left(x - a e^\mu\right)\right) . \tag{2.28}$$

To restore gauge invariance, it is insufficient for the gluon fields to take values on the lattice sites. Instead, they are represented by the link variables

$$U^\mu(x) \equiv \mathcal{P} \exp\left( i\, g \int_x^{x + a e^\mu} \mathrm{d}z A^\mu(z)\right) , \tag{2.29}$$

which take values on the links between orthogonally adjacent lattice sites, as illustrated in Fig. 2.2. Under local gauge transformations, these link variables transform as

$$U^{ab\,\mu}(x) \xrightarrow{\Omega(x)} \Omega^{ac}(x)\, U^{cd\,\mu}(x)\, \Omega^{\dagger\, db}(x + a e^\mu) \tag{2.30a}$$

$$U^{\dagger\, ab\,\mu}(x) \xrightarrow{\Omega(x)} \Omega^{ac}(x + a e^\mu)\, U^{\dagger\, cd\,\mu}(x)\, \Omega^{\dagger\, db}(x) . \tag{2.30b}$$

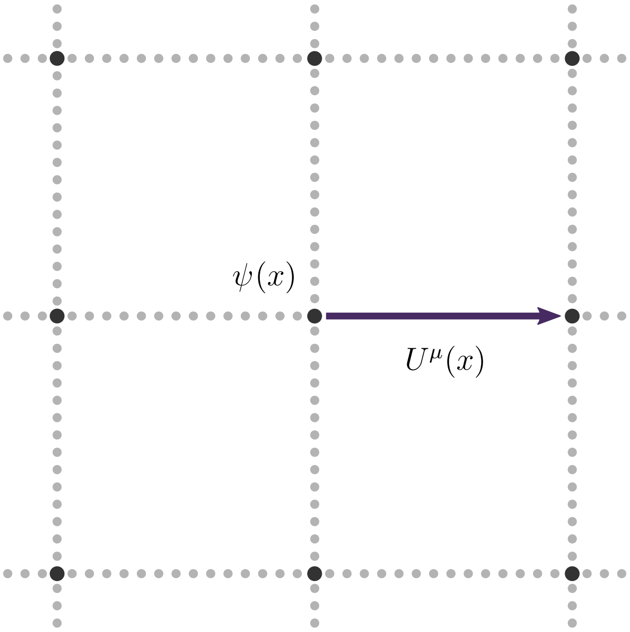

Figure 2.2: On the lattice, the quark fields $\psi(x)$ take values on the lattice sites, and the gluons are represented by the link variables $U^\mu(x)$ between the lattice sites

It is then possible to define the covariant finite difference operator

$$\nabla^{ab\,\mu}\psi_i^b(x) \equiv \frac{1}{2a}\left(U^{ab\,\mu}(x)\,\psi_i^b\left(x+ae^\mu\right) - U^{\dagger\,ab\,\mu}(x-ae^\mu)\,\psi_i^b\left(x-ae^\mu\right)\right)\,, \tag{2.31}$$

which transforms as desired under local gauge transformations

$$\nabla^{ab\,\mu}\psi_i^b(x) \xrightarrow{\Omega(x)} \Omega^{ab}(x)\nabla^{bc\,\mu}\psi_i^c(x) \tag{2.32}$$

and satisfies $\nabla^{ab\,\mu} \to D^{ab\,\mu}$ as $a \to 0$.

Now that we have formulated our quark fields, gluon fields, integrals and covariant derivative on the lattice, we seek a discretised form of the QCD action

$$\mathcal{S}_{\mathrm{QCD}}^{Latt}[\psi,\overline{\psi},U^\mu] = \mathcal{S}_{\mathrm{G}}^{Latt}[U^\mu] + \mathcal{S}_{\mathrm{F}}^{Latt}[\psi,\overline{\psi},U^\mu]\;. \tag{2.33}$$

### 2.2.3 Gluonic action

We begin with the gluonic action $\mathcal{S}_{\mathrm{G}}^{Latt}[U^\mu]$. In the continuum limit $a \to 0$, we want our lattice action to take the form of the Euclidean gauge action

$$\int \mathrm{d}^4x\,\frac{1}{2}G^{ab\,\mu\nu}(x)G^{ba\,\mu\nu}(x)\,. \tag{2.34}$$

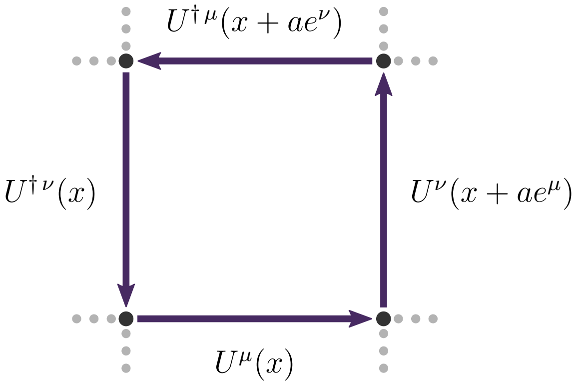

Figure 2.3: The plaquette $P^{\mu\nu}(x)$ is the product of four link variables.

On the lattice, this integral takes the form

$$a^4 \sum_x \frac{1}{2} G^{ab\,\mu\nu}(x) G^{ba\,\mu\nu}(x) = a^4 \sum_x \sum_{\mu>\nu} G^{ab\,\mu\nu}(x) G^{ba\,\mu\nu}(x)\,. \tag{2.35}$$

So we seek a gauge invariant expression which takes the form $\sum_{\mu>\nu} G^{ab\,\mu\nu}(x)G^{ba\,\mu\nu}(x)$ in the continuum limit.

To this end, we consider products of gauge links around closed paths, which form gauge invariant quantities known as Wilson loops. The simplest Wilson loop is the $1 \times 1$ plaquette,

$$P^{ab\,\mu\nu}(x) = U^{ac\,\mu}(x)\, U^{cd\,\nu}(x+ae^\mu)\, U^{\dagger\,de\,\mu}(x+ae^\nu)\, U^{\dagger\,eb\,\nu}(x)\,, \tag{2.36}$$

which is illustrated in Fig. 2.3. The plaquette takes the value

$$P^{\mu\nu}(x) = \exp\!\left[ig\left(a^2 G^{\mu\nu}(x) + O(a^3)\right)\right]\,. \tag{2.37}$$

So by considering its Taylor expansion, we find that the real part of the plaquette contains the gluonic interaction term

$$\frac{1}{2}\left(P^{ac\,\mu\nu}(x) + P^{\dagger\,ac\,\mu\nu}(x)\right) = 3 - \frac{g^2 a^4}{2} G^{ab\,\mu\nu}(x) G^{bc\,\mu\nu}(x) + O(a^6)\,, \tag{2.38}$$

so we can write the gluonic action as a colour trace

$$\begin{aligned} \mathcal{S}_\mathrm{G}^W[U^\mu] &\equiv \beta \sum_x \sum_{\mu>\nu} \mathrm{Tr}\left[1 - \frac{1}{6}\left(P^{\mu\nu}(x) + P^{\dagger\,\mu\nu}(x)\right)\right] \\ &= a^4 \left[\sum_x \sum_{\mu>\nu} G^{ab\,\mu\nu}(x) G^{ba\,\mu\nu}(x) + O(a^2)\right]\,, \end{aligned} \tag{2.39}$$

where the lattice coupling $\beta \equiv 6/g^2$ is defined to recover the continuum action in the limit $a \to 0$. This action is called the Wilson gauge action, and has errors of $O(a^2)$. Improvements to this discretisation error can be made by introducing larger Wilson loops such as the $1 \times 2$ rectangle to cancel off the higher order terms in $a$. This is known as Symanzik improvement [26, 27]. This process proceeds as above, with the only difficulty lying in determining the renormalisation of the coefficients of the differently-sized Wilson loops. There are a variety of prescriptions for determining the renormalisation of these coefficients, such as the tree-level calculation of Ref [28], or the renormalisation group approach outlined by Iwasaki in Ref. [29]. The latter approach is adopted throughout this thesis.

### 2.2.4 Quark action

We now consider the quark action $\mathcal{S}_{\mathrm{F}}^{Latt}[\psi, \overline{\psi}, U^{\mu}]$. We seek a gauge invariant expression which in the continuum limit takes the form of the Euclidean fermion action

$$\mathcal{S}_{\mathrm{F}}^{Cont}[\psi, \overline{\psi}, A^{\mu}] = \int \mathrm{d}^4x \, \overline{\psi}_i^a(x) \left( \not{D}_{ij}^{ab}(x) + \delta^{ab}\delta_{ij} m \right) \psi_j^b(x) \,. \tag{2.40}$$

Replacing the covariant derivative by the covariant finite difference operator $\nabla^{ab\,\mu}$ defined in Eq. (2.31), we obtain the naïve discretisation of the fermion action

$$\mathcal{S}_{\mathrm{F}}^{N}[\psi, \overline{\psi}, U^{\mu}] \equiv a^4 \sum_x \overline{\psi}_i^a(x) \left( \nabla_{ij}^{ab}(x) + \delta^{ab}\delta_{ij} m \right) \psi_j^b(x) \,. \tag{2.41}$$

This takes the form

$$\mathcal{S}_{\mathrm{F}}^{N}[\psi, \overline{\psi}, U^{\mu}] = a^4 \sum_x \overline{\psi}_i^a(x) \left( \delta^{ab} \not{\partial}_{ij} + ig \not{A}_{ij}^{ab}(x) + \delta^{ab}\delta_{ij} m + O(a^2) \right) \psi_j^b(x) \,. \tag{2.42}$$

So this action has errors of $O(a^2)$. In addition, this action preserves the chiral symmetry described in Ref. [30].

However, this action has a serious flaw: it produces fifteen unphysical quark species known as fermion doublers. In coordinate space, the Hermitian implementation of the finite difference operator only couples fermion fields separated by two lattice sites. This leads to a decoupling between the even and odd lattice sites along each space-time axis, which gives $2^4 = 16$ decoupled fermion fields. In momentum space, the finite difference operator takes a sinusoidal form, resulting in multiple zeros at 0 and the cutoff $\pi/a$ in each dimension. These zeros lead to spurious poles in the quark propagator in the $m \to 0$ limit, which result in the extra quark species.

In order to get rid of the fermion doublers, we must remove the spurious momentum-space zeros of the finite difference operator in such a way that we still recover the correct continuum limit of the action. The solution proposed by Wilson is to add the so-called Wilson term,

$$\overline{\psi}_i^a(x)\,\Delta^{ab}\,\psi_i^b(x) \equiv \frac{1}{a^2}\sum_{\mu=1}^{4}\overline{\psi}_i^a(x)\Big(2\psi_i^a(x) - U^{ab\,\mu}(x)\,\psi_i^b(x+ae^\mu) \\ -U^{\dagger\,ab\,\mu}(x-ae^\mu)\,\psi_i^b(x-ae^\mu)\Big)\,, \qquad (2.43)$$

producing the Wilson action

$$\mathcal{S}_{\mathrm{F}}^{W}[\psi,\overline{\psi},U^\mu] \equiv a^4\sum_x \overline{\psi}_i^a(x)\left(\nabla_{ij}^{ab}(x) + \delta_{ij}\frac{ra}{2}\Delta^{ab} + \delta^{ab}\delta_{ij}m\right)\psi_j^b(x)\,, \qquad (2.44)$$

where $r$ is the Wilson parameter, which is generally set to 1. The Wilson term is an irrelevant second order derivative operator with an energy dimension of five. As a result it has a coefficient including the fifth power of the lattice spacing. A factor of $a^4$ is absorbed into the discretisation of the integral, $a^4\sum_x \to \int \mathrm{d}^4x$ as $a \to 0$, leaving a single factor of the lattice spacing in the coefficient, as seen in Eq. (2.44). This remaining factor of $a$ ensures that the coefficient for the Wilson term goes to zero in the continuum limit, allowing us to recover the correct action.

It is conventional to rescale the fermion fields

$$\psi_i^a(x) \to \frac{\psi_i^a(x)}{\sqrt{2\kappa}}\,,\ \text{where}\ \kappa = \frac{1}{2ma+8r}\,. \qquad (2.45)$$

which allows the fermion action to be written as

$$\mathcal{S}_{\mathrm{F}}^{W}[\psi,\overline{\psi},U^\mu] = a^4\sum_x \overline{\psi}_i^a(x)\,M_{ij}^{W\,ab}(x,y)\,\psi_j^b(x)\,, \qquad (2.46)$$

with the Wilson fermion matrix

$$M_{ij}^{W\,ab}(x,y) = \delta_{xy} - \kappa\sum_\mu\big[(r-\gamma^\mu)\,U^\mu(x)\,\delta_{x+ae^\mu,y} \\ +\,(r+\gamma^\mu)\,U^{\dagger\,\mu}(x-ae^\mu)\,\delta_{x-ae^\mu,y}\big]\ . \qquad (2.47)$$

The parameter $\kappa$ is the hopping parameter, which couples the fermion field at each lattice site to its nearest neighbours.

The Wilson action is free from fermion doublers for any $r > 0$. Unfortunately, the Wilson term introduces two new problems: it introduces new discretisation errors at $O(a)$, and it explicitly breaks chiral symmetry.

The $O(a)$ discretisation errors can be cancelled out by adding the so-called clover term

$$-\frac{iga\,C_{SW}\,r}{4}\sigma_{ij}^{\mu\nu}F^{ab\,\mu\nu}(x)\,, \qquad (2.48)$$

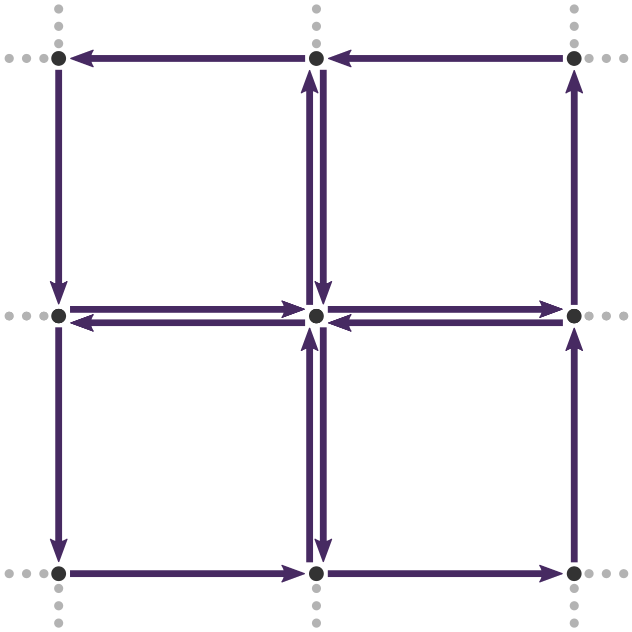

Figure 2.4: The clover loop $C^{\mu\nu}(x)$ is the product of 16 link variables.

where

$$F^{\mu\nu}(x) = \frac{-i}{8a^2 g}\left[C^{\mu\nu}(x) - C^{\mu\nu}(x)\right] , \tag{2.49}$$

is composed of the clover loop

$$\begin{aligned} C^{ab\,\mu\nu}(x) = {} & U^{ac\,\mu}(x)\, U^{cd\,\nu}(x+ae^{\mu})\, U^{\dagger\,de\,\mu}(x+ae^{\nu})\, U^{\dagger\,eb\,\nu}(x) \\ & + U^{ac\,\nu}(x)\, U^{\dagger\,cd\,\mu}(x-ae^{\mu}+ae^{\nu})\, U^{\dagger\,de\,\nu}(x-ae^{\mu})\, U^{eb\,\mu}(x-ae^{\mu}) \\ & + U^{\dagger\,ac\,\mu}(x-ae^{\mu})\, U^{\dagger\,cd\,\nu}(x-ae^{\mu}-ae^{\nu})\, U^{de\,\mu}(x-ae^{\mu}-ae^{\nu})\, U^{eb\,\nu}(x-ae^{\nu}) \\ & + U^{\dagger\,ac\,\nu}(x-ae^{\nu})\, U^{cd\,\mu}(x-ae^{\nu})\, U^{de\,\nu}(x+ae^{\mu}-ae^{\nu})\, U^{\dagger\,eb\,\mu}(x) \, , \end{aligned} \tag{2.50}$$

as illustrated in Fig. 2.4. This gives the Sheikholeslami-Wohlert, or clover fermion action [31],

$$\mathcal{S}_{\mathrm{F}}^{SW}[\psi,\overline{\psi},U^{\mu}] = \mathcal{S}_{\mathrm{F}}^{W}[\psi,\overline{\psi},U^{\mu}] - a^4 \sum_x \overline{\psi}_i^a(x)\,\frac{iga\,C_{SW}\,r}{4}\sigma_{ij}^{\mu\nu} F^{ab\,\mu\nu}(x)\,\psi_j^b(x)\,. \tag{2.51}$$

The clover coefficient $C_{SW}$ is tuned to properly remove the $O(a)$ errors. In this thesis, we use a non-perturbatively tuned value for this coefficient, as described in Ref. [32].

Restoring chiral symmetry is much more difficult. In fact, fully restoring chiral symmetry on the lattice is not possible without reintroducing fermion doublers [33]. However, restoring a lattice generalisation of chiral symmetry [34] is possible. This leads to both the overlap action [35,36] and domain wall fermions [37]. These approaches are computationally expensive, so in practice are only used for applications where chiral symmetry is particularly important.

When specifying these actions, we are free to select any mass for our quarks, either through the bare mass $m$, or the hopping parameter $\kappa$. When every quark in the simulation is tuned to have its physical mass, we say the simulation is at the physical point. It turns out that the computational expense associated with these actions is particularly high when the quark mass is small. This makes it difficult to generate gauge field configurations at the physical point, due to the light quark masses of the up and down quarks. In addition, some statistical errors are associated with the mass of the pion, so at lighter quark masses where the pion is lighter, these effects are more significant. Because of both of these effects, it is common to perform lattice QCD simulations with unphysically heavy up and down quarks, and then extrapolate back to the physical point. However, in recent years as algorithms improve, and more supercomputing resources become available, it is becoming more common to perform simulations at or very near the physical point for so-called "gold-plated" calculations, as in Refs. [38–41].

An additional problem with Wilson fermions in particular is the additive renormalisation of the quark mass admitted by chiral symmetry breaking. At tree level (that is, to lowest order in perturbation theory), a quark mass of zero is attained at $\kappa = \kappa_{\mathrm{cr}} \equiv 1/8$, as can be seen from Eq. 2.45. However, nonperturbative effects lead to a non-zero renormalised quark mass at $\kappa = \kappa_{\mathrm{cr}}$ and make it difficult to make a direct connection between $\kappa$ and the renormalised quark mass. Hence, rather than working directly with the quark mass, we use the squared pion mass $m_\pi^2$, which is proportional to the renormalised quark mass, as a measure of proximity to the physical point.

### 2.2.5 Lattice units

When performing calculations in lattice QCD, the physical variables are replaced by dimensionless counterparts in 'lattice units'

$$\begin{aligned}
m_{lat} &= a\, m_{phys}\,, && \text{(2.52a)}\\
x_{lat} &= a^{-1}\, x_{phys}\,, && \text{(2.52b)}\\
\Big[\psi_i^a(x)\Big]_{lat} &= a^{3/2}\Big[\psi_i^a(x)\Big]_{phys}\,, && \text{(2.52c)}\\
\Big[\overline{\psi}_i^a(x)\Big]_{lat} &= a^{3/2}\Big[\overline{\psi}_i^a(x)\Big]_{phys}\,, && \text{(2.52d)}\\
\Big[\partial^\mu\psi_i^a(x)\Big]_{lat} &= a^{5/2}\Big[\partial^\mu\psi_i^a(x)\Big]_{phys}\,, && \text{(2.52e)}\\
&\text{etc.}
\end{aligned}$$

The physical units can be easily recovered by multiplying or dividing by the appropriate powers of the lattice spacing $a$, and $\hbar c \approx 0.197\,327\,\mathrm{GeV\,fm}$. For example, the physical mass in units of energy is given by $\frac{\hbar c}{a}\, m_{lat}$. For the rest of this thesis, variables other than the lattice spacing are expressed in lattice units unless otherwise stated.

### 2.2.6 Path integrals

Now that we have discretised the QCD Lagrangian on a finite volume of Euclidean space-time, we are finally in a position to compute the path integrals from Sec. 2.2.1. If we consider the QCD partition function

$$\begin{aligned} Z &= \int \mathcal{D}\psi\, \mathcal{D}\overline{\psi}\, \mathcal{D}U^{\mu}\ \exp\bigl(-\mathcal{S}^{Latt}_{\mathrm{QCD}}[\psi,\overline{\psi},U^{\mu}]\bigr) \\ &= \int \mathcal{D}\psi\, \mathcal{D}\overline{\psi}\, \mathcal{D}U^{\mu}\ \exp\bigl(-\mathcal{S}^{Latt}_{\mathrm{G}}[U^{\mu}] - \mathcal{S}^{Latt}_{\mathrm{F}}[\psi,\overline{\psi},U^{\mu}]\bigr) \\ &= \int \mathcal{D}U^{\mu}\ \exp\bigl(-\mathcal{S}^{Latt}_{\mathrm{G}}[U^{\mu}]\bigr) \int \mathcal{D}\psi\, \mathcal{D}\overline{\psi}\ \exp\bigl(-\mathcal{S}^{Latt}_{\mathrm{F}}[\psi,\overline{\psi},U^{\mu}]\bigr)\ . \end{aligned} \tag{2.53}$$

We can then express the quark action $\mathcal{S}^{Latt}_{\mathrm{F}}$ in terms of a $({N_s}^3 \cdot N_t \cdot N_c \cdot N_D)$-dimensional fermion matrix $M$, where $N_c = 3$ is the number of colour charges and $N_D = 4$ is the number of Dirac spin components

$$\mathcal{S}^{Latt}_{\mathrm{F}}[\psi,\overline{\psi},U^{\mu}] = \sum_{x,y} \overline{\psi}^{a}_{i}(x)\, M^{ab}_{ij}(x,y)\, \psi^{b}_{j}(y)\,. \tag{2.54}$$

Since the fermion fields behave as Grassmann variables, the fermionic integral can be evaluated explicitly

$$\int \mathcal{D}\psi\, \mathcal{D}\overline{\psi}\ \exp\left( -\sum_{x,y} \overline{\psi}^{a}_{i}(x)\, M^{ab}_{ij}(x,y)\, \psi^{b}_{j}(y) \right) = \det(M)\ , \tag{2.55}$$

as described in Ref. [42]. Hence, we can integrate out the fermion degrees of freedom, reducing the partition function to

$$\begin{aligned} Z &= \int \mathcal{D}U^{\mu}\ \exp\bigl(-\mathcal{S}^{Latt}_{\mathrm{G}}[U^{\mu}]\bigr)\ \det(M[U^{\mu}]) \\ &= \int \mathcal{D}U^{\mu}\ \exp(-\mathcal{S}_{\mathrm{Eff}}[U^{\mu}])\ , \end{aligned} \tag{2.56}$$

where we define the effective action $\mathcal{S}_{\mathrm{Eff}}[U^{\mu}] \equiv \mathcal{S}^{Latt}_{\mathrm{G}}[U^{\mu}] - \ln(\det(M[U^{\mu}]))$.

A similar procedure can be applied to the expression for the vacuum expectation value

$$\langle\Omega|\mathcal{O}[\psi,\overline{\psi},U^{\mu}]\,|\Omega\rangle = \frac{1}{\mathcal{Z}} \int \mathcal{D}\psi\, \mathcal{D}\overline{\psi}\, \mathcal{D}U^{\mu}\ \mathcal{O}[\psi,\overline{\psi},U^{\mu}]\ \exp\bigl(-\mathcal{S}^{Latt}_{\mathrm{QCD}}[\psi,\overline{\psi},U^{\mu}]\bigr)\ , \tag{2.57}$$

however care must be taken when the operator is dependent on the quark fields, as this changes the integrand in Eq. (2.55). The quark-field dependence of such an operator can be expressed in terms of products of equal numbers of fermion and anti-fermion fields, so the fermionic part of the integral becomes

$$\begin{aligned}\int \mathcal{D}\psi\,\mathcal{D}\overline{\psi}\;\psi_{i_1}^{a_1}(x_1)\cdots\psi_{i_n}^{a_n}(x_n)\,\overline{\psi}_{j_1}^{b_1}(y_1)\cdots\overline{\psi}_{j_n}^{b_n}(y_n)&\\ \times\exp\left(-\sum_{x,y}\overline{\psi}_i^a(x)\,M_{ij}^{ab}(x,y)\,\psi_j^b(y)\right)&\,. \qquad (2.58)\end{aligned}$$

This integral can be evaluated explicitly by considering the following generating functional

$$\begin{aligned}\tilde{\mathcal{Z}}[\eta,\overline{\eta}]\equiv\int\mathcal{D}\psi\,\mathcal{D}\overline{\psi}\;\exp\Bigg(&-\sum_{x,y}\overline{\psi}_i^a(x)\,M_{ij}^{ab}(x,y)\,\psi_j^b(y)\\ &+\sum_x\left(\overline{\psi}_i^a(x)\,\eta_i^a(x)+\overline{\eta}_i^a(x)\,\psi_i^a(x)\right)\Bigg)\,, \qquad (2.59)\end{aligned}$$

which is constructed such that our fermionic integral can be accessed by taking its derivative

$$\begin{aligned}\int\mathcal{D}\psi\,\mathcal{D}\overline{\psi}\;\psi_{i_1}^{a_1}(x_1)\cdots\psi_{i_n}^{a_n}(x_n)\,\overline{\psi}_{j_1}^{b_1}(y_1)\cdots\overline{\psi}_{j_n}^{b_n}(y_n)&\\ \times\exp\left(-\sum_{x,y}\overline{\psi}_i^a(x)\,M_{ij}^{ab}(x,y)\,\psi_j^b(y)\right)&\\ =\left[\frac{\partial}{\partial\overline{\eta}_{i_1}^{a_1}(x_1)}\cdots\frac{\partial}{\partial\overline{\eta}_{i_n}^{a_n}(x_n)}\,\tilde{\mathcal{Z}}[\eta,\overline{\eta}]\,\frac{\overleftarrow{\partial}}{\partial\eta_{j_1}^{b_1}(y_1)}\cdots\frac{\overleftarrow{\partial}}{\partial\eta_{j_n}^{b_n}(y_n)}\right]_{\eta=\overline{\eta}=0}&\,, \qquad (2.60)\end{aligned}$$

where $\frac{\partial}{\partial\overline{\eta}}$ and $\frac{\overleftarrow{\partial}}{\partial\eta}$ are the left and right Grassmann derivatives respectively. We can evaluate the left derivative by bringing $\overline{\eta}$ all the way to the left and then applying the rule $\frac{\partial}{\partial\overline{\eta}}\,\overline{\eta}=1$, and the right derivative by bringing $\eta$ all the way to the left and then applying the rule $\eta\,\frac{\overleftarrow{\partial}}{\partial\eta}=1$.

To evaluate this generating functional, we introduce the quark propagator $S[U^\mu]$, which is defined as the Green's function of the fermion matrix, that is

$$\sum_{x,a,i}M_{ki}^{ca}(z,x)\,S_{ij}^{ab}(x,y)\equiv\delta^{cb}\,\delta_{kj}\,\delta_{zy}\,. \qquad (2.61)$$

We can then perform a change of variables

$$\psi_i'^{\,a}(x)\equiv\psi_i^a(x)-\sum_y S_{ij}^{ab}(x,y)\,\eta_j^b(y)\,, \qquad (2.62a)$$

$$\overline{\psi}_i'^{\,a}(x)\equiv\overline{\psi}_i^a(x)-\sum_y\overline{\eta}_j^b(y)\,S_{ji}^{ba}(y,x)\,, \qquad (2.62b)$$

which allows us to rewrite the generating functional as

$$\tilde{\mathcal{Z}}[\eta,\overline{\eta}] \equiv \left[\int \mathcal{D}\psi'\,\mathcal{D}\overline{\psi}'\;\exp\left(-\sum_{x,y}\overline{\psi}_i'^{\,a}(x)\,M_{ij}^{ab}(x,y)\,\psi_j'^{\,b}(y)\right)\right] \\ \times\exp\left(\sum_{x,y}\overline{\eta}_i^a(x)\,S_{ij}^{ab}(x,y)\,\eta_j^b(y)\right). \tag{2.63}$$

The first term can then be evaluated similarly to Eq. (2.55), giving the final result of

$$\tilde{\mathcal{Z}}[\eta,\overline{\eta}] = \det(M)\;\exp\left(\sum_{x,y}\overline{\eta}_i^a(x)\,S_{ij}^{ab}(x,y)\,\eta_j^b(y)\right). \tag{2.64}$$

For more detail on this process, see Ref [42].

Taking the partial derivatives of this result as in Eq. (2.60) produces terms consisting of products of quark propagators for every permutation of fermion anti-fermion pairs. This corresponds to taking the terms corresponding to each possible full set of Wick contractions [43] of the fermion fields in the operator and replacing each contraction with a quark propagator with the corresponding colour, Dirac and spatial indices. The sign of each term is governed by the rearrangement required to place each pair of contracted Grassmann fields next to one another with $\psi$ on the left. For example, in the simplest case of one fermion field and one anti-fermion field

$$\int \mathcal{D}\psi\,\mathcal{D}\overline{\psi}\;\psi_{i_1}^{a_1}(x_1)\,\overline{\psi}_{j_1}^{b_1}(y_1)\;\exp\left(-\sum_{x,y}\overline{\psi}_i^a(x)\,M_{ij}^{ab}(x,y)\,\psi_j^b(y)\right) \\ = \det(M)\;S_{i_1j_1}^{a_1b_1}(x_1,y_1). \tag{2.65}$$

As such, it is sufficient to consider effective operators,

$$\mathcal{O}_{\text{Eff}}[U^\mu, S[U^\mu]] \tag{2.66}$$

where all fermion fields have been fully Wick contracted and replaced by quark propagators. Thus, to compute vacuum expectation values of such operators, it suffices to generate a sub-ensemble of gauge field configurations $\{U^{\mu\,i}\}$ distributed according to the probability factor

$$P\left[U^{\mu\,i}\right] = \exp\left(-\mathcal{S}_{\text{Eff}}\left[U^{\mu\,i}\right]\right)\,, \tag{2.67}$$

evaluate the quark propagator $S[U^{\mu\,i}]$ on each configuration, and then calculate the average value of the operator across the sub-ensemble

$$\langle\Omega|\mathcal{O}[\psi,\overline{\psi},U^\mu]\,|\Omega\rangle \approx \frac{1}{N}\sum_{i=1}^{N}\mathcal{O}_{\text{Eff}}\left[U^{\mu\,i}, S\left[U^{\mu\,i}\right]\right]. \tag{2.68}$$

### 2.2.7 Hybrid Monte-Carlo

In order to generate a sub-ensemble of gauge field configurations $\{U^{\mu\,i}\}$ with the desired probability distribution $P[U^{\mu\,i}] = \exp\left(-\mathcal{S}_{\text{Eff}}[U^{\mu\,i}]\right)$, the hybrid Monte-Carlo (HMC) algorithm [44] is used. The HMC algorithm works by iteratively proposing new gauge field configurations via a molecular dynamics algorithm, then accepting or rejecting the configurations with some probability $\rho$. The value of $\rho$ is carefully chosen such that after sufficiently many iterations, the distribution of accepted configurations approaches $P[U^{\mu\,i}i]$.

The molecular dynamics algorithm requires introducing the non-physical constructs $\Pi^\mu(x)$, the conjugate momenta of $U^\mu(x)$, and the simulation time $\tau$. We then describe the new extended system by the Hamiltonian

$$\mathcal{H}[U^\mu, \Pi^\mu] = \sum_{x,\mu} \frac{1}{2}\,\mathrm{Tr}\,\Pi^\mu(x)^2 + \mathcal{S}_{\text{Eff}}[U^\mu]\ . \tag{2.69}$$

Starting from an initial gauge field configuration $U$, we apply the following process [45]:

1. Select a random $\Pi^\mu(x)$ from an ensemble distributed according to

$$P[\Pi^\mu] \propto \exp\left(-\frac{1}{2}\,\mathrm{Tr}\,\Pi^2\right) \tag{2.70}$$

2. Perform molecular dynamics updates with step size $\Delta\tau$, evolving $U^\mu$ to to $U^{\mu\prime}$ and $\Pi^\mu$ to $\Pi^{\mu\prime}$ by the discretised equations of motion

$$U^\mu(x, \tau + \Delta\tau) = U^\mu(x,\tau)\exp(i\,\Delta\tau\,\Pi^\mu(x,\tau)) \tag{2.71a}$$

$$\Pi^\mu(x, \tau + \Delta\tau) = \Pi^\mu(x,\tau) - \Delta\tau\,U^\mu(x,\tau)\,\frac{\delta\mathcal{S}_{\text{Eff}}}{\delta U^\mu(x,\tau)}\ . \tag{2.71b}$$

These equations of motion ensure that $\frac{d\mathcal{H}}{d\tau} \approx 0$.

3. After some $n$ updates, providing a trajectory length of $n\,\Delta\tau$, we accept or reject the new configuration with probability

$$\rho = \min(1, \mathrm{e}^{-\Delta\mathcal{H}})\,,\ \text{where}\ \Delta\mathcal{H} = \mathcal{H}[U,\Pi] - \mathcal{H}[U',\Pi']\,. \tag{2.72}$$

Combining a molecular dynamics update with an accept/reject step in this way allows us to efficiently traverse the phase space via the molecular dynamics integration whilst using the acceptance probability to prevent any numerical errors in the integration from affecting the distribution of the sub-ensemble produced.

If we repeat this process sufficiently many times, we get a gauge field configuration ${U^\mu}^0$ which is independent from our initial configuration. We then say that our sequence of configurations is thermalised. We can then sample more configurations ${U^\mu}^1$, ${U^\mu}^2$, etc., separated by sufficiently many trajectories to ensure independence. This gives us a sub-ensemble $\{{U^\mu}^i\}$ with probability distribution $P[{U^\mu}^i]$ as required.

### 2.2.8 Hadronic operators

Having computed a sub-ensemble of gauge field configurations, we are able to calculate the vacuum expectation value of any operator which depends only on the gauge fields

$$\langle\Omega|\mathcal{O}[U^\mu]\,|\Omega\rangle \approx \frac{1}{N}\sum_{i=1}^{N}\mathcal{O}\left[{U^\mu}^i\right] \,. \tag{2.73}$$

However, if we have a more general operator $\mathcal{O}[\psi,\overline{\psi},U^\mu]$ which also depends on the quark fields, we need to consider the integral

$$\int \mathcal{D}\psi\,\mathcal{D}\overline{\psi}\;\mathcal{O}[\psi,\overline{\psi},U^\mu]\,\exp(-\psi M\overline{\psi})\,, \tag{2.74}$$

which takes a more complicated form than simply $\mathcal{O}[U^\mu]\,\det(M)$.

Such operators arise when investigating hadrons on the lattice. In such an investigation, we consider the interpolating fields $\chi(x)$ and $\overline{\chi}(x) = \chi^\dagger(x)\,\gamma^4$ which respectively annihilate and create states with the quantum numbers of the hadron of interest. Due to the complex dynamics of QCD, it is infeasible to directly formulate an interpolator that only produces the state of interest, so in general our interpolators will couple with varying strength to all states on the lattice with the chosen quantum numbers.

For baryons we use linear combinations of local interpolators of the form

$$\left[\,\chi(x)\right]_i = \epsilon^{abc}\left(q^a_j(x)\,C_{jm}\,\Gamma_{mk}\,r^b_k(x)\right)\tilde{\Gamma}_{il}s^c_l(x)\,, \tag{2.75}$$

where $q^a_j(x)$, $r^b_k(x)$ and $s^c_l(x)$ are quark fields corresponding to the valence quarks of the baryon of interest, and $C_{jm}$ is the charge conjugation matrix. The matrices $\Gamma_{mk}$ and $\tilde{\Gamma}_{il}$ are combinations of $\gamma$-matrices that couple the quark spins to give the desired quantum numbers. In particular, to ensure correct behaviour under Lorentz transformations, $\tilde{\Gamma}_{il}$ must be either $\gamma^5$ or $\mathbb{I}$. Similarly, for mesons we use linear combinations of local interpolators of the form

$$\chi(x) = \overline{q}^a_i(x)\,\Gamma_{ij}\,r^a_j(x)\,. \tag{2.76}$$

Using such interpolators, we can form the two point correlation function

$$\mathcal{G}(\boldsymbol{p}\,;t) = \sum_{\boldsymbol{x}} \mathrm{e}^{-i\boldsymbol{p}\cdot\boldsymbol{x}} \, \langle\Omega|\, \chi(x)\, \overline{\chi}(0)\, |\Omega\rangle \;, \tag{2.77}$$

which describes how the hadronic system propagates from 0 to $x$. We can then interpret this correlation function as a sum over a tower of exponentials each depending on the energy of some energy eigenstate the interpolator couples to. To make this connection, we first insert the complete set of states

$$\mathbb{I} = \sum_{\alpha,\tilde{p},s} |\alpha\,;\tilde{p}\,;s\rangle\,\langle\alpha\,;\tilde{p}\,;s| \tag{2.78}$$

between the interpolators $\chi(x)$ and $\overline{\chi}(0)$, giving

$$\mathcal{G}(\boldsymbol{p}\,;t) = \sum_{\alpha,\tilde{p},s}\sum_{\boldsymbol{x}} \mathrm{e}^{-i\boldsymbol{p}\cdot\boldsymbol{x}} \, \langle\Omega|\, \chi(x)\, |\alpha\,;\tilde{p}\,;s\rangle\,\langle\alpha\,;\tilde{p}\,;s|\, \overline{\chi}(0)\, |\Omega\rangle \;. \tag{2.79}$$

Noting our use of Euclidean time, we can then invoke operator translation

$$\chi(x) = \mathrm{e}^{Ht}\mathrm{e}^{-i\boldsymbol{P}\cdot\boldsymbol{x}}\chi(0)\mathrm{e}^{-Ht}\mathrm{e}^{+i\boldsymbol{P}\cdot\boldsymbol{x}} \,, \tag{2.80}$$

and the identity

$$\sum_{\boldsymbol{x}} \mathrm{e}^{i(\boldsymbol{p}-\boldsymbol{p}')\cdot\boldsymbol{x}} = \delta_{\boldsymbol{p}\boldsymbol{p}'} \,, \tag{2.81}$$

to simplify Eq. (2.79) to

$$\begin{aligned}
\mathcal{G}(\boldsymbol{p}\,;t) &= \sum_{\alpha,\tilde{p},s}\sum_{\boldsymbol{x}} \mathrm{e}^{-i\boldsymbol{p}\cdot\boldsymbol{x}} \, \langle\Omega|\, \mathrm{e}^{Ht}\mathrm{e}^{-i\boldsymbol{P}\cdot\boldsymbol{x}}\,\chi(0)\,\mathrm{e}^{-Ht}\mathrm{e}^{+i\boldsymbol{P}\cdot\boldsymbol{x}}\, |\alpha\,;\tilde{p}\,;s\rangle\,\langle\alpha\,;\tilde{p}\,;s|\, \overline{\chi}(0)\, |\Omega\rangle \\
&= \sum_{\alpha,\tilde{p},s}\sum_{\boldsymbol{x}} \mathrm{e}^{i(\tilde{\boldsymbol{p}}-\boldsymbol{p})\cdot\boldsymbol{x}}\mathrm{e}^{-E_\alpha(\boldsymbol{p})\,t} \, \langle\Omega|\, \chi(0)\, |\alpha\,;\tilde{p}\,;s\rangle\,\langle\alpha\,;\tilde{p}\,;s|\, \overline{\chi}(0)\, |\Omega\rangle \\
&= \sum_{\alpha,s} \mathrm{e}^{-E_\alpha(\boldsymbol{p})\,t} \, \langle\Omega|\, \chi(0)\, |\alpha\,;p\,;s\rangle\,\langle\alpha\,;p\,;s|\, \overline{\chi}(0)\, |\Omega\rangle \;.
\end{aligned} \tag{2.82}$$

We can see that the correlator has contributions from all eigenstates $\alpha$ consistent with the quantum numbers of the interpolating field. This means that in addition to the ground state in any channel, we also observe a tower of its excited states, including multi-particle scattering states. Each term is the product of an exponential of the state's energy, which encodes the time dependence, and interpolator overlap factors which can be parameterised as

$$\langle\Omega|\, \chi(0)\, |\alpha\,;p\,;s\rangle = \lambda_\alpha(\boldsymbol{p}) \times \{\text{spin terms}\} \,, \tag{2.83}$$

with the factor $\lambda_\alpha(\boldsymbol{p})$ encoding the coupling strength of the interpolator $\chi(0)$ to the eigenstate $|\alpha\,;p\,;s\rangle$. In the case of baryon interpolators, these spin terms give the correlation function the form of a matrix in Dirac spin space. To remove this spin structure, it is conventional to take the spinor trace of this matrix with some spin-structure projector $\Gamma_S$ to give the spinor-projected correlation function.

$$G(\Gamma_S\,;\boldsymbol{p}\,;t) \equiv \mathrm{Tr}\big(\Gamma_S\,\mathcal{G}_{ij}(\boldsymbol{p}\,;t)\big)\ . \tag{2.84}$$

This leaves us with a sum of scalar terms each with an exponential time dependence. As the coefficient of each exponential is the energy of the corresponding state, in the large Euclidean time limit all other contributions will be suppressed relative to the state with the lowest energy. Therefore by examining the correlator at large times, we can access the inertial properties of the lowest lying state in the channel under consideration. In particular, by forming the ratio of the correlator at successive times with the hadron at rest, we can access the effective mass of the eigenstate

$$m_{\mathrm{Eff}} \equiv \frac{1}{\delta t}\ln\!\left(\frac{\mathcal{G}(\boldsymbol{0}\,;t)}{\mathcal{G}(\boldsymbol{0}\,;t+\delta t)}\right)\ . \tag{2.85}$$

In order to actually calculate such two point correlation functions in lattice QCD, we need to deal with the dependence of the operators on the fermion fields. For baryons, our interpolators take the form given in Eq. (2.75), so the correlation function becomes

$$\begin{aligned}\mathcal{G}(\boldsymbol{p}\,;t) = \sum_{\boldsymbol{x}} \mathrm{e}^{-i\boldsymbol{p}\cdot\boldsymbol{x}}\ \langle\Omega|\,\epsilon^{abc}\Big(q^a_j(x)\,C_{jm}\,\Gamma_{mk}\,r^b_k(x)\Big)\tilde{\Gamma}_{il}\,s^c_l(x)&\\ \epsilon^{a'b'c'}\,\overline{s}{}'^{c'}_{l'}(0)\,\overline{\tilde{\Gamma}}{}'_{l'i'}\Big(\overline{r}{}'^{b'}_{k'}(0)\,\overline{\Gamma}{}'_{k'm'}\,C_{m'j'}\,\overline{q}{}'^{a'}_{j'}(0)\Big)\,|\Omega\rangle\ ,&\end{aligned} \tag{2.86}$$

where $\overline{\Gamma}_{ij} = \gamma^4_{ik}\Gamma^\dagger_{kl}\gamma^4_{lj}$, and $\overline{\tilde{\Gamma}}_{ij} = \gamma^4_{ik}\tilde{\Gamma}^\dagger_{kl}\gamma^4_{lj}$. We then need to evaluate the Grassmann integral

$$\begin{aligned}\int \mathcal{D}\psi\,\mathcal{D}\overline{\psi}\,\epsilon^{abc}\Big(q^a_j(x)\,C_{jm}\,\Gamma_{mk}\,r^b_k(x)\Big)\tilde{\Gamma}_{il}\,s^c_l(x)&\\ \epsilon^{a'b'c'}\,\overline{s}{}'^{c'}_{l'}(0)\,\overline{\tilde{\Gamma}}{}'_{l'i'}\Big(\overline{r}{}'^{b'}_{k'}(0)\,\overline{\Gamma}{}'_{k'm'}\,C_{m'j'}\,\overline{q}{}'^{a'}_{j'}(0)\Big)\ \exp(-\psi M\overline{\psi})\ .&\end{aligned} \tag{2.87}$$

We can do this via Wick's theorem [43], performing all possible Wick contractions of the quark field, replacing each by the corresponding quark propagator $S^{ab}_{ij}(x,y)$. The quark propagator is the Green's function of the fermion matrix, that is, the solution to the equation

$$\sum_{x,a,i} M^{ca}_{ki}(z,x)\,S^{ab}_{ij}(x,y) = \delta^{cb}\,\delta_{kj}\,\delta_{zy}\,. \tag{2.88}$$

This gives rise to six terms, each corresponding to a separate set of contractions

$$
\begin{aligned}
\Big[\mathcal{G}(\boldsymbol{p}\,;t)\Big]_{ii'} &= \sum_{\boldsymbol{x}} \mathrm{e}^{-i\boldsymbol{p}\cdot\boldsymbol{x}} \Big\langle \epsilon^{abc}\,\epsilon^{a'b'c'} \\
&\Big\{\tilde{\Gamma}_{il} S^{cc'}_{s\,ll'}(x,0)\overline{\tilde{\Gamma}}_{l'i'} \Big[C_{jm}\Gamma_{mk} S^{bb'}_{r\,kk'}(x,0)\overline{\Gamma}_{k'm'}C_{m'j'}S^{aa'}_{q\,jj'}(x,0)\Big]\delta_{qq'}\delta_{rr'}\delta_{ss'} \\
&- \tilde{\Gamma}_{il} S^{cc'}_{s\,ll'}(x,0)\overline{\tilde{\Gamma}}_{l'i'} \Big[\Gamma_{mk}C_{jm} S^{ab'}_{q\,jk'}(x,0)\overline{\Gamma}_{k'm'}C_{m'j'}S^{ba'}_{r\,kj'}(x,0)\Big]\delta_{qr'}\delta_{rq'}\delta_{ss'} \\
&+ \Big(\tilde{\Gamma}_{il} S^{cb'}_{s\,lk'}(x,0)\overline{\Gamma}_{k'm'}C_{m'j'} S^{ba'}_{r\,kj'}(x,0)\Gamma_{mk}C_{jm}S^{ac'}_{q\,jl'}(x,0)\overline{\tilde{\Gamma}}_{l'i'}\Big)\delta_{qs'}\delta_{rq'}\delta_{sr'} \\
&- \Big(\tilde{\Gamma}_{il} S^{cb'}_{s\,lk'}(x,0)\overline{\Gamma}_{k'm'}C_{m'j'} S^{aa'}_{q\,jj'}(x,0)C_{jm}\Gamma_{mk}S^{bc'}_{r\,kl'}(x,0)\overline{\tilde{\Gamma}}_{l'i'}\Big)\delta_{qq'}\delta_{rs'}\delta_{sr'} \\
&+ \Big(\tilde{\Gamma}_{il} S^{ca'}_{s\,lj'}(x,0)C_{m'j'}\overline{\Gamma}_{k'm'} S^{ab'}_{q\,jk'}(x,0)C_{jm}\Gamma_{mk}S^{bc'}_{r\,kl'}(x,0)\overline{\tilde{\Gamma}}_{l'i'}\Big)\delta_{qr'}\delta_{rs'}\delta_{sq'} \\
&- \Big(\tilde{\Gamma}_{il} S^{ca'}_{s\,lj'}(x,0)C_{m'j'}\overline{\Gamma}_{k'm'} S^{bb'}_{r\,kk'}(x,0)\Gamma_{mk}C_{jm}S^{ac'}_{q\,jl'}(x,0)\overline{\tilde{\Gamma}}_{l'i'}\Big)\delta_{qs'}\delta_{rr'}\delta_{sq'}\Big\}\Big\rangle\,. \qquad (2.89)
\end{aligned}
$$

The Kronecker delta, $\delta$, describes which contractions are allowed for the given interpolator $\chi$ and leads to a non-zero contribution only when the contracted quark fields are of the same flavour.

Similarly, for mesons we have the correlation function

$$
\mathcal{G}(\boldsymbol{p}\,;t) = \sum_{\boldsymbol{x}} \mathrm{e}^{-i\boldsymbol{p}\cdot\boldsymbol{x}}\ \langle\Omega|\,\overline{q}^{a}_{i}(x)\,\Gamma_{ij}\,r^{a}_{j}(x)\,\overline{r}'^{a'}_{j'}(0)\,\overline{\Gamma}_{j'i'}\,q'^{a'}_{i'}(0)\,|\Omega\rangle\ . \qquad (2.90)
$$

For this correlator, the Wick contractions reduce to two terms

$$
\begin{aligned}
\mathcal{G}(\boldsymbol{p}\,;t) = \sum_{\boldsymbol{x}} \mathrm{e}^{-i\boldsymbol{p}\cdot\boldsymbol{x}} \Big\langle &\Big[S^{aa}_{r\,ji}(x,x)\Gamma_{ij}\Big]\Big[S^{a'a'}_{q'\,i'j'}(0,0)\overline{\Gamma}_{j'i'}\Big]\delta_{qr}\delta_{q'r'} \\
&- \Big[S^{a'a}_{q'\,i'i}(0,x)\Gamma_{ij}S^{aa'}_{r\,jj'}(x,0)\overline{\Gamma}_{j'i'}\Big]\delta_{qq'}\delta_{rr'}\Big\rangle\,. \qquad (2.91)
\end{aligned}
$$

In this case, due to the presence of both quark and anti-quark fields in the interpolator, in addition to the forwards propagator $S(x,0)$ from the baryon correlator, we have contractions that both result in loop propagators $S(x,x)$, and in backwards propagators $S(0,x)$. As will be discussed below, the loop propagator is difficult to calculate. However, as indicated by the delta functions, the first term is only present in the case where both the quark and the anti-quark fields in the interpolator have the same flavour. Hence, correlation functions for mesons consisting of a quark and anti-quark of differing flavours do not contain the loop propagator. Additionally, isospin symmetry can provide a cancellation of these contributions from different quark flavours, as in the case of the pion. While correlation functions for isoscalar mesons (such as the $\eta$, $\eta'$, $\sigma$, and $\omega$) necessarily contain the loop propagators, correlation functions for isovector mesons (such as the $\pi$ and $\rho$) do not.

For the backwards propagator, we are able to make use of the $\gamma^5$-hermiticity of the fermion matrix to express it in terms of the corresponding forwards propagator

$$S^{ab}_{ij}(0,x) = \gamma^5_{jk}\, S^{ba}_{kl}(x,0)^* \gamma^5_{li}\,. \tag{2.92}$$

In order to compute the quark propagators, we need to solve Eq. (2.88). For the Wilson fermion action and its improvements, the fermion matrix $M$ contains only local and nearest neighbour interactions, so it is possible to use well-established sparse matrix inversion techniques to efficiently solve this equation. Such techniques allow us to solve against some source vector $\eta^c_k(z)$ to obtain a solution vector $\Phi^a_i(x)$ satisfying

$$\sum_{x,a,i} M^{ca}_{ki}(z,x)\, \Phi^a_i(x) = \eta^c_k(z)\,. \tag{2.93}$$

To obtain the full all-to-all propagator, or a loop propagator, we need to perform this inversion once for each combination of $y$, $b$, and $j$, setting

$$\eta^c_k(z) = \delta^{cb}\, \delta_{kj}\, \delta_{zy}\,, \tag{2.94}$$

solving for $\Phi^a_i(x)$, and then letting

$$S^{ab}_{ij}(x,y) = \Phi^a_i(x)\,. \tag{2.95}$$

This means that we need to perform a huge number $({N_s}^3 \cdot N_t \cdot N_c \cdot N_D)$ of such inversions, which is computationally intractable. Fortunately, if we only need forward propagators, we can simply consider propagation from a single space-time point to all other points. Thus, the source only varies in the colour and spin dimensions, so we need to perform just $N_c \cdot N_D = 12$ inversions per gauge field configuration. In some other cases the full all-to-all propagator is still required, for example when considering scattering states on the lattice. In such situations, it is possible to estimate the all-to-all propagator using stochastic techniques [46, 47] or the distillation method [48].

In computing the quark propagator, we once again need to choose boundary conditions for our fields. The boundary conditions in the spatial directions are usually chosen to be the same as used when generating the gauge fields, although sometimes other boundary conditions can be useful. For example, twisted boundary conditions [49] can be used to access quantised momenta offset from those usually accessible on the lattice [50]. The boundary condition in the temporal direction affects the way our correlation function wraps around the finite time extent of the lattice. There are three commonly used options, each with their own complications:

1. **Periodic boundary conditions**

   Our interpolators couple to both forward and backward-running states, so if periodic boundary conditions are chosen, sufficiently light states can wrap around the lattice and intrude on the forward-running correlation Since they are travelling backwards in time, they appear in the sum of exponentials with the opposite sign in their time dependence, and if they are baryons, they appear with opposite parity. These backward-running states can be a problem if the temporal extent of the lattice is short, or the particles being studied are particularly light, for example near-physical pions. The contributions from backward-running states can sometimes be isolated by simultaneously fitting to both forward and backward-running states.

2. **Anti-periodic boundary conditions**
   Anti-periodic boundary conditions have similar problems to periodic boundary conditions, but the contributions to the correlators from the backwards propagating baryons come in with the opposite sign. Up to any changes in sign due to time-reversal of the operator (which show up for both periodic and anti-periodic boundary conditions), backward-running mesons come in with the same sign under anti-periodic boundary conditions. The differing sign for backward-running baryons can make their effect on the correlation function more pronounced. Similar to periodic boundary conditions, the contributions from backward-running states can sometimes be isolated by simultaneously fitting to both forward and backward-running states.

3. **Fixed boundary conditions**
   Fixed (or Dirichlet) boundary conditions set links in the time direction at the boundary to zero, $U^4(\boldsymbol{x}, N_t) = 0$. This eliminates the problem of correlators wrapping around the lattice entirely. Instead we find that states can reflect off the boundary. Both forward- and backward-running states can reflect off the boundary and return to contaminate the correlator.

In this work, we choose fixed boundary conditions for the temporal direction, as we have found that as long as the source is placed sufficiently far from the boundary, the effects of the reflected states are usually less significant than the backward-propagating states allowed by either of the other two options. For the rest of this chapter, we assume that our source is sufficiently far from any fixed boundaries and that our lattice has a sufficient time extent that any reflections or backwards-running states can be neglected, regardless of boundary condition used.

Returning to considering the tower of forward-running states, we note that while the space-time delta function in Eq. (2.94) gives the simplest form for a source vector, it is not a realistic representation for the distribution of a quark field within a hadron. Because of this, it does not couple well to the states of interest. In order to study a given eigenstate, we want an interpolator that has maximal overlap with that state relative to others. To maximise the overlap of our interpolator with the states we are interested in, we want a source vector that reflects the quark wave function for the system in question. In the absence of interactions, this suggests we should try an extended, spherically symmetric source. To produce such a source, we utilise a procedure known as gauge-invariant Gaussian smearing [51]. We start with a point source

$$\eta_k^{(0)\,c}(z) = \delta^{cb}\,\delta_{kj}\,\delta_{zy} \tag{2.96}$$

and iteratively apply the spatial smearing operator

$$F^{ab}(x,x') = (1-\alpha)\;\delta_{x',x}\,\delta^{ab} + \frac{\alpha}{6}\sum_{\mu=1}^{3}\left\{U^{ab\,\mu}(x)\,\delta_{x',x+e^\mu} + U^{\dagger\,ab\,\mu}(x-e^\mu)\,\delta_{x',x-e^\mu}\right\}\;, \tag{2.97}$$

giving

$$\eta_k^{(i)\,c}(x) = \sum_{x'} F^{cb}(x,x')\,\eta_k^{(i-1)\,b}(x')\,. \tag{2.98}$$

The smearing fraction $\alpha$ determines the degree of smearing on each application of the operator which, along with the number of sweeps of smearing $i$, determines the width of the source.

### 2.2.9 Variational analysis

Smeared sources provide improved overlap with the ground state, but it is desirable to produce even better interpolators, in particular to produce interpolators with maximal overlap with individual energy eigenstates. For this, we turn to the variational method [12,13]. We begin with some set of basis interpolators $\{\chi_i\}$, for example a selection of smearing levels and spin couplings, and seek a set of of optimised interpolators $\{\phi_{\boldsymbol{p}\,\alpha}(x)\}$ each of which each couple only to a single energy eigenstate

$$\langle\Omega|\phi_{\boldsymbol{p}\,\alpha}(0)|\beta\,;p\,;s\rangle = \delta_{\alpha\beta}\,z_{\boldsymbol{p}\,\alpha}\;\times\{\text{spin terms}\}\,, \tag{2.99}$$

for some coupling strength $z_{\boldsymbol{p}\,\alpha}$. To construct these optimised interpolators, we take linear combinations of our basis interpolators

$$\phi_{\boldsymbol{p}\,\alpha}(x) = \sum_i v_{\alpha\,i}(\boldsymbol{p})\,\chi_i(x)\,,\qquad \overline{\phi}_{\boldsymbol{p}\,\alpha}(x) = \sum_j \overline{\chi}_j(x)\,u_{\alpha\,j}(\boldsymbol{p})\,, \tag{2.100}$$

where the weights $v_{\alpha\,i}(\boldsymbol{p})$, and $u_{\alpha\,j}(\boldsymbol{p})$ need to be determined by analysing the correlation functions.

In practice, the operator basis may be insufficient to isolate individual energy eigenstates, resulting in some non-zero coupling of the optimised operators to states other than those they are optimised for. When this occurs, we leverage Euclidean time evolution to suppress excited-state contaminations and access the lowest lying energy eigenstate each optimised operator couples to.

Beginning with the matrix of two-point correlation functions created from our basis interpolators

$$\mathcal{G}_{ij}(\boldsymbol{p}\,;t) = \sum_{\boldsymbol{x}} \mathrm{e}^{-i\boldsymbol{p}\cdot\boldsymbol{x}} \, \langle\Omega|\chi_i(x)\,\overline{\chi}_j(0)|\Omega\rangle \;, \tag{2.101}$$

we can establish a recurrence relation by considering

$$\begin{aligned}
\mathcal{G}_{ij}(\boldsymbol{p}\,;t)\,u_{\alpha\,j}(\boldsymbol{p}) &= \sum_{\boldsymbol{x}} \mathrm{e}^{-i\boldsymbol{p}\cdot\boldsymbol{x}} \, \langle\Omega|\,\chi_i(x)\,\left(\overline{\chi}_j(0)\,u_{\alpha\,j}(\boldsymbol{p})\right)\,|\Omega\rangle \\
&= \sum_{\boldsymbol{x}} \mathrm{e}^{-i\boldsymbol{p}\cdot\boldsymbol{x}} \, \langle\Omega|\,\chi_i(x)\,\overline{\phi}_{\boldsymbol{p}\,\alpha}(0)\,|\Omega\rangle \\
&= \sum_{\beta,s} \mathrm{e}^{-E_\beta(\boldsymbol{p})\,t} \, \langle\Omega|\,\chi_i(0)\,|\beta\,;p\,;s\rangle\,\langle\beta\,;p\,;s|\,\overline{\phi}_{\boldsymbol{p}\,\alpha}(0)\,|\Omega\rangle \\
&= \mathrm{e}^{-E_\alpha(\boldsymbol{p})\,t} \sum_{s} \langle\Omega|\,\chi_i(0)\,|\alpha\,;p\,;s\rangle\,\langle\alpha\,;p\,;s|\,\overline{\phi}_{\boldsymbol{p}\,\alpha}(0)\,|\Omega\rangle \;,
\end{aligned} \tag{2.102}$$

where we have made use of Eq. (2.99) in order to establish that the only term that contributes to the sum is that of the state $\alpha$, allowing us to factor out the exponential. Then, since the exponential contains all of the time dependence,

$$\begin{aligned}
\mathcal{G}_{ij}(\boldsymbol{p}\,;t_0+\Delta t)\,u_{\alpha\,j}(\boldsymbol{p}) &= \mathrm{e}^{-E_\alpha(\boldsymbol{p})\,(t_0+\Delta t)} \sum_{s} \langle\Omega|\,\chi_i(0)\,|\alpha\,;p\,;s\rangle\,\langle\alpha\,;p\,;s|\,\overline{\phi}_{\boldsymbol{p}\,\alpha}(0)\,|\Omega\rangle \\
&= \mathrm{e}^{-E_\alpha(\boldsymbol{p})\,\Delta t}\,\mathcal{G}_{ij}(\boldsymbol{p}\,;t_0)\,u_{\alpha\,j}(\boldsymbol{p})\,.
\end{aligned} \tag{2.103}$$

An analogous expression can be obtained for $v_{\alpha\,i}(\boldsymbol{p})\,\mathcal{G}_{ij}(\boldsymbol{p}\,;t_0+\Delta t)$. It follows that the required weights are the eigenvector solutions to the generalised eigenvalue problems

$$\mathcal{G}_{ij}(\boldsymbol{p}\,;t_0+\Delta t)\,u_{\alpha\,j}(\boldsymbol{p}) = \mathrm{e}^{-E_\alpha(\boldsymbol{p})\,\Delta t}\,\mathcal{G}_{ij}(\boldsymbol{p}\,;t_0)\,u_{\alpha\,j}(\boldsymbol{p}) \tag{2.104a}$$

$$v_{\alpha\,i}(\boldsymbol{p})\,\mathcal{G}_{ij}(\boldsymbol{p}\,;t_0+\Delta t) = \mathrm{e}^{-E_\alpha(\boldsymbol{p})\,\Delta t}\,v_{\alpha\,i}(\boldsymbol{p})\,\mathcal{G}_{ij}(\boldsymbol{p}\,;t_0)\,. \tag{2.104b}$$

After solving these generalised eigenvalue problems, it is then straightforward to produce a correlator optimised for a single energy eigenstate

$$\mathcal{G}(\boldsymbol{p}\,;t\,;\alpha) = v_{\alpha\,i}(\boldsymbol{p})\,\mathcal{G}_{ij}(\boldsymbol{p}\,;t)\,u_{\alpha\,j}(\boldsymbol{p})\,. \tag{2.105}$$

When solving these generalised eigenvalue problems across jackknife or bootstrap sub-ensembles, it is important to have a means of identifying which eigenvectors in each analysis correspond to the same physical state. This is necessary even in the case where two or more states have nearly degenerate energy levels. Simply identifying states by the ordering of their energy levels is clearly insufficient in this case. Instead, we consider the structure of the optimised operators. The generalised eigenvectors give the relative contributions from the various operators used to produce the optimised operator for a given eigenstate. As a result, they can be considered as a “fingerprint” of the structure of the state.

The simplest approach to using the generalised eigenvectors to identify states is to take the scalar product of the left (or right) generalised eigenvectors from one variational analysis with those from another, and finding which pairs have the largest overlap. However, these eigenvectors do not form an orthogonal set. As a result, a single eigenvector from one variational analysis may have significant overlap with multiple eigenvectors from the other analysis, giving rise to potential eigenstate misidentification. In order to resolve this issue, it is desirable to change our basis in such a way as to make the generalised eigenvectors orthogonal.

The first step in doing this is to ensure that our correlation matrix is perfectly symmetric. By CP symmetry and translational invariance, any given value for the correlation matrix is equally likely to occur as its transpose. Hence, we work with the symmetrised correlation matrix

$$\mathcal{G}_{ij}(\boldsymbol{p}\,;t) \to \frac{1}{2}\left[\mathcal{G}_{ij}(\boldsymbol{p}\,;t) + \mathcal{G}_{ji}(\boldsymbol{p}\,;t)\right]\,, \tag{2.106}$$

enforcing the symmetry on a configuration-by-configuration basis and producing an improved unbiased estimator. Improved unbiased estimators will be discussed in slightly more detail in Section 2.2.11.

Assuming that this has been done, and hence the correlation matrix is perfectly symmetric, then the matrix square root $\mathcal{G}_{ij}^{1/2}(\boldsymbol{p}\,;t)$ is well defined. Then, as long as the correlation matrix is invertible, we can rewrite Eq. (2.104a) as

$$\mathcal{G}_{ij}^{-1}(\boldsymbol{p}\,;t_0)\,\mathcal{G}_{jk}(\boldsymbol{p}\,;t_0+\Delta t)\,u_{\alpha\,k}(\boldsymbol{p}) = \mathrm{e}^{-E_\alpha(\boldsymbol{p})\,\Delta t}\,u_{\alpha\,i}(\boldsymbol{p})\,. \tag{2.107}$$

Pre-multiplying by $\mathcal{G}_{ij}^{1/2}(\boldsymbol{p}\,;t_0)$, and inserting $\mathbb{I}_{jk} = \mathcal{G}_{ij}^{-1/2}(\boldsymbol{p}\,;t_0)\,\mathcal{G}_{jk}^{1/2}(\boldsymbol{p}\,;t_0)$, we obtain

$$\begin{aligned}\mathcal{G}_{ij}^{-1/2}(\boldsymbol{p}\,;t_0)\,\mathcal{G}_{jk}(\boldsymbol{p}\,;t_0+\Delta t)\,\mathcal{G}_{kl}^{-1/2}(\boldsymbol{p}\,;t_0)\,\mathcal{G}_{lm}^{1/2}(\boldsymbol{p}\,;t_0)\,u_{\alpha\,m}\boldsymbol{p}&\\ = \mathrm{e}^{-E_\alpha(\boldsymbol{p})\,\Delta t}\,\mathcal{G}_{ij}^{1/2}(\boldsymbol{p}\,;t_0)\,u_{\alpha\,j}\boldsymbol{p}\,.&\end{aligned} \tag{2.108}$$

Identifying

$$w_{\alpha\,i}\boldsymbol{p} = \mathcal{G}_{ij}^{1/2}(\boldsymbol{p}\,;t_0)\,u_{\alpha\,j}(\boldsymbol{p})\,, \tag{2.109}$$

and

$$\mathcal{H}_{ij}(\boldsymbol{p}\,;t_0\,,\Delta t = \mathcal{G}_{ik}^{-1/2}(\boldsymbol{p}\,;t_0)\,\mathcal{G}_{kl}(\boldsymbol{p}\,;t_0+\Delta t)\,\mathcal{G}_{lj}^{-1/2}(\boldsymbol{p}\,;t_0)\,, \tag{2.110}$$

noting that $\mathcal{H}_{ij}(\boldsymbol{p}\,; t_0\,, \Delta t$ is real and symmetric, we arrive at the eigenvalue equation

$$\mathcal{H}_{ij}(\boldsymbol{p}\,; t_0\,, \Delta t\, w_{\alpha\, j}(\boldsymbol{p}) = \mathrm{e}^{-E_\alpha(\boldsymbol{p})\,\Delta t}\, w_{\alpha\, i}(\boldsymbol{p})\,. \tag{2.111}$$

Since the $\{w_\alpha\}$ are the eigenvectors of a real symmetric matrix, they are guaranteed to be orthogonal, as we set out to achieve. Hence, we can identify states by taking the scalar product of these orthogonal eigenvectors from one variational analysis with those from another, and finding which pairs have the largest overlap.

This technique for identifying eigenstates can be extended beyond identifying states across sub-ensembles to identifying states at a range of light quark masses [16], or over a range of momenta. In both of these cases, it is important to identify states at one momentum or mass with a nearby momentum or mass and then chain the identification across the whole range to be considered, rather than sorting against a single reference analysis. This is to ensure that the correlation matrix and hence the eigenvector set is as similar as possible to maintain approximate orthogonality.

### 2.2.10 Current operators

Performing a variational analysis on two point correlation functions provides access to the inertial properties of the excited-state spectrum of lattice QCD. However, these states are not point-like and have some internal structure that is not directly accessible through the standard two point correlators. To investigate this internal structure, we wish to observe the interaction of the states of interest with some external probe. For example, we can gain insight into the electromagnetic structure by considering the vector current, which in the continuum is $j^\mu(x) = \overline{q}^a_i(x)\,\gamma^\mu_{ik}\,q^a_k(x)$.

The response of a given hadron $\alpha$ to some external probe $\mathcal{J}(x)$ can be accessed through the three point correlation function

$$\mathcal{G}^3(\mathcal{J}; \boldsymbol{p}', \boldsymbol{p}\,; t_2\,, t_1\,; \alpha) \equiv \sum_{\boldsymbol{x}_2, \boldsymbol{x}_1} \mathrm{e}^{-i\boldsymbol{p}'\cdot\boldsymbol{x}_2}\, \mathrm{e}^{i(\boldsymbol{p}'-\boldsymbol{p})\cdot\boldsymbol{x}_1}\, \langle\Omega|\, \phi_{\boldsymbol{p}'\,\alpha}(x_2)\, \mathcal{J}(x_1)\, \overline{\phi}_{\boldsymbol{p}\,\alpha}(0)\, |\Omega\rangle\ . \tag{2.112}$$

Similar to the two point correlator, this can be interpreted by invoking the completeness relation and operator translation

$$\begin{aligned}
&\mathcal{G}^3(\mathcal{J}; \boldsymbol{p}', \boldsymbol{p}\,; t_2\,, t_1\,; \alpha) \\
&\quad= \sum_{\beta', \tilde{p}', s'} \sum_{\beta, \tilde{p}, s} \sum_{\boldsymbol{x}_2, \boldsymbol{x}_1} \mathrm{e}^{-i\boldsymbol{p}'\cdot\boldsymbol{x}_2}\, \mathrm{e}^{i(\boldsymbol{p}'-\boldsymbol{p})\cdot\boldsymbol{x}_1} \\
&\qquad\times \langle\Omega|\, \phi_{\boldsymbol{p}'\,\alpha}(x_2)\, |\beta'\,; \tilde{p}'\,; s'\rangle\langle\beta'\,; \tilde{p}'\,; s'|\, \mathcal{J}(x_1)\, |\beta\,; \tilde{p}\,; s\rangle\langle\beta\,; \tilde{p}\,; s|\, \overline{\phi}_{\boldsymbol{p}\,\alpha}(0)\, |\Omega\rangle \\
&\quad\approx \sum_{s, s'} \mathrm{e}^{-E_\alpha(\boldsymbol{p}')\,(t_2 - t_1)}\, \mathrm{e}^{-E_\alpha(\boldsymbol{p})\,t_1}\, \langle\alpha\,; p'\,; s'|\, \mathcal{J}(0)\, |\alpha\,; p\,; s\rangle \\
&\qquad\times \langle\Omega|\, \phi_{\boldsymbol{p}'\,\alpha}(0)\, |\alpha\,; p'\,; s'\rangle\, \langle\alpha\,; p\,; s|\, \overline{\phi}_{\boldsymbol{p}\,\alpha}(0)\, |\Omega\rangle\ ,
\end{aligned} \tag{2.113}$$

where the matrix element $\langle \alpha \,; p' \,; s' | \, \mathcal{J}(0) \, | \alpha \,; p \,; s \rangle$ encodes the behaviour we are interested in.

We note that the optimised interpolators do not have to correspond to the same state and hence we can access the transition amplitude $\langle \beta \,; p' \,; s' | \mathcal{J}(0) | \alpha \,; p \,; s \rangle$ from some hadron $\alpha$ to another hadron $\beta$ via

$$
\begin{aligned}
\mathcal{G}^3(\mathcal{J}; \boldsymbol{p}', \boldsymbol{p} \,; t_2 \,, t_1 \,; \alpha \to \beta) \equiv & \sum_{\boldsymbol{x}_2, \boldsymbol{x}_1} \mathrm{e}^{-i\boldsymbol{p}' \cdot \boldsymbol{x}_2} \, \mathrm{e}^{i(\boldsymbol{p}'-\boldsymbol{p}) \cdot \boldsymbol{x}_1} \, \langle \Omega | \, \phi_{\boldsymbol{p}' \, \beta}(x_2) \, \mathcal{J}(x_1) \, \overline{\phi}_{\boldsymbol{p}' \, \alpha}(0) \, | \Omega \rangle \\
\approx & \sum_{s, s'} \mathrm{e}^{-E_\beta(\boldsymbol{p}') \, (t_2 - t_1)} \, \mathrm{e}^{-E_\alpha(\boldsymbol{p}) t_1} \, \langle \beta \,; p' \,; s' | \, \mathcal{J}(0) \, | \alpha \,; p \,; s \rangle \\
& \times \langle \Omega | \, \phi_{\boldsymbol{p}' \, \beta}(0) \, | \beta \,; p' \,; s' \rangle \, \langle \alpha \,; p \,; s | \, \overline{\phi}_{\boldsymbol{p} \, \alpha}(0) \, | \Omega \rangle \; . \qquad (2.114)
\end{aligned}
$$

To extract the matrix element, we take a ratio of three and two point correlators [52]

$$
R(p, p') = \sqrt{\frac{\langle \mathcal{G}^3(\mathcal{J} \,; \boldsymbol{p}', \boldsymbol{p} \,; t_2 \,, t_1 \,; \alpha \to \beta) \rangle \, \langle \mathcal{G}^3(\mathcal{J} \,; \boldsymbol{p} \,, \boldsymbol{p}'; t_2 \,, t_1 \,; \beta \to \alpha) \rangle}{\langle \mathcal{G}(\boldsymbol{p}'; t_2 \,; \beta) \rangle \, \langle \mathcal{G}(\boldsymbol{p} \,; t_2 \,; \alpha) \rangle}} \qquad (2.115)
$$

This ratio is chosen such that (in the case of perfect eigenstate isolation), it cancels out the time dependence of the correlators, as well as the dependence on the coupling of the optimised interpolators to the states we are studying. If the eigenstate isolation is imperfect, Euclidean time dependence will be re-introduced into the correlation function ratio. In this case, care must be taken to select a Euclidean time region in which only one state is dominant, and the single-state ansatz is satisfied.

In order to calculate this ratio, we need the three point correlation function for both momentum transfers $+\boldsymbol{q} = \boldsymbol{p}' - \boldsymbol{p}$ and $-\boldsymbol{q} = \boldsymbol{p} - \boldsymbol{p}'$.

These matrix elements can be expressed as

$$
\langle \beta \,; p' \,; s' | \, \mathcal{J}(0) \, | \alpha \,; p \,; s \rangle = \overline{u}_\beta(p', s') \, \Gamma(Q^2 \,, p')p \, u_\alpha(p, s) \qquad (2.116)
$$

where the terms $u_\alpha(p, s)$ are relevant mathematical objects that properly encode the spin structure of the state $\alpha$ carrying momentum $p$ and spin $s$. All of the dynamics describing the interaction of the state(s) with the current are encoded within the vertex function $\Gamma(Q^2 \,, p')p$. This vertex function can be expressed as the sum of all Lorentz covariant structures multiplied by scalar functions called covariant vertex functions. These functions must depend only on scalar invariant variables, and the only such variable is the squared momentum transfer $q^2$, where $q = p' - p$.Hence, we can rewrite the vertex function as

$$
\Gamma(Q^2 \,, p')p = \sum_i \mathcal{X}^i c^i(q^2) \,, \qquad (2.117)
$$

where $\mathcal{X}^i$ are the Lorentz covariant structures and $c^i(q^2)$ are the covariant vertex functions. We can often take linear combinations of the covariant vertex functions to form experimentally measurable quantities known as form factors. For consistency with experimental determinations, we choose to express the form factors in terms of the variable

$$Q^2 \equiv \boldsymbol{q}^2 - \left(E_\alpha(\boldsymbol{p}') - E_\beta(\boldsymbol{p})\right)^2 \tag{2.118}$$

which is the squared momentum with an explicit sign convention regardless of representation. In the Pauli representation used here, $Q^2 = q^2$.

In this work, we use the $O(a)$-improved [53] conserved vector current

$$j^\mu_{CI}(x) \equiv j^\mu_C(x) + \frac{r}{2}\partial^\rho \left(\overline{q}^a_i(x)\, \sigma^{\rho\mu}_{ik}\, q^a_k(x)\right) , \tag{2.119}$$

as found in Ref. [54]. This current is derived from the standard conserved vector current for the Wilson action

$$\begin{aligned} j^\mu_C(x) \equiv \frac{1}{4}\Big[ & \overline{q}^a_i(x)\,(\gamma^\mu_{ik} - r\,\delta_{ik})\,U^{ab\,\mu}(x)\,q^b_k(x+e^\mu) \\ & + \overline{q}^a_i(x+e^\mu)\,(\gamma^\mu_{ik} + r\,\delta_{ik})\,U^{\dagger\,ab\,\mu}(x)\,q^b_k(x) \\ & + \overline{q}^a_i(x-e^\mu)\,(\gamma^\mu_{ik} - r\,\delta_{ik})\,U^{ab\,\mu}(x-e^\mu)\,q^b_k(x) \\ & + \overline{q}^a_i(x)\,(\gamma^\mu_{ik} + r\,\delta_{ik})\,U^{\dagger\,ab\,\mu}(x-e^\mu)\,q^b_k(x-e^\mu)\Big] . \end{aligned} \tag{2.120}$$

The $O(a)$ improvement term is also derived from the fermion action and is constructed as a four-divergence to preserve charge conservation. This four-divergence is given by

$$\partial^\rho \left(\overline{q}^a_i(x)\, \sigma^{\rho\mu}_{ik}\, q^a_k(x)\right) = \overline{q}^a_i(x) \left(\overleftarrow{\nabla}^{ab\,\rho} + \overrightarrow{\nabla}^{ab\,\rho}\right) \sigma^{\rho\mu}_{ik}\, q^b_k(x) , \tag{2.121}$$

where

$$\overrightarrow{\nabla}^{ab\,\mu} q^b_i(x) \equiv \frac{1}{2}\left(U^{ab\,\mu}(x)\,q^b_i(x+e^\mu) - U^{\dagger\,ab\,\mu}(x-e^\mu)\,q^b_i(x-e^\mu)\right) \tag{2.122a}$$

$$\overline{q}^a_i(x)\overleftarrow{\nabla}^{ab\,\mu} \equiv \frac{1}{2}\left(\overline{q}^a_i(x+e^\mu)\,U^{\dagger\,ab\,\mu}(x) - \overline{q}^a_i(x-e^\mu)\,U^{ab\,\mu}(x-e^\mu)\right) . \tag{2.122b}$$

Unlike the naïve vector current on the lattice, this improved conserved vector current does not need to be renormalised.

The matrix element for the vector current interacting with a fermion can be expressed in terms of the Dirac and Pauli form factors $F_2(Q^2)$ and $F_1(Q^2)$ as

$$\langle \alpha\,; p'\,; s' |\, j^\mu \,| \alpha\,; p\,; s\rangle = \overline{u}_\alpha(p', s') \left(\gamma^\mu\, F_{2\,\alpha}(Q^2) - \frac{\sigma^{\mu\nu} q^\nu}{2m_\alpha}\, F_{1\,\alpha}(Q^2)\right) u_\alpha(p, s) . \tag{2.123}$$

These can be related to the Sachs electric and magnetic form factors by

$$G_{E\,\alpha}(Q^2) = F_{2\,\alpha}(Q^2) - \frac{Q^2}{(2m_\alpha)^2}\, F_{1\,\alpha}(Q^2) , \text{ and} \tag{2.124a}$$

$$G_{M\,\alpha}(Q^2) = F_{2\,\alpha}(Q^2) + F_{1\,\alpha}(Q^2)\,. \tag{2.124b}$$

The electric form factor $G_{E\,\alpha}(Q^2)$ is related to the distribution of charge within the baryon, and the magnetic form factor $G_{M\,\alpha}(Q^2)$ is related to its magnetic structure. These form factors are experimentally determined with some accuracy for the ground-state proton and neutron, and so calculating them is a good way to make contact with experiment.

Computing these three point functions so that we can extract the matrix elements requires the inclusion the current operator $\mathcal{J}(x)$ in our Grassmann integrals. Restricting ourselves to currents of the form $\mathcal{J}(x) = \overline{t}'^{\,d}_{n}(x)\,\Gamma^{d'd}_{\mathcal{J}\,n'n}\,t^{d}_{n}(x)$ (such as the vector current), we begin by considering baryons, for which

$$\begin{aligned}
&\sum_{\boldsymbol{x}_2,\boldsymbol{x}_1} \mathrm{e}^{-i\boldsymbol{p}'\cdot\boldsymbol{x}_2}\,\mathrm{e}^{i(\boldsymbol{p}'-\boldsymbol{p})\cdot\boldsymbol{x}_1}\,\langle\Omega|\,\chi(x_2)\,\mathcal{J}(x_1)\,\overline{\chi}(0)\,|\Omega\rangle \\
&\quad= \sum_{\boldsymbol{x}_2,\boldsymbol{x}_1} \mathrm{e}^{-i\boldsymbol{p}'\cdot\boldsymbol{x}_2}\,\mathrm{e}^{i(\boldsymbol{p}'-\boldsymbol{p})\cdot\boldsymbol{x}_1}\,\langle\Omega|\,\epsilon^{abc}\left(q^a_j(x_2)\,C_{jm}\,\Gamma_{mk}\,r^b_k(x_2)\right)\tilde{\Gamma}_{il}\,s^c_l(x_2)\,\overline{t}'^{\,d}_{n}(x_1)\,\Gamma^{d'd}_{\mathcal{J}\,n'n}\,t^d_n(x_1) \\
&\qquad\qquad\qquad\qquad \epsilon^{a'b'c'}\,\overline{s}'^{\,c}_{l}(0)\,\overline{\tilde{\Gamma}}'_{li}\left(\overline{r}'^{\,b}_{k}(0)\,\overline{\Gamma}'_{km}\,C_{m'j'}\,\overline{q}'^{\,a}_{j}(0)\right)|\Omega\rangle\;.
\end{aligned} \tag{2.125}$$

The Wick contractions for this expression give rise to 24 terms, which are easily divided into two distinct categories as illustrated in Fig. 2.5. The first kind includes

$$\begin{aligned}
&\sum_{\boldsymbol{x}_2,\boldsymbol{x}_1} \mathrm{e}^{-i\boldsymbol{p}'\cdot\boldsymbol{x}_2}\,\mathrm{e}^{i(\boldsymbol{p}'-\boldsymbol{p})\cdot\boldsymbol{x}_1}\,S^{dd'}_{t\,nn'}(x_1,x_1)\,\Gamma^{d'd}_{\mathcal{J}\,n'n}\,\epsilon^{abc}\,\epsilon^{a'b'c'}\tilde{\Gamma}_{il}S^{cc'}_{s\,ll'}(x_2,0)\overline{\tilde{\Gamma}}_{l'i'} \\
&\qquad\times\left[C_{jm}\Gamma_{mk}S^{bb'}_{r\,kk'}(x_2,0)\overline{\Gamma}_{k'm'}C_{m'j'}S^{aa'}_{q\,jj'}(x_2,0)\right]\delta_{tt'}\delta_{ss'}\delta_{rr'}\delta_{qq'}\;,
\end{aligned} \tag{2.126}$$

and similar terms. There are six such terms, which take the form of the six terms from the two point correlator in Eq. (2.89), each multiplied by $\delta_{tt'}S^{dd'}_{t\,nn'}(x_1,x_1)\,\Gamma^{d'd}_{\mathcal{J}\,n'n}$. These terms are illustrated in Fig. 2.5a and are known as disconnected loop contributions. They require the calculation of a loop propagator which as described above is computationally difficult. Because of this it is common to either ignore these terms and only present the connected contribution, or to cancel them out through the consideration of isovector quantities.

The second kind of term in the Wick contraction includes

$$\begin{aligned}
&\sum_{\boldsymbol{x}_2,\boldsymbol{x}_1} \mathrm{e}^{-i\boldsymbol{p}'\cdot\boldsymbol{x}_2}\,\mathrm{e}^{i(\boldsymbol{p}'-\boldsymbol{p})\cdot\boldsymbol{x}_1}\,\epsilon^{abc}\,\epsilon^{a'b'c'}\tilde{\Gamma}_{il}S^{cd'}_{s\,ln'}(x_2,x_1)\Gamma^{d'd}_{\mathcal{J}\,n'n}S^{dc'}_{t\,nl'}(x_1,0)\overline{\tilde{\Gamma}}_{l'i'} \\
&\qquad\times\left[C_{jm}\Gamma_{mk}S^{bb'}_{r\,kk'}(x_2,0)\overline{\Gamma}_{k'm'}C_{m'j'}S^{aa'}_{q\,jj'}(x_2,0)\right]\delta_{st'}\delta_{ts'}\delta_{rr'}\delta_{qq'}\;,
\end{aligned} \tag{2.127}$$

and similar terms. These terms are illustrated in Fig. 2.5b and are known as connected contributions. The contribution from these terms will be studied in Chapters 5 and 6.

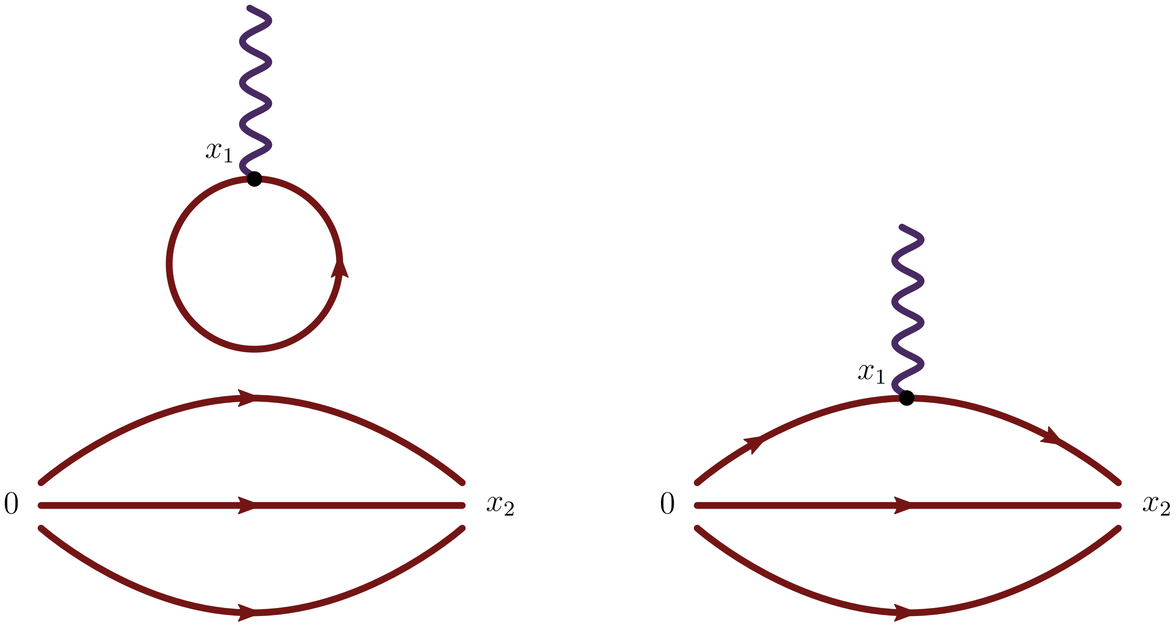

(a) Disconnected contributions

(b) Connected contributions

Figure 2.5: Applying Wick's theorem to a current interacting with a baryon gives two classes of diagram, the disconnected contributions and the connected contributions.

There are 18 such terms which correspond to the six terms in Eq. (2.89) with each of the three quark propagators in each term replaced in turn by a modified propagator [54, 55]. For example $S^{cc'}_{s\,ll'}(x_2,0)\,\delta_{ss'}$ is replaced by $S^{cc'}_{\mathcal{J}\,t\,ll'}(x_2,t_1,0;\boldsymbol{q})\,\delta_{st'}\,\delta_{ts'}$, where

$$S^{cc'}_{\mathcal{J}\,t\,ll'}(x_2,t_1,0;\boldsymbol{q}) \equiv \sum_{\boldsymbol{x}_1} \mathrm{e}^{i\boldsymbol{q}\cdot\boldsymbol{x}_1}\, S^{cd'}_{s\,ln'}(x_2,x_1)\,\Gamma^{d'd}_{\mathcal{J}\,n'n}\,S^{dc'}_{t\,nl'}(x_1,0)\,. \tag{2.128}$$

While at first this term may appear to require the calculation of an all-to-all propagator, we can evaluate it using sequential source techniques (SST) [56]. We make use of the fact that $S^{cd'}_{s\,ln'}(x_2,x_1)$ is the Green's function of the fermion matrix to write

$$\begin{aligned}\sum_{x_2} M^{ac}_{il}(z,x_2)\,S^{cc'}_{\mathcal{J}\,t\,ll'}(x_2,t_1,0;\boldsymbol{q}) &= \sum_{x_1,x_2} \mathrm{e}^{i\boldsymbol{q}\cdot\boldsymbol{x}_1}\, M^{ac}_{il}(z,x_2)\,S^{cd'}_{s\,ln'}(x_2,x_1)\,\Gamma^{d'd}_{\mathcal{J}\,n'n}\,S^{dc'}_{t\,nl'}(x_1,0)\\ &= \sum_{x_1} \mathrm{e}^{i\boldsymbol{q}\cdot\boldsymbol{x}_1}\,\delta_{z,x_1}\,\delta^{ad'}\,\delta_{in'}\,\Gamma^{d'd}_{\mathcal{J}\,n'n}\,S^{dc'}_{t\,nl'}(x_1,0)\\ &= \mathrm{e}^{i\boldsymbol{q}\cdot\boldsymbol{z}}\,\delta_{t_z,t_1}\,\Gamma^{ad}_{\mathcal{J}\,in}\,S^{dc'}_{t\,nl'}(z,0)\,.\end{aligned} \tag{2.129}$$

So by inverting against the source vector

$$\eta^a_i(z) = \mathrm{e}^{i\boldsymbol{q}\cdot\boldsymbol{z}}\,\delta_{t_z,t_1}\,\Gamma^{ad}_{\mathcal{J}\,in}\,S^{dc'}_{t\,nl'}(z,0)\,. \tag{2.130}$$

we can obtain the desired SST propagator from the solution vector

$$S^{cc'}_{\mathcal{J}\,t\,ll'}(x_2, t_1, 0; \boldsymbol{q}) = \Phi^c_l(x_2)\,. \tag{2.131}$$

Obtaining SST propagators in this manner requires us to fix the momentum transfer $\boldsymbol{q}$ and current operator, however the source and sink are left free, allowing us to reuse these propagators for any number of hadron interpolators. An alternate construction involving an inversion through the sink requires the source and sink to be fixed, but does allow the current to be varied. For more details on the latter method and a comparison of both methods, see Ref. [57], where it is concluded that inverting through the current as described above is superior when the number of operators to be inserted (and current momenta to be considered) is sufficiently small.

We can follow a similar procedure for mesons, and similar to the two point case we find that in order to avoid difficult-to-calculate disconnected loops, we can only investigate isovector mesons. For such mesons, we find that it is simple to calculate the connected contributions from SST propagators as above.

### 2.2.11 The $U + U^*$ trick

When calculating these two and three point correlation functions in lattice QCD, we wish to minimise statistical errors arising from our finite Monte-Carlo sampling of gauge field configurations. The simplest way to do this is to increase the number of gauge fields we consider in our sub-ensemble, but limitations in available computing power mean that we can only take this approach so far. A complementary approach is to enforce symmetries that must be true across the whole ensemble on a configuration-by-configuration basis. Given some such symmetry, for each configuration in our sub-ensemble we can consider all configurations related to it by that symmetry in evaluating our (unbiased) estimator. This removes our sensitivity to statistical fluctuations away from these symmetries. It can be shown by the Rao-Blackwell theorem that this results in an improved unbiased estimator. One way we produce an improved unbiased estimator in this work is the symmetrisation of correlation matrices described in Section 2.2.9.

Another way we produce an improved unbiased estimator is by a process known as the $U + U^*$ trick [58]. We begin by noting the invariance of the QCD action under transformations $U \to U^*$. This means that the link variables $\{U\}$ and $\{U^*\}$ have equal weighting in the ensemble average, and we can use this symmetry to construct an improved unbiased estimator. As we will show below, by including the complex conjugate of each gauge field we consider, we can enforce the ensemble average $\boldsymbol{p} \to -\boldsymbol{p}$ transformation properties of our two and three point correlation functions on each $U + U^*$ pair. In addition, the zero momentum two point correlation functions (which already obey their ensemble average $\boldsymbol{p} \to -\boldsymbol{p}$ transformation on each configuration) become purely real [59].

In principal, calculating our propagators on the $\{U^*\}$ configurations would require inverting the fermion matrix again for every single gauge field configuration sampled. These additional inversions would lead to twice the computational cost as considering the $\{U\}$ configurations alone. However, this additional computational cost can be avoided by calculating the $\{U^*\}$ propagators directly from the $\{U\}$ propagators. To do this, we note that the fermion matrix on a $\{U^*\}$ configuration is related to the fermion matrix on the corresponding $\{U\}$ configuration by

$$M^{ab}_{ij}[U^*] = \left(\tilde{C}_{ik}\, M^{ab}_{km}[U]\; \tilde{C}^{-1}_{mj}\right)^* , \tag{2.132}$$

where $\tilde{C} = C\,\gamma^5$. Hence, we can write the $\{U^*\}$ propagator as

$$S^{ab}_{ij}(x,0;\{U^*\}) = \left(\tilde{C}_{ik}\, S^{ab}_{km}(x,0;\{U\})\, \tilde{C}^{-1}_{mj}\right)^* , \tag{2.133}$$

eliminating the need for further inversions.

In the case of SST propagators, care must be taken with the transformation of the current when applying Eq. (2.132). Considering the definition of the SST propagator from Eq. (2.128), we obtain

$$\begin{aligned}
&\left(\tilde{C}_{ik}\, S^{ab}_{\mathcal{J}\,kl}(x_2,t_1,0;\boldsymbol{q};\{U\})\, \tilde{C}^{-1}_{lj}\right)^* \\
&\quad = \sum_{\boldsymbol{x}_1} \mathrm{e}^{-i\boldsymbol{q}\cdot\boldsymbol{x}_1} \left(\tilde{C}_{ik}\, S^{ac}_{kl}(x_2,x_1;\{U\})\, \tilde{C}^{-1}_{lm}\tilde{C}_{mn}\, \Gamma^{cd}_{\mathcal{J}\,np}\, \tilde{C}^{-1}_{pq}\tilde{C}_{qr}\, S^{db}_{rs}(x_1,0;\{U\})\, \tilde{C}^{-1}_{sj}\right)^* \\
&\quad = \sum_{\boldsymbol{x}_1} \mathrm{e}^{-i\boldsymbol{q}\cdot\boldsymbol{x}}\, S^{ac}_{im}(x_2,x_1;\{U^*\}) \left(\tilde{C}_{mn}\, \Gamma^{cd}_{\mathcal{J}\,np}\, \tilde{C}^{-1}_{pq}\right)^* S^{db}_{qj}(x_1,0;\{U^*\}) \,.
\end{aligned} \tag{2.134}$$

Thus, as long as the operator describing the current vertex satisfies

$$\left(\tilde{C}_{ik}\, \Gamma^{ab}_{\mathcal{J}\,kl}\, \tilde{C}^{-1}_{lj}\right)^* = s_C\, \Gamma^{ab}_{\mathcal{J}\,ij} \,, \tag{2.135}$$

where $s_C$ is ±1, then the SST propagator on a $\{U^*\}$ configuration is given by

$$S^{ab}_{\mathcal{J}\,ij}(x_2,t_1,0,+\boldsymbol{q};\{U^*\}) = s_C\left(\tilde{C}_{ik}\, S^{ab}_{\mathcal{J}\,kl}(x_2,t_1,0,-\boldsymbol{q};\{U\})\tilde{C}^{-1}_{lj}\right)^* . \tag{2.136}$$

The identity in Eq. (2.135) is satisfied with $s_C = +1$ for the improved conserved vector current described in Section 2.2.10. Hence, we can calculate the $+\boldsymbol{q}$ and $-\boldsymbol{q}$ SST propagators on the $\{U^*\}$ configurations from the $-\boldsymbol{q}$ and $+\boldsymbol{q}$ SST propagators on the $\{U\}$ configurations. If we only required the $+\boldsymbol{q}$ propagators, this would mean that including the $\{U^*\}$ configurations would require twice as many inversions. However, as we are calculating the ratio in Eq. (2.115), we need both of these propagators anyway and there are no extra inversions required.

Having established a computationally efficient technique for calculating propagators on the $\{U^*\}$ configurations, we now turn our attention to the correlation functions formed from these propagators. We first consider the baryon two point correlation function expressed in terms of quark propagators as in Eq. (2.89). By substituting in the $\{U^*\}$ propagator from Eq. (2.133), we can show that as long as the spin-structure matrices from the interpolating fields obey the relations $(\tilde{C}_{ik}\,\Gamma_{kl}\,\tilde{C}^{-1}_{lj})^* = \pm\Gamma_{ij}$ and $(\tilde{C}_{ik}\,\tilde{\Gamma}_{kl}\,\tilde{C}^{-1}_{lj})^* = \pm\tilde{\Gamma}_{ij}$ (where the signs of those two expressions need not be the same), then

$$\mathcal{G}(\boldsymbol{p}\,;t\,;\{U^*\}) = \left(\tilde{C}^{-1}\,\mathcal{G}(-\boldsymbol{p}\,;t\,;\{U\})\,\tilde{C}\right)^* . \tag{2.137}$$

Importantly, the sign of the momentum is reversed due to the complex conjugate. This means that the spin-structure projected correlator on the $\{U^*\}$ configurations is

$$\begin{aligned} G(\Gamma_S\,;\boldsymbol{p}\,;t\,;\{U^*\}) &= \operatorname{Tr}\Gamma_S\left(\tilde{C}^{-1}\,\mathcal{G}(-\boldsymbol{p}\,;t\,;\{U\})\,\tilde{C}\right)^* \\ &= \operatorname{Tr}\left(\tilde{C}^*\,\Gamma_S\,\tilde{C}^{-1\,*}\right)\mathcal{G}^*(-\boldsymbol{p}\,;t\,;\{U\})\,. \end{aligned} \tag{2.138}$$

Hence, as long as $\Gamma_S$ obeys the relation

$$\left(\tilde{C}^{-1}_{ik}\,\Gamma_{S\,kl}\,\tilde{C}_{lj}\right)^* = s_S\,\Gamma_{S\,ij}\,, \tag{2.139}$$

we have

$$G(\Gamma_S\,;\boldsymbol{p}\,;t\,;\{U^*\}) = s_S\,G^*(\Gamma_S\,;-\boldsymbol{p}\,;t\,;\{U\})\,. \tag{2.140}$$

In the ensemble average, we expect the correlation function to transform definitely under $\boldsymbol{p} \to -\boldsymbol{p}$, that is

$$\langle G(\Gamma_S\,;-\boldsymbol{p}\,;t)\rangle = s_P\,\langle G(\Gamma_S\,;\boldsymbol{p}\,;t)\rangle\,, \tag{2.141}$$

for $s_P = \pm 1$. If $s_P = s_S$ ($s_P = -s_S$), then when both $\{U\}$ and $\{U^*\}$ configurations are included in the sub-ensemble the ensemble average is real (imaginary) and the real (imaginary) component of the correlation function obeys the expected $\boldsymbol{p} \to -\boldsymbol{p}$ transformation on a configuration-by-configuration basis. This can be seen from the average of the $\{U\}$ and $\{U^*\}$ correlation functions

$$\begin{aligned} &\frac{1}{2}\left[\,G(\Gamma_S\,;\boldsymbol{p}\,;t\,;\{U\}) + G(\Gamma_S\,;\boldsymbol{p}\,;t\,;\{U^*\})\,\right] \\ &\quad = \frac{1}{2}\left[\,G(\Gamma_S\,;\boldsymbol{p}\,;t\,;\{U\}) + s_S\,G^*(\Gamma_S\,;-\boldsymbol{p}\,;t\,;\{U\})\,\right] \\ &\quad = \frac{1}{2}\left[\,G(\Gamma_S\,;\boldsymbol{p}\,;t\,;\{U\}) \pm s_P\,G^*(\Gamma_S\,;-\boldsymbol{p}\,;t\,;\{U\})\,\right], \end{aligned} \tag{2.142}$$

which in the ensemble average becomes

$$\begin{aligned}
&\frac{1}{2}\,\langle G(\Gamma_S\,;\boldsymbol{p}\,;t\,;\{U\}) + G(\Gamma_S\,;\boldsymbol{p}\,;t\,;\{U^*\})\rangle \\
&\quad= \frac{1}{2}\,\langle G(\Gamma_S\,;\boldsymbol{p}\,;t\,;\{U\})\rangle \pm s_P\,\langle G^*(\Gamma_S\,;-\boldsymbol{p}\,;t\,;\{U\})\rangle \\
&\quad= \frac{1}{2}\,\langle G(\Gamma_S\,;\boldsymbol{p}\,;t\,;\{U\})\rangle \pm s_P^2\,\langle G^*(\Gamma_S\,;\boldsymbol{p}\,;t\,;\{U\})\rangle \\
&\quad= \frac{1}{2}\,\langle G(\Gamma_S\,;\boldsymbol{p}\,;t\,;\{U\})\rangle \pm \langle G(\Gamma_S\,;\boldsymbol{p}\,;t\,;\{U\})\rangle^*\,. \qquad (2.143)
\end{aligned}$$

Baryon three point correlation functions behave similarly, with the inclusion of a factor of $s_C$ introduced by the transformation of the SST propagator. The same conclusions follow, with the condition on $s_P$ replaced by $s_P = s_S\,s_C$ ($s_P = -s_S\,s_C$).

Meson correlation functions can be shown to behave similarly, except there is one less spin-structure matrix in the interpolator, and there is no spin-structure projector, so there is no factor of $s_C$. Hence, the same conclusions hold, with $s_S$ replaced by +1.

In the special case of two point correlation functions at $\boldsymbol{p} = 0$, the relation $G(\Gamma_S\,;-\boldsymbol{p}\,;t) = \langle G(\Gamma_S\,;\boldsymbol{p}\,;t)\rangle$ is satisfied exactly on a configuration-by-configuration basis. As a result, when the $\{U\}$ and $\{U^*\}$ correlators are averaged, the correlation function is perfectly real (imaginary) on a configuration-by-configuration basis.

By using this technique, we can significantly improve the statistical uncertainties in our correlation functions with minimal additional computation time.

# Chapter 3

# Centre Clusters in the Yang-Mills Vacuum

*The content of this chapter is based on the publication: "Visualizations of coherent center domains in local Polyakov loops" by F. M. Stokes et al. [9]*

*Links to the online animations produced as part of this work are provided in the following text, indicated by the use of blue font.*

## 3.1 Introduction

In QCD, the self-coupling of gluons through the colour charge gives rise to a non-trivial vacuum structure, confining quarks and generating mass through dynamical chiral symmetry breaking. This physics underlies all hadronic properties and thus underpins the results of this thesis. In this chapter we explore one particular aspect of this vacuum structure: the topologically non-trivial structures known as centre clusters. Centre clusters are of particular interest in this work because they govern the quark core of hadrons, playing a critical role in shaping the structure which we observe in later chapters.

Centre clusters also play an important role in the phase transition of the QCD vacuum from the hadronic confined phase to a deconfined phase. In a vacuum, this transition occurs at the critical temperature $T_C \approx 160\,\mathrm{MeV}$ [60–63], or around two trillion degrees Kelvin. Above the critical temperature, confinement breaks down, resulting in the formation of a quark-gluon plasma. Understanding the nature of this transition is critical to understanding the formation of hadronic matter in the early universe, the nature of neutron stars, and observations at RHIC and the LHC [64–67].

In this chapter, we work in a lattice formulation of pure SU(3) Yang-Mills theory in order to make quantitative comparisons with other work [7, 8, 10, 68–71]. More recent work has shown qualitatively similar results in full QCD [72]. SU(3) Yang-Mills theory describes the interactions of gluons in the absence of quark fields. In the absence of light dynamical quarks, the critical temperature increases to $T_C \approx 270\,\mathrm{MeV}$ [73].

To observe the phase transition in lattice simulations, one examines the behaviour of the Polyakov loop. The Polyakov loop is a complex-valued quantity which acts as an order parameter for the phase transition. It has an expectation value of zero in the confined phase and transitions to a nonzero expectation value in the deconfined phase [8]. As we will observe, this transition occurs through the growth of centre clusters, regions of space where the Polyakov loop prefers a single complex phase associated with the centre of SU(3). It is these clusters that we analyse in this chapter.

## 3.2 Background

### 3.2.1 Centre Symmetry

The local Polyakov loop is defined to be

$$\begin{aligned} L(\boldsymbol{x}) &\equiv \mathrm{Tr}\left(\mathcal{P}\exp\left[ig\int \mathrm{d}x^4 A^4(x)\right]\right) \\ &= \mathrm{Tr}\prod_{t=1}^{N_t} U^4(t,\boldsymbol{x})\,, \end{aligned} \tag{3.1}$$

where $U^4$ is the time-oriented link variable, as defined in Chapter 2. These link variables transform under a local gauge transformation $\Omega(x) \in \mathrm{SU}(3)$ as

$$U^{\mu}(x) \xrightarrow{\Omega(x)} \Omega(x)\, U^{\mu}(x)\; \Omega^{\dagger}(x + e^{\mu}\, a)\,. \tag{3.2}$$

So given the standard periodic boundary conditions in time, the Polyakov loop is invariant under local gauge transformations.

The spatially averaged Polyakov loop is defined to be

$$P \equiv \frac{1}{V}\sum_{\boldsymbol{x}} L(\boldsymbol{x})\,. \tag{3.3}$$

The local Polyakov loop $L(\boldsymbol{x})$ has the same vacuum expectation value as the spatially averaged loop $P$, due to translational invariance. Its value is related to the free energy of a static quark $F_q$ by

$$\langle L(\boldsymbol{x})\rangle = \langle P\rangle \propto \exp(-F_q/T)\,. \tag{3.4}$$

The free energy of a static quark is related to confinement. In the confined phase, the free energy is infinite, so $\langle L(\boldsymbol{x})\rangle = \langle P\rangle = 0$; in the deconfined phase the free energy is finite, so $\langle L(\boldsymbol{x})\rangle = \langle P\rangle \neq 0$ [68]. Thus, the Polyakov loop is an order parameter for confinement.

The pure SU(3) Yang-Mills theory action is invariant under centre transformations

$$U^4\left(t_0, \boldsymbol{x}\right) \rightarrow z\, U^4\left(t_0, \boldsymbol{x}\right)\ \forall \boldsymbol{x} \text{ for some } z \in C,\ t_0\,, \tag{3.5}$$

where C is the centre of SU(3), which is defined as

$$C \equiv \left\{z \in \mathrm{SU}(3) | zg = gz\, \forall g \in \mathrm{SU}(3)\right\}. \tag{3.6}$$

That is, in a centre transformation all time-oriented links on some time slice $t_0$ are multiplied by some element in the centre of SU(3). These transformations form a global symmetry of the theory known as the centre symmetry. Polyakov loops transform non-trivially under centre transformations:

$$L(\boldsymbol{x}) \rightarrow z\, L(\boldsymbol{x})\,, \tag{3.7}$$

so if the centre symmetry is conserved, $\langle L(\boldsymbol{x})\rangle = 0$ [74]. Thus, the Polyakov loop is an order parameter for the centre symmetry and deconfinement corresponds to a spontaneous breaking of the centre symmetry.

As it is defined here, the Polyakov loop would be exactly zero in both phases, as in pure SU($N$) Yang-Mills theory, all N sectors are equally weighted in the partition function. Therefore it is common to use the absolute value of the Polyakov loop as an order parameter. We take an alternative approach, removing this remaining symmetry by performing centre transformations to bring the most dominant centre sector in each configuration to the same phase. In full QCD the fermion determinant introduces a preferred phase, causing the peak with a phase of zero to always become dominant above the critical temperature [68], so this would no longer be a concern. Herein, we similarly bring the dominant centre sector of each configuration to a phase of zero.

On the lattice, the expectation value of the Polyakov loop below the critical temperature is not exactly zero, due to finite volume effects. However, the volumes we work with are large enough that it is close to zero. In the thermodynamic limit, the Polyakov loop truly vanishes below the critical temperature.

In SU(3) Yang-Mills theory below the critical temperature, it has been observed [8,68] that the complex phase of the local Polyakov loops ($\phi(\boldsymbol{x})$ in $L(\boldsymbol{x}) = \rho(\boldsymbol{x})\, \mathrm{e}^{i\phi(\boldsymbol{x})}$) is distributed evenly between three peaks, one at each of the three centre phases of SU(3) (0, $\frac{2\pi}{3}$, and $\frac{-2\pi}{3}$). We have seen a similar effect in our own simulations as shown in Fig. 3.1a. As the distribution of $L(\boldsymbol{x})$ is uniform about the three centre phases, the expectation value $\langle L(\boldsymbol{x})\rangle$ vanishes. Above the critical temperature, the centre symmetry is spontaneously broken and one of the three peaks becomes dominant. We have replicated this in our simulations as shown in Fig. 3.1b. As a result, the expectation value $\langle L(\boldsymbol{x})\rangle$ is non-zero.

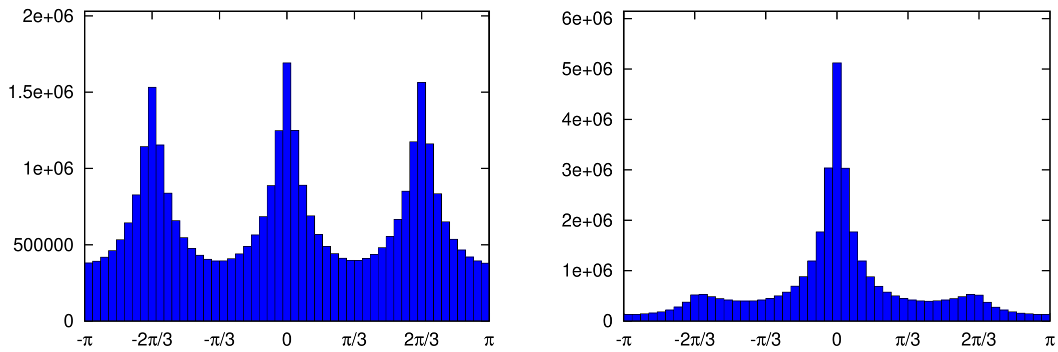

(a) $T < T_C$, approximately equal occupation

(b) $T > T_C$, there is a single dominant centre phase

Figure 3.1: Histograms of the distribution of complex phases of local loops across a gauge field ensemble, showing differing occupation of the three centre phases.

### 3.2.2 Anisotropic Gauge Action

On the lattice, the temperature $T$ is related to the temporal extent $aN_t$ by $T = \frac{1}{aN_t}$. The volume $V = (aN_s)^3$ depends on the spatial extent of the lattice $aN_s$. Most studies of centre clusters change the temperature by varying the lattice spacing [8, 68, 69, 75]. This is undesirable because the volume of the lattice is changed as the temperature changes. The only way one can change the temperature of an isotropic lattice without changing the volume is by adding or removing lattice sites in the time direction. In order to be able to adjust the temperature in a continuous manner, we instead introduce anisotropy into the lattice, replacing the single lattice spacing $a$ with both a spatial lattice spacing $a_s$ and a temporal lattice spacing $a_t$. In this way we can vary the temperature $T = \frac{1}{a_t N_t}$ while maintaining a constant volume $V = (a_s N_s)^3$ by varying $a_t$ whilst holding $a_s$ fixed. This allows us to observe the evolution of the centre clusters in gauge field configurations moving from a confined configuration to a deconfined configuration under the HMC algorithm with no change in physical volume. This cannot be done with any of the previous methods and is the first such presentation.

In order to introduce this anisotropy, we use the anisotropic Iwasaki action [76]. This action introduces the anisotropy parameter $\gamma_G$. This separates the Wilson loops in the planes defined by pairs of spatial directions from the Wilson loops in the planes defined by the temporal direction paired with each individual spatial direction. The gauge action is

$$\begin{aligned}\mathcal{S}_{\mathrm{G}}^{Anis}[U^\mu] = \beta \Bigg\{ & \frac{1}{\gamma_G} \sum_{x,i>j} \left\{ c_0^s P^{ij}(x) + c_1^s (R^{ij}(x) + R^{ji}(x)) \right\} \\ & + \gamma_G \sum_{x,k} \left\{ c_0^t P^{k\,4}(x) + c_1^t R^{k\,4}(x) + c_2^t R^{4\,k}(x) \right\} \Bigg\}, \qquad (3.8)\end{aligned}$$

where $i$, $j$, $k$ signify spatial directions, and $P^{\mu\nu}(x)$ and $R^{\mu\nu}(x)$ are respectively the $1 \times 1$ plaquette and $1 \times 2$ rectangular loop in the $\mu - \nu$ plane. The parameter $\beta$ governs the strong coupling, while $\gamma_G$ governs the anisotropy. The improvement coefficients used are from Ref. [76], and take the values

$$c_1^s = c_1^t = c_2^t = -0.331 \tag{3.9a}$$

$$c_0^s = c_0^t = 3.648\,. \tag{3.9b}$$

Since we are working in pure Yang-Mills theory, the fermion action $\mathcal{S}_{\mathrm{F}}$ discussed in Chapter 2 is set to zero.

### 3.2.3 Lattice Spacings and Temperature

The lattice spacings $a_s$ and $a_t$ depend non-trivially on $\beta$ and $\gamma_G$. In order to determine $a_s$ and $a_t$ for a given $(\beta, \gamma_G)$ pair, we first perform a lattice simulation at zero temperature (high temporal extent). We can then compute the values of the spatially averaged Wilson loops,

$$\begin{aligned} W^{\mu\nu}(r,t) \equiv \frac{1}{V}\sum_x \mathrm{Tr}\Bigg[ & \prod_{z=0}^{(r-1)} U^{\mu}(x + z\,e^{\mu}) \\ & \times \prod_{z=0}^{(t-1)} U^{\nu}(x + r\,e^{\mu} + z\,e^{\nu}) \\ & \times \prod_{z=1}^{r} U^{\dagger\,\mu}(x + r\,e^{\mu} + t\,e^{\nu} - z\,e^{\mu}) \\ & \times \prod_{z=1}^{t} U^{\dagger\,\nu}(x + t\,e^{\nu} - z\,e^{\nu})\Bigg]\,. \end{aligned} \tag{3.10}$$

An example of such a loop is illustrated in Fig.3.2. These values can then be fit to an exponential

$$W^{\mu\nu}(r,t) \propto \exp(-V_q(r)\,t)\ , \tag{3.11}$$

where $V_q(r)$ is the static quark potential

$$V_q(r) \approx V_0 + \sigma r - e \cdot \left[\frac{1}{r}\right] + l \cdot \left(\left[\frac{1}{r}\right] - \frac{1}{r}\right)\,. \tag{3.12}$$

Here $\left[\frac{1}{r}\right]$ denotes the tree-level lattice Coulomb term [77].

This ansatz for the static quark potential is sensitive to discretisation effects at extremely small $r$ and noise starts to dominate at large $r$. This means that when fitting to this ansatz we need a lower and upper cutoff for $r$. Once this is done, we can extract values for the string tension $\sigma$ from the fits.

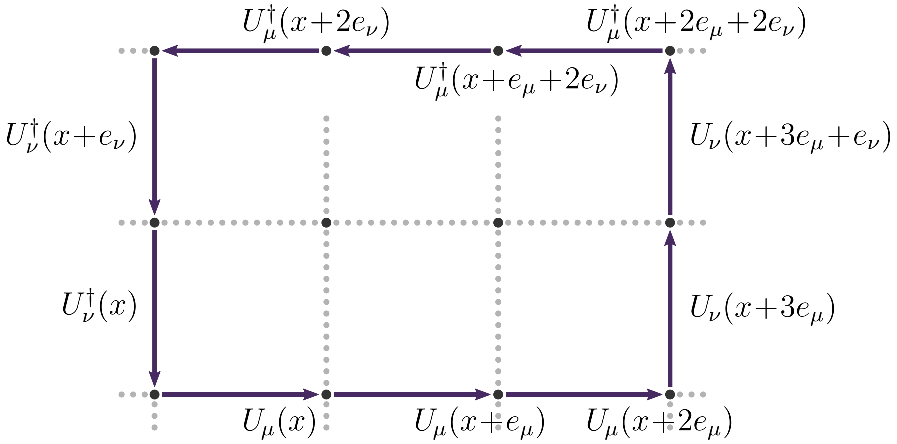

Figure 3.2: The Wilson loop $W^{\mu\nu}(3,2)$ is the product of 10 link variables forming a closed loop around a $3 \times 2$ rectangle.

On an anisotropic lattice, the fit for the space-space loops ($W^{ij}(r,t)$) gives a purely spatial string tension $\sigma_{ss}$. This can be related to the spatial lattice spacing $a_s$ through the physical value for the string tension

$$\frac{\sqrt{\sigma_{ss}}}{a_s}\,\hbar c = \sqrt{\sigma_{phys}} = 0.44\,\mathrm{GeV}\,. \tag{3.13}$$

On the other hand, the space-time loops, ($W^{k\,4}(r,t)$) and the time-space loops ($W^{4\,k}(r,t)$) give a mixed string tension $\sigma_{st}$, which can be related to the geometric mean of the spatial and temporal lattice spacings

$$\sqrt{\frac{\sigma_{st}}{a_s a_t}}\,\hbar c = \sqrt{\sigma_{phys}} = 0.44\,\mathrm{GeV}\,. \tag{3.14}$$

Hence, by computing both of these string tensions, we can extract $a_s$ and $a_t$

By finding $a_s$ and $a_t$ for a variety of $(\beta, \gamma_G)$ pairs, the relationship between $\beta$ and $\gamma_G$ necessary to keep $a_s$ constant can be determined. This allows us to choose a set of $(\beta, \gamma_G)$ pairs that give us access to a range of temperatures at a fixed volume as shown in Table 3.1.

We also find that the renormalised anisotropy,

$$\xi = \frac{a_s}{a_t}\,, \tag{3.15}$$

is approximately equal to the bare anisotropy, $\gamma_G$, in the region we studied.

### 3.2.4 Potts Model

Finite temperature phase transitions in SU(3) Yang-mills theory and other (3 + 1) dimensional gauge theories have universal properties related to those in 3-dimensional

Table 3.1: The $(\beta, \gamma_G)$ pairs obtained from pure gauge simulations of $24^3 \times 48$ lattices and the corresponding temperatures for a $24^3 \times 8$ lattice.

| $\beta$ | $\gamma_G$ | $a_s$ (fm) | $a_t$ (fm) | $\xi$ | $T$ (MeV) |
|---|---|---|---|---|---|
| 2.620 | 1.000 | 0.1016(5) | 0.1028(11) | 0.988(12) | 240(3) |
| 2.645 | 1.125 | 0.1014(4) | 0.0912(8) | 1.112(12) | 270(2) |
| 2.670 | 1.250 | 0.1019(6) | 0.0803(10) | 1.245(19) | 307(4) |
| 2.695 | 1.375 | 0.1014(4) | 0.0761(8) | 1.335(25) | 324(3) |
| 2.720 | 1.500 | 0.1002(9) | 0.0673(10) | 1.489(31) | 366(5) |
| 2.740 | 1.625 | 0.1007(12) | 0.0622(8) | 1.618(39) | 396(5) |
| 2.760 | 1.750 | 0.1019(8) | 0.0567(9) | 1.796(38) | 434(7) |

spin models [74, 78]. Thus, it is of interest to compare the behaviour of the Polyakov loops in QCD with the three dimensional 3-state Potts model [79], a generalisation of the Ising spin model. In the 3-state Potts model, each lattice site can assume one of three spin directions and these form spin aligned domains. After the phase transition, one direction dominates the space, just as in the QCD deconfinement transition. Thus, the Potts model is a candidate for a simplified model of deconfinement.

The 3-state Potts model for a three dimensional lattice of points $\boldsymbol{x} \in \mathbb{L} \subset \mathbb{Z}^3$ with spin $\sigma(\boldsymbol{x}) = 1, 2$ or 3 at each lattice site is described by the partition function

$$Z = \mathrm{e}^{-\beta E[\sigma]}\,, \tag{3.16}$$

where

$$E[\sigma] = J \sum_{\boldsymbol{x}} \sum_{i} \delta_{\sigma(\boldsymbol{x}),\sigma(\boldsymbol{x}+e^i)}\,, \tag{3.17}$$

is summed over the points of the lattice and the three spatial directions, $J$ is a coupling constant determining the strength of the interactions between adjacent sites, $e^i$ is the unit vector in the positive $i$ direction, and $\delta_{j,k}$ is the Kronecker delta. That is, $E[\sigma]$ is proportional to the total number of spin-aligned nearest-neighbour pairs. Here, $\beta = 1/(k_B T)$ is the inverse temperature in natural units, defined in terms of the Boltzmann constant $k_B$ and the temperature $T$.

We can simulate this using the Metropolis-Hastings algorithm [80], studying the behaviour of spin-aligned domains near the critical temperature and making a comparison to the behaviour of centre clusters in SU(3) Yang-Mills theory near $T_C$.

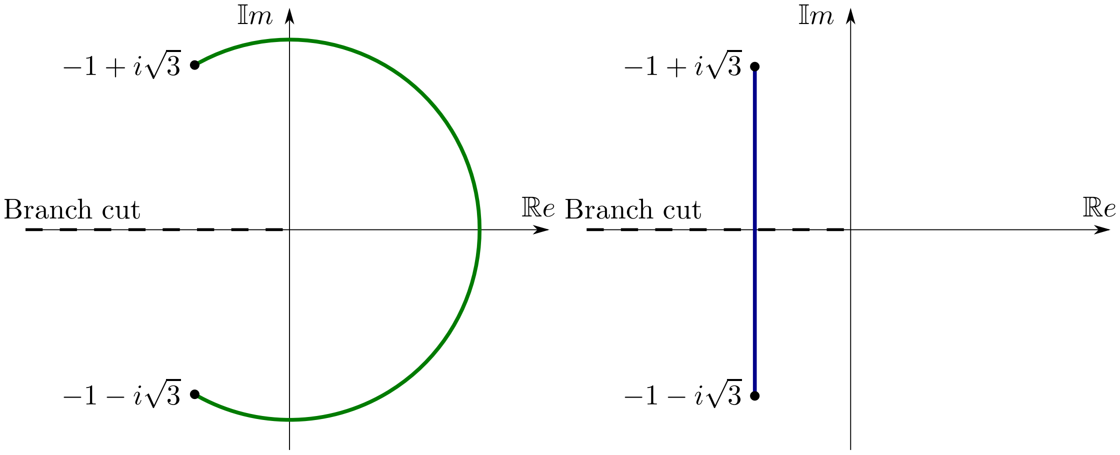

(a) Interpolation of phase (b) Interpolation of complex value

Figure 3.3: Diagrams showing path followed by different interpolation methods.

## 3.3 Results

In generating the results presented in this chapter, we used the HMC algorithm (described in Section 2.2.7). In the HMC simulation, we use 150 molecular dynamics steps per trajectory with step size $\Delta\tau = \frac{1}{150}$. In order to make the animation smoother, when producing visualisations we store the state of the Polyakov loops every 30 molecular dynamics steps, or five times per trajectory. Of course, these snapshots are dropped if the configuration is not accepted in the Metropolis accept/reject step. The acceptance rates we observed when generating our gauge field configurations varied between 75 % and 90 %, depending on the volume and temperature of the configurations being generated. Large volumes and high temperatures have the lowest acceptance rates.

Independent gauge fields are saved every 50 trajectories, an order of magnitude more separation than the 5 trajectories often used in dynamical QCD. As we will see, correlations in the centre clusters are associated with a time scale of 20 to 30 trajectories, or 4 to 6 seconds in the animations.

### 3.3.1 Visualisation

In order to analyse the behaviour of the Polyakov loops at the critical temperature, we generate gauge field configurations on several $24^3 \times 8$ lattices with the same spatial lattice spacing but different temporal spacings, using the parameters described in Table 3.1. We note that while we only present visualisations on a $24^3$ spatial volume, they are representative of the other volumes considered later in the chapter.

Visualising the Polyakov loop data presents a difficulty. We wish to render the phase $\phi(\boldsymbol{x})$ of the local Polyakov loops as expressed in polar form

$$L(\boldsymbol{x}) = \rho(\boldsymbol{x})\, \mathrm{e}^{i\,\phi(\boldsymbol{x})}\,. \tag{3.18}$$

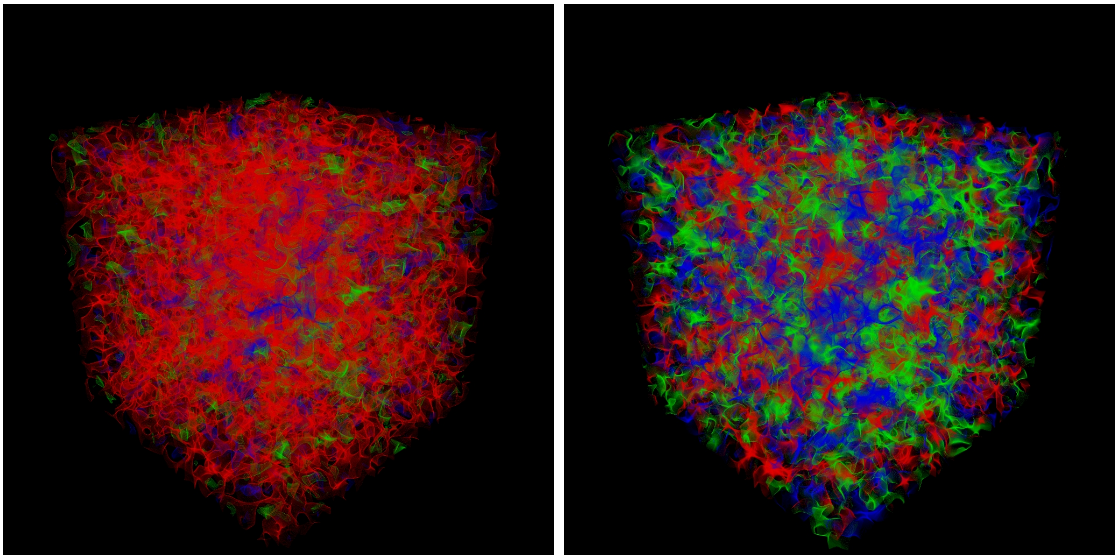

(a) Interpolation of phase (artefacts) (b) Interpolation of complex value

Figure 3.4: Visualisations demonstrating the (red) artefacts produced by the incorrect phase interpolation on the left. On the right, the correct complex interpolation shows an equal centre phase distribution.

Most visualisation software that has the ability to render volumetric data takes in a three dimensional grid of real values and uses trilinear interpolation to fill in the gaps. However, if we try to do this with the complex phase of our Polyakov loop values (with a branch cut at $\pi$), we find that the interpolation has problems near the branch cut. For example, if two adjacent data points have complex values $-1 \pm i\sqrt{3}$ (corresponding to complex phases of $\phi = \frac{\pm 2\pi}{3}$) then interpolating the phase linearly between the two points takes it through $\phi = 0$ as in Fig. 3.3a, rather than crossing the branch cut as in Fig. 3.3b. This behaviour is incorrect and produces artefacts in the final image that look like thin shells or films between regions of transparency. This leads to much more red (corresponding to $\phi = 0$) than either of green or blue ($\phi = \frac{2\pi}{3}$ and $\phi = \frac{-2\pi}{3}$ respectively) as seen in Fig. 3.4a.

Instead, we want to directly interpolate the complex numbers and *then* calculate the phase, resulting in the phase going directly between the two endpoints, across the branch cut as in Fig. 3.3b. This results in a significantly different visualisation as seen in Fig. 3.4b.

To perform this corrected interpolation, we have developed a custom volume renderer for complex valued scalar fields. The details of the rendering algorithm are given in Appendix B. There we present two ways of visualising the centre clusters.

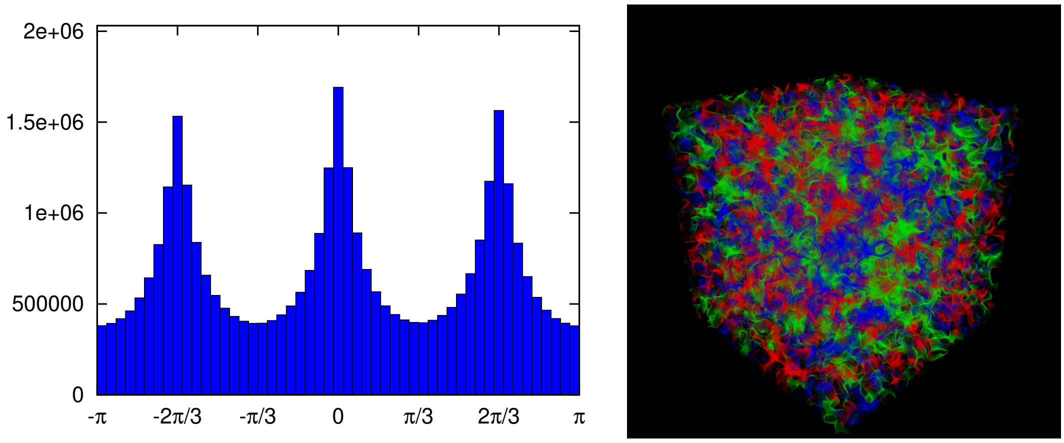

Figure 3.5: Histogram of the phase $\phi(\boldsymbol{x})$ and a visualisation of the centre clusters in the local Polyakov loop values at $T = 0.89(1)\,T_C$. All three centre phases are present in small clusters with approximately equal density.

### 3.3.2 Critical Temperature

Using this custom volume renderer, four animations are produced showing the evolution of centre clusters under the HMC algorithm. These animations are available online at `http://www.physics.adelaide.edu.au/cssm/lattice/centreclusters/`. Two different rendering techniques are used. As discussed in Appendix B, these include both rendering based on the proximity of $\phi(\boldsymbol{x})$ to one of the three centre phases of SU(3), and rendering based on the magnitude $\rho(\boldsymbol{x})$. Each are rendered from the original configurations as well as configurations smoothed with four sweeps of stout-link smearing, as discussed in greater detail below.

The animations reveal the evolution of centre clusters as a function of the HMC simulation time, with five frames per unit trajectory. The evolution of the centre clusters is governed by the evolution of the gauge field configurations under the HMC algorithm, and therefore the timescale of these animations is not a physical scale but an algorithmic scale. However, while it may have no direct physical significance, the evolution of the centre clusters during thermalisation gives novel insights into the nature of the HMC algorithm and the way it brings the gauge field to a physical configuration. In addition, once thermalisation is complete, every frame in itself is a physically representative state and thus we can observe a number of possible structures for the centre clusters and gain extensive insight.

We commence with a thermalised configuration at $T = 240(3)\,\text{MeV}$ or $T/T_C = 0.89(1)$. To show the nature of the HMC updates, we present 750 frames corresponding to 150 HMC trajectories. At our frame rate of 25 frames per second, this lasts 30 seconds. A snapshot of the centre clusters at this temperature is provided in Fig. 3.5. On the left-hand plot, a histogram of the distribution of the phases of the Polyakov loops across a gauge field ensemble at this temperature shows that all three centre phases,

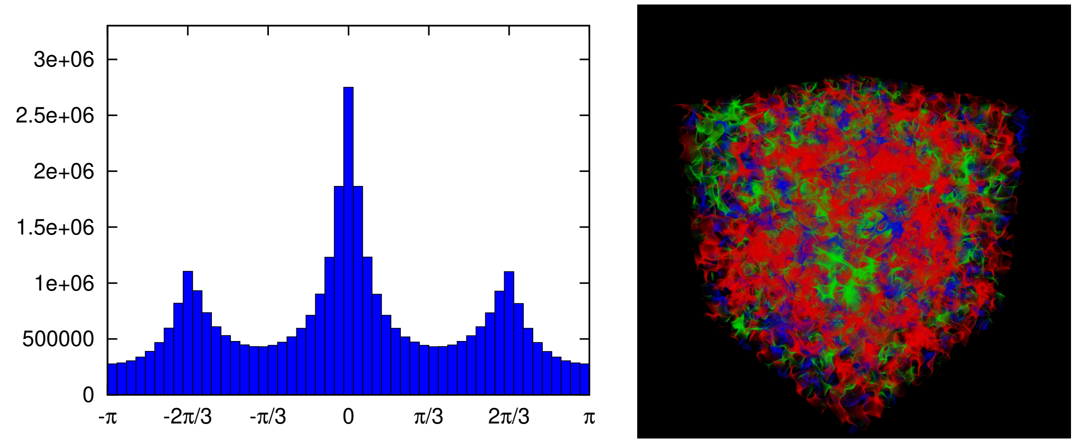

Figure 3.6: Histogram and visualisation as in Fig. 3.5 at $T = 1.14(2)\,T_C$. A single (red) phase is beginning to dominate, signalling deconfinement.

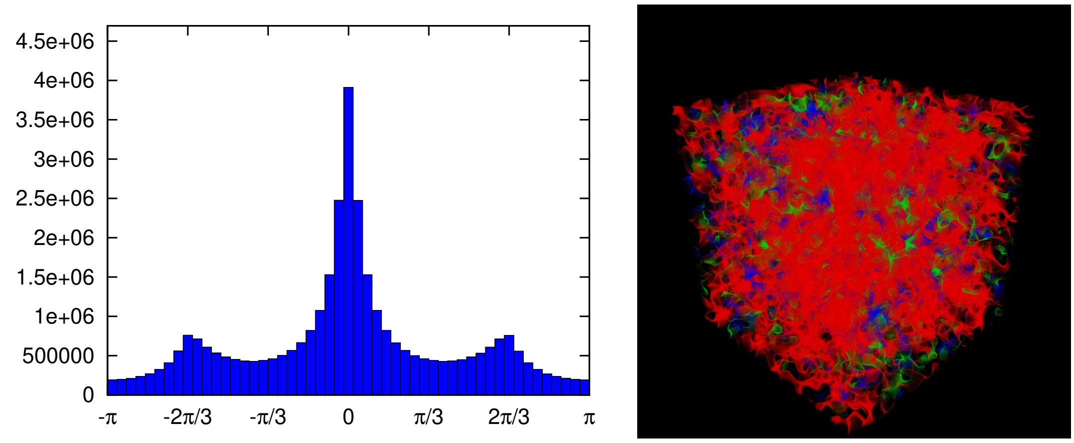

Figure 3.7: Histogram and visualisation at $T = 1.36(2)\,T_C$. A single (red) cluster dominates the entire space.

observable as peaks in the histogram, are approximately equally occupied, signalling confinement. The right-hand plot shows a single frame from the animation, in which the three centre-phase peaks observed in the histogram correspond to blue (left), red (centre), and green (right). All three centre phases are present in small clusters with approximately equal density.

At this point (0:30 in the animation), the temperature is increased to $T = 307(4)\,\text{MeV}$ or $T/T_C = 1.14(2)$ and the response of the gauge field is illustrated in the animations. Fig. 3.6 shows the red centre phase becoming dominant with the other two beginning to be suppressed, signalling the onset of deconfinement. In the animation, we can see that the three centre phases start out equally dominant and fluctuate in size until the red clusters come to dominate.

After 600 HMC trajectories or 120 seconds, at 2:30 in the animation, the configuration has finished responding to the temperature change and we increase the temperature again, this time to $T = 366(5)\,\text{MeV}$ or $T/T_C = 1.36(2)$. At this temperature, the

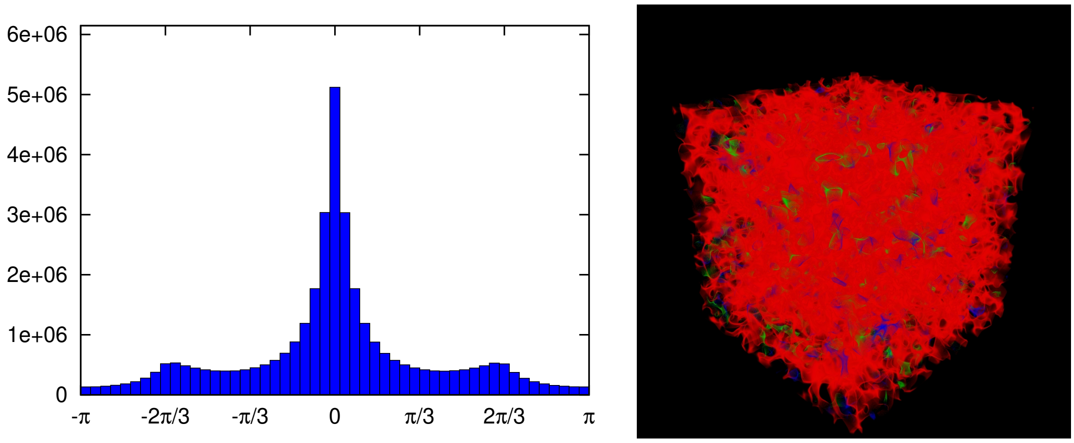

Figure 3.8: Histogram and visualisation at $T = 1.61(3)\,T_C$. The same (red) phase is still dominant.

animation shows that the red clusters continue to grow, occupying almost the entire space. This can be seen in the snapshot provided in Fig. 3.7.

After 250 more HMC trajectories or 50 seconds, at 3:20 in the animation, we increase the temperature again, to $T = 434(7)$ MeV or $T/T_C = 1.61(3)$. At this temperature, the red phase remains dominant in the animation and the other two phases are suppressed even further. Fig. 3.8 provides a snapshot at this temperature, showing the red phase almost completely dominant. We show 250 HMC trajectories at this temperature over the remaining 50 seconds of the animation.

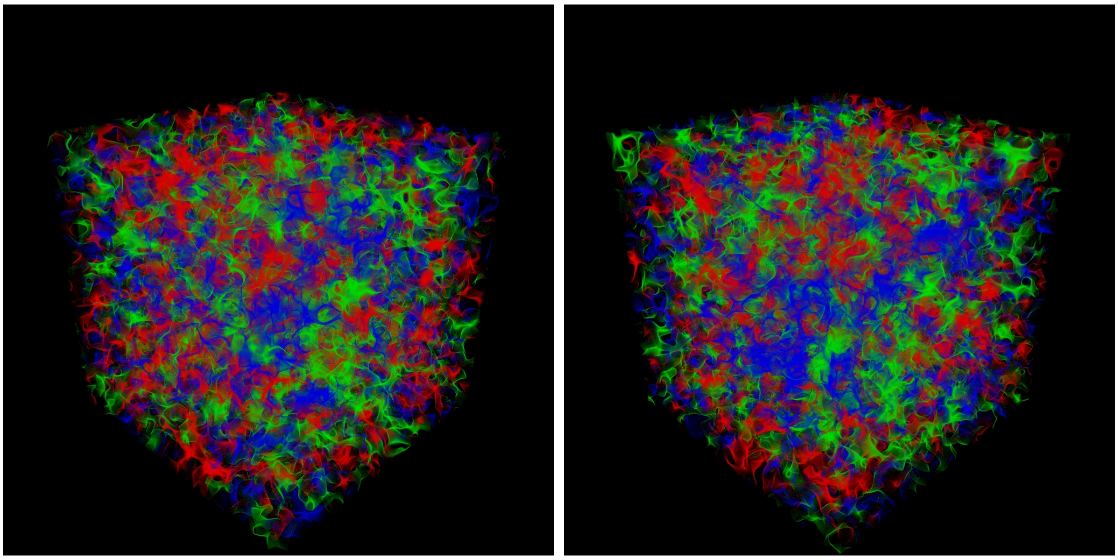

(a) Thermalised configuration

(b) After one unit HMC trajectory

Figure 3.9: Evolution of centre clusters with simulation time at $T = 0.89(1)\,T_C$.

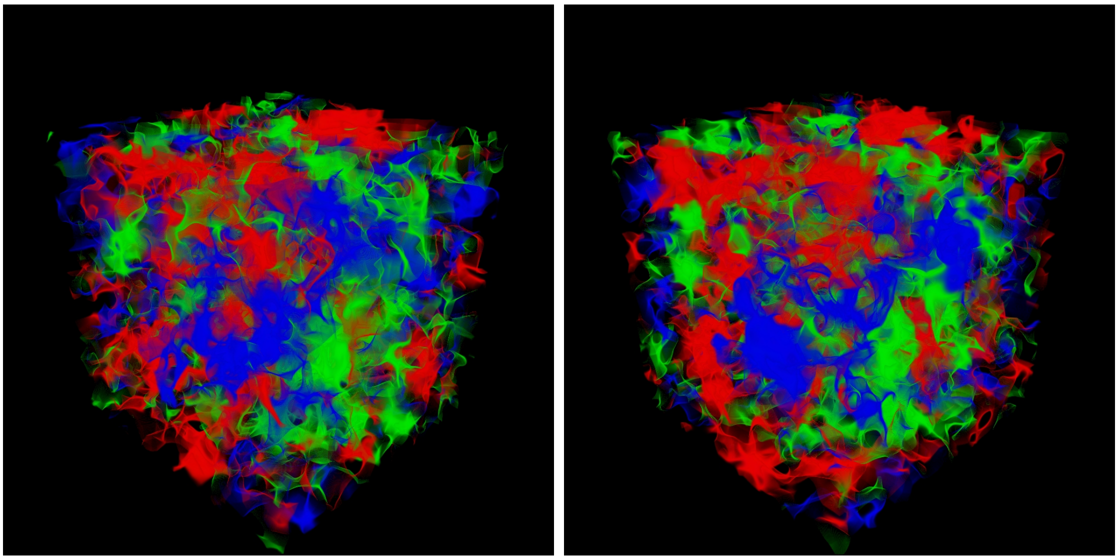

(a) Thermalised configuration (b) After one unit HMC trajectory

Figure 3.10: Evolution of centre clusters with simulation time at $T = 0.89(1)\,T_C$. Four sweeps of stout-link smearing are applied to the gauge links prior to calculating the Polyakov loops.

### 3.3.3 Monte-Carlo Evolution

By examining visualisations of the centre clusters on gauge field configurations separated by a single HMC trajectory, we can observe the evolution of the centre clusters with simulation time. The auto-correlation times for different observables under HMC evolution can vary, so it is of interest to observe the timescales over which the centre clusters evolve. We can see that over the course of a single unit trajectory, the small scale structure of the loops changes significantly, as shown in Fig. 3.9. This suggests that the small scale structure of the centre clusters evolves very quickly under the HMC algorithm and thus has short auto-correlation times.

To investigate the larger scale behaviour of the clusters, we remove the small scale noise by performing four sweeps of stout-link smearing [81] prior to calculating the Polyakov loops. The results are illustrated in Fig. 3.10. In these visualisations, we see that over the course of one trajectory, the centre clusters are slowly moving, with some change around the boundaries of the clusters. Observing the evolution of the centre clusters in the corresponding animation, we see correlations in the centre clusters persisting for approximately 5 seconds corresponding to 25 trajectories, suggesting an approximate length for the auto-correlation time of the larger scale structure of the clusters. After approximately 50 trajectories, the large scale structure of the loops has become completely decorrelated. This is supported by Fig. 3.11, which shows the phase of the average Polyakov loop on a small $(6 \times 6 \times 6)$ subsection of the lattice. We can see that the phase becomes completely decorrelated within 50 trajectories. This supports

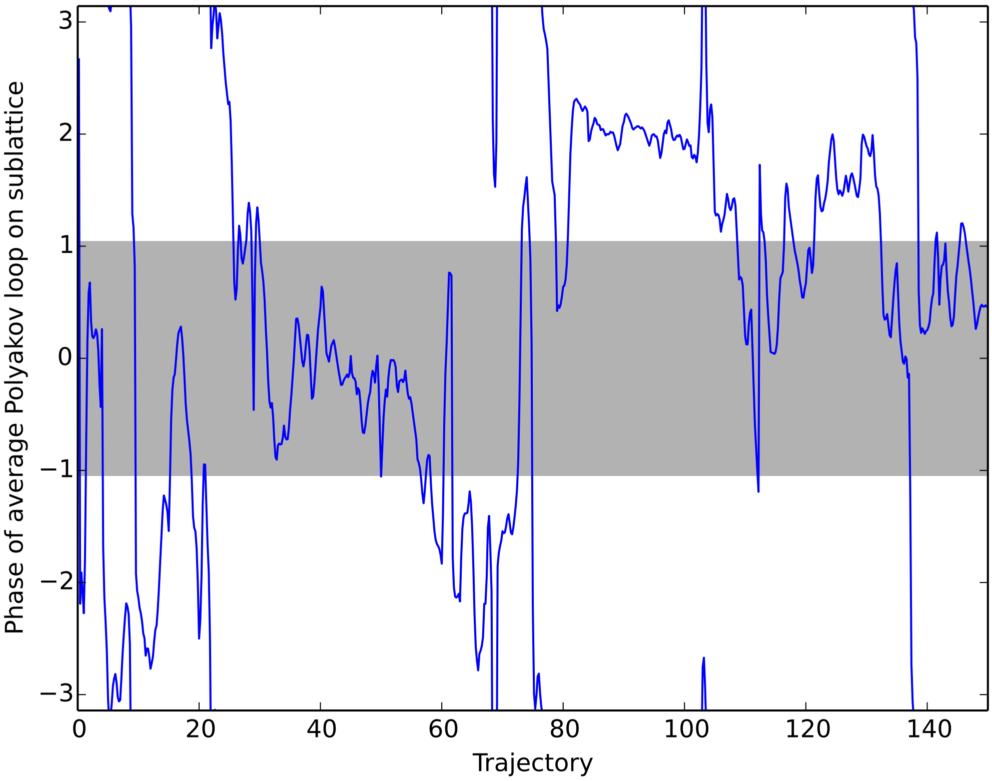

Figure 3.11: Evolution of phase of average Polyakov loop on $6 \times 6 \times 6$ sub-lattice with simulation time at $T = 0.89(1)\,T_C$. Four sweeps of stout-link smearing are applied to the gauge links prior to calculating the Polyakov loops. Since the phase is $2\pi$-periodic, we see the graph wrapping around on the y-axis.

our choice of separation for independent configurations.

The evolution observed in SU(3) gauge theory is consistent with the behaviour of spin-aligned domains in the three dimensional 3-state Potts model [79] just below the critical temperature under Metropolis-Hastings algorithm simulations, as seen in Fig. 3.12.

We can also see that once a particular centre phase comes to dominate the space, that phase remains dominant for the rest of the simulation. That is, in this first investigation of the behaviour of the Polyakov loop under Monte-Carlo evolution, we find that the dominant phase is highly stable under the process of HMC updates.

### 3.3.4 Magnitude-Based Clusters

If we use the alternate rendering style based on the magnitude $\rho(x)$, we can see that peaks in the magnitude lie approximately within the centre clusters, as shown in Fig. 3.13. The magnitude peaks are each coloured corresponding to a single centre phase and they appear to line up with peaks in the corresponding phase based visualisation. However

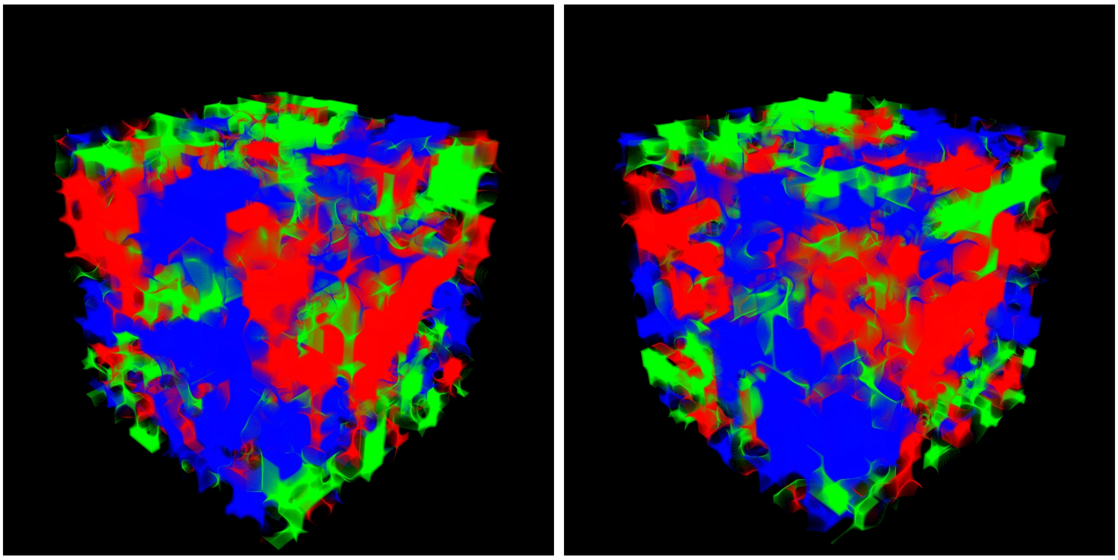

(a) Thermalised configuration (b) After 4096 single-site Metropolis updates

Figure 3.12: Evolution of spin-aligned domains in the three dimensional 3-state Potts model at $\beta = 0.55$ on a $16^3$ lattice.

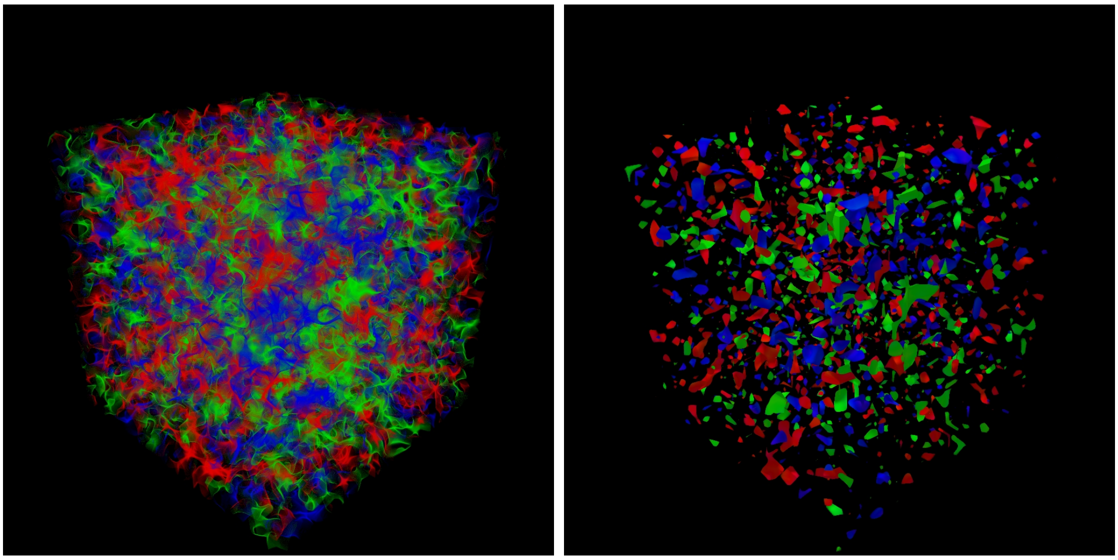

(a) Opacity based on $\phi(\boldsymbol{x})$ (b) Opacity based on $\rho(\boldsymbol{x})$

Figure 3.13: Comparison of complex phase $\phi(\boldsymbol{x})$ and magnitude $\rho(\boldsymbol{x})$ clusters at $T = 0.89(1)\, T_C$.

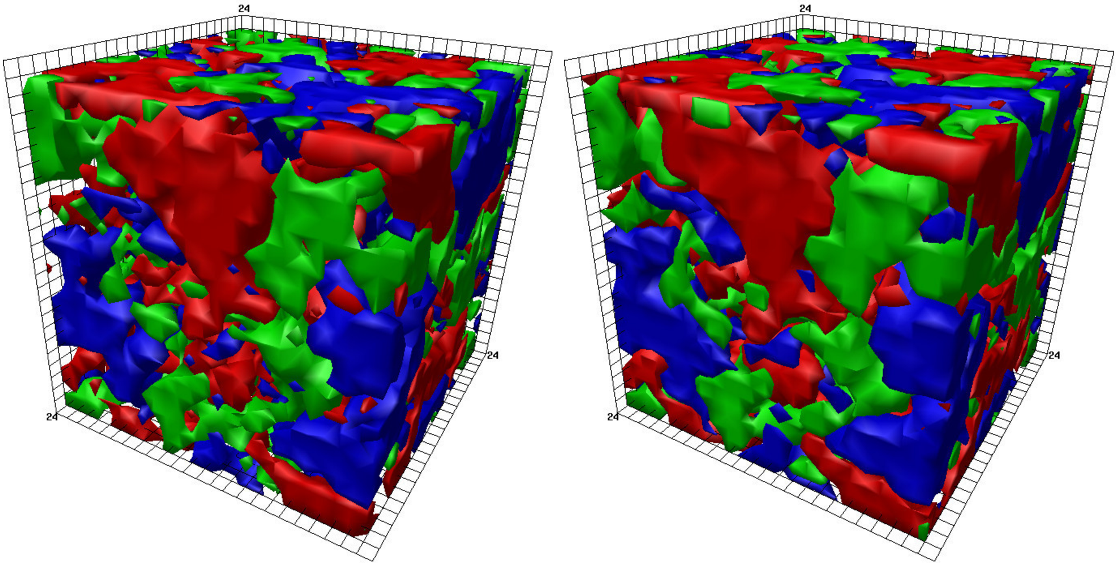

(a) Clusters based on $\phi(\boldsymbol{x})$ (b) Clusters based on $\rho(\boldsymbol{x})$

Figure 3.14: Comparison of phase $\phi(\boldsymbol{x})$ and magnitude $\rho(\boldsymbol{x})$ clusters at $T = 0.89(1)\,T_C$ after four sweeps of stout-link smearing using the isovolume renderer. The rendering thresholds for $\phi(\boldsymbol{x})$ and $\rho(\boldsymbol{x})$ are 0.5 and 0.2 respectively.

it is not necessarily clear that each centre cluster corresponds to a peak in the modulus, $\rho(\boldsymbol{x})$.

In order to look more closely at the correlation between these clusters, we again perform four sweeps of stout-link smearing, making it easier to observe larger scale structures, and render both the phase and magnitude based clusters using an isovolume rendering developed in AVS/Express [82] that makes the boundaries of the clusters more clear. For each cluster, we colour the isovolume based on the nearest centre phase $\phi_c$ to the Polyakov loop values in the cluster. We render isovolumes for the phase-based clusters where $|\phi(\boldsymbol{x}) - \phi_c(\boldsymbol{x})|/(\pi/3)$ is less than some cut. We also calculate the maximum magnitude of the Polyakov loop on the lattice and render isovolumes for the magnitude-based clusters where $\rho(x)/\rho_{\max}$ is less than some cut.

When we do this, as shown in Figs. 3.14 and 3.15, it becomes clear that there is an approximate one-to-one relationship between the peaks in the magnitude $\rho(\boldsymbol{x})$ and the proximity of $\phi(\boldsymbol{x})$ to a centre phase.

We can also observe this correlation by looking at a scatter plot of $\rho(x)/\rho_{\max}$ vs $|\phi(\boldsymbol{x}) - \phi_c(\boldsymbol{x})|$ as in Fig. 3.16. This observed correlation of $\rho(\boldsymbol{x})$ becoming small as $\phi(\boldsymbol{x})$ moves away from a centre phase is the first direct confirmation of the underlying assumption of Ref. [64], which links the centre domain walls to unanticipated phenomena observed at RHIC [83] and the LHC [65–67].

These peaks in the magnitude of the local Polyakov loops mean that the free energy of a quark-antiquark pair is minimised in the core of a centre cluster. Thus we have a confining potential with local minima at the cores of centre clusters. Below the critical

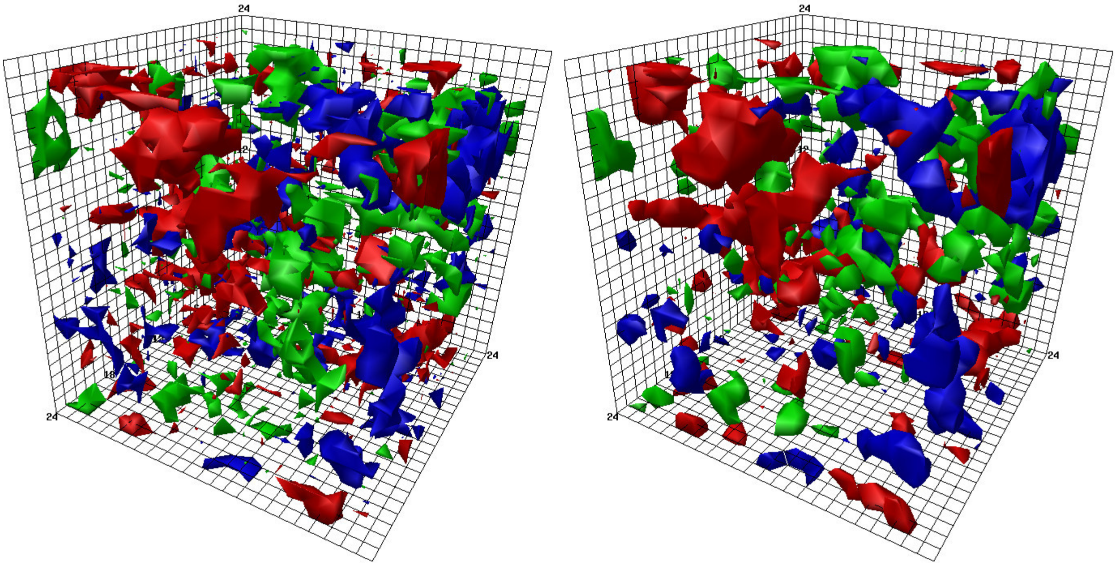

(a) Clusters based on $\phi(\boldsymbol{x})$ (b) Clusters based on $\rho(\boldsymbol{x})$

Figure 3.15: Comparison of phase $\phi(\boldsymbol{x})$ and magnitude $\rho(\boldsymbol{x})$ clusters at $T = 0.89(1)\,T_C$ after four sweeps of stout-link smearing, using the isovolume renderer, cut much closer into the peaks than Fig. 3.14. Here, the rendering thresholds for $\phi(\boldsymbol{x})$ and $\rho(\boldsymbol{x})$ are 0.9 and 0.5 respectively.

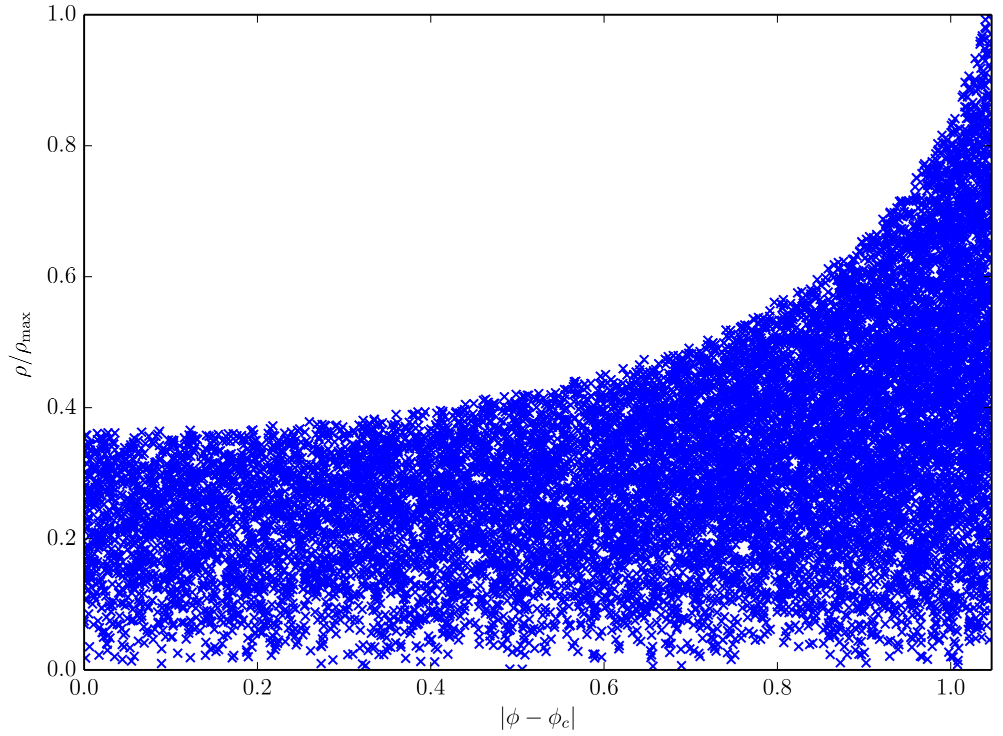

Figure 3.16: Scatter plot of centre phase proximity and modulus, showing a clear correlation between proximity to a centre phase and maxima of the modulus.

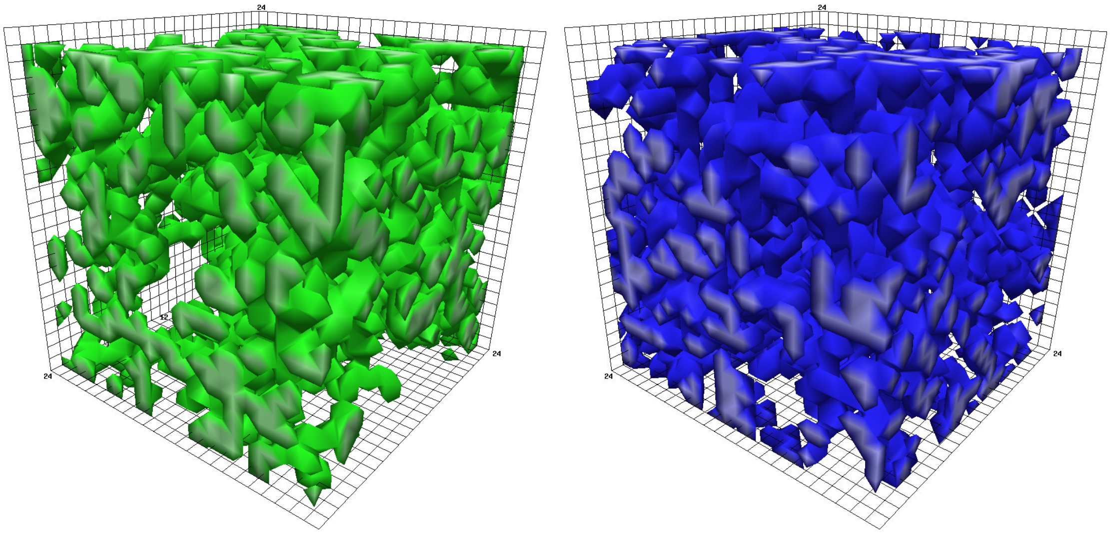

Figure 3.17: Two of the three percolating clusters in a representative $24^3 \times 8$ gauge field configuration at $T = 0.89(1)\, T_C$ when using a cut parameter of zero.

temperature the peaks are sharp so the gradient of the potential is steep, resulting in a strong restoring force confining the quarks to the core of the cluster. Above the critical temperature, the peaks become much broader so the gradient is significantly smaller and the restoring force is greatly reduced.

Animations showing the HMC time evolution of the magnitude-based centre clusters are available online for both unsmeared and smeared gauge field configurations.

### 3.3.5 Centre Clusters

In order to observe the structure of individual clusters, we use the definition by Gattringer and Schmidt [8]. Two neighbouring points $\boldsymbol{x}$ and $\boldsymbol{y}$ belong to the same cluster if and only if $n(\boldsymbol{x}) = n(\boldsymbol{y})$, where the sector number $n(\boldsymbol{x})$ is defined to be

$$n(\boldsymbol{x}) := \begin{cases} -1 & \text{for}\, \phi(\boldsymbol{x}) \in [-\pi + \delta, -\frac{\pi}{3} - \delta], \\ 0 & \text{for}\, \phi(\boldsymbol{x}) \in [-\frac{\pi}{3} + \delta, \frac{\pi}{3} - \delta], \\ 1 & \text{for}\, \phi(\boldsymbol{x}) \in [\frac{\pi}{3} + \delta, \pi - \delta]. \end{cases} \tag{3.19}$$

If we include every site in a cluster (i.e. we set the cut parameter $\delta$ to zero), then below the critical temperature each sector is equally occupied so each sector occupies approximately one third of the sites. This means that if our sectors were randomly distributed, our clustering would be equivalent to random site percolation theory with an occupation probability of $p \approx 0.3333$. This is above the critical percolation probability of $p_c \approx 0.3116$ [84]. Even though our sectors are not randomly distributed, their distribution tends to clump together, which should increase the likelihood of percolation. Thus, with a cut parameter of zero, we expect to see at least one percolating cluster

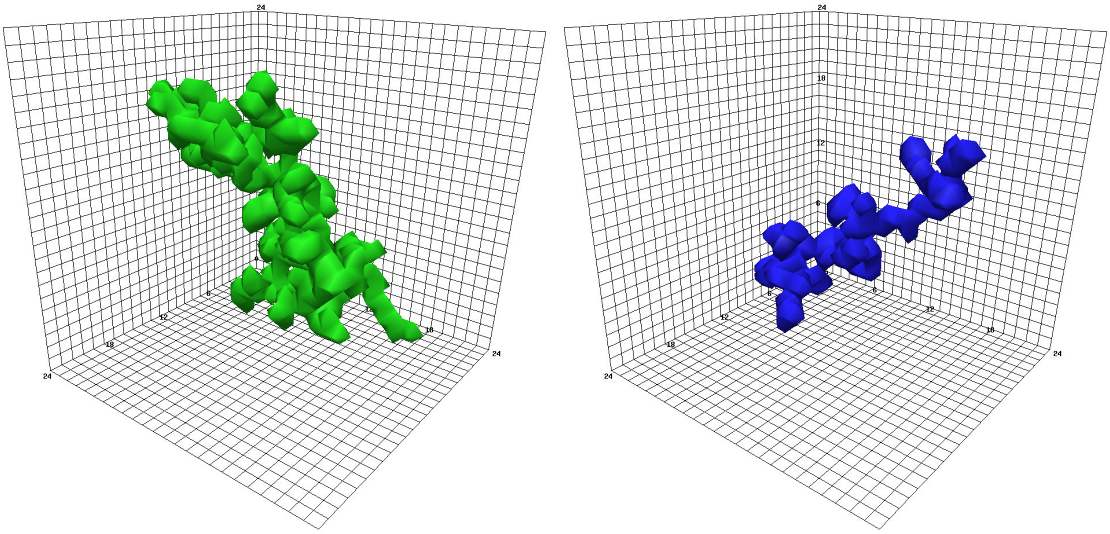

Figure 3.18: One of the non-percolating clusters broken off from each of the clusters in Fig. 3.17 when the cut parameter is increased to 0.3.

(i.e. a cluster that has at least one site in each of the $3N_s$ spatial planes) for each phase. Thus, if we define the clusters in this way, due to the nature of three dimensional space they are not localised, and instead extend over the entire lattice, as seen in Fig. 3.17.

In order to study localised clusters below the critical temperature, we instead introduce a cut parameter as in Ref. [8]. This cut results in smaller, localised clusters scattered across the lattice. We show examples of such localised clusters in Fig. 3.18. We can see that these clusters have a one dimensional, finger-like quality to their structure and this supports the determination by Endrődi, Gattringer and Schadler [10] that the centre clusters have a fractal dimension of $D \approx 1.4$ to $1.7$.

As illustrated in Fig.3.16, the selection of a cut in $\phi(\boldsymbol{x})$ identifies a subset of points where $\rho(\boldsymbol{x})$ is small. Hence, our inclusion of a cut parameter in our cluster definition leads to a set of localised centre clusters separated from one another by domain walls of finite thickness within which the magnitude of the Polyakov loop is small.

Now that we have defined these localised clusters, we seek to understand their physical significance. We consider the effect of these clusters on the correlation function $\langle L(\boldsymbol{x}) L^\dagger(\boldsymbol{y}) \rangle$:

1. If $\boldsymbol{x}$ and $\boldsymbol{y}$ lie within a single cluster, $\phi(\boldsymbol{x}) \approx \phi(\boldsymbol{y})$ and

$$\begin{aligned} \langle L(\boldsymbol{x}) L^\dagger(\boldsymbol{y}) \rangle &= \langle \rho(\boldsymbol{x}) \rho(\boldsymbol{y}) \mathrm{e}^{i(\phi(\boldsymbol{x}) - \phi(\boldsymbol{y}))} \rangle \\ &\approx \langle \rho(\boldsymbol{x}) \rho(\boldsymbol{y}) \rangle \neq 0 \,. \end{aligned} \tag{3.20}$$

   That is, the phases at $\boldsymbol{x}$ and $\boldsymbol{y}$ cancel out, and the correlation function is non-zero.

2. If $\boldsymbol{x}$ and $\boldsymbol{y}$ lie within different clusters, $\phi(\boldsymbol{x}) \neq \phi(\boldsymbol{y})$ in general and thus there is no correlation between the phases. These uncorrelated phases combine to give

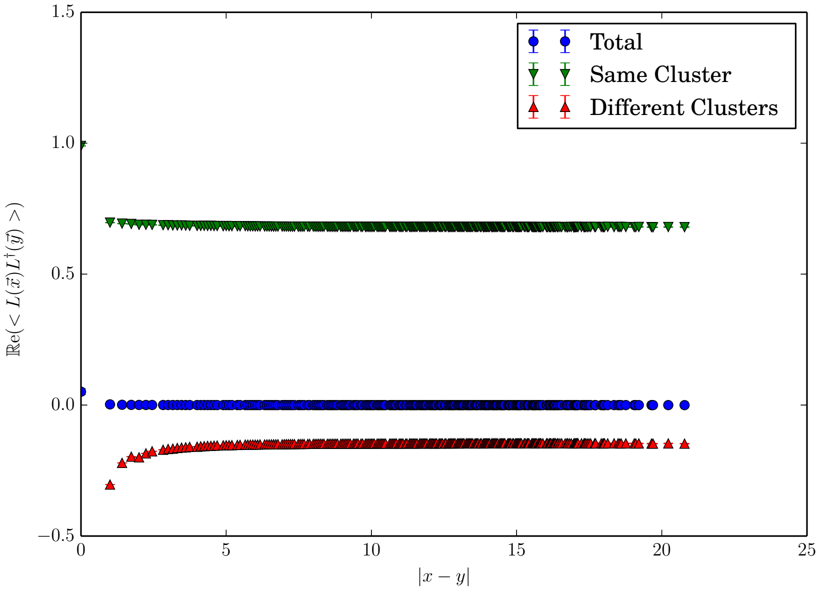

Figure 3.19: Comparison of real component of correlation function for points in the same and in different clusters and averaged across all points. Generated from $24^3 \times 8$ lattice at $T = 0.89(1)\,T_C$ with a cut parameter of 0.0.

a phase which will be symmetrically distributed between the three centre phase peaks. Thus, the complex values average to zero across an ensemble, giving

$$\langle L(\boldsymbol{x})L^\dagger(\boldsymbol{y})\rangle = 0 \tag{3.21}$$

We can observe the effect of the clusters on the value of $\langle L(\boldsymbol{x})L^\dagger(\boldsymbol{y})\rangle$ in Figs. 3.19-3.21, produced from an ensemble of 100 independent gauge field configurations. We see that the real component of the correlator is nonzero and positive for pairs of points in the same cluster and plateaus to a small negative value for pairs of points in different clusters. The imaginary component is negligible.

The nonzero negative value of the plateau for points in different clusters observed at low cut parameters can be understood to be a combination of percolation and finite volume effects.

In a given region of the volume containing multiple clusters, we expect approximately equal numbers of clusters associated with each centre phase. Hence, if $\boldsymbol{x}$ and $\boldsymbol{y}$ are in separate clusters in separate regions of the volume, there should be no correlation between their phases. However, if the cluster containing $\boldsymbol{x}$ extends into the neighbourhood of $\boldsymbol{y}$, then requiring that $\boldsymbol{y}$ be in a different cluster to $\boldsymbol{x}$ effectively biases the distribution of phases that the loop at $\boldsymbol{y}$ could take. This occurs because we are taking a region with clusters equally distributed between the three phases and then effectively

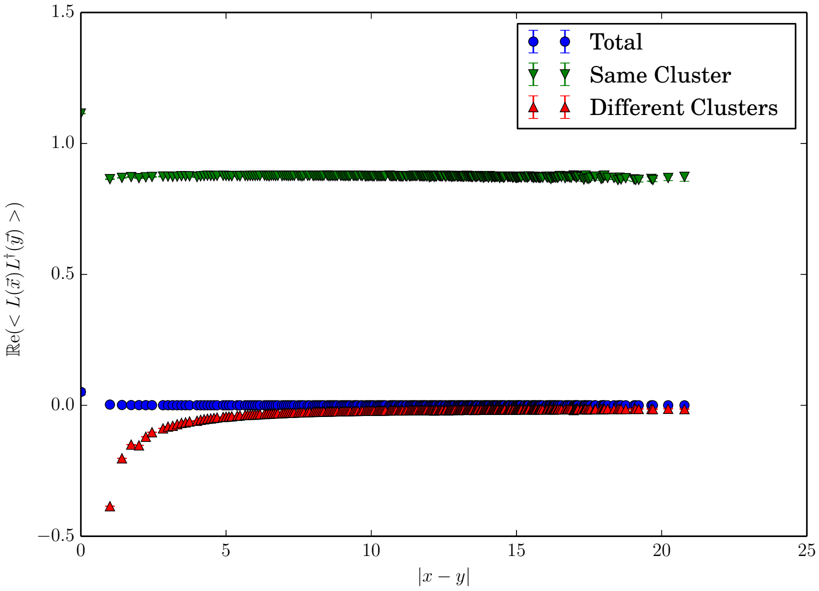

Figure 3.20: Comparison of real component of correlation function for points in the same and in different clusters and averaged across all points. Generated from $24^3 \times 8$ lattice at $T = 0.89(1)\, T_C$ with a cut parameter of 0.3.

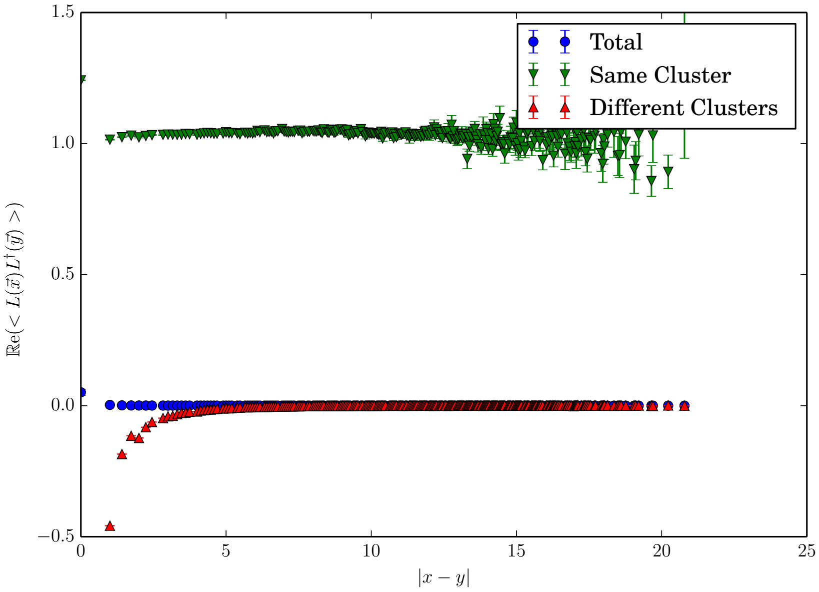

Figure 3.21: Comparison of real component of correlation function for points in the same and in different clusters and averaged across all points. Generated from $24^3 \times 8$ lattice at $T = 0.89(1)\, T_C$ with a cut parameter of 0.5.

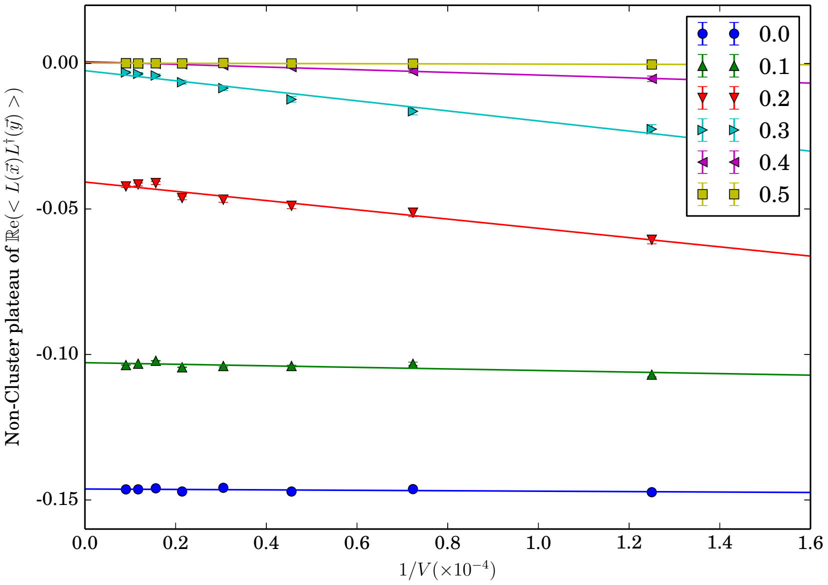

Figure 3.22: Volume and cut parameter dependence of the plateau in the correlation function for different clusters at $T = 0.89(1)\,T_C$. Cut parameters are indicated in the legend.

removing one cluster with a specific phase from consideration.

Hence, in order for the correlation function to vanish we need both a sufficiently large cut parameter to give the clusters a finite size, and a volume significantly larger than that cluster size. This then allows us to separate points sufficiently to avoid this bias. As can be seen from Fig. 3.22, the value of the plateau does indeed go to zero in the infinite volume limit for sufficiently large values of the cut parameter.

The two point correlation function $\langle L(\boldsymbol{x})L^\dagger(\boldsymbol{y})\rangle$ is related to the free energy of a static quark-antiquark pair (a meson) separated by $\boldsymbol{x}-\boldsymbol{y}$ [74]:

$$\langle L(\boldsymbol{x})L^\dagger(\boldsymbol{y})\rangle \propto \exp(-F_{q\bar{q}}(\boldsymbol{x}-\boldsymbol{y})/T)\,. \tag{3.22}$$

Thus:

1. If $\langle L(\boldsymbol{x})L^\dagger(\boldsymbol{y})\rangle \neq 0$, then $F_{q\bar{q}}(\boldsymbol{x}-\boldsymbol{y})$ is finite. Since this corresponds to $\boldsymbol{x}$ and $\boldsymbol{y}$ lying within the same cluster, this means that creating a quark-antiquark pair within a single cluster is energetically favourable.

2. If $\langle L(\boldsymbol{x})L^\dagger(\boldsymbol{y})\rangle = 0$, then $F_{q\bar{q}}(\boldsymbol{x}-\boldsymbol{y})$ is infinite. Since this corresponds to $\boldsymbol{x}$ and $\boldsymbol{y}$ lying within different clusters, this means that creating a quark-antiquark pair across a cluster boundary is energetically unfavourable.

Hence, mesons are confined to within the scale of a cluster.

We now consider the similar effect of the clusters on the three point correlation function $\langle L(\boldsymbol{x})L(\boldsymbol{y})L(\boldsymbol{z})\rangle$:

1. If $\boldsymbol{x}$, $\boldsymbol{y}$, and $\boldsymbol{z}$ lie within a single cluster, $\phi(\boldsymbol{x}) \approx \phi(\boldsymbol{y}) \approx \phi(\boldsymbol{z}) \approx \frac{2n\pi}{3}$ for some $n \in \{-1, 0, 1\}$, so

$$\begin{aligned} \langle L(\boldsymbol{x})L(\boldsymbol{y})L(\boldsymbol{z})\rangle &= \langle \rho(\boldsymbol{x})\rho(\boldsymbol{y})\rho(\boldsymbol{z})\mathrm{e}^{i(\phi(\boldsymbol{x})+\phi(\boldsymbol{y})+\phi(\boldsymbol{z}))}\rangle \\ &\approx \langle \rho(\boldsymbol{x})\rho(\boldsymbol{y})\rho(\boldsymbol{z})\mathrm{e}^{i(3\times\frac{2n\pi}{3})}\rangle \\ &\approx \langle \rho(\boldsymbol{x})\rho(\boldsymbol{y})\rho(\boldsymbol{z})\rangle \neq 0\,. \end{aligned} \tag{3.23}$$

   That is, the three phases cancel out, and the correlation function is non-zero.

2. If any of $\boldsymbol{x}$, $\boldsymbol{y}$ and $\boldsymbol{z}$ lie within different clusters, their phases are not correlated. These uncorrelated phases combine to give a phase which will be symmetrically distributed between the three centre phase peaks. Thus, the complex values average to zero across an ensemble, giving

$$\langle L(\boldsymbol{x})L(\boldsymbol{y})L(\boldsymbol{z})\rangle = 0 \tag{3.24}$$

The correlation function $\langle L(\boldsymbol{x})L(\boldsymbol{y})L(\boldsymbol{z})\rangle$ is related to the free energy of a quark triplet (a baryon):

$$\langle L(\boldsymbol{x})L^{\dagger}(\boldsymbol{y})\rangle \propto \exp(-F_{qqiq}(\boldsymbol{x},\boldsymbol{y},\boldsymbol{z})/T)\,. \tag{3.25}$$

Thus:

1. If $\langle L(\boldsymbol{x})L(\boldsymbol{y})L(\boldsymbol{z})\rangle \neq 0$, then $F_{qqq}(\boldsymbol{x},\boldsymbol{y},\boldsymbol{z})$ is finite. Since this corresponds to $\boldsymbol{x}$, $\boldsymbol{y}$, and $\boldsymbol{z}$ lying within the same cluster, this means that creating a quark triplet within a single cluster is energetically favourable.

2. If $\langle L(\boldsymbol{x})L(\boldsymbol{y})L(\boldsymbol{z})\rangle = 0$, then $F_{qqq}(\boldsymbol{x},\boldsymbol{y},\boldsymbol{z})$ is infinite. Since this corresponds to one of $\boldsymbol{x}$, $\boldsymbol{y}$, and $\boldsymbol{z}$ lying within different clusters, this means that creating a quark triplet across a cluster boundary is energetically unfavourable.

Hence, baryons are also confined to the scale of a cluster.

The cluster size thus has a physical significance, governing the confining scale of the theory. From a model perspective, this scale governs the size of the quark core of hadrons which is dressed by the mesonic cloud. Above the critical temperature, as a single cluster grows to encompass the entire space, the quarks become deconfined [8].

## 3.4 Conclusion

We simulated SU(3) Yang-Mills theory on anisotropic $24^3 \times 8$ lattices with the Iwasaki gauge action, considering renormalised anisotropy ranging from $\xi \approx 0.99$ to $\xi \approx 1.80$ with a spatial lattice spacing of $a_s \approx 0.1\,\mathrm{fm}$. We explored temperatures ranging from $0.89(1)\,T_C$ to $1.61(3)\,T_C$. We focused on the structure and evolution of the centre clusters associated with Polyakov loops.

In doing so, we developed a volume rendering program that correctly deals with the interpolation of three dimensional complex fields such as the local Polyakov loop, and clearly displays their phase (and/or absolute value). This allows us to observe the evolution of centre clusters with HMC simulation time.

For the first time, we were able to reveal the evolution of centre clusters as they transitioned from the confined to the deconfined phase. The cluster behaviour is consistent with that of spin aligned domains in the three dimensional 3-state Potts model. This supports the idea that the phase transition in QCD is comparable to that of a three state spin system.

We also observe an approximate one to one correspondence between peaks in the magnitude of local Polyakov loops and the locations of centre clusters defined by the proximity of the phase of the Polyakov loops to a centre phase. We observe that the magnitude of the Polyakov loop is suppressed within the domain walls between the clusters. This supports the underlying assumption of Ref. [64], linking the centre domain walls to phenomena observed at RHIC [83] and the LHC [65–67].

The creation of a domain wall of finite thickness between clusters through the cut parameter $\delta$ [8] produces clusters in which the quark-antiquark correlation function $\langle L(\boldsymbol{x}) L^\dagger(\boldsymbol{y}) \rangle$ vanishes when both quarks do not reside in the same cluster, setting a scale for confinement.

Below the critical temperature, these clusters correspond to sharp peaks in the Polyakov loop magnitude. Through considerations of the free energy of multi-quark systems, this results in a minimum of the quark-antiquark potential in the core of each centre cluster with a steep gradient resulting in a strong restoring force confining the quarks within the cluster. Above the critical temperature the peak structure becomes smooth and the region covered by the cluster becomes large. When averaged over an ensemble, any remaining fluctuations in the Polyakov loops are smoothed out and the restoring force becomes negligible. In this way, quarks become deconfined.

# Chapter 4

# Parity Expanded Variational Analysis

*The content of this chapter is based on the publication: "Parity-expanded variational analysis for nonzero momentum " by F. M. Stokes et al. [85]*

## 4.1 Introduction

One of the most widely recognised successes of lattice QCD has been its application to light hadron spectroscopy [11, 86–88]. The rest masses of the ground states have been established and agree well with experiment [89], but this is just the beginning. A multitude of excited states can be extracted through a combination of effective mass calculations and variational analysis techniques. Significant progress has been made within the baryon sector [14–23]. However, the study of baryon excited states in lattice QCD is still a challenging endeavour and has not reached the maturity of ground state computations. As yet, there are no studies that isolate all excited states within a region of interest at or near the physical pion mass and also include a full continuum extrapolation.

Once an understanding of the spectra is obtained, the logical progression is to investigate the structure of these hadrons, and again lattice QCD provides the tools needed for the precise determination of hadronic matrix elements. Key to lattice QCD's ability to investigate hadronic structure is the computation of two- and three-point correlation functions for each hadronic state of interest at both zero and non-zero final state momenta. While the zero momentum two-point case corresponds to the rest mass analysis and is well understood, at non-zero momentum more care must be taken to ensure the energy eigenstates are cleanly extracted, especially when investigating excited states.

In this chapter, we investigate the use of variational analysis techniques to extract correlation functions for excited states of spin-½ baryons at non-zero momentum. In Section 4.2, we briefly describe the conventional approach and highlight how states of the opposite parity can intrude into the analysis. Section 4.3 introduces the parity-expanded variational analysis (PEVA) technique, an original approach to overcoming this shortfall, created herein. This method will be central to baryon form-factor calculations involving excited states, for example the analysis of electromagnetic structure described in Chapter 6. It will also be particularly important in future investigations of baryon transitions.

In Section 4.4, we present results comparing the conventional parity projection approach to the PEVA technique, demonstrating the removal of opposite parity contaminations from two-point correlators through strong cross-parity contributions to the interpolator structure of the four lowest-lying states. These results are calculated on the PACS-CS $(2+1)$-flavour full-QCD ensembles [87], made available through the ILDG [90]. They are $32^3 \times 64$ lattices with $\beta = 1.90$, and employ a renormalisation-group improved Iwasaki gauge action and non-perturbatively $O(a)$-improved Wilson quarks, with $C_{SW} = 1.715$. In particular, we demonstrate proof of principle on the ensemble with the second lightest quark mass. This ensemble consists of 400 gauge field configurations with $\kappa_{\mathrm{u,d}} = 0.13770$, corresponding to a pion mass of 280 MeV, and a lattice spacing of $a = 0.0951(13)$ fm as set by the Sommer parameter with $r_0 = 0.49$ fm. When generating quark propagators, we utilise fixed boundary conditions in the time direction, and place the source at $t_{src} = L_t/4 = 16$, striking a balance between sufficient separation from the boundary in the negative time direction to suppress backwards-running states, and giving sufficient room in the positive time direction for forwards-running states to propagate before they approach possible reflections off the far boundary.

## 4.2 Parity Mixing at Non-Zero Momentum

We begin by briefly reviewing conventional variational analysis to highlight where opposite parity contaminations enter. In order to discuss opposite parity contaminations, we need to be able to categorise states by their parity. However, eigenstates of non-zero momentum are not eigenstates of parity, so the boosted states do not have a well-defined parity. Instead, we categorise states by their rest frame parity. We call states that transform positively under parity in their rest frame "positive-parity states" (and label them $B^+$), and states that transform negatively under parity in their rest frame "negative-parity states" ($B^-$).

To perform a conventional variational analysis on spin-½ baryons, we begin with a basis of $n$ conventional baryon interpolating fields $\{\chi_i\}$ (e.g. $\chi_1 = (u^\top (C\gamma^5) d) u$). Such interpolators couple to both positive and negative-parity states as

$$\langle\Omega|\,\chi_i(0)\,|B^+;p\,;s\rangle = \lambda_{B^+i}(\boldsymbol{p})\sqrt{\frac{m_{B^+}}{E_{B^+}(\boldsymbol{p})}}\,u_{B^+}(p,s)\,, \tag{4.1a}$$

$$\langle\Omega|\,\chi_i(0)\,|B^-;p\,;s\rangle = \lambda_{B^-i}(\boldsymbol{p})\sqrt{\frac{m_{B^-}}{E_{B^-}(\boldsymbol{p})}}\,\gamma^5\,u_{B^-}(p,s)\,, \tag{4.1b}$$

where $u_B(p,s)$ is the Dirac spinor for a spin-½ baryon with momentum $p$ and spin polarisation $s$, as defined in Appendix C. Note that the only difference between the spinors for positive and negative-parity states is the mass of the states in question. Under parity transformations, such interpolators transform as

$$\chi_i \xrightarrow{P} \gamma^4\,\chi_i\,. \tag{4.2}$$

We use this basis to construct an $n\times n$ matrix of two-point correlation functions

$$\mathcal{G}_{ij}(\boldsymbol{p}\,;t) \equiv \sum_{\boldsymbol{x}} \mathrm{e}^{-i\boldsymbol{p}\cdot\boldsymbol{x}}\ \langle\Omega|\,\chi_i(x)\ \overline{\chi}_j(0)\,|\Omega\rangle\ . \tag{4.3}$$

A described in Chapter 2, inserting the complete set of states

$$\mathbb{I} = \sum_{B,p,s} |B\,;p\,;s\rangle\,\langle B\,;p\,;s| \tag{4.4}$$

between the two interpolators allows us to rewrite the correlation functions as

$$\mathcal{G}_{ij}(\boldsymbol{p}\,;t) = \sum_{B,s} \mathrm{e}^{-E_B(\boldsymbol{p})\,t}\ \langle\Omega|\,\chi_i(0)\,|B\,;p\,;s\rangle\,\langle B\,;p\,;s|\,\overline{\chi}_j(0)\,|\Omega\rangle\ . \tag{4.5}$$

The sum over states $B$ contains both positive and negative-parity states so we can consider them separately, giving

$$\begin{aligned}\mathcal{G}_{ij}(\boldsymbol{p}\,;t) =& \sum_{B^+,s} \mathrm{e}^{-E_{B^+}(\boldsymbol{p})\,t}\ \langle\Omega|\,\chi_i(0)\,|B^+;p\,;s\rangle\,\langle B^+;p\,;s|\,\overline{\chi}_j(0)\,|\Omega\rangle \\ &+ \sum_{B^-,s} \mathrm{e}^{-E_{B^-}(\boldsymbol{p})\,t}\ \langle\Omega|\,\chi_i(0)\,|B^-;p\,;s\rangle\,\langle B^-;p\,;s|\,\overline{\chi}_j(0)\,|\Omega\rangle \\ =& \sum_{B^+,s} \mathrm{e}^{-E_{B^+}(\boldsymbol{p})\,t}\,\lambda_{B^+i}(\boldsymbol{p})\ \overline{\lambda}_{B^+j}(\boldsymbol{p})\ \frac{m_{B^+}}{E_{B^+}(\boldsymbol{p})}\,u_{B^+}(p,s)\,\overline{u}_{B^+}(p,s) \\ &- \sum_{B^-,s} \mathrm{e}^{-E_{B^-}(\boldsymbol{p})\,t}\,\lambda_{B^-i}(\boldsymbol{p})\ \overline{\lambda}_{B^-j}(\boldsymbol{p})\ \frac{m_{B^-}}{E_{B^-}(\boldsymbol{p})}\,\gamma^5\,u_{B^-}(p,s)\,\overline{u}_{B^-}(p,s)\,\gamma^5\,.\end{aligned} \tag{4.6}$$

In the Pauli representation,

$$\sum_s u_B(p,s)\,\overline{u}_B(p,s) = \frac{-i\,\gamma^\mu\,p^\mu + m_B}{2m_B}\,, \tag{4.7}$$

so we can take the spin sum of the correlation functions to give

$$\begin{aligned}
\mathcal{G}_{ij}(\boldsymbol{p}\,;t) = &\sum_{B^+} \mathrm{e}^{-E_{B^+}(\boldsymbol{p})\,t}\,\lambda_{B^+i}(\boldsymbol{p})\,\overline{\lambda}_{B^+j}(\boldsymbol{p})\,\frac{-i\,\gamma^\mu\,p^\mu + m_{B^+}}{2E_{B^+}(\boldsymbol{p})} \\
&- \sum_{B^-} \mathrm{e}^{-E_{B^-}(\boldsymbol{p})\,t}\,\lambda_{B^-i}(\boldsymbol{p})\,\overline{\lambda}_{B^-j}(\boldsymbol{p})\,\gamma^5\,\frac{-i\,\gamma^\mu\,p^\mu + m_{B^-}}{2E_{B^-}(\boldsymbol{p})}\,\gamma^5 \\
= &\sum_{B^+} \mathrm{e}^{-E_{B^+}(\boldsymbol{p})\,t}\,\lambda_{B^+i}(\boldsymbol{p})\,\overline{\lambda}_{B^+j}(\boldsymbol{p})\,\frac{-i\,\gamma^\mu\,p^\mu + m_{B^+}}{2E_{B^+}(\boldsymbol{p})} \\
&- \sum_{B^-} \mathrm{e}^{-E_{B^-}(\boldsymbol{p})\,t}\,\lambda_{B^-i}(\boldsymbol{p})\,\overline{\lambda}_{B^-j}(\boldsymbol{p})\,\frac{+i\,\gamma^\mu\,p^\mu + m_{B^-}}{E_{B^-}(\boldsymbol{p})}\,. \qquad (4.8)
\end{aligned}$$

So the Dirac structure of the two point correlation functions is given by

$$\mathcal{G}_{ij}(\boldsymbol{p}\,;t) = \sum_{B^\pm} \mathrm{e}^{-E_{B^\pm}(\boldsymbol{p})\,t}\,\lambda_{B^\pm i}(\boldsymbol{p})\,\overline{\lambda}_{B^\pm j}(\boldsymbol{p})\,\frac{-i\,\gamma^\mu\,p^\mu \pm m_{B^\pm}}{2E_{B^\pm}(\boldsymbol{p})}\,. \qquad (4.9)$$

For clarity, Eq. (4.9) is formulated for the case of a fixed boundary condition in the temporal direction, as used herein. It is also applicable to the common case of a periodic or anti-periodic boundary condition on lattices with large Euclidean time extents, where the contributions of backward-running baryon states are negligible. The case of non-negligible backward-running states is presented at the end of Sec. 4.3.1.

These correlation functions contain states of both parities, so conventionally we take the spinor trace with some spin-structure projector $\Gamma_S$, defining $G_{ij}(\Gamma_S\,;\boldsymbol{p}\,;t) \equiv \mathrm{Tr}\big(\Gamma_S\,\mathcal{G}_{ij}(\boldsymbol{p}\,;t)\big)$. If we choose $\Gamma_S = \Gamma^\pm \equiv (\gamma^4 \pm \mathbb{I})/2$, we get the parity projected correlators

$$\begin{aligned}
G_{ij}(\Gamma^\pm;\boldsymbol{p}\,;t) &\equiv \mathrm{Tr}\big(\Gamma^\pm\,\mathcal{G}_{ij}(\boldsymbol{p}\,;t)\big) \\
&= \sum_{B^+} \mathrm{e}^{-E_{B^+}(\boldsymbol{p})\,t}\,\lambda_{B^+i}(\boldsymbol{p})\,\overline{\lambda}_{B^+j}(\boldsymbol{p})\,\frac{E_{B^+}(\boldsymbol{p}) \pm m_{B^+}}{2E_{B^+}(\boldsymbol{p})} \\
&\quad + \sum_{B^-} \mathrm{e}^{-E_{B^-}(\boldsymbol{p})\,t}\,\lambda_{B^-i}(\boldsymbol{p})\,\overline{\lambda}_{B^-j}(\boldsymbol{p})\,\frac{E_{B^-}(\boldsymbol{p}) \mp m_{B^-}}{2E_{B^-}(\boldsymbol{p})}\,. \qquad (4.10)
\end{aligned}$$

At zero momentum, $E_B(\boldsymbol{0}) = m_B$, so the parity projected correlators contain only contributions from states of a single parity:

$$G_{ij}(\Gamma^+;\boldsymbol{0}\,;t) = \sum_{B^+} \mathrm{e}^{-m_{B^+}t}\,\lambda_{B^+i}(\boldsymbol{0})\,\overline{\lambda}_{B^+j}(\boldsymbol{0}) \qquad (4.11a)$$

$$G_{ij}(\Gamma^-;\boldsymbol{0}\,;t) = \sum_{B^-} \mathrm{e}^{-m_{B^-}t}\,\lambda_{B^-i}(\boldsymbol{0})\,\overline{\lambda}_{B^-j}(\boldsymbol{0})\,. \qquad (4.11b)$$

However, at non-zero momentum, $E_B(\boldsymbol{p}) \neq m_B$ and the parity projected correlators include $O(E - m)$ opposite parity contaminations. This situation was investigated in [91], where an improved projector of the form

$$\Gamma^{\pm}_{Imp}(\boldsymbol{p}) \equiv \frac{1}{2}\left(\frac{m_{B^{\mp}}}{E_{B^{\mp}}(\boldsymbol{p})}\,\gamma^4 \pm \mathbb{I}\right)\,, \tag{4.12}$$

was introduced to remove a single contaminating state, the lowest state of the opposite parity. However, if there is more than one nearby state contaminating the correlation function, the additional contaminating state will still remain.

Clearly, variational analysis techniques applied to baryons at non-zero momentum are vulnerable to opposite parity contaminations. To properly investigate the structure of baryons on the lattice, we require a robust technique for removing opposite parity contaminations, even if multiple such contaminations are present.

One option is to take the trace with $\gamma^4$ to get

$$G_{ij}(\gamma^4\,;\boldsymbol{p}\,;t) = \sum_{B} \mathrm{e}^{-E_B(\boldsymbol{p})\,t}\,\lambda_{B\,i}(\boldsymbol{p})\,\overline{\lambda}_{B\,j}(\boldsymbol{p})\,, \tag{4.13}$$

where the sum over $B$ now contains both parities. We can then use standard correlation matrix techniques to isolate the excited-state spectrum of both parities simultaneously. A technique similar to this appears to be used by Lang and Verduci in Ref. [92]. However, this technique requires isolating both positive and negative-parity states in a single correlation matrix rather than in separate positive- and negative-parity-projected correlation matrices. For a given interpolator basis, we are hence only able to isolate half as many states of each parity. We are also destroying the parity information encoded in the Dirac structure, preventing one from distinguishing whether a particular state has positive or negative rest-frame parity.

Instead, we want a technique that allow us to extract the same number of states as a conventional parity projected analysis, while maintaining a clear signal of each state's rest-frame parity.

## 4.3 Using a Parity-Expanded Interpolator Basis

### 4.3.1 Physics at the Hadronic Level

To solve this problem of opposite parity contaminations at finite momentum, we developed the PEVA technique [85]. In this section, we summarise the PEVA technique, and describe how it applies to form factor calculations.

The PEVA technique works by expanding the basis of the correlation matrix to isolate states of both rest-frame parities simultaneously, while maintaining a clear signature of the states' rest-frame parity. This requires the introduction of novel interpolating fields that utilise the Dirac structure of the states to couple to individual parity sectors at zero momentum and probe the mixing between these sectors at finite momentum.

We consider the Dirac structure of the correlation function

$$\sum_{\boldsymbol{x}} \mathrm{e}^{-i\boldsymbol{p}\cdot\boldsymbol{x}} \, \langle\Omega|\,\gamma^5\chi_i(x)\,\overline{\chi}_j(0)\,|\Omega\rangle \,, \tag{4.14}$$

which captures the cross-parity mixing. The on-diagonal blocks of this Dirac matrix are proportional to $\sigma^k\,p^k$. To access this signal, we need a projector with a $\gamma^5\,\gamma^k\,\widehat{\boldsymbol{p}}^k$ term. Hence, we introduce a novel momentum-dependent projector

$$\Gamma_{\boldsymbol{p}} \equiv \frac{1}{4}\left(\mathbb{I}+\gamma^4\right)\left(\mathbb{I}-i\gamma^5\,\gamma^k\,\widehat{\boldsymbol{p}}^k\right) \tag{4.15}$$

which allows us to construct a set of “parity-signature” projected interpolating fields

$$\chi_{\boldsymbol{p}\,i}(x) = \Gamma_{\boldsymbol{p}}\,\chi_i(x)\,, \tag{4.16a}$$

$$\chi_{\boldsymbol{p}\,i'}(x) = \Gamma_{\boldsymbol{p}}\,\gamma^5\,\chi_i(x)\,. \tag{4.16b}$$

The primed indices on $\chi_{\boldsymbol{p}}$ denote the inclusion of $\gamma^5$, inverting the way the interpolators transform under parity.

Unlike the conventional baryon interpolators $\{\,\chi_i\,\}$, these interpolating fields have definite parity at zero momentum and hence transform as eigenstates of parity

$$\chi_{\boldsymbol{0}\,i} \to \chi_{\boldsymbol{0}\,i}\,, \tag{4.17a}$$

$$\chi_{\boldsymbol{0}\,i'} \to -\chi_{\boldsymbol{0}\,i'}\,. \tag{4.17b}$$

Making use of this property, we introduce the nomenclature that interpolators with unprimed indices are “positive-parity interpolators” ($\chi^+$) and interpolators with primed indices are “negative-parity interpolators” ($\chi^-$). We use these terms in quotes here as these interpolators are only definite in parity at zero momentum, and while the interpolators at non-zero momentum have a clear connection to the definite parity interpolators at zero momentum, they are not themselves definite in parity.

Drawing on the spinor structure for an on-shell baryon of momentum $\boldsymbol{p}$, as given in Appendix C, we find that

$$\Gamma_{\boldsymbol{p}}\,u(p,\uparrow) = \frac{1}{2}\sqrt{\frac{E(\boldsymbol{p})+m}{2m}}\begin{pmatrix} 1-\widehat{\boldsymbol{p}}^3 \\ -\widehat{\boldsymbol{p}}^1 - i\,\widehat{\boldsymbol{p}}^2 \\ 0 \\ 0 \end{pmatrix}, \text{ and} \tag{4.18a}$$

$$\Gamma_{\boldsymbol{p}}\,\gamma^5\,u(p,\uparrow) = \frac{1}{2}\,\frac{|\boldsymbol{p}|}{E(\boldsymbol{p})+m}\sqrt{\frac{E(\boldsymbol{p})+m}{2m}}\begin{pmatrix} 1-\widehat{\boldsymbol{p}}^3 \\ -\widehat{\boldsymbol{p}}^1 - i\,\widehat{\boldsymbol{p}}^2 \\ 0 \\ 0 \end{pmatrix} \tag{4.18b}$$

so the PEVA projector acting on $\gamma^5$ times a spinor gives

$$\Gamma_{\boldsymbol{p}}\,\gamma^5\,u(p,\uparrow) = \frac{|\boldsymbol{p}|}{E(\boldsymbol{p})+m}\Gamma_{\boldsymbol{p}}\,u(p,\uparrow)\,, \tag{4.19a}$$

which is proportional to the PEVA projector acting directly on a spinor. Similarly, we find that

$$\Gamma_{\boldsymbol{p}}\,\gamma^5\,u(p,\downarrow) = \frac{|\boldsymbol{p}|}{E(\boldsymbol{p})+m}\Gamma_{\boldsymbol{p}}\,u(p,\downarrow)\,. \tag{4.19b}$$

As a result, these interpolators couple to the states of interest as

$$\langle\Omega|\,\chi_{\boldsymbol{p}\,i}\,|B^+;p\,;s\rangle = \lambda_{B^+i}(\boldsymbol{p})\,\sqrt{\frac{m_{B^+}}{E_{B^+}(\boldsymbol{p})}}\,\Gamma_{\boldsymbol{p}}\,u_{B^+}(p,s)\,, \tag{4.20a}$$

$$\langle\Omega|\,\chi_{\boldsymbol{p}\,i}\,|B^-;p\,;s\rangle = \lambda_{B^-i}(\boldsymbol{p})\,\frac{|\boldsymbol{p}|}{E_{B^-}(\boldsymbol{p})+m_{B^-}}\sqrt{\frac{m_{B^-}}{E_{B^-}(\boldsymbol{p})}}\,\Gamma_{\boldsymbol{p}}\,u_{B^-}(p,s)\,, \tag{4.20b}$$

$$\langle\Omega|\,\chi_{\boldsymbol{p}\,i'}\,|B^+;p\,;s\rangle = \lambda_{B^+i}(\boldsymbol{p})\,\frac{|\boldsymbol{p}|}{E_{B^+}(\boldsymbol{p})+m_{B^+}}\sqrt{\frac{m_{B^+}}{E_{B^+}(\boldsymbol{p})}}\,\Gamma_{\boldsymbol{p}}\,u_{B^+}(p,s)\,, \tag{4.20c}$$

$$\langle\Omega|\,\chi_{\boldsymbol{p}\,i'}\,|B^-;p\,;s\rangle = \lambda_{B^-i}(\boldsymbol{p})\,\sqrt{\frac{m_{B^-}}{E_{B^-}(\boldsymbol{p})}}\,\Gamma_{\boldsymbol{p}}\,u_{B^-}(p,s)\,. \tag{4.20d}$$

We see that the coupling of both primed and unprimed interpolators to a particular state $B$ has a consistent Dirac structure of $\Gamma_{\boldsymbol{p}}\,u_B(p,s)$. Hence we can take linear combinations of such interpolators to enhance or eliminate the coupling to a particular state. We can see in these expressions that at zero momentum, $\chi_{\boldsymbol{0}\,i}$ and $\chi_{\boldsymbol{0}\,i'}$ couple only to states of positive and negative parity respectively. However, as we boost to non-zero momenta, the interpolators clearly couple to states of both parities.

We can use these novel interpolating fields as an expanded basis, forming a correlation matrix from the blocks

$$\mathcal{G}_{ij}(\boldsymbol{p}\,;t) \equiv \sum_{\boldsymbol{x}} \mathrm{e}^{-i\boldsymbol{p}\cdot\boldsymbol{x}}\ \langle\Omega|\,\chi_{\boldsymbol{p}\,i}(x)\,\overline{\chi}_{\boldsymbol{p}\,j}(0)\,|\Omega\rangle\ , \tag{4.21a}$$

$$\mathcal{G}_{ij'}(\boldsymbol{p}\,;t) \equiv \sum_{\boldsymbol{x}} \mathrm{e}^{-i\boldsymbol{p}\cdot\boldsymbol{x}}\ \langle\Omega|\,\chi_{\boldsymbol{p}\,i}(x)\,\overline{\chi}_{\boldsymbol{p}\,j'}(0)\,|\Omega\rangle\ , \tag{4.21b}$$

$$\mathcal{G}_{i'j}(\boldsymbol{p}\,;t) \equiv \sum_{\boldsymbol{x}} \mathrm{e}^{-i\boldsymbol{p}\cdot\boldsymbol{x}}\ \langle\Omega|\,\chi_{\boldsymbol{p}\,i'}(x)\,\overline{\chi}_{\boldsymbol{p}\,j}(0)\,|\Omega\rangle\ , \tag{4.21c}$$

$$\mathcal{G}_{i'j'}(\boldsymbol{p}\,;t) \equiv \sum_{\boldsymbol{x}} \mathrm{e}^{-i\boldsymbol{p}\cdot\boldsymbol{x}}\ \langle\Omega|\,\chi_{\boldsymbol{p}\,i'}(x)\,\overline{\chi}_{\boldsymbol{p}\,j'}(0)\,|\Omega\rangle\ . \tag{4.21d}$$

If we begin with $n$ interpolators $\{\chi_i\}$ then each of these blocks is $n \times n$, so the expanded basis $\{\chi_{\boldsymbol{p}\,i}, \chi_{\boldsymbol{p}\,i'}\}$ gives us a $2n \times 2n$ correlation matrix.

We can factor out the Dirac structure from this correlation matrix. We begin by once again inserting a complete set of states to give (in the absence of backward-running state contributions)

$$\begin{aligned}
\mathcal{G}_{ij}(\boldsymbol{p}\,;t) &= \sum_{B,s} \mathrm{e}^{-E_B(\boldsymbol{p})\,t}\, \langle\Omega|\, \chi_{\boldsymbol{p}\,i}(0)\, |B\,;p\,;s\rangle\, \langle B\,;p\,;s|\, \overline{\chi}_{\boldsymbol{p}\,j}(0)\, |\Omega\rangle \,, && (4.22\text{a})\\
\mathcal{G}_{ij'}(\boldsymbol{p}\,;t) &= \sum_{B,s} \mathrm{e}^{-E_B(\boldsymbol{p})\,t}\, \langle\Omega|\, \chi_{\boldsymbol{p}\,i}(0)\, |B\,;p\,;s\rangle\, \langle B\,;p\,;s|\, \overline{\chi}_{\boldsymbol{p}\,j'}(0)\, |\Omega\rangle \,, && (4.22\text{b})\\
\mathcal{G}_{i'j}(\boldsymbol{p}\,;t) &= \sum_{B,s} \mathrm{e}^{-E_B(\boldsymbol{p})\,t}\, \langle\Omega|\, \chi_{\boldsymbol{p}\,i'}(0)\, |B\,;p\,;s\rangle\, \langle B\,;p\,;s|\, \overline{\chi}_{\boldsymbol{p}\,j}(0)\, |\Omega\rangle \,, && (4.22\text{c})\\
\mathcal{G}_{i'j'}(\boldsymbol{p}\,;t) &= \sum_{B,s} \mathrm{e}^{-E_B(\boldsymbol{p})\,t}\, \langle\Omega|\, \chi_{\boldsymbol{p}\,i'}(0)\, |B\,;p\,;s\rangle\, \langle B\,;p\,;s|\, \overline{\chi}_{\boldsymbol{p}\,j'}(0)\, |\Omega\rangle \,, && (4.22\text{d})
\end{aligned}$$

where the sum over $B$ includes both $B^+$ and $B^-$ states. We can then substitute in the expressions for the interpolator couplings from Eq. (4.20), once again take the spin sum and use the relation

$$\Gamma_{\boldsymbol{p}}\,(-i\,\gamma^\mu\,p^\mu + m_B)\,\Gamma_{\boldsymbol{p}} = \Gamma_{\boldsymbol{p}}\,(E_B(\boldsymbol{p}) + m_B) \qquad (4.23)$$

to write

$$\begin{aligned}
\mathcal{G}_{ij}(\boldsymbol{p}\,;t) =& \sum_{B^+} \mathrm{e}^{-E_{B^+}(\boldsymbol{p})\,t}\, \lambda_{B^+i}(\boldsymbol{p})\, \lambda_{B^+j}(\boldsymbol{p})\, \Gamma_{\boldsymbol{p}}\, \frac{-i\,\gamma^\mu\,p^\mu + m_{B^+}}{2E_{B^+}(\boldsymbol{p})}\, \Gamma_{\boldsymbol{p}}\\
&+ \sum_{B^-} \mathrm{e}^{-E_{B^-}(\boldsymbol{p})\,t}\, \lambda_{B^-i}(\boldsymbol{p})\, \lambda_{B^-j}(\boldsymbol{p})\, \left(\frac{E_{B^-}(\boldsymbol{p}) - m_{B^-}}{E_{B^-}(\boldsymbol{p}) + m_{B^-}}\right) \Gamma_{\boldsymbol{p}}\, \frac{-i\,\gamma^\mu\,p^\mu + m_{B^-}}{2E_{B^-}(\boldsymbol{p})}\, \Gamma_{\boldsymbol{p}}\\
=& \,\Gamma_{\boldsymbol{p}} \left[\sum_{B^\pm} \mathrm{e}^{-E_{B^\pm}(\boldsymbol{p})\,t}\, \lambda_{B^\pm i}(\boldsymbol{p})\, \lambda_{B^\pm j}(\boldsymbol{p})\, \frac{E_{B^\pm}(\boldsymbol{p}) \pm m_{B^\pm}}{2E_{B^\pm}(\boldsymbol{p})}\right], \qquad (4.24\text{a})\\
\mathcal{G}_{ij'}(\boldsymbol{p}\,;t) =& \,\mathcal{G}_{i'j}(\boldsymbol{p}\,;t)\\
=& \sum_{B^\pm} \mathrm{e}^{-E_{B^\pm}(\boldsymbol{p})\,t}\, \lambda_{B^\pm i}(\boldsymbol{p})\, \lambda_{B^\pm j}(\boldsymbol{p})\, \frac{|\boldsymbol{p}|}{E_{B^\pm}(\boldsymbol{p}) + m_{B^\pm}}\, \Gamma_{\boldsymbol{p}}\, \frac{-i\,\gamma^\mu\,p^\mu + m_{B^\pm}}{2E_{B^\pm}(\boldsymbol{p})}\, \Gamma_{\boldsymbol{p}}\\
=& \,\Gamma_{\boldsymbol{p}} \left[\sum_{B^\pm} \mathrm{e}^{-E_{B^\pm}(\boldsymbol{p})\,t}\, \lambda_{B^\pm i}(\boldsymbol{p})\, \lambda_{B^\pm j}(\boldsymbol{p})\, \frac{|\boldsymbol{p}|}{2E_{B^\pm}(\boldsymbol{p})}\right], \qquad (4.24\text{b})\\
\mathcal{G}_{i'j'}(\boldsymbol{p}\,;t) =& \sum_{B^+,s} \mathrm{e}^{-E_{B^+}(\boldsymbol{p})\,t}\, \lambda_{B^+i}(\boldsymbol{p})\, \lambda_{B^+j}(\boldsymbol{p})\, \left(\frac{E_{B^+}(\boldsymbol{p}) - m_{B^+}}{E_{B^+}(\boldsymbol{p}) + m_{B^+}}\right) \Gamma_{\boldsymbol{p}}\, \frac{-i\,\gamma^\mu\,p^\mu + m_{B^+}}{2E_{B^+}(\boldsymbol{p})}\, \Gamma_{\boldsymbol{p}}\\
&+ \sum_{B^-,s} \mathrm{e}^{-E_{B^-}(\boldsymbol{p})\,t}\, \lambda_{B^-i}(\boldsymbol{p})\, \lambda_{B^-j}(\boldsymbol{p})\, \Gamma_{\boldsymbol{p}}\, \frac{-i\,\gamma^\mu\,p^\mu + m_{B^-}}{2E_{B^-}(\boldsymbol{p})}\, \Gamma_{\boldsymbol{p}}\\
=& \,\Gamma_{\boldsymbol{p}} \left[\sum_{B^\pm} \mathrm{e}^{-E_{B^\pm}(\boldsymbol{p})\,t}\, \lambda_{B^\pm i}(\boldsymbol{p})\, \lambda_{B^\pm j}(\boldsymbol{p})\, \frac{E_{B^\pm}(\boldsymbol{p}) \mp m_{B^\pm}}{2E_{B^\pm}(\boldsymbol{p})}\right]. \qquad (4.24\text{c})
\end{aligned}$$

Noting that $\mathrm{Tr}(\Gamma_{\boldsymbol{p}}) = 1$, the spinor trace of the correlation matrix

$$G(\boldsymbol{p}\,;t) \equiv \mathrm{Tr}\ \mathcal{G}(\boldsymbol{p}\,;t)\,, \tag{4.25}$$

obeys the relation $\mathcal{G}(\boldsymbol{p}\,;t) = \Gamma_{\boldsymbol{p}}\,G(\boldsymbol{p}\,;t)$. We can take this traced correlation matrix $G(\boldsymbol{p}\,;t)$ and perform a variational analysis as outlined in Chapter 2, producing optimised interpolators $\phi_{\boldsymbol{p}\,B}(x)$ for each of the $2n$ states accessible via the chosen operator basis. By inspecting the generalised eigenvectors corresponding to one of these states, we can gain insight into its rest-frame parity and parity mixing. At zero momentum, a parity eigenstate should only have nonzero eigenvector components for PEVA interpolators corresponding to the same parity. The interpolating fields corresponding to the opposite parity couple to an entirely distinct set of states and thus their eigenvector components should be zero. At non-zero momentum, the eigenvector components corresponding to opposite-parity interpolators should be non-zero, and give insight into the opposite-parity contaminations.

In the case of non-negligible backward-running states on a periodic or anti-periodic lattice with temporal extent $L_t$, we can generalise Eq. (4.22) to include the backward-running baryons as in the meson case [93]

$$\begin{aligned}
\mathcal{G}_{ij}(\boldsymbol{p}\,;t) =& \sum_{B,s} \mathrm{e}^{-E_B(\boldsymbol{p})\,t}\,\langle\Omega|\,\chi_{\boldsymbol{p}\,i}(0)\,|B\,;p\,;s\rangle\,\langle B\,;p\,;s|\,\overline{\chi}_{\boldsymbol{p}\,j}(0)\,|\Omega\rangle \\
&\mp \sum_{\overline{B},s} \mathrm{e}^{-E_B(\boldsymbol{p})\,(L_t-t)}\,\langle\Omega|\,\overline{\chi}_{\boldsymbol{p}\,j}(0)\,|\overline{B};p\,;s\rangle\,\langle\overline{B};p\,;s|\,\chi_{\boldsymbol{p}\,i}(0)\,|\Omega\rangle\ , \qquad (4.26)\\
\mathcal{G}_{ij'}(\boldsymbol{p}\,;t) =& \sum_{B,s} \mathrm{e}^{-E_B(\boldsymbol{p})\,t}\,\langle\Omega|\,\chi_{\boldsymbol{p}\,i}(0)\,|B\,;p\,;s\rangle\,\langle B\,;p\,;s|\,\overline{\chi}_{\boldsymbol{p}\,j'}(0)\,|\Omega\rangle \\
&\mp \sum_{\overline{B},s} \mathrm{e}^{-E_B(\boldsymbol{p})\,(L_t-t)}\,\langle\Omega|\,\overline{\chi}_{\boldsymbol{p}\,j'}(0)\,|\overline{B};p\,;s\rangle\,\langle\overline{B};p\,;s|\,\chi_{\boldsymbol{p}\,i}(0)\,|\Omega\rangle\ , \qquad (4.27)\\
\mathcal{G}_{i'j}(\boldsymbol{p}\,;t) =& \sum_{B,s} \mathrm{e}^{-E_B(\boldsymbol{p})\,t}\,\langle\Omega|\,\chi_{\boldsymbol{p}\,i'}(0)\,|B\,;p\,;s\rangle\,\langle B\,;p\,;s|\,\overline{\chi}_{\boldsymbol{p}\,j}(0)\,|\Omega\rangle \\
&\mp \sum_{\overline{B},s} \mathrm{e}^{-E_B(\boldsymbol{p})\,(L_t-t)}\,\langle\Omega|\,\overline{\chi}_{\boldsymbol{p}\,j}(0)\,|\overline{B};p\,;s\rangle\,\langle\overline{B};p\,;s|\,\chi_{\boldsymbol{p}\,i'}(0)\,|\Omega\rangle\ , \qquad (4.28)\\
\mathcal{G}_{i'j'}(\boldsymbol{p}\,;t) =& \sum_{B,s} \mathrm{e}^{-E_B(\boldsymbol{p})\,t}\,\langle\Omega|\,\chi_{\boldsymbol{p}\,i'}(0)\,|B\,;p\,;s\rangle\,\langle B\,;p\,;s|\,\overline{\chi}_{\boldsymbol{p}\,j'}(0)\,|\Omega\rangle \\
&\mp \sum_{\overline{B},s} \mathrm{e}^{-E_B(\boldsymbol{p})\,(L_t-t)}\,\langle\Omega|\,\overline{\chi}_{\boldsymbol{p}\,j'}(0)\,|\overline{B};p\,;s\rangle\,\langle\overline{B};p\,;s|\,\chi_{\boldsymbol{p}\,i'}(0)\,|\Omega\rangle\ , \qquad (4.29)
\end{aligned}$$

where the source is taken to be on the boundary, at $t = 0$, and the sign of the second term reflects periodic/anti-periodic boundary conditions respectively.

The interpolator overlaps for the backward-running baryons $\overline{B}$ are given by

$$\langle\overline{B}^{+};p\,;s|\,\chi_{\boldsymbol{p}\,i}\,|\Omega\rangle = \lambda_{B^{-}i}(\boldsymbol{p})\,\sqrt{\frac{m_{B^{-}}}{E_{B^{-}}(\boldsymbol{p})}}\,\Gamma_{\boldsymbol{p}}\,\gamma^{5}\,v_{\overline{B}^{+}}(p,s)\,, \tag{4.30a}$$

$$\langle \overline{B}^{-} ; p \,; s |\, \chi_{\boldsymbol{p}\, i} \,|\Omega\rangle = \lambda_{B^{+} i}(\boldsymbol{p}) \, \frac{|\boldsymbol{p}|}{E_{B^{-}}(\boldsymbol{p}) + m_{B^{-}}} \sqrt{\frac{m_{B^{+}}}{E_{B^{+}}(\boldsymbol{p})}} \, \Gamma_{\boldsymbol{p}} \, \gamma^{5} \, v_{\overline{B}^{-}}(p, s) \,, \tag{4.30b}$$

$$\langle \overline{B}^{+} ; p \,; s |\, \chi_{\boldsymbol{p}\, i} \,|\Omega\rangle = \lambda_{B^{-} i}(\boldsymbol{p}) \, \frac{|\boldsymbol{p}|}{E_{B^{-}}(\boldsymbol{p}) + m_{B^{-}}} \sqrt{\frac{m_{B^{-}}}{E_{B^{-}}(\boldsymbol{p})}} \, \Gamma_{\boldsymbol{p}} \, \gamma^{5} \, v_{\overline{B}^{+}}(p, s) \,, \tag{4.30c}$$

$$\langle \overline{B}^{-} ; p \,; s |\, \chi_{\boldsymbol{p}\, i} \,|\Omega\rangle = \lambda_{B^{+} i}(\boldsymbol{p}) \sqrt{\frac{m_{B^{+}}}{E_{B^{+}}(\boldsymbol{p})}} \, \Gamma_{\boldsymbol{p}} \, \gamma^{5} \, v_{\overline{B}^{-}}(p, s) \,. \tag{4.30d}$$

With these definitions, the formalism described above may be applied in the same manner, noting

$$\sum_{s} v_{\overline{B}^{\pm}}(p, s) \, \overline{v}_{\overline{B}^{\pm}}(p, s) = -\frac{i \, \gamma^{\mu} \, p^{\mu} + m_{B^{\mp}}}{2 m_{B^{\mp}}} \,. \tag{4.31}$$

The backward-running states will appear as opposite-parity partners to each of the forward-running states. Due to their time dependence on $L_t - t$ instead of $t$, these states will have negative effective energies, and their couplings will be effectively suppressed by a factor of $\mathrm{e}^{-E_B(\boldsymbol{p})\, L_t}$. Thus, given a sufficiently large interpolator basis, the PEVA technique can be used unmodified to simultaneously isolate both forward and backward-running states.

### 4.3.2 Calculation at the Quark Level

To simplify the numerical calculation of $G(\boldsymbol{p} \,; t)$, we use the idempotence of $\Gamma_{\boldsymbol{p}}$ and the invariance of the trace operation under cyclic permutations to rewrite it as

$$\begin{aligned}
G_{ij}(\boldsymbol{p} \,; t) &= \mathrm{Tr}\left( \sum_{\boldsymbol{x}} \mathrm{e}^{-i\boldsymbol{p}\cdot\boldsymbol{x}} \; \langle\Omega|\, \Gamma_{\boldsymbol{p}} \, \chi_i(x) \, \overline{\chi}_j(0) \, \Gamma_{\boldsymbol{p}} \,|\Omega\rangle \right) \\
&= \mathrm{Tr}\left( \Gamma_{\boldsymbol{p}} \sum_{\boldsymbol{x}} \mathrm{e}^{-i\boldsymbol{p}\cdot\boldsymbol{x}} \; \langle\Omega|\, \chi_i(x) \; \overline{\chi}_j(0) \,|\Omega\rangle \right) \\
&= G_{ij}(\Gamma_{\boldsymbol{p}} \,; \boldsymbol{p} \,; t) \,, && (4.32\mathrm{a}) \\
G_{ij'}(\boldsymbol{p} \,; t) &= \mathrm{Tr}\left( \sum_{\boldsymbol{x}} \mathrm{e}^{-i\boldsymbol{p}\cdot\boldsymbol{x}} \; \langle\Omega|\, \Gamma_{\boldsymbol{p}} \, \chi_i(x) \left( -\overline{\chi}_j(0) \, \gamma^5 \, \Gamma_{\boldsymbol{p}} \right) |\Omega\rangle \right) \\
&= \mathrm{Tr}\left( -\gamma^5 \, \Gamma_{\boldsymbol{p}} \sum_{\boldsymbol{x}} \mathrm{e}^{-i\boldsymbol{p}\cdot\boldsymbol{x}} \; \langle\Omega|\, \chi_i(x) \; \overline{\chi}_j(0) \,|\Omega\rangle \right) \\
&= G_{ij}(-\gamma^5 \, \Gamma_{\boldsymbol{p}} \,; \boldsymbol{p} \,; t) \,, && (4.32\mathrm{b}) \\
G_{i'j}(\boldsymbol{p} \,; t) &= \mathrm{Tr}\left( \sum_{\boldsymbol{x}} \mathrm{e}^{-i\boldsymbol{p}\cdot\boldsymbol{x}} \; \langle\Omega|\, \Gamma_{\boldsymbol{p}} \, \gamma^5 \, \chi_i(x) \, \overline{\chi}_j(0) \, \Gamma_{\boldsymbol{p}} \,|\Omega\rangle \right) \\
&= G_{ij}(\Gamma_{\boldsymbol{p}} \, \gamma^5 \,; \boldsymbol{p} \,; t) \,, && (4.32\mathrm{c}) \\
G_{i'j'}(\boldsymbol{p} \,; t) &= \mathrm{Tr}\left( \sum_{\boldsymbol{x}} \mathrm{e}^{-i\boldsymbol{p}\cdot\boldsymbol{x}} \; \langle\Omega|\, \Gamma_{\boldsymbol{p}} \, \gamma^5 \, \chi_i(x) \left( -\overline{\chi}_j(0) \, \gamma^5 \, \Gamma_{\boldsymbol{p}} \right) |\Omega\rangle \right) \\
&= G_{ij}(-\gamma^5 \, \Gamma_{\boldsymbol{p}} \, \gamma^5 \,; \boldsymbol{p} \,; t) \,, && (4.32\mathrm{d})
\end{aligned}$$

Thus if we consider $n$ interpolators, $\chi_i$, $i = 1, \ldots, n$, we can calculate each of the four $n \times n$ blocks of our full $2n \times 2n$ correlation matrix simply by taking the spinor trace of the unprojected correlators with the appropriate combination of $\Gamma_{\boldsymbol{p}}$ and $\gamma^5$, much like we would with $\Gamma_\pm$ in a conventional parity projection at $\boldsymbol{p} = 0$.

At zero momentum, the off-diagonal blocks $G_{ij'}(\boldsymbol{p}\,;t)$ and $G_{i'j}(\boldsymbol{p}\,;t)$ will be zero, as they are proportional to $|\boldsymbol{p}|$, so we can treat the top-left and bottom-right blocks separately. Since at zero momentum $\chi_{\boldsymbol{p}\,i}$ couples only to positive-parity states and $\chi_{\boldsymbol{p}\,i'}$ couples only to negative-parity states, the top-left block will contain only positive-parity states and the bottom-right only negative. Thus, we can effectively solve the generalised eigenvalue equation for the positive and negative parity sectors separately. This is equivalent to the conventional parity-projected analysis using $\Gamma^\pm = \frac{1}{2}(\gamma^4 \pm \mathbb{I})$. However, at non-zero momentum there will be contributions from states of both parities in all four blocks, and the conventional technique will suffer from opposite-parity contaminations. This is where the expanded basis of the PEVA technique is necessary to correctly isolate energy eigenstates of both rest-frame parities.

## 4.4 Results

As a first investigation of the PEVA approach, we isolate the four lowest lying states of the nucleon excited by local three-quark operators on the lattice: the ground state, the first two negative-parity excitations, and the first positive-parity excitation observed at $\sim$1.9 GeV. We use the PEVA technique to expand an $8 \times 8$ correlation matrix to a $16 \times 16$ correlation matrix. We compare the results to those given by conventional parity projectors $\Gamma_+$ and $\Gamma_-$ acting on the original $8 \times 8$ correlation matrix. The original eight-interpolator basis is formed from the conventional spin-½ nucleon interpolators

$$\begin{aligned}\chi_1 =& \epsilon^{abc}[u^{a\top}\,(C\gamma^5)\,d^b]u^c\,, \text{ and}\\ \chi_2 =& \epsilon^{abc}[u^{a\top}\,(C)\,d^b]\gamma^5 u^c\,,\end{aligned} \tag{4.33}$$

with 16, 35, 100, or 200 sweeps of gauge-invariant Gaussian smearing [51] with a smearing fraction of $\alpha = 0.7$, applied at the quark source and sinks in creating the propagators. This smearing technique is described in Chapter 2. Before performing the Gaussian smearing, the gauge links to be used are smoothed by applying four sweeps of four-dimensional isotropic stout-link smearing [94] with $\rho = 0.1$. For each level of Gaussian smearing, we calculate 3200 quark propagators by making use of circular shifts of the gauge fields to access a total of eight source locations on each of the 400 gauge field configurations. We perform both analyses and extract the effective energies of the states at the seven momenta described in Table 4.1, ranging from $\boldsymbol{p}^2 = 0.166\,\mathrm{GeV}^2$ to $\boldsymbol{p}^2 = 0.996\,\mathrm{GeV}^2$.

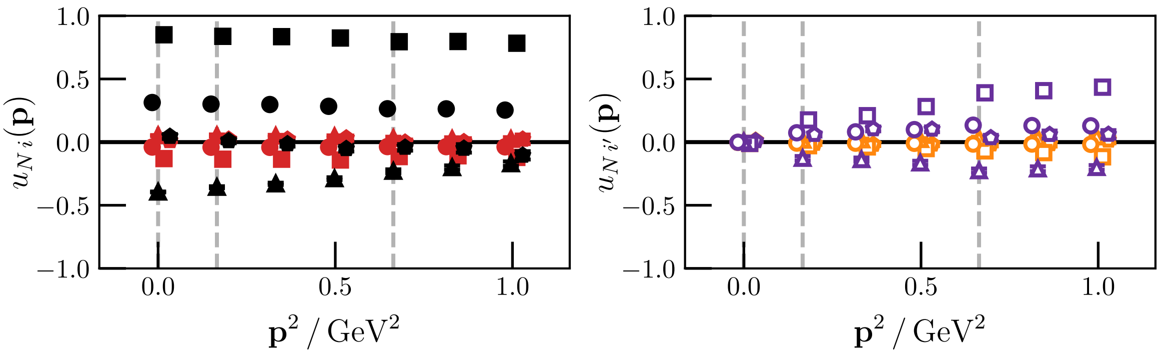

(a) The positive parity ground-state nucleon.

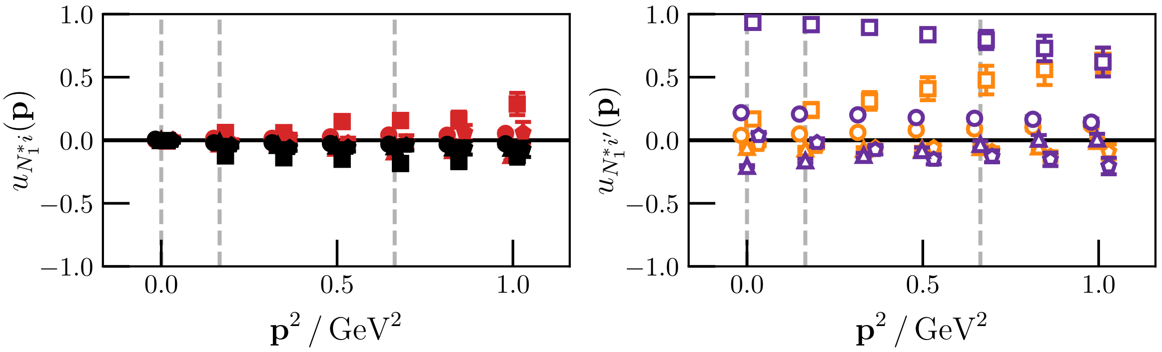

(b) The first negative-parity excitation of the nucleon.

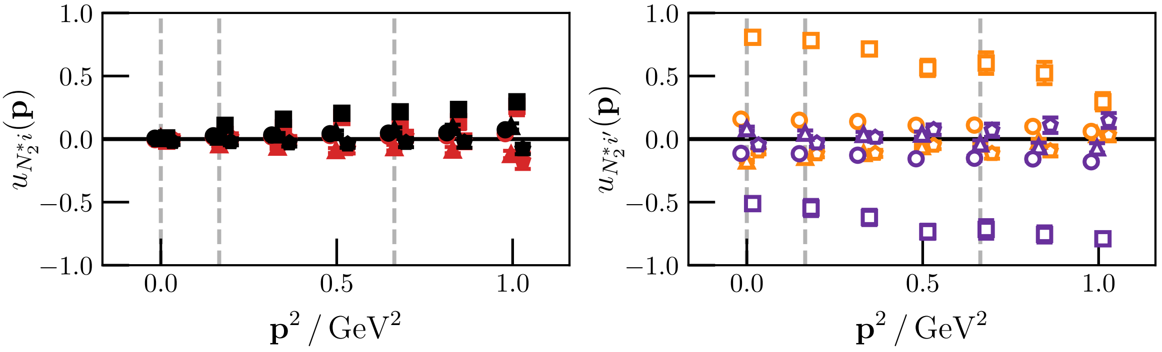

(c) The second negative-parity excitation of the nucleon.

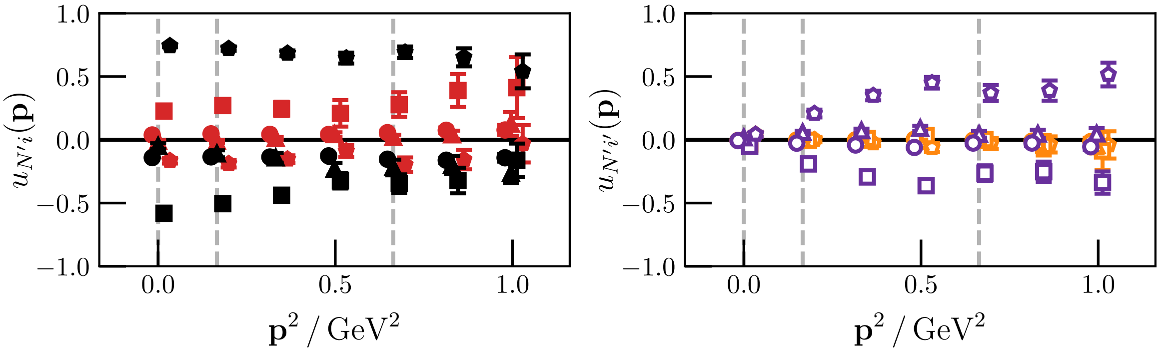

(d) The first positive-parity excitation of the nucleon.

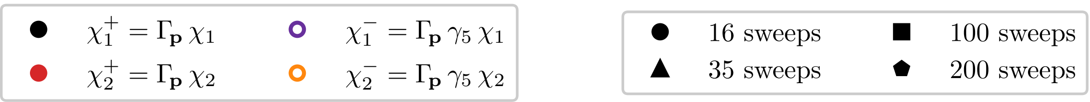

Figure 4.1: Momentum-squared dependence of the PEVA eigenvectors associated with the ground-state nucleon and first three excitations. Vertical dashed lines denote the on-axis momenta.

Table 4.1: Momenta used in this analysis. Physical units are obtained from the lattice momentum $\boldsymbol{p}_{lat}$ by multiplying by $2\pi/32a$, with $a = 0.0951\,\text{fm}$

| # | $\boldsymbol{p}_{lat}$ | $\boldsymbol{p}^2\,/\,\text{GeV}^2$ |
|---|---|---|
| 1 | $(0,0,0)$ | 0.000 |
| 2 | $(1,0,0)$ | 0.166 |
| 3 | $(1,1,0)$ | 0.332 |
| 4 | $(1,1,1)$ | 0.498 |
| 5 | $(2,0,0)$ | 0.664 |
| 6 | $(2,1,0)$ | 0.830 |
| 7 | $(2,1,1)$ | 0.996 |

We can gain insight into the amount of “leakage” between different parity sectors by examining the eigenvectors produced by the variational analysis. The primary indicator of this “leakage” is the magnitude of the elements corresponding to interpolators of the opposite parity to the state being isolated. In Fig. 4.1 we plot the eigenvector components of the four lowest-lying states isolated by the 16 × 16 PEVA correlation matrix at each of the seven momenta. The coloration of the data points correspond to the interpolator structure associated with that component of the eigenvector ($\chi_1^+ = \Gamma_{\boldsymbol{p}}\,\chi_1$, $\chi_2^+ = \Gamma_{\boldsymbol{p}}\,\chi_2$, $\chi_1^- = \Gamma_{\boldsymbol{p}}\,\gamma^5\,\chi_1$, or $\chi_2^- = \Gamma_{\boldsymbol{p}}\,\gamma^5\,\chi_2$) and the shapes of the data points correspond to the number of sweeps of gauge-invariant Gaussian smearing applied in creating the propagators.

If we start by examining the first extracted state, shown in Fig. 4.1a, we see that the eigenvectors at all momenta are dominated by the components in the left-hand plot, corresponding to the positive-parity interpolators. In particular, at zero momentum, the contributions from the negative-parity interpolators (in the right-hand plot) are consistent with zero. This clearly indicates that it is a positive-parity state, as expected for the ground-state nucleon. If we now look at the next extracted state, shown in Fig. 4.1b, we see that this time the eigenvectors are dominated by the components in the right-hand plot, corresponding to the negative-parity interpolators, and the contribution from positive-parity interpolators at zero momentum is consistent with zero. This clearly indicates that this is a negative-parity state, the first negative-parity excitation of the nucleon. The next two states, shown in Fig. 4.1c and 4.1d, show similarly clear parity signals, corresponding to the second negative-parity and the first positive-parity excitation of the nucleon respectively.

While the contributions from opposite-parity interpolators at zero momentum are consistent with zero, at non-zero momentum we see statistically significant contributions from interpolators of both parities. This is observed for all four states, even at a single lattice unit of momentum. This demonstrates that parity mixing has a significant effect on the optimised interpolator structure of states at all non-zero momenta accessible on the lattice. This will have non-trivial implications for calculating three-point functions, but it is informative to first consider the simplest case of two-point functions and determinations of the effective energy.

For each state, we fit the effective energy of the eigenstate-projected correlators at $\boldsymbol{p} = (0,0,0)$ with a single-state ansatz and find a fit window which produces an acceptable $\chi^2/\text{dof}$. We then step through the lattice momenta listed in Table 4.1 in ascending order, keeping the lower bound of the fit window fixed. The upper bound of the fit window is reduced as necessary to remove excessively noisy points. Due to the block-diagonal nature of the PEVA correlation matrix at zero momentum, the same eigenstate-projected correlators are produced at $\boldsymbol{p} = (0,0,0)$ by both the $16 \times 16$ PEVA correlation matrix and the conventional $8 \times 8$ correlation matrices. Hence, this process results in the same fit windows for states extracted by both methods. For both methods, the $\chi^2/\text{dof}$ is calculated for each fit to our single state ansatz.

Figure 4.2 provides a comparison of the states extracted by the conventional $8 \times 8$ correlation matrices and the states extracted by the $16 \times 16$ PEVA correlation matrix. The upper plot of Fig. 4.2 shows the effective energies for each state as a function of momentum. Due to the localised nature of our interpolators, and hence the states they couple to, we expect the effective energies of the extracted states to approximately follow the dispersion relation $E_\alpha(\boldsymbol{p}) \approx \sqrt{{m_\alpha}^2 + \boldsymbol{p}^2}$. This dispersion relation is plotted on the graph as a shaded band for each state $\alpha$, with $m_\alpha$ set by the effective energy at $\boldsymbol{p} = (0,0,0)$. The lower plot of Fig. 4.2 shows the $\chi^2/\text{dof}$ values for each of these fits. Contamination of our projected states shows up as a failure of the single state ansatz as indicated by a high $\chi^2/\text{dof}$.

We see an acceptable $\chi^2/\text{dof}$ distribution for all fits other than those for the first negative-parity excitation extracted by the conventional $\Gamma_-$ projected $8 \times 8$ correlation matrix (open orange triangles). For the ground state, the faster-decaying exponential dependence of excited-state contaminations means that the effective energy can be extracted reasonably well even when contaminated by opposite parity states.

The effective energies of the first positive-parity excitation and the second negative-parity excitation also do not appear to suffer from significant cross-parity contamination effects. However, the eigenvector structure shown in Fig. 4.1c and 4.1d suggests that these states do have non-trivial opposite parity contributions at finite momentum. A possible explanation for this is that the contaminating state or states are close in energy to the eigenstate being projected, so they do not significantly change the two-point correlator. Since these two states have opposite parities and similar energies, this seems to be a reasonable assumption. We will see in Chapter 6, in which we investigate the form factors of these states, that there are indeed large opposite-parity contaminations in the excitations extracted via the conventional analysis.

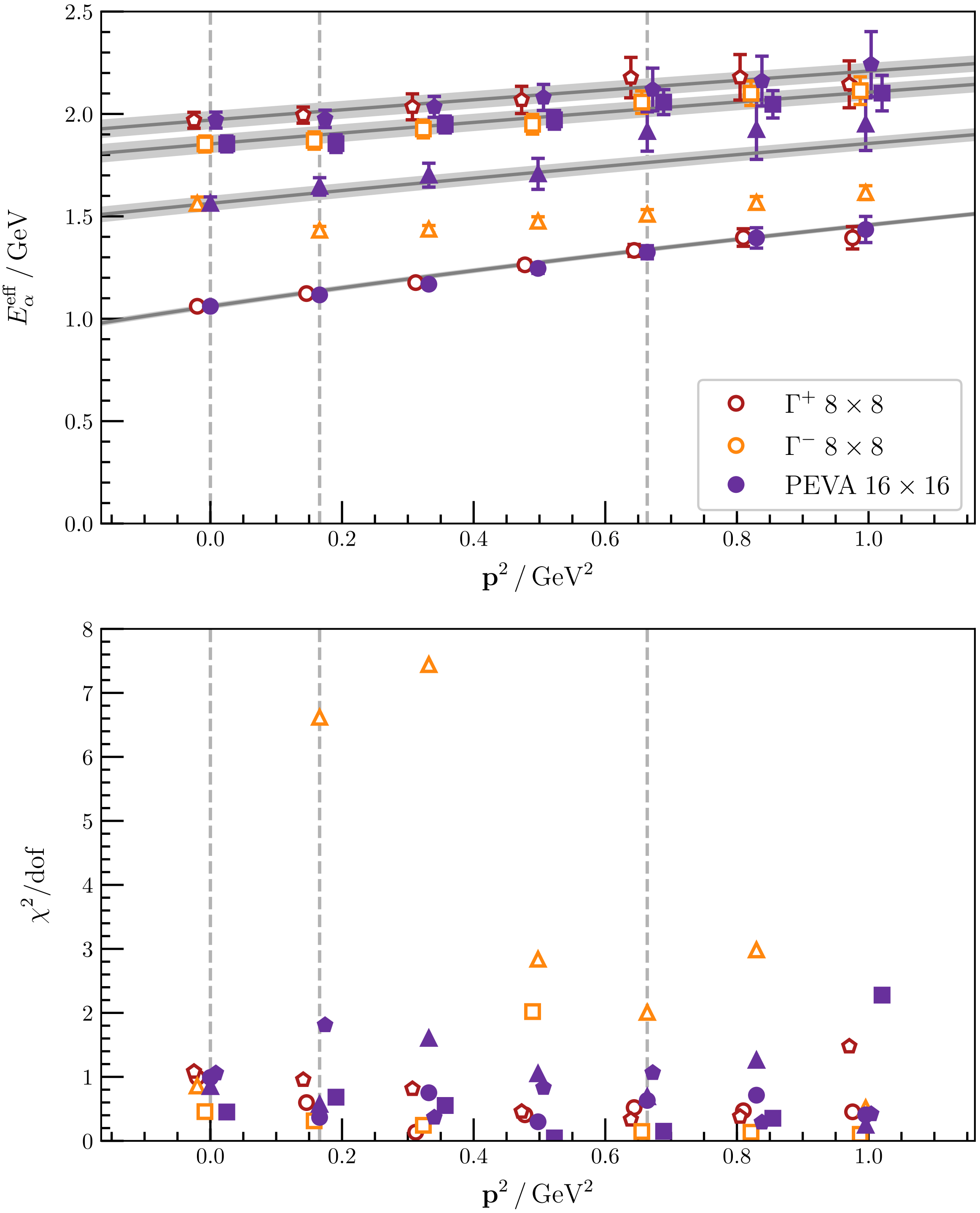

Figure 4.2: Momentum-squared dependence of the effective energy fits (upper) and associated $\chi^2$/dof (lower) for the ground state (○), first (△) and second (□) negative parity excitations, and first positive-parity excitation (⬠) of the nucleon. Results are plotted for both the full 16 × 16 PEVA technique (filled blue points) and the conventional 8 × 8 analyses projected by $\Gamma^+$ (open red points) and $\Gamma^-$ (open orange points). Shaded bands indicate the expected dispersion relation ($E_\alpha(\boldsymbol{p}) = \sqrt{m_\alpha{}^2 + \boldsymbol{p}^2}$). The ground state and first negative-parity excitation extracted by the PEVA technique are displayed at the actual momenta used, while other points are offset where necessary for clarity.

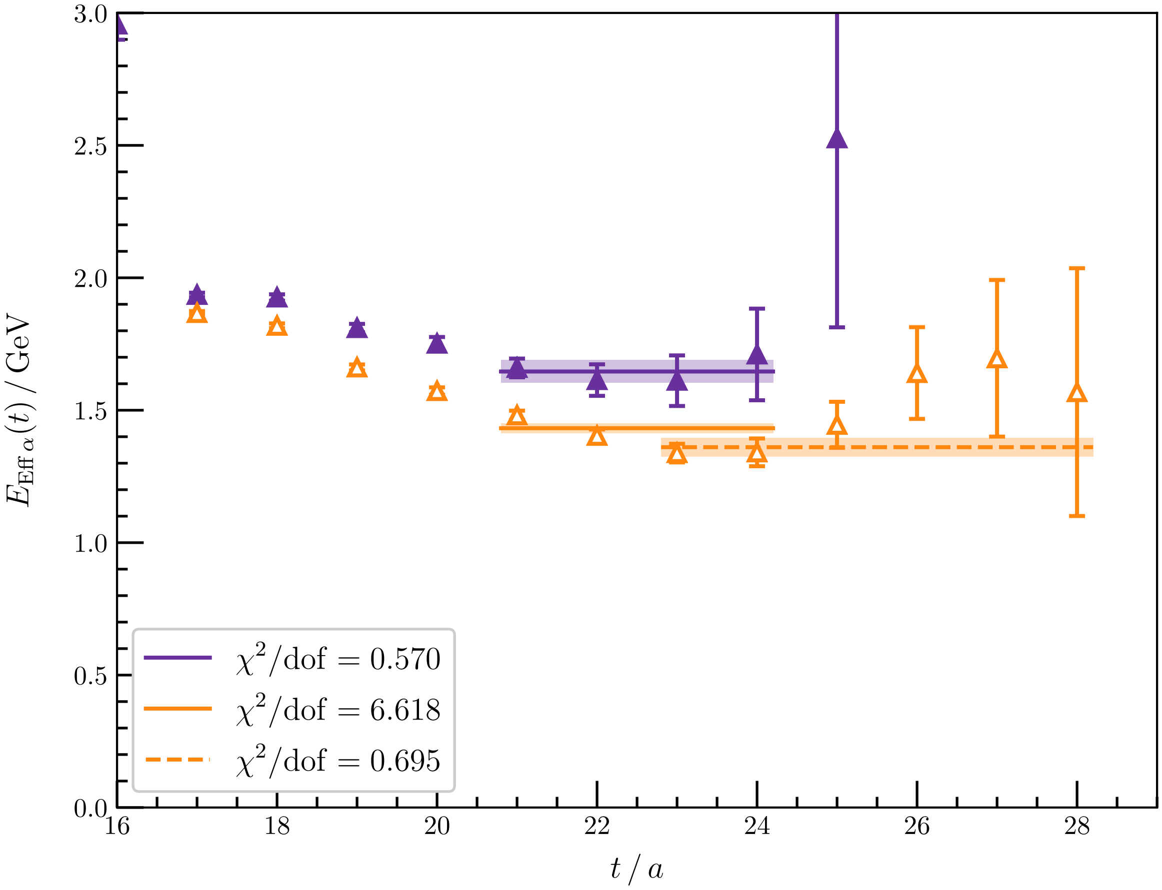

Figure 4.3: Euclidean time dependence of the effective energy of the first negative-parity excitation at $\boldsymbol{p} = (1, 0, 0)$ ($\boldsymbol{p}^2 = 0.166\,\mathrm{GeV}^2$). The effective energy of the state isolated by the conventional $8 \times 8$ correlation matrix (open orange symbols) has a clear non-trivial time dependence all the way up to the point where the signal disappears into noise, with no clear plateau. It lies significantly below the state projected by the $16 \times 16$ PEVA correlation matrix (filled blue symbols). The fits indicated by the solid lines are obtained using the systematic method described in Section 4.4 and give the values used in Fig. 4.2. In the case of the conventional $8 \times 8$ correlation matrix, this fit has an unfavourable $\chi^2$/dof of 6.6, indicating multiple states are present in the correlator. A significant deviation from the systematic approach used here would allow us to move the lower bound of the fit window to a later time slice of $t/a = 24$, and take advantage of the degradation of the signal-to-noise ratio to find an acceptable $\chi^2$/dof. This fit, indicated by the dashed line, has a $\chi^2$/dof of 0.70 and a value of $1.36 \pm 0.04(\mathrm{stat.}) \pm 0.14(\mathrm{sys.})$, where the estimate of the systematic error is obtained by considering multiple fit windows with acceptable $\chi^2$/dof.

In the case of the first negative-parity excitation, significant opposite-parity contamination is manifest in the effective energies. For the conventional 8 × 8 correlation matrix analysis the extracted effective energies lie between the dispersion relations for the first negative-parity excitation and the ground state, which along with high $\chi^2/\text{dof}$ values clearly indicates contamination by the (opposite parity) ground state. By contrast the PEVA technique provides fits with an acceptable $\chi^2/\text{dof}$ distribution that closely follow the expected dispersion relation. This clearly demonstrates removal of these opposite-parity contaminations and clean isolation of this state, as illustrated in Fig. 4.3.

It should be noted that the excited states reported here lie near or above a number of infinite-volume multi-particle scattering state thresholds with the same quantum numbers. In isolating the states reported here, only localised three-quark operators are used. Without the use of multi-hadron operators, we are unable to isolate non-local multi-particle scattering states [95, 96]. Hence, it is possible for such states to contaminate the localised states we do isolate.

However, the observed satisfaction of the single-state ansatz suggests that such contaminations are small. Our most comprehensive analysis of the sensitivity of the excited state spectrum to missing states demonstrates that single-state fits to projected correlators are robust, even when lower-lying states are missing [15]. Hence, while the inclusion of multi-hadron operators is desirable for precision studies of these states, the basis used here is sufficient for a first study of the effects of opposite-parity contaminations.

## 4.5 Conclusion

We have shown that conventional baryon spectroscopy methods applied at non-zero momentum can produce correlators that are significantly contaminated by opposite parity states. This could in turn lead to significant errors in the determination of three-point correlation functions. We present the PEVA technique to address and resolve this issue. The method is equivalent to conventional parity-projection methods at zero momentum, but at non-zero momentum effectively removes opposite parity contaminations. This can have a marked effect on two-point correlation functions, such as that for the lowest-lying negative-parity excitation of the nucleon as shown in Section 4.4. The approach is cost effective as the basis expansion amounts to simply pre- or post-multiplying (or both) the projection matrix $\Gamma_{\boldsymbol{p}}$ by $\gamma^5$. The PEVA technique isolates non-zero-momentum energy eigenstates while maintaining a signature of the state's rest-frame parity, key to understanding the content of finite momentum spectra in lattice QCD.

# Chapter 5

# Form Factors of the Proton and Neutron

*Some of the content in this chapter is based on the conference proceeding: "Electromagnetic Form Factors of Excited Nucleons via Parity-Expanded Variational Analysis" by F. M. Stokes et al. [97]*

## 5.1 Introduction

In Chapter 4 we established both the importance and the effectiveness of the PEVA technique at isolating individual baryons on the lattice at a range of momenta. The logical next step is to investigate the structure of these states and determine the importance of the PEVA technique to extracting the correct results. We can do this by probing the states of interest with some external current, for example the vector current $j^\mu$. As outlined in Chapter 2, the response of the states to such a current can be parameterised in terms of experimentally measurable quantities known as form factors.

In this chapter we study the Sachs electric and magnetic form factors $G_E(Q^2)$ and $G_M(Q^2)$ of the ground-state proton and neutron. The Sachs form factors describe the response of a baryon to the vector current. At low $Q^2$, these form factors give information about the large-scale electromagnetic structure of the state, such as its charge radius and magnetic moment; at high $Q^2$ they give information about the short-distance internal structure of the state. These form factors can be determined experimentally to high accuracy. Computing them in *ab-initio* lattice QCD provides an important confrontation of theory with experiment.

In addition, computing these form factors on the lattice gives us unique insight into the physics underlying the experimental results. For example, on the lattice it is possible to separately compute the contributions to the form factors from connected diagrams (as studied in this thesis) and disconnected diagrams, giving insight into the role sea quarks play in the structure of the proton and the neutron. One can also alter the electric charges of the quarks, readily illustrating the quark-flavour structure of the nucleon.

We probe the values of these form factors by creating an incoming nucleon on the lattice, having it interact with a vector current with some momentum transfer $\boldsymbol{q}$, and then annihilating the outgoing nucleon with a fixed momentum $\boldsymbol{p}'$. By momentum conservation, the incoming state must have momentum $\boldsymbol{p} = \boldsymbol{p}' - \boldsymbol{q}$. Due to the way we include the vector current on the lattice, we only consider a small number of fixed momentum transfers $\boldsymbol{q}$. By varying the three-momenta of the outgoing state and hence the incoming state, we gain access to the form factors at a range of

$$Q^2 = \boldsymbol{q}^2 - \left(\sqrt{{m_N}^2 + \boldsymbol{p}'^2} - \sqrt{{m_N}^2 + \boldsymbol{p}^2}\right)^2 . \tag{5.1}$$

In particular, these boosts provide access to values close to $Q^2 = 0$, well below $|\boldsymbol{q}_{\mathrm{min}}|^2 = (2\pi/L_s)^2$, without requiring the use of twisted boundary conditions. By accessing a range of values, we gain insight into the $Q^2$ dependence of the form factors, and can make a comparison with various models and experiment. By studying the low-$Q^2$ dependence of the electric form factor, we can make an *ab-initio* determination of the charge radius of the proton. In addition, we observe that when considering the contributions from each quark flavour independently, $G_E(Q^2)$ and $G_M(Q^2)$ have a similar $Q^2$ dependence in the range considered. Hence, we can access the magnetic dipole moments of the proton and neutron by taking ratios of the quark-sector form factors.

## 5.2 Baryon matrix elements

In this section, we establish the formalism to extend the PEVA technique to the computation of baryon form factors. Both the original PEVA technique and its extension to form factor calculations are original work developed for this thesis. To perform the extension, we consider three-point correlation functions, inspecting their Dirac structure to extract the signal of interest. We then take ratios with two point functions to remove the time dependence and cancel out dependence on the interpolator couplings. The calculations are performed in the most generalised kinematics that can be realised.

Due to a lattice Ward identity associated with the conserved current, the three-point correlation functions for the electric form factor normalised to unit charge must approach the two-point correlation functions exactly on a configuration-by-configuration basis as $Q^2 \to 0$. As a result, the two- and three-point correlation functions are highly correlated at low $Q^2$. The ratios we take facilitate the cancellation of statistical fluctuations, significantly reducing the statistical uncertainties in our extracted form factors.

By performing a parity-expanded variational analysis as described in Chapter 4, we construct optimised operators $\phi_{\boldsymbol{p}\,\alpha}(x)$ that couple to each state $\alpha$. When defining

$$\Gamma_{\boldsymbol{p}} \equiv \frac{1}{4}\left(\mathbb{I}+\gamma^4\right)\left(\mathbb{I}-i\gamma^5\gamma^k\widehat{\boldsymbol{p}}^k\right) , \tag{5.2}$$

we make an arbitrary sign choice in the $i\gamma^5\gamma^k\widehat{\boldsymbol{p}}^k$ term, so it is convenient to define the equally valid projector

$$\Gamma'_{\boldsymbol{p}} \equiv \frac{1}{4}\left(\mathbb{I}+\gamma^4\right)\left(\mathbb{I}+i\gamma^5\gamma^k\widehat{\boldsymbol{p}}^k\right) = \Gamma_{-\boldsymbol{p}} , \tag{5.3}$$

We can then use this alternate projector in constructing an alternate sink operator $\phi'_{\boldsymbol{p}\,\alpha}(x) = \phi_{-\boldsymbol{p}\,\alpha}(x)$, while leaving the source operator unchanged. The consideration of $\phi'_{\boldsymbol{p}\,\alpha}(x)$ is required to optimise the extraction of the form factors for general kinematics. We can use these operators to calculate the three point correlation functions

$$\mathcal{G}^3_+(\mathcal{J};\boldsymbol{p}',\boldsymbol{p}\,;t_2\,,t_1\,;\alpha) \equiv \sum_{\boldsymbol{x}_2,\boldsymbol{x}_2} \mathrm{e}^{-i\boldsymbol{p}'\cdot\boldsymbol{x}_2}\,\mathrm{e}^{i(\boldsymbol{p}'-\boldsymbol{p})\cdot\boldsymbol{x}_1} \left\langle\Omega\right|\phi_{\boldsymbol{p}'\,\alpha}(x_2)\,\mathcal{J}(x_1)\,\overline{\phi}_{\boldsymbol{p}\,\alpha}(0)\left|\Omega\right\rangle , \tag{5.4}$$

$$\begin{aligned}\mathcal{G}^3_-(\mathcal{J};\boldsymbol{p}',\boldsymbol{p}\,;t_2\,,t_1\,;\alpha) &\equiv \sum_{\boldsymbol{x}_2,\boldsymbol{x}_2} \mathrm{e}^{-i\boldsymbol{p}'\cdot\boldsymbol{x}_2}\,\mathrm{e}^{i(\boldsymbol{p}'-\boldsymbol{p})\cdot\boldsymbol{x}_1} \left\langle\Omega\right|\phi'_{\boldsymbol{p}'\,\alpha}(x_2)\,\mathcal{J}(x_1)\,\overline{\phi}_{\boldsymbol{p}\,\alpha}(0)\left|\Omega\right\rangle \\ &= \sum_{\boldsymbol{x}_2,\boldsymbol{x}_2} \mathrm{e}^{-i\boldsymbol{p}'\cdot\boldsymbol{x}_2}\,\mathrm{e}^{i(\boldsymbol{p}'-\boldsymbol{p})\cdot\boldsymbol{x}_1} \left\langle\Omega\right|\phi_{-\boldsymbol{p}'\,\alpha}(x_2)\,\mathcal{J}(x_1)\,\overline{\phi}_{\boldsymbol{p}\,\alpha}(0)\left|\Omega\right\rangle , \end{aligned}\tag{5.5}$$

where $\mathcal{J}(x)$ is some current operator, which is inserted with a momentum transfer $\boldsymbol{q} = \boldsymbol{p}' - \boldsymbol{p}$.

By inserting the complete set of states

$$\mathbb{I} = \sum_{B,p,s} \left|B\,;p\,;s\right\rangle\left\langle B\,;p\,;s\right| \tag{5.6}$$

on either side of the current, and noting the use of Euclidean time and fixed boundary conditions (or negligible backward-running state contributions), we can rewrite this three point correlation function as

$$\begin{aligned}&\mathcal{G}^3_\pm(\mathcal{J};\boldsymbol{p}',\boldsymbol{p}\,;t_2\,,t_1\,;\alpha) \\ &\quad= \sum_{s',s}\sum_{B',B} \mathrm{e}^{-E_B(\boldsymbol{p})\,t_1}\,\mathrm{e}^{-E_{B'}(\boldsymbol{p}')\,(t_2-t_1)} \\ &\qquad\qquad \times \left\langle\Omega\right|\phi_{\pm\boldsymbol{p}'\,\alpha}(0)\left|B'\,;p'\,;s'\right\rangle\left\langle B'\,;p'\,;s'\right|\mathcal{J}(0)\left|B\,;p\,;s\right\rangle\left\langle B\,;p\,;s\right|\overline{\phi}_{\boldsymbol{p}\,\alpha}(0)\left|\Omega\right\rangle \\ &\quad= \sum_{s',s} \mathrm{e}^{-E_\alpha(\boldsymbol{p})\,t_1}\,\mathrm{e}^{-E_\alpha(\boldsymbol{p}')\,(t_2-t_1)} \\ &\qquad\qquad \times \left\langle\Omega\right|\phi_{\pm\boldsymbol{p}'\,\alpha}(0)\left|\alpha\,;p'\,;s'\right\rangle\left\langle\alpha\,;p'\,;s'\right|\mathcal{J}(0)\left|\alpha\,;p\,;s\right\rangle\left\langle\alpha\,;p\,;s\right|\overline{\phi}_{\boldsymbol{p}\,\alpha}(0)\left|\Omega\right\rangle . \end{aligned}\tag{5.7}$$

Note, the formalism presented here assumes perfect state isolation such that each optimised operator couples only to a single state.

We see that the time dependence of this three point correlator is entirely contained within exponentials of the energy, and the remaining structure depends on both the overlap of the optimised operator with its corresponding state

$$\langle\Omega|\,\phi_{\pm\boldsymbol{p}'\,\alpha}(0)\,|\alpha\,;p\,;s\rangle = z_{\boldsymbol{p}\,\alpha}\sqrt{\frac{m_\alpha}{E_\alpha(\boldsymbol{p})}}\,\Gamma_{\pm\boldsymbol{p}}\,u_\alpha(p,s)\,, \tag{5.8}$$

and the matrix element for the current operator, $\langle\alpha\,;p'\,;s'|\,\mathcal{J}(0)\,|\alpha\,;p\,;s\rangle$.

In this chapter, we investigate the electromagnetic properties of the proton and neutron by choosing the current operator $\mathcal{J}(x)$ to be a vector current. In particular, we use the $O(a)$-improved [53] conserved vector current described in Chapter 2 and used in Ref. [54], denoted $j^\mu_{CI}(x)$. This choice of operator gives the matrix element

$$\begin{aligned}&\langle\alpha\,;p'\,;s'|\,j^\mu_{CI}(0)\,|\alpha\,;p\,;s\rangle\\ &\quad=\sqrt{\frac{m_\alpha}{E_\alpha(\boldsymbol{p})}}\sqrt{\frac{m_\alpha}{E_\alpha(\boldsymbol{p}')}}\,\overline{u}_\alpha(p',s')\left(\gamma^\mu\,F_{1\,\alpha}(Q^2)-\frac{\sigma^{\mu\nu}\,q^\nu}{2m_\alpha}\,F_{2\,\alpha}(Q^2)\right)u_\alpha(p,s)\,,\end{aligned} \tag{5.9}$$

where $Q^2=\boldsymbol{q}^2-(E_\alpha(\boldsymbol{p}')-E_\alpha(\boldsymbol{p}))^2$ is the squared four-momentum with the conventional sign, and the invariant scalar functions $F_1(Q^2)$ and $F_2(Q^2)$ are respectively the Dirac and Pauli form factors.

Hence, using Eqs. (5.8) and (5.9) we can rewrite the correlator as

$$\begin{aligned}&\mathcal{G}^3_\pm(j^\mu_{CI}\,;\boldsymbol{p}',\boldsymbol{p}\,;t_2\,,t_1\,;\alpha)\\ &\quad=\sum_{s',s}\mathrm{e}^{-E_\alpha(\boldsymbol{p})\,t_1}\,\mathrm{e}^{-E_\alpha(\boldsymbol{p}')\,(t_2-t_1)}\,\frac{m_\alpha}{E_\alpha(\boldsymbol{p})}\,\frac{m_\alpha}{E_\alpha(\boldsymbol{p}')}\,z_{\boldsymbol{p}\,\alpha}\,\overline{z}_{\boldsymbol{p}\,\alpha}\\ &\qquad\times\Gamma_{\pm\boldsymbol{p}'}\,u_\alpha(p',s')\,\overline{u}_\alpha(p',s')\left(\gamma^\mu F_{1\,\alpha}(Q^2)-\frac{\sigma^{\mu\nu}q^\nu}{2m_\alpha}F_{2\,\alpha}(Q^2)\right)u_\alpha(p,s)\,\overline{u}_\alpha(p,s)\,\Gamma_{\boldsymbol{p}}\,.\end{aligned} \tag{5.10}$$

Using the spin sum

$$\sum_s u_B(p,s)\,\overline{u}_B(p,s)=\frac{-i\,\gamma\cdot p+m_B}{2m_B}\,, \tag{5.11}$$

the three-point function is

$$\begin{aligned}&\mathcal{G}^3_\pm(j^\mu_{CI}\,;\boldsymbol{p}',\boldsymbol{p}\,;t_2\,,t_1\,;\alpha)\\ &\quad=\mathrm{e}^{-E_\alpha(\boldsymbol{p})\,t_1}\,\mathrm{e}^{-E_\alpha(\boldsymbol{p}')\,(t_2-t_1)}\,z_{\boldsymbol{p}\,\alpha}\,\overline{z}_{\boldsymbol{p}\,\alpha}\\ &\qquad\times\Gamma_{\pm\boldsymbol{p}'}\frac{-i\,\gamma\cdot p'+m_\alpha}{2E_\alpha(\boldsymbol{p}')}\left(\gamma^\mu F_{1\,\alpha}(Q^2)-\frac{\sigma^{\mu\nu}\,q^\nu}{2m_\alpha}F_{2\,\alpha}(Q^2)\right)\frac{-i\,\gamma\cdot p+m_\alpha}{2E_\alpha(\boldsymbol{p})}\,\Gamma_{\boldsymbol{p}}\,.\end{aligned} \tag{5.12}$$

To extract our desired signal from this spinor structure, we can take the spinor trace with some spin-structure projector $\Gamma_S$. This trace is then called the spinor-projected three-point correlation function

$$
\begin{aligned}
&G^3_\pm(\Gamma_S\,;j^\mu_{CI}\,;\boldsymbol{p}',\boldsymbol{p}\,;t_2\,,t_1\,;\alpha)\\
&\quad\equiv \mathrm{Tr}\big(\,\Gamma_S\,\mathcal{G}^3_\pm(j^\mu_{CI}\,;\boldsymbol{p}',\boldsymbol{p}\,;t_2\,,t_1\,;\alpha)\,\big)\\
&\quad= \mathrm{e}^{-E_\alpha(\boldsymbol{p})\,t_1}\,\mathrm{e}^{-E_\alpha(\boldsymbol{p}')\,(t_2-t_1)}\,z_{\boldsymbol{p}\,\alpha}\,\overline{z}_{\boldsymbol{p}\,\alpha}\\
&\qquad\times\Bigg(\mathrm{Tr}\bigg(\Gamma_S\,\Gamma_{\boldsymbol{p}'}\,\frac{-i\,\gamma\cdot p'+m_\alpha}{2E_\alpha(\boldsymbol{p}')}\,\gamma^\mu\,\frac{-i\,\gamma\cdot p+m_\alpha}{2E_\alpha(\boldsymbol{p})}\,\Gamma_{\boldsymbol{p}}\bigg)\,F_{1\,\alpha}(Q^2)\\
&\qquad\quad-\mathrm{Tr}\bigg(\Gamma_S\,\Gamma_{\boldsymbol{p}'}\,\frac{-i\,\gamma\cdot p'+m_\alpha}{2E_\alpha(\boldsymbol{p}')}\,\frac{\sigma^{\mu\nu}\,q^\nu}{2m_\alpha}\,\frac{-i\,\gamma\cdot p+m_\alpha}{2E_\alpha(\boldsymbol{p})}\,\Gamma_{\boldsymbol{p}}\bigg)\,F_{2\,\alpha}(Q^2)\Bigg)\,. \qquad (5.13)
\end{aligned}
$$

If we consider the function

$$
F'_\pm(\Gamma_S,\,\mathcal{J})\equiv 8E_\alpha(\boldsymbol{p})E_\alpha(\boldsymbol{p}')\;\mathrm{Tr}\bigg(\Gamma_S\,\Gamma_{\pm\boldsymbol{p}'}\,\frac{-i\,\gamma\cdot p'+m_\alpha}{2E_\alpha(\boldsymbol{p}')}\,\mathcal{J}\,\frac{-i\,\gamma\cdot p+m_\alpha}{2E_\alpha(\boldsymbol{p})}\,\Gamma_{\boldsymbol{p}}\bigg)\,, \qquad (5.14)
$$

where the prime on $F'_\pm(\Gamma_S,\,\mathcal{J})$ denotes the presence of the PEVA projectors, we can express Eq. (5.13) as

$$
\begin{aligned}
&G^3_\pm(\Gamma_S\,;j^\mu_{CI}\,;\boldsymbol{p}',\boldsymbol{p}\,;t_2\,,t_1\,;\alpha)\\
&\quad= \mathrm{e}^{-E_\alpha(\boldsymbol{p})\,t_1}\,\mathrm{e}^{-E_\alpha(\boldsymbol{p}')\,(t_2-t_1)}\,z_{\boldsymbol{p}\,\alpha}\,\overline{z}_{\boldsymbol{p}\,\alpha}\,\frac{1}{8E_\alpha(\boldsymbol{p})E_\alpha(\boldsymbol{p}')}\\
&\qquad\times\bigg(F'_\pm(\Gamma_S,\gamma^\mu)\,F_{1\,\alpha}(Q^2)-\frac{q^\nu}{2m_\alpha}\,F'_\pm(\Gamma_S,\sigma^{\mu\nu})\,F_{2\,\alpha}(Q^2)\bigg)\,. \qquad (5.15)
\end{aligned}
$$

The values that $F'_\pm$ takes for a variety of $\Gamma_S$ and $\mathcal{J}$ are given in Appendix A. This appendix also contains values for $F$, the equivalent function that arises in the corresponding conventional analysis. $F$ is defined in the same way as $F'_\pm$ save for the absence of the PEVA projectors $\Gamma_{\pm\boldsymbol{p}'}$ and $\Gamma_{\boldsymbol{p}}$ in the trace, and a factor of 4 in the normalisation.

These spinor-projected correlation functions have a nontrivial time dependence, which can be removed by constructing the ratio

$$
\begin{aligned}
&R_\pm(\boldsymbol{p}',\boldsymbol{p}\,;\alpha\,;r,s)\\
&\quad\equiv\sqrt{\left|\frac{r^\mu\,G^3_\pm(s^\nu\,\Gamma_\nu\,;j^\mu_{CI}\,;\boldsymbol{p}',\boldsymbol{p}\,;t_2\,,t_1\,;\alpha)\;r^\rho\,G^3_\pm(s^\sigma\,\Gamma_\sigma\,;j^\rho_{CI}\,;\boldsymbol{p}\,,\boldsymbol{p}';t_2\,,t_1\,;\alpha)}{\mathcal{G}(\boldsymbol{p}'\,;t_2\,;\alpha)\,\mathcal{G}(\boldsymbol{p}\,;t_2\,;\alpha)}\right|}\\
&\qquad\times\mathrm{sign}\big(r^\lambda\,G^3_\pm(s^\eta\,\Gamma_\eta\,;j^\lambda_{CI}\,;\boldsymbol{p}',\boldsymbol{p}\,;t_2\,,t_1\,;\alpha)\big)\,, \qquad (5.16)
\end{aligned}
$$

where $\Gamma_4=(\mathbb{I}+\gamma^4)/2$ and $\Gamma_k=(\mathbb{I}+\gamma^4)(i\,\gamma^5\,\gamma^k)/2$ form the basis for the projectors we use, and $r_\mu$ and $s_\mu$ are coefficients selected to determine the form factors. In addition, due to a charge conservation, as the momentum transfer $\boldsymbol{q}\to\boldsymbol{0}$ the temporal component of the three point correlator for the conserved vector current becomes exactly proportional to the two point correlator on each gauge field configuration, that is $G^3_{\pm}(s^\nu\,\Gamma_\nu\,;j^4_{CI}\,;\boldsymbol{p}\,,\boldsymbol{p};t_2\,,t_1\,;\alpha) \propto \mathcal{G}(\boldsymbol{p}\,;t_2\,;\alpha)$. Because of this, taking the ratio in Eq. (5.16) facilitates the cancellation of statistical fluctuations in the two- and three-point correlators, providing results with small statistical uncertainties, at least in the case of $G_E(Q^2)$.

We can then define the reduced ratio,

$$\overline{R}_{\pm}(\boldsymbol{p}',\boldsymbol{p}\,;\alpha\,;r,s) \equiv \sqrt{\frac{2E_\alpha(\boldsymbol{p})}{E_\alpha(\boldsymbol{p})+m_\alpha}}\sqrt{\frac{2E_\alpha(\boldsymbol{p}')}{E_\alpha(\boldsymbol{p}')+m_\alpha}}\,R_{\pm}(\boldsymbol{p}',\boldsymbol{p}\,;\alpha\,;r,s)\,. \tag{5.17}$$

Taking this reduced ratio and substituting in the expressions for the projected correlation functions, we obtain

$$\begin{aligned}\overline{R}_{\pm}(\boldsymbol{p}',\boldsymbol{p}\,;\alpha\,;r,s) = {} & \frac{r_\mu\,s_\nu}{16E_\alpha(\boldsymbol{p})E_\alpha(\boldsymbol{p}')(E_\alpha(\boldsymbol{p})+m_\alpha)\,(E_\alpha(\boldsymbol{p}')+m_\alpha)} \\ & \times\left(F'_{\pm}(\Gamma_\nu,\gamma^\mu)\,F_{1\,\alpha}(Q^2) - \frac{q_\rho}{2m_\alpha}\,F'_{\pm}(\Gamma_\mu,\sigma^{\mu\rho})\,F_{2\,\alpha}(Q^2)\right)\,.\end{aligned} \tag{5.18}$$

By investigating the $r^\mu$ and $s^\sigma$ dependence of this ratio, we find that the clearest signals are given by

$$R^T_{\pm} = \frac{2}{1\pm\widehat{\boldsymbol{p}}\cdot\widehat{\boldsymbol{p}}'}\,\overline{R}_{\pm}\left(\boldsymbol{p}',\boldsymbol{p}\,;\alpha\,;(1,\boldsymbol{0}),(1,\boldsymbol{0})\right)\text{ , and} \tag{5.19a}$$

$$R^S_{\mp} = \frac{2}{1\pm\widehat{\boldsymbol{p}}\cdot\widehat{\boldsymbol{p}}'}\,\overline{R}_{\mp}\left(\boldsymbol{p}',\boldsymbol{p}\,;\alpha\,;(0,\widehat{\boldsymbol{r}}),(0,\widehat{\boldsymbol{s}})\right)\,, \tag{5.19b}$$

where $\widehat{\boldsymbol{s}}$ is chosen such that $\boldsymbol{p}\cdot\widehat{\boldsymbol{s}} = 0 = \boldsymbol{p}'\cdot\widehat{\boldsymbol{s}}$, $\widehat{\boldsymbol{r}}$ is equal to $\widehat{\boldsymbol{q}}\times\widehat{\boldsymbol{s}}$, and the sign $\pm$ in Eq. (5.19) is chosen such that $1\pm\widehat{\boldsymbol{p}}\cdot\widehat{\boldsymbol{p}}'$ is maximised. This choice maximises the signal in the lattice determination of the correlation function ratios.

We can then find the Sachs electric and magnetic form factors,

$$\begin{aligned}G_{E\,\alpha}(Q^2) &\equiv F_{1\,\alpha}(Q^2) - \frac{Q^2}{(2m_\alpha)^2}\,F_{2\,\alpha}(Q^2) \\ &= \Big[Q^2\,(E_\alpha(\boldsymbol{p}')+E_\alpha(\boldsymbol{p}))\,\big((E_\alpha(\boldsymbol{p})+m_\alpha)\,(E_\alpha(\boldsymbol{p}')+m_\alpha)\mp|\boldsymbol{p}||\boldsymbol{p}'|\big)\,R^T_{\pm} \\ &\qquad \pm 2|\boldsymbol{q}|\,(1\mp\widehat{\boldsymbol{p}}\cdot\widehat{\boldsymbol{p}}')\,|\boldsymbol{p}||\boldsymbol{p}'|\,\big((E_\alpha(\boldsymbol{p})+m_\alpha)\,(E_\alpha(\boldsymbol{p}')+m_\alpha)\pm|\boldsymbol{p}||\boldsymbol{p}'|\big)\,R^S_{\mp}\Big] \\ &\quad /\left[4m_\alpha\left[\big(E_\alpha(\boldsymbol{p})\,E_\alpha(\boldsymbol{p}')+{m_\alpha}^2\mp|\boldsymbol{p}||\boldsymbol{p}'|\big)\,|\boldsymbol{q}|^2+4|\boldsymbol{p}|^2|\boldsymbol{p}'|^2\,(1\mp\widehat{\boldsymbol{p}}\cdot\widehat{\boldsymbol{p}}')\right]\right]\end{aligned} \tag{5.20a}$$

$$\begin{aligned}G_{M\,\alpha}(Q^2) &\equiv F_{1\,\alpha}(Q^2) + F_{2\,\alpha}(Q^2) \\ &= \Big[\pm 2\,(1\mp\widehat{\boldsymbol{p}}\cdot\widehat{\boldsymbol{p}}')\,|\boldsymbol{p}||\boldsymbol{p}'|\,\big((E_\alpha(\boldsymbol{p})+m_\alpha)\,(E_\alpha(\boldsymbol{p}')+m_\alpha)\pm|\boldsymbol{p}||\boldsymbol{p}'|\big)\,R^T_{\pm} \\ &\qquad -|\boldsymbol{q}|\,(E_\alpha(\boldsymbol{p}')+E_\alpha(\boldsymbol{p}))\,\big((E_\alpha(\boldsymbol{p})+m_\alpha)\,(E_\alpha(\boldsymbol{p}')+m_\alpha)\mp|\boldsymbol{p}||\boldsymbol{p}'|\big)\,R^S_{\mp}\Big] \\ &\quad /\left[2\left[\big(E_\alpha(\boldsymbol{p})\,E_\alpha(\boldsymbol{p}')+{m_\alpha}^2\mp|\boldsymbol{p}||\boldsymbol{p}'|\big)\,|\boldsymbol{q}|^2+4|\boldsymbol{p}|^2|\boldsymbol{p}'|^2\,(1\mp\widehat{\boldsymbol{p}}\cdot\widehat{\boldsymbol{p}}')\right]\right]\,.\end{aligned} \tag{5.20b}$$

Table 5.1: Details of the gauge field ensembles used in this analysis, including the number of gauge field configurations in each ensemble and the number of sources used on each configuration. For each ensemble we list both the pion mass given in Ref. [87], with the lattice spacing set by hadronic inputs, and our determination of the the squared pion mass with the lattice spacing listed in the table, which is set by the Sommer parameter with $r_0 = 0.4921(64)\,\mathrm{fm}$ [87].

| PACS-CS $m_\pi\,/\,\mathrm{MeV}$ | $a\,/\,\mathrm{fm}$ | $m_\pi^2\,/\,\mathrm{GeV}$ | # conf. | # src per conf. |
|---|---|---|---|---|
| 702 | 0.1022(15) | 0.3884(113) | 399 | 1 |
| 570 | 0.1009(15) | 0.2654(81) | 397 | 1 |
| 411 | 0.0961(13) | 0.1525(43) | 449 | 2 |
| 296 | 0.0951(13) | 0.0784(25) | 400 | 2 |
| 156 | 0.0933(13) | 0.0285(12) | 197 | 4 |

A similar procedure can be applied to extract the relevant form factors from any current.

We have shown how the PEVA technique can be applied to the calculation of baryon form factors for arbitrary kinematics. Doing so ensures that these form factors are free from opposite parity contaminations.

## 5.3 Sachs Electric Form Factor

We now apply this technique to calculate the Sachs electric form factors of the proton and the neutron. This gives us insight into the distribution of charge within these states.

The results in this and the following chapters are calculated on the PACS-CS $(2+1)$-flavour full-QCD ensembles [87], made available through the ILDG [90]. These ensembles use a $32^3 \times 64$ lattice, and employ a renormalisation-group improved Iwasaki gauge action with $\beta = 1.90$ and non-perturbatively $O(a)$-improved Wilson quarks, with $C_{SW} = 1.715$. We use five ensembles, with stated pion masses [87] from $m_\pi = 702\,\mathrm{MeV}$ to $156\,\mathrm{MeV}$, and set the scale using the Sommer parameter with $r_0 = 0.4921(64)\,\mathrm{fm}$ [87]. More details of the individual ensembles are presented in Table 5.1, including the squared pion masses in the Sommer scale. When fitting correlators, the $\chi^2/\mathrm{dof}$ is calculated with the full covariance matrix, and the $\chi^2$ values of all fits are consistent with an appropriate $\chi^2$ distribution, as discussed in Chapter 4.

At the lighter pion masses considered, the relativistic components of the baryon spinor will be enhanced. As a result, the parity-mixing at finite momentum will be increasingly problematic. However, at lighter pion masses, the gauge noise is more significant, and can occlude the parity-mixing effects if the statistics are insufficient.

For the variational analyses in this chapter, we use the same basis of operators as

Table 5.2: Different kinematics used in our analysis to access a range of $Q^2$ values. The $Q^2$ value listed is for the ground-state nucleon at the middle pion mass of $m_\pi = 411\,\mathrm{MeV}$. The statistical error listed for $Q^2$ comes from both the determination of the mass of the state and the conversion to physical units. In the so-called Breit frame kinematics, where the incoming and outgoing energies are equal, the correlated statistical errors from the mass cancel exactly, and as such the only source of errors is uncertainty in the lattice spacing used in converting to physical units.

| Source momentum $\boldsymbol{p}$ | Sink momentum $\boldsymbol{p}'$ | Momentum transfer $\boldsymbol{q}$ | $Q^2\,/\,\mathrm{GeV}^2$ |
|---|---|---|---|
| $(2,0,0)$ | $(3,0,0)$ | $(1,0,0)$ | 0.0924(26) |
| $(2,0,1)$ | $(3,0,1)$ | $(1,0,0)$ | 0.0970(27) |
| $(1,0,0)$ | $(2,0,0)$ | $(1,0,0)$ | 0.1278(35) |
| $(1,0,1)$ | $(2,0,1)$ | $(1,0,0)$ | 0.1309(36) |
| $(0,0,0)$ | $(1,0,0)$ | $(1,0,0)$ | 0.1578(43) |
| $(0,0,1)$ | $(1,0,1)$ | $(1,0,0)$ | 0.1583(43) |
| $(2,0,0)$ | $(3,1,0)$ | $(1,1,0)$ | 0.2272(62) |
| $(1,0,0)$ | $(2,1,0)$ | $(1,1,0)$ | 0.2660(73) |
| $(0,0,0)$ | $(1,1,0)$ | $(1,1,0)$ | 0.3072(84) |
| $(0,-1,0)$ | $(1,0,0)$ | $(1,1,0)$ | 0.3251(89) |
| $(1,0,0)$ | $(3,0,0)$ | $(2,0,0)$ | 0.4466(123) |
| $(0,0,0)$ | $(2,0,0)$ | $(2,0,0)$ | 0.5851(160) |
| $(-1,0,0)$ | $(1,0,0)$ | $(2,0,0)$ | 0.6502(177) |

used to isolate the nucleon excited-state spectrum in Chapter 4.

To extract the form factors, we fix the source at time slice $N_t/4 = 16$, and (utilising the sequential source technique [56]) invert through the current, fixing the current insertion at time slice 21. We choose time slice 21 by inspecting the two point correlation functions associated with each state and observing that excited-state contaminations in the eigenstate-projected correlators are suppressed by time slice 21. This is evaluated by fitting the effective mass in this region to a single state ansatz verifying that the full covariant $\chi^2/\mathrm{dof}$ is satisfactory. We then extract the form factors as outlined in Section 5.2 for every possible sink time and once again look for a plateau consistent with a single-state ansatz.

Performing the sequential source technique through the current requires us to choose our current operators and momentum transfers at inversion time. However, this allows us to vary the sink momentum, and by extension the source momentum, as well as varying the form of the interpolation functions at the sink. This gives us access to several states, as well as a range of values of

$$Q^2 = \boldsymbol{q}^2 - \left(E_\alpha(\boldsymbol{p}') - E_\alpha(\boldsymbol{p})\right)^2 . \tag{5.21}$$

In particular, values of $Q^2$ well below that encountered in the frames with $\boldsymbol{p}$, or

$\boldsymbol{p}' = (0,0,0)$ are accessed via kinematics such as $\boldsymbol{p} = (1,0,0)$, $\boldsymbol{p}' = (2,0,0)$. The main alternative approach to accessing $Q^2$ values in this region is to use twisted boundary conditions to change the momentum discretisation, allowing the valence quarks to take different momentum values from the sea quarks. In our approach, all momenta attained by the valence quarks are present in the sea, and thus we avoid the complexities of partial quenching effects inherent in the twisted boundary approach. Table 5.2 summarises the kinematics considered herein.

To begin, we inspect the Euclidean time dependence of $G_E(Q^2)$, extracted as outlined in Section 5.2. We consider independently the connected contributions to $G_E(Q^2)$ from single valence quarks of unit charge. The two flavours considered are the doubly represented quark flavour, or the up quark in the proton ($u_p$); and the singly represented quark flavour, or the down quark in the proton ($d_p$). As discussed later, we can combine these contributions together, weighted by the number of that quark flavour and the physical charges to get the connected contributions to the form factors for the proton and neutron.

In the case of perfect optimised operators, there should be no Euclidean time dependence, and the extracted form factors should be perfectly constant (up to statistical fluctuations) after the current insertion. However, in practice a finite operator basis is insufficient to perfectly isolate each state, leading to residual excited-state contaminations. These show up as enhanced or suppressed form factors at early Euclidean times. In light of this, care must be taken to select a Euclidean time region in which these excited-state contaminations are suppressed and the single state ansatz is satisfied.

In Figs. 5.1 and 5.2 we plot both PEVA and conventional extractions of $G_E(Q^2)$ with respect to Euclidean sink time at the heaviest pion mass of $m_\pi = 702\,\mathrm{MeV}$ and the lowest-momentum kinematics of $\boldsymbol{p} = (0,0,0)$ and $\boldsymbol{p}' = (1,0,0)$. We see that starting from time slice 22, which is immediately after the source, both extractions of $G_E(Q^2)$ are quite flat across all time slices considered. However, the errors on $G_E(Q^2)$ are sufficiently small to identify a small Euclidean time dependence at early time slices. We find that this dependence is suppressed by time slice 26 and are able to find a clear and clean plateau from 26–31 for both extractions. For both quark flavours considered, there is no significant difference in the fit ranges, extracted values or errors between the two extractions. We believe this is because the opposite-parity contaminations are small, and come from heavier states that are suppressed by Euclidean time evolution.

As the pion mass decreases, for example at $m_\pi = 296\,\mathrm{MeV}$ as seen in Figs. 5.3 and 5.4, the statistical noise in the form factor extractions increases, and the plateau region shifts somewhat. However for all five masses, the qualitative behaviour described above remains true, save for the following anomalies. At $m_\pi = 570\,\mathrm{MeV}$, the plateaus from PEVA start two time slices earlier than those from the conventional analysis. This is potentially a signal of opposite-parity contaminations entering into the analysis.

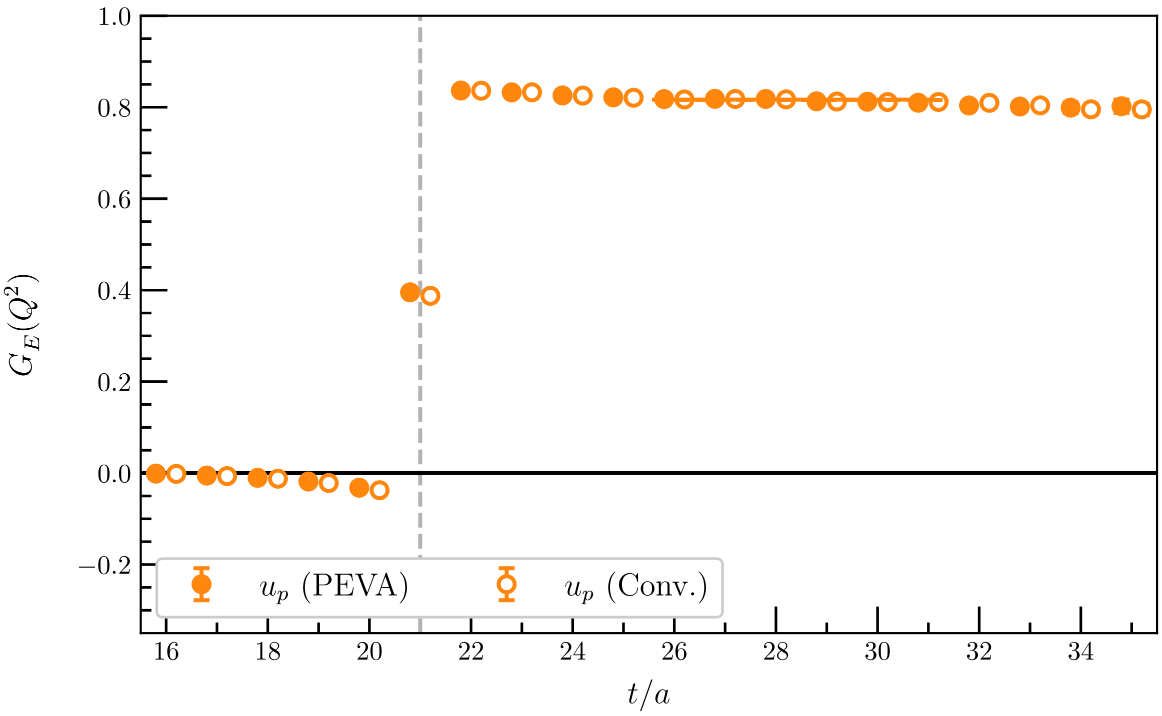

Figure 5.1: The contribution to the electric form factor from the doubly represented quark flavour for the ground-state nucleon at $m_\pi = 702\,\mathrm{MeV}$, for the lowest-momentum kinematics, providing $Q^2 = 0.1410(41)\,\mathrm{GeV}^2$. We plot the conventional analysis with open markers and the new PEVA analysis with filled markers. Our fits to the plateaus are illustrated by shaded bands, with the central value indicated by dashed fit lines for the conventional analysis, and solid fit lines for the PEVA analysis. The source is at time slice 16, and the current is inserted at time slice 21, with the latter indicated by the vertical dashed line. Both the conventional and PEVA fits are from time slice 26–31.

However, there is no statistically significant difference in the fit values from the two methods and the different plateaus do not show up at any of the other masses considered, so it is inconclusive. At $m_\pi = 411\,\mathrm{MeV}$, the plateaus are forced out to begin at time slice 29 by a kink in the correlator at time slice 28. This is much later than the plateaus at any other mass. There is no physical source for such a kink in the correlator, so it is likely to be a statistical anomaly. Fitting after the kink does not have a statistically significant effect on the value of the plateau, although it does increase the uncertainty. We choose to fit after the kink in part to encapsulate potential systematic errors in the increased statistical errors.

We can also consider changing the momenta of the initial and final states, both by changing the momentum transfer, and by boosting both the initial and final states without changing the three-momentum transfer. If we do this for the $m_\pi = 570\,\mathrm{MeV}$ ensemble, where we previously found inconsistent plateaus between PEVA and a conventional analysis, we continue to find discrepancies. In Figs. 5.5 and 5.6, we increase both the initial and final state momenta to $\boldsymbol{p} = (1,0,0)$ and $\boldsymbol{p}' = (2,0,0)$,

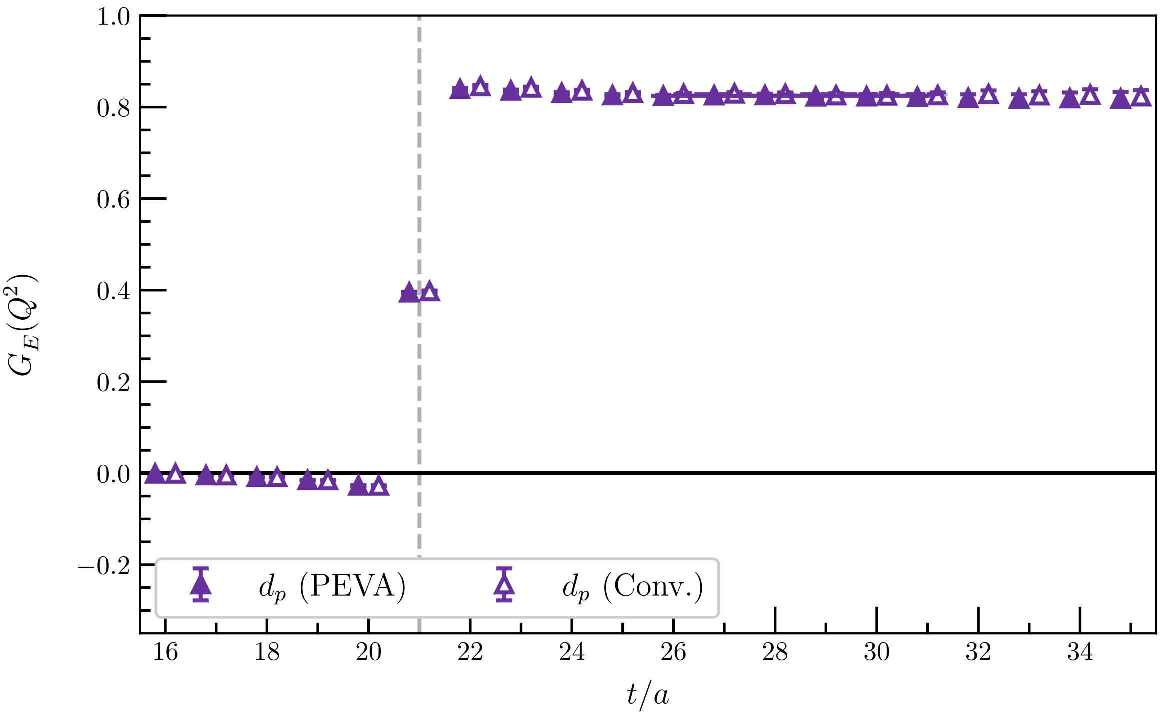

Figure 5.2: The contribution to the electric form factor from the singly represented quark flavour for the ground-state nucleon. The conventions used in this plot are the same as used for the other quark flavour in Fig. 5.1. The pion mass and kinematics are also the same, with $m_\pi = 702\,\text{MeV}$, and $Q^2 = 0.1410(41)\,\text{GeV}^2$. Both the conventional and PEVA fits are from time slice 26–31.

leaving the three-momentum transfer the same, but leading to a reduction in $Q^2$. In this case, we find that the PEVA and conventional plateaus start on the same time slices and have consistent plateau values. Any opposite-parity contaminations do not seem to be affecting the plateau ranges or values for these kinematics. In Figs. 5.7 and 5.8, we increase the momentum transfer, leading to an increase in $Q^2$. In this case, and in most other kinematics at this mass, we find a result similar to our original kinematics, with the conventional plateau starting later than the PEVA plateau, but having a consistent value within statistical errors. These results suggest that there are problems extracting $G_E(Q^2)$ with the conventional analysis at this mass, but are not enough to categorically ascribe these problems to opposite-parity contamination.

For the other four masses, almost all kinematics have identical plateaus in $G_E(Q^2)$ from both analyses. It is unclear why $m_\pi = 570\,\text{MeV}$ has inconsistent plateaus at a range of kinematics when the other four masses don't. However, it is clear that whatever opposite-parity contaminations are occurring, they are not affecting the $G_E(Q^2)$ values extracted, at least within our current statistical uncertainties.

Across all five masses, we consistently find that at higher momenta there is more statistical noise in the extraction of $G_E(Q^2)$.

In Fig. 5.9, we take the plateau values from each of the kinematics listed in Table 5.2

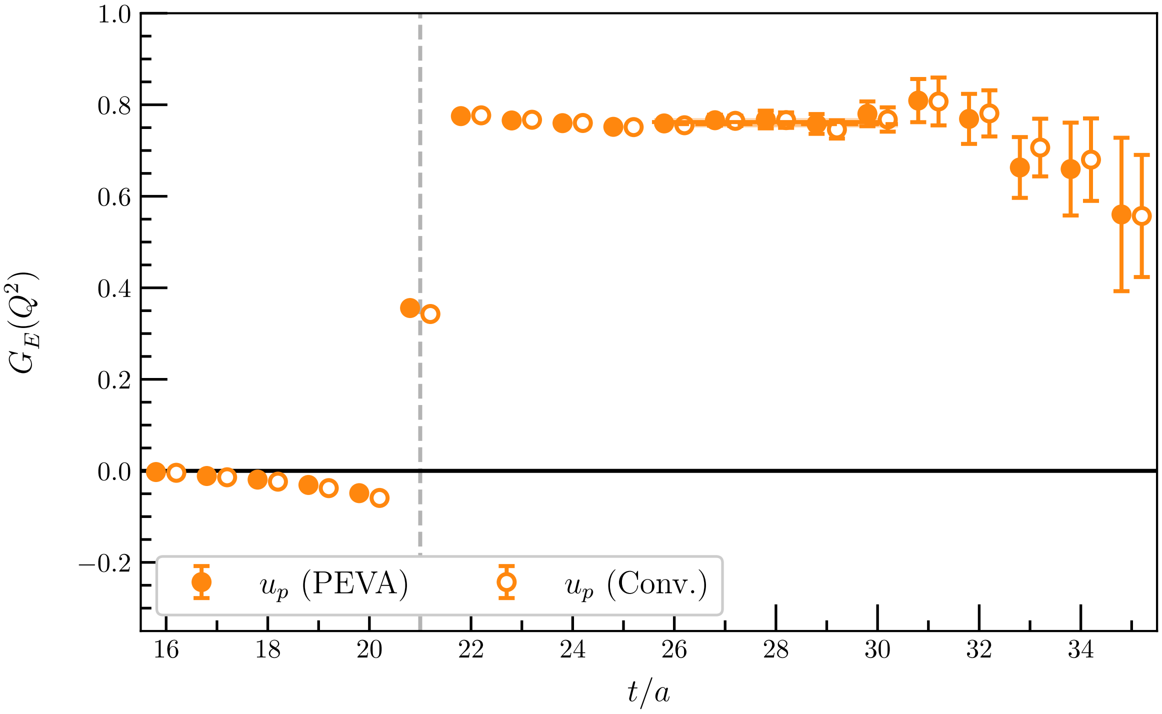

Figure 5.3: Contributions to ground state $G_E(Q^2)$ from $u_p$ at $m_\pi = 296\,\text{MeV}$, for the lowest-momentum kinematics, providing $Q^2 = 0.1605(44)\,\text{GeV}^2$. The conventions used in this plot are the same as in Fig. 5.1. Both fits are from time slice 26–30.

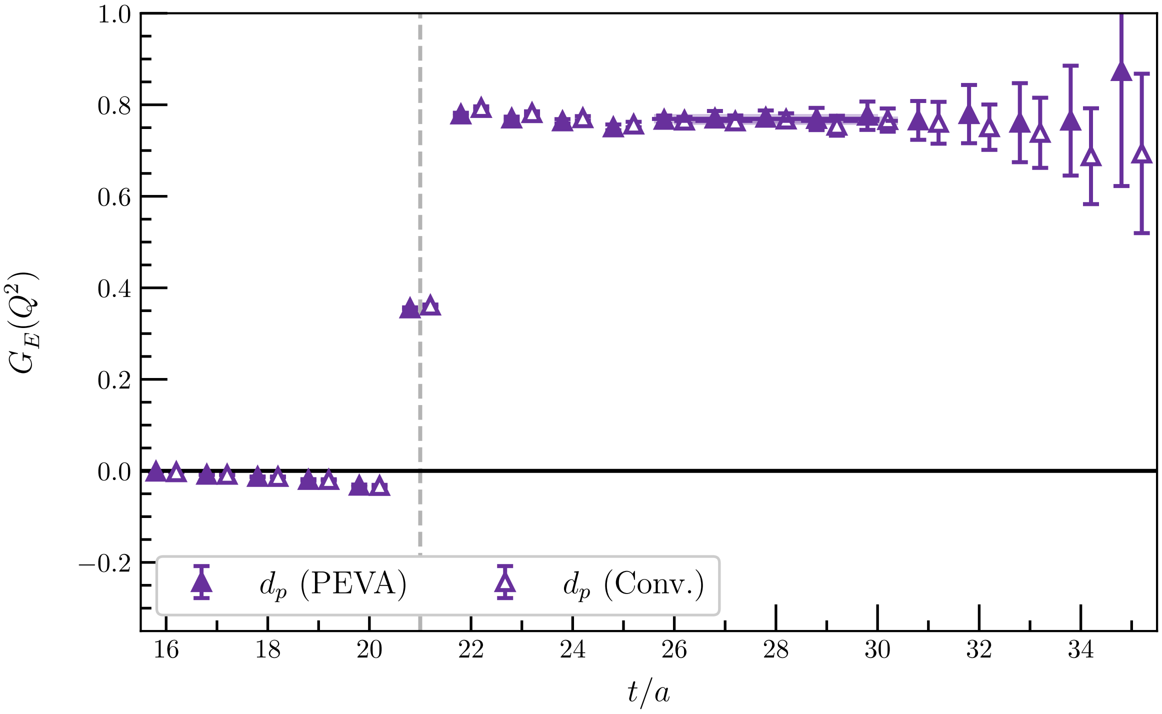

Figure 5.4: Contributions to ground state $G_E(Q^2)$ from $d_p$. Pion mass and kinematics are as in Fig. 5.3 above. The conventions used in this plot are the same as in Fig. 5.1. Both fits are from time slice 26–30.

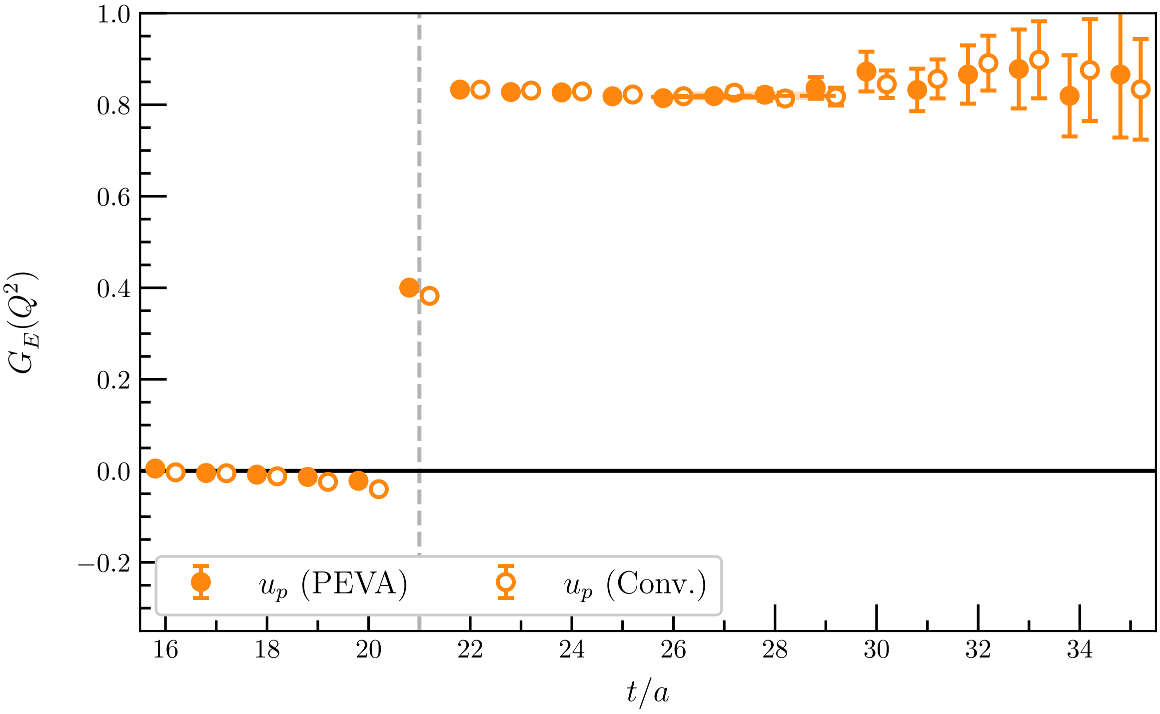

Figure 5.5: Contributions to ground state $G_E(Q^2)$ from $u_p$ at $m_\pi = 570\,\mathrm{MeV}$ for $\boldsymbol{p} = (1,0,0)$ and $\boldsymbol{p}' = (2,0,0)$, providing $Q^2 = 0.1236(38)\,\mathrm{GeV}^2$. The conventions used in this plot are the same as in Fig. 5.1. Both fits start from time slice 26.

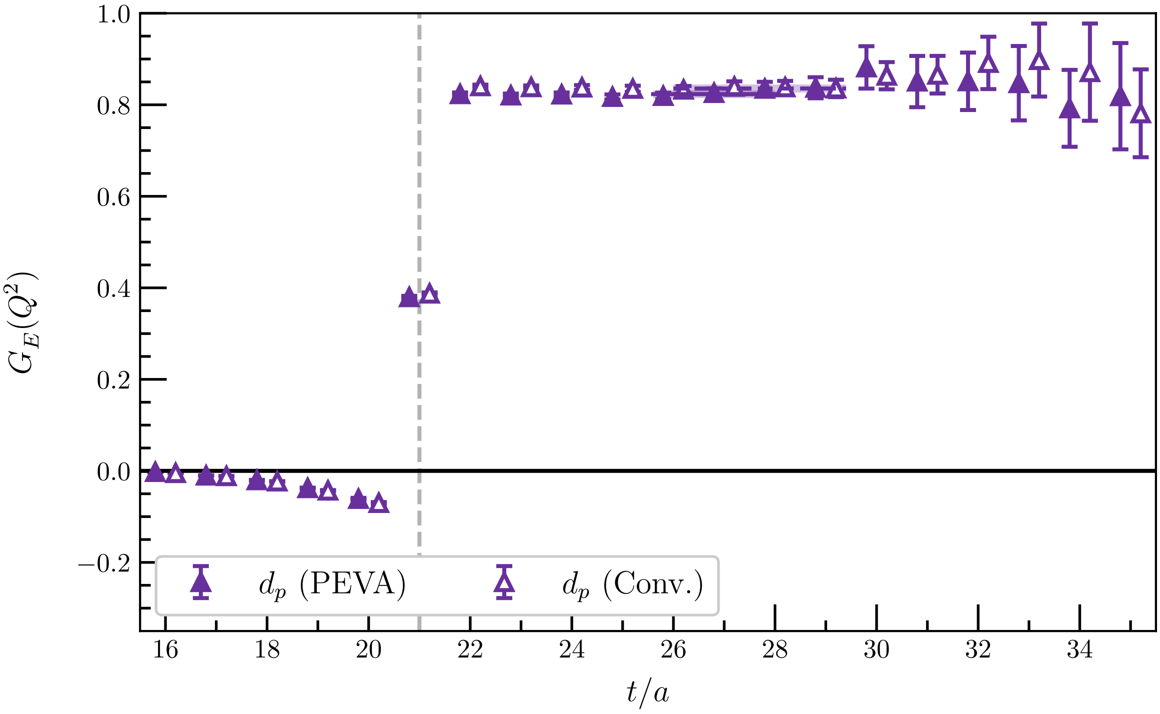

Figure 5.6: Contributions to ground state $G_E(Q^2)$ from $d_p$. Pion mass and kinematics are as in Fig. 5.5 above. The conventions used in this plot are the same as in Fig. 5.1. Both fits start from time slice 26.

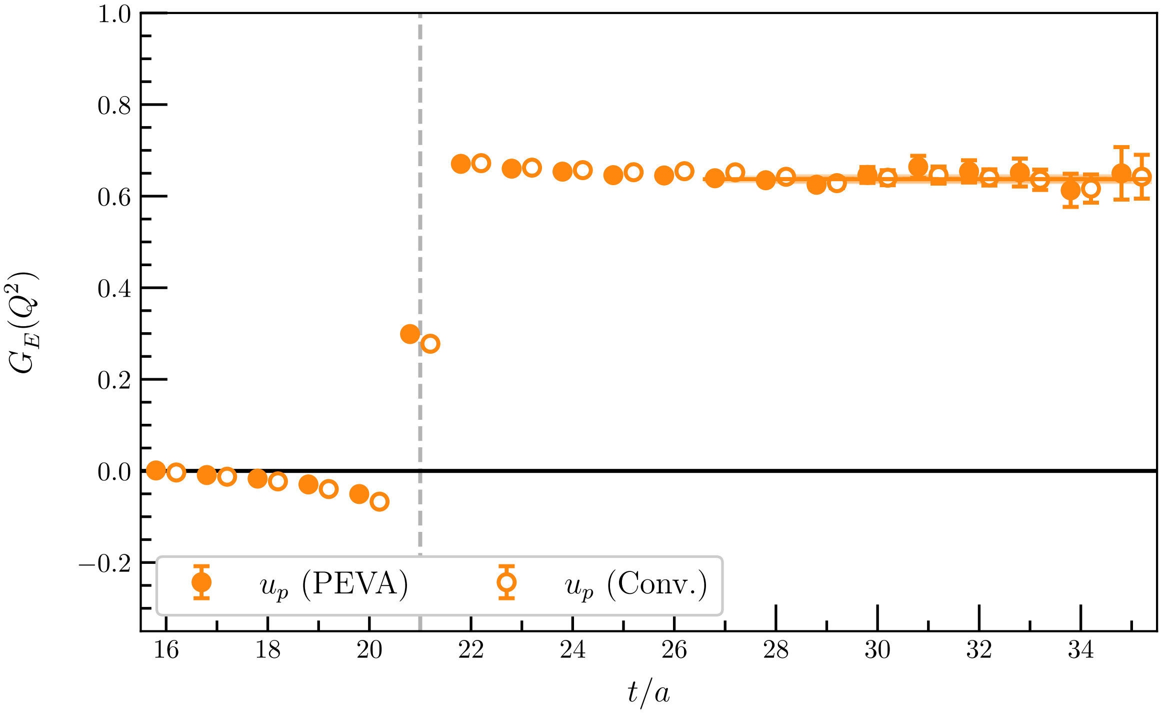

Figure 5.7: Contributions to ground state $G_E(Q^2)$ from $u_p$ at $m_\pi = 570\,\mathrm{MeV}$ for $\boldsymbol{p} = (0, 0, 0)$ and $\boldsymbol{p}' = (1, 1, 0)$, providing $Q^2 = 0.2831(86)\,\mathrm{GeV}^2$. The conventions used in this plot are the same as in Fig. 5.1. The PEVA fit starts from time slice 27, but the conventional analysis fit starts from time slice 28.

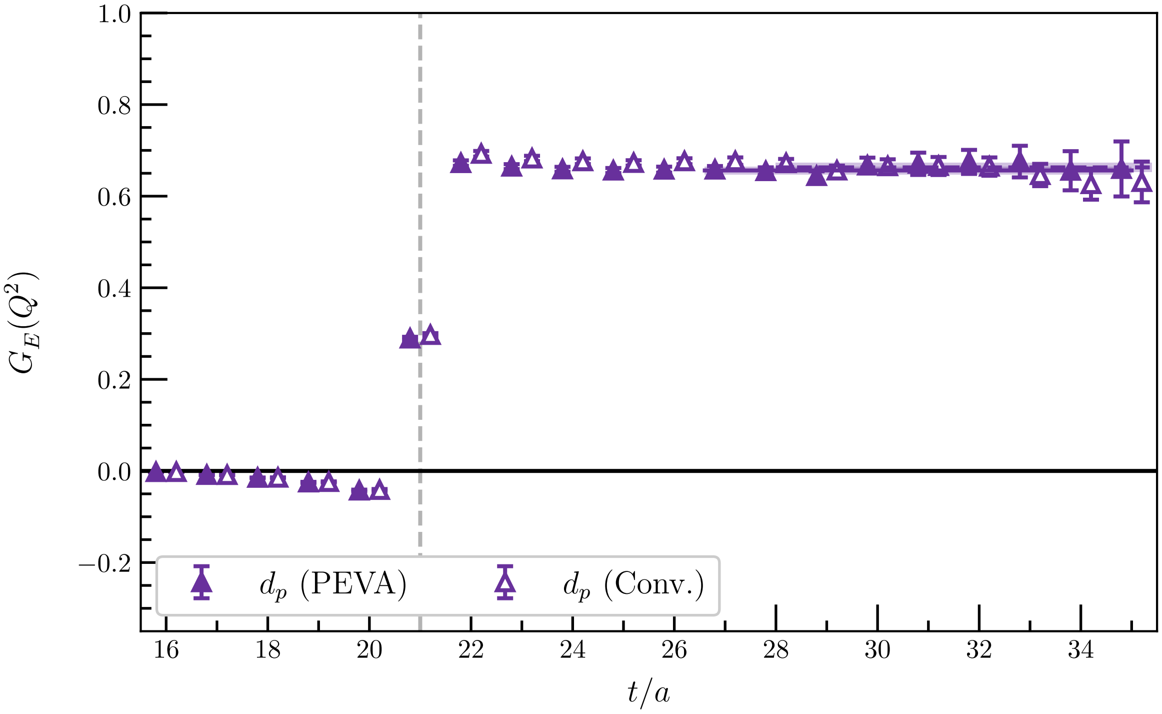

Figure 5.8: Contributions to ground state $G_E(Q^2)$ from $d_p$. Pion mass and kinematics are as in Fig. 5.7 above. The conventions used in this plot are the same as in Fig. 5.1. The PEVA fit starts from time slice 27, but the conventional analysis fit starts from time slice 28.

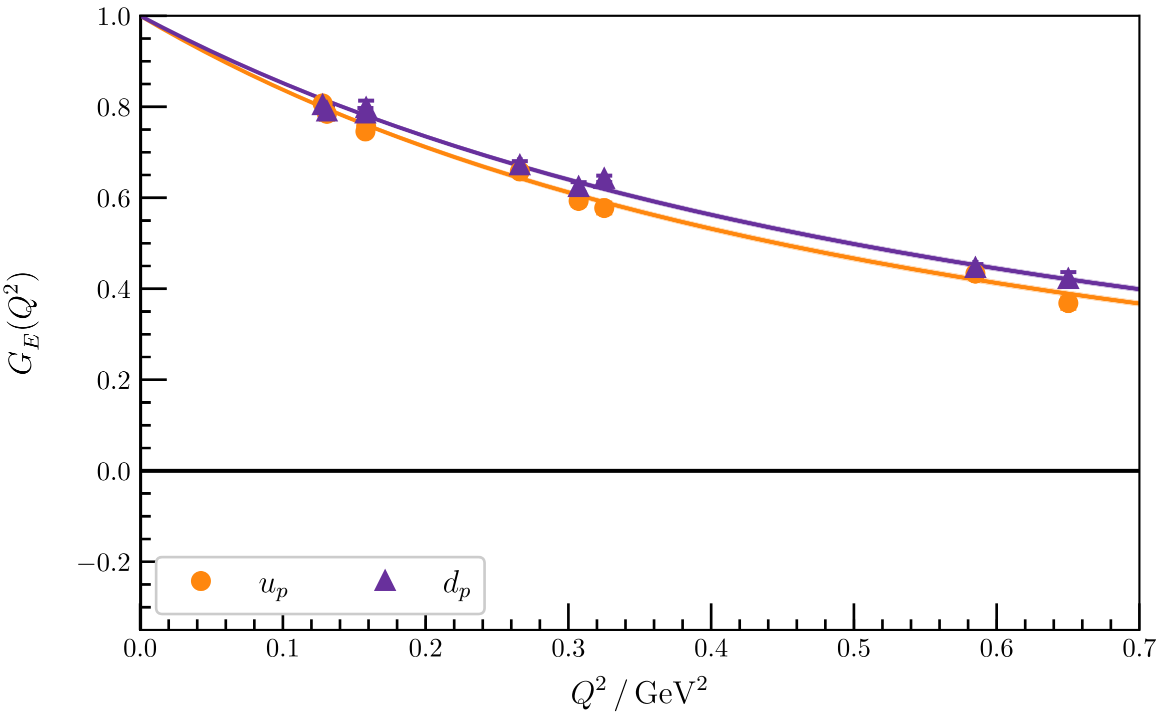

Figure 5.9: Contributions from individual quark flavours to the electric form factor of the ground-state nucleon at $m_\pi = 411\,\mathrm{MeV}$. The shaded regions are dipole fits to the form factor, with lines indicating the central values. The $y$-axis intercept is fixed to one, as we are using an improved conserved vector current and the quarks are taken with unit charge. The errors on these fits are small enough that the shaded bands are barely distinguishable from the central lines. The fits correspond to a charge radius of $0.658(12)\,\mathrm{fm}$ for the doubly represented quark ($u_p$) and $0.624(11)\,\mathrm{fm}$ for the singly represented quark ($d_p$).

at $m_\pi = 411\,\mathrm{MeV}$ and plot their $Q^2$ dependence. We exclude any kinematics for which we are unable to find a clear plateau, or the variational analysis produces a negative generalised eigenvalue (as negative eigenvalues indicate issues with the variational analysis, and can cause problems with state identification). We see the contributions from both quark flavours are very similar and each agrees well with a dipole ansatz

$$G_D(Q^2) = \frac{G_0}{\left(1 + Q^2/\Lambda^2\right)^2}\,, \tag{5.22}$$

with $G_0$ fixed to one, as we are working with quarks of unit charge. These fits correspond to an RMS charge radius of $\langle r^2 \rangle^{1/2} = \sqrt{12}/\Lambda = 0.658(12)\,\mathrm{fm}$ for the doubly represented quark flavour and $0.624(11)\,\mathrm{fm}$ for the singly represented quark flavour. For brevity, we omit similar plots for the other four masses from this chapter. The omitted plots are available in Appendix D for the interested reader.

In order to compute the form factors of the proton, $G_{E\,p}(Q^2)$, and neutron, $G_{E\,n}(Q^2)$, we need to take the correct linear combinations of the contributions from the doubly represented quark flavour ($G_{E\,u_p}(Q^2)$) and the singly represented quark flavour ($G_{E\,d_p}(Q^2)$)

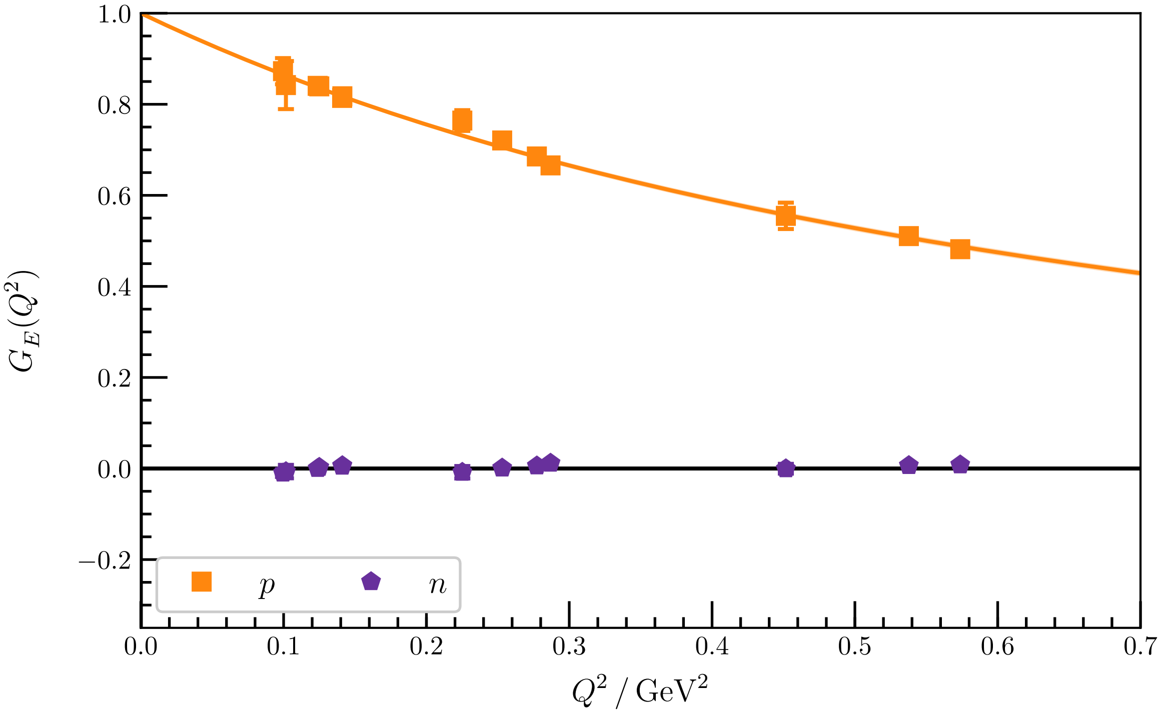

Figure 5.10: $G_E(Q^2)$ for the ground-state proton and neutron at $m_\pi = 702\,\mathrm{MeV}$. The shaded region corresponds to a dipole fit to the proton form factor, with a charge radius of 0.593(11) fm .

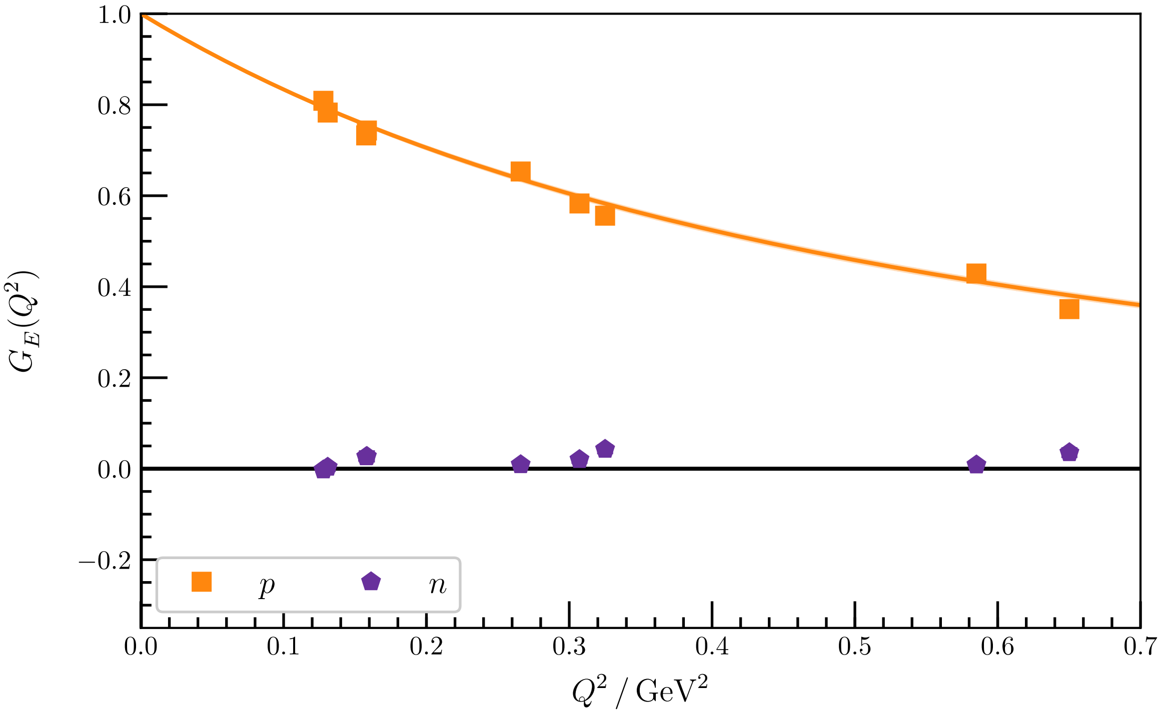

Figure 5.11: $G_E(Q^2)$ for the ground-state proton and neutron at $m_\pi = 411\,\mathrm{MeV}$. The shaded region corresponds to a dipole fit to the proton form factor, with a charge radius of 0.667(13) fm .

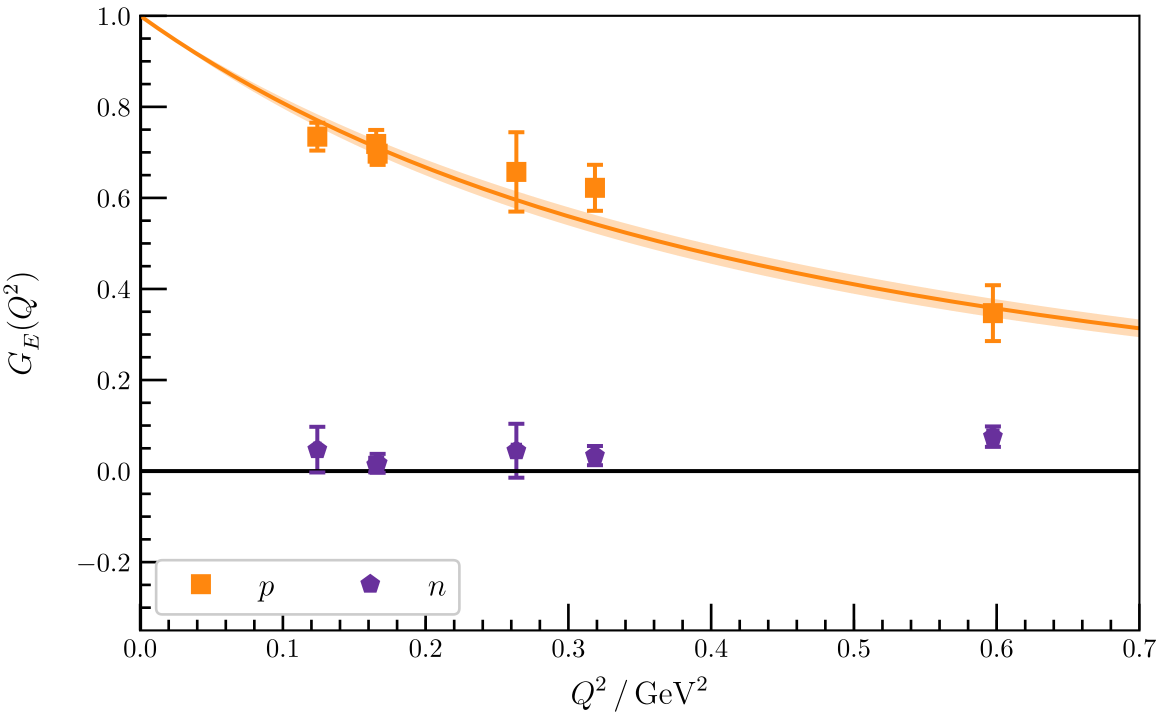

Figure 5.12: $G_E(Q^2)$ for the ground-state proton and neutron at $m_\pi = 156\,\mathrm{MeV}$. The shaded region corresponds to a dipole fit to the proton form factor, with a charge radius of 0.724(28) fm .

to reintroduce the multiplicity of the doubly represented quark and the physical charges of the up and down quarks:

$$G_{E\,p}(Q^2) = 2 \times \left(+\frac{2}{3}\right) G_{E\,u_p}(Q^2) + \left(-\frac{1}{3}\right) G_{E\,d_p}(Q^2)\,, \text{ and} \tag{5.23}$$

$$G_{E\,n}(Q^2) = 2 \times \left(-\frac{1}{3}\right) G_{E\,u_p}(Q^2) + \left(+\frac{2}{3}\right) G_{E\,d_p}(Q^2)\,. \tag{5.24}$$

In Figs. 5.10–5.12, we plot the electric form factors obtained by these combinations for three of the five pion masses. Plots for all five masses are available in Appendix D.

The form factor for the neutrally charged neutron is close to zero for all masses considered, as expected. Similar to the linear combinations taken for the form factors, we can combine the squared charge radii from the individual quark sectors with the appropriate multiplicities and charge factors to obtain the squared charge radius of the neutron. For all five pion masses, we find a small negative value. For example, at $m_\pi = 411\,\mathrm{MeV}$, the neutron's squared charge radius is −0.030(5) fm . This is qualitatively consistent with the negative squared charge radii observed in experiment. A more quantitative discussion of this effect requires knowledge of the disconnected loop contributions, which are not considered in this work.

The form factor of the proton matches well with a dipole fit with $G_0$ fixed to one (the charge of the proton). As expected, the charge radii extracted from these dipole

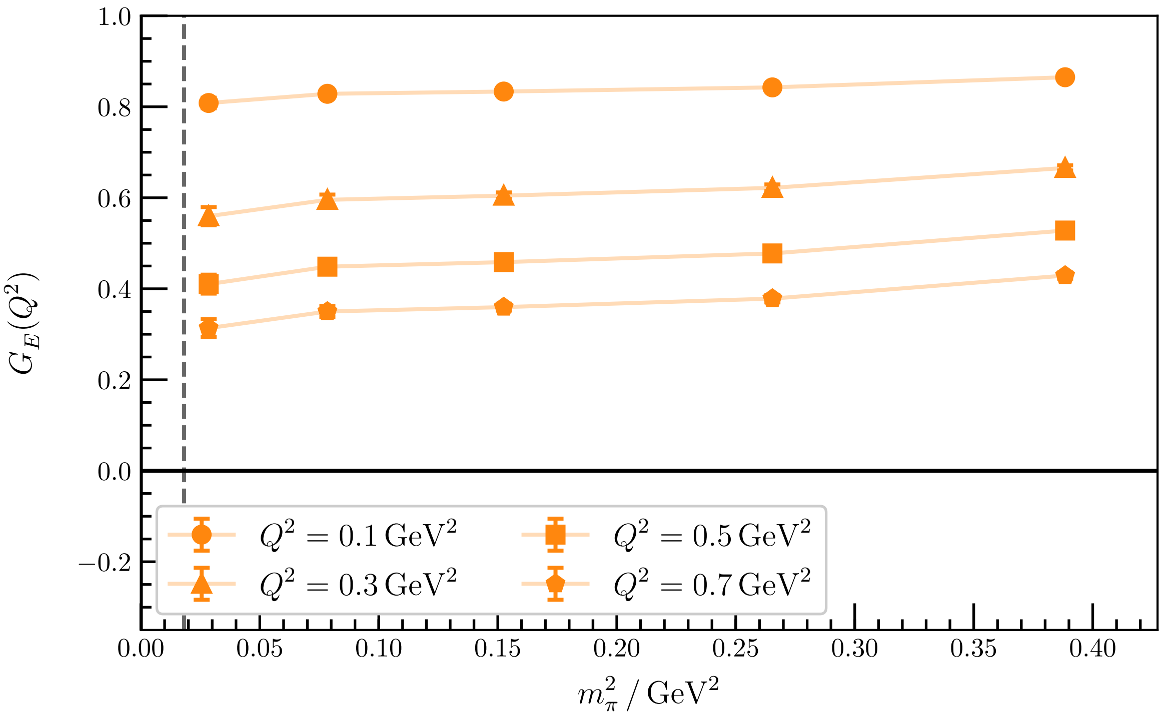

Figure 5.13: Quark-mass dependence of dipole fits to $G_E(Q^2)$ for the ground-state proton. The different marker shapes correspond to taking the fit value at different $Q^2$ slices, and the dashed line corresponds to the physical pion mass.

fits approach the experimentally measured proton charge radius from below as the pion mass is reduced towards the physical point.

As discussed in Refs. [98, 99], the exact physical value of the proton radius has been a puzzle for the last seven years, since precision laser spectroscopy of muonic hydrogen yielded a proton radius of 0.840 87(39) fm [100] in 2010. This value is 4.6 %, or $5.6\sigma$ lower than the CODATA 2014 world average of 0.8751(61) fm [101], from a combination of laser spectroscopy of electronic hydrogen and deuterium, and elastic electron scattering. Recent precision results from new laser spectroscopy of electronic hydrogen provide a proton radius of 0.8335(95) fm [102], which agrees with the muonic hydrogen radius. This suggests that the discrepancy is likely due to systematic errors in the existing results for electronic hydrogen and elastic electron scattering.

Returning to our results, in Fig. 5.13, we plot the values of the dipole fits on various $Q^2$ slices as a function of the squared pion mass. We see that the pion-mass dependence is quite smooth, suggesting that the structure of the state is fairly consistent at all five masses considered here. It has a clear trend downwards as the mass is reduced, corresponding to the increasing charge radius.

For all pion masses and kinematics considered in this chapter, in the specific case of the electric form factor, there is no conclusive evidence of opposite parity contaminations. Both the PEVA and conventional variational analysis show clear and clean plateaus in $G_E(Q^2)$ with good excited state control. This supports previous work demonstrating the utility of variational analysis techniques in calculating baryon matrix elements [103, 104]. By using such techniques we are able to cleanly isolate precise values for the Sachs electric form factor of the ground-state proton and neutron.

## 5.4 Sachs Magnetic Form Factor

Moving on to $G_M(Q^2)$, we once again begin with the heaviest pion mass and the lowest momenta. In Fig. 5.14, we see that while the signal is noisier than $G_E(Q^2)$, the excited-state contaminations seem to be less significant, and for both the PEVA and conventional analyses we are able to find a plateau from time slice 23 to time slice 29. We are cautious in fitting noisy data and restrict fit regimes to avoid large fluctuations.

Contrary to the electric case, there is actually a statistically significant difference in the values of the plateaus from the PEVA and conventional analysis for the singly represented quark flavour. If we take the correlated ratio of $G_M(Q^2)$ from the conventional analysis to $G_M(Q^2)$ from the PEVA analysis, we get a value of 0.988(4) for the

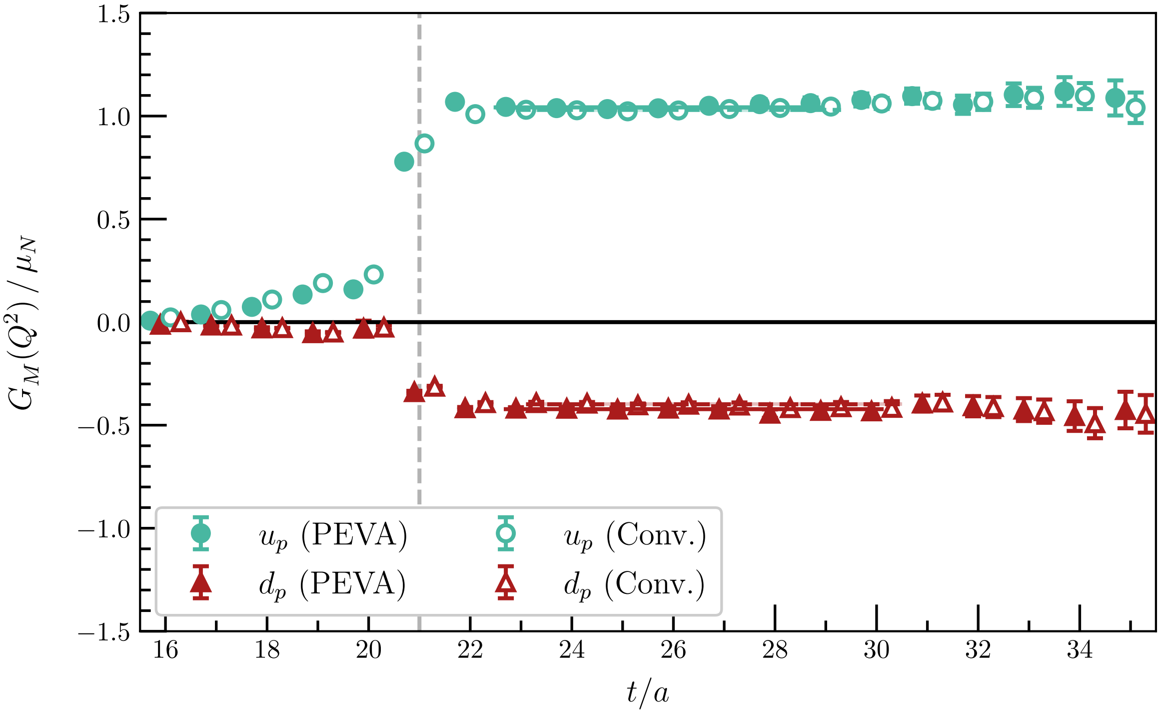

Figure 5.14: The contributions to the magnetic form factor from single quarks of unit charge for the ground-state nucleon at $m_\pi = 702\,\mathrm{MeV}$ for the lowest-momentum kinematics, providing $Q^2 = 0.1410(41)\,\mathrm{GeV}^2$. We plot the conventional analysis with open markers and the new PEVA analysis with filled markers. Our fits to the plateaus are illustrated by shaded bands, with the central value indicated by dashed lines for the conventional analysis, and solid lines for the PEVA analysis. The plateau regions for both analyses are consistent, starting from time slice 23 for all four fits, but the value of the conventional plateau for the singly represented quark ($d_p$) has a magnitude approximately 5 % lower than the PEVA plateau.

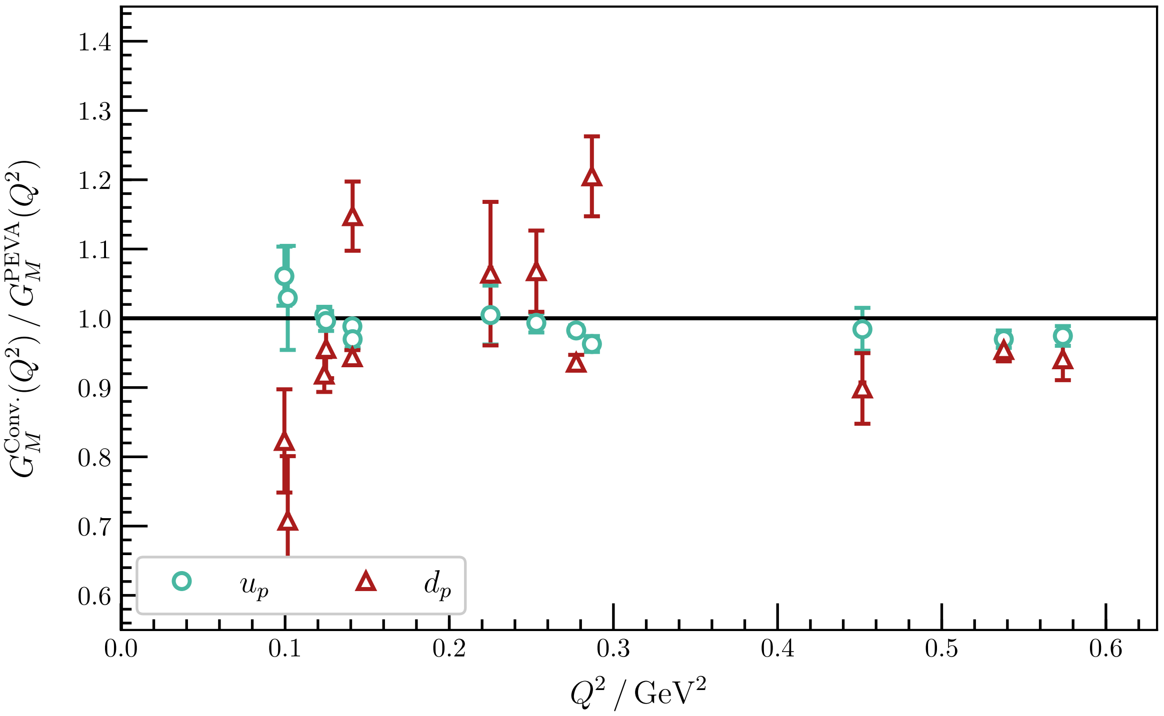

Figure 5.15: Ratios of conventional plateaus to PEVA plateaus for ground state $G_M(Q^2)$ at $m_\pi = 702\,\mathrm{MeV}$. If the plateaus were consistent, the points should be distributed about 1.0. For the doubly represented quark flavour ($u_p$), the points are often slightly further from unity than would be expected, suggesting that the conventional variational analysis may be contaminated by opposite-parity states. The singly represented quark flavour ($d_p$) shows significantly more scatter, strongly supporting the presence of opposite-parity contaminations. These results indicate systematic errors of 5–10 % for $d_p$, and perhaps more for some specific kinematics.

doubly represented quark and 0.944(10) for the singly represented quark. This ratio is clearly less than 1 for both quark flavours. The effect is more pronounced for the singly represented quark flavour, indicating that despite finding a plateau, the conventional analysis is being affected by opposite-parity contaminations that are introducing a systematic error of approximately 5 %.

We see similar behaviour across all kinematics considered, with the conventional plateaus often showing a statistically significant deviation from the PEVA plateaus despite having the same fit regions and acceptable $\chi^2$ values. In Fig. 5.15, we plot the correlated ratio discussed above for all kinematics with acceptable plateaus and positive generalised eigenvalues at $m_\pi = 702\,\mathrm{MeV}$. We see that while the ratio falls both above and below unity for different kinematics, there is a statistically significant deviation from the expectation that the plateaus from both analyses should be consistent, corresponding to a ratio of one. Clearly, there should be some statistical scatter about this value, but the ratios lie significantly further from one than their errors would suggest.

This is particularly clear for the singly represented quark flavour, for which the ratio clearly differs from one for almost all kinematics. If we focus only on the points with small error bars, say the six points with the smallest statistical errors, we see that they all sit near 0.95. This means that for this quark flavour, the well constrained points see an underestimation of the magnitude of $G_M(Q^2)$ of approximately 5 %.

Moving on to the second heaviest mass, Fig. 5.16 shows the magnetic form factor plateaus for the lowest-momentum kinematics at $m_\pi = 570\,\mathrm{MeV}$. Similar to $G_E(Q^2)$, we find that decreasing the pion mass leads to increased statistical noise. Once again, the magnitude of the contribution to $G_M(Q^2)$ from the singly represented quark flavour is slightly underestimated, as can be seen in from the ratios plotted in Fig. 5.17. We can see that the doubly represented quark flavour still has some small but statistically significant deviations, and the singly represented quark flavour sees an underestimation of the magnitude of the form factor of approximately 10 % for all points with small statistical errors. This is an even more significant effect than at the heaviest mass.

Fig. 5.18 shows the plateaus for the lowest-momentum kinematics at $m_\pi = 411\,\mathrm{MeV}$. We see continuations of the same trends with slightly increased statistical noise compared to the lighter pion masses, and the conventional results once again sitting below the PEVA plateau values. In fact, Fig. 5.19 shows that the effects of opposite-parity contaminations are larger again. The disagreement for the doubly represented quark flavour has grown, particularly at higher $Q^2$, where the form factor is consistently underestimated by at least 5 %. At this mass, the statistical errors for the singly represented quark flavour are growing, making the disagreement between the two analyses harder to pin down. However, with the exception of a few very noisy points, all of the ratios for the singly represented quark sector lie at or below 1.0. The opposite-parity contaminations are clearly still present in the well-constrained points, and if anything is larger than at the heavier masses, sitting at 10–20 %.

As we move to $m_\pi = 296\,\mathrm{MeV}$, the plateau plot in Fig. 5.20 shows that the statistical noise gets larger again, but we are still able to find clear and unambiguous plateaus. As shown in Fig. 5.21, the number of kinematics with acceptable plateaus is significantly reduced, and the noise for both quark flavours is continuing to increase. However, save for one point with very large statistical errors, the results for the singly represented quark flavour show that the conventional analysis still underestimates the plateau amplitude by approximately 10 %.

At the lightest mass, Fig. 5.22 shows that the statistical noise is getting even stronger, but acceptable plateaus are still possible. As Fig. 5.23 shows, for the lowest-momentum kinematics, the results from the conventional analysis continue to sit significantly below the PEVA results. However, for the other kinematics, the statistical errors in the fits are too large to clearly resolve any discrepancy between the conventional and PEVA analyses at this mass. Higher statistics are required to resolve the differences between the analyses for the remaining kinematics at this mass.

These results provide strong evidence for opposite-parity contaminations in conven-

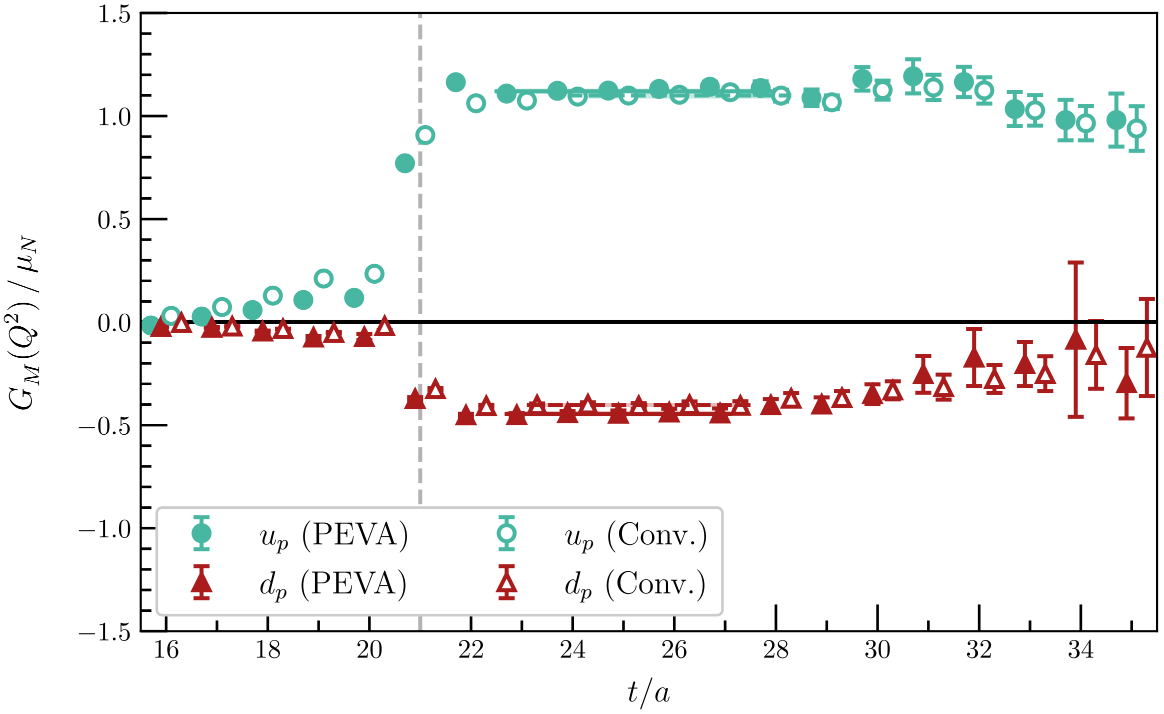

Figure 5.16: Quark-flavour contributions to ground state $G_M(Q^2)$ at $m_\pi = 570\,\text{MeV}$ for the lowest-momentum kinematics, providing $Q^2 = 0.1444(44)\,\text{GeV}^2$. The conventions used in this plot are the same as in Fig. 5.14. Both PEVA fits start from time slice 23, and for $d_p$, so does the conventional fit. For $u_p$, the conventional fit starts at time slice 24.

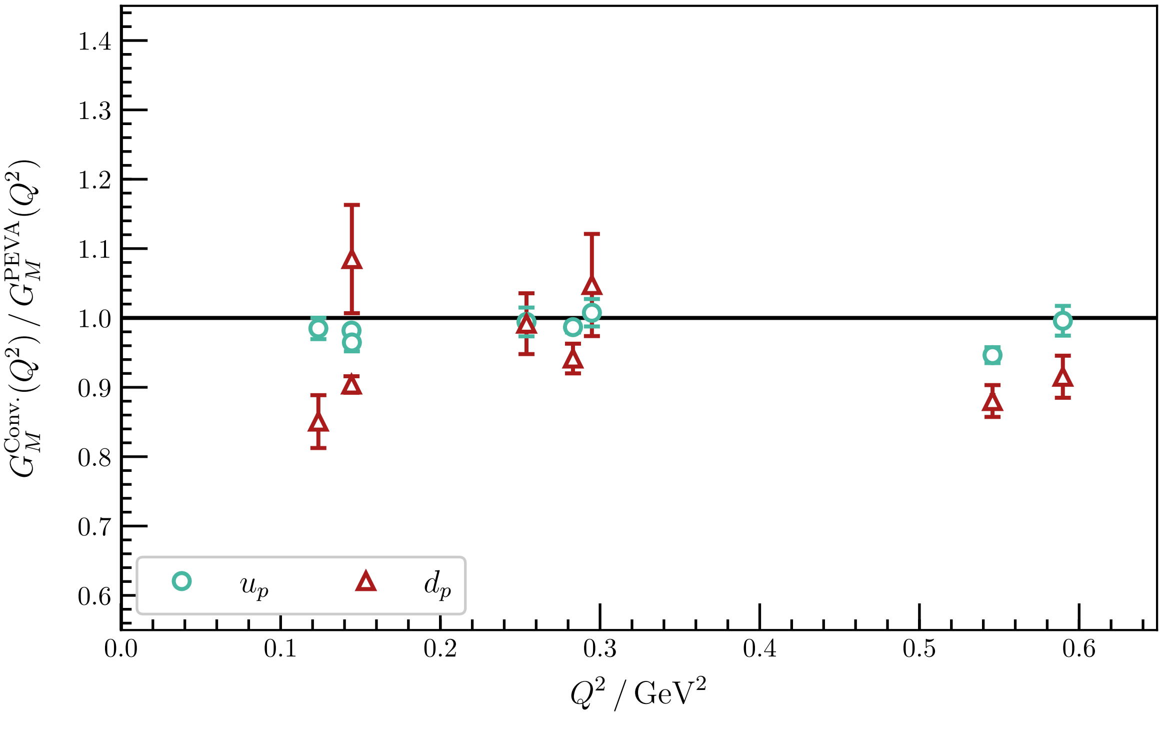

Figure 5.17: Ratios of conventional plateaus to PEVA plateaus for ground state $G_M(Q^2)$ at $m_\pi = 570\,\text{MeV}$. Most of the $d_p$ ratios show a significant departure from one, particularly those with smaller statistical errors.

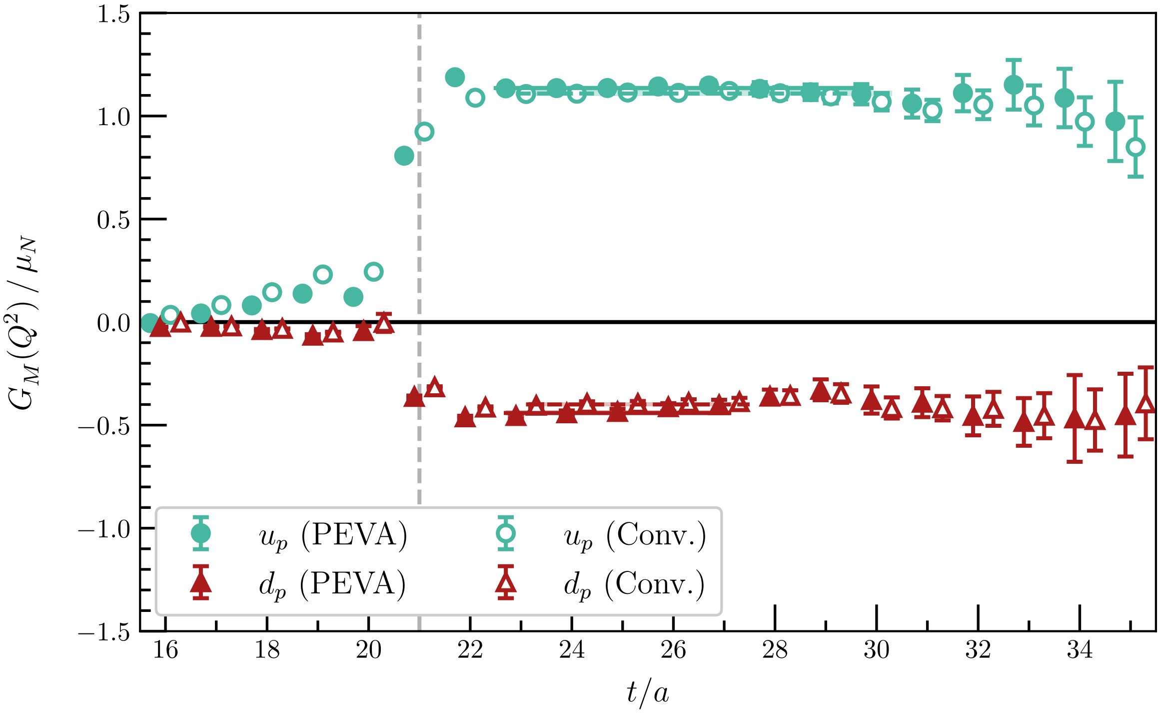

Figure 5.18: Quark-flavour contributions to ground state $G_M(Q^2)$ at $m_\pi = 411\,\text{MeV}$ for the lowest-momentum kinematics, providing $Q^2 = 0.1578(43)\,\text{GeV}^2$. The conventions used in this plot are the same as in Fig. 5.14. All four fits start at time slice 23. The ends of the fit regions differ between the two quark flavours due to an earlier onset of noise for $d_p$.

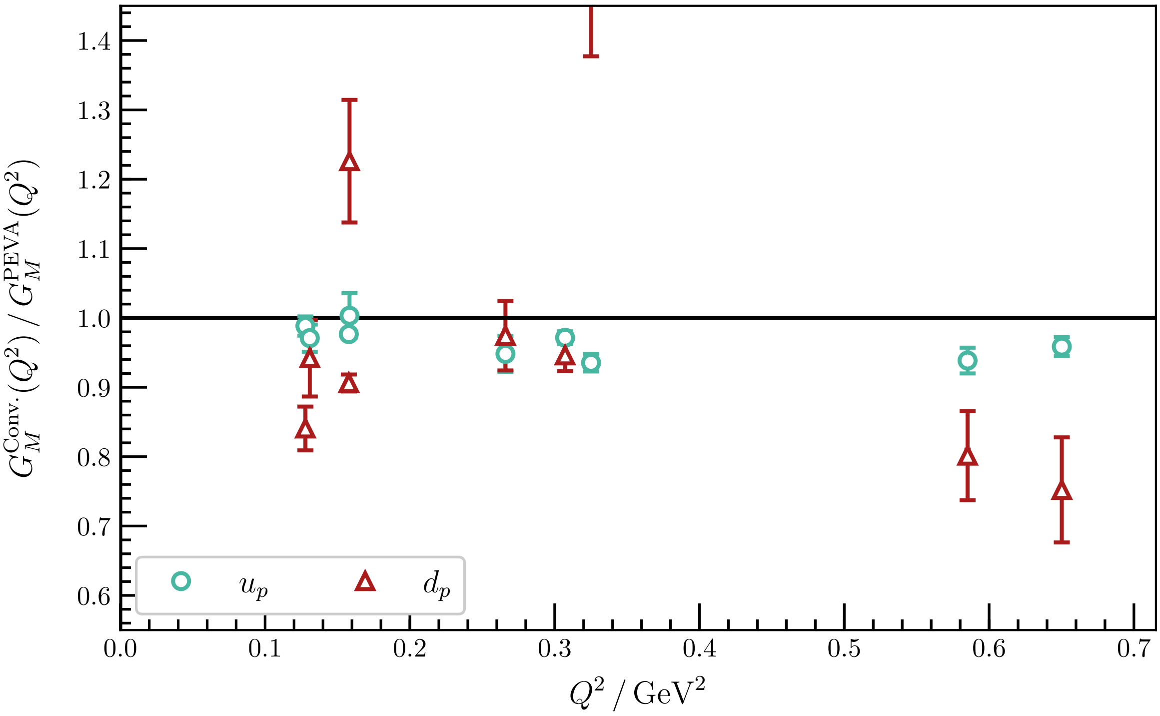

Figure 5.19: Ratios of conventional plateaus to PEVA plateaus for ground state $G_M(Q^2)$ at $m_\pi = 411\,\text{MeV}$. Most of the $d_p$ ratios show a significant departure from one. In addition, at higher $Q^2$ values, all of the $u_p$ ratios are clearly less than one.

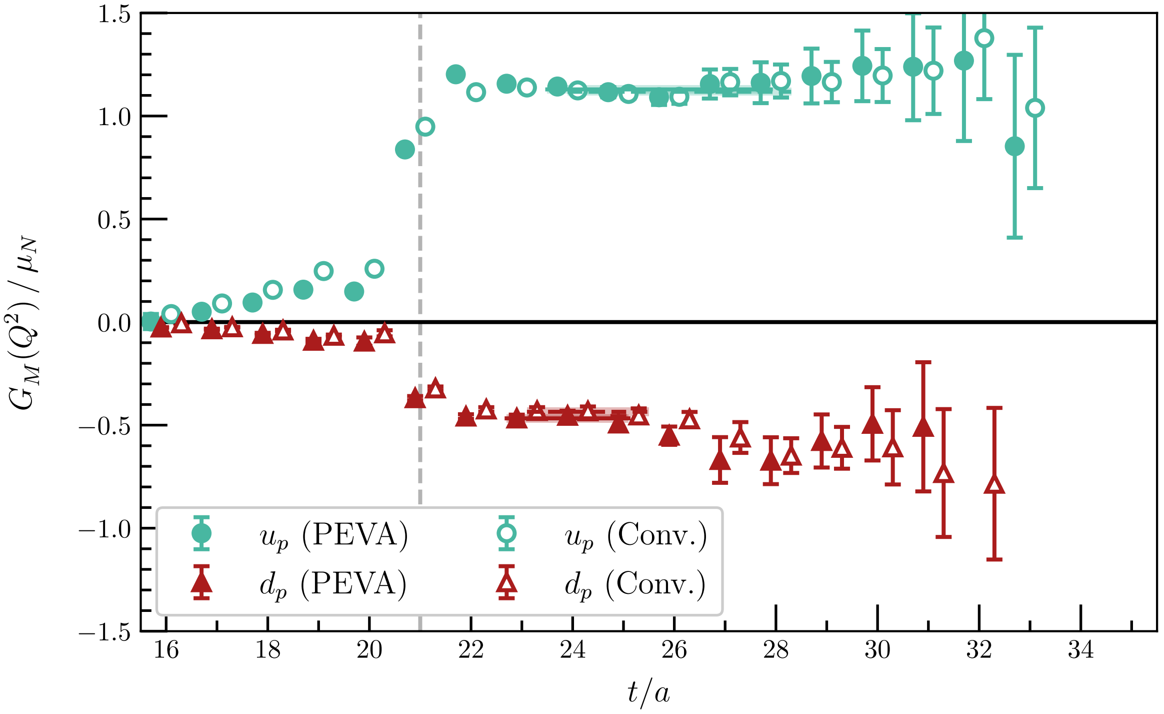

Figure 5.20: Quark-flavour contributions to ground state $G_M(Q^2)$ at $m_\pi = 296\,\text{MeV}$ for the lowest-momentum kinematics, providing $Q^2 = 0.1605(44)\,\text{GeV}^2$. The conventions used in this plot are the same as in Fig. 5.14. Both fits for $u_p$ are from time slice 24–28. Both fits for $d_p$ are slightly earlier, at 23–25.

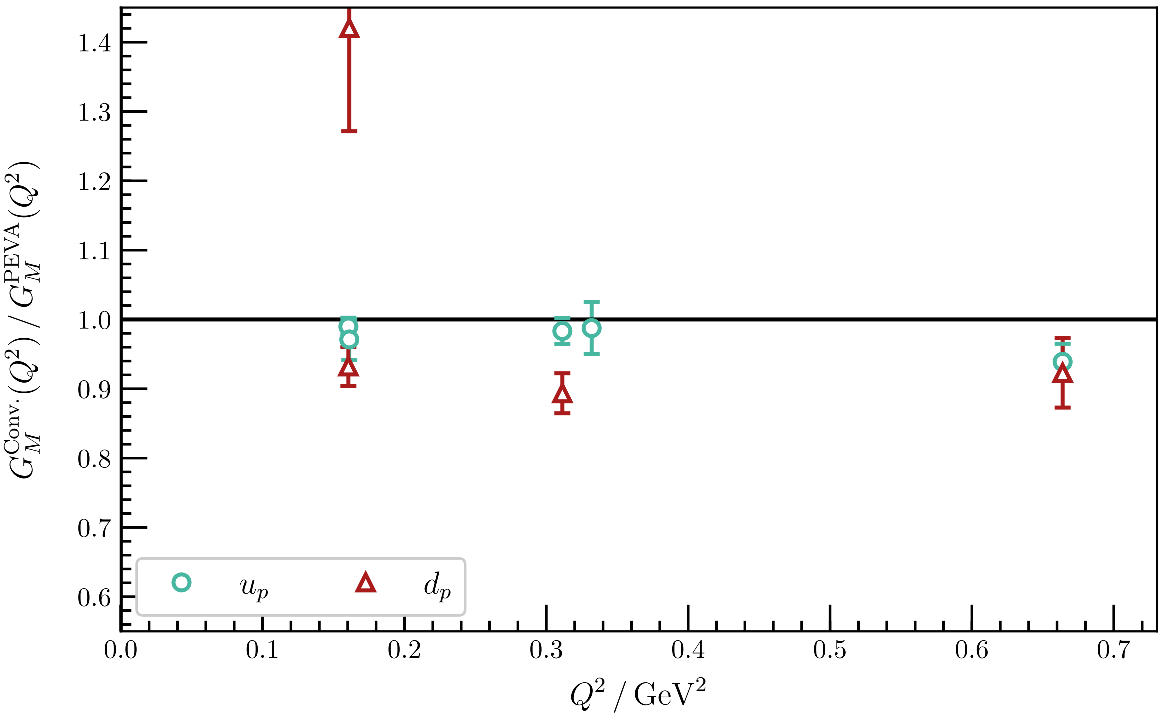

Figure 5.21: Ratios of conventional plateaus to PEVA plateaus for ground state $G_M(Q^2)$ at $m_\pi = 296\,\text{MeV}$. Most of the kinematics have been excluded due to unacceptable plateaus or failure of the variational analysis, but for those that remain, all of the $d_p$ ratios show a significant departure from one.

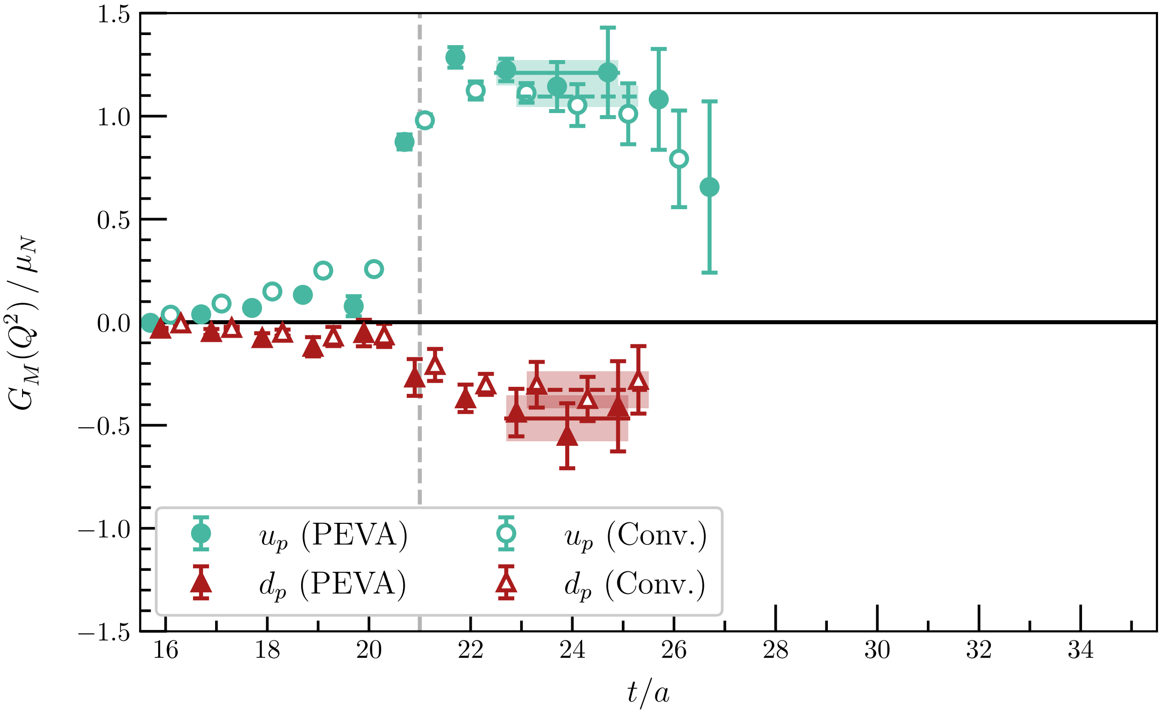

Figure 5.22: Quark-flavour contributions to the ground state $G_M(Q^2)$ at $m_\pi = 156\,\mathrm{MeV}$ for the lowest-momentum kinematics, providing $Q^2 = 0.1654(48)\,\mathrm{GeV}^2$. The conventions used in this plot are the same as in Fig. 5.14. All four fits are from time slice 23–25.

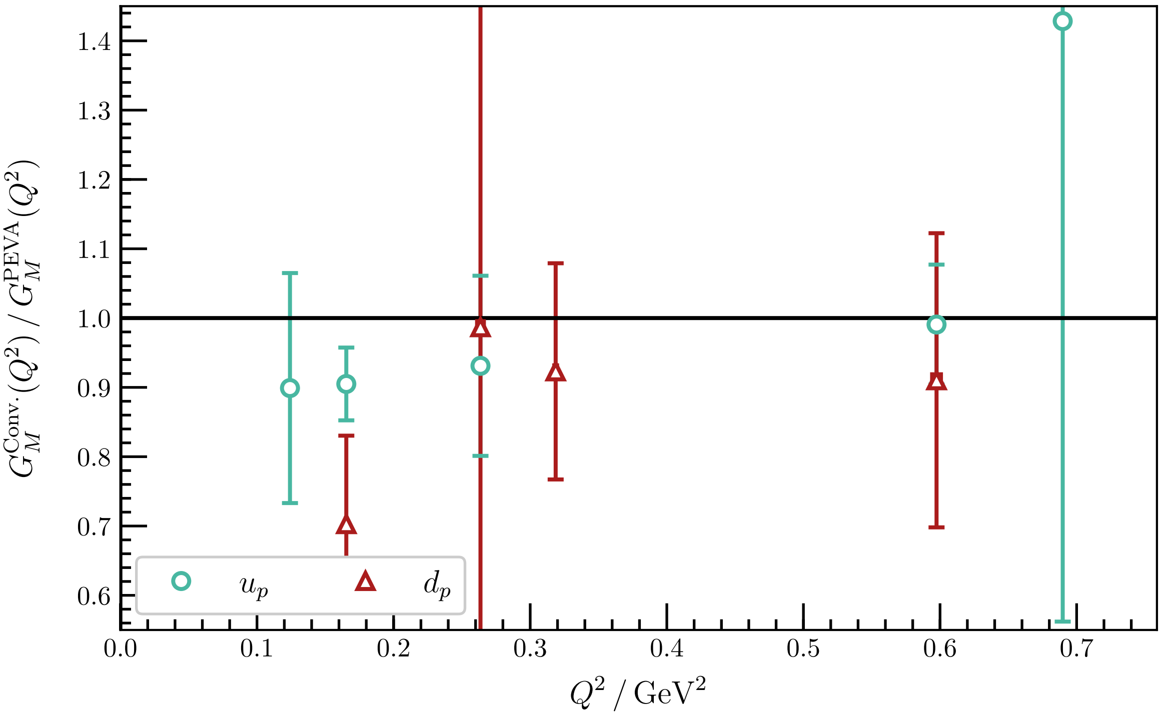

Figure 5.23: Ratios of conventional plateaus to PEVA plateaus for ground state $G_M(Q^2)$ at $m_\pi = 156\,\mathrm{MeV}$. Any disagreement between the plateaus at this mass is buried in the statistical noise, save for the kinematics with $\boldsymbol{p} = (0,0,0)$ and $\boldsymbol{p}' = (1,0,0)$, where the ratios for both quark flavours are significantly below one.

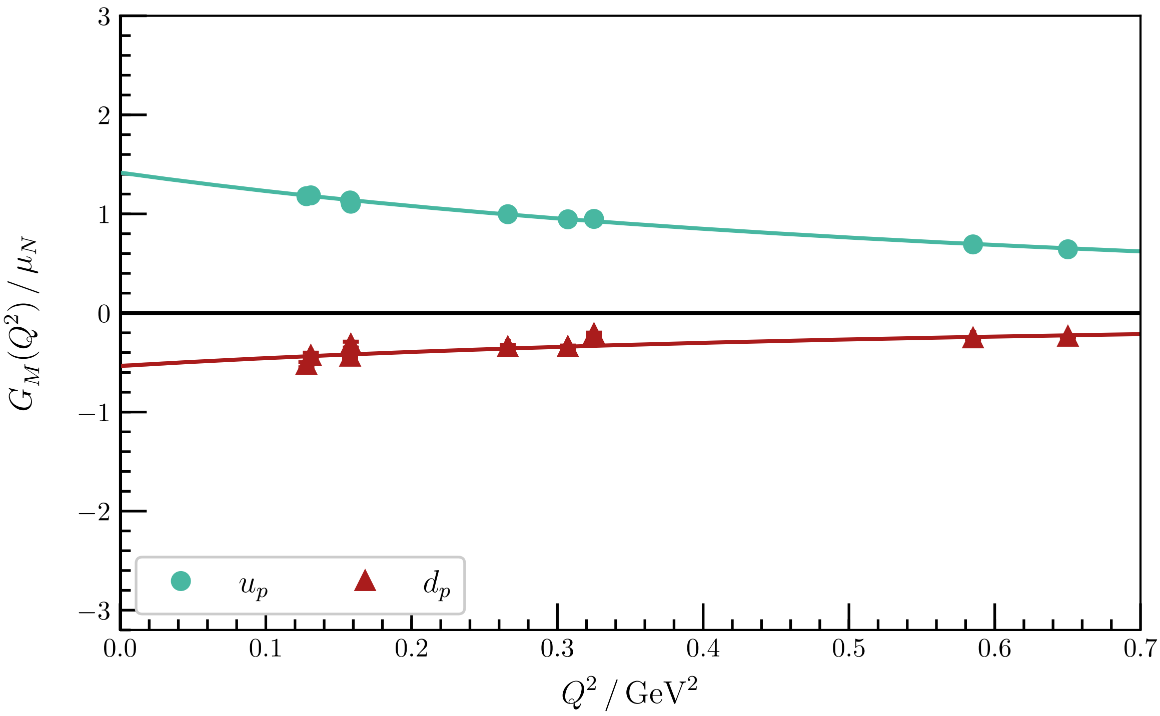

Figure 5.24: Quark-flavour contributions to ground state $G_M(Q^2)$ at $m_\pi = 411\,\mathrm{MeV}$. The shaded regions are dipole fits to the form factor, corresponding to magnetic radii of 0.583(13) fm for the doubly represented quark flavour ($u_p$) and 0.623(26) fm for the singly represented quark flavour ($d_p$).

tional extractions. These contaminations have a clear effect on the extracted magnetic form factor at all five pion masses, on the order of 10 %. Moving forward, use of the PEVA technique will be critical in precision calculations of $G_M(Q^2)$ for the ground-state nucleon, for which such systematic errors are unacceptable.

We now proceed to examine the extracted form factors. In light of the opposite-parity contaminations present in the conventional extractions, we focus only on the PEVA results. Fig. 5.24 shows the $Q^2$ dependence of the contribution to $G_M(Q^2)$ from each quark flavour at $m_\pi = 411\,\mathrm{MeV}$. We see good agreement with a dipole ansatz, with magnetic radii of 0.583(13) fm for the doubly represented quark flavour and 0.623(26) fm for the singly represented quark flavour. Similar plots for the other four masses are available in Appendix D.

Similar to the electric form factor case described in Section 5.3, we take linear combinations of the contributions from the doubly represented quark flavour ($G_{M\,u_p}(Q^2)$) and the singly represented quark flavour ($G_{M\,d_p}(Q^2)$) to obtain the magnetic form factors of the proton ($G_{M\,p}(Q^2)$) and neutron ($G_{M\,n}(Q^2)$):

$$G_{M\,p}(Q^2) = 2\times\left(+\frac{2}{3}\right)G_{M\,u_p}(Q^2) + \left(-\frac{1}{3}\right)G_{M\,d_p}(Q^2)\,,\ \text{and} \tag{5.25}$$

$$G_{M\,n}(Q^2) = 2\times\left(-\frac{1}{3}\right)G_{M\,u_p}(Q^2) + \left(+\frac{2}{3}\right)G_{M\,d_p}(Q^2)\,. \tag{5.26}$$

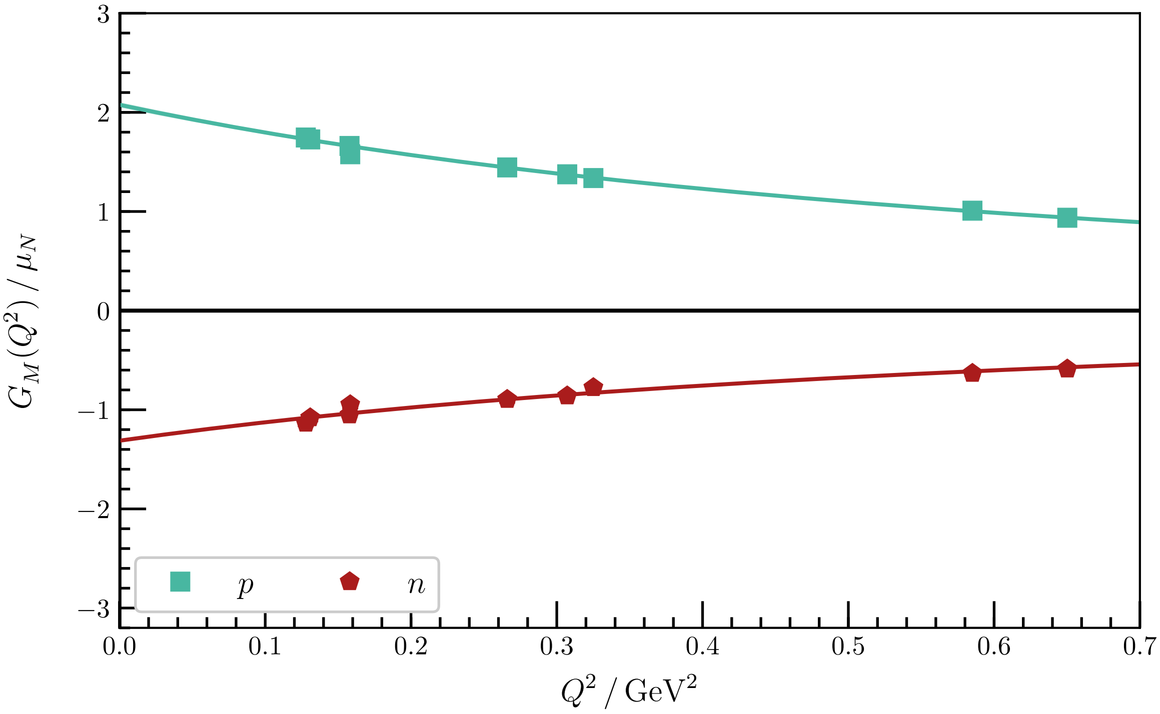

Figure 5.25: $G_M(Q^2)$ for the ground-state proton and neutron at $m_\pi = 411$ MeV. The shaded regions correspond to dipole fits to the form factors, with a magnetic radius of 0.592(12) fm for the proton and 0.609(13) fm for the neutron.

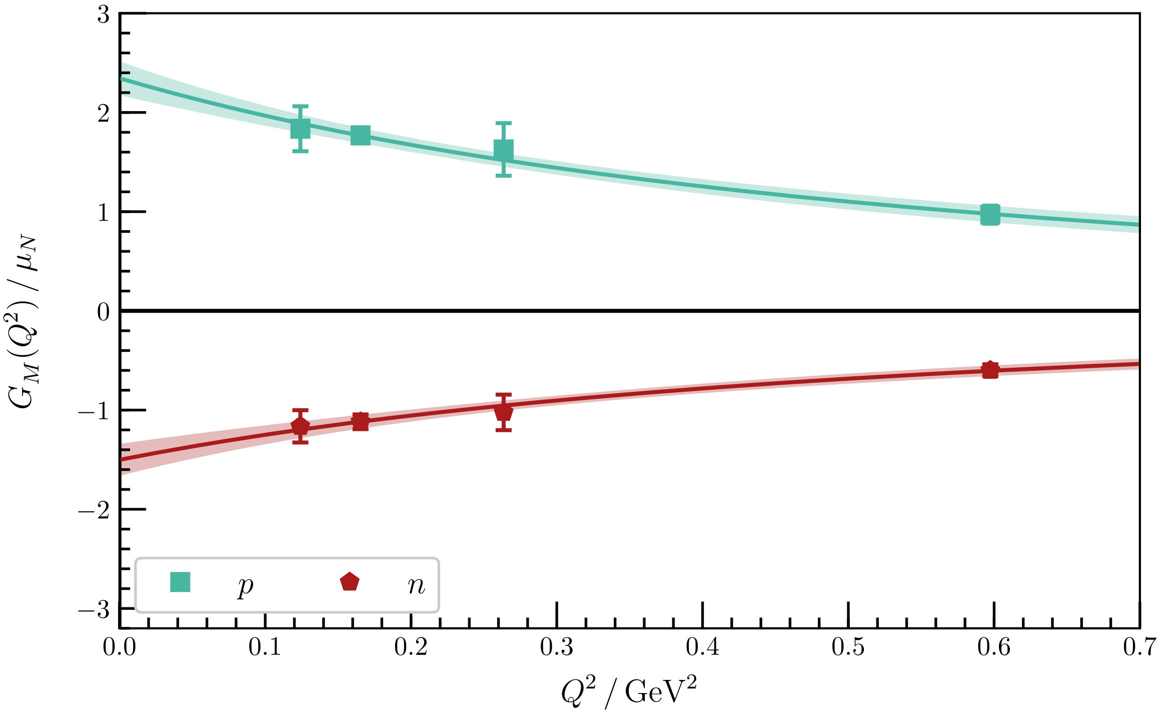

Figure 5.26: $G_M(Q^2)$ for the ground-state proton and neutron at $m_\pi = 156$ MeV. The shaded region corresponds to a dipole fit to the form factor, with a magnetic radius of 0.655(63) fm for the proton and 0.671(77) fm for the neutron.

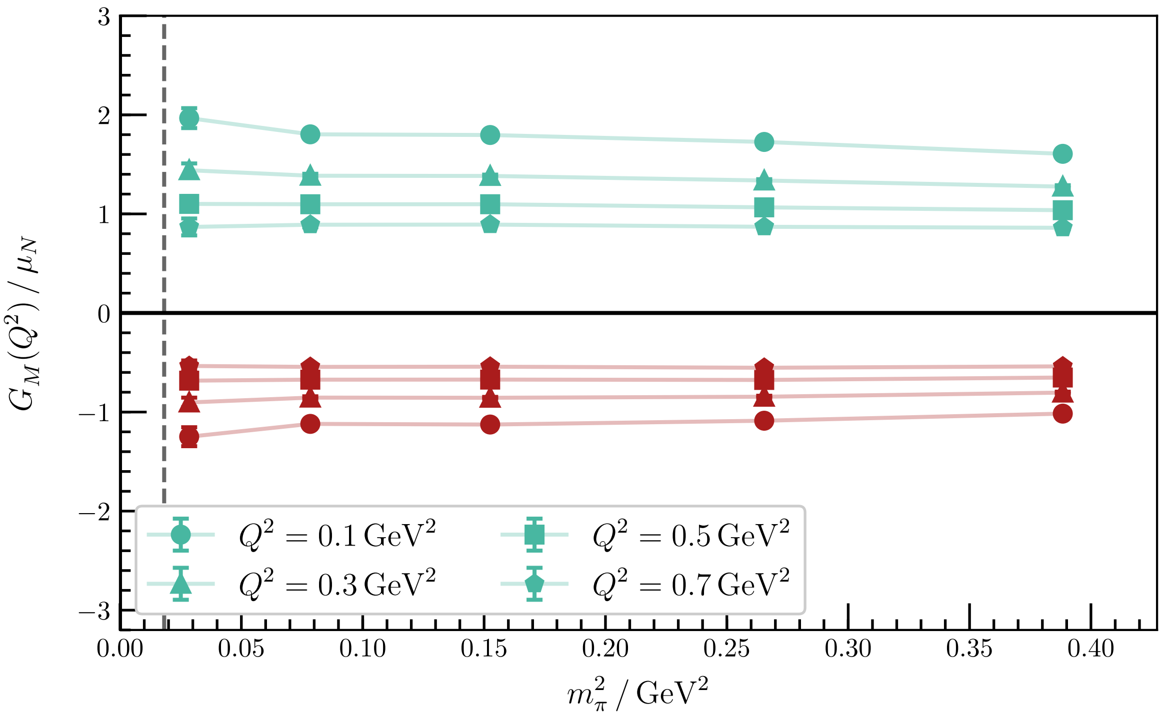

Figure 5.27: Quark-mass dependence of dipole fits to $G_M(Q^2)$ for the ground-state proton and neutron. The proton is represented by the light green symbols and takes only positive values, and the neutron is represented by dark red symbols and takes only negative values. As in Fig. 5.13, the marker shapes represent different $Q^2$ slices and the dashed line corresponds to the physical pion mass.

We plot these combinations for the middle and lightest pion masses in Figs. 5.25 and 5.26. Similar plots for the other three masses are available in Appendix D. At all five masses, the magnetic form factors of both the proton and the neutron agree well with a dipole fit. The magnetic radius obtained from each of these fits is close to the electric charge radius of the proton extracted from $G_E(Q^2)$ at the same pion mass.

In Fig. 5.27, we plot the quark-mass dependence of the dipole fits to $G_M(Q^2)$. We can once again see a quark-mass dependence, with the different $Q^2$ slices fanning out at lower masses, due to the simultaneous increase in the size of the state and the increasing value of $G_M(0)$, as expected in chiral perturbation theory [105, 106].

In this section, we demonstrated the importance of the PEVA technique in controlling systematic errors arising from opposite-parity contaminations in extractions of the magnetic form factor for the ground-state nucleon. Due to these opposite-parity contaminations, the conventional analysis underestimates the contribution to the magnetic form factor from the singly represented quark sector by approximately 10 %, whereas the PEVA technique removes the contaminations and gives improved results.

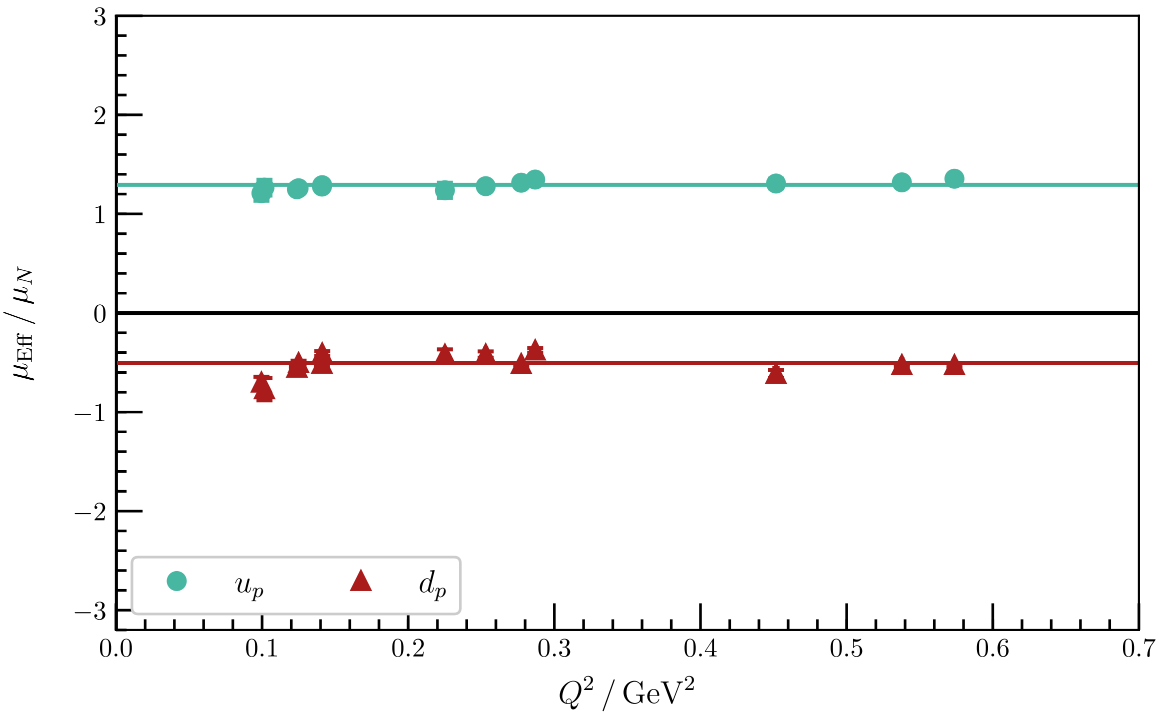

Figure 5.28: $\mu_{\mathrm{Eff}}$ for individual quark flavours in the ground state nucleon at $m_\pi = 702\,\mathrm{MeV}$. The narrow shaded bands are constant fits to the effective magnetic moment. They correspond to magnetic moment contributions of 1.294(24) $\mu_N$ for the doubly represented quark and −0.505(14) $\mu_N$ for the singly represented quark.

## 5.5 Magnetic Dipole Moment

Returning to the individual quark flavour contributions,and noting that the observed $Q^2$ dependence of $G_E(Q^2)$ and $G_M(Q^2)$ is very similar, we hypothesise that $G_M(Q^2)$ and $G_E(Q^2)$ have the same scaling in $Q^2$ over the range considered here. If this hypothesis is valid, then the ratio of $G_M(Q^2)$ to $G_E(Q^2)$ should be independent of $Q^2$. Since we are working with an improved conserved vector current, and single quarks of unit charge, $G_E(0) = 1$ exactly, and $G_M(0)$ should be the contribution of the quark flavour to the magnetic moment (up to scaling by the physical charge). Hence, the ratio

$$\mu_{\mathrm{Eff}}(Q^2) \equiv \frac{G_M(Q^2)}{G_E(Q^2)}\,, \tag{5.27}$$

should be constant in $Q^2$, and equal to the contribution to the magnetic moment from the given quark flavour.

Experimental results show that at high $Q^2$, $\mu\, G_E(Q^2)/G_M(Q^2)$ diverges significantly from unity [107], so our hypothesis must break down at sufficiently high $Q^2$. However, over the low $Q^2$ range we consider here, these experimental results show that $\mu\, G_E(Q^2)/G_M(Q^2)$ is close to one, and hence within this range $G_M(Q^2)/G_E(Q^2)$ approximates the magnetic moment.

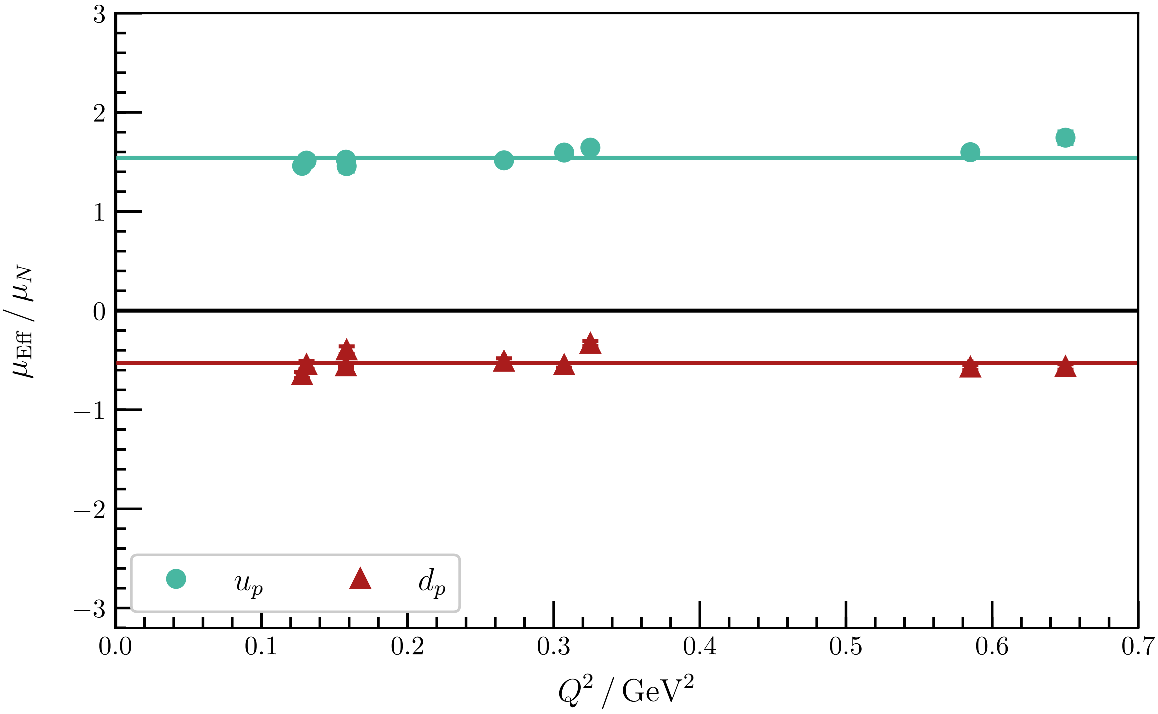

Figure 5.29: $\mu_{\mathrm{Eff}}$ for individual quark flavours in the ground state nucleon at $m_\pi = 411\,\mathrm{MeV}$. The narrow shaded bands are constant fits to the effective magnetic moment. They correspond to magnetic moment contributions of $1.542(29)\ \mu_N$ for the doubly represented quark and $-0.528(17)\ \mu_N$ for the singly represented quark.

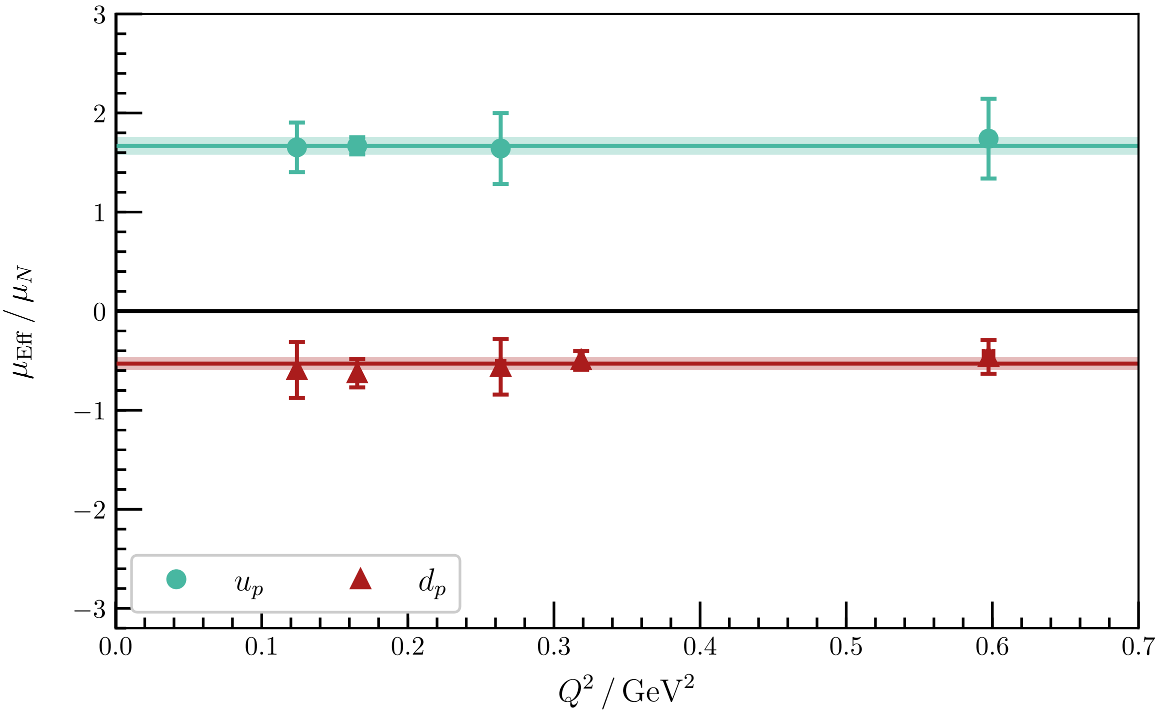

Figure 5.30: $\mu_{\mathrm{Eff}}$ for individual quark flavours in the ground state nucleon at $m_\pi = 156\,\mathrm{MeV}$. The shaded bands are constant fits to the effective magnetic moment. They correspond to magnetic moment contributions of $1.669(93)\ \mu_N$ for the doubly represented quark and $-0.529(66)\ \mu_N$ for the singly represented quark.

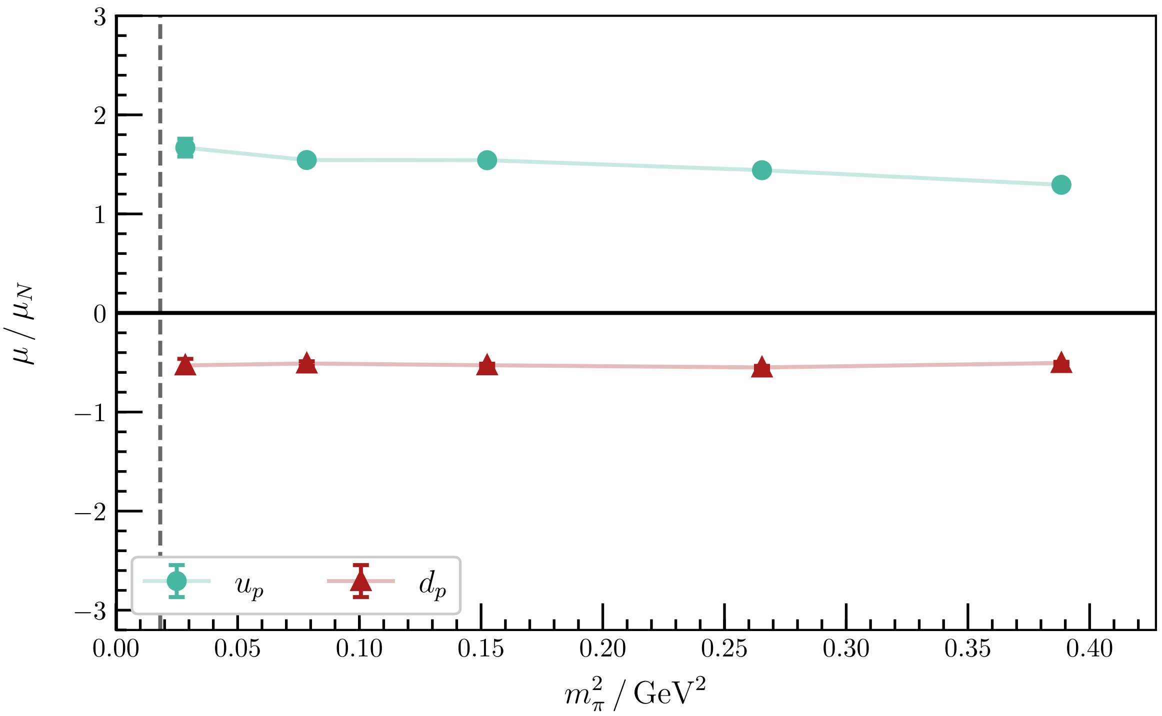

Figure 5.31: Pion-mass dependence of contributions to the ground-state magnetic moment from the doubly represented quark sector ($u_p$) and the singly represented quark sector ($d_p$). The vertical dashed line shows the physical pion mass.

For all five pion masses, we find that $\mu_{\text{Eff}}(Q^2)$ is indeed approximately constant across the $Q^2$ range considered. For example, Figs. 5.28–5.30 show the $Q^2$ dependence of $\mu_{\text{Eff}}(Q^2)$ at three of the masses. The remaining masses show very similar $Q^2$ dependence, and the corresponding plots are available in Appendix D. By taking a constant fit across all kinematics we obtain a robust estimate for the contributions to the magnetic moment of the nucleon from single quarks of unit charge. In the graphs shown here, the statistical errors on this fit are small, and the shaded band showing these errors is almost indistinguishable from the solid line indicating the central value of the fit. Fig. 5.31 shows the pion mass dependence of these fits. These individual quark-flavour contributions show a smooth pion-mass dependence with an enhancement of the magnetic moments at low pion mass consistent with chiral perturbation theory [105,106].

We can take the linear combinations discussed in Section 5.3 to obtain the magnetic moments of the ground-state proton and neutron. The quark mass dependence of these combinations is illustrated in Fig. 5.32. We see that the magnetic moments of the proton and neutron have a similar quark mass dependence to the individual quark-flavour contributions and are close to the experimental values of $2.792\,847\,350\,8(85)\ \mu_N$ for the proton, and $-1.913\,042\,73(45)\ \mu_N$ for the neutron [101]. The small discrepancy between our results and the physical values is due to a combination of disconnected loop contributions which are not included in our calculation, and finite-volume effects. There is no a priori reason that the disconnected loops could not be included in a

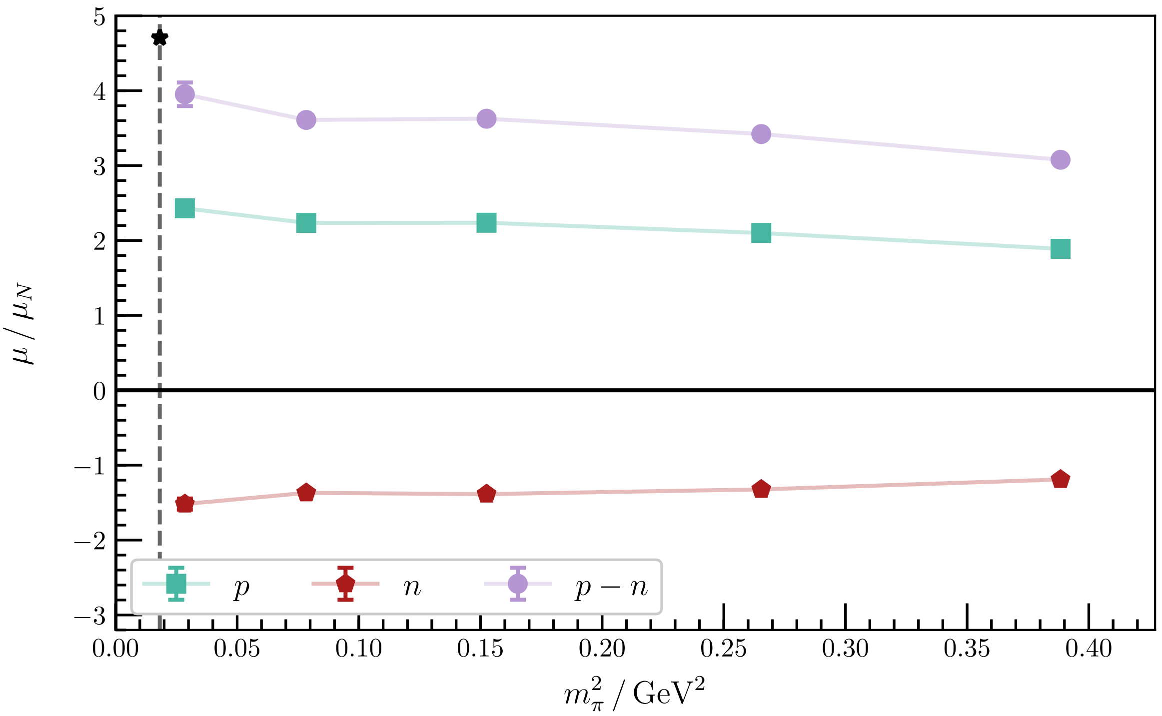

Figure 5.32: Pion-mass dependence of the extracted magnetic moment for the ground-state proton and neutron. To cancel out any disconnected loop contributions, we plot the isovector combination $\mu_p - \mu_n$. As the physical point is approached, the trend in this combination approaches but doesn't quite reach the physical value of $4.70\,\mu_N$ [101], represented by a black star.

PEVA calculation. They were simply omitted from the analysis presented here for computational efficiency. The disconnected loop contributions to the proton and neutron should be approximately the same (exactly the same in our lattice calculations, as we are in the isospin symmetric limit). Hence, if we take the isovector combination $\mu_{\mathrm{Eff}\,p} - \mu_{\mathrm{Eff}\,n}$, the disconnected loop contributions will cancel. Comparing this combination of our lattice results to the equivalent combination of the experimentally determined magnetic moments, we find that we underestimate the experimental value by around $10\,\%$. This remaining discrepancy is likely due to finite volume corrections [108] which are not accounted for in this analysis, which focuses on the importance of the PEVA technique.

## 5.6 Conclusion

In this chapter, we extended the PEVA technique to the calculation of elastic form factors, and applied it to calculating the Sachs electric and magnetic form factors $G_E(Q^2)$ and $G_M(Q^2)$ of the ground-state proton and neutron. This required inspection of the Dirac structure of the three point correlation function and careful selection of appropriate spinor projectors to extract the desired form factors with maximised signal.

Nucleon structure is a vibrant and rich field of study, and there have been a number of investigations of the Sachs electric and magnetic form factors of the ground state nucleon [109–117]. In this chapter we focused specifically on the application of the PEVA technique to form factor calculations and on the systematic errors introduced through opposite-parity contaminations.

We demonstrated the efficacy of variational analysis techniques in general, and PEVA specifically, at controlling excited-state contaminations in the electric form factor. Both the PEVA and conventional variational analysis show clear and clean plateaus, supporting previous work demonstrating the utility of variational analysis in calculating baryon matrix elements [103, 104].

In the case of the magnetic form factor, we found evidence that the conventional analysis was contaminated by opposite-parity states. For many of the kinematics considered here, we observe a 5–20 % underestimation of the magnitude of the contributions to the magnetic form factor from the singly represented quark flavour. For all of the highest-precision results, this underestimation is very consistent and of order 10 %. This indicates that the PEVA technique is critical for precision measurements of the nucleon form factors, where such systematic errors are unacceptable.

By utilising the PEVA technique, we are able to successfully extract the Sachs form factors of the ground-state nucleon at a range of $Q^2$ values. These extractions allow us to investigate the $Q^2$ dependence of these form factors. By taking ratios of the form factors, we are also able to extract the magnetic moments of both the ground-state proton and the ground-state neutron.

In the next chapter, we will extend this analysis to world-first calculations of the form factors for the the excited states of the nucleon, where the PEVA technique plays an even more significant role.

# Chapter 6

# Elastic Form Factors of Nucleon Excitations

*Some of the content in this chapter is based on the conference proceeding: "Electromagnetic Form Factors of Excited Nucleons via Parity-Expanded Variational Analysis" by F. M. Stokes et al. [97]*

## 6.1 Introduction

In Chapter 5, we presented a method for extracting the form factors of a baryonic state on the lattice using the PEVA technique, and established its effectiveness for accessing the structure of the ground-state nucleon. We now use this method to investigate the structure of the excitations of the proton and neutron observed in Lattice QCD.

On the lattice, we observe a tower of stable excitations of each ground state. These towers of stable finite-volume eigenstates are associated in a non-trivial manner with unstable finite-width resonances in nature. Understanding the structure of the states observed in Lattice QCD will enable predictions of the infinite-volume observables of nature via effective field theory techniques [95, 118].

Investigating the structure of excited states in lattice QCD is recognised as an important frontier in the field. Progress has already been made in the meson sector, where the issues of parity mixing are not present [119, 120]. Here we tackle the more challenging problem of calculating such quantities in the baryon sector.

While experimental measurements of resonance transition amplitudes have been made, it is much harder to measure elastic form factors in the resonance regime. This is because elastic form factors parameterise interactions where both the initial and final state are the same. To measure them for an (unstable) resonance, we need to first produce that resonance, and then probe it during the extremely short time window before it decays. On the other hand, the transition form factors parameterise the transformation of one state into another. We can probe a stable target such as a ground state proton and measure how it is excited into the unstable resonance of interest through an examination of its decay products.

It has been suggested that the magnetic dipole moment of the $N^*(1535)$ resonance could be measured through the $\gamma p \to \gamma\eta p$ process [121] using the Crystal Barrel/TAPS detector at ELSA or Crystal Ball @ MAMI, but this measurement has yet to be realised. The difficulty of measuring such quantities experimentally provides the opportunity for Lattice QCD to lead experiment and create new knowledge.

By using local three-quark operators on the lattice, both the CSSM [16, 122] and the Hadron Spectrum Collaboration (HSC) [18, 19] observe two low-lying odd-parity states in the resonance regimes of the $N^*(1535)$ and $N^*(1650)$. The local operators used only couple well to localised states. As a result, the states accessed by such analyses will usually be quark-model-like states dressed by a meson cloud, similar to the ground-state nucleon. Existing Hamiltonian effective field theory (HEFT) calculations [96] describe this energy spectrum as the finite volume spectrum of the $N^*(1535)$ resonance. However, given the presence of two resonances in this region, this is not necessarily the full picture, and a determination of the structure of these states on the lattice can give important insight. By comparing the structure of the observed states to quark model predictions, we gain insight into the expected makeup of the states in HEFT, as the bare states in the HEFT roughly correspond to the quark model states. HEFT also holds the promise of linking our lattice results to experiment.

In this chapter we present a determination of the Sachs electric and magnetic form factors for three localised spin-½ nucleon eigenstates on the lattice. Two of these states are negative-parity nucleon excitations, which we label $N_1^*$ (or $p_1^*$ for the proton excitation and $p_1^*$ for the neutron excitation), and $N_2^*$ (or the equivalent labels for the excited proton and neutron). The remaining eigenstate is a positive-parity excitation, and is denoted $N'$, $p'$, or $n'$. We compare the magnetic moments predicted from the negative-parity results to constituent quark model predictions for the magnetic moments of the $N^*(1535)$ and $N^*(1650)$ resonances [121, 123]. Such quark model calculations can be extended to include effects from the pion cloud. We also compare our lattice results to two such extensions [123, 124]. From these comparisons, we make connections to the basis states to be considered in HEFT [96].

## 6.2 Negative parity excitations

The results presented in this chapter use the same variational analysis and gauge field ensembles as in Chapter 5, in which we studied the electromagnetic form factors of the ground-state nucleon. The three heaviest pion masses available among these ensembles span $m_\pi = 411\,\mathrm{MeV}$–$702\,\mathrm{MeV}$, a typical range for studies of baryon excitations. As such, these masses are appropriate for this world-first study of the electromagnetic structure of nucleon excitations. In presenting our discoveries, we will focus on the results at the lightest of these three masses, $m_\pi = 411\,\mathrm{MeV}$. There are two even lighter masses, at $m_\pi = 156\,\mathrm{MeV}$ and $296\,\mathrm{MeV}$. These approach the physical point, presenting a significant challenge in terms of gauge noise and computational cost, but offer the possibility of insight into important chiral physics.

We once again use the operator basis described in Chapter 4, where we extracted the nucleon excited-state spectrum. We study the first three excitations extracted by this basis. As we will see in the results presented below, the PEVA technique is very important in correctly extracting form factors of these excitations.

A particular concern in this analysis is the possibility of contamination by nearby multi-particle scattering states that have not been isolated by the current correlation-matrix analysis using local operators [15, 16, 122]. However, HEFT calculations indicate that such contaminations are less than 10 %, and a careful search for these contaminations in the negative-parity spectrum showed their effects to be contained within the statistical uncertainties [125]. In the following analysis, we demand that our two- and three-point correlators are consistent with a single-state ansatz within the Euclidean time regions considered. As one proceeds to precision calculation of these form factors, it will be important to examine the scattering-state contributions to the form factors in detail.

### 6.2.1 $G_E$ for the first negative-parity excitation

Beginning with the lowest-lying negative-parity excitation observed in this study, we study the dependence of $G_E(Q^2)$ as extracted by both PEVA and a conventional analysis on the Euclidean time of the sink. In Fig. 6.1, we plot $G_E(Q^2)$ for both quark flavours present in the nucleon interpolator at $m_\pi = 702\,\mathrm{MeV}$ with the lowest-momentum kinematics of $\boldsymbol{p} = (0, 0, 0)$ and $\boldsymbol{p}' = (1, 0, 0)$. As with most of the graphs in this chapter, for ease of comparison we use the same axis ranges as used in the previous chapter for the corresponding results for the ground-state nucleon.

We see that the conventional extraction sits well below the PEVA extraction for all time slices between the current insertion and the point at which the signal is lost to noise. The conventional extraction also has a more significant time dependence than the PEVA extraction, forcing the conventional fit one time slice later. Both of these effects indicate that the conventional analysis is affected by opposite-parity contaminations, which are having a significant effect on the extracted form factor, introducing a systematic error of 12(4) % for the singly represented quark flavour and 25(5) % for the doubly represented flavour.

The lighter pion masses show a similar behaviour, The conventional analysis con-

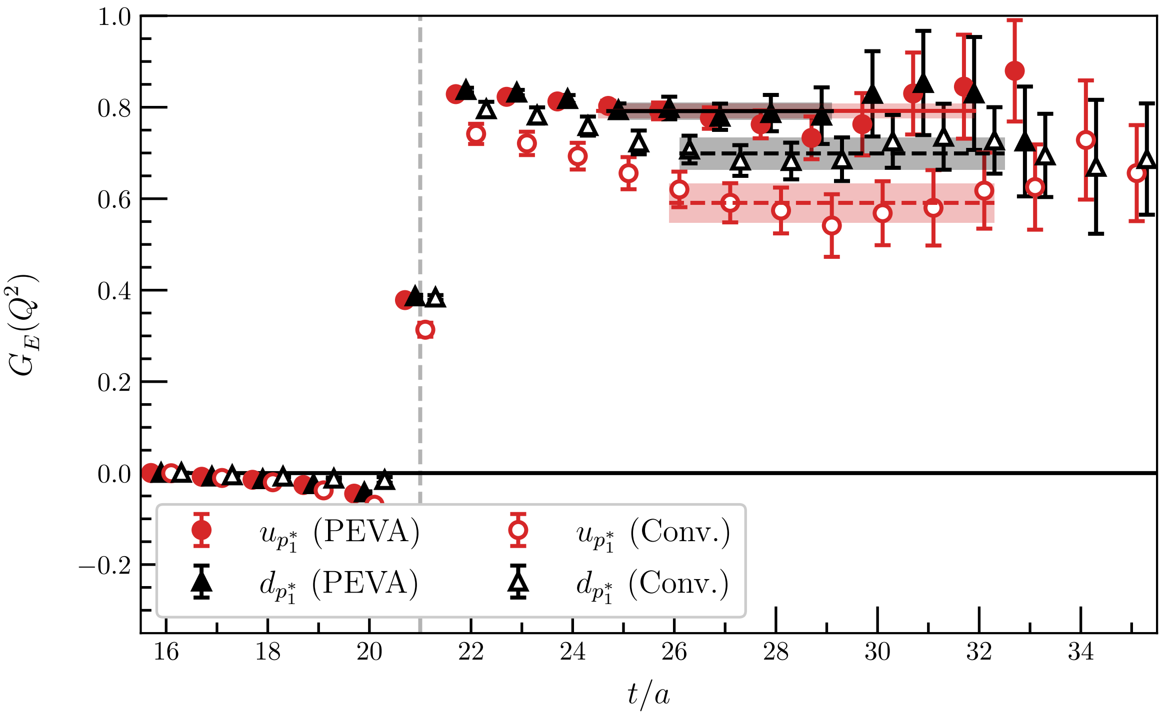

Figure 6.1: Quark-flavour contributions to the electric form factor for the first negative-parity excitation of the nucleon at $m_\pi = 702\,\mathrm{MeV}$ for the lowest-momentum kinematics, providing $Q^2 = 0.1422(41)\,\mathrm{GeV}^2$. We plot the conventional analysis with open markers and the new PEVA analysis with filled markers. Our fits to the plateaus are illustrated by shaded bands, with dashed fit lines for the conventional analysis, and solid fit lines for PEVA. The source is at time slice 16, and the current is inserted at time slice 21, as indicated by the vertical dashed line. Both PEVA fits are from time slice 25, whereas the conventional fits both start at 26, and have significantly lower values than the PEVA fits.

sistently has a plateau which starts later than the PEVA analysis and sits significantly lower. For example Fig. 6.2 shows this behaviour at $m_\pi = 296\,\mathrm{MeV}$. The magnitudes of the conventional plateaus with these low-momentum kinematics are systematically underestimated by 14(4) % and 32(5) % for the singly and doubly represented quark flavours respectively.

We can also consider changing the momenta to access different kinematics. By boosting the initial and final states while keeping the momentum transfer constant, we can access smaller values of $Q^2$, as discussed in Chapter 5. We can also increase the momentum transfer, giving access to larger values of $Q^2$. For such kinematics at all masses we find that in general, the conventional plateaus are later in time and take smaller values than the PEVA plateaus.

These results indicate that the PEVA technique is critical to the correct extraction of the electric form factors of this nucleon excitation. The conventional analysis is clearly contaminated by opposite-parity states, and when these states are removed by the PEVA technique it has a significant effect on the extracted form factor values.

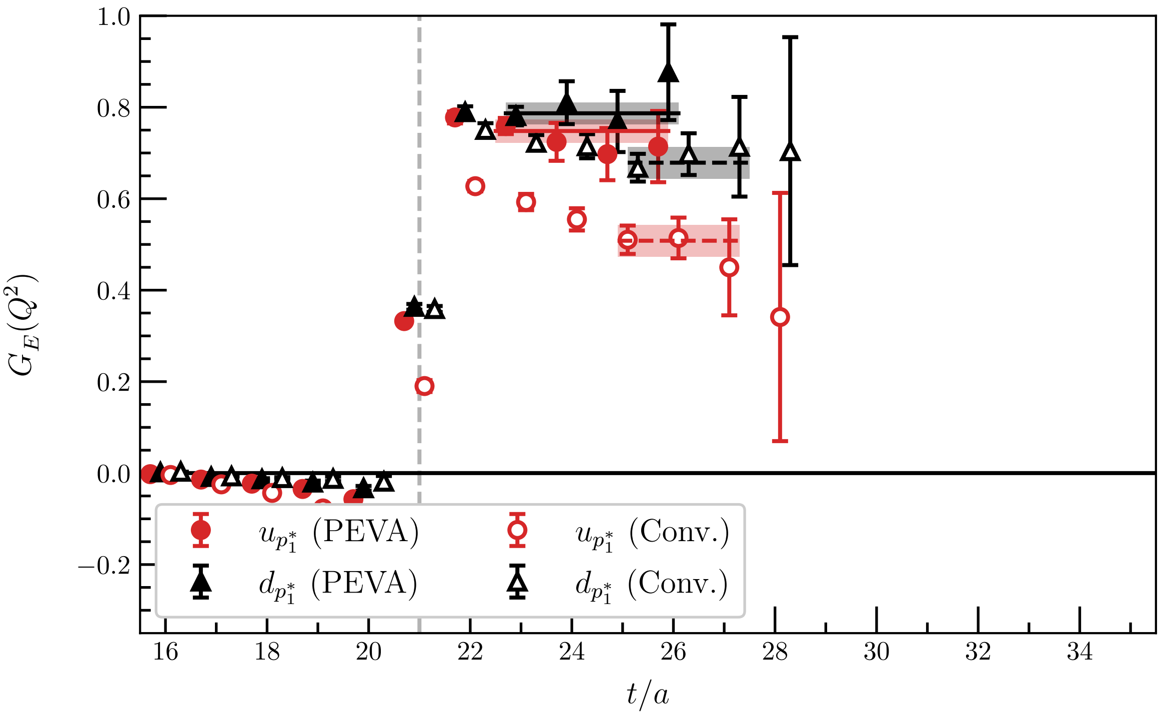

Figure 6.2: Quark-flavour contributions to the electric form factor for the first negative-parity excitation of the nucleon at $m_\pi = 296\,\mathrm{MeV}$ for the lowest-momentum kinematics, providing $Q^2 = 0.1632(45)\,\mathrm{GeV}^2$. The conventions used in this plot are the same as in Fig. 6.1. Both PEVA fits start from time slice 23, but the conventional analysis fits start from 25, and have lower values.

Hence, we now focus our attention only on the PEVA results.

In Fig. 6.3, we plot the $Q^2$ dependence of the electric form factor at $m_\pi = 411\,\mathrm{MeV}$. The set of kinematics used to access the various $Q^2$ values is the same as listed in Chapter 5, and we once again exclude any fits for which there is no acceptable plateau, or the variational analysis fails. We see that the two quark flavours have very similar contributions to the electric form factor. They both agree well with a dipole ansatz (as discussed in Chapter 5), with a charge radius of $0.646(18)\,\mathrm{fm}$ for the doubly represented quark flavour and $0.670(26)\,\mathrm{fm}$ for the singly represented quark flavour. These charge radii are similar to the charge radii of the individual quark sectors in the ground state examined in Chapter 5, ($0.658(12)\,\mathrm{fm}$ for the doubly represented quark flavour and $0.624(11)\,\mathrm{fm}$ for the singly represented quark flavour). The doubly represented quark sector agrees to within one standard deviation. However, the singly represented quark sector in the excitation has a charge radius approximately 1.5 standard deviations larger than the ground state.

We see similar behaviour for the other four masses. The plots for these masses are omitted from this chapter for the sake of brevity. For the interested reader, they are available in Appendix D.

In order to compute the form factors of the first negative-parity excitation of

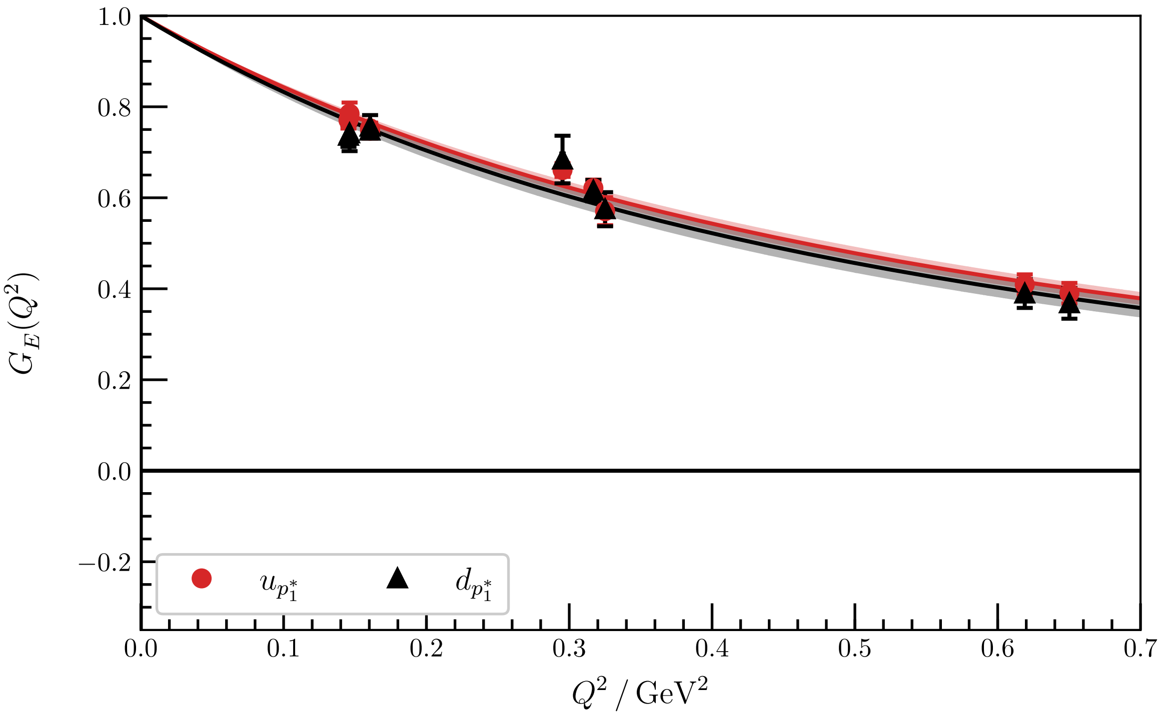

Figure 6.3: Quark-flavour contributions to the electric form factor for the first negative-parity excitation at $m_\pi = 411$ MeV. The shaded regions are dipole fits to the form factors, with the $y$-intercept fixed to unity. They correspond to charge radii of 0.646(18) fm for the doubly represented quark flavour ($u_{p_1^*}$) and 0.670(26) fm for the singly represented quark flavour ($d_{p_1^*}$).

the proton ($G_{E\,p_1^*}(Q^2)$) and neutron ($G_{E\,n_1^*}(Q^2)$), we need to take the correct linear combinations of the contributions from the doubly represented quark flavour ($G_{E\,u_{p_1^*}}(Q^2)$) and the singly represented quark flavour ($G_{E\,d_{p_1^*}}(Q^2)$). As in Chapter 5,

$$G_{E\,p_1^*}(Q^2) = 2 \times \left(+\frac{2}{3}\right) G_{E\,u_{p_1^*}}(Q^2) + \left(-\frac{1}{3}\right) G_{E\,d_{p_1^*}}(Q^2)\,, \text{ and} \tag{6.1}$$

$$G_{E\,n_1^*}(Q^2) = 2 \times \left(-\frac{1}{3}\right) G_{E\,u_{p_1^*}}(Q^2) + \left(+\frac{2}{3}\right) G_{E\,d_{p_1^*}}(Q^2)\,. \tag{6.2}$$

In Fig. 6.4, we plot the electric form factors obtained by taking these combinations of the form factors at $m_\pi = 411$ MeV. The form factor for the neutron excitation is close to zero, reflecting the similar charge radii of the individual quark flavours. The electric form factor for the first excited state of the proton agrees well with a dipole ansatz. If we do this for all five pion masses (see Appendix D), we find that the dipole fits correspond to charge radii ranging from 0.577(18) fm–0.697(47) fm, increasing with decreasing pion mass. For each pion mass considered, the extracted charge radius is consistent with the radius of the ground-state proton at the same mass, as obtained in Chapter 5. This suggests that the size of this state is similar to that of the ground-state nucleon.

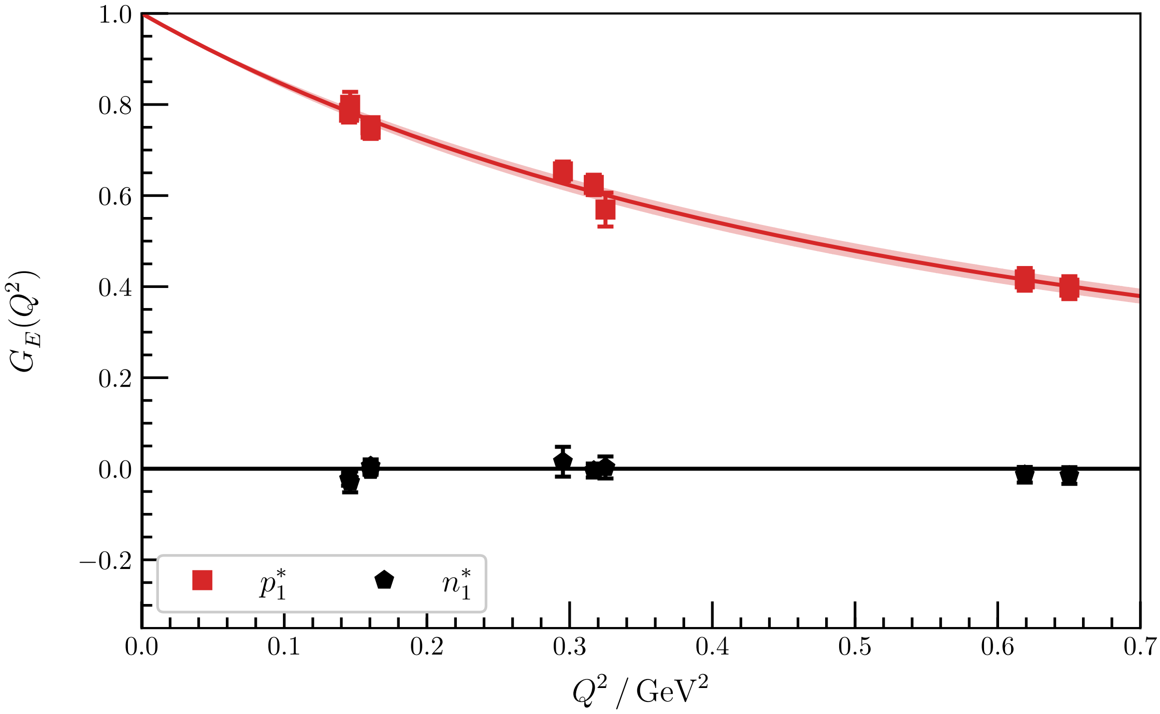

Figure 6.4: $G_E(Q^2)$ for the first negative-parity excitations of the proton and neutron at $m_\pi = 411\,\mathrm{MeV}$. The shaded region corresponds to a dipole fit to the electric form factor for the proton excitation with the $y$-intercept fixed to unity. This fit corresponds to a charge radius of 0.645(20) fm .

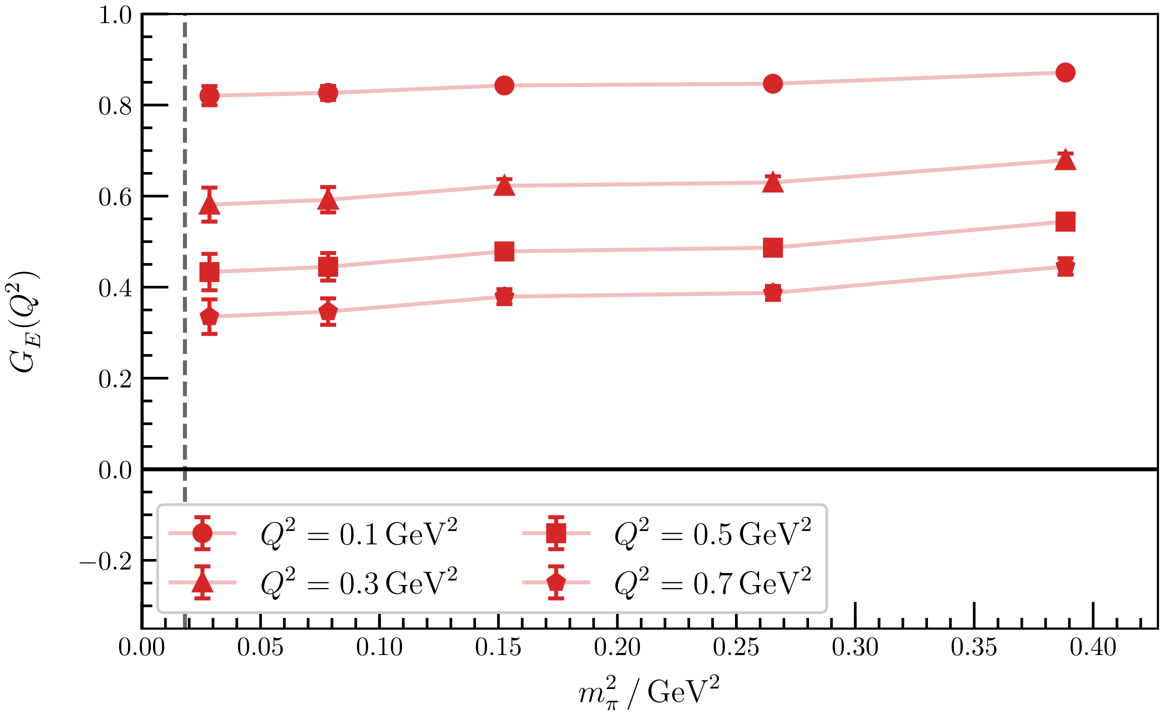

Figure 6.5: Quark-mass dependence of dipole fits to the electric form factor for the first negative-parity excitation of the proton. We can see a mild pion-mass dependence, with the form factor dropping in magnitude as the pion mass is reduced towards the physical point. This is consistent with the increasing charge radius as the quark mass drops.

In Fig. 6.5, we plot the pion-mass dependence of the dipole fits to the electric form factor for the proton excitation on a number of $Q^2$ slices. We see that, similar to the ground state, the pion-mass dependence is fairly smooth, and has a clear trend to lower values at lower pion masses, consistent with the increasing charge radius. However, there is no hint of significant non-analytic behaviour in the quark-mass dependence.

In a similar way, we can take a linear combination of the squared charge radii for the individual quark flavours to obtain the squared charge radius of the excited neutron. In contrast to the ground state neutron, which has a significant negative squared charge radius, this excitation has a squared charge radius that is much closer to zero, or perhaps even positive. For example, at $m_\pi = 411\,\mathrm{MeV}$, the squared charge radius of the first negative parity excitation of the neutron is $\langle {r_{n_1^*}}^2 \rangle = 0.021(18)\,\mathrm{fm}$.

### 6.2.2 $G_M$ for first negative-parity excitation

We now proceed to the magnetic form factor. In Fig. 6.6, we plot the plateaus for the heaviest pion mass and the lowest momenta. While the conventional and PEVA plateaus for the doubly represented quark flavour are consistent, both in fit region and value, the conventional plateau for the singly represented quark flavour starts later and has a significantly more negative value than the PEVA plateau. We see a similar effect at the lighter masses and other kinematics. For example, Fig. 6.7 shows this behaviour at $m_\pi = 411\,\mathrm{MeV}$ with the same lowest-momentum kinematics.

Having fit the form factor plateaus, we can investigate the $Q^2$ dependence of $G_M(Q^2)$. In Fig. 6.8, we plot the contributions to $G_M(Q^2)$ from both the singly represented quark flavour and the doubly represented quark flavour at $m_\pi = 411\,\mathrm{MeV}$. Both quark flavours are consistent with a dipole fit with a magnetic radius of $0.533(46)\,\mathrm{fm}$ for the doubly represented quark flavour and $0.664(194)\,\mathrm{fm}$ for the singly represented quark flavour. This $Q^2$ dependence is similar to that for $G_E(Q^2)$, and the same is true for the other pion masses considered. Plots demonstrating this are available in Appendix D.

As described in Section 6.2.1 above, we can take linear combinations of the individual quark flavour contributions to compute the magnetic form factors of the excited proton and neutron. We plot these combinations for $m_\pi = 411\,\mathrm{MeV}$ in Fig. 6.9. For all five masses, we find that these form factors are described well by dipole fits. Graphs of these fits for all five masses are available in Appendix D for the interested reader. These fits mostly agree with the charge radii from $G_E(Q^2)$, although the magnetic charge radii at $m_\pi = 702\,\mathrm{MeV}$ and $411\,\mathrm{MeV}$ are slightly lower than the corresponding electric charge radii.

In Figs. 6.10 and 6.11, we plot the pion-mass dependence of the dipole fits to $G_M(Q^2)$ for the excited proton and neutron. We observe a discontinuity at the second lightest mass, which suggests that there could be a change in the structure of this state at that

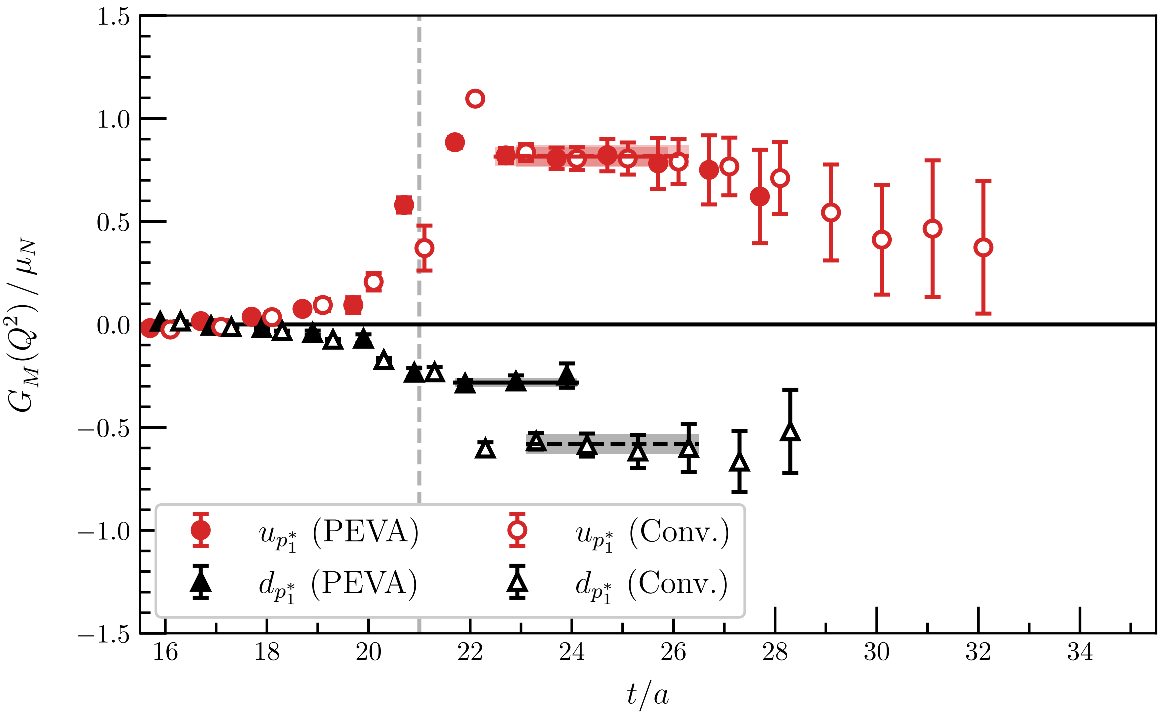

Figure 6.6: Quark-flavour contributions to $G_M(Q^2)$ for the first negative-parity excitation at $m_\pi = 702\,\mathrm{MeV}$ for the lowest-momentum kinematics, providing $Q^2 = 0.1422(41)\,\mathrm{GeV}^2$. As in Fig. 6.1, we plot the conventional analysis with open markers and dashed fit lines and the new PEVA analysis with filled markers and solid fit lines. For the doubly represented quark flavour, the plateaus for both analyses are from 23–26 and take consistent values. For the singly represented quark flavour, the PEVA fit is from 22–25, while the conventional fit is from 23–26, and has a significantly more negative value.

mass. However, there is no corresponding change in $G_E(Q^2)$. At the lightest mass, the form factors appear to once again be consistent with the heavy-mass behaviour. Hence, it is unclear whether the behaviour at the second lightest mass indicates a change in the nature of the state, or is a result of increasing gauge noise at lighter pion masses. Further research with increased statistics will be required to determine which of these two possibilities is realised.

Returning to the individual quark sector results, we note that $G_M(Q^2)$ and $G_E(Q^2)$ have a similar $Q^2$ dependence over the range considered. As in Chapter 5, we consider the ratio $\mu_{\mathrm{Eff}}(Q^2) \equiv G_M(Q^2)/G_E(Q^2)$. In Fig. 6.12, we plot this ratio at $m_\pi = 411\,\mathrm{MeV}$ as a function of $Q^2$. We see that the ratio is once again approximately constant across the $Q^2$ range considered. This holds true for all five pion masses considered, as can be seen in the supplementary plots presented in Appendix D. This supports the underlying hypothesis that the $Q^2$ scaling of the contributions to $G_E(Q^2)$ and $G_M(Q^2)$ is the same, and hence suggests that $\mu_{\mathrm{Eff}}$ is a good estimate for the magnetic moment of this state.

We take constant fits to $\mu_{\mathrm{Eff}}$ at each quark mass, and plot their pion-mass dependence in Fig. 6.13. By taking linear combinations of these fits as described for $G_E(Q^2)$

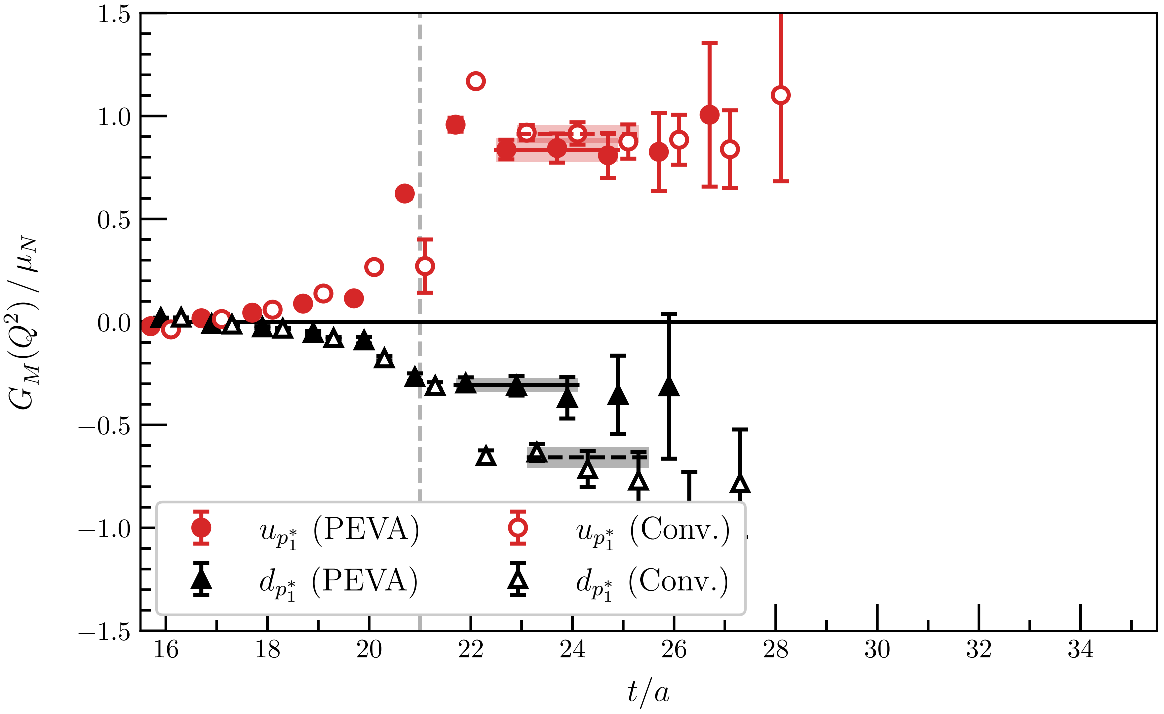

Figure 6.7: Quark-flavour contributions to $G_M(Q^2)$ for the first negative-parity excitation at $m_\pi = 411\,\mathrm{MeV}$ for the lowest-momentum kinematics, providing $Q^2 = 0.1604(44)\,\mathrm{GeV}^2$. The conventions used in this plot are the same as in Fig. 6.6. For $u_{p_1^*}$, both analyses are consistent. For $d_{p_1^*}$, the conventional plateau is a time slice later and much more negative.

and $G_M(Q^2)$ above, we obtain magnetic moment estimates for the excited proton and neutron, as plotted in Fig. 6.14. For the heaviest three pion masses, the effective magnetic moments show little pion mass dependence and have tight error bars. The lightest two pion masses have much larger errors, and once again we observe the discontinuity in $G_M(Q^2)$ at the the second lightest mass, appearing this time as significantly smaller magnetic moments for both states. At the lightest mass, the magnetic moments appear to return to consistency with the values from the heavier masses.

In this section, we have demonstrated the importance of PEVA in correctly extracting both the electric and magnetic form factors of the first negative-parity nucleon. We extracted the electric and magnetic form factors at all five masses, leading to determinations of the charge radii and magnetic moments.

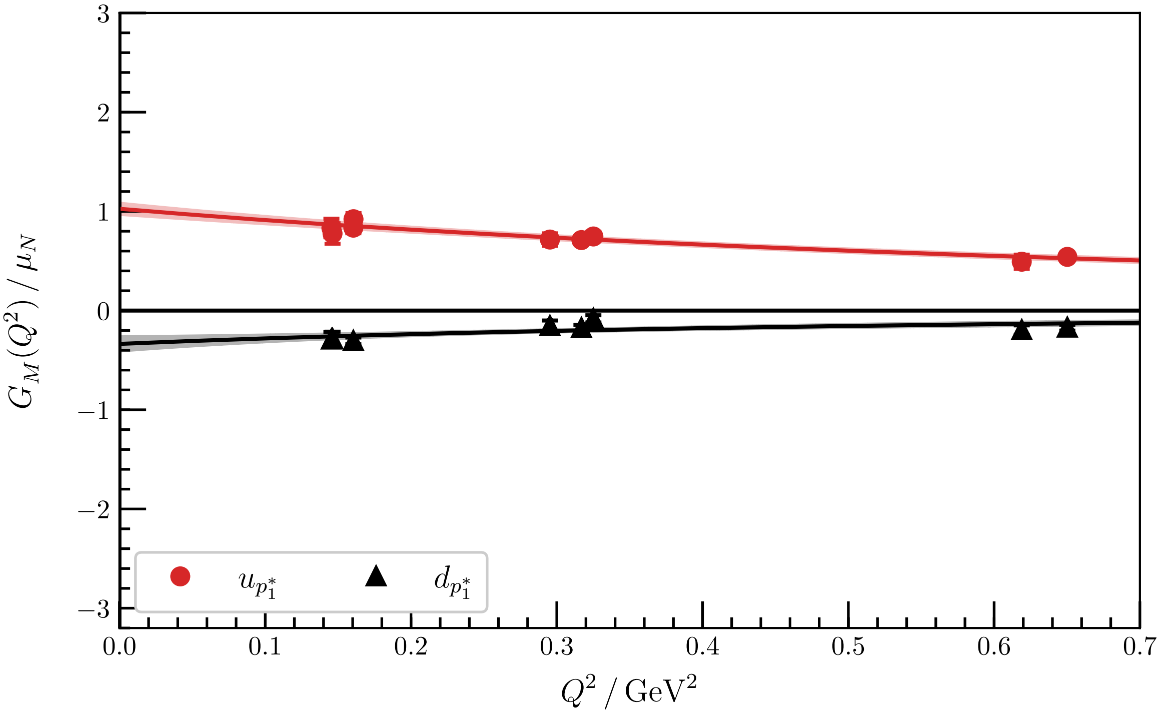

Figure 6.8: Quark-flavour contributions to $G_M(Q^2)$ for the first negative-parity excitation at $m_\pi = 411\,\text{MeV}$. The shaded regions are dipole fits to the form factor, corresponding to magnetic charge radii of 0.533(46) fm for $u_{p_1^*}$ and 0.664(194) fm for $d_{p_1^*}$.

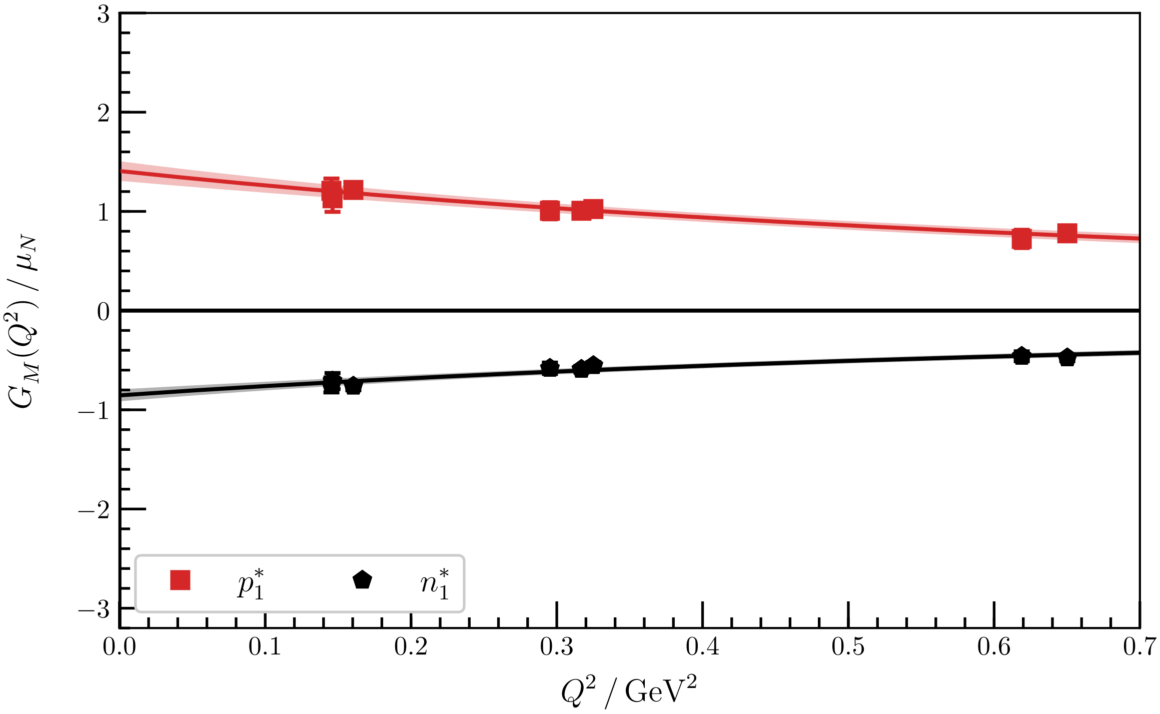

Figure 6.9: $G_M(Q^2)$ for the first negative-parity excitations of the proton and neutron at $m_\pi = 411\,\text{MeV}$. The shaded regions correspond to dipole fits to the form factor, with a magnetic charge radius of 0.511(44) fm for the excited proton and 0.528(45) fm for the excited neutron.

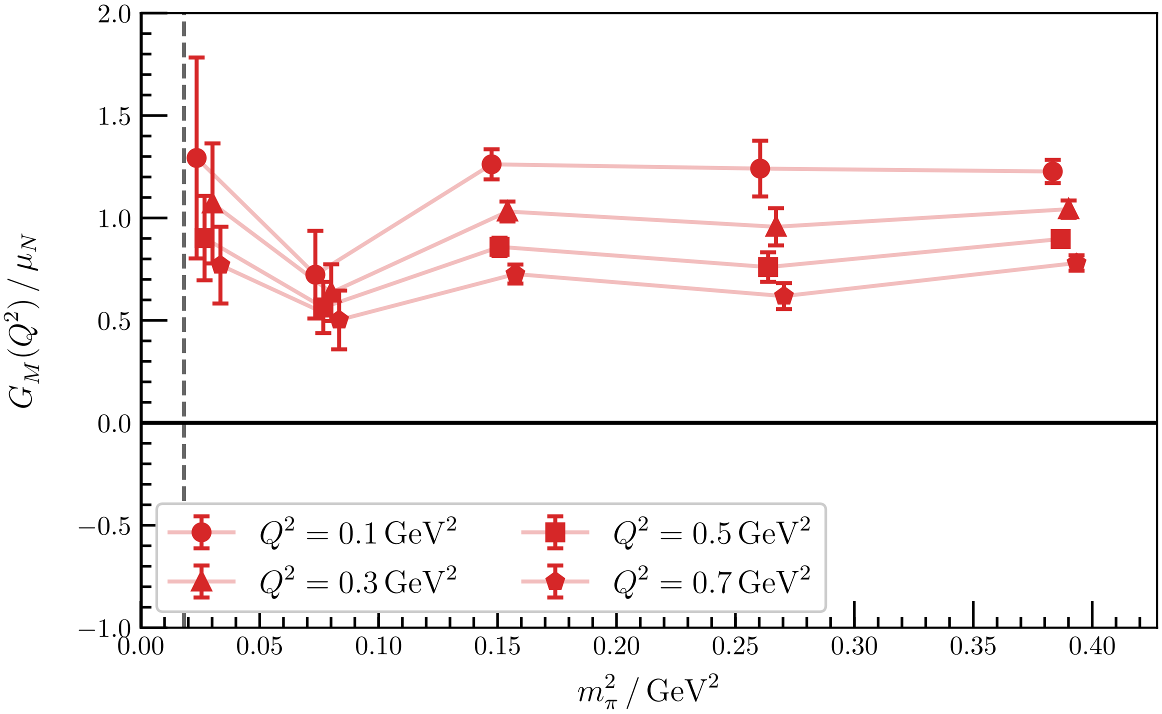

Figure 6.10: Quark-mass dependence of dipole fits to $G_M(Q^2)$ for the first negative-parity excitation of the proton. The marker shapes represent different $Q^2$ slices and the dashed line corresponds to the physical pion mass. The points have been offset symmetrically for clarity.

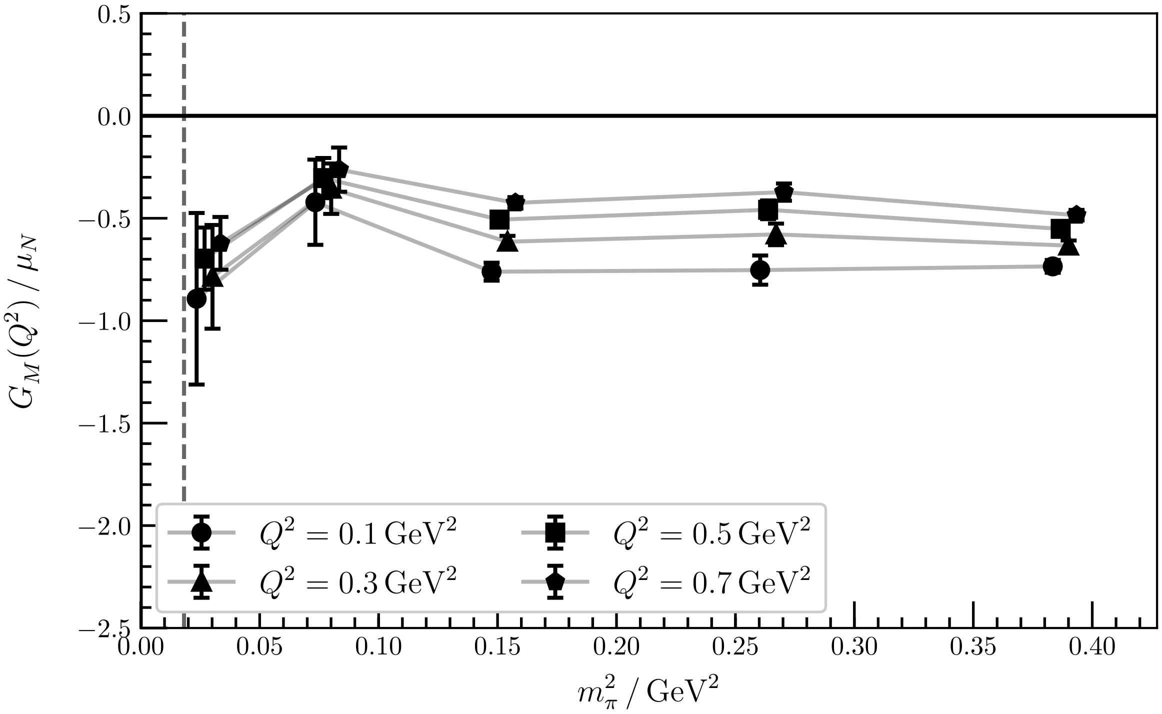

Figure 6.11: Quark-mass dependence of dipole fits to $G_M(Q^2)$ for the first negative-parity excitation of the neutron. The conventions used in this plot are the same as in Fig 6.10 above.

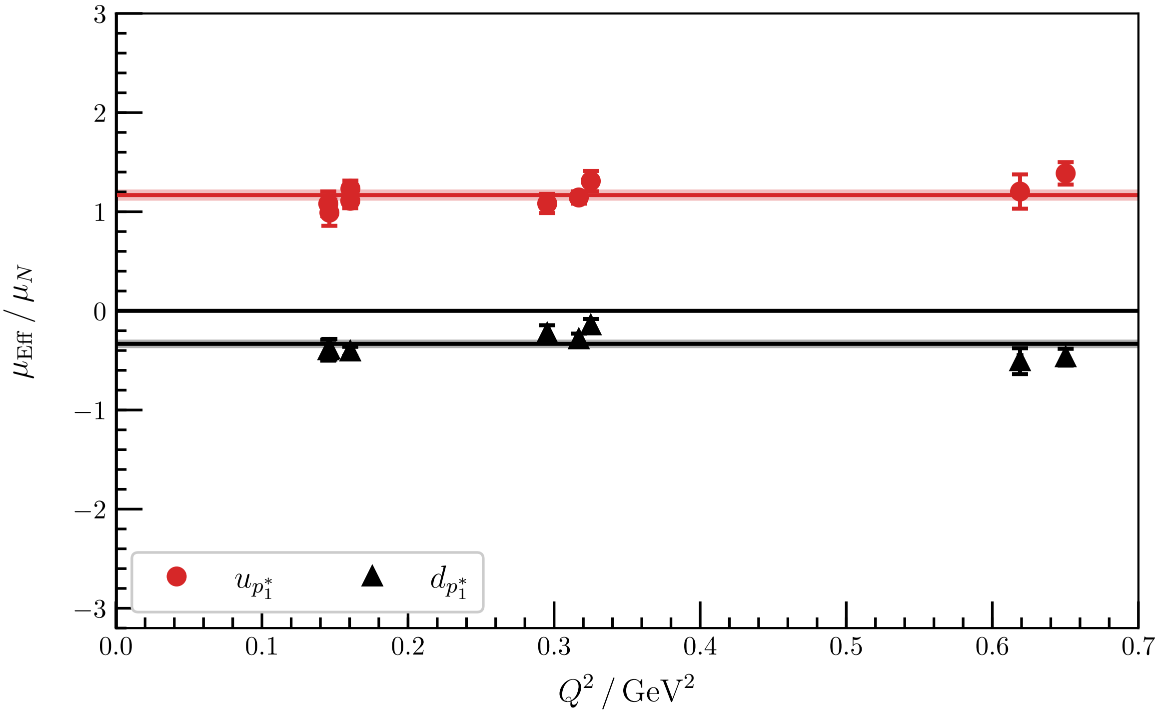

Figure 6.12: $\mu_{\mathrm{Eff}}$ for individual quarks of unit charge in the first negative-parity nucleon excitation at $m_\pi = 411\,\mathrm{MeV}$. The shaded bands are constant fits to the effective magnetic moment that have reasonable agreement with the data, and correspond to magnetic moment contributions of $1.168(59)\ \mu_N$ for the doubly represented quark and $-0.333(43)\ \mu_N$ for the singly represented quark.

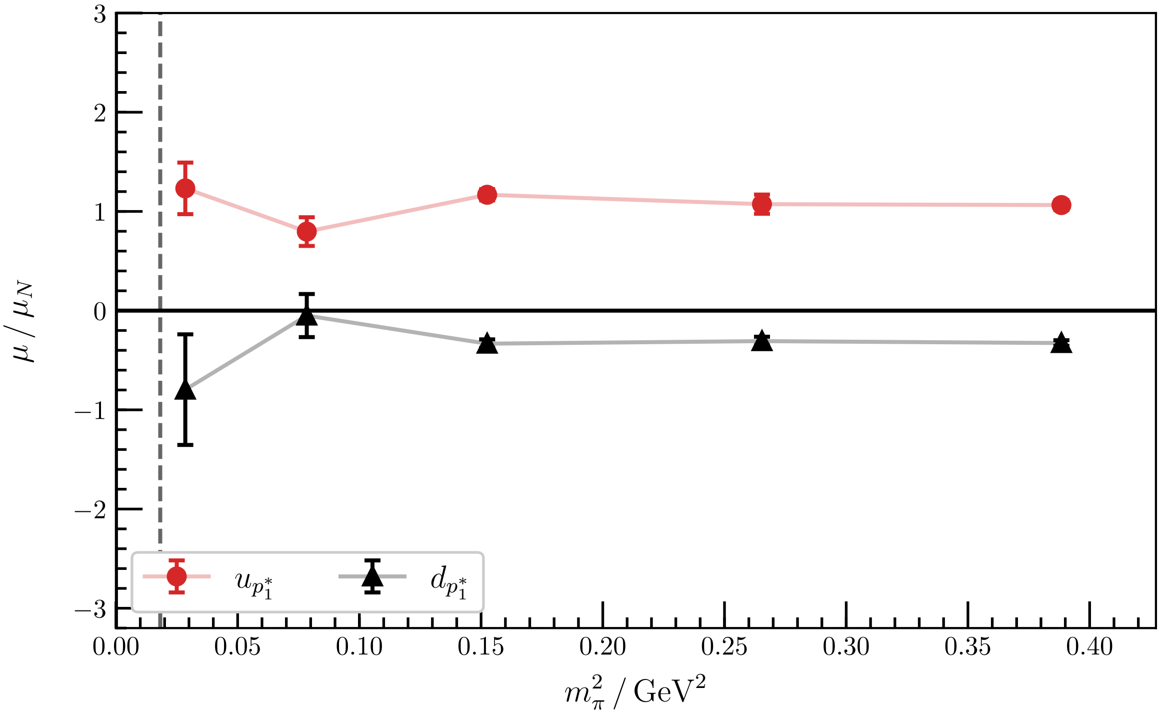

Figure 6.13: Quark-mass dependence of contributions from individual unit-charge quarks to the magnetic moment of the first negative-parity nucleon excitation. The vertical dashed line corresponds to the physical pion mass.

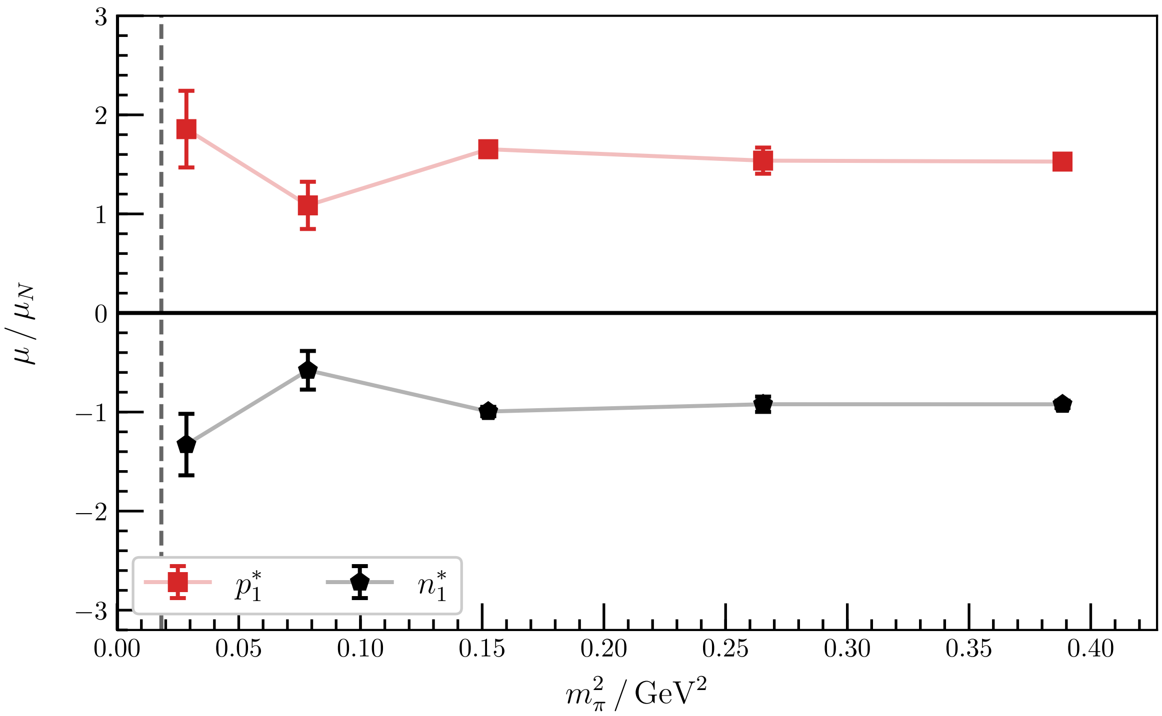

Figure 6.14: Quark-mass dependence of the magnetic moment of the first negative-parity excitations of the proton and neutron.

### 6.2.3 $G_E$ for the second negative-parity excitation

We now proceed to examine the next negative-parity excitation observed in this study, $N_2^*$. In Fig. 6.15, we plot $G_E(Q^2)$ as a function of sink time for both quark flavours at $m_\pi = 702\,\mathrm{MeV}$ with the lowest-momentum kinematics. We see that the conventional extraction sits even further below the PEVA extraction than the first negative-parity excitation. While the PEVA fits start at time slice 24, the conventional fits are forced all the way out to time slice 28 and sit at only just above half of the values of the PEVA fits.

Moving on to the lighter pion masses, the discrepancy between the extracted form factors continues at $m_\pi = 570\,\mathrm{MeV}$ and $411\,\mathrm{MeV}$, with the conventional analysis giving consistently lower values than PEVA. For example, Fig. 6.16 shows the plateaus at $m_\pi = 570\,\mathrm{MeV}$. At the lightest two pion masses, the signal gets significantly noisier, and the difference between the two techniques gets harder to distinguish. Increased statistics are required in order to clearly identify the effects of opposite-parity contaminations of this state at these masses. However, in principle, the enhancement of relativistic components of the baryon spinors at light quark masses is expected to increase parity mixing in the conventional analysis.

We find similar results for all other kinematics: for all masses for which the noise is sufficiently low, the conventional fits still sit significantly lower than the PEVA fits.

Once again, these results clearly indicate that PEVA is critical to the correct

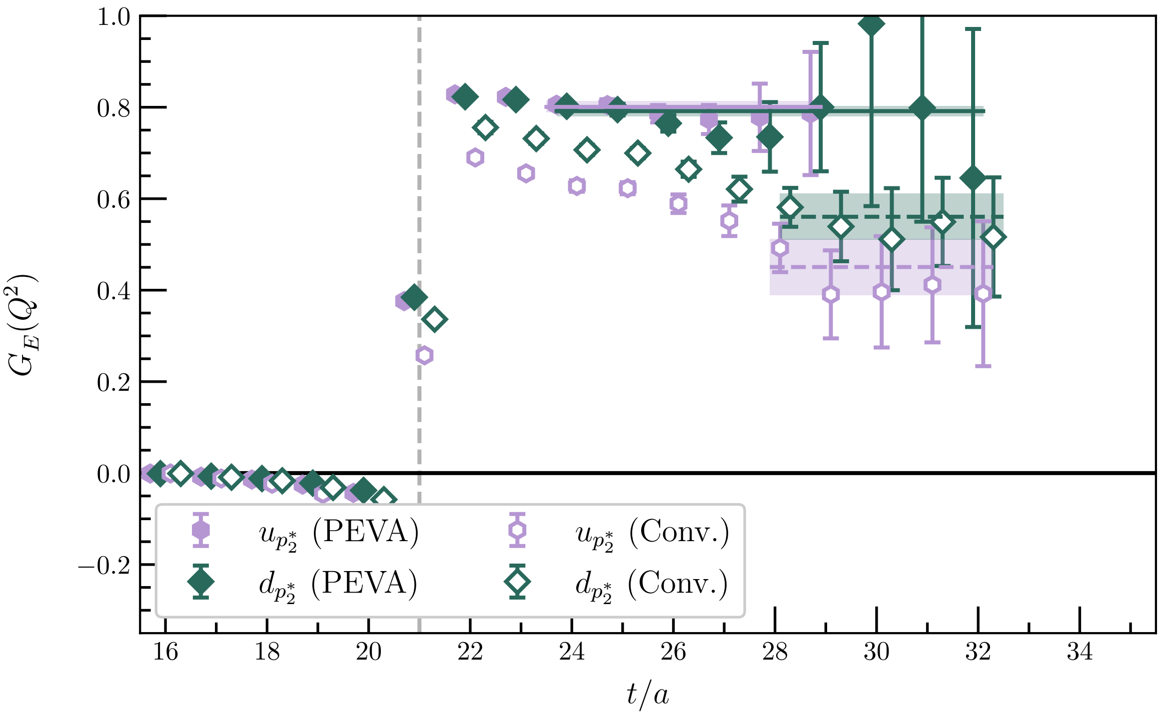

Figure 6.15: Quark-flavour contributions to the electric form factor for the second negative-parity nucleon excitation at $m_\pi = 702\,\mathrm{MeV}$ for the lowest-momentum kinematics, providing $Q^2 = 0.1422(41)\,\mathrm{GeV}^2$. We plot the conventional analysis with open markers and dashed fit lines and the new PEVA analysis with filled markers and solid fit lines. Results for both the singly represented quark flavour ($d_{p_2^*}$) and the doubly represented quark flavour ($u_{p_2^*}$) are shown for single quarks of unit charge. Both PEVA fits are from time slice 24, whereas the conventional fits both start at time slice 28. The values for both conventional fits are significantly lower than the corresponding PEVA fits.

extraction of the electric form factors of this nucleon excitation. The opposite-parity contaminations admitted by the conventional analysis lead to significant underestimation of the value of the electric form factor. Hence, we now focus our attention only on the PEVA results.

Plotting the acceptable plateaus as a function of $Q^2$ reveals that the contributions from the two quark flavours are once again very similar, and agree well with a dipole ansatz. For example, Fig. 6.17 shows dipole fits to the two quark flavours at $m_\pi = 411\,\mathrm{MeV}$, with a charge radius of $0.650(21)\,\mathrm{fm}$ for the doubly represented quark flavour and $0.670(22)\,\mathrm{fm}$ for the singly represented quark flavour. These results are very similar to the first negative-parity excitation. Similar plots are available for the other four masses in Appendix D.

We once again take the linear combinations discussed in Section 6.2.1 to form the excited proton and neutron. For example, in Fig. 6.18, we plot the electric form factors obtained by these combinations at $m_\pi = 411\,\mathrm{MeV}$. Similar plots are available for the other four masses in Appendix D. At all five masses, the electric form factor for the

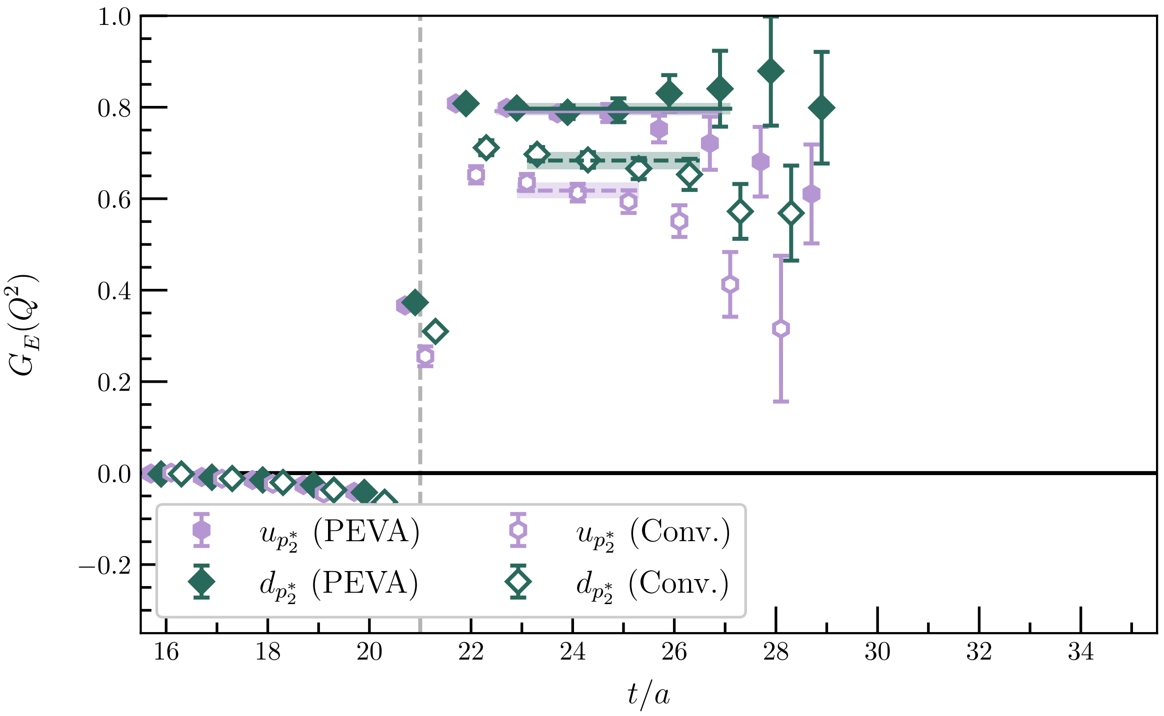

Figure 6.16: Quark-flavour contributions to $G_E(Q^2)$ for the second negative-parity excitation at $m_\pi = 570\,\mathrm{MeV}$ for the lowest-momentum kinematics, providing $Q^2 = 0.1458(44)\,\mathrm{GeV}^2$. The conventions used in this plot are the same as in Fig 6.15. All four fits start at time slice 23, but the conventional fits have significantly lower values than the PEVA fits.

second negative-parity excitation of the neutron is approximately zero. For the proton excitation, the electric form factor once again agrees with a dipole fit with a radius consistent with the ground-state proton at the same mass, as obtained in Chapter 5. This suggests that this excitation is also of similar size to the ground-state nucleon.

We can also examine the squared charge radius of the excited neutron. Once again, we find that it is much closer to zero than the ground state, or perhaps even positive. For example, at $m_\pi = 411\,\mathrm{MeV}$, the squared charge radius of the first negative parity excitation of the neutron is $\langle {r_{n_1^*}}^2 \rangle = 0.017(16)\,\mathrm{fm}$.

In Fig. 6.19, we plot the pion-mass dependence of the dipole fits to the electric form factor for the proton excitation on a number of $Q^2$ slices. We once again see that the pion-mass dependence is fairly smooth, and has a clear trend to lower values of the form factor at lower pion masses, consistent with the increasing charge radius. The lightest mass sees an increase in the rate of change with pion mass, suggesting a significant non-analytic dependence on the quark mass.

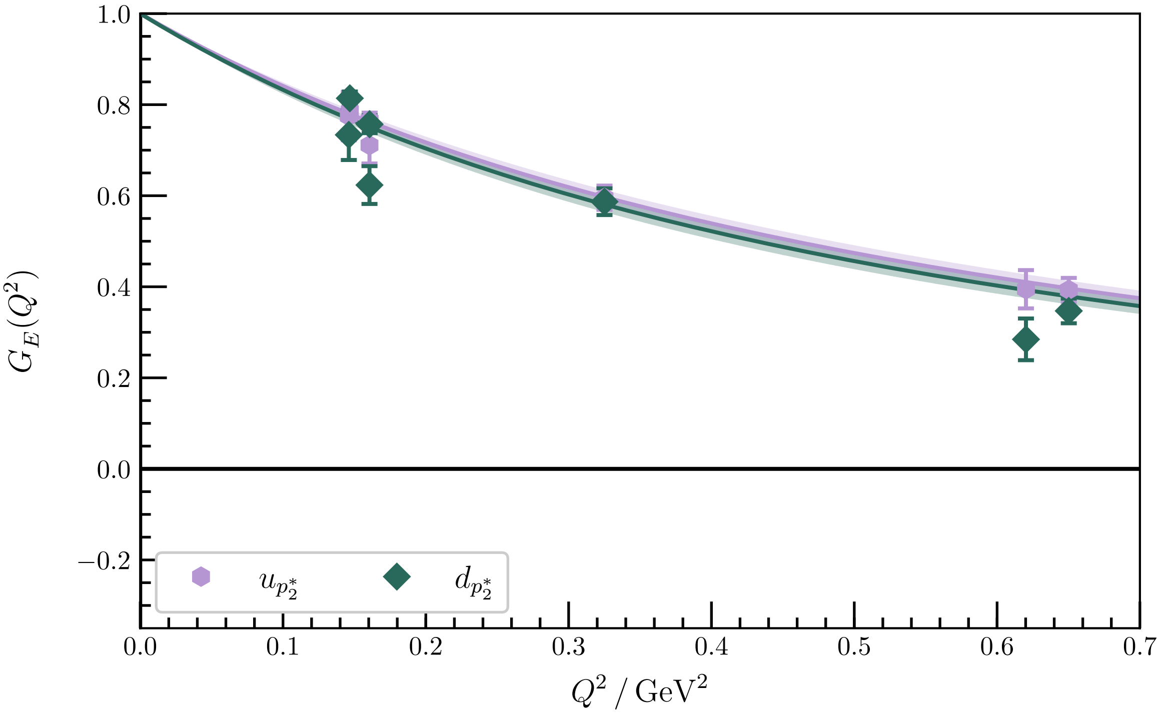

Figure 6.17: Quark-flavour contributions to $G_E(Q^2)$ for the second negative-parity excitation at $m_\pi = 411\,\text{MeV}$. The shaded regions are dipole fits to the form factor, with the $y$-intercept fixed to unity. They correspond to charge radii of 0.650(21) fm for the doubly represented quark ($u_p$) and 0.670(22) fm for the singly represented quark ($d_p$).

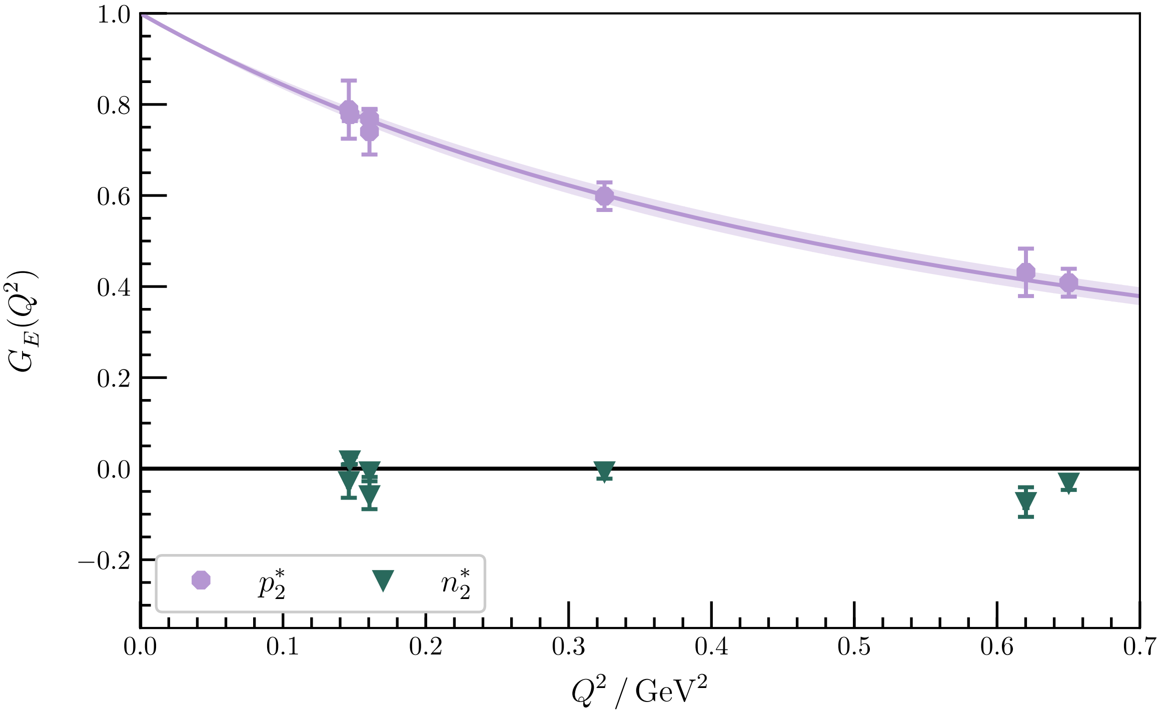

Figure 6.18: $G_E(Q^2)$ for the second negative-parity excitation of the proton and neutron at $m_\pi = 411\,\text{MeV}$. The shaded region corresponds to a dipole fit to the excited proton, with a charge radius of 0.646(23) fm .

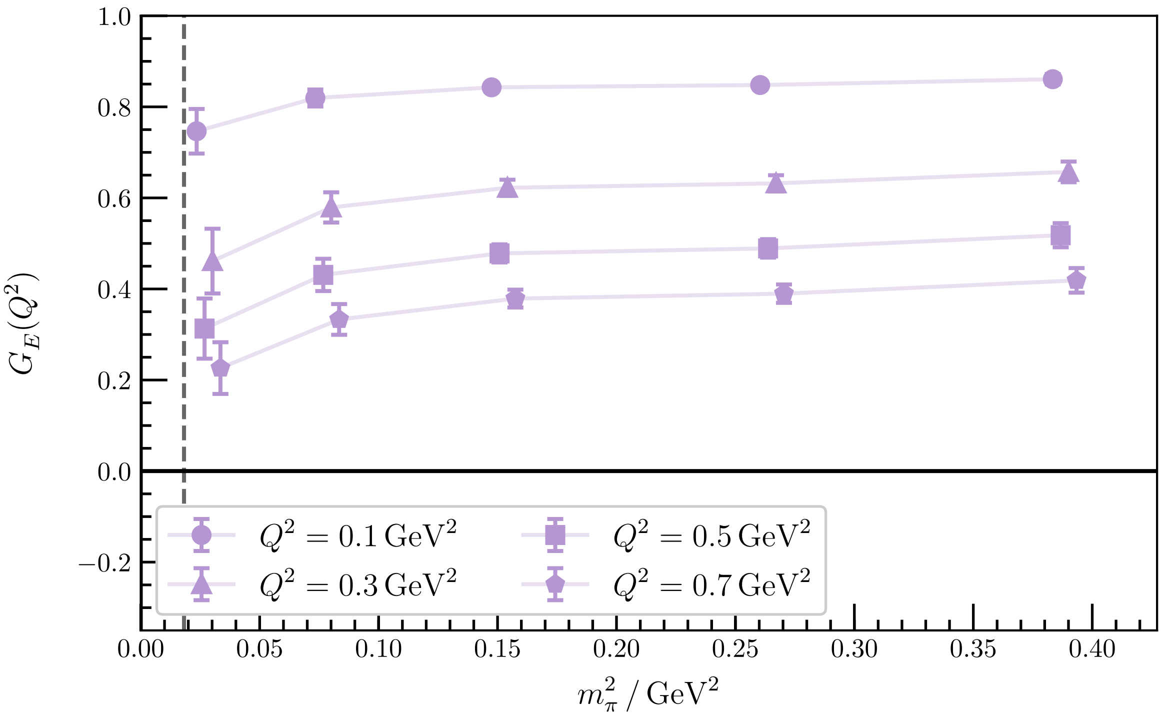

Figure 6.19: Quark-mass dependence of dipole fits to $G_E(Q^2)$ for the second negative-parity excitation of the proton. Similar to previous plots of the pion-mass dependence, the vertical dashed line corresponds to the physical pion mass, and the points have been offset symmetrically for clarity.

### 6.2.4 $G_M$ for the second negative-parity excitation

We now advance to the magnetic form factor of this state. In Fig. 6.20, we plot the heaviest pion mass of $m_\pi = 702\,\mathrm{MeV}$ and the lowest-momentum kinematics. While the plateau regions for the PEVA and conventional analysis are consistent, the values of those plateaus are very different, and in fact change order between the two extractions. We see a similar effect at $m_\pi = 411\,\mathrm{MeV}$ and $570\,\mathrm{MeV}$, with similar inversions of the magnetic form factors between the two analyses. At $m_\pi = 296\,\mathrm{MeV}$, Fig. 6.21 shows that there is still a noticeable difference between the two analyses, despite the fact that the errors are larger, and the difference is harder to distinguish. At the lightest mass, the correlators are too noisy to distinguish any difference between the plateaus from the two analyses. We see similar patterns for the other kinematics, with significantly different plateau values between the two analyses when the statistical noise is low enough to distinguish them.

It is clear that PEVA is once again crucial to extracting the correct form factors. Hence, we focus only on the PEVA results. Inspecting the $Q^2$ dependence of these form factors, we find that the contributions from both quark flavours agree well with a dipole ansatz. For example, Fig. 6.22 shows the form factors at $m_\pi = 411\,\mathrm{MeV}$. Here we have held the $y$-scale fixed to match previous plots, for ease of comparison. The most notable

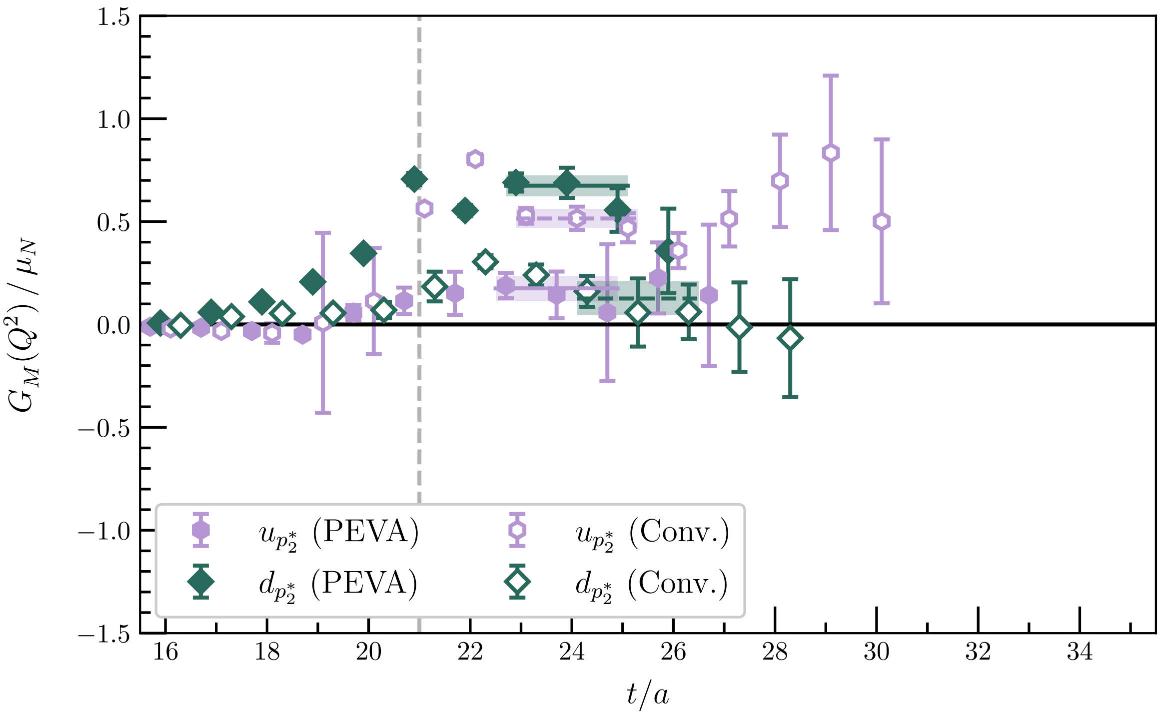

Figure 6.20: Quark-flavour contributions to $G_M(Q^2)$ for the second negative-parity excitation of the nucleon at $m_\pi = 702\,\mathrm{MeV}$ for the lowest-momentum kinematics, providing $Q^2 = 0.1422(41)\,\mathrm{GeV}^2$. The conventions used in this plot are the same as in Fig 6.15. The plateaus for the PEVA analysis both start at time slice 23. The plateaus for the conventional analysis start at time slice 23 for $u_{p_2^*}$ and time slice 24 for $d_{p_2^*}$. The difference in the plateau values between the two analyses is enough to change the ordering of the two quark flavours.

feature of these results is their small magnitude compared to the other three states investigated so far in this thesis. The dipole fits to these results correspond to magnetic radii of 0.860(188) fm for the doubly represented quark flavour and 0.779(86) fm for the singly represented quark flavour. While the central values of these magnetic radii are larger than the charge radii from the dipole fits to $G_E(Q^2)$, the errors are also large, so they are still consistent. We see similar behaviour at the other four masses. Plots showing this behaviour at all five masses are available in Appendix D.

By taking linear combinations based on the multiplicity and charge of each quark flavour, as described in Section 6.2.1, we can obtain the magnetic form factors for the excited proton and neutron. Fig. 6.23 shows these combinations for $m_\pi = 411\,\mathrm{MeV}$. For this and the other four masses (plots available in Appendix D), we find that these form factors are described well by dipole fits. The magnetic charge radii are consistent with the charge radii from $G_E(Q^2)$, although they often have very large errors due to the very small values of the magnetic form factors amplifying the effects of statistical fluctuations.

In Figs. 6.24 and 6.25, we plot the pion-mass dependence of the dipole fits to $G_M(Q^2)$

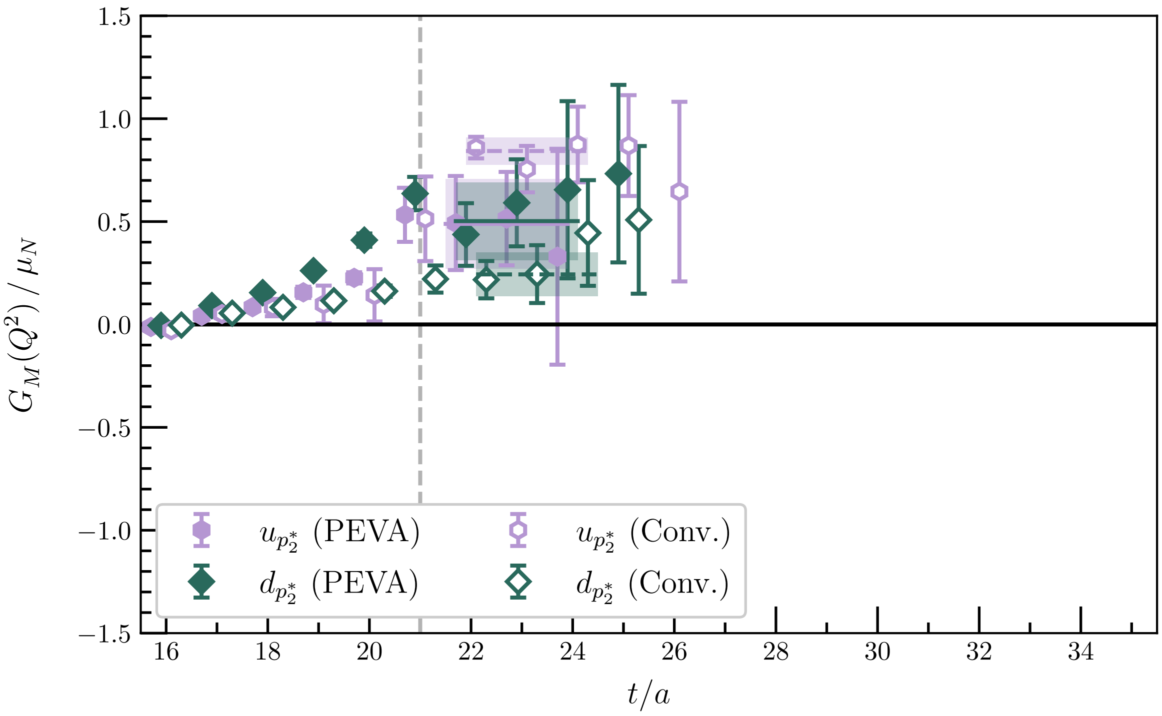

Figure 6.21: Quark-flavour contributions to $G_M(Q^2)$ for the second negative-parity excitation at $m_\pi = 296\,\mathrm{MeV}$, for the lowest-momentum kinematics, providing $Q^2 = 0.1641(45)\,\mathrm{GeV}^2$. The conventions used in this plot are the same as in Fig 6.15. All fits are from time slice 22–24.

for the second negative-parity excitations of the proton and neutron. At the heaviest three masses, the magnetic form factor for the excited proton is very close to zero, and the form factor for the excited neutron has a small but nonzero value. We see a significant shift in the values and statistical errors of the magnetic form factors at the lightest two masses. The form factor for the excited proton and neutron change places, with the excited proton taking a clearly non-zero value and the excited neutron approaching zero. This suggests that there may be a change in the structure of this state at the lightest two pion masses. There is no corresponding discontinuity in $G_E(Q^2)$ at these masses, though the change in slope discussed above could indicate a change in the distribution of the quarks that may be contributing to the observed effects in $G_M(Q^2)$. However, as discussed above, the fits at these masses are very noisy, and a higher statistics study should be performed to confirm that this result is robust.

Returning to the individual quark sector results with unit charge, and noting that the $Q^2$ dependence for $G_E(Q^2)$ and $G_M(Q^2)$ is similar, we once again take the ratio $\mu_{\mathrm{Eff}}(Q^2) \equiv G_M(Q^2)/G_E(Q^2)$. We find that this ratio is once again approximately flat for all five pion masses. For example, Fig. 6.26 shows the $Q^2$ dependence of the ratio at $m_\pi = 411\,\mathrm{MeV}$. The $Q^2$ dependence for all five masses can be found in Appendix D. We can extract the contributions to the magnetic moment from both quark flavours from constant fits to this ratio.

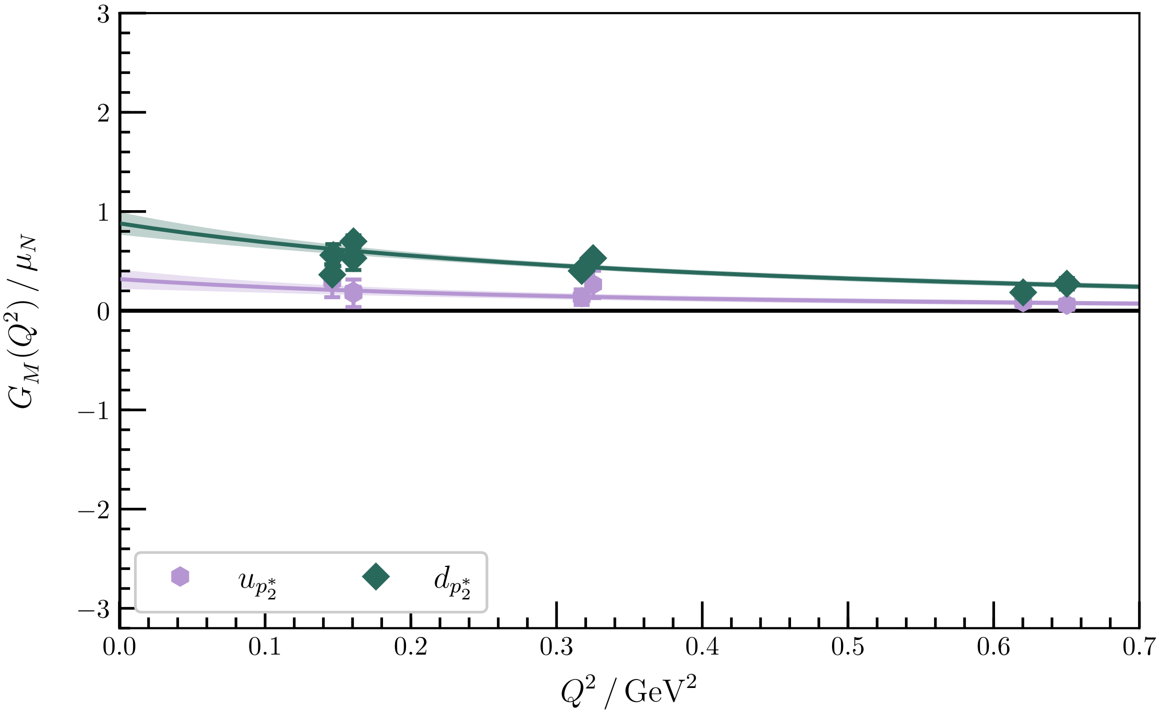

Figure 6.22: Quark-flavour contributions to $G_M(Q^2)$ for the second negative-parity excitation at $m_\pi = 411\,\mathrm{MeV}$. The shaded regions are dipole fits to the form factor, corresponding to magnetic radii of 0.860(188) fm for the doubly represented quark flavour ($u_p$) and 0.779(86) fm for the singly represented quark flavour ($d_p$).

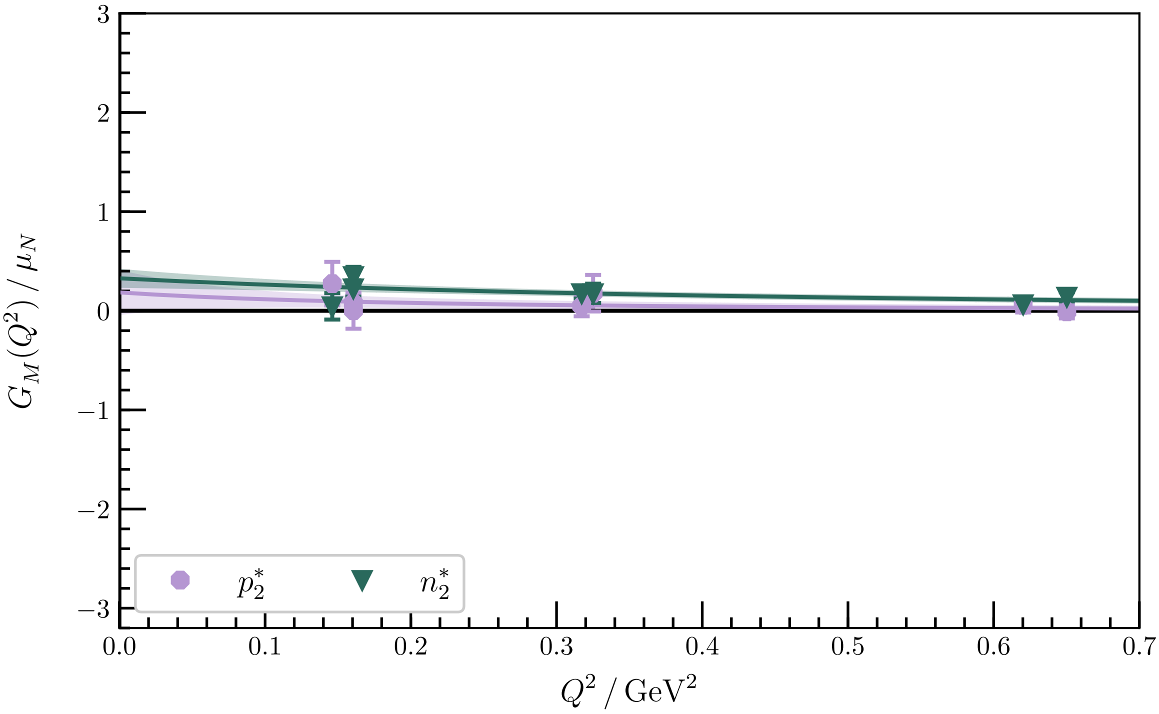

Figure 6.23: $G_M(Q^2)$ for the excited proton and neutron at $m_\pi = 411\,\mathrm{MeV}$. The shaded regions correspond to dipole fits to the form factors, with a magnetic radius of 1.111(912) fm for the proton and 0.733(186) fm for the neutron.

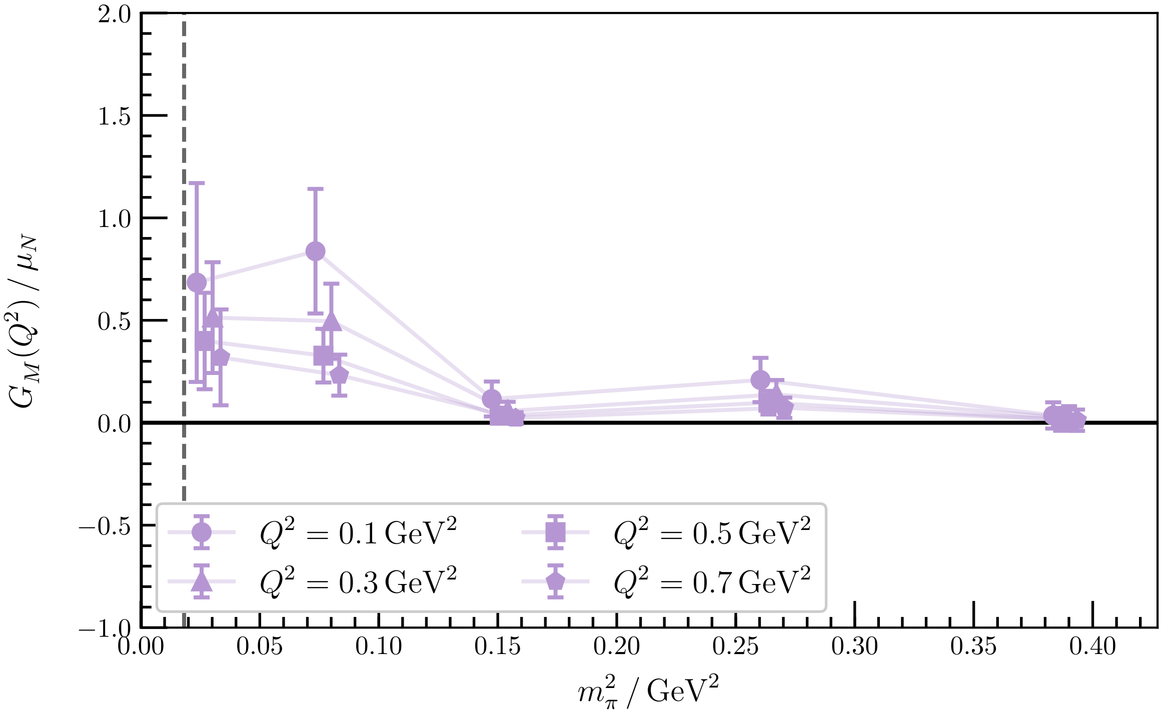

Figure 6.24: Quark-mass dependence of dipole fits to $G_M(Q^2)$ excited proton. The points have been offset symmetrically for clarity.

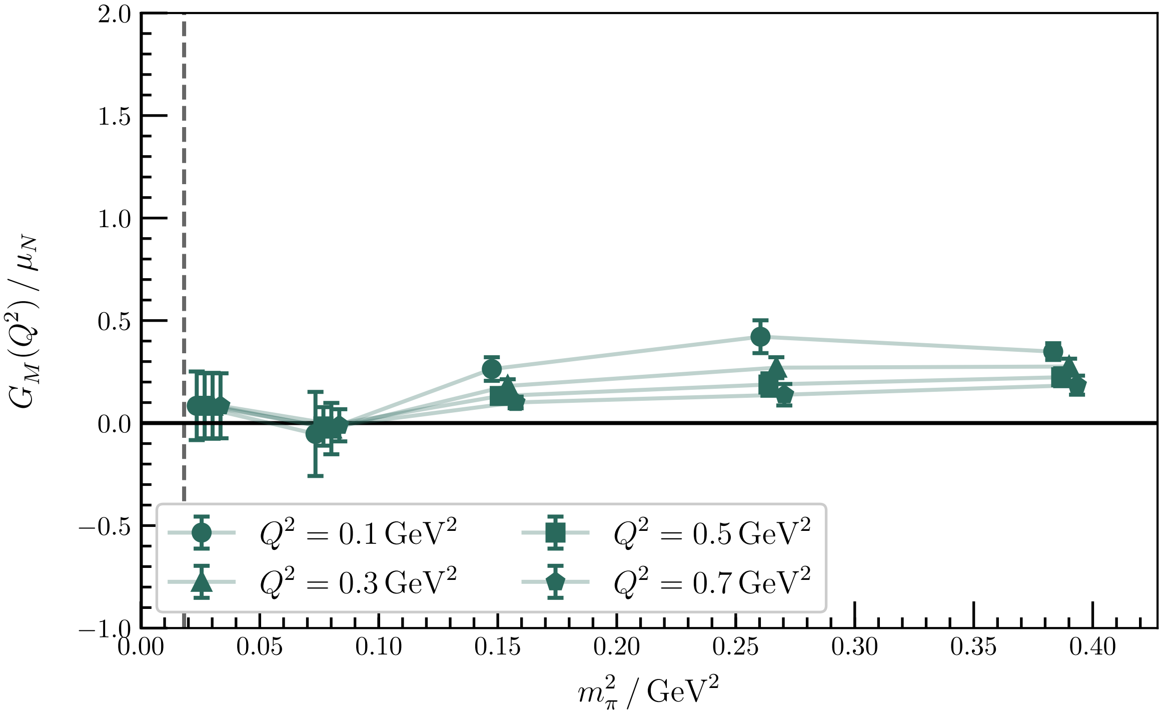

Figure 6.25: Quark-mass dependence of dipole fits to $G_M(Q^2)$ for the excited neutron. As above, the points have been offset symmetrically for clarity

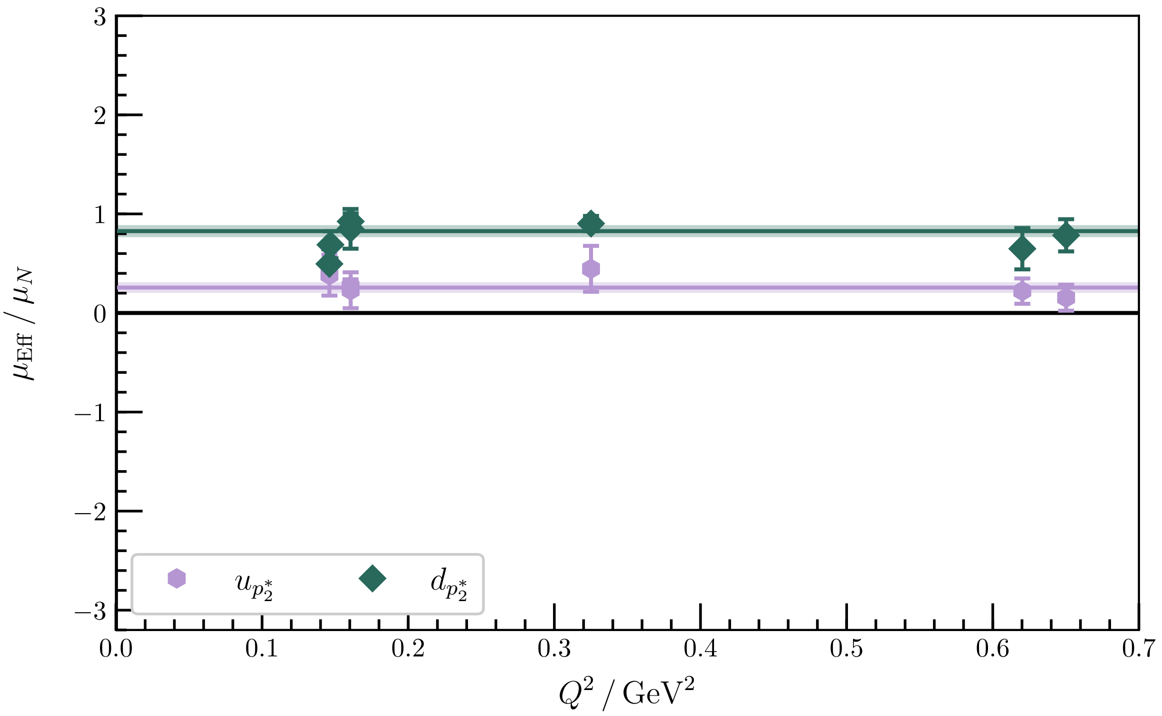

Figure 6.26: $\mu_{\mathrm{Eff}}$ for individual quarks of unit charge in the second negative-parity excitation at $m_\pi = 411\,\mathrm{MeV}$. The shaded bands are constant fits to the effective magnetic moment, corresponding to magnetic moment contributions of 0.257(54) $\mu_N$ for the doubly represented quark and 0.826(62) $\mu_N$ for the singly represented quark.

Fig. 6.27 shows the pion-mass dependence of these extracted magnetic moment contributions. It is remarkable that both quark flavours contribute with the same sign.

By taking the linear combinations discussed above, we can combine these individual quark flavour results to get the predicted magnetic moments for the second negative-parity excitations of the proton and neutron. In Fig. 6.28 we plot the dependence of these combinations on the squared pion mass. For the heaviest three pion masses, the effective magnetic moments show little pion mass dependence and have tight error bars. The magnetic moment of the proton excitation sits very close to zero, and the magnetic moment of the neutron excitation has a small but nonzero positive value. For the lightest two masses, the ordering of the two states flips, with the proton excitation taking on a significant magnetic moment, and the neutron excitation dropping to be consistent with zero. This strongly supports the interpretation of the change in the slope of the electric form factor at these masses observed in Fig. 6.19 as arising from a fundamental change in the structure of the state. This is likely to arise from an increasing role of meson-baryon scattering states at these lighter pion masses. The channels that are likely to contribute to this effect are $\pi N$, $\eta N$, $K\Lambda$, and $K\Sigma$. It is interesting to note that the $N_2^*$ lies just below the $K\Sigma$ scattering threshold. This is reminiscent of the $\Lambda(1405)$ lying just below the $\overline{K}N$ threshold, where it is now understood that the $\overline{K}N$ is a significant feature of the $\Lambda(1405)$ [126].

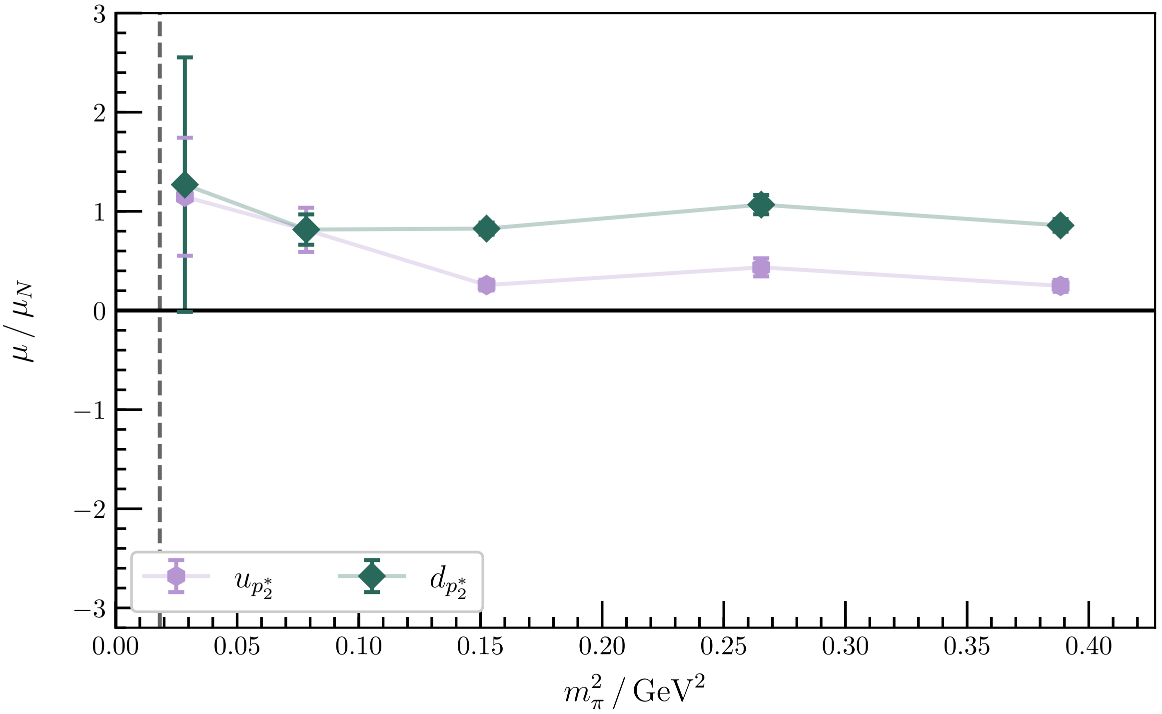

Figure 6.27: Quark-mass dependence of contributions from individual unit-charge quarks to the magnetic moment of the second negative-parity excitation of the nucleon. The vertical dashed line corresponds to the physical pion mass.

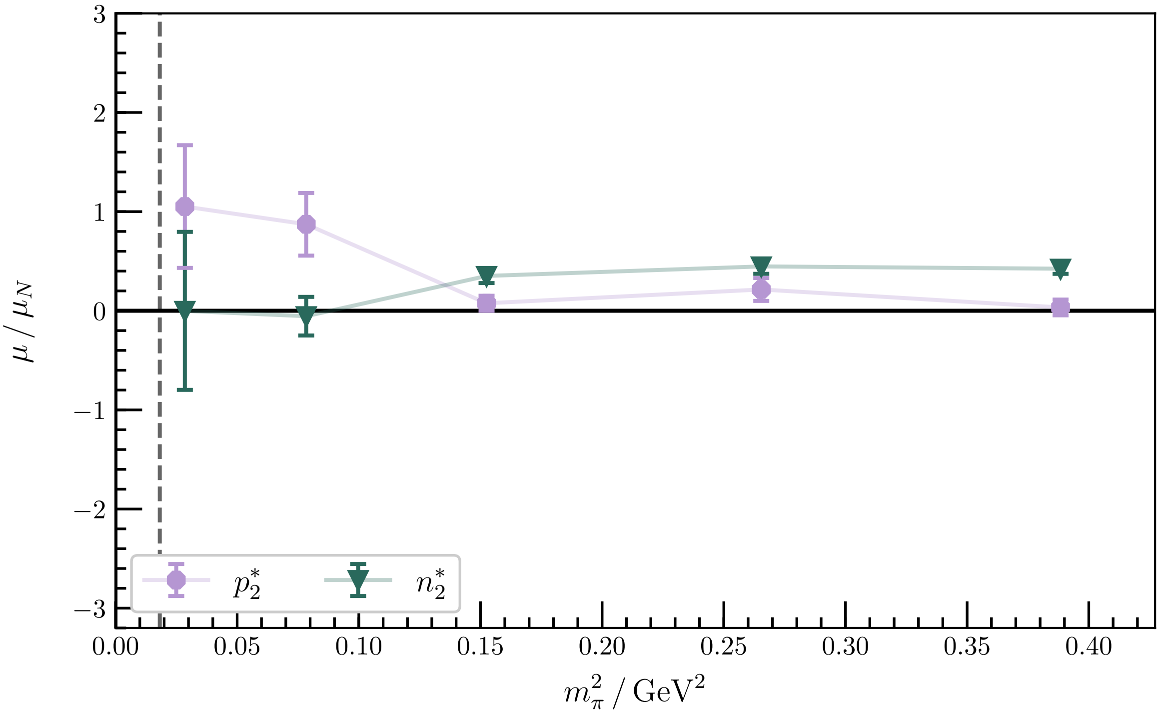

Figure 6.28: Quark-mass dependence of the magnetic moment of the second negative-parity excitations of the proton and neutron. The dashed line corresponds to the physical pion mass. There is a clear change at the lightest two pion masses, which signals a significant shift in the structure of the states.

The most notable feature of the $N_2^*$ at these lightest two masses is the symmetry between the two quark sectors taking on equal contributions to the magnetic moment, up to factors of charge and multiplicity. This does not match well with predictions from any one of the four meson-baryon scattering states listed above, suggesting that multiple scattering states and quark-model-like three-quark states are likely to be involved.

It is clear that the PEVA technique is crucial for extracting both the electric and magnetic form factors of the second negative-parity excitations of the proton and neutron. It has allowed us to successfully extract the electric and magnetic form factors at all five masses, leading to a determination of the charge radii and magnetic moments of the proton and neutron excitations. The pion-mass dependence of the extracted magnetic form factors and magnetic moments provides evidence for a possible change in the structure of the states at the lightest two masses.

### 6.2.5 Model comparison

In Section 6.1, we introduced the two localised negative-parity excitations of the proton and neutron observed on the lattice by the CSSM and the HSC. Existing Hamiltonian Effective Field Theory (HEFT) calculations [96] describe this energy spectrum as the finite volume spectrum of a single physical resonance: the $N^*(1535)$ resonance. However, there is another resonance in the energy region of these states: the $N^*(1650)$ resonance. This resonance may also play an important role in the observed finite-volume spectrum.

In order to investigate the role the $N^*(1650)$ resonance might play in the finite-volume spectrum, we consider the electromagnetic properties of the observed lattice states. In particular, we focus on the magnetic moments of the two states, as calculated in sections 6.2.2 and 6.2.4. To date there have been no experimental determinations of the magnetic moments of these states, so we turn to theory to interpret these results.

A HEFT description of these states would express them as a strongly interacting superposition of "bare" baryonic states and non-interacting meson-baryon states with definite relative momenta. Due to the localised nature of the interpolating operators used in this study, the only states the interpolators will have a significant overlap with are localised states with a significant bare-state component. These bare states are associated with simple quark model states, so to understand our magnetic moment results, we turn to quark model predictions of the magnetic moments of the $N^*(1535)$ and $N^*(1650)$ resonances. We consider two constituent quark model (QM) predictions of the magnetic moments from Refs. [121, 123], and two chiral constituent quark model ($\chi$QM) calculations which take the quark model calculations and include effects from the pion cloud [123, 124].

In Fig. 6.29, we compare our magnetic moments extracted at $m_\pi = 702\,\text{MeV}$ with these quark model predictions, which are calculated at the physical point. We can see

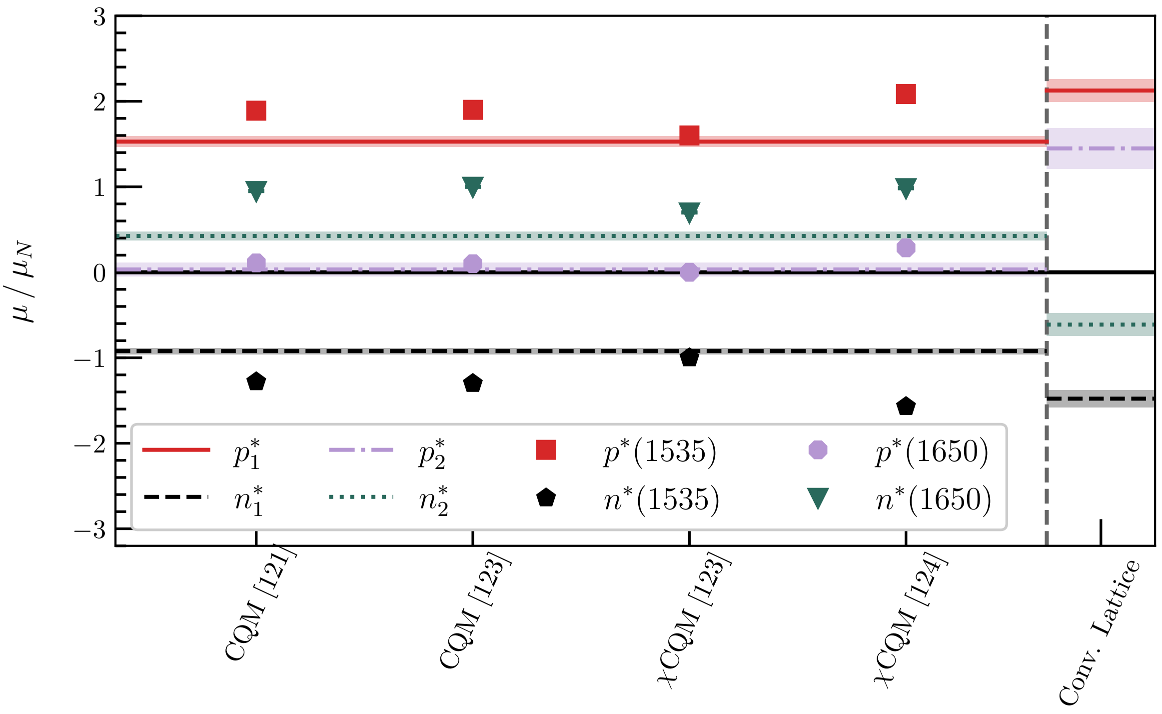

Figure 6.29: Comparison between lattice calculations of the magnetic moments of two negative-parity nucleon excitations at $m_\pi = 702\,\mathrm{MeV}$ and quark model predictions for the $N^*(1535)$ and $N^*(1650)$ resonances. The shaded bands on the left-hand side of the plot indicate the magnetic moments calculated via the PEVA technique, and symbols denote the quark model predictions. Lattice calculations of the magnetic moments using conventional parity projection are plotted to the right of the vertical dashed line.

that qualitatively, the results for the first negative-parity lattice excitation match up with the quark model $N^*(1535)$, and the second negative-parity lattice excitation with the quark model $N^*(1650)$. In fact, despite being at significantly different pion masses, the results are quantitatively very similar, with the lattice results sitting within the scatter of the model predictions for all states save the second negative-parity nucleon excitation, which sits slightly below all of the model predictions.

For comparison, we also plot lattice results produced using the conventional analysis. For these results, $\mu_{\mathrm{Eff}}(Q^2)$ varies significantly for different kinematics, so rather than taking a constant fit across kinematics, we present only the result from the lowest-momentum ($\boldsymbol{p} = (0,0,0)$, $\boldsymbol{p}' = (1,0,0)$) kinematics, which we expect to have the smallest opposite-parity contaminations. We see that the conventional results are significantly different to the PEVA results. In particular, the conventional extraction of the second negative-parity excitation is completely different to both the PEVA result and the quark model results. This once again demonstrates how critical the PEVA technique is to obtaining the results presented in this chapter.

This trend continues for $m_\pi = 570\,\mathrm{MeV}$ and $411\,\mathrm{MeV}$, as shown in Figs. 6.30 and 6.31. Since the pion-mass dependence of the magnetic moments between these three

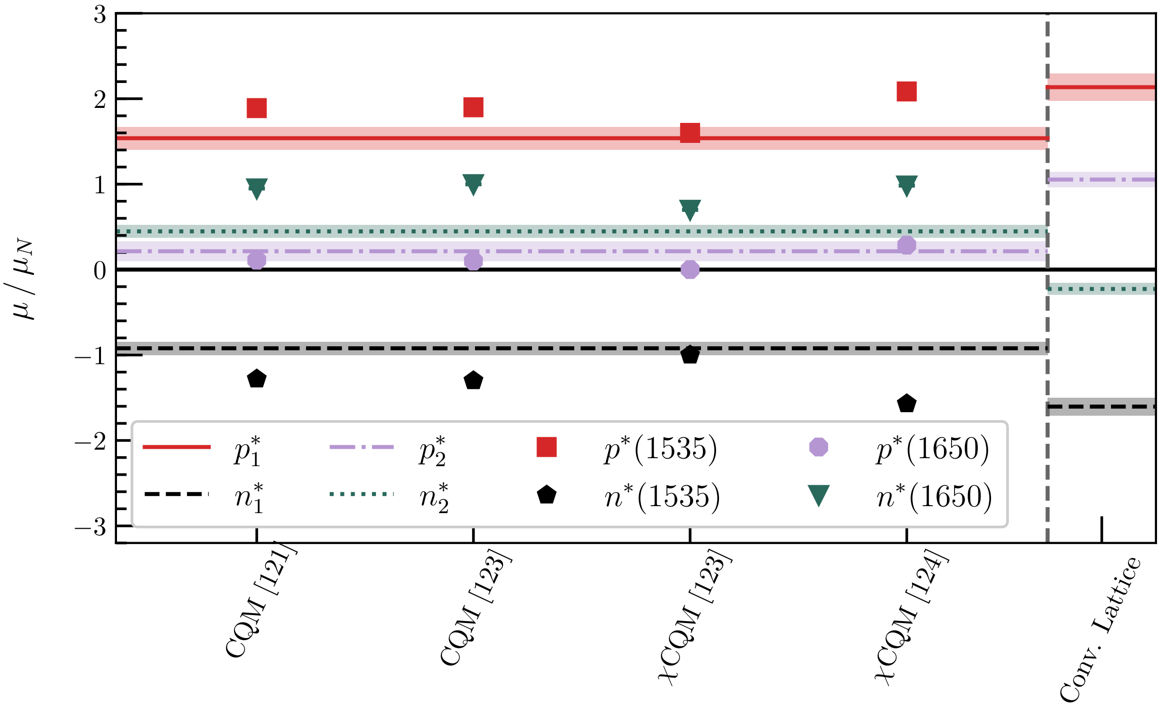

Figure 6.30: Comparison between magnetic moments from lattice calculations at $m_\pi = 570\,\mathrm{MeV}$ and quark model predictions for the $N^*(1535)$ and $N^*(1650)$. The shaded bands indicate the PEVA calculations on the left, and the conventional analysis on the right. The markers show the quark model predictions.

masses is quite small, the quantitative agreement remains good. This strongly suggests that these lattice states are dominated by two different bare states, corresponding to the two quark model states, at least at the three heaviest masses. This suggests that future HEFT studies of this resonance region should include two bare states, corresponding to the quark model $N^*(1535)$ and $N^*(1650)$ states.

Moving on to the lightest two masses, Figs. 6.32 and 6.33 show that the lattice results depart from the model predictions. The first negative-parity excitations of the neutron and proton have a smaller magnitude than the quark model results (as well as the PEVA results at the other masses) at $m_\pi = 296\,\mathrm{MeV}$. However, this discrepancy is not present at $m_\pi = 156\,\mathrm{MeV}$, suggesting that it may just be a statistical anomaly resulting from worsening signal to noise ratios at these lighter masses. On the other hand, the second negative-parity excitations of the neutron and proton have values that are clearly different to the quark model results both quantitatively and qualitatively at both masses. This suggests that meson-baryon scattering states may play a greater role in structure of these states at these lightest two pion masses.

Despite the PEVA results shifting away from the quark model predictions, Fig. 6.32 shows that there is still a significant disagreement between the conventional and PEVA results at $m_\pi = 296\,\mathrm{MeV}$. It remains clear that PEVA is necessary to extract the correct magnetic moments, despite the changing structure of the states

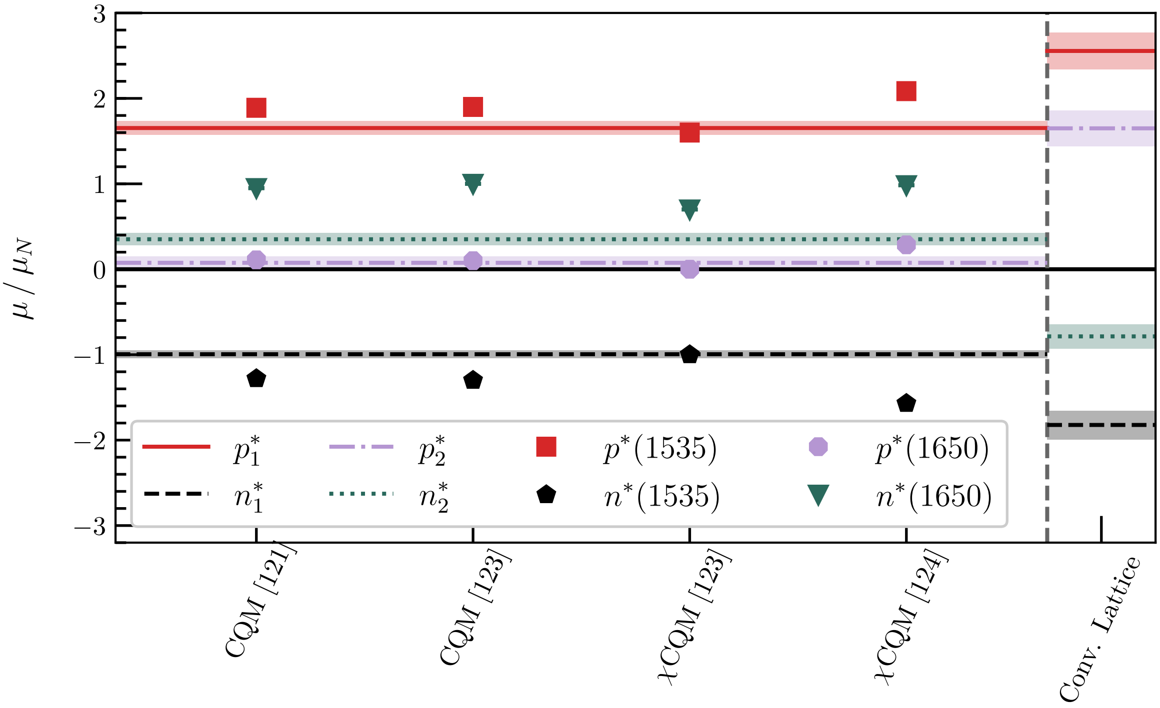

Figure 6.31: Comparison between magnetic moments from lattice calculations at $m_\pi = 411\,\mathrm{MeV}$ and quark model predictions for the $N^*(1535)$ and $N^*(1650)$. The shaded bands indicate the PEVA calculations on the left, and the conventional analysis on the right. The markers show the quark model predictions.

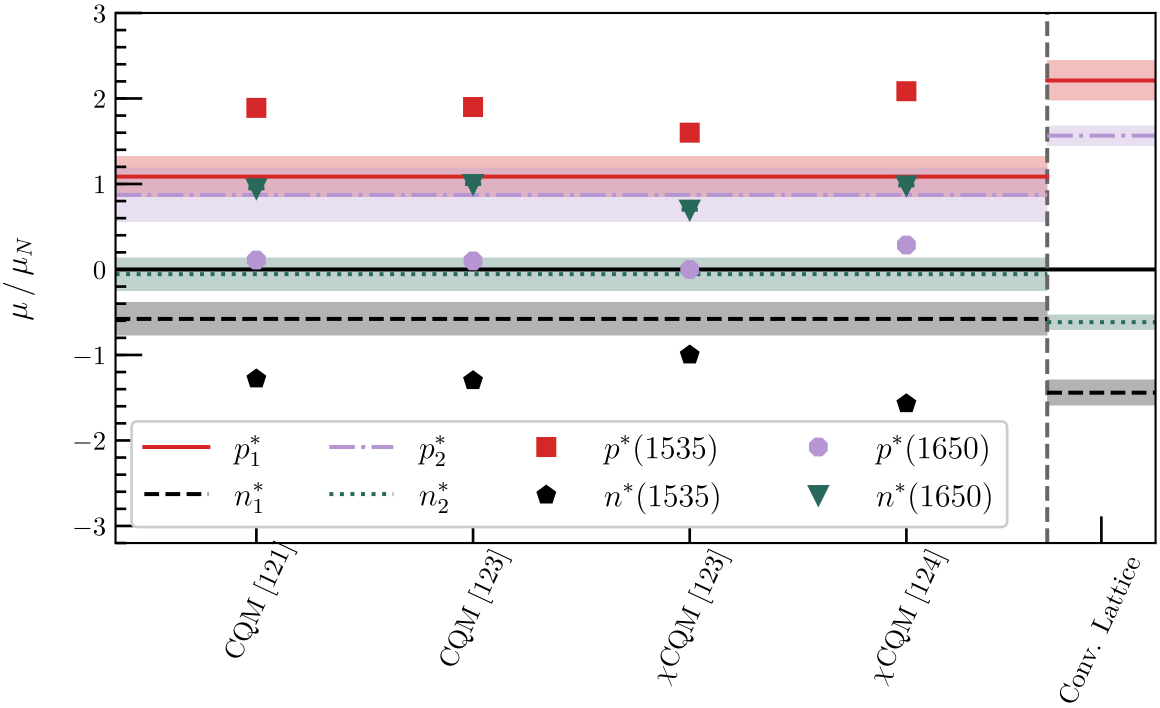

Figure 6.32: Comparison between magnetic moments from lattice calculations at $m_\pi = 296\,\mathrm{MeV}$ and quark model predictions for the $N^*(1535)$ and $N^*(1650)$. The shaded bands indicate the PEVA calculations on the left, and the conventional analysis on the right. The markers show the quark model predictions.

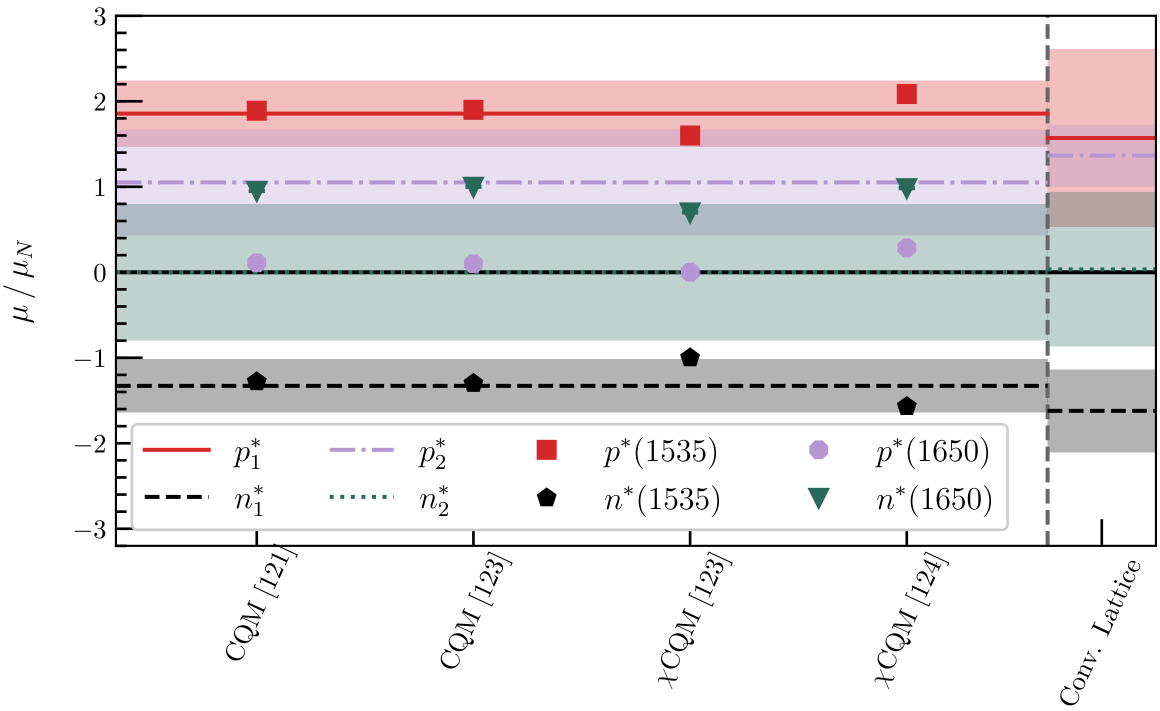

Figure 6.33: Comparison between magnetic moments from lattice calculations at $m_\pi = 156\,\mathrm{MeV}$ and quark model predictions for the $N^*(1535)$ and $N^*(1650)$. The shaded bands indicate the PEVA calculations on the left, and the conventional analysis on the right. The markers show the quark model predictions.

At the lightest mass, Fig. 6.33 shows that the statistical errors are too large to resolve any differences between the PEVA and conventional analyses. To observe any difference between the analyses at this mass, more statistics are required.

The results presented in this section provide new insight into the structure of the negative-parity nucleon excitations observed in Lattice QCD. At the heavier pion masses considered, the two negative-parity excitations agree well with quark-model descriptions of the $N^*(1535)$ and $N^*(1650)$. This gives significant insight into the nature of these finite-volume eigenstates. Coupled with the observed single-particle dispersion relations seen in Chapter 4, these results indicate that the states are highly localised and behave like three-quark constituent-quark-model states. At the lightest two pion masses, the picture appears more complex, suggesting an increasing role for meson-baryon dressings. Here, a description of this state as a molecular bound state of $K\Sigma$ dressed by $K\Lambda$, $\eta N$ and $\pi N$ is an interesting possibility, analogous to the description of the odd-parity $\Lambda(1405)$ excitation as a molecular bound state of $\overline{K}N$ dressed by $\pi\Sigma$ [126, 127]. Further statistics will be required to pin down the exact behaviour at these light pion masses and refine this picture. In addition, the inclusion of multi-hadron operators could improve overlap with these states, and would allow for the investigation of other excitations in this region, providing more insight into the changing role of meson-baryon dressings at these masses.

As the conventional analysis clearly gives the wrong result, these groundbreaking results are made possible by the PEVA technique. The insights provided will be an important guide for future HEFT calculations.

## 6.3 Positive parity excitation

We now move to the positive parity sector, studying the first positive-parity excitation of the nucleon observed on the lattice. This state sits at an effective mass of approximately 2 GeV for all five pion masses, well above 1.43(2) GeV, the mass of the Roper resonance observed in nature [128]. This has long been a puzzle for the particle physics community, but recent HEFT results strongly suggest that the Roper resonance is dynamically generated from meson-baryon scattering states [95], and hence the lattice spectrum in this energy region has poor overlap with local three-quark operators. This means that the lattice state studied here is likely associated with the $N^*(1710)$, $N^*(1880)$, and/or $N^*(2100)$ resonances.

### 6.3.1 Electric form factor

We plot the dependence of $G_E(Q^2)$ on the Euclidean sink time at $m_\pi = 702\,\mathrm{MeV}$ in Figs. 6.34 and 6.35. The form factor values extracted from the PEVA and conventional analyses for each sink time look very similar, and this is reflected in the fits. The conventional and PEVA extractions both have clear plateaus over the same range of sink times, and these plateaus have consistent values.

This trend continues for lighter pion masses: the PEVA and conventional analyses have the same fit ranges and consistent fit values. This is also true for all kinematics for which we are able to find acceptable plateaus. This suggests there are no significant effects from opposite-parity contaminations on $G_E(Q^2)$ for this state, at least for this level of statistics.

Focusing on the PEVA results, in Fig. 6.36, we plot the $Q^2$ dependence of the electric form factor for the two valence quark flavours at $m_\pi = 411\,\mathrm{MeV}$. We see that the two quark flavours make very similar contributions to the electric form factor and agree well with a dipole fit corresponding to charge radii of 0.88(4) fm for the doubly represented quark flavour and 0.89(5) fm for the singly represented quark flavour. This is significantly larger than the ground-state nucleon. Similar behaviour is seen for the other four masses, and plots demonstrating this are available in Appendix D.

As above, we take linear combinations of the individual quark flavour contributions, including the charges of the quark flavours and their multiplicity, to get the electric form factors for the first positive-parity excitations of the proton and neutron. In Fig. 6.37, we plot these combinations at $m_\pi = 411\,\mathrm{MeV}$. At this and the other four

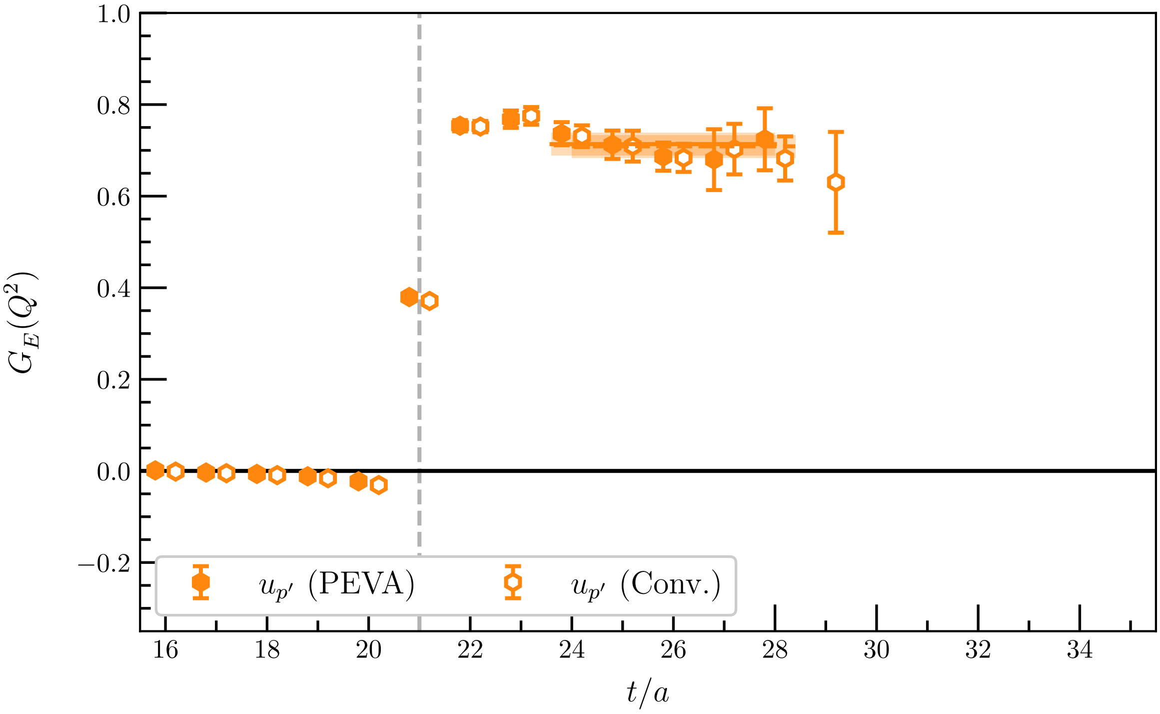

Figure 6.34: Contributions to $G_E(Q^2)$ from the doubly represented quark flavour for the first positive-parity nucleon excitation at $m_\pi = 702\,\mathrm{MeV}$ with the lowest-momentum kinematics, providing $Q^2 = 0.1422(41)\,\mathrm{GeV}^2$. We plot the conventional analysis with open markers and dashed fit lines and the PEVA analysis with filled markers and solid fit lines. Both fits are from time slice 24–28.

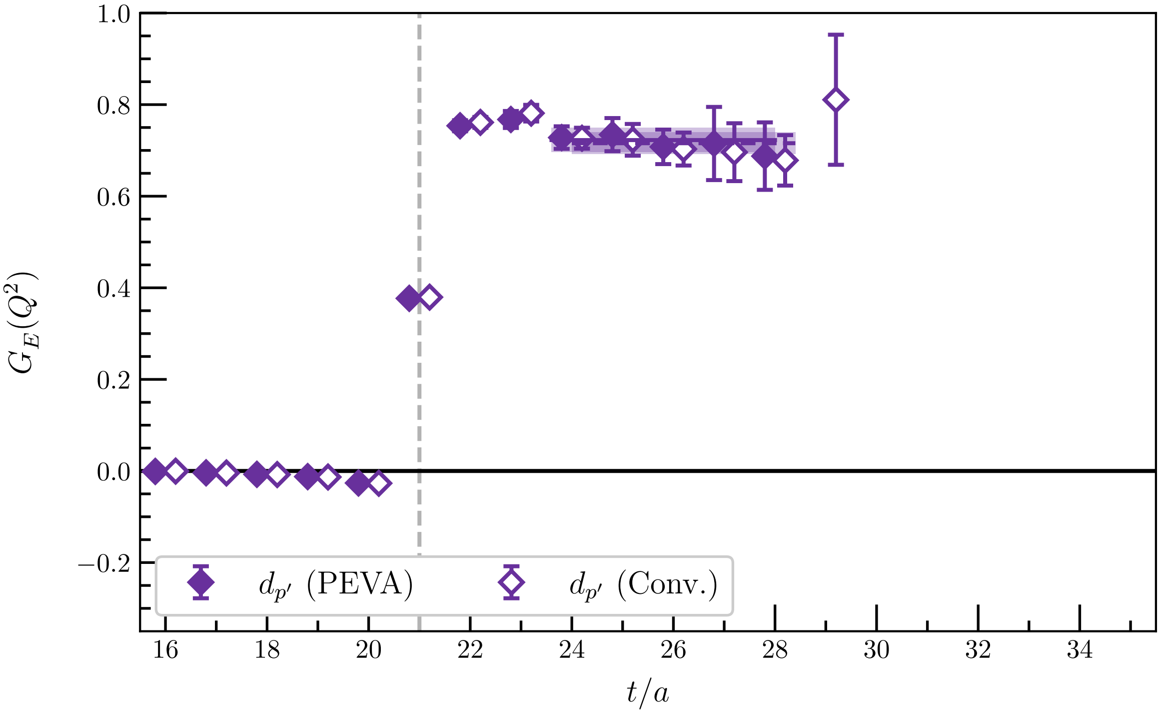

Figure 6.35: Contributions to $G_E(Q^2)$ from the singly represented quark flavour for the first positive-parity nucleon excitation. The pion mass, kinematics and plotting convention are the same as in Fig. 6.34 above. Both fits are from time slice 24–28.

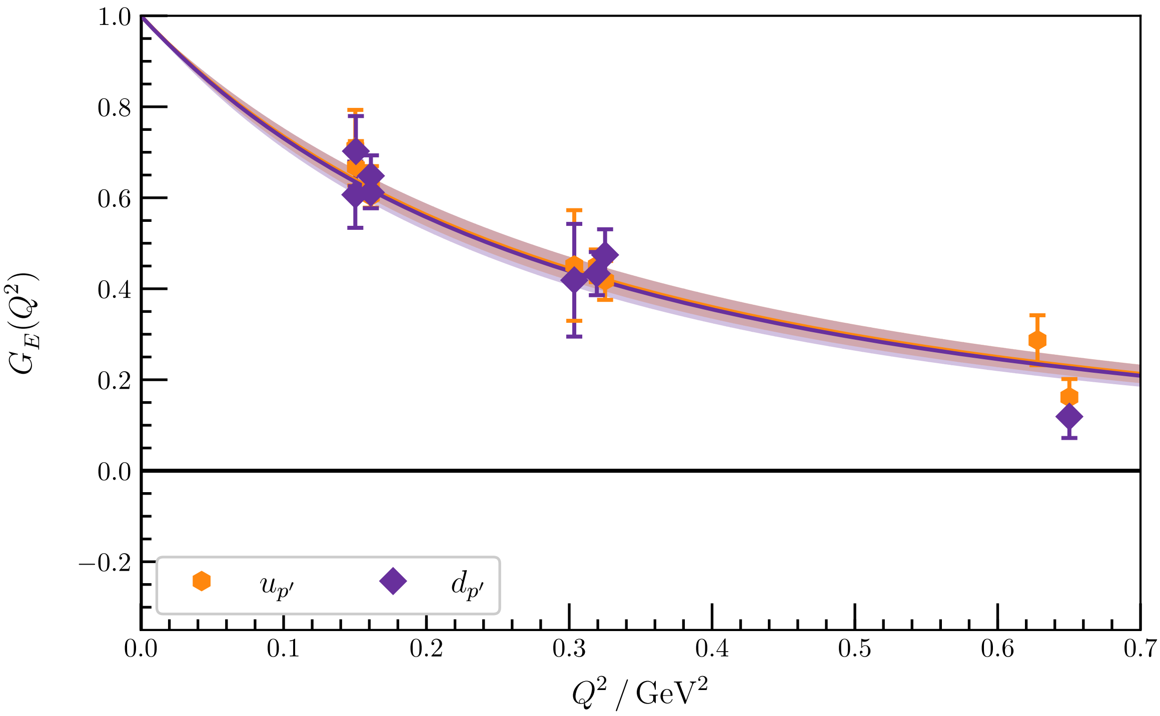

Figure 6.36: Quark-flavour contributions to $G_E(Q^2)$ for the first positive-parity excitation at $m_\pi = 411\,\mathrm{MeV}$. The shaded regions are dipole fits to the form factor, with lines indicating the central values. The fits correspond to charge radii of 0.887(40) fm for the doubly represented quark flavour ($u_{p'}$) and 0.890(49) fm for the singly represented quark flavour ($d_{p'}$).

masses (plots available in Appendix D), we find that the electric form factor for the neutron excitation is approximately zero, and the electric form factor for the proton excitation agrees well with a dipole fit which has been constrained to intersect the $y$-axis at unity (corresponding to a charge of +1).

For the heaviest three masses, these fits have charge radii ranging from 0.817(44) fm –0.890(44) fm , increasing with decreasing pion mass. These radii are all significantly larger than the charge radius of the ground-state proton at the corresponding mass. This indicates that the second positive-parity excitation is a larger state than the ground state proton, at least at these pion masses.

At the lightest two masses, the central values of the radii are smaller, but the statistical errors are large enough that they are consistent with the radii at the heavier masses (as well as being consistent with the ground-state proton radii at the corresponding masses). For example, Fig. 6.38 shows the form factors at $m_\pi = 296\,\mathrm{MeV}$. The dipole fit to the electric form factor for the excited proton at this mass corresponds to a charge radius of 0.787(125) fm .

In Fig. 6.39, we plot the pion-mass dependence of these dipole fits to the electric form factor for the proton excitation on a number of $Q^2$ slices. We clearly see here this different behaviour at the lightest two masses, which appears to indicate a partial loss

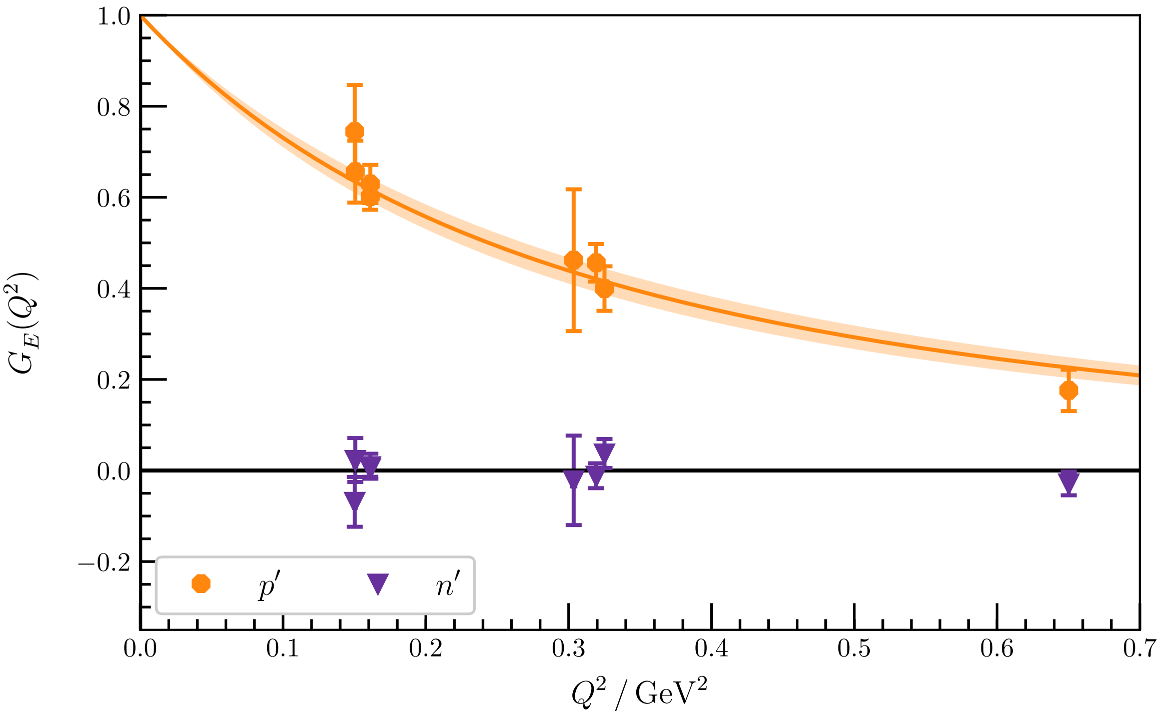

Figure 6.37: $G_E(Q^2)$ for the first positive-parity excitations of the proton and neutron at $m_\pi = 411\,\text{MeV}$. The shaded region corresponds to a dipole fit to the form factor for the proton, with a charge radius of $0.890(44)\,\text{fm}$ .

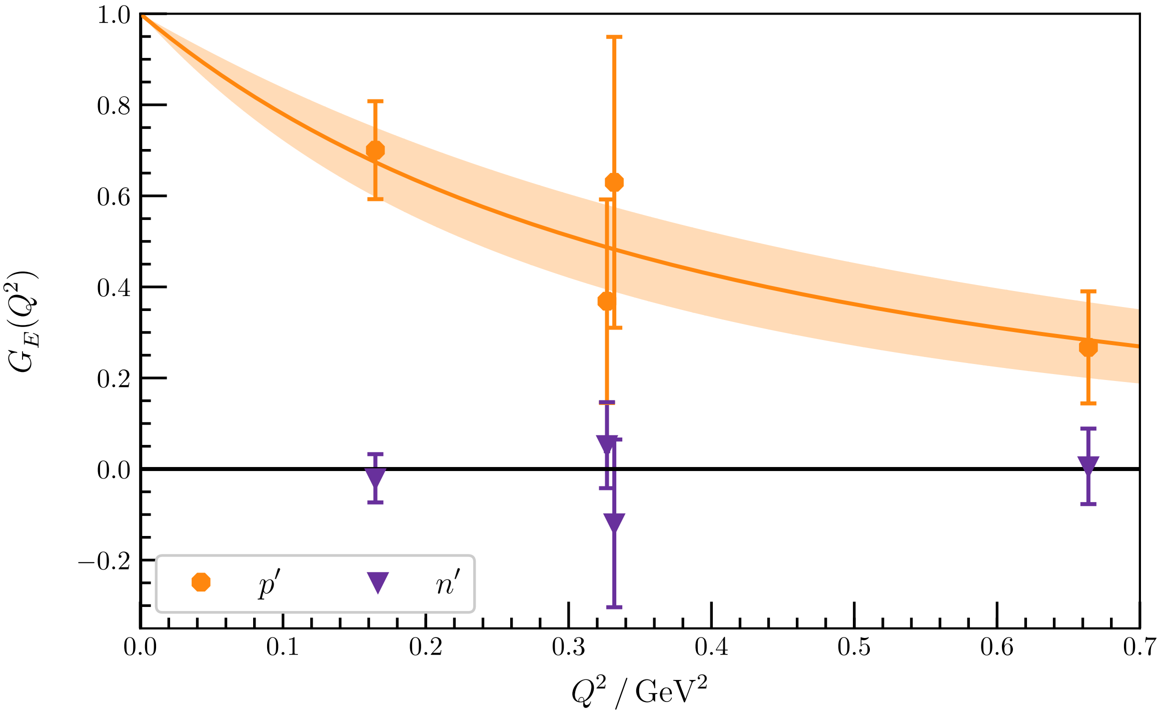

Figure 6.38: $G_E(Q^2)$ for the first positive-parity excitations of the proton and neutron at $m_\pi = 296\,\text{MeV}$. The shaded region corresponds to a dipole fit to the proton form factor, with a charge radius of $0.787(125)\,\text{fm}$ .

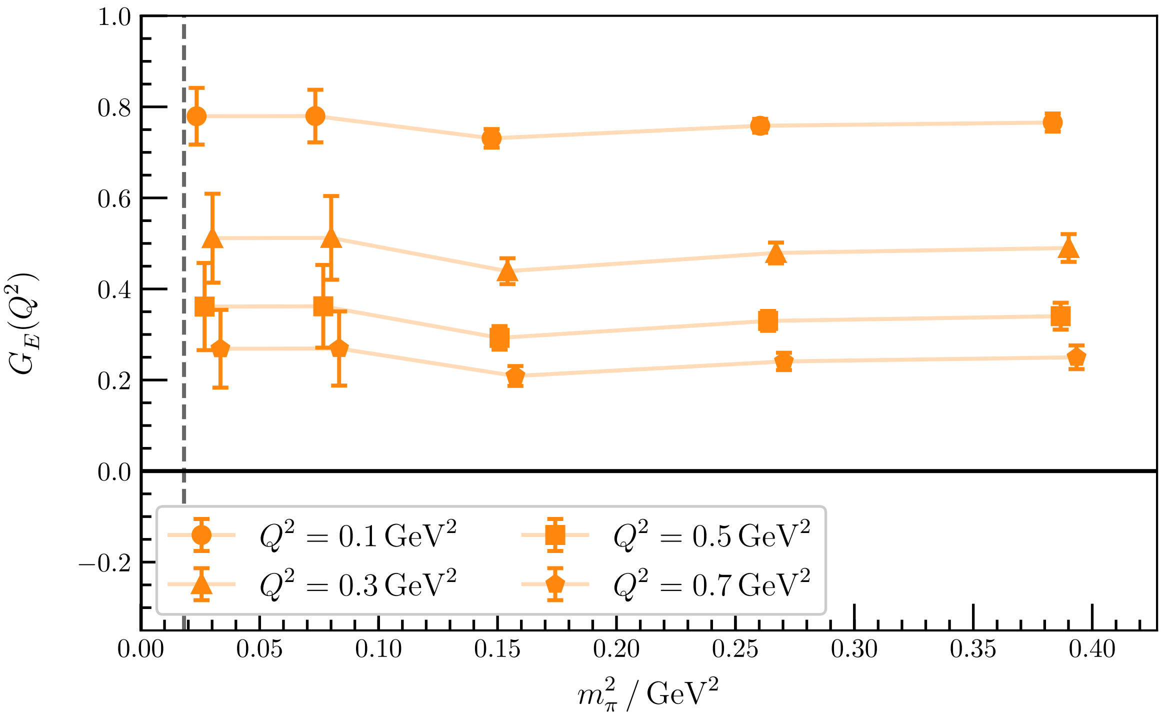

Figure 6.39: Quark-mass dependence of dipole fits to $G_E(Q^2)$ for the first positive-parity excitation of the proton. The different marker shapes correspond to taking the fit value at different $Q^2$ slices, and the dashed line corresponds to the physical pion mass. The points have been offset symmetrically for clarity.

of signal, though it could hint at this state also changing structure at these masses. Repeating the calculations with increased statistics at these masses should allow these results to be more clearly resolved, and any physics concealed within these large error bars to be revealed.

### 6.3.2 Magnetic form factor

Having investigated the electric form factor for this state, we now consider the magnetic form factor. In Fig. 6.40 we plot the Euclidean sink-time dependence of the extracted form factors at $m_\pi = 702\,\mathrm{MeV}$, with the lowest-momentum kinematics. We see that the form factors and plateaus for both analyses are very similar, and there is no evidence for excited-state contamination of this state. We see similar results for the other masses and kinematics, with no clear differences between the conventional and PEVA plateaus. For example, Fig. 6.41 shows this behaviour at $m_\pi = 411\,\mathrm{MeV}$ with the same lowest-momentum kinematics. This suggests that, like $G_E(Q^2)$, $G_M(Q^2)$ for the first positive-parity excitation is not affected by opposite parity excitations, at least at this level of statistics.

Focusing on the PEVA results, we plot the $Q^2$ dependence of the plateau fits for the two valence quark flavours at $m_\pi = 411\,\mathrm{MeV}$ in Fig. 6.42. We see that both quark flavours agree well with a dipole ansatz. This is also true for the two heavier pion masses, and the two lighter masses are also consistent, though they are too noisy to significantly constrain the fit. Plots of these results are available in Appendix D.

As discussed above, we can take appropriate combinations of the quark flavour contributions to form the excitations of the proton and neutron. In Fig. 6.43, we plot these combinations at $m_\pi = 411\,\text{MeV}$. Plots for the other masses are available in Appendix D. At this and the heavier two masses, we find that the magnetic form factors for the proton and neutron excitations agree well with a dipole fit. These fits have magnetic charge radii that are consistent with the corresponding excited proton charge radius. The magnetic form factors at the lightest two masses are too noisy to properly constrain a dipole fit. This can be seen in Figs. 6.44 and 6.45, in which we plot the pion-mass dependence of the dipole fits to the form factors at a range of $Q^2$ slices. These plots show fairly consistent results for the heavier three masses, with some pion-mass dependence, whereas the lightest two masses have much larger errors. This is a similar result to $G_E(Q^2)$, and supports the conclusion that we are losing most of the signal at these masses.

Returning to the individual quark sector results and noting that once again the electric and magnetic form factors have a similar $Q^2$ dependence, we take the ratio $\mu_{\text{Eff}}(Q^2) \equiv G_M(Q^2)/G_E(Q^2)$. In Fig. 6.46, we plot this ratio as a function of $Q^2$ for

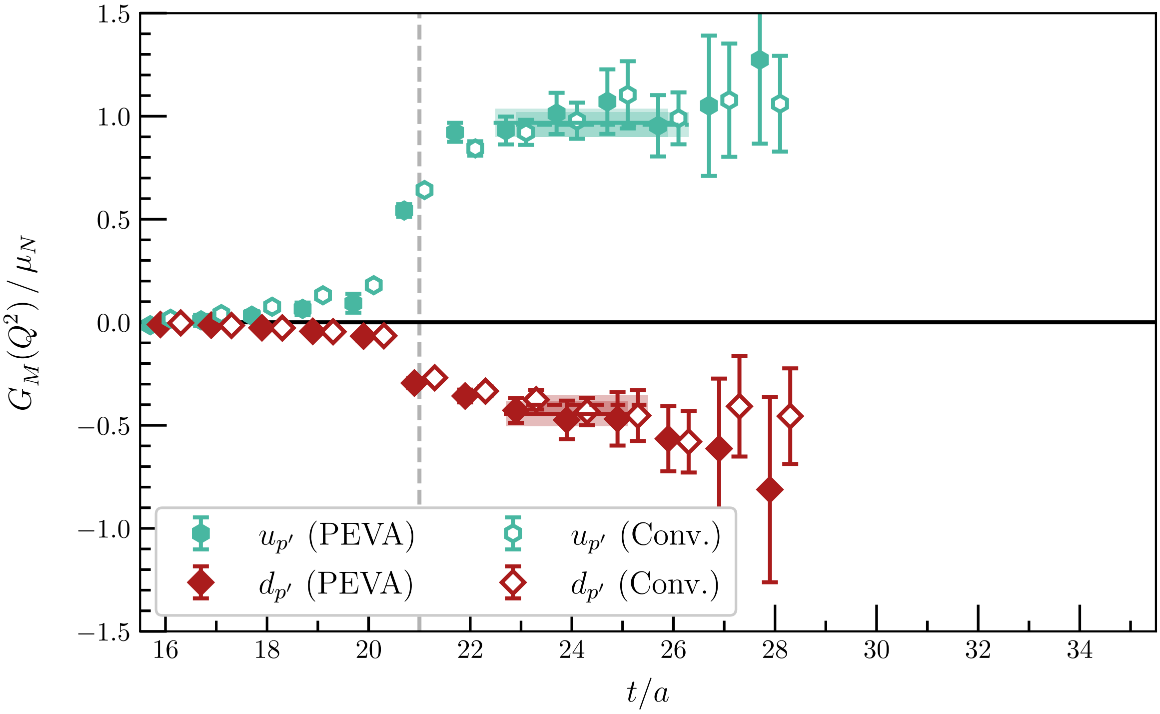

Figure 6.40: Quark-flavour contributions to the magnetic form factor for the first positive-parity excitation of the nucleon at $m_\pi = 702\,\text{MeV}$ for the lowest-momentum kinematics, providing $Q^2 = 0.1422(41)\,\text{GeV}^2$. Results are for single quarks of unit charge. All four fits start from time slice 23 and have consistent values.

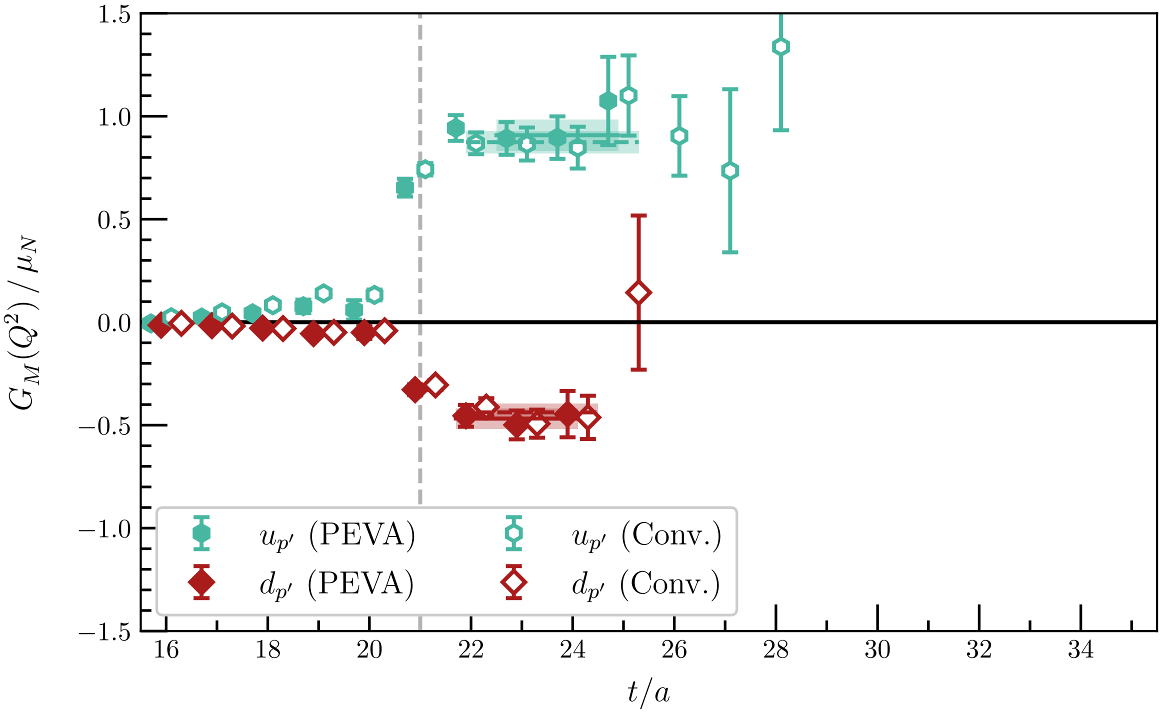

Figure 6.41: Quark-flavour contributions to $G_M(Q^2)$ for the first positive-parity excitation of the nucleon at $m_\pi = 570\,\text{MeV}$ for the lowest-momentum kinematics, providing $Q^2 = 0.146\,\text{GeV}^2$.

$m_\pi = 411\,\text{MeV}$. Plots of the $Q^2$ dependence for all five pion masses are available in Appendix D. We find that the ratio is once again very flat in $Q^2$, supporting our hypothesis that the form factors have the same $Q^2$ scaling in this region, and the validity of $\mu_{\text{Eff}}$ as an estimate of the magnetic moment.

In Fig. 6.47, we plot the pion-mass dependence of $\mu_{\text{Eff}}$ for individual quarks of unit charge. We see that the three heaviest masses have reasonably small error bars, but the lightest two masses have large errors. We can once again take combinations of the individual quark-flavour contributions to get the excited proton and neutron. In Fig. 6.48, we plot the pion-mass dependence of these combinations.

We see that the excited-state magnetic moments agree well with the ground-state magnetic moments. The agreement at the heaviest three masses is impressive. Thus, the results are in accord with a simple 2S constituent-quark-model state.

In this section, we have shown that the first positive-parity excitation of the nucleon has no obvious opposite-parity contaminations. However, variational analysis techniques in general have given good access to this state at several pion masses. This has allowed us to ascertain that these states have a larger radius than the ground-state nucleon, but have very similar magnetic moments. This is consistent with these states being a radial 2S excitation of the ground-state nucleon as seen in Ref. [129].

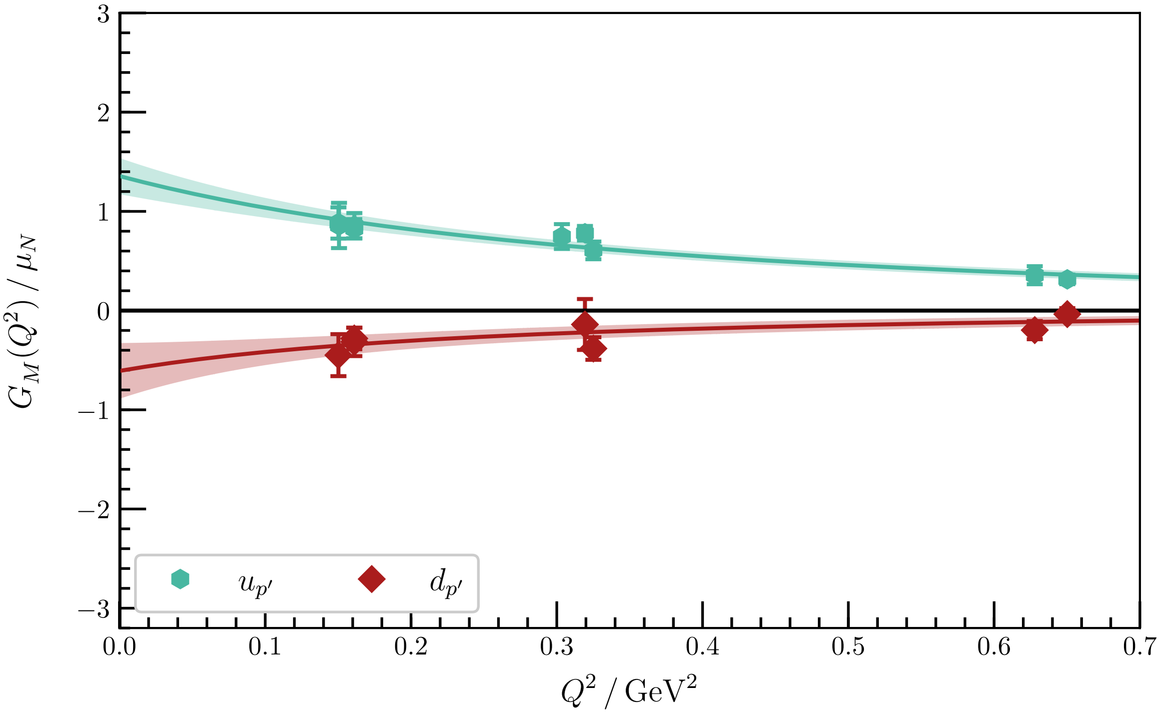

Figure 6.42: Quark-flavour contributions to $G_M(Q^2)$ for the first positive-parity excitation at $m_\pi = 411\,\mathrm{MeV}$. The shaded regions are dipole fits to the form factor, corresponding to magnetic charge radii of 0.820(84) fm for $u_{p'}$ and 0.986(301) fm for $d_{p'}$.

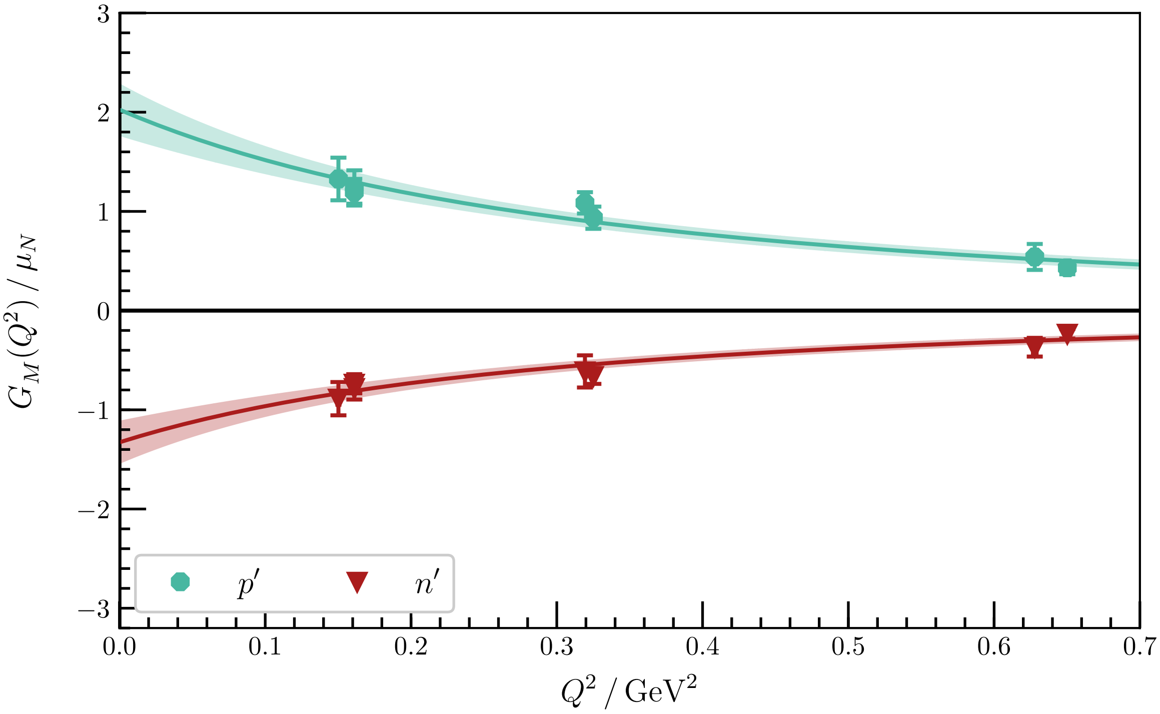

Figure 6.43: $G_M(Q^2)$ for the first positive-parity excitations of the proton and neutron at $m_\pi = 411\,\mathrm{MeV}$. The shaded region corresponds to a dipole fit to the form factor, with a magnetic charge radius of 0.852(80) fm for the proton excitation and 0.902(104) fm for the neutron excitation.

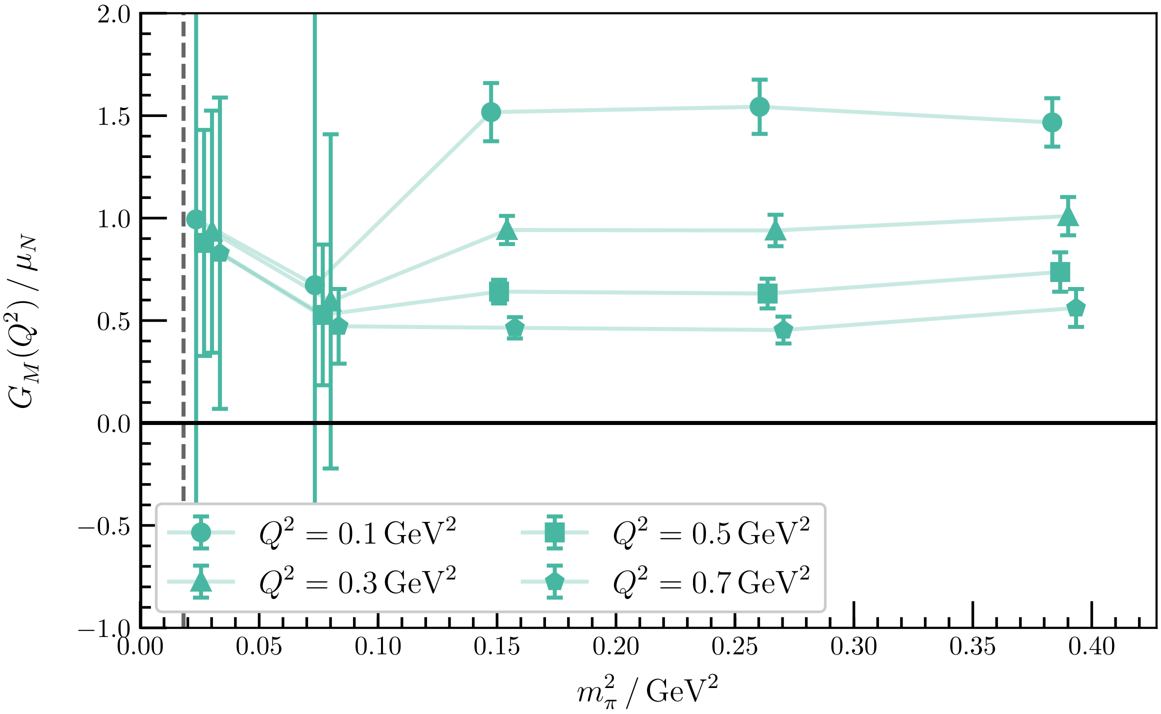

Figure 6.44: Quark-mass dependence of dipole fits to $G_M(Q^2)$ for the first positive-parity excitation of the proton. The marker shapes represent different $Q^2$ slices and the vertical dashed line corresponds to the physical pion mass. The points have been offset symmetrically for clarity.

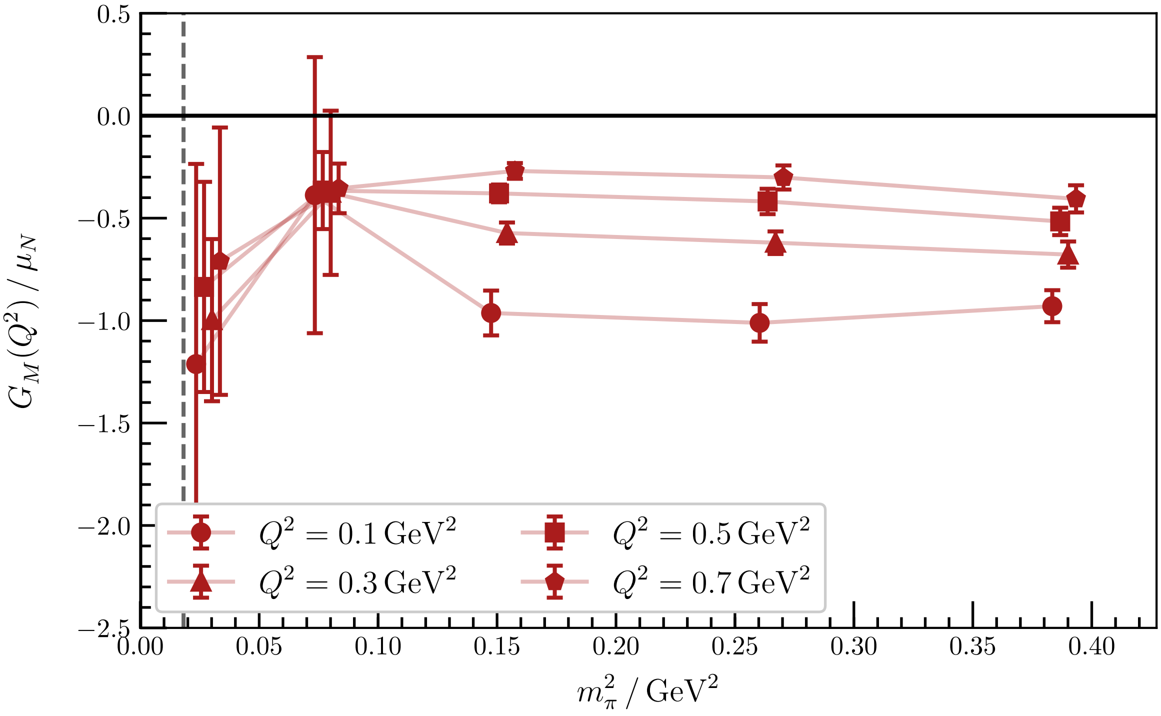

Figure 6.45: Quark-mass dependence of dipole fits to $G_M(Q^2)$ for the first positive-parity excitation of the neutron. The conventions for this plot are the same as in Fig. 6.44 above.

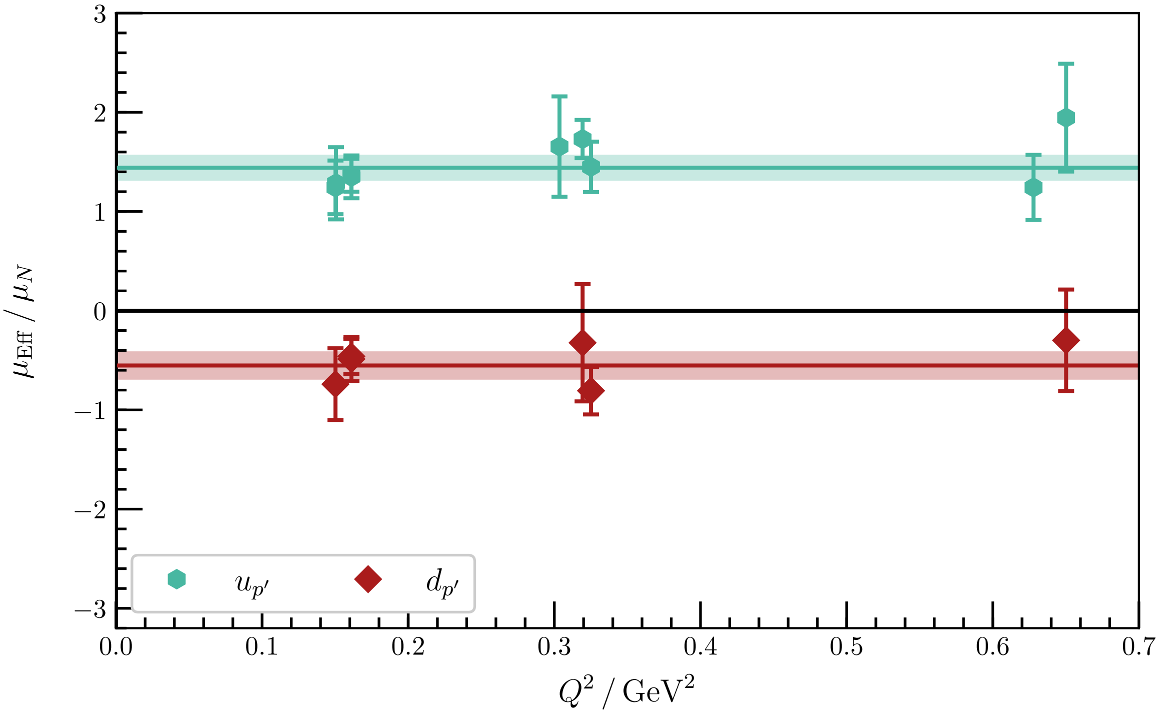

Figure 6.46: $\mu_{\text{Eff}}$ for individual quarks of unit charge in the first positive-parity excitation at $m_\pi = 411\,\text{MeV}$. The shaded bands are constant fits to the effective magnetic moments which provide magnetic moment contributions of $1.441(133)\ \mu_N$ for the doubly represented quark and $-0.552(143)\ \mu_N$ for the singly represented quark.

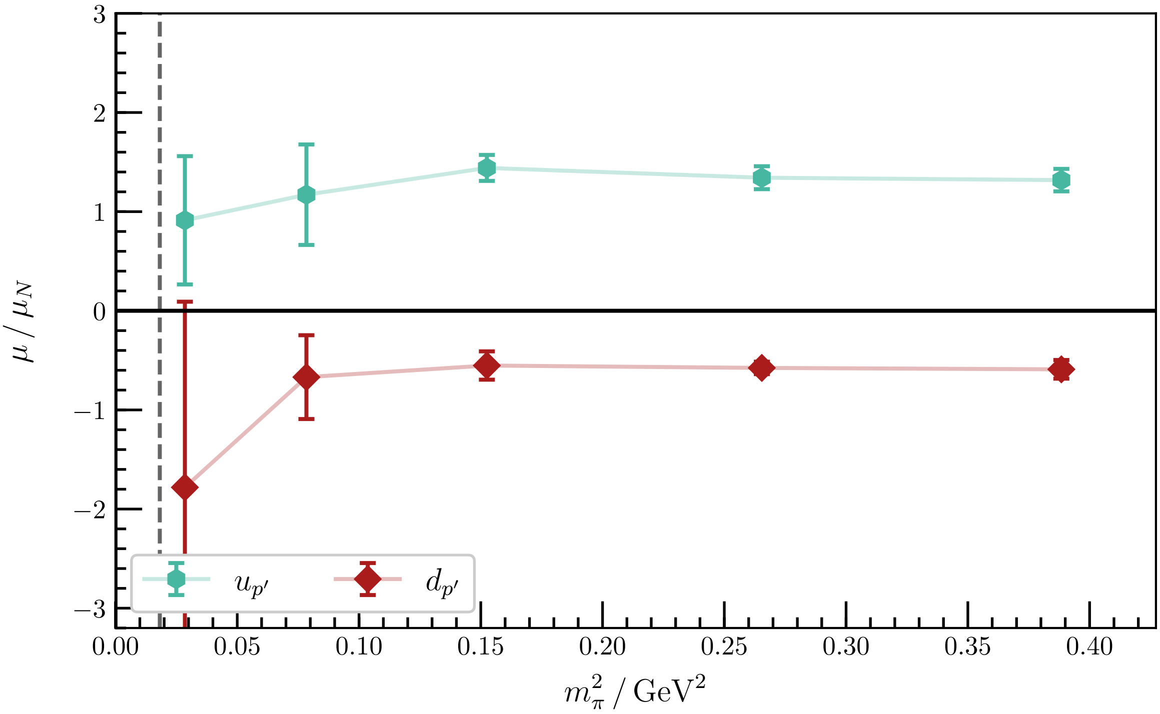

Figure 6.47: Quark-mass dependence of contributions from individual unit-charge quarks to the magnetic moment of the first positive-parity excitation of the nucleon. The vertical dashed line corresponds to the physical pion mass.

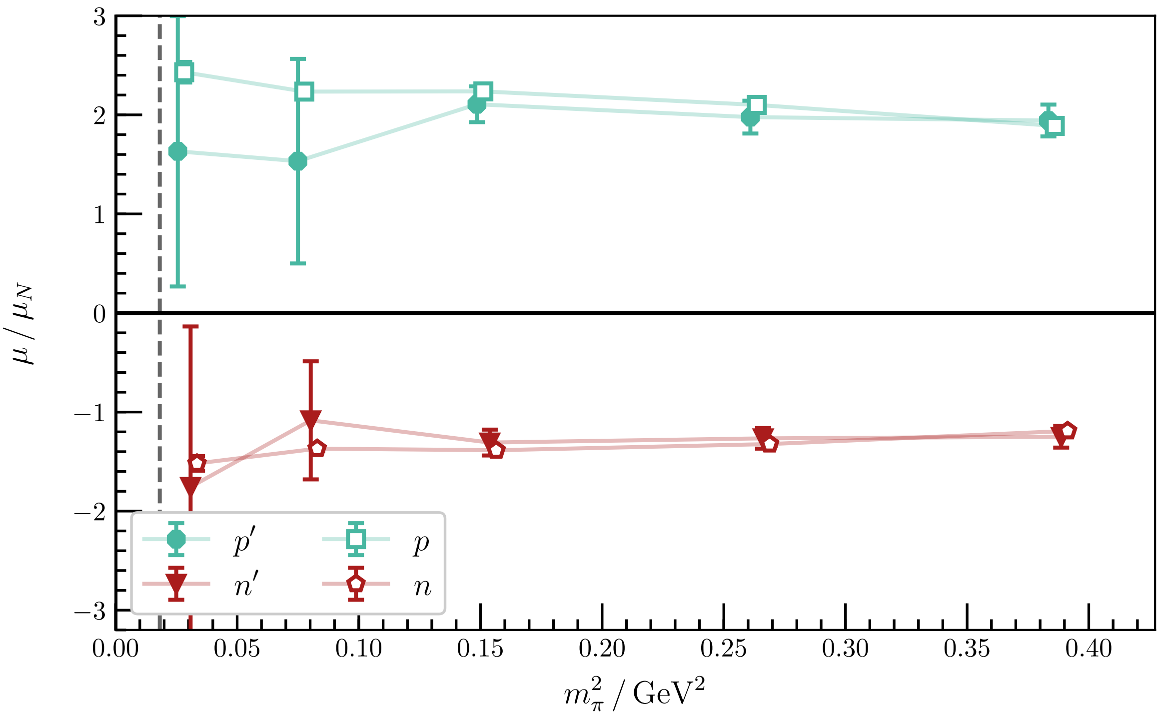

Figure 6.48: Quark-mass dependence of the magnetic moments of the first positive-parity excitations of the proton and neutron. The vertical dashed line corresponds to the physical pion mass, and the ground state is plotted with open markers. Points have been offset symmetrically for clarity.

## 6.4 Conclusion

In this chapter, we have shown that the PEVA technique is critical to correctly extracting the form factors of proton and neutron excitations on the lattice. Such extractions give us insight into the structure of the states seen on the lattice.

The first negative-parity excitation observed is consistent with the $N^*(1535)$ of the quark model, as predicted by HEFT. However, the second negative-parity excitation observed is not consistent with the $N^*(1535)$, and instead has the properties of the quark model $N^*(1650)$. This suggests that the simple HEFT interpretation of these states as both generated by the $N^*(1535)$ resonance is incomplete. Future HEFT studies should incorporate two bare basis states associated with the two different localised states observed herein. At the lightest two pion masses, we observe a rearrangement in the structure of the second negative-parity excitation. This is evident in both a significant shift in the magnetic moments of the excited proton and neutron, and significant non-analytic behaviour in the pion-mass dependence of of the electric form factor. The possibility of a molecular bound state of $K\Sigma$ dressed by $K\Lambda$ (analogous to the $\overline{K}N$ molecular structure of the $\Lambda(1405)$) is intriguing.

The positive-parity excitation observed in this study is difficult to isolate, and has proven quite noisy in previous lattice studies. To extract its form factors is a remarkable achievement, which can only be attained through the cancellation of statistical uncertainties enabled by the combination of a conserved current and an appropriately selected correlator ratio. This state has a charge radius approximately 30 % larger than the ground state, but it has nearly identical magnetic moments. This is consistent with the state being a radial excitation of the ground-state nucleon as seen in Ref. [129].

In this chapter we presented world-first calculations of the elastic form factors of these excitations of the nucleon. Accessing these form factors free from opposite-parity contaminations was not possible before we developed the PEVA technique. Now that this technique has been developed, it should become a staple of baryon excited state studies.

# Chapter 7

# Conclusion

In this thesis, we investigated the structure of the nucleon and its excitations in lattice QCD. We began in Chapter 3 with a study of QCD vacuum structure. We investigated centre clusters in pure SU(3) Yang-Mills gauge theory. We used a custom volume renderer developed specifically to overcome deficiencies in existing software, allowing us to render the centre clusters in 3D. By visualising the centre clusters and their evolution with HMC simulation time, we gained insight both into the effect of HMC updates on the vacuum structure, and into the nature of the centre clusters themselves and the role they play in confinement. The phenomenon of confinement is critical to hadron structure, as it governs the existence of hadrons and the structure of their quark core.

Having studied the role the vacuum plays in producing hadronic states, we then turned our attention to these states themselves, specifically baryonic states. In Chapter 4, we discussed how baryonic energy eigenstates can be isolated on the lattice. The conventional application of variational analysis techniques is vulnerable to opposite-parity contamination at finite momentum. To remove these contaminations, we developed the novel parity-expanded variational analysis (PEVA) technique. We demonstrated the efficacy of the PEVA technique at removing these opposite-parity contaminations and correctly extracting the excited-state spectrum of the nucleon at finite momentum. This result paved the way for the next phase of our research, investigating the structure of these states.

In Chapter 5, we extended the PEVA technique to the calculation of form factors. We then applied this extension to the calculation of the Sachs electric and magnetic form factors for the ground-state nucleon with general kinematics. The results for the electric form factor demonstrate the efficacy of variational techniques in general at extracting ground-state form factors. The results for the magnetic form factor show clear opposite-parity contaminations for the singly represented quark flavour. These contaminations lead to underestimations of the contributions to the form factor from this quark flavour of 5–20 % in conventional analyses, depending on the specific quark mass and kinematics. This indicates that the PEVA technique will be critical to precision calculations of nucleon form factors.

Having demonstrated the success and importance of the PEVA technique for extracting the form factors of the ground-state nucleon, we proceeded to examine its excitations. In Chapter 6 we presented world-first results for the first three excitations of the nucleon observed on the lattice when using local operators. A summary of some key features of these results along with the corresponding ground-state results is presented in Table 7.1. We observe two low-lying negative-parity excitations, both with proton charge radii consistent with the ground-state nucleon.

We also investigated the squared charge radius for the neutron and its excited states. For the ground state, we found a significant negative squared charge radius for all pion masses. This is consistent with experiment. This ground-state effect can be understood as the result of the pion in $\pi^- p$ dressings of the neutron carrying negative charge out to large radii. For the negative-parity excitations, the squared charge radius is closer to zero, suggesting an increased symmetry between the distributions of the individual quark flavours. Reproducing this shift is an interesting challenge for theoretical models of these states.

For the heaviest three pion masses considered, the lighter of the two states has magnetic moments consistent with constituent quark model predictions for the $N^*(1535)$, whereas the heavier state is consistent with constituent quark model predictions for the $N^*(1650)$. This is in contrast to Hamiltonian effective field theory calculations [96], which suggest that the two states can both be described as finite-volume dressings of the quark-model $N^*(1535)$. Our results suggest that future HEFT studies of this resonance region should include two bare states, corresponding to the two quark model states. At the lightest two pion masses, the heavier of the two negative-parity states departs from the quark-model predictions, suggesting an increasing role for meson-baryon scattering states.

The final state considered was the lowest-lying localised positive-parity excitation on the lattice. This state has a larger charge radius than the ground-state nucleon, but has the same magnetic moments. This suggests that it may be a radial excitation of the ground-state, as seen in Ref. [129].

This approach to calculating the elastic form factors can be extended to the calculation of transition amplitudes. The introduction of a different final state mass complicates the kinematics, but the expressions in Appendix A are general enough to accommodate this. Another consequence of the mass gap between the initial and final states is a significant negative offset in the values of $Q^2$. As a result, small momentum transfers such as $\boldsymbol{q} = (1, 0, 0)$ result in timelike $Q^2 < 0$. Most experimental results for transition amplitudes are for spacelike $Q^2 > 0$, so larger momentum transfers such as $\boldsymbol{q} = (1, 1, 0)$ and $(2, 0, 0)$ will be very important. Performing this analysis would be an interesting project to commence as a postdoctoral research associate.

In this thesis we focused on the systematic errors arising from opposite-parity contaminations in conventional variational analyses and the development of the PEVA technique to remove these contaminations. These systematic errors are catastrophic for excited states and important for ground state baryon form factors. In addition, there are other sources of systematic error to be considered and the modern lattice QCD techniques used herein ensure they are controlled and kept to a minimum. The form factor analyses were performed at five different pion masses approaching the physical point, allowing observation of the pion-mass dependence of the observed quantities. The fermion action employed was a non-perturbatively $O(a)$ improved action which eliminates $O(a)$ discretisation errors and fortuitously has small $O(a^2)$ errors [130]. The finite volume effects on the elastic form factors can be analysed in effective field theory as in Ref. [131].

In summary, we have gained great insight into the structure of the excitations of the nucleon in QCD. New visualisation techniques have provided insight into the role the QCD vacuum plays in confining quarks into hadrons with finite size. The development of the PEVA technique has allowed for the clean excitation of the baryons observed on the lattice at finite momentum for the first time. An extension of the PEVA technique proved effective at controlling excited-state contaminations in form factor extractions for the ground-state nucleon. This same extension has allowed for world-first extractions of the form factors of excited-state nucleons on the lattice free from opposite-parity contaminations. These results have provided great insight into the nature of the states observed on the lattice, and will be an important input into future studies of the connection between the finite-volume eigenstates observed in lattice QCD and the infinite-volume resonances of nature. The PEVA technique has played a critical role in all of the form factor results presented here, and will become a staple of baryon excited state studies.

Table 7.1: Summary of PEVA lattice results from previous chapters. We present the mass of the nucleon ($m$), the electric charge radius of the proton (${\langle {r_p}^2 \rangle}^{1/2}$), the squared electric charge radius of the neutron ($\langle {r_n}^2 \rangle$), and the magnetic moments of the proton and neutron ($\mu_p$ and $\mu_n$ respectively). Results are presented for all five pion masses considered herein. We consider the ground state ($N$), the two lowest-lying localised negative-parity excitations ($N_1^*$ and $N_2^*$), and the first localised positive-parity excitation ($N'$).

| | $m_\pi$ / MeV | $N$ | $N_1^*$ | $N_2^*$ | $N'$ |
|---|---|---|---|---|---|
| $m$ / GeV | 702 | 1.42(1) | 1.99(2) | 2.00(4) | 2.03(8) |
| | 570 | 1.30(1) | 1.85(3) | 1.78(5) | 1.95(7) |
| | 411 | 1.15(1) | 1.75(3) | 1.79(4) | 2.10(6) |
| | 296 | 1.08(1) | 1.53(6) | 1.88(6) | 2.28(18) |
| | 156 | 0.98(2) | 1.64(6) | 1.62(9) | 2.13(8) |
| ${\langle {r_p}^2 \rangle}^{1/2}$ / fm | 702 | 0.593(11) | 0.577(19) | 0.603(29) | 0.817(44) |
| | 570 | 0.646(13) | 0.636(19) | 0.634(24) | 0.832(35) |
| | 411 | 0.667(13) | 0.645(20) | 0.646(23) | 0.890(44) |
| | 296 | 0.679(17) | 0.683(36) | 0.699(43) | 0.787(125) |
| | 156 | 0.724(28) | 0.697(48) | 0.858(104) | 0.787(134) |
| $\langle {r_n}^2 \rangle$ / fm$^2$ | 702 | −0.009(3) | 0.008(12) | 0.014(17) | −0.024(27) |
| | 570 | −0.019(5) | −0.016(12) | 0.004(15) | −0.049(21) |
| | 411 | −0.030(5) | 0.021(18) | 0.017(16) | 0.009(43) |
| | 296 | −0.022(9) | −0.039(25) | −0.028(33) | 0.020(110) |
| | 156 | −0.056(32) | −0.015(39) | −0.109(99) | 0.162(215) |
| $\mu_p$ / $\mu_N$ | 702 | 1.89(3) | 1.53(7) | 0.03(8) | 1.94(16) |
| | 570 | 2.10(4) | 1.54(13) | 0.21(12) | 1.98(17) |
| | 411 | 2.24(4) | 1.65(8) | 0.08(8) | 2.11(18) |
| | 296 | 2.23(5) | 1.09(24) | 0.87(32) | 1.53(103) |
| | 156 | 2.43(11) | 1.86(39) | 1.05(62) | 1.63(136) |
| $\mu_n$ / $\mu_N$ | 702 | −1.19(2) | −0.92(4) | 0.42(5) | −1.25(11) |
| | 570 | −1.32(3) | −0.92(8) | 0.45(8) | −1.27(11) |
| | 411 | −1.39(3) | −0.99(5) | 0.35(7) | −1.31(13) |
| | 296 | −1.37(3) | −0.58(20) | −0.05(19) | −1.08(60) |
| | 156 | −1.52(8) | −1.33(31) | −0.00(80) | −1.76(162) |

# Appendix A

# F-Functions in the Pauli Representation

$$F\left(\Gamma, \mathcal{J}\right) \equiv 2EE' \,\mathrm{Tr}\left(\Gamma\,\frac{-i\gamma\cdot p' + \mathbb{I}M'}{2E'}\,\mathcal{J}\,\frac{-i\gamma\cdot p + \mathbb{I}M}{2E}\right) \tag{A.1}$$

$$\begin{aligned}
F\left(\Gamma_4, \mathbb{I}\right) &= \left(\left(E+M\right)\left(E'+M'\right) - \boldsymbol{p}\cdot\boldsymbol{p}'\right)\\
F\left(\Gamma_4, \gamma^i\right) &= -i\left(p_i\left(E'+M'\right) + p'_i\left(E+M\right)\right)\\
F\left(\Gamma_4, \gamma^4\right) &= \left(\left(E+M\right)\left(E'+M'\right) + \boldsymbol{p}\cdot\boldsymbol{p}'\right)\\
F\left(\Gamma_4, \gamma^5\right) &= 0\\
F\left(\Gamma_4, \gamma^i\gamma^5\right) &= -\epsilon_{ijk}p_j p'_k\\
F\left(\Gamma_4, \gamma^4\gamma^5\right) &= 0\\
F\left(\Gamma_4, \sigma^{4i}\right) &= -\left(p_i\left(E'+M'\right) - p'_i\left(E+M\right)\right)\\
F\left(\Gamma_4, \sigma^{ij}\right) &= -i\left(p_i p'_j - p_j p'_i\right)\\
F\left(\Gamma_i, \mathbb{I}\right) &= i\epsilon_{ijk}p_j p'_k\\
F\left(\Gamma_i, \gamma^j\right) &= \epsilon_{ijk}\left(p_k\left(E'+M'\right) - p'_k\left(E+M\right)\right)\\
F\left(\Gamma_i, \gamma^4\right) &= -i\epsilon_{ijk}p_j p'_k\\
F\left(\Gamma_i, \gamma^5\right) &= -\left(p_i\left(E'+M'\right) - p'_i\left(E+M\right)\right)\\
F\left(\Gamma_i, \gamma^j\gamma^5\right) &= i\left(\left(p_i p'_j + p_j p'_i\right) + \delta_{ij}\left(\left(E+M\right)\left(E'+M'\right) - \boldsymbol{p}\cdot\boldsymbol{p}'\right)\right)\\
F\left(\Gamma_i, \gamma^4\gamma^5\right) &= -\left(p_i\left(E'+M'\right) + p'_i\left(E+M\right)\right)\\
F\left(\Gamma_i, \sigma^{4j}\right) &= -i\epsilon_{ijk}\left(p_k\left(E'+M'\right) + p'_k\left(E+M\right)\right)\\
F\left(\Gamma_i, \sigma^{jk}\right) &= -\epsilon_{jkl}\left(\left(p_i p'_l + p_l p'_i\right) - \delta_{il}\left(\left(E+M\right)\left(E'+M'\right) + \boldsymbol{p}\cdot\boldsymbol{p}'\right)\right)
\end{aligned}$$

$$F'_+\left(\Gamma,\mathcal{J}\right) \equiv 8EE'\,\mathrm{Tr}\Bigg(\Gamma\,\Gamma_{\boldsymbol{p}'}\,\frac{-i\gamma\cdot p' + \mathbb{I}M'}{2E'}\,\mathcal{J}\,\frac{-i\gamma\cdot p + \mathbb{I}M}{2E}\,\Gamma_{\boldsymbol{p}}\Bigg) \tag{A.2}$$

$$\begin{aligned}
F'_+\left(\Gamma_4,\mathbb{I}\right) &= \left(\left(E+M\right)\left(E'+M'\right) - |\boldsymbol{p}||\boldsymbol{p}'|\right)\left(1+\hat{\boldsymbol{p}}\cdot\hat{\boldsymbol{p}}'\right)\\
F'_+\left(\Gamma_4,\gamma^i\right) &= -\left(|\boldsymbol{p}|\left(E'+M'\right) + |\boldsymbol{p}'|\left(E+M\right)\right)\left(\epsilon_{ijk}\hat{p}_j\hat{p}'_k + i\left(\hat{p}_i+\hat{p}'_i\right)\right)\\
F'_+\left(\Gamma_4,\gamma^4\right) &= \left(\left(E+M\right)\left(E'+M'\right) + |\boldsymbol{p}||\boldsymbol{p}'|\right)\left(1+\hat{\boldsymbol{p}}\cdot\hat{\boldsymbol{p}}'\right)\\
F'_+\left(\Gamma_4,\gamma^5\right) &= \left(|\boldsymbol{p}|\left(E'+M'\right) - |\boldsymbol{p}'|\left(E+M\right)\right)\left(1+\hat{\boldsymbol{p}}\cdot\hat{\boldsymbol{p}}'\right)\\
F'_+\left(\Gamma_4,\gamma^i\gamma^5\right) &= -\left(\left(E+M\right)\left(E'+M'\right) + |\boldsymbol{p}||\boldsymbol{p}'|\right)\left(\epsilon_{ijk}\hat{p}_j\hat{p}'_k + i\left(\hat{p}_i+\hat{p}'_i\right)\right)\\
F'_+\left(\Gamma_4,\gamma^4\gamma^5\right) &= \left(|\boldsymbol{p}|\left(E'+M'\right) + |\boldsymbol{p}'|\left(E+M\right)\right)\left(1+\hat{\boldsymbol{p}}\cdot\hat{\boldsymbol{p}}'\right)\\
F'_+\left(\Gamma_4,\sigma^{4i}\right) &= i\left(|\boldsymbol{p}|\left(E'+M'\right) - |\boldsymbol{p}'|\left(E+M\right)\right)\left(\epsilon_{ijk}\hat{p}_j\hat{p}'_k + i\left(\hat{p}_i+\hat{p}'_i\right)\right)\\
F'_+\left(\Gamma_4,\sigma^{ij}\right) &= -\left(\left(E+M\right)\left(E'+M'\right) - |\boldsymbol{p}||\boldsymbol{p}'|\right)\left(\epsilon_{ijk}\left(\hat{p}_k+\hat{p}'_k\right) - i\left(\hat{p}_i\hat{p}'_j - \hat{p}_j\hat{p}'_i\right)\right)\\
F'_+\left(\Gamma_i,\mathbb{I}\right) &= -i\left(\left(E+M\right)\left(E'+M'\right) - |\boldsymbol{p}||\boldsymbol{p}'|\right)\left(\epsilon_{ijk}\hat{p}_j\hat{p}'_k - i\left(\hat{p}_i+\hat{p}'_i\right)\right)\\
F'_+\left(\Gamma_i,\gamma^j\right) &= i\left(|\boldsymbol{p}|\left(E'+M'\right) + |\boldsymbol{p}'|\left(E+M\right)\right)\\
&\quad\times\left(\left(\hat{p}_i\hat{p}'_j + \hat{p}_j\hat{p}'_i\right) - i\epsilon_{ijk}\left(\hat{p}_k-\hat{p}'_k\right) + \delta_{ij}\left(1-\hat{\boldsymbol{p}}\cdot\hat{\boldsymbol{p}}'\right)\right)\\
F'_+\left(\Gamma_i,\gamma^4\right) &= -i\left(\left(E+M\right)\left(E'+M'\right) + |\boldsymbol{p}||\boldsymbol{p}'|\right)\left(\epsilon_{ijk}\hat{p}_j\hat{p}'_k - i\left(\hat{p}_i+\hat{p}'_i\right)\right)\\
F'_+\left(\Gamma_i,\gamma^5\right) &= -i\left(|\boldsymbol{p}|\left(E'+M'\right) - |\boldsymbol{p}'|\left(E+M\right)\right)\left(\epsilon_{ijk}\hat{p}_j\hat{p}'_k - i\left(\hat{p}_i+\hat{p}'_i\right)\right)\\
F'_+\left(\Gamma_i,\gamma^j\gamma^5\right) &= i\left(\left(E+M\right)\left(E'+M'\right) + |\boldsymbol{p}||\boldsymbol{p}'|\right)\\
&\quad\times\left(\left(\hat{p}_i\hat{p}'_j + \hat{p}_j\hat{p}'_i\right) - i\epsilon_{ijk}\left(\hat{p}_k-\hat{p}'_k\right) + \delta_{ij}\left(1-\hat{\boldsymbol{p}}\cdot\hat{\boldsymbol{p}}'\right)\right)\\
F'_+\left(\Gamma_i,\gamma^4\gamma^5\right) &= -i\left(|\boldsymbol{p}|\left(E'+M'\right) + |\boldsymbol{p}'|\left(E+M\right)\right)\left(\epsilon_{ijk}\hat{p}_j\hat{p}'_k - i\left(\hat{p}_i+\hat{p}'_i\right)\right)\\
F'_+\left(\Gamma_i,\sigma^{4j}\right) &= \left(|\boldsymbol{p}|\left(E'+M'\right) - |\boldsymbol{p}'|\left(E+M\right)\right)\\
&\quad\times\left(\left(\hat{p}_i\hat{p}'_j + \hat{p}_j\hat{p}'_i\right) - i\epsilon_{ijk}\left(\hat{p}_k-\hat{p}'_k\right) + \delta_{ij}\left(1-\hat{\boldsymbol{p}}\cdot\hat{\boldsymbol{p}}'\right)\right)\\
F'_+\left(\Gamma_i,\sigma^{jk}\right) &= \left(\left(E+M\right)\left(E'+M'\right) - |\boldsymbol{p}||\boldsymbol{p}'|\right)\epsilon_{jkl}\\
&\quad\times\left(\left(\hat{p}_i\hat{p}'_l + \hat{p}_l\hat{p}'_i\right) - i\epsilon_{ilm}\left(\hat{p}_m-\hat{p}'_m\right) + \delta_{il}\left(1-\hat{\boldsymbol{p}}\cdot\hat{\boldsymbol{p}}'\right)\right)
\end{aligned}$$

$$F'_-\left(\Gamma,\mathcal{J}\right) \equiv 8EE'\,\mathrm{Tr}\biggl(\Gamma\,\Gamma_{\boldsymbol{p}'}\,\frac{-i\gamma\cdot p'+\mathbb{I}M'}{2E'}\,\mathcal{J}\,\frac{-i\gamma\cdot p+\mathbb{I}M}{2E}\,\Gamma_{\boldsymbol{p}}\biggr) \tag{A.3}$$

$$\begin{aligned}
F'_-\left(\Gamma_4,\mathbb{I}\right) &= \left(\left(E+M\right)\left(E'+M'\right)+|\boldsymbol{p}||\boldsymbol{p}'|\right)\left(1-\hat{\boldsymbol{p}}\cdot\hat{\boldsymbol{p}}'\right)\\
F'_-\left(\Gamma_4,\gamma^i\right) &= -\left(|\boldsymbol{p}|\left(E'+M'\right)-|\boldsymbol{p}'|\left(E+M\right)\right)\left(\epsilon_{ijk}\hat{p}_j\hat{p}'_k+i\left(\hat{p}_i-\hat{p}'_i\right)\right)\\
F'_-\left(\Gamma_4,\gamma^4\right) &= \left(\left(E+M\right)\left(E'+M'\right)-|\boldsymbol{p}||\boldsymbol{p}'|\right)\left(1-\hat{\boldsymbol{p}}\cdot\hat{\boldsymbol{p}}'\right)\\
F'_-\left(\Gamma_4,\gamma^5\right) &= -\left(|\boldsymbol{p}|\left(E'+M'\right)+|\boldsymbol{p}'|\left(E+M\right)\right)\left(1-\hat{\boldsymbol{p}}\cdot\hat{\boldsymbol{p}}'\right)\\
F'_-\left(\Gamma_4,\gamma^i\gamma^5\right) &= \left(\left(E+M\right)\left(E'+M'\right)-|\boldsymbol{p}||\boldsymbol{p}'|\right)\left(\epsilon_{ijk}\hat{p}_j\hat{p}'_k+i\left(\hat{p}_i-\hat{p}'_i\right)\right)\\
F'_-\left(\Gamma_4,\gamma^4\gamma^5\right) &= -\left(|\boldsymbol{p}|\left(E'+M'\right)-|\boldsymbol{p}'|\left(E+M\right)\right)\left(1-\hat{\boldsymbol{p}}\cdot\hat{\boldsymbol{p}}'\right)\\
F'_-\left(\Gamma_4,\sigma^{4i}\right) &= i\left(|\boldsymbol{p}|\left(E'+M'\right)+|\boldsymbol{p}'|\left(E+M\right)\right)\left(\epsilon_{ijk}\hat{p}_j\hat{p}'_k+i\left(\hat{p}_i-\hat{p}'_i\right)\right)\\
F'_-\left(\Gamma_4,\sigma^{ij}\right) &= \left(\left(E+M\right)\left(E'+M'\right)+|\boldsymbol{p}||\boldsymbol{p}'|\right)\left(\epsilon_{ijk}\left(\hat{p}_k-\hat{p}'_k\right)-i\left(\hat{p}_i\hat{p}'_j-\hat{p}_j\hat{p}'_i\right)\right)\\
F'_-\left(\Gamma_i,\mathbb{I}\right) &= i\left(\left(E+M\right)\left(E'+M'\right)+|\boldsymbol{p}||\boldsymbol{p}'|\right)\left(\epsilon_{ijk}\hat{p}_j\hat{p}'_k-i\left(\hat{p}_i-\hat{p}'_i\right)\right)\\
F'_-\left(\Gamma_i,\gamma^j\right) &= i\left(|\boldsymbol{p}|\left(E'+M'\right)-|\boldsymbol{p}'|\left(E+M\right)\right)\\
&\quad\times\left(\left(\hat{p}_i\hat{p}'_j+\hat{p}_j\hat{p}'_i\right)-i\epsilon_{ijk}\left(\hat{p}_k+\hat{p}'_k\right)-\delta_{ij}\left(1+\hat{\boldsymbol{p}}\cdot\hat{\boldsymbol{p}}'\right)\right)\\
F'_-\left(\Gamma_i,\gamma^4\right) &= i\left(\left(E+M\right)\left(E'+M'\right)-|\boldsymbol{p}||\boldsymbol{p}'|\right)\left(\epsilon_{ijk}\hat{p}_j\hat{p}'_k-i\left(\hat{p}_i-\hat{p}'_i\right)\right)\\
F'_-\left(\Gamma_i,\gamma^5\right) &= -i\left(|\boldsymbol{p}|\left(E'+M'\right)+|\boldsymbol{p}'|\left(E+M\right)\right)\left(\epsilon_{ijk}\hat{p}_j\hat{p}'_k-i\left(\hat{p}_i-\hat{p}'_i\right)\right)\\
F'_-\left(\Gamma_i,\gamma^j\gamma^5\right) &= -i\left(\left(E+M\right)\left(E'+M'\right)-|\boldsymbol{p}||\boldsymbol{p}'|\right)\\
&\quad\times\left(\left(\hat{p}_i\hat{p}'_j+\hat{p}_j\hat{p}'_i\right)-i\epsilon_{ijk}\left(\hat{p}_k+\hat{p}'_k\right)-\delta_{ij}\left(1+\hat{\boldsymbol{p}}\cdot\hat{\boldsymbol{p}}'\right)\right)\\
F'_-\left(\Gamma_i,\gamma^4\gamma^5\right) &= -i\left(|\boldsymbol{p}|\left(E'+M'\right)-|\boldsymbol{p}'|\left(E+M\right)\right)\left(\epsilon_{ijk}\hat{p}_j\hat{p}'_k-i\left(\hat{p}_i-\hat{p}'_i\right)\right)\\
F'_-\left(\Gamma_i,\sigma^{4j}\right) &= \left(|\boldsymbol{p}|\left(E'+M'\right)+|\boldsymbol{p}'|\left(E+M\right)\right)\\
&\quad\times\left(\left(\hat{p}_i\hat{p}'_j+\hat{p}_j\hat{p}'_i\right)-i\epsilon_{ijk}\left(\hat{p}_k+\hat{p}'_k\right)-\delta_{ij}\left(1+\hat{\boldsymbol{p}}\cdot\hat{\boldsymbol{p}}'\right)\right)\\
F'_-\left(\Gamma_i,\sigma^{jk}\right) &= -\left(\left(E+M\right)\left(E'+M'\right)+|\boldsymbol{p}||\boldsymbol{p}'|\right)\epsilon_{jkl}\\
&\quad\times\left(\left(\hat{p}_i\hat{p}'_l+\hat{p}_l\hat{p}'_i\right)-i\epsilon_{ilm}\left(\hat{p}_m+\hat{p}'_m\right)-\delta_{il}\left(1+\hat{\boldsymbol{p}}\cdot\hat{\boldsymbol{p}}'\right)\right)
\end{aligned}$$

# Appendix B

# Visualising Centre Clusters

*This rendering software was developed as part of my honours work, the year before I began my PhD and has already been submitted as part of my honours thesis. It is included here because it underpins the new work presented in Chapter 3.*

## B.1 Algorithm

In order to visualise centre clusters, we use a ray-traced volume renderer. For each pixel in the final image, a single ray is traced out directly away from the viewer through the volume to be rendered, accruing colour and opacity based on the volumetric data.

Given a RGB (red, green, blue) colour vector $C^{vol}(\vec{x})$ and an opacity $\alpha^{vol}(\vec{x})$ at every point $\vec{x}$ in the volume, we accrue colour and opacity along a ray $\vec{x}(z)$ $(0 \leq z \leq 1$, where $\vec{x}(0)$ is the point where the ray enters the volume and $\vec{x}(1)$ the point where it exits) by the differential equations,

$$\begin{aligned}\frac{d\alpha^{ray}(z)}{dz} &= \left(1-\alpha^{ray}(z)\right)\alpha^{vol}\left(\vec{x}(z)\right) \ , \\ \frac{dC^{ray}(z)}{dz} &= \left(1-\alpha^{ray}(z)\right)C^{vol}\left(\vec{x}(z)\right) \ .\end{aligned}$$

To solve these differential equations, we use Euler's method, with a finite step size $\Delta z$ [132]:

$$\begin{aligned}\alpha^{ray}_{n+1} &= \alpha^{ray}_{n} + \Delta z\left(1-\alpha^{ray}_{n}\right)\alpha^{vol}\left(\vec{x}(z_n)\right) \ , \\ C^{ray}_{n+1} &= C^{ray}_{n} + \Delta z\left(1-\alpha^{ray}_{n}\right)C^{vol}\left(\vec{x}(z_n)\right) \ .\end{aligned}$$

In order to perform these calculations, we use OpenGL [133], a 2D and 3D graphics API that allows us to leverage the powerful hardware available in modern GPUs which is designed specifically for rendering graphics. OpenGL provides a flexible graphics processing pipeline which for our purposes consists of a vertex shader followed by a fragment shader. The vertex shader takes in information about the position and shape of three dimensional objects to be rendered and transforms them into the two dimensional space of the screen. The fragment shader runs once for each pixel on the screen, taking information about the polygon visible at that point from the vertex shader and determining the colour the pixel should be.

In our particular case, we adapt a technique by Krüger and Westermann [134] which involves repeatedly rendering a single cube with a sequence of different shader pairs. The vertex shader is the same every time and performs a simple transformation on the cube and calculates the mapping between points on the surface of the cube and points in the volume data that is being rendered. We then have three different fragment shaders that are run in sequence to produce the desired output. A feature that we make extensive use of in order to store interim data is rendering to a framebuffer, an image in memory that serves as a virtual screen, allowing us to store the result of one fragment shader and then use it in a later shading run.

The first fragment shader is run with only the outside faces of the cube visible, so the vertex shader gives the coordinates of the point a ray cast through the current pixel would enter the volume. We store these directly in the red, green, and blue channels of a framebuffer. We then run the second shader with only the inside faces of the cube visible, so the vertex shader gives the coordinates of the point the ray would leave the volume. We then access the entry coordinates from the framebuffer and calculate the direction and length of the ray inside the volume and store them in the red, green, blue, and alpha channels of a new framebuffer.

We can then use a more complicated fragment shader to preform the integration, indexing into a 3D texture containing the volume data and calculating $C^{vol}(\vec{x})$ and $\alpha^{vol}(\vec{x})$ at each step. By setting the interpolation mode on the texture, we can tell OpenGL to automatically and efficiently perform trilinear interpolation on the data.

By transforming the cube, we can transform the volume being rendered. Thus we perform standard OpenGL model/view and projection transformations on the cube to place the volume in the centre of the screen with perspective and continuously rotate it so that it is possible to see all sides of the volume and observe the 3D structure it contains.

We can then load the pixel data produced by the GPU back into main memory and convert it into a range of formats for later use. In particular, we use DevIL [135] to convert a single frame into a static image, or we use FFmpeg [136] to combine a sequence of frames into a video.

## B.2 Optimisation

Implementing this algorithm naïvely is rather inefficient for all but the most sparse data sets, as much of the volume is obscured by opaque or nearly opaque regions and has little to no effect on the final image. In order to eliminate this inefficiency, we introduce early ray termination, that is we stop integrating rays once they reach a certain opacity threshold.

We do this by introducing another fragment shader that writes to the depth buffer without changing the colour or opacity. The depth buffer is a special texture used by OpenGL to determine what geometry should be obscured by other geometry. If the opacity has reached a certain threshold, our shader writes the minimum possible value to the depth buffer, effectively terminating the ray.

This shader is then interleaved with the integrating shader, which writes to a framebuffer to store its interim result. This method is also used to stop integrating rays that have left the volume, simply by setting their opacity to 1 if they are outside the volume (equivalent to hitting a solid black backdrop).

In order to maximise efficiency, the integrating shader performs batches of several steps at a time, starting from zero opacity and colour. The result is then appended to the previously calculated integration by using OpenGL blending with the blending mode set to

$$\alpha \to \alpha + (1-\alpha)\alpha_{new} \,,$$

$$C \to C + (1-\alpha)C_{new} \,.$$

This tells OpenGL how to mix the new colour produced by the fragment shader ($C_{new}$ and $\alpha_{new}$) with the current value of the render target ($C$ and $\alpha$). We can show that combining batches of integration in this way is equivalent to integrating the entire ray in a single batch.

## B.3 Rendering Styles

In this particular case, we take the local Polyakov loops defined at each lattice site and, using trilinear interpolation, get a complex field $L(\vec{x})$ defined everywhere on the volume. We then calculate the complex phase of the loops and the distance to the closest centre phase:

$$\phi(\vec{x}) = \arg\left(L(\vec{x})\right) \,,$$

$$\Delta\phi(\vec{x}) = \min\left( |\phi(\vec{x})| \,, \left|\phi(\vec{x}) - \frac{2\pi}{3}\right| , \left|\phi(\vec{x}) + \frac{2\pi}{3}\right| \right) \,.$$

We then define $C^{vol}(\vec{x})$ and $\alpha^{vol}(\vec{x})$ to be

$$C^{vol}(\vec{x}) = \mathrm{hsv}\left(\frac{\phi(\vec{x})}{2\pi}, 1, 1\right),$$

$$\alpha^{vol}(\vec{x}) = \begin{cases} 100(1 - 20\Delta\phi(\vec{x}))^4 & \text{if } \Delta\phi(\vec{x}) < 0.05 \\ 0 & \text{if } \Delta\phi(\vec{x}) \geq 0.05 \end{cases}$$

where hsv maps a colour expressed in HSV (hue, saturation, value) to its RGB representation:

$$\mathrm{hsv}(h, s, v) = \begin{cases} v \cdot (1, 1 - s(1 - 6h), 1 - s) & \text{if } 0 \leq h < \frac{1}{6} \\ v \cdot (1 - s(6h - 1), 1, 1 - s) & \text{if } \frac{1}{6} \leq h < \frac{2}{6} \\ v \cdot (1 - s, 1, 1 - s(3 - 6h)) & \text{if } \frac{2}{6} \leq h < \frac{3}{6} \\ v \cdot (1 - s, 1 - s(6h - 3), 1) & \text{if } \frac{3}{6} \leq h < \frac{4}{6} \\ v \cdot (1 - s(5 - 6h), 1 - s, 1) & \text{if } \frac{4}{6} \leq h < \frac{5}{6} \\ v \cdot (1, 1 - s, 1 - s(6h - 5)) & \text{if } \frac{5}{6} \leq h < 1 \end{cases}$$

This maps $\phi = 0$ ($h = 0$) to red, $\phi = \frac{2\pi}{3}$ ($h = \frac{1}{3}$) to green, and $\phi = \frac{-2\pi}{3}$ ($h = \frac{2}{3}$) to blue.

We also use an alternative rendering style where the colour is still determined in the same way, but the opacity is determined by the absolute value rather than the phase:

$$\alpha^{vol}(\vec{x}) = \begin{cases} 200\left(|L(\vec{x})|^2 - 0.2\right) & \text{if } |L(\vec{x})|^2 > 0.2 \\ 0 & \text{if } |L(\vec{x})|^2 \leq 0.2 \end{cases}$$

This allows us to study the relationship between the phase and the absolute value.

# Appendix C

# Pauli Representation

In this thesis we work in the Pauli representation for the $\gamma$-matrices. This representation is formulated with a Euclidean metric $g^{\mu\nu} = \delta^{\mu\nu}$

$$\{\gamma^\mu, \gamma^\nu\} = 2\,\delta_{\mu\nu}\,. \tag{C.1}$$

In this representation, we have

$$\gamma^i \equiv \begin{pmatrix} 0 & -i\,\sigma_i \\ i\,\sigma_i & 0 \end{pmatrix}, \qquad \text{for } i = 1, 2, 3\,, \tag{C.2}$$

$$\gamma^4 \equiv \begin{pmatrix} \mathbb{I}_2 & 0 \\ 0 & -\mathbb{I}_2 \end{pmatrix}, \tag{C.3}$$

with

$$\begin{aligned} \gamma^5 &\equiv \frac{1}{4!}\,\epsilon_{\mu\nu\sigma\tau}\,\gamma^\mu\,\gamma^\nu\,\gamma^\sigma\,\gamma^\tau \\ &= -\begin{pmatrix} 0 & \mathbb{I}_2 \\ \mathbb{I}_2 & 0 \end{pmatrix}, \end{aligned} \tag{C.4}$$

and

$$\begin{aligned} \sigma^{\mu\nu} &\equiv \frac{1}{2i}\,[\gamma^\mu, \gamma^\nu] \\ &= -i\,\gamma^\mu\,\gamma^\nu \qquad \text{for } \mu \neq \nu\,. \end{aligned} \tag{C.5}$$

The charge conjugation matrix is given by

$$C \equiv \gamma^4\,\gamma^2\,. \tag{C.6}$$

Given these definitions,

$$\sigma^{ij} = \epsilon_{ijk} \begin{pmatrix} \sigma_k & 0 \\ 0 & \sigma_k \end{pmatrix}, \qquad \text{for } i, j = 1, 2, 3\,, \tag{C.7}$$

$$\sigma^{k4} = \epsilon_{ijk} \begin{pmatrix} 0 & \sigma_k \\ \sigma_k & 0 \end{pmatrix} = -\sigma^{4k}\,, \qquad \text{for } k = 1, 2, 3\,, \tag{C.8}$$

$$i\,\gamma^5\,\gamma^k = \begin{pmatrix} \sigma_k & 0 \\ 0 & -\sigma_k \end{pmatrix}, \qquad \text{for } k = 1, 2, 3\,, \tag{C.9}$$

$$i\,\gamma^5\,\gamma^4 = \begin{pmatrix} 0 & \mathbb{I}_2 \\ -\mathbb{I}_2 & 0 \end{pmatrix}, \qquad \text{for } k = 1, 2, 3\,, \tag{C.10}$$

$$\{\gamma^5, \gamma^\mu\} = 0\,, \qquad \text{for } \mu = 1, 2, 3, 4\,, \tag{C.11}$$

$$(\gamma^\mu)^2 = \mathbb{I}_4\,, \qquad \text{for } \mu = 1, 2, 3, 4\,, \tag{C.12}$$

$$\left(\gamma^5\right)^2 = \mathbb{I}_4\,, \tag{C.13}$$

$$\gamma^{\mu\dagger} = \gamma^\mu\,, \qquad \text{for } \mu = 1, 2, 3, 4\,, \tag{C.14}$$

$$\gamma^{5\dagger} = \gamma^5\,, \tag{C.15}$$

$$C^\dagger = C^{-1} = C^\top = -C\,. \tag{C.16}$$

The Hermitian nature of $\gamma^\mu$ is a feature of this representation. Combined with the Euclidean metric, it is particularly amenable to lattice QCD calculations in Euclidean space via $t \to -i\,t$.

Free particle spinors in this representation take the form

$$u(p,\uparrow) \equiv \sqrt{\frac{E+m}{2m}} \begin{pmatrix} 1 \\ 0 \\ \frac{p_3}{E(\boldsymbol{p})+m} \\ \frac{p_1+i\,p_2}{E(\boldsymbol{p})+m} \end{pmatrix}, \tag{C.17}$$

$$u(p,\downarrow) \equiv \sqrt{\frac{E+m}{2m}} \begin{pmatrix} 0 \\ 1 \\ \frac{p_1-i\,p_2}{E(\boldsymbol{p})+m} \\ \frac{-p_3}{E(\boldsymbol{p})+m} \end{pmatrix}, \tag{C.18}$$

and the corresponding anti-spinors take the form

$$v(p,\uparrow) \equiv -\sqrt{\frac{E+m}{2m}} \begin{pmatrix} \frac{p_1-i\,p_2}{E(\boldsymbol{p})+m} \\ \frac{-p_3}{E(\boldsymbol{p})+m} \\ 0 \\ 1 \end{pmatrix}, \tag{C.19}$$

$$v(p,\downarrow) \equiv \quad \sqrt{\frac{E+m}{2m}} \begin{pmatrix} \frac{p_3}{E(\boldsymbol{p})+m} \\ \frac{p_1+i\,p_2}{E(\boldsymbol{p})+m} \\ 1 \\ 0 \end{pmatrix} . \tag{C.20}$$

# Appendix D

# Form Factor Results

In Chapters 5 and 6, we presented extractions of the Sachs electric and magnetic form factors of the ground-state nucleon and three of its excitations on the lattice. For the sake of brevity, some of these results were elided from these chapters. In this Appendix, we present the elided results in full. Figures are listed in the index below according to the excitation under consideration, then by the quantity being graphed in each of the five figures in the set. One figure is included for each pion mass ensemble from 702 MeV down to 156 MeV.

For further details on the quantities being graphed, see Chapters 5 and 6. The form factor data plotted here is available in tabular form from `http://www.physics.adelaide.edu.au/cssm/lattice/formfactors`.

### Ground state nucleon

**Figs. D.1–D.5** $G_E(Q^2)$, contributions of individual quark sectors

**Figs. D.6–D.10** $G_E(Q^2)$, comparison of ground state proton and neutron

**Figs. D.11–D.15** $G_M(Q^2)$, contributions of individual quark sectors

**Figs. D.16–D.20** $G_M(Q^2)$, comparison of ground state proton and neutron

**Figs. D.21–D.25** $\mu_{\text{Eff}}$ of ground state nucleon, contributions of individual quark sectors

### First negative parity excitation

**Figs. D.26–D.30** $G_E(Q^2)$, contributions of individual quark sectors

**Figs. D.31–D.35** $G_E(Q^2)$, comparison of first negative parity excitation of the proton and neutron

**Figs. D.36–D.40** $G_M(Q^2)$, contributions of individual quark sectors

**Figs. D.41–D.45** $G_M(Q^2)$, comparison of first negative parity excitation of the proton and neutron

**Figs. D.46–D.50** $\mu_{\text{Eff}}$ of first negative parity excitation, contributions of individual quark sectors

### Second negative parity excitation

**Figs. D.51–D.55** $G_E(Q^2)$, contributions of individual quark sectors

**Figs. D.56–D.60** $G_E(Q^2)$, comparison of second negative parity excitation of the proton and neutron

**Figs. D.61–D.65** $G_M(Q^2)$, contributions of individual quark sectors

**Figs. D.66–D.70** $G_M(Q^2)$, comparison of second negative parity excitation of proton and neutron

**Figs. D.71–D.75** $\mu_{\text{Eff}}$ of second positive parity excitation, contributions of individual quark sectors

### First positive parity excitation

**Figs. D.76–D.80** $G_E(Q^2)$, contributions of individual quark sectors

**Figs. D.81–D.85** $G_E(Q^2)$,comparison of first positive parity excitation of the proton and neutron

**Figs. D.86–D.90** $G_M(Q^2)$, contributions of individual quark sectors

**Figs. D.91–D.95** $G_M(Q^2)$,comparison of first positive parity excitation of the proton and neutron

**Figs. D.96–D.100** $\mu_{\text{Eff}}$ of first positive parity excitation, contributions of individual quark sectors

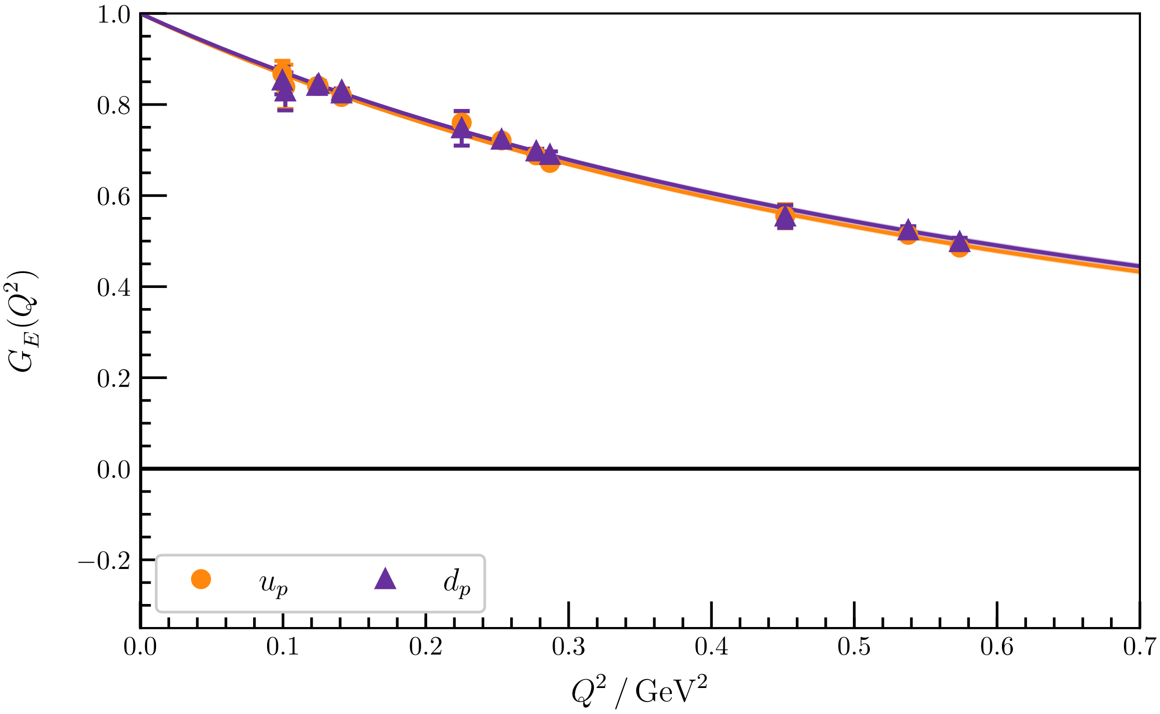

Figure D.1: Contributions from individual quark sectors to the electric form factor of the ground-state nucleon at $m_\pi = 702\,\mathrm{MeV}$. The shaded regions are dipole fits to the form factor, with lines indicating the central values. The y-axis intercept is fixed to one. The errors on these fits are small enough that the shaded bands are barely distinguishable from the central lines.

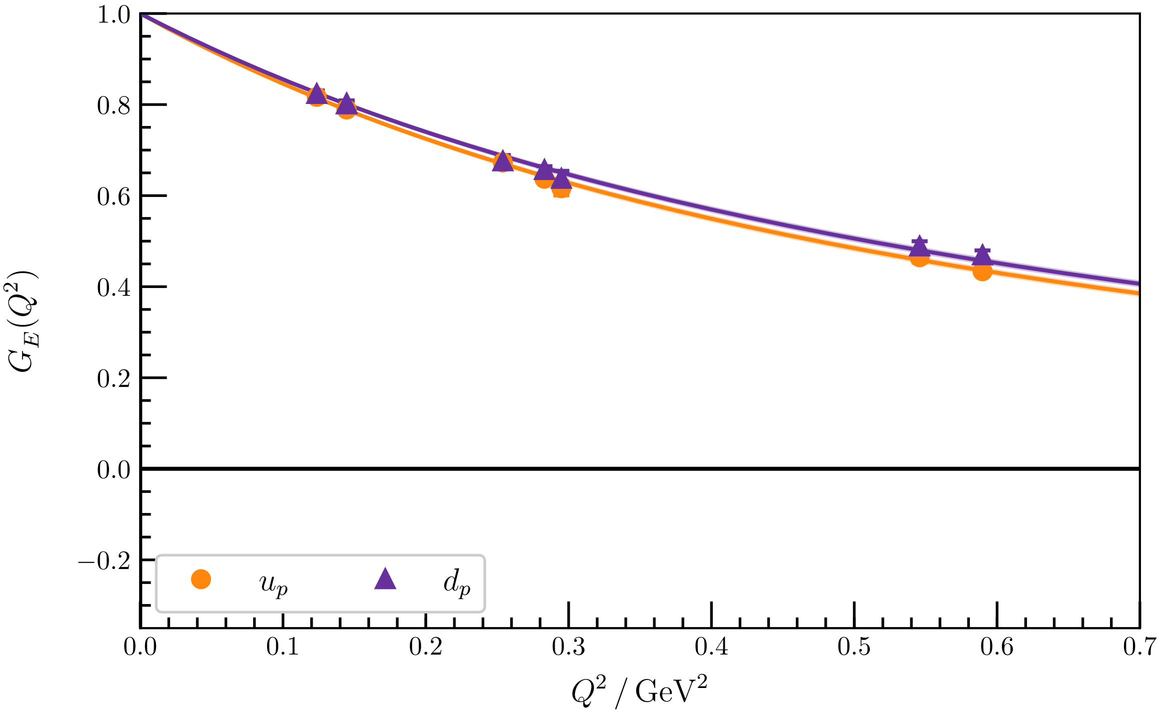

Figure D.2: Contributions from individual quark sectors to the electric form factor of the ground-state nucleon at $m_\pi = 570\,\mathrm{MeV}$. The shaded regions are dipole fits to the form factor, with lines indicating the central values.

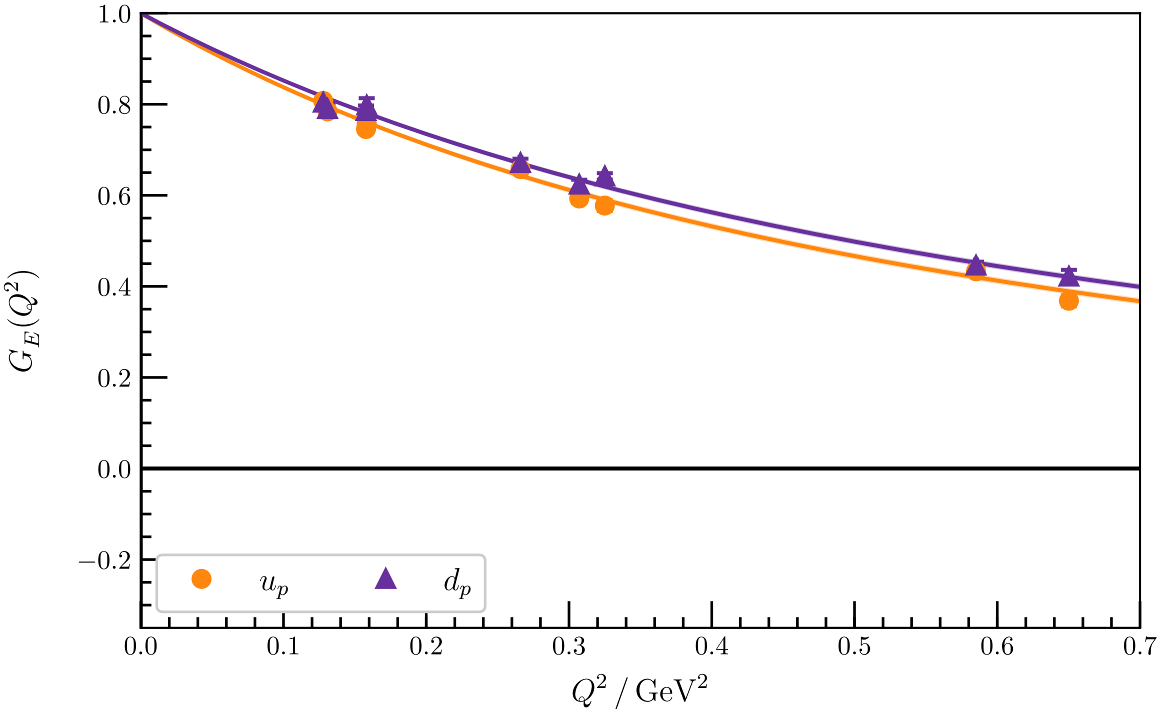

Figure D.3: Contributions from individual quark sectors to the electric form factor of the ground-state nucleon at $m_\pi = 411\,\text{MeV}$. The shaded regions are dipole fits to the form factor, with lines indicating the central values.

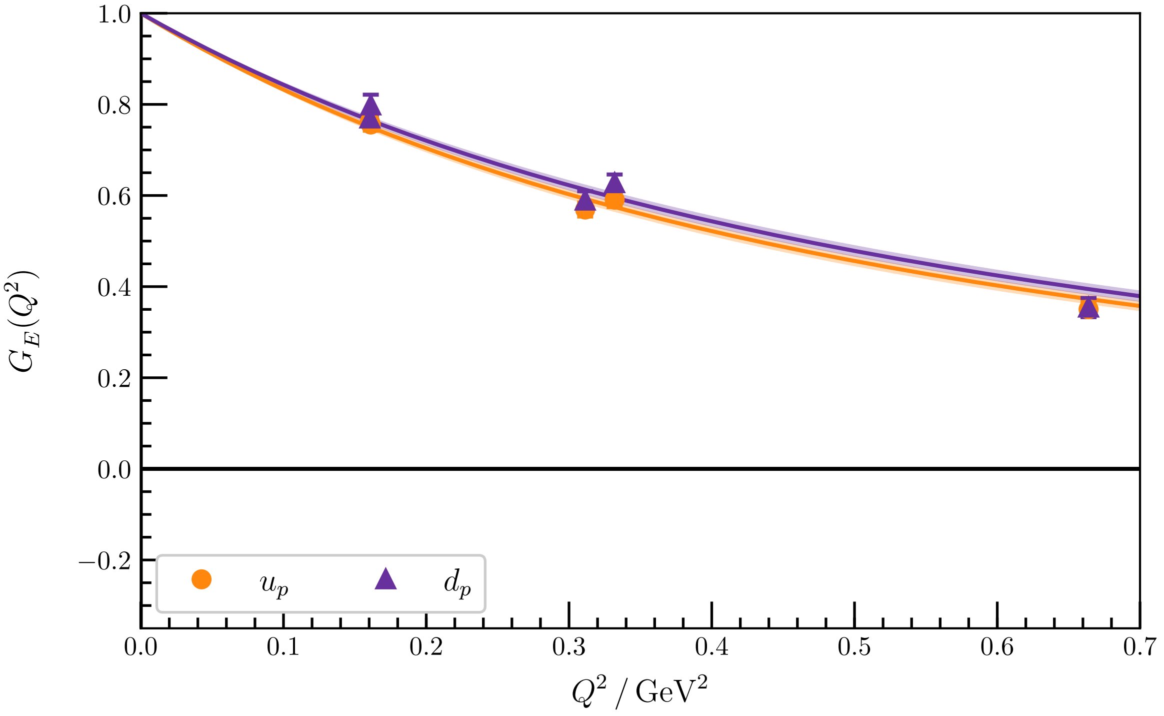

Figure D.4: Contributions from individual quark sectors to the electric form factor of the ground-state nucleon at $m_\pi = 296\,\text{MeV}$. The shaded regions are dipole fits to the form factor, with lines indicating the central values.

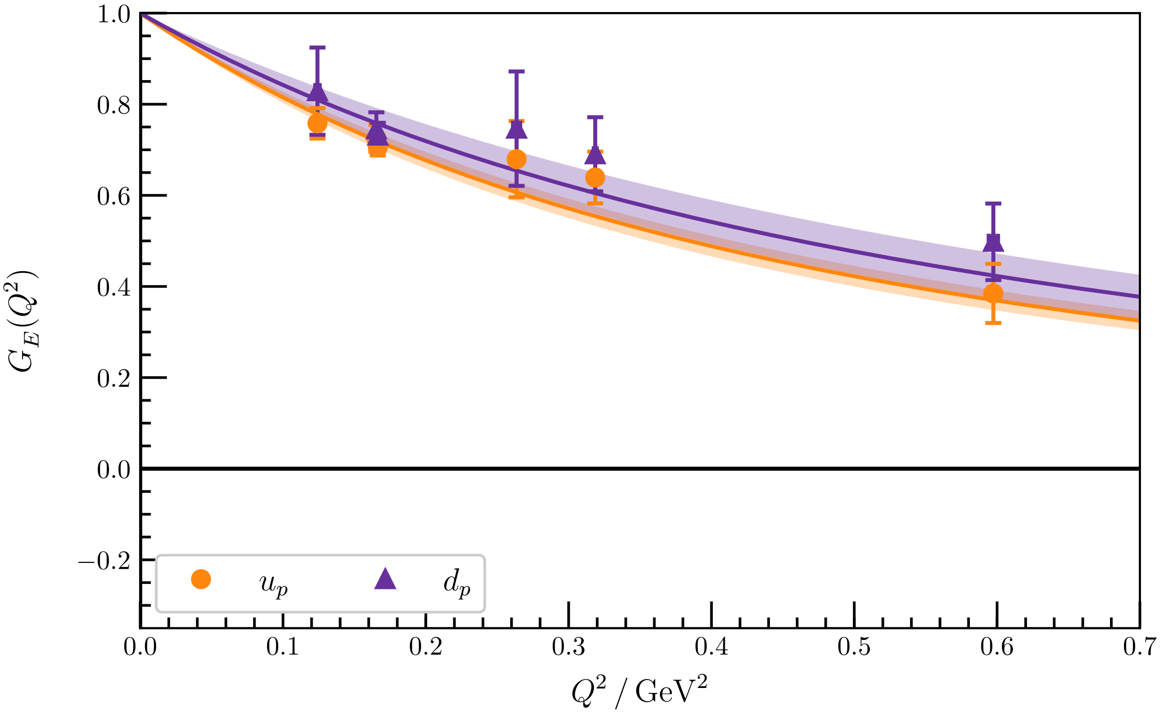

Figure D.5: Contributions from individual quark sectors to the electric form factor of the ground-state nucleon at $m_\pi = 156\,\text{MeV}$. The shaded regions are dipole fits to the form factor, with lines indicating the central values.

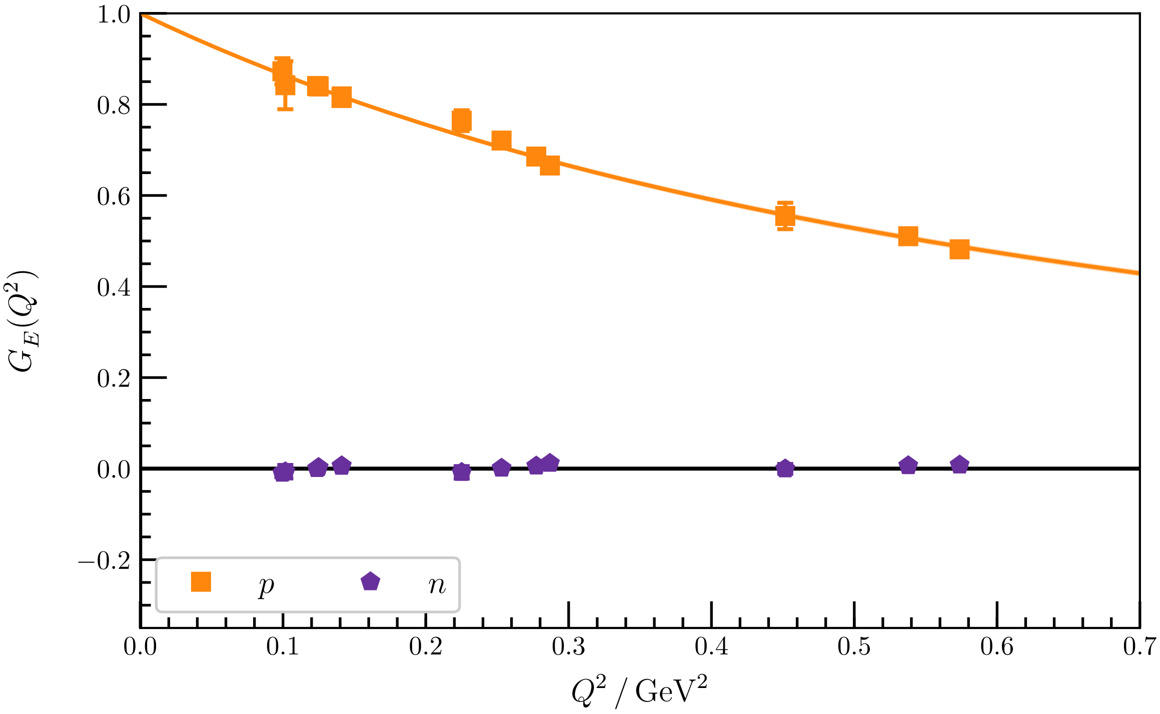

Figure D.6: $G_E(Q^2)$ for the ground-state proton and neutron at $m_\pi = 702\,\text{MeV}$. These are obtained by taking the appropriate linear combination of the individual quark flavour contributions. The shaded region corresponds to a dipole fit to the form factor, with a charge radius of 0.593(7) fm.

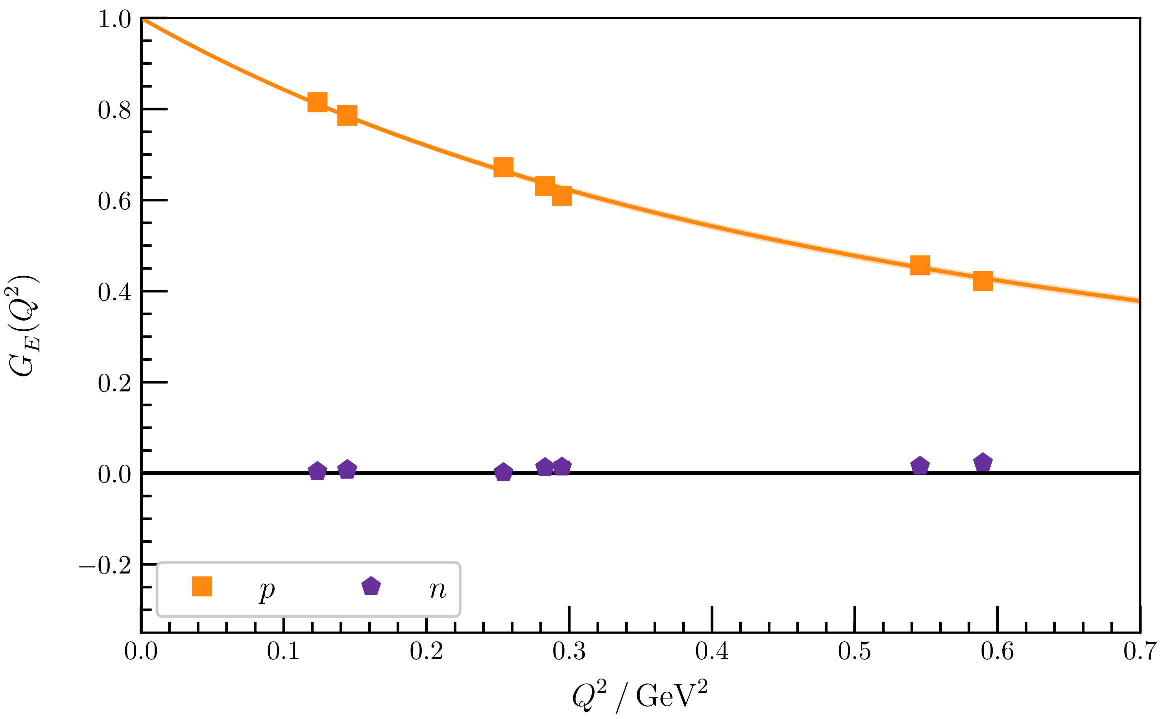

Figure D.7: $G_E(Q^2)$ for the ground-state proton and neutron at $m_\pi = 570\,\mathrm{MeV}$. The shaded region corresponds to a dipole fit to the form factor, with a charge radius of 0.646(9) fm.

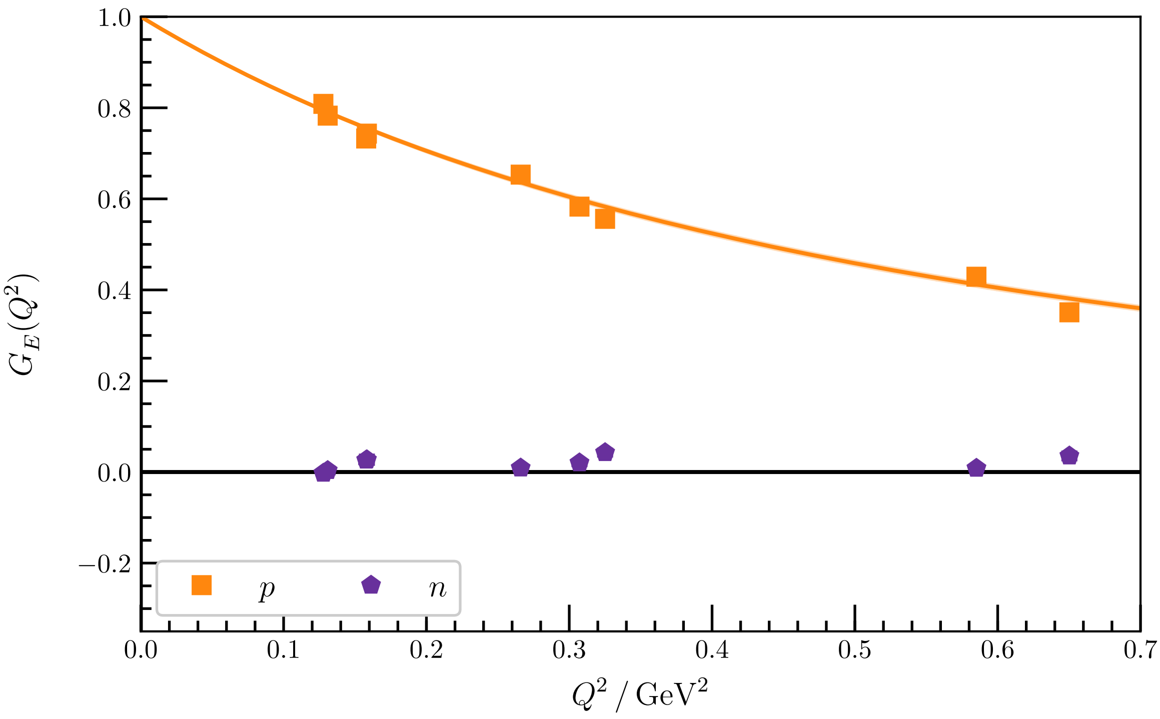

Figure D.8: $G_E(Q^2)$ for the ground-state proton and neutron at $m_\pi = 411\,\mathrm{MeV}$. The shaded region corresponds to a dipole fit to the form factor, with a charge radius of 0.667(9) fm.

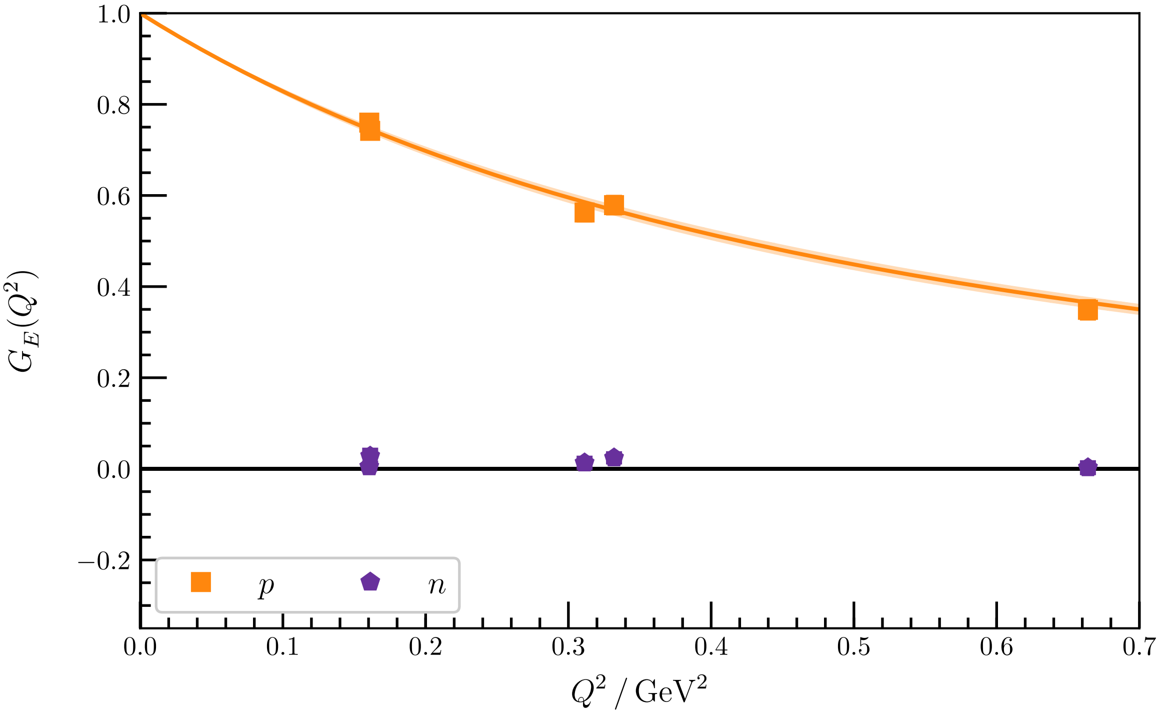

Figure D.9: $G_E(Q^2)$ for the ground-state proton and neutron at $m_\pi = 296\,\mathrm{MeV}$. The shaded region corresponds to a dipole fit to the form factor, with a charge radius of 0.679(14) fm.

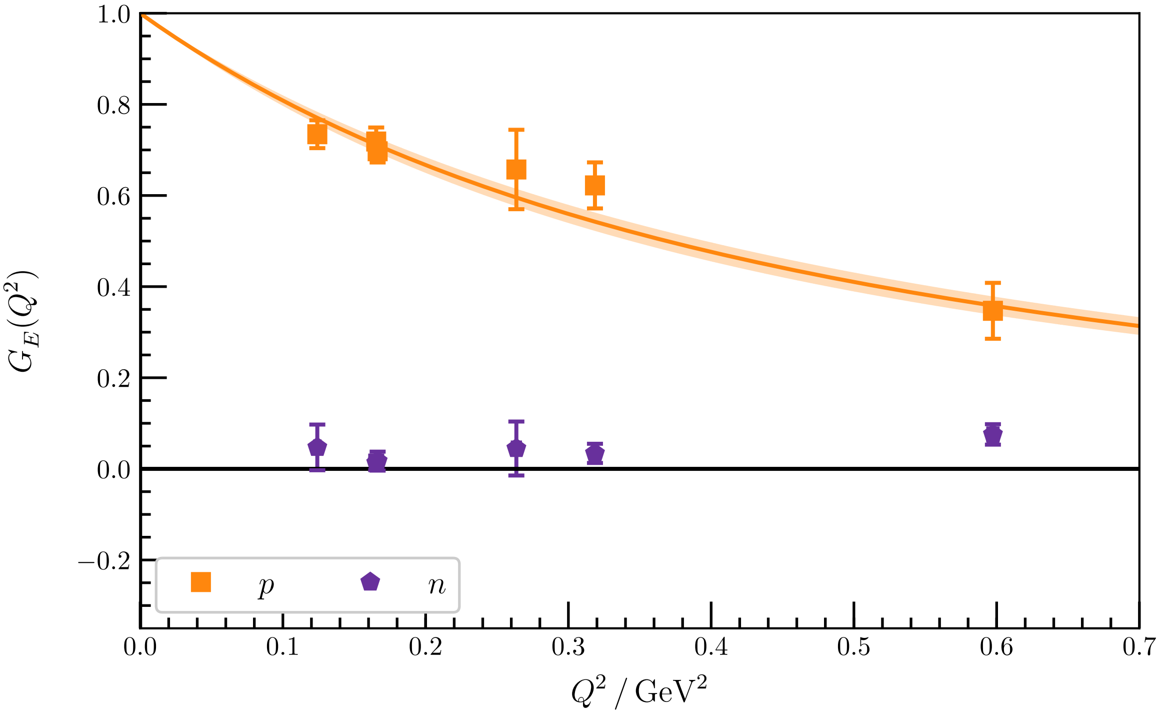

Figure D.10: $G_E(Q^2)$ for the ground-state proton and neutron at $m_\pi = 156\,\mathrm{MeV}$. The shaded region corresponds to a dipole fit to the form factor, with a charge radius of 0.724(26) fm.

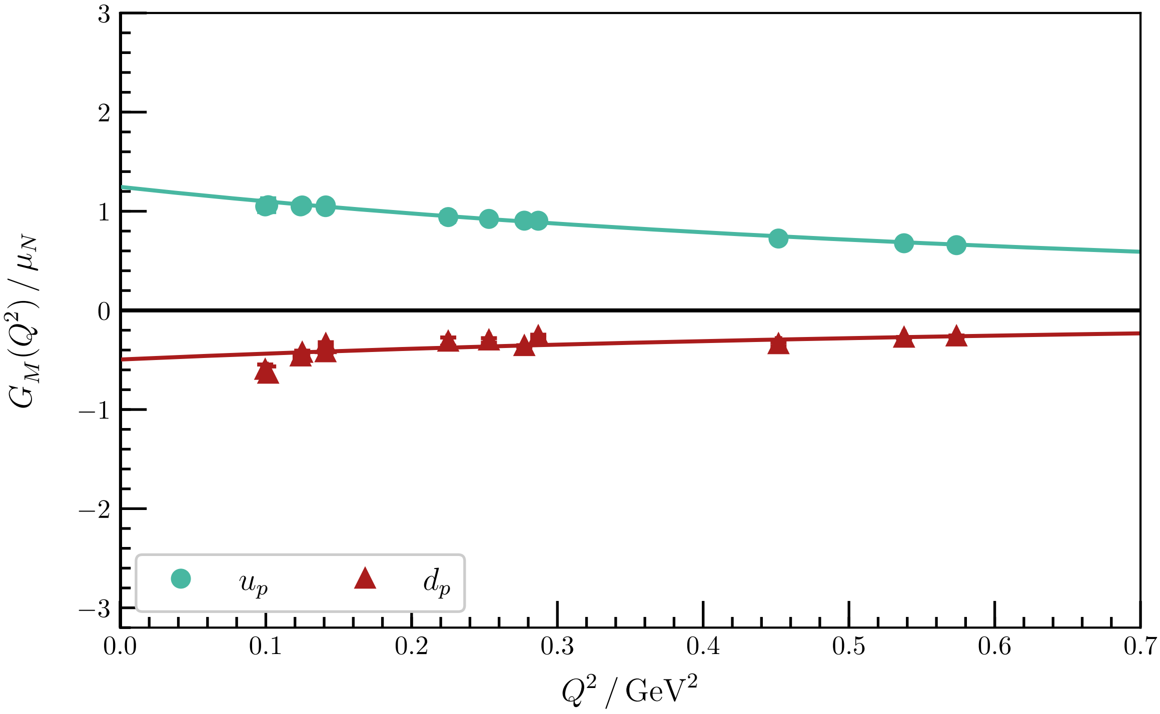

Figure D.11: Quark-flavour contributions to ground state $G_M(Q^2)$ at $m_\pi = 702\,\mathrm{MeV}$. The shaded regions are dipole fits to the form factor.

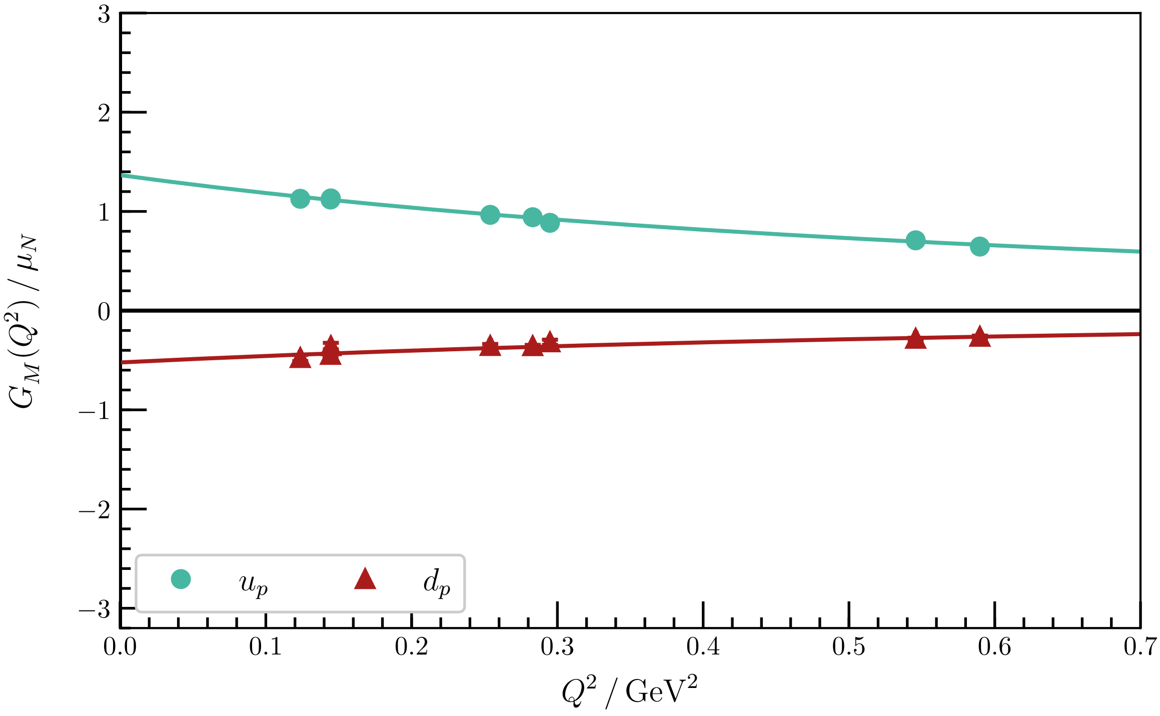

Figure D.12: Quark-flavour contributions to ground state $G_M(Q^2)$ at $m_\pi = 570\,\mathrm{MeV}$. The shaded regions are dipole fits to the form factor.

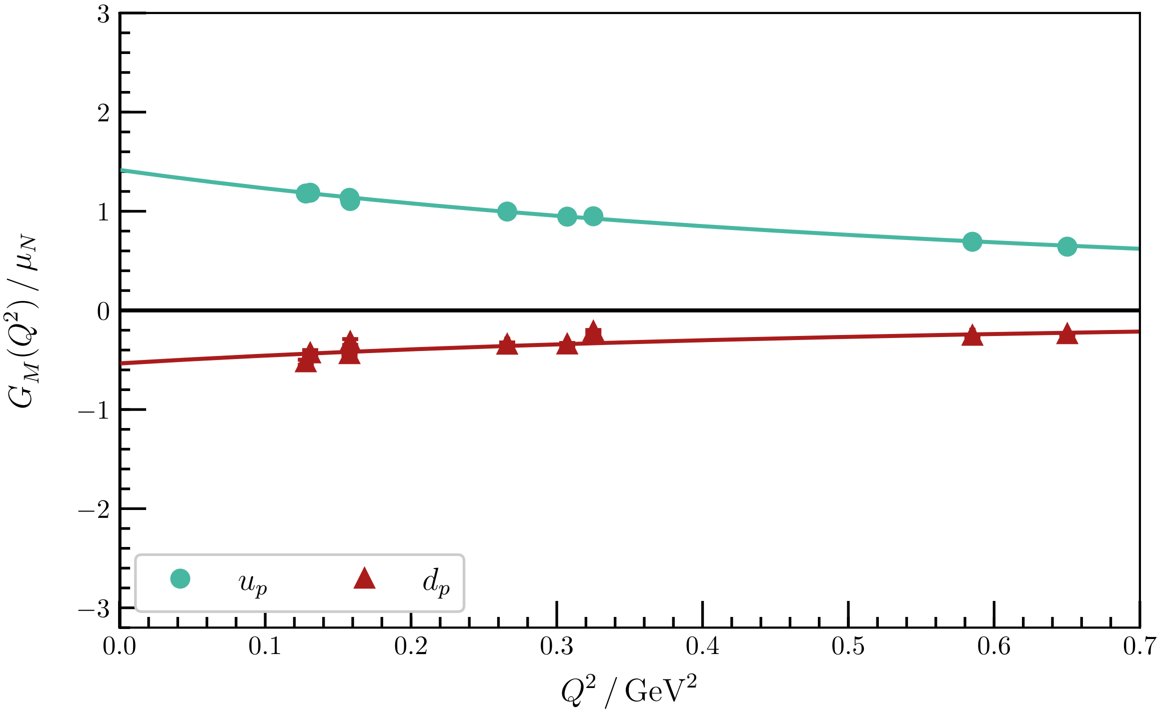

Figure D.13: Quark-flavour contributions to ground state $G_M(Q^2)$ at $m_\pi = 411\,\text{MeV}$. The shaded regions are dipole fits to the form factor.

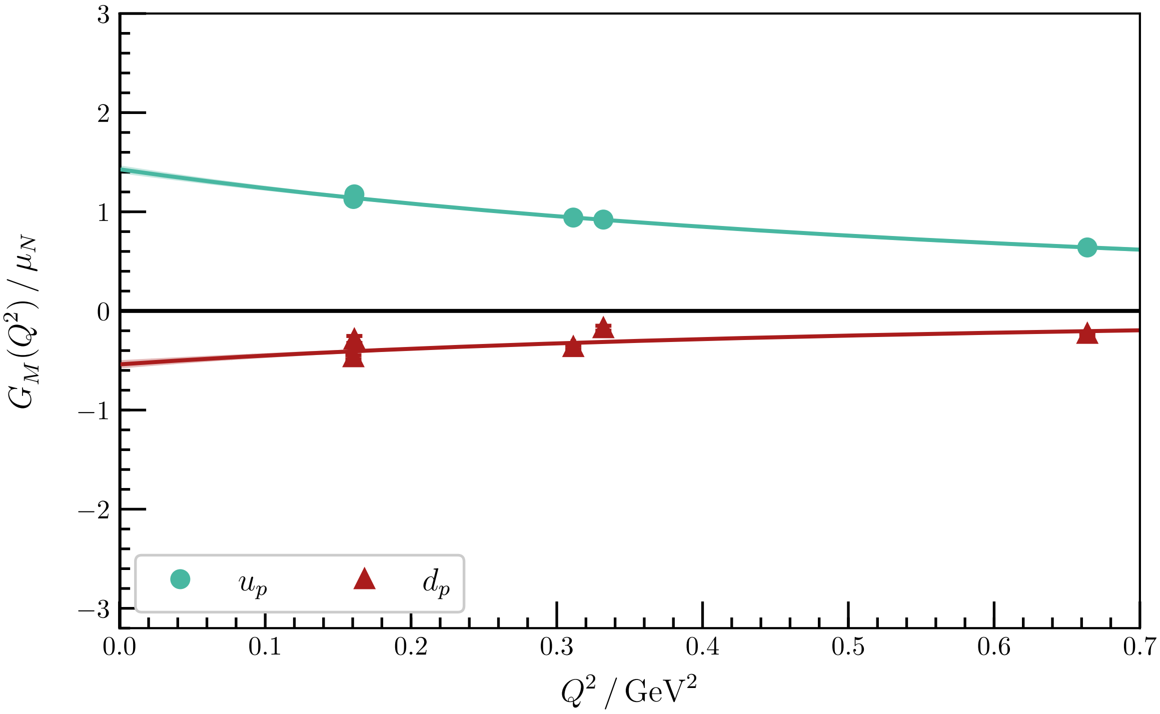

Figure D.14: Quark-flavour contributions to ground state $G_M(Q^2)$ at $m_\pi = 296\,\text{MeV}$. The shaded regions are dipole fits to the form factor.

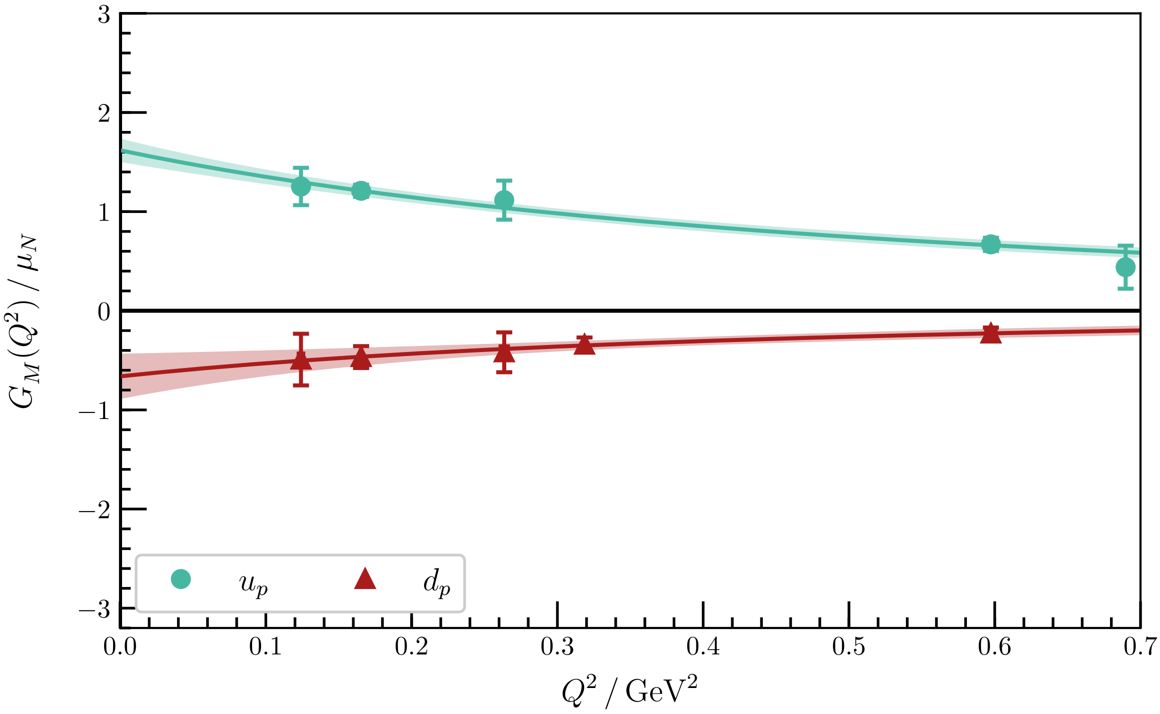

Figure D.15: Quark-flavour contributions to ground state $G_M(Q^2)$ at $m_\pi = 156\,\mathrm{MeV}$. The shaded regions are dipole fits to the form factor.

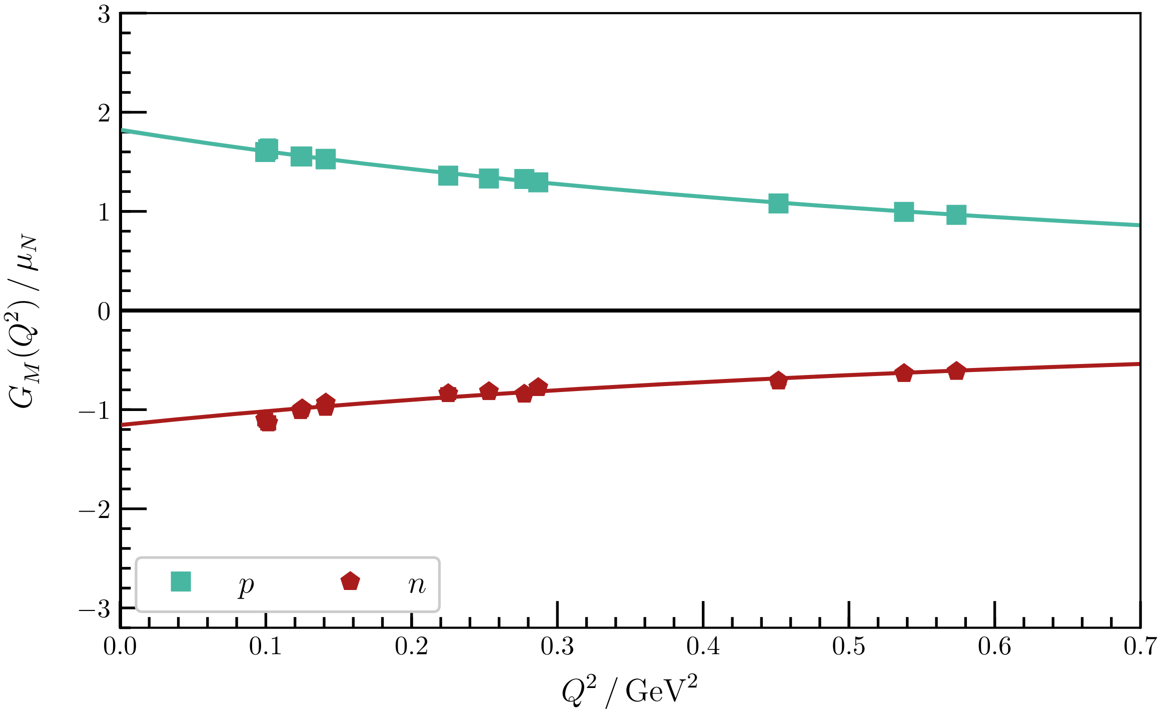

Figure D.16: $G_M(Q^2)$ for the ground-state proton and neutron at $m_\pi = 702\,\mathrm{MeV}$. The shaded region corresponds to a dipole fit to the form factor, with a magnetic charge radius of 0.551(9) fm for the proton and 0.556(9) fm for the neutron.

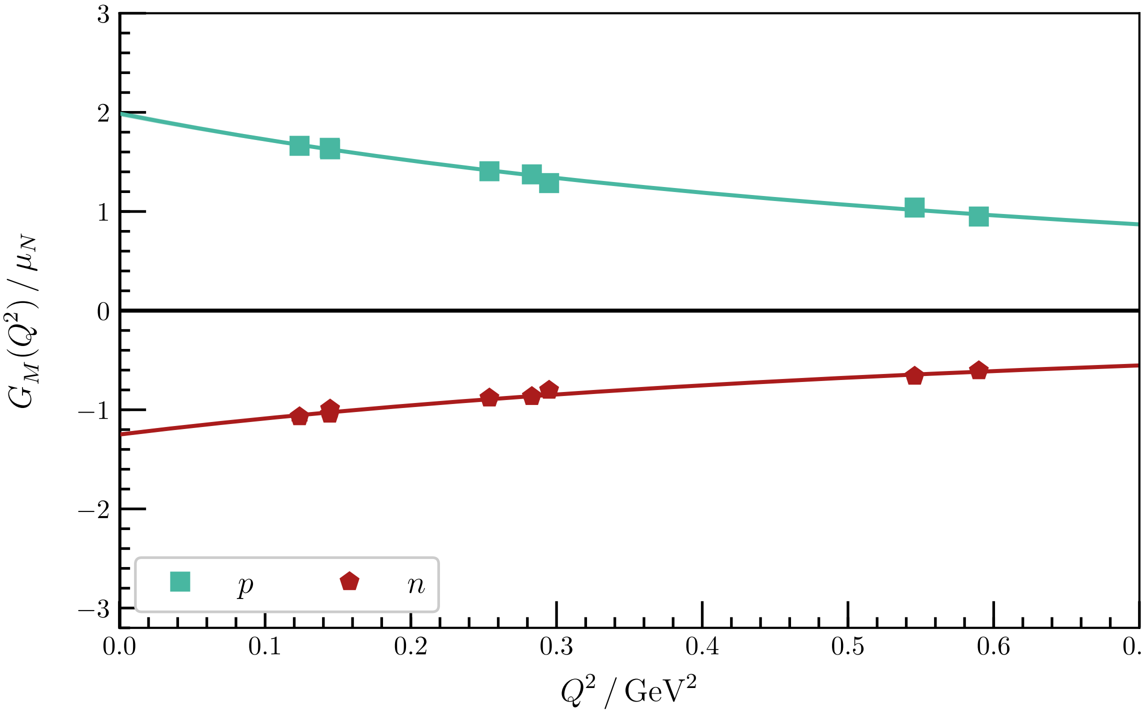

Figure D.17: $G_M(Q^2)$ for the ground-state proton and neutron at $m_\pi = 570\,\mathrm{MeV}$. The shaded region corresponds to a dipole fit to the form factor, with a magnetic charge radius of 0.584(10) fm for the proton and 0.580(10) fm for the neutron.

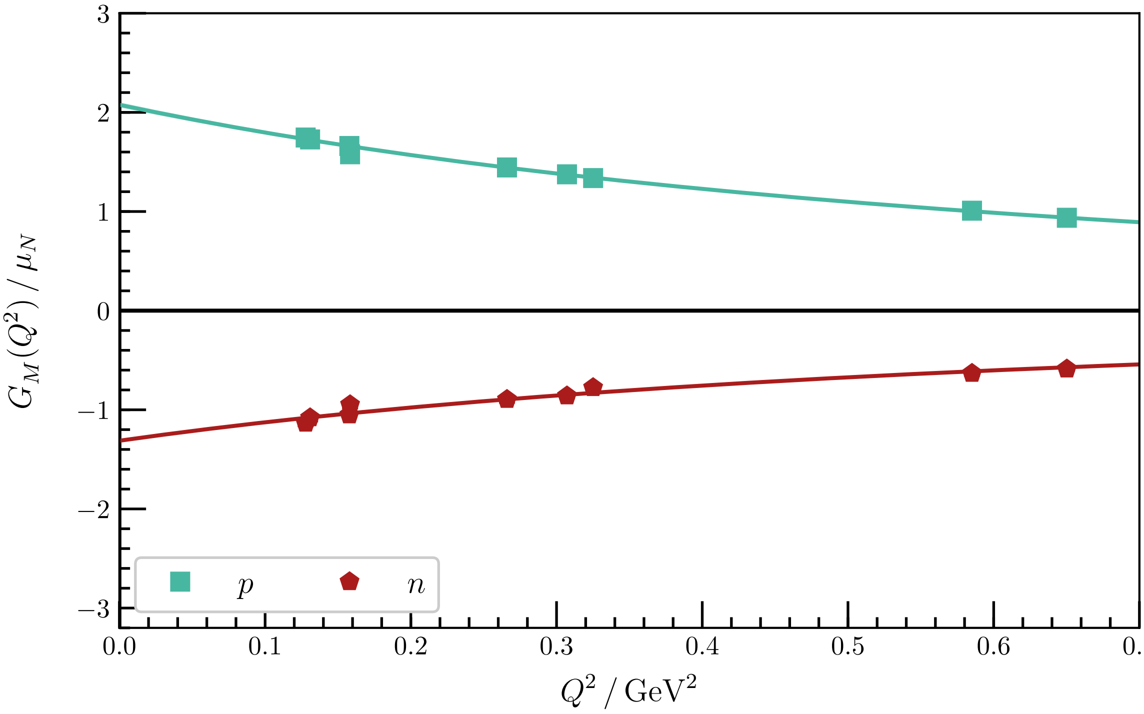

Figure D.18: $G_M(Q^2)$ for the ground-state proton and neutron at $m_\pi = 411\,\mathrm{MeV}$. The shaded region corresponds to a dipole fit to the form factor, with a magnetic charge radius of 0.592(9) fm for the proton and 0.609(9) fm for the neutron.

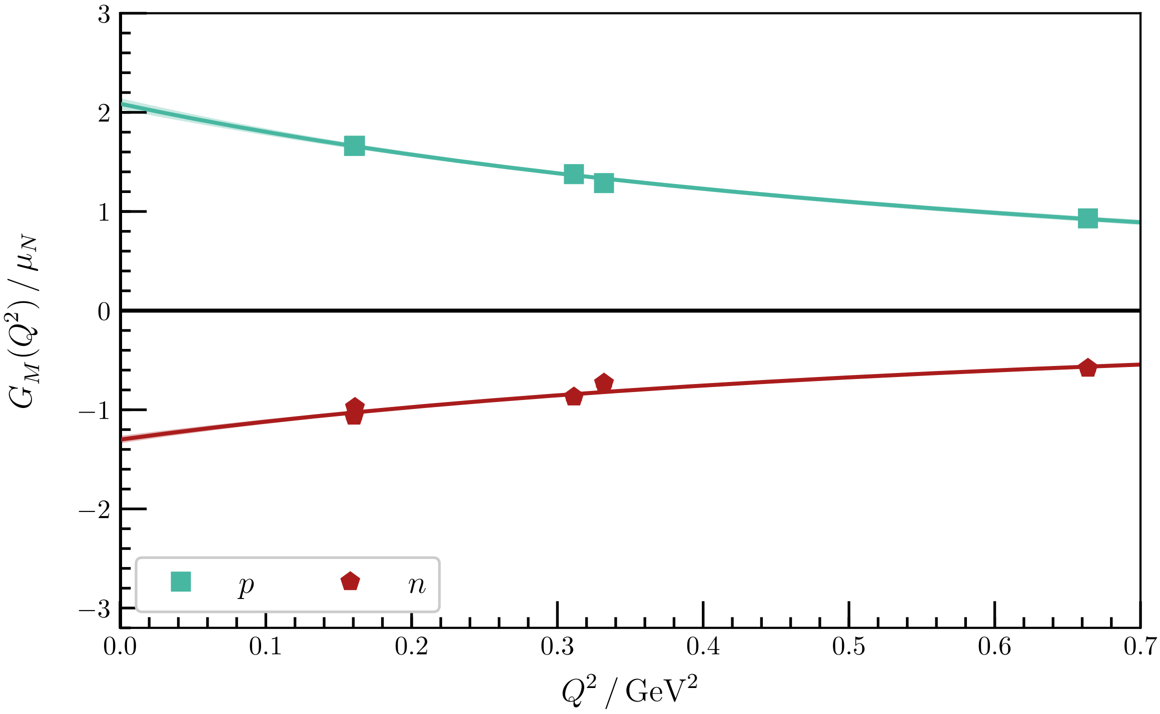

Figure D.19: $G_M(Q^2)$ for the ground-state proton and neutron at $m_\pi = 296\,\mathrm{MeV}$. The shaded region corresponds to a dipole fit to the form factor, with a magnetic charge radius of 0.595(21) fm for the proton and 0.604(21) fm for the neutron.

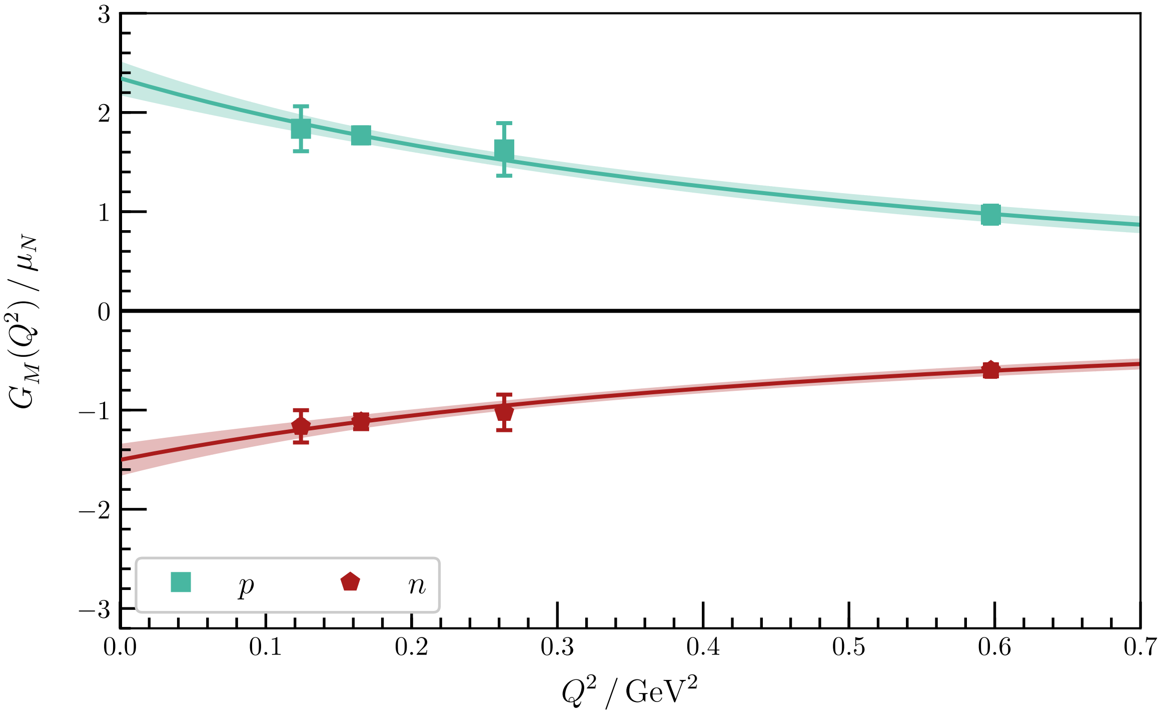

Figure D.20: $G_M(Q^2)$ for the ground-state proton and neutron at $m_\pi = 156\,\mathrm{MeV}$. The shaded region corresponds to a dipole fit to the form factor, with a magnetic charge radius of 0.655(62) fm for the proton and 0.671(77) fm for the neutron.

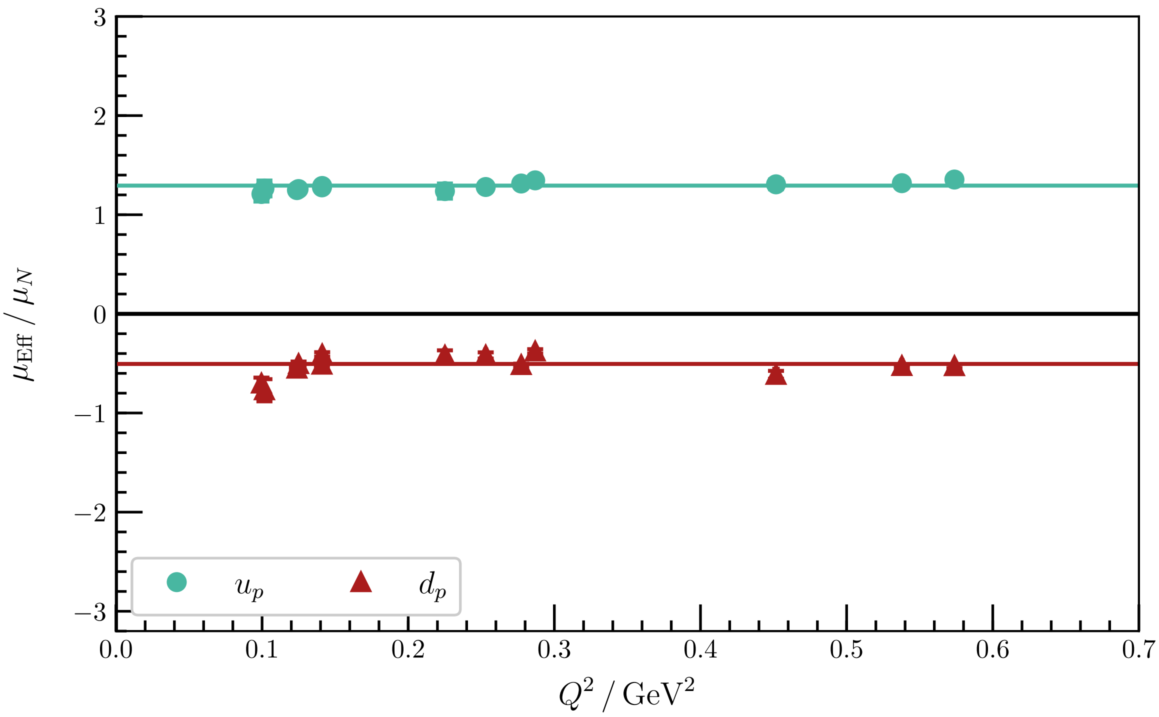

Figure D.21: Quark-flavour contributions to ground state $\mu_{\mathrm{Eff}}$ at $m_\pi = 702\,\mathrm{MeV}$. The narrow shaded bands are constant fits to the effective magnetic moment that correspond to magnetic moment contributions of $1.294(15)\ \mu_N$ for the doubly represented quark and $-0.505(12)\ \mu_N$ for the singly represented quark.

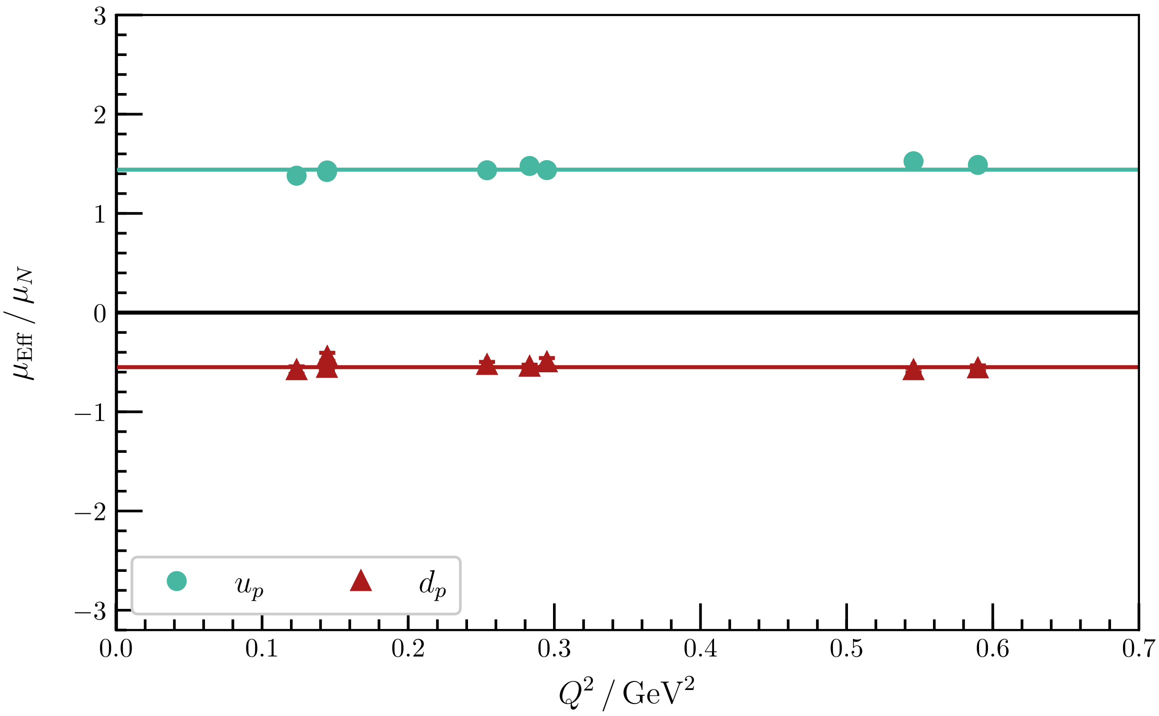

Figure D.22: Quark-flavour contributions to ground state $\mu_{\mathrm{Eff}}$ at $m_\pi = 570\,\mathrm{MeV}$. The narrow shaded bands are constant fits to the effective magnetic moment that correspond to magnetic moment contributions of $1.441(18)\ \mu_N$ for the doubly represented quark and $-0.550(16)\ \mu_N$ for the singly represented quark.

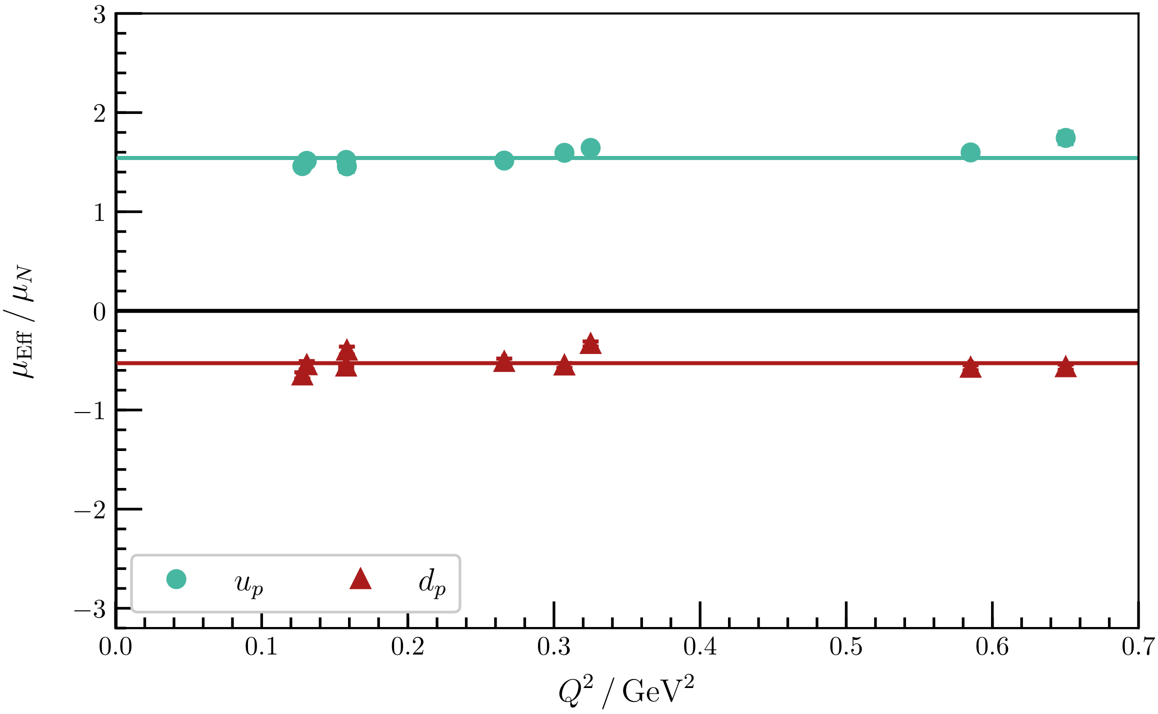

Figure D.23: Quark-flavour contributions to ground state $\mu_{\mathrm{Eff}}$ at $m_\pi = 411\,\mathrm{MeV}$. The narrow shaded bands are constant fits to the effective magnetic moment that correspond to magnetic moment contributions of 1.542(21) $\mu_N$ for the doubly represented quark and −0.528(16) $\mu_N$ for the singly represented quark.

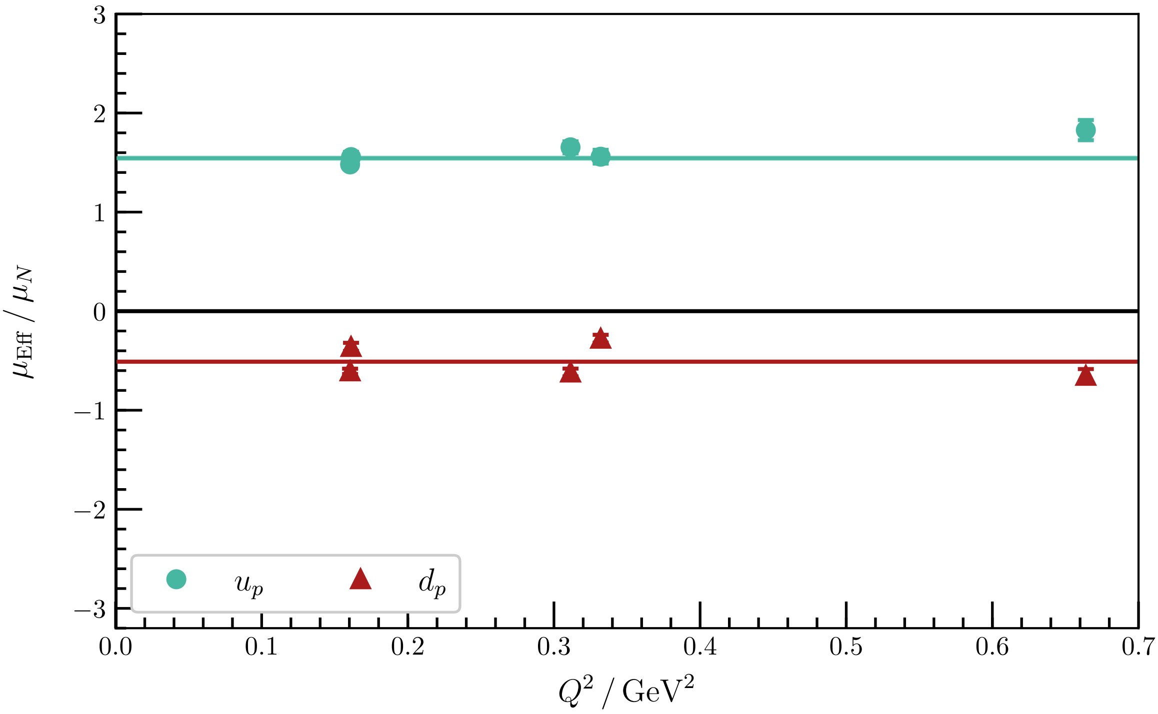

Figure D.24: Quark-flavour contributions to ground state $\mu_{\mathrm{Eff}}$ at $m_\pi = 296\,\mathrm{MeV}$. The narrow shaded bands are constant fits to the effective magnetic moment that correspond to magnetic moment contributions of 1.544(28) $\mu_N$ for the doubly represented quark and −0.510(22) $\mu_N$ for the singly represented quark.

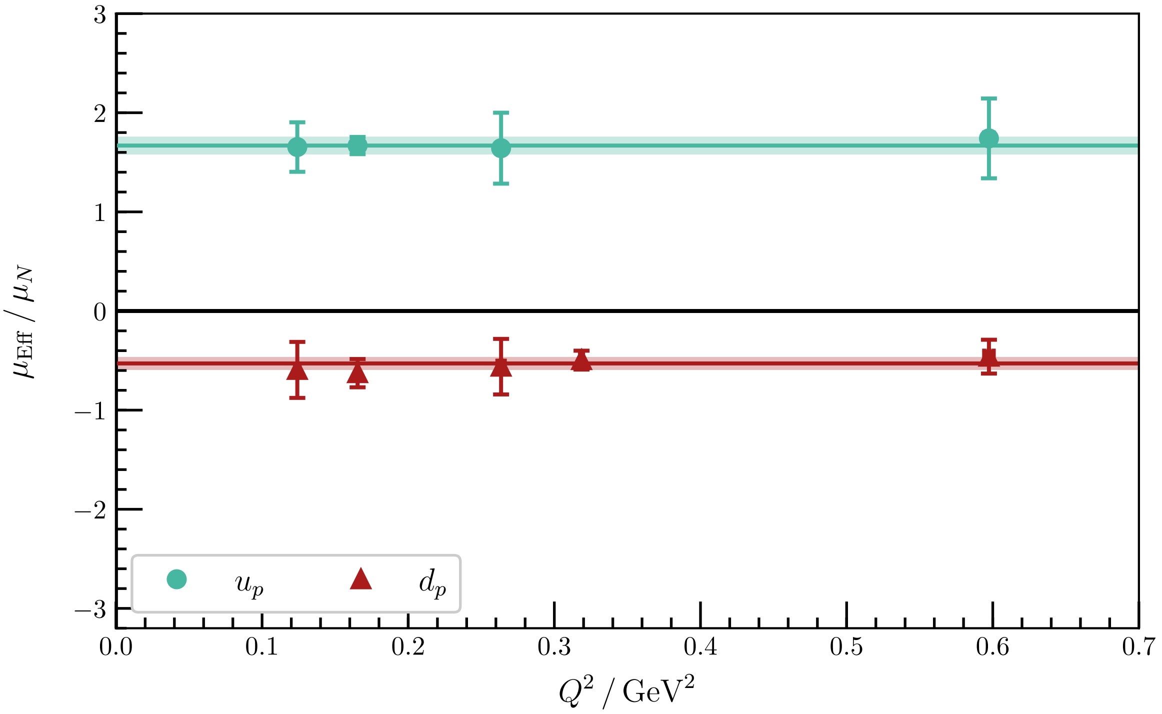

Figure D.25: Quark-flavour contributions to ground state $\mu_{\mathrm{Eff}}$ at $m_\pi = 156\,\mathrm{MeV}$. The shaded bands are constant fits to the effective magnetic moment that correspond to magnetic moment contributions of 1.669(90) $\mu_N$ for the doubly represented quark and −0.529(66) $\mu_N$ for the singly represented quark.

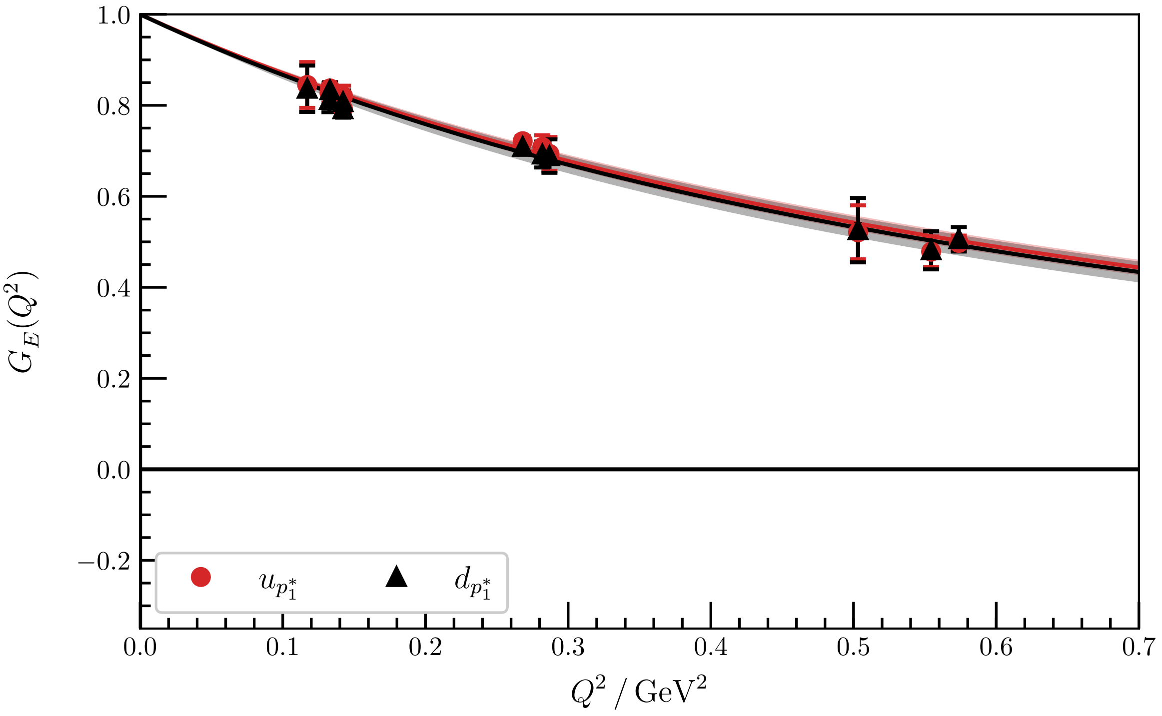

Figure D.26: Contributions to the electric form factor from both quark flavours for the first negative parity excitation at $m_\pi = 702\,\mathrm{MeV}$. The shaded regions are dipole fits to the form factors, with the y-intercept fixed to unity.

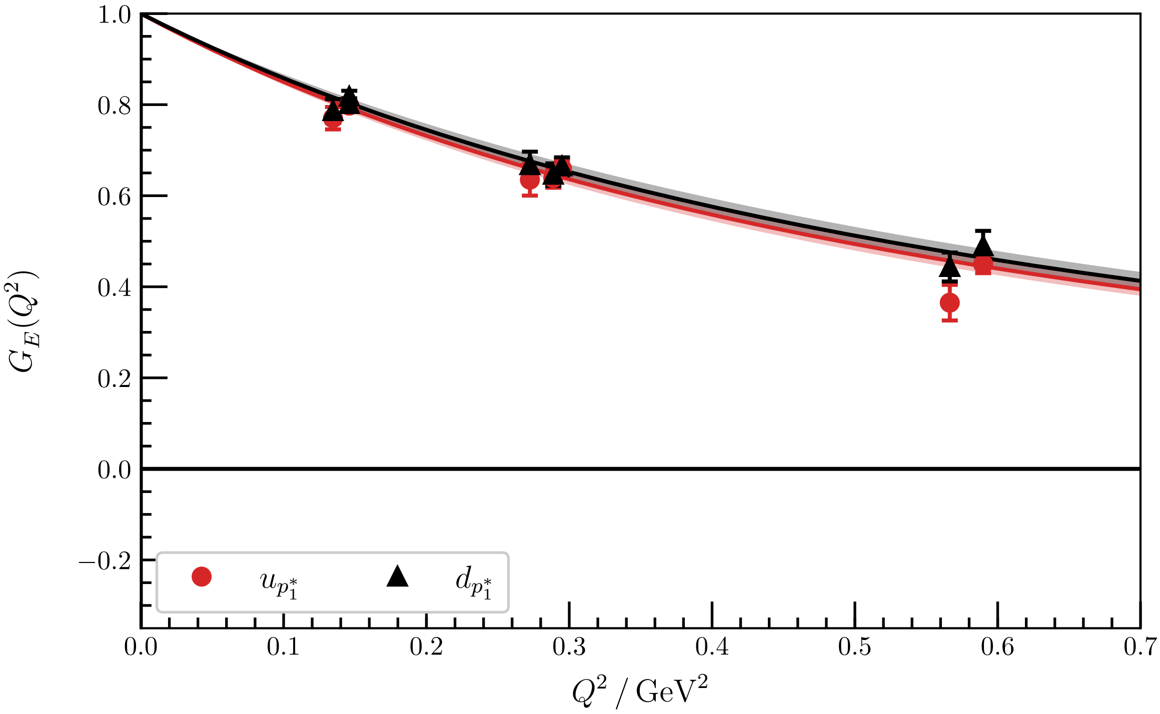

Figure D.27: Contributions to the electric form factor from both quark flavours for the first negative parity excitation at $m_\pi = 570\,\text{MeV}$. The shaded regions are dipole fits to the form factors, with the y-intercept fixed to unity.

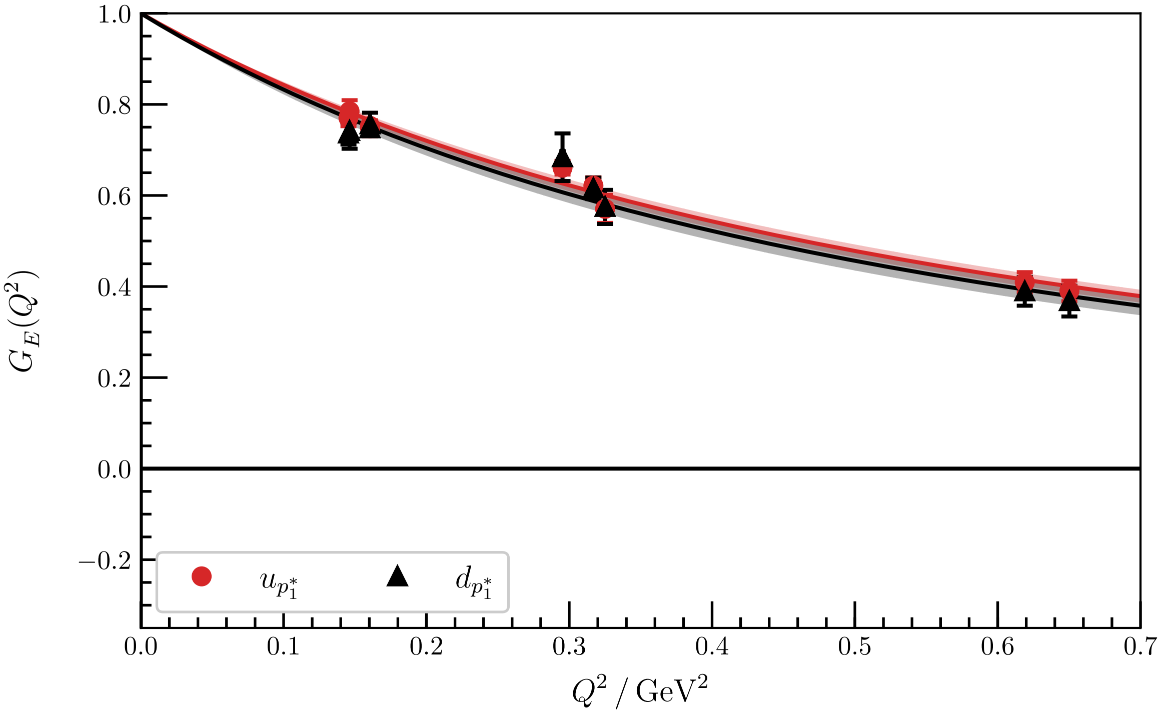

Figure D.28: Contributions to the electric form factor from both quark flavours for the first negative parity excitation at $m_\pi = 411\,\text{MeV}$. The shaded regions are dipole fits to the form factors, with the y-intercept fixed to unity. The solid lines indicate the central values of the fits.

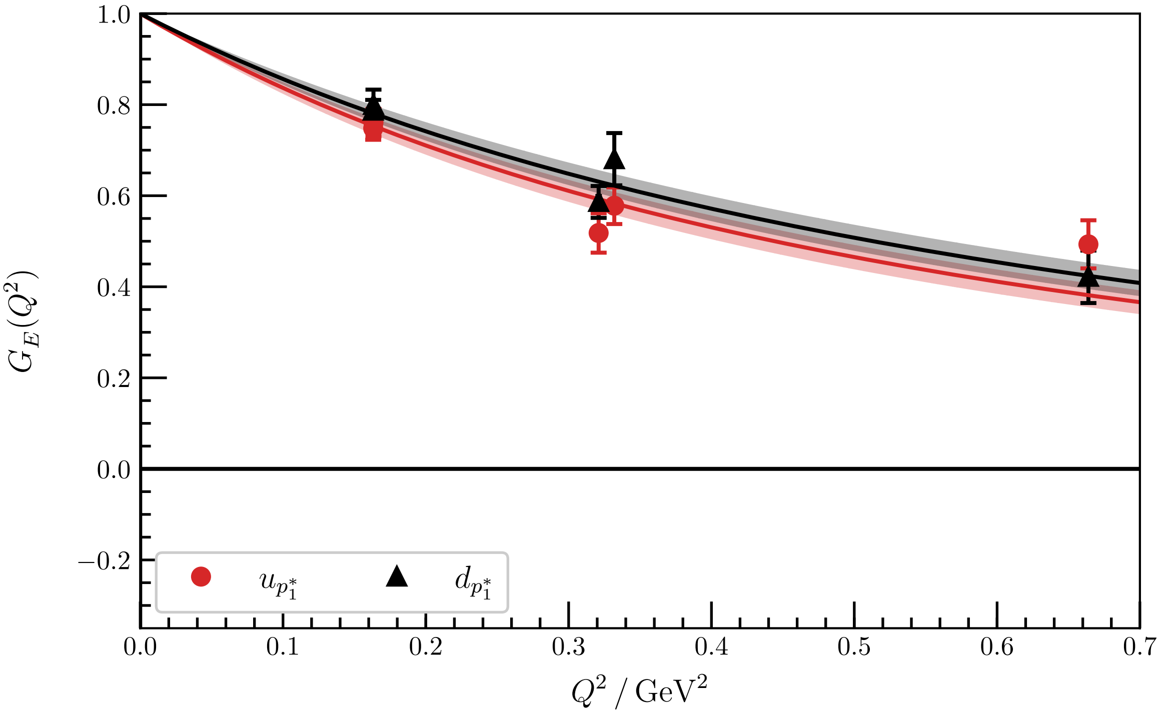

Figure D.29: Contributions to the electric form factor from both quark flavours for the first negative parity excitation at $m_\pi = 296\,\text{MeV}$. The shaded regions are dipole fits to the form factors, with the y-intercept fixed to unity. The solid lines indicate the central values of the fits.

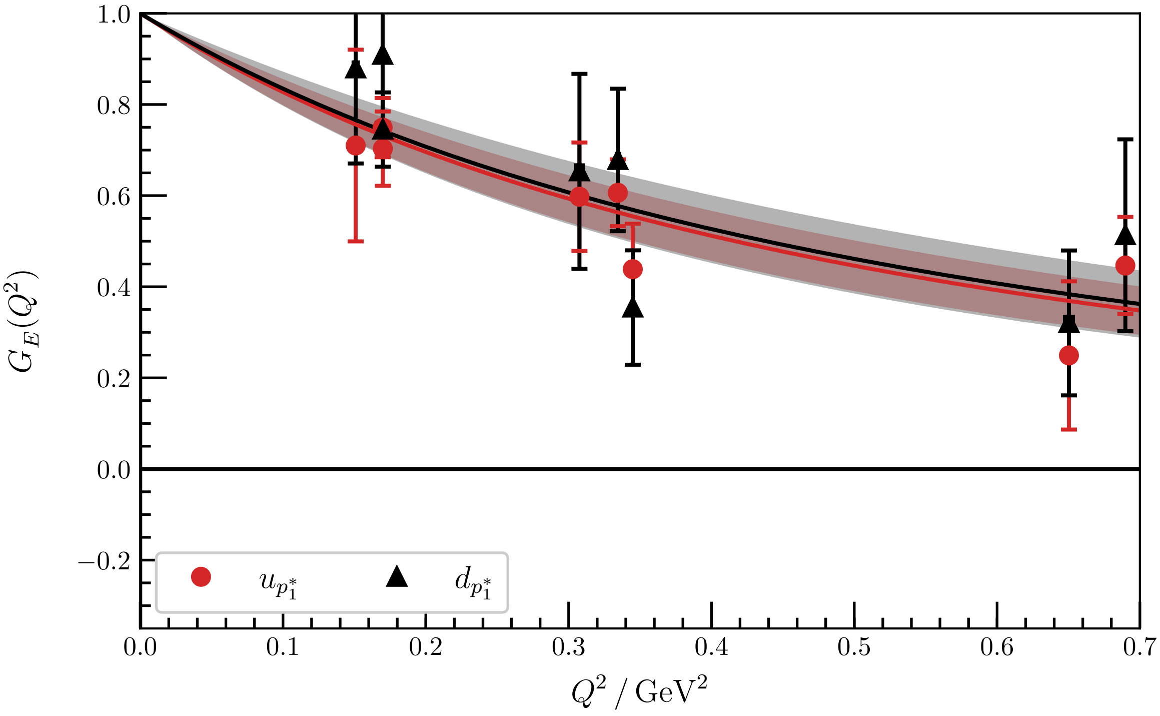

Figure D.30: Contributions to the electric form factor from both quark flavours for the first negative parity excitation at $m_\pi = 156\,\text{MeV}$. The shaded regions are dipole fits to the form factors, with the y-intercept fixed to unity.

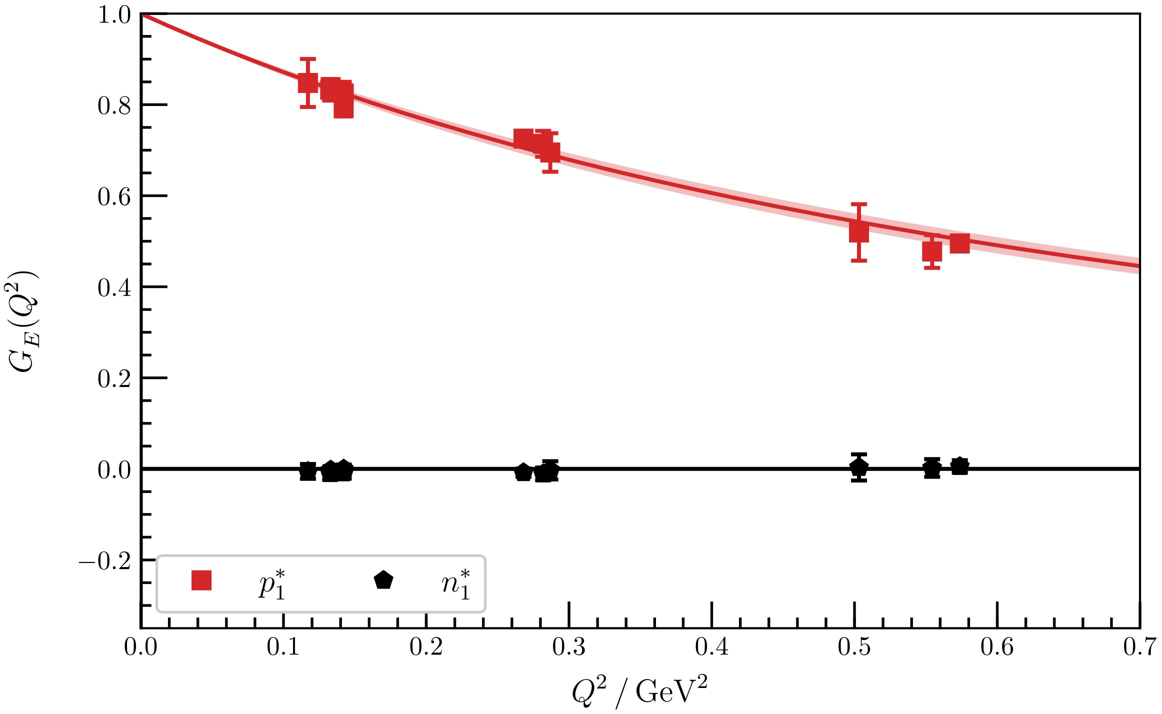

Figure D.31: $G_E(Q^2)$ for the first negative-parity excitations of the proton and neutron at $m_\pi = 702\,\text{MeV}$. The shaded region corresponds to a dipole fit to the electric form factor for the proton excitation, with the y-intercept fixed to unity. This fit corresponds to a charge radius of 0.577(18) fm.

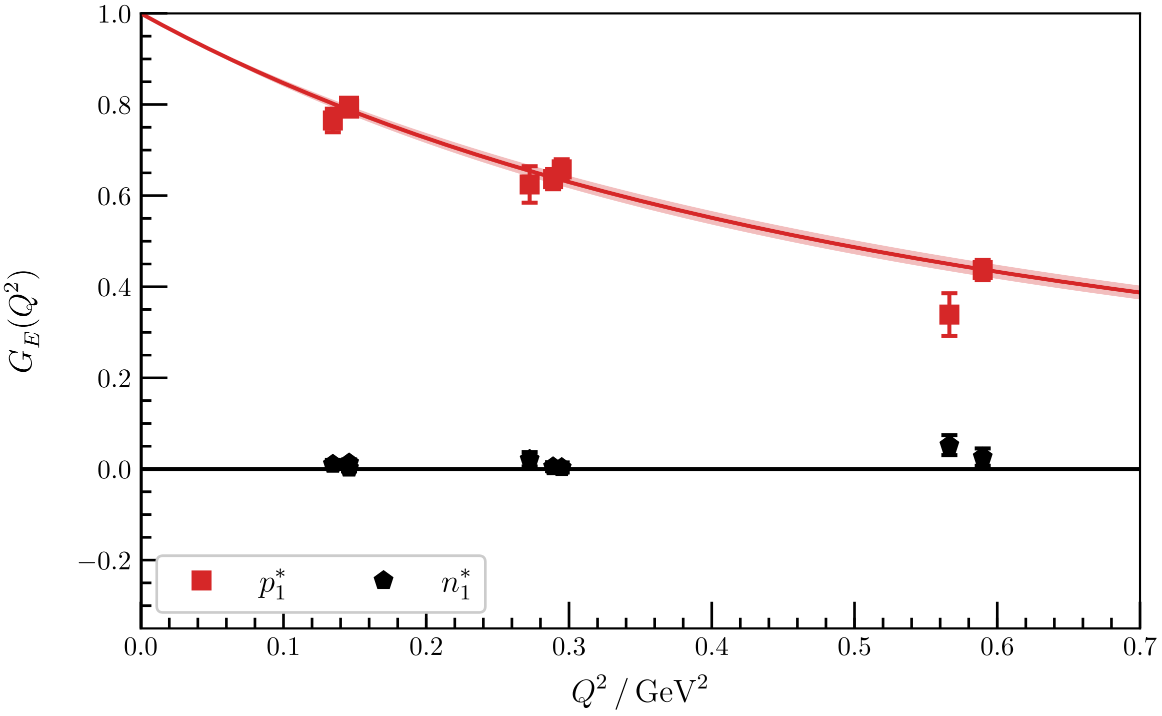

Figure D.32: $G_E(Q^2)$ for the first negative-parity excitations of the proton and neutron at $m_\pi = 570\,\text{MeV}$. The shaded region corresponds to a dipole fit to the form factor for the proton excitation, with a charge radius of 0.636(17) fm.

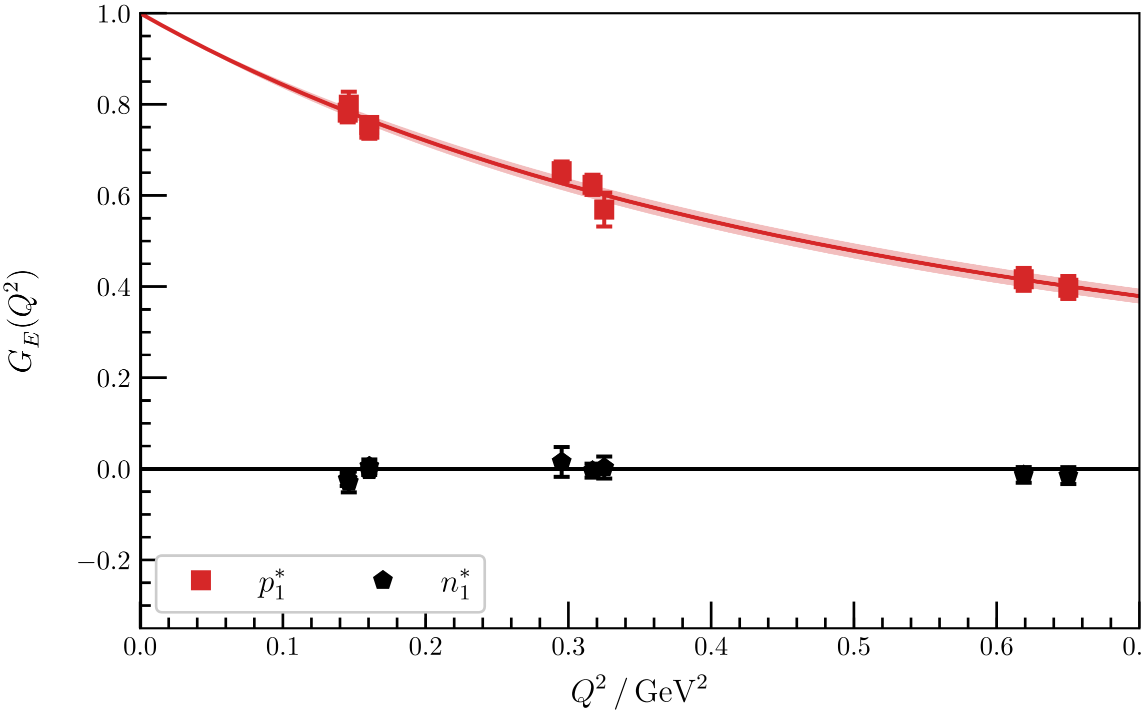

Figure D.33: $G_E(Q^2)$ for the first negative-parity excitations of the proton and neutron at $m_\pi = 411$ MeV. The shaded region corresponds to a dipole fit to the form factor for the proton excitation, with a charge radius of 0.645(18) fm.

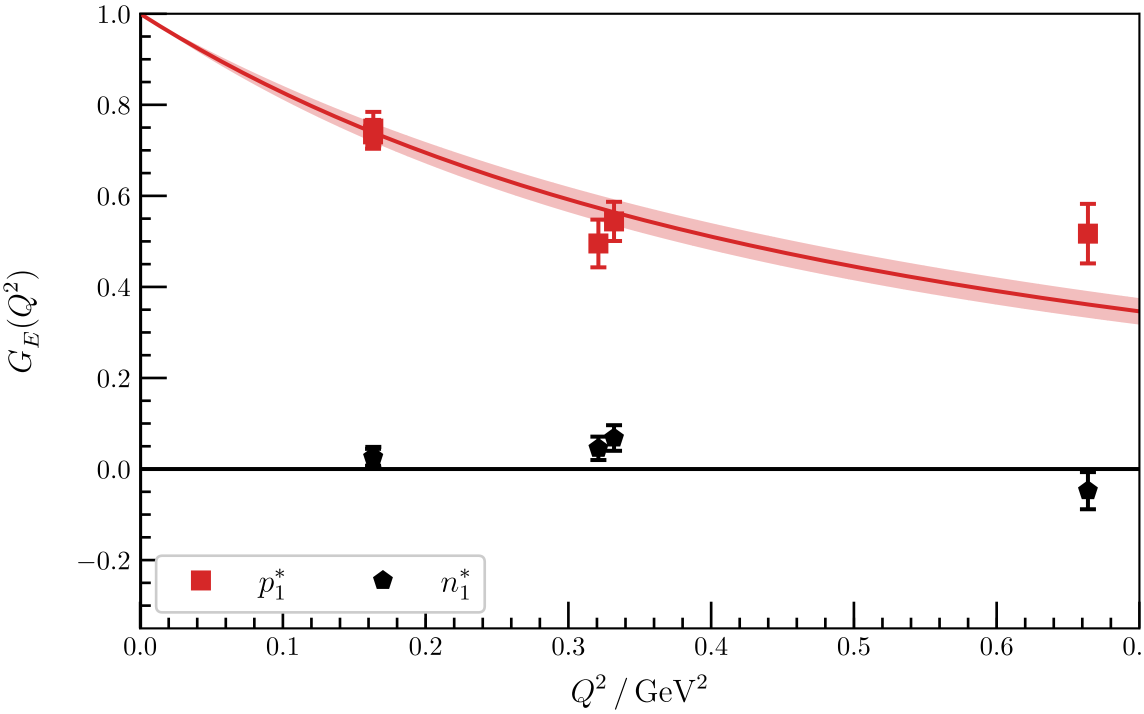

Figure D.34: $G_E(Q^2)$ for the first negative-parity excitations of the proton and neutron at $m_\pi = 296$ MeV. The shaded region corresponds to a dipole fit to the form factor for the proton excitation, with a charge radius of 0.683(35) fm.

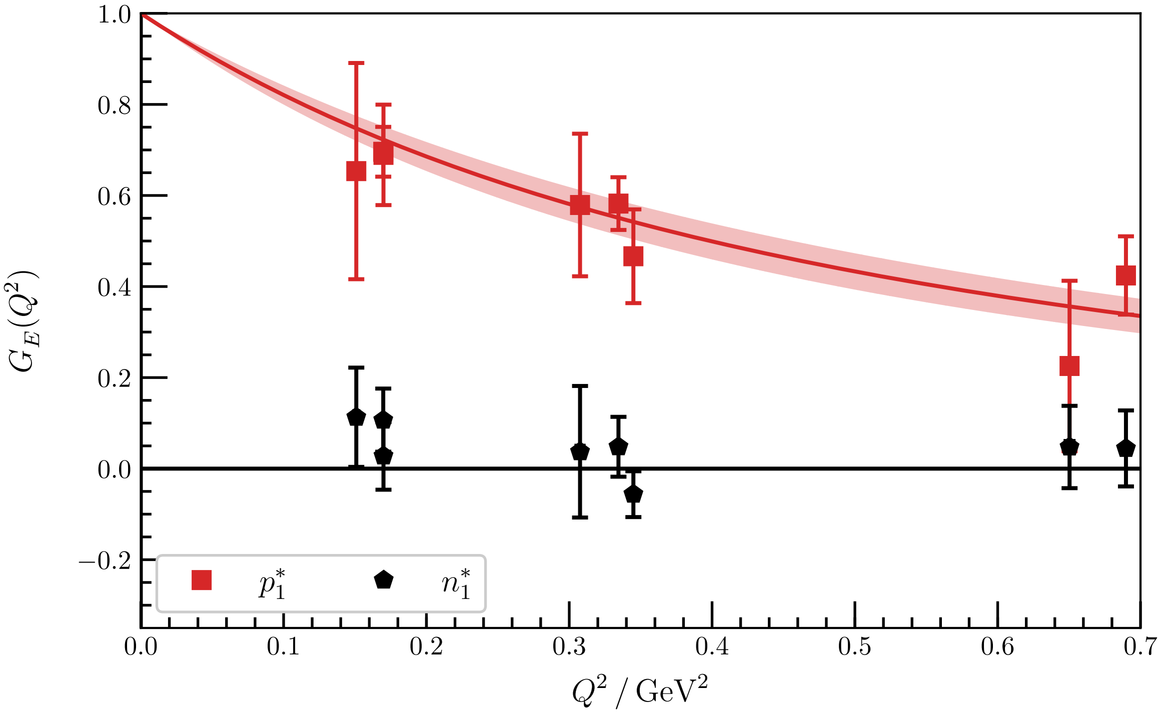

Figure D.35: $G_E(Q^2)$ for the first negative-parity excitations of the proton and neutron at $m_\pi = 156$ MeV. The shaded region corresponds to a dipole fit to the form factor for the proton excitation, with a charge radius of 0.697(47) fm.

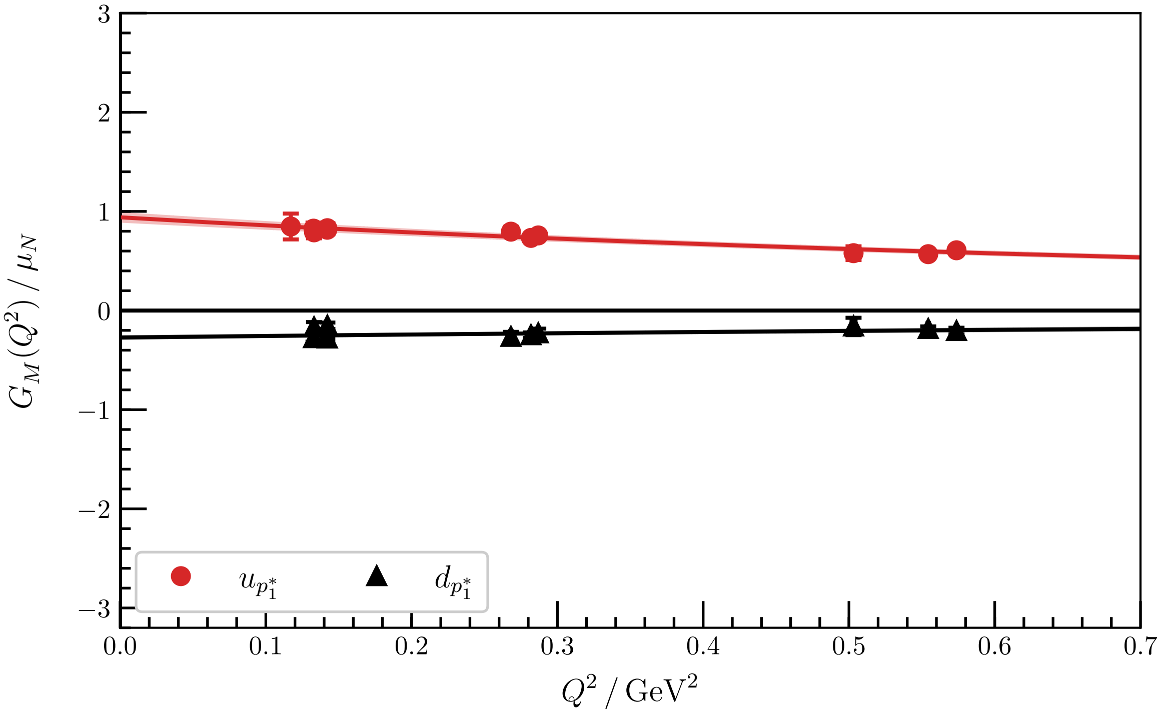

Figure D.36: Quark-flavour contributions to $G_M(Q^2)$ for the first negative-parity excitation at $m_\pi = 702$ MeV. The shaded regions are dipole fits to the form factor.

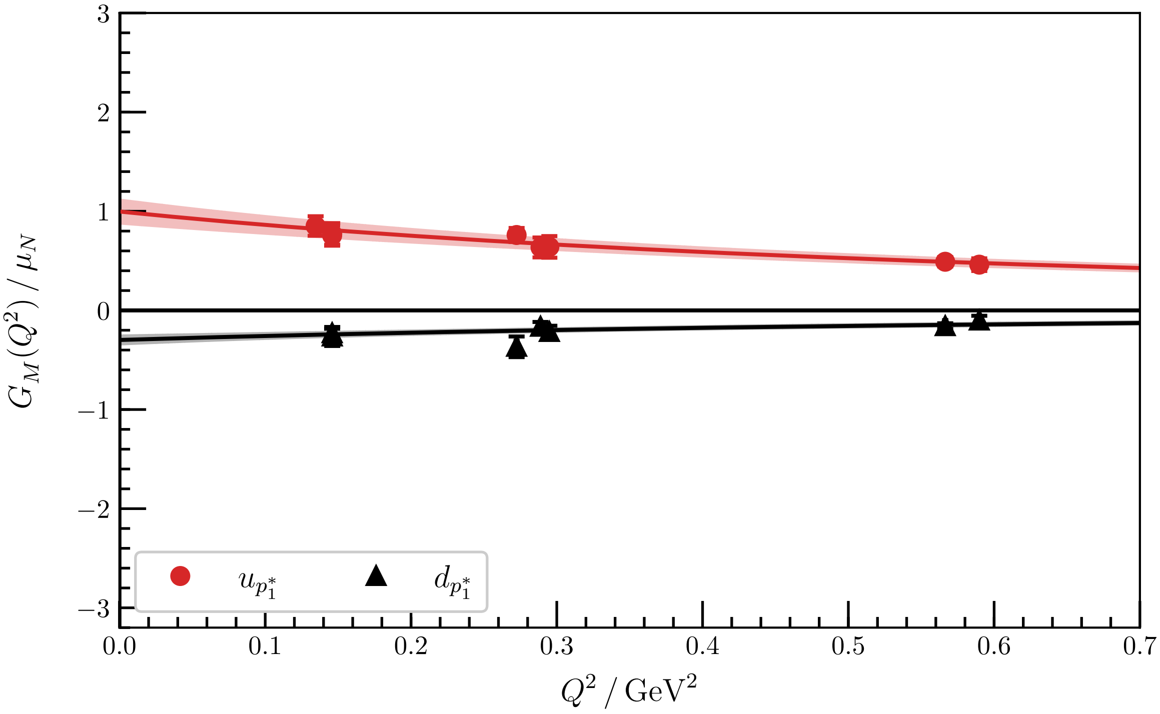

Figure D.37: Quark-flavour contributions to $G_M(Q^2)$ for the first negative-parity excitation at $m_\pi = 570\,\mathrm{MeV}$. The shaded regions are dipole fits to the form factor.

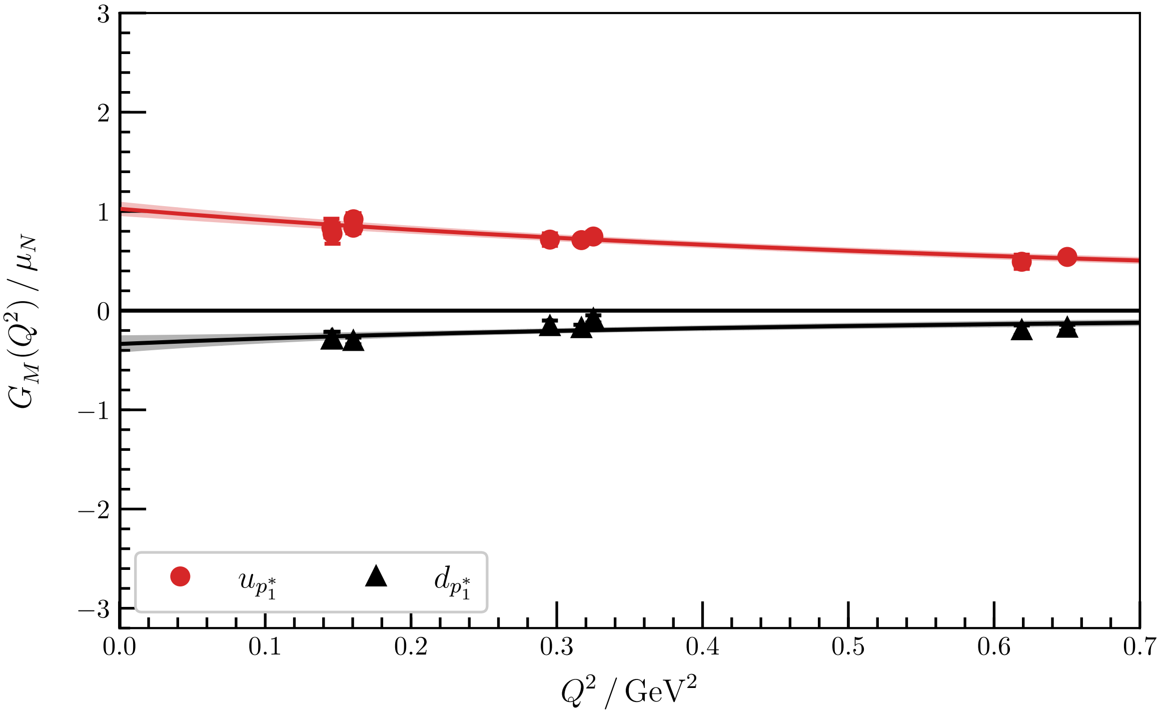

Figure D.38: Quark-flavour contributions to $G_M(Q^2)$ for the first negative-parity excitation at $m_\pi = 411\,\mathrm{MeV}$. The shaded regions are dipole fits to the form factor.

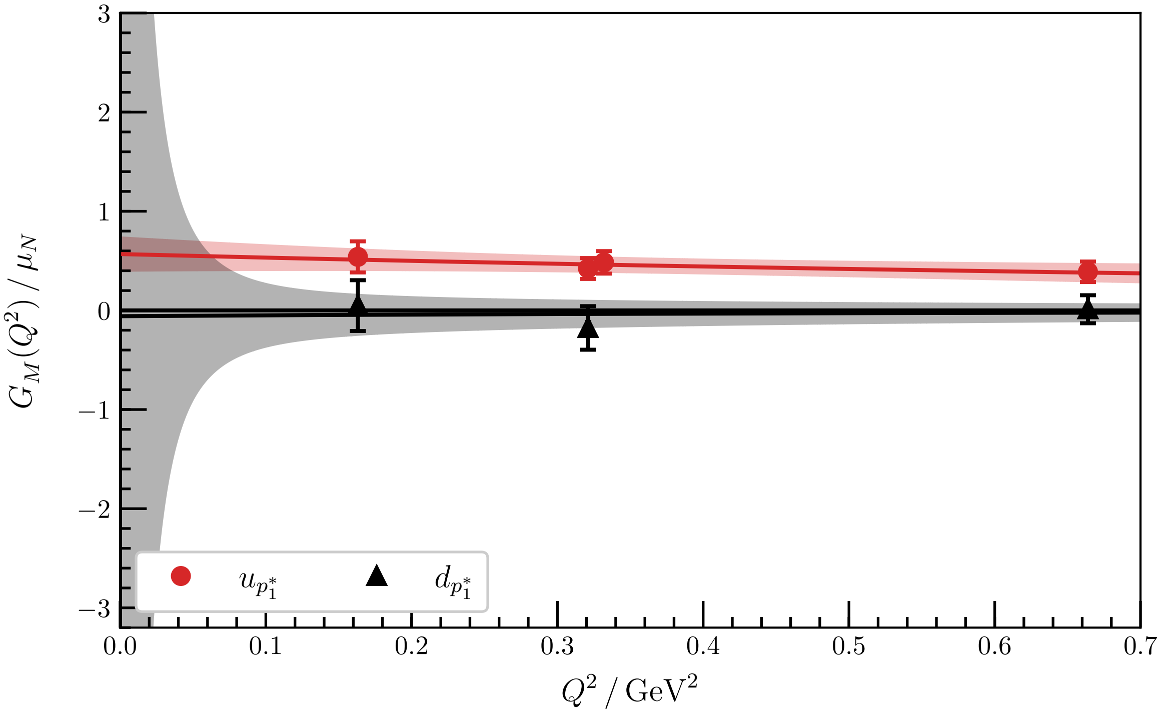

Figure D.39: Quark-flavour contributions to $G_M(Q^2)$ for the first negative-parity excitation at $m_\pi = 296\,\mathrm{MeV}$. The shaded regions are dipole fits to the form factor.

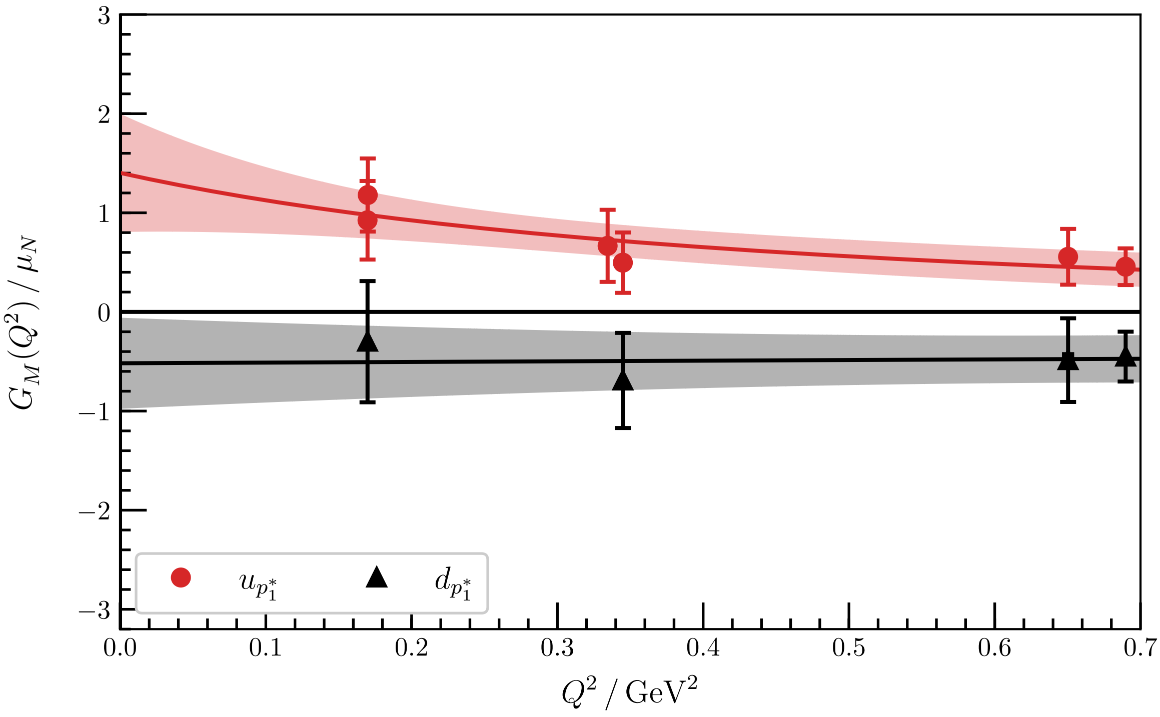

Figure D.40: Quark-flavour contributions to $G_M(Q^2)$ for the first negative-parity excitation at $m_\pi = 156\,\mathrm{MeV}$. The shaded regions are dipole fits to the form factor.

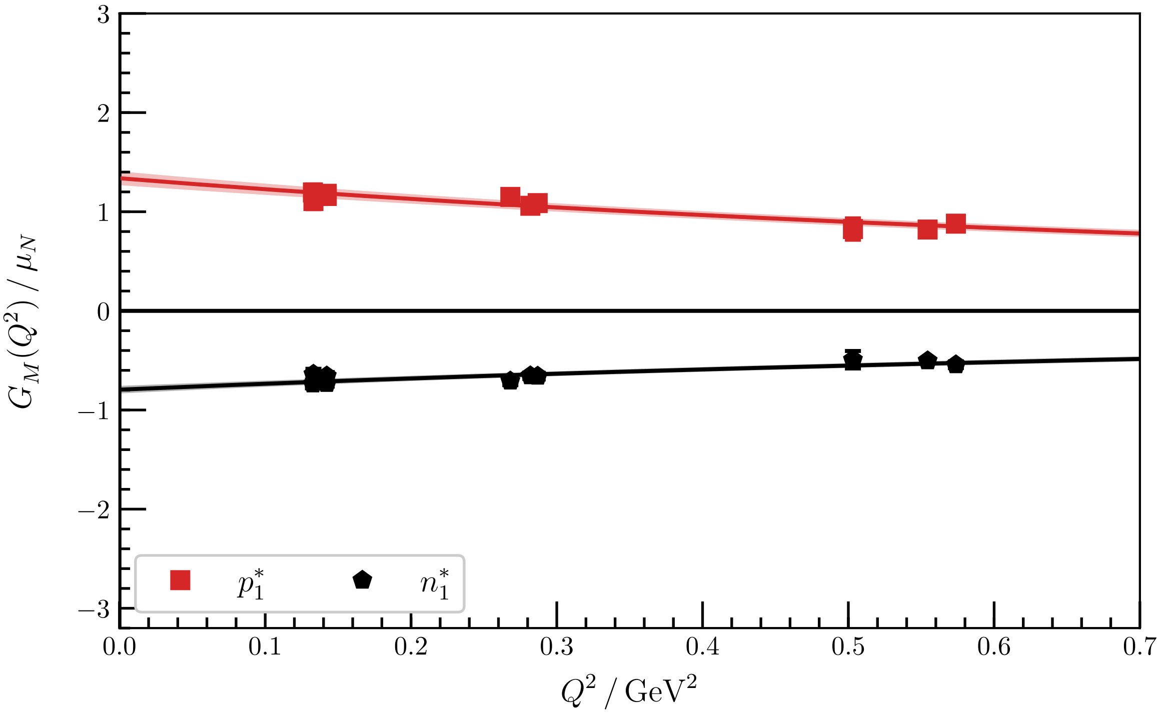

Figure D.41: $G_M(Q^2)$ for the first negative-parity excitations of the proton and neutron at $m_\pi = 702$ MeV. The shaded region corresponds to a dipole fit to the form factor, with a magnetic charge radius of 0.454(28) fm for the excited proton and 0.433(32) fm for the excited neutron.

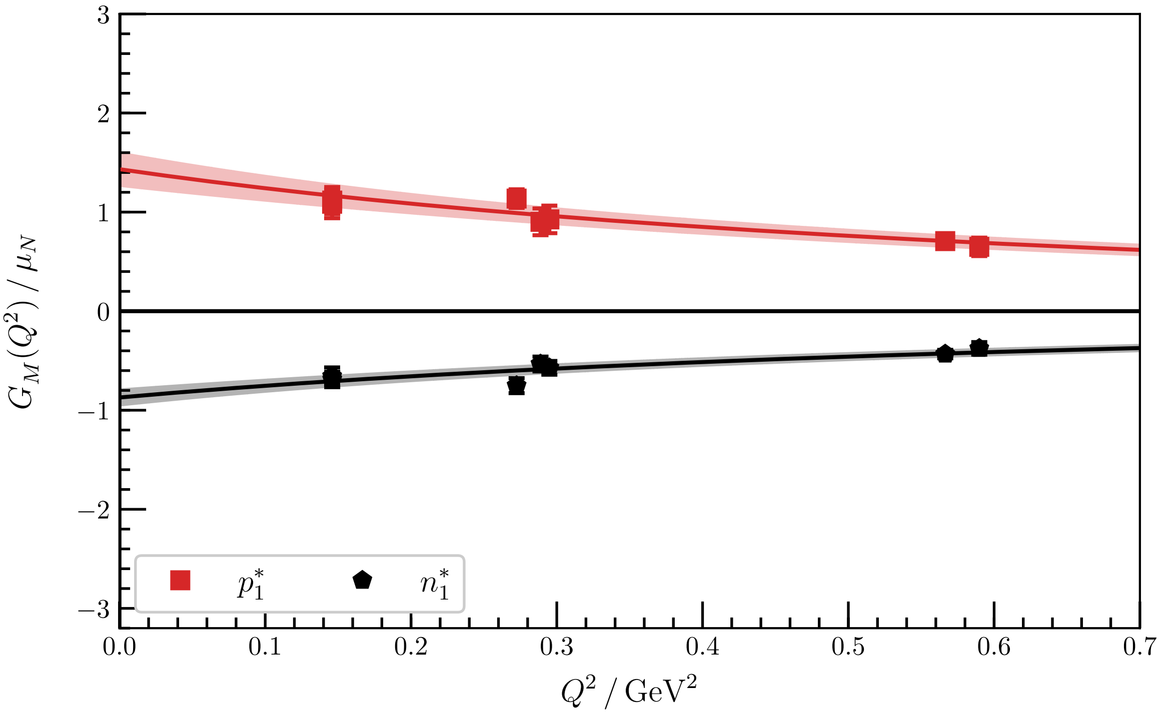

Figure D.42: $G_M(Q^2)$ for the first negative-parity excitations of the proton and neutron at $m_\pi = 570$ MeV. The shaded region corresponds to a dipole fit to the form factor, with a magnetic charge radius of 0.590(53) fm for the excited proton and 0.595(52) fm for the excited neutron.

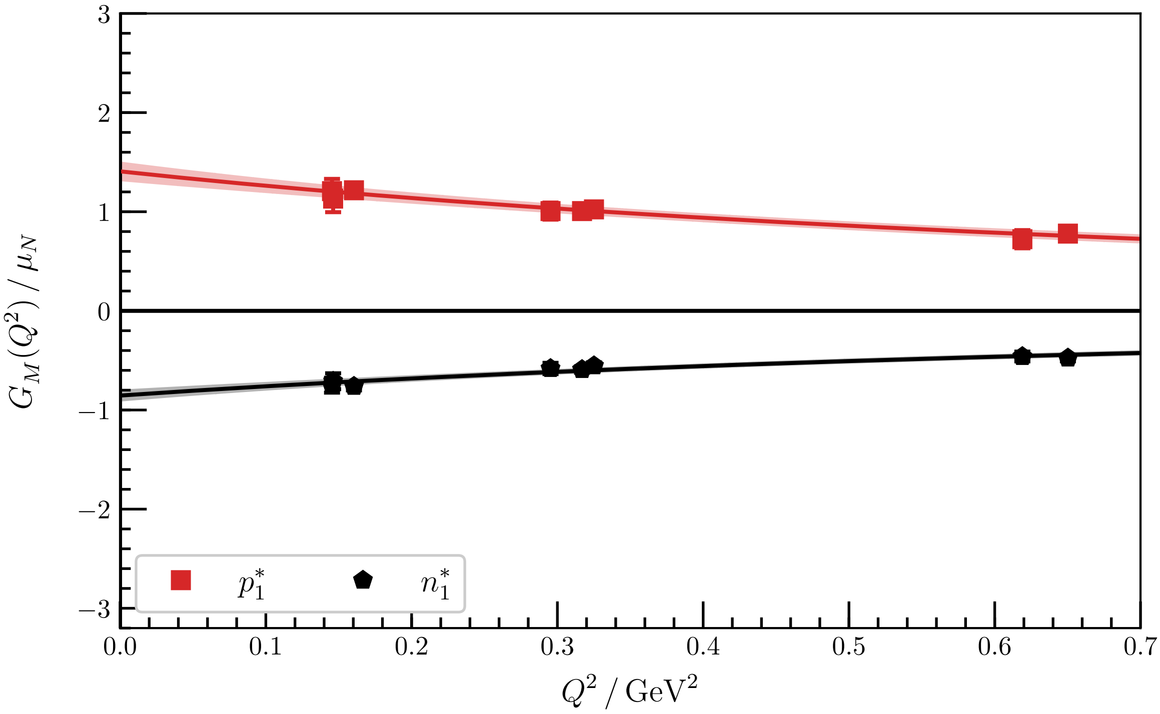

Figure D.43: $G_M(Q^2)$ for the first negative-parity excitations of the proton and neutron at $m_\pi = 411\,\mathrm{MeV}$, The shaded region corresponds to a dipole fit to the form factor, with a magnetic charge radius of 0.511(43) fm for the excited proton and 0.528(45) fm for the excited neutron.

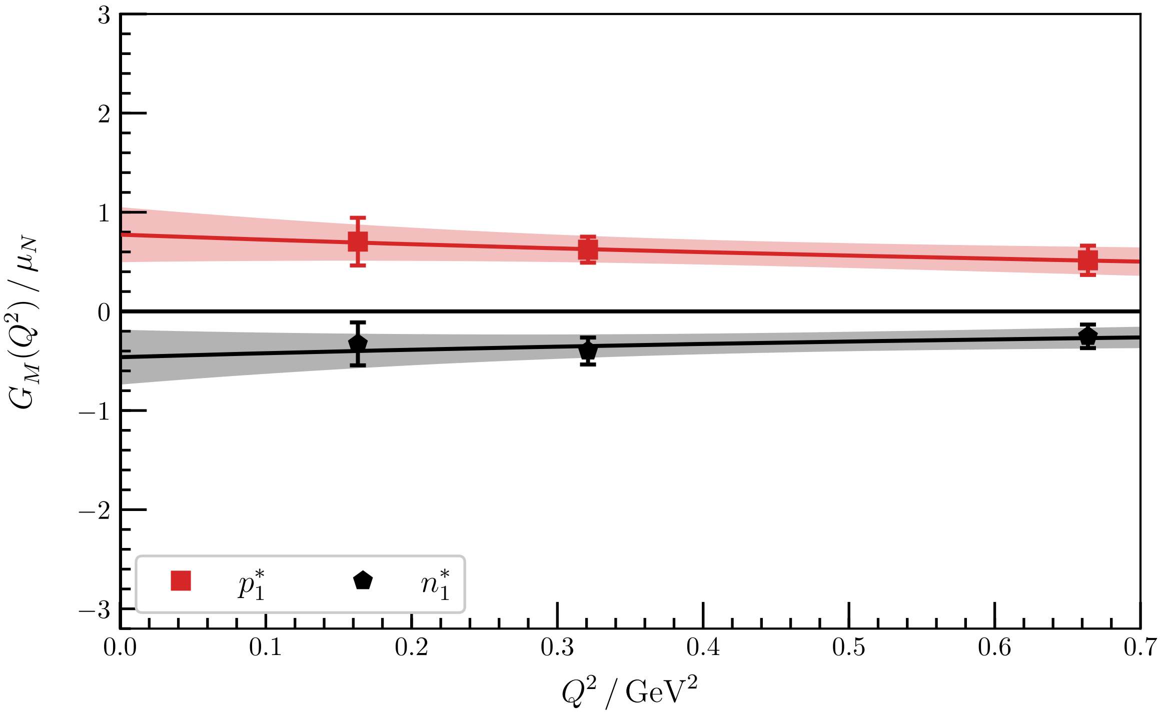

Figure D.44: $G_M(Q^2)$ for the first negative-parity excitations of the proton and neutron at $m_\pi = 296\,\mathrm{MeV}$. The shaded region corresponds to a dipole fit to the form factor, with a magnetic charge radius of 0.40(26) fm for the excited proton and 0.47(41) fm for the excited neutron.

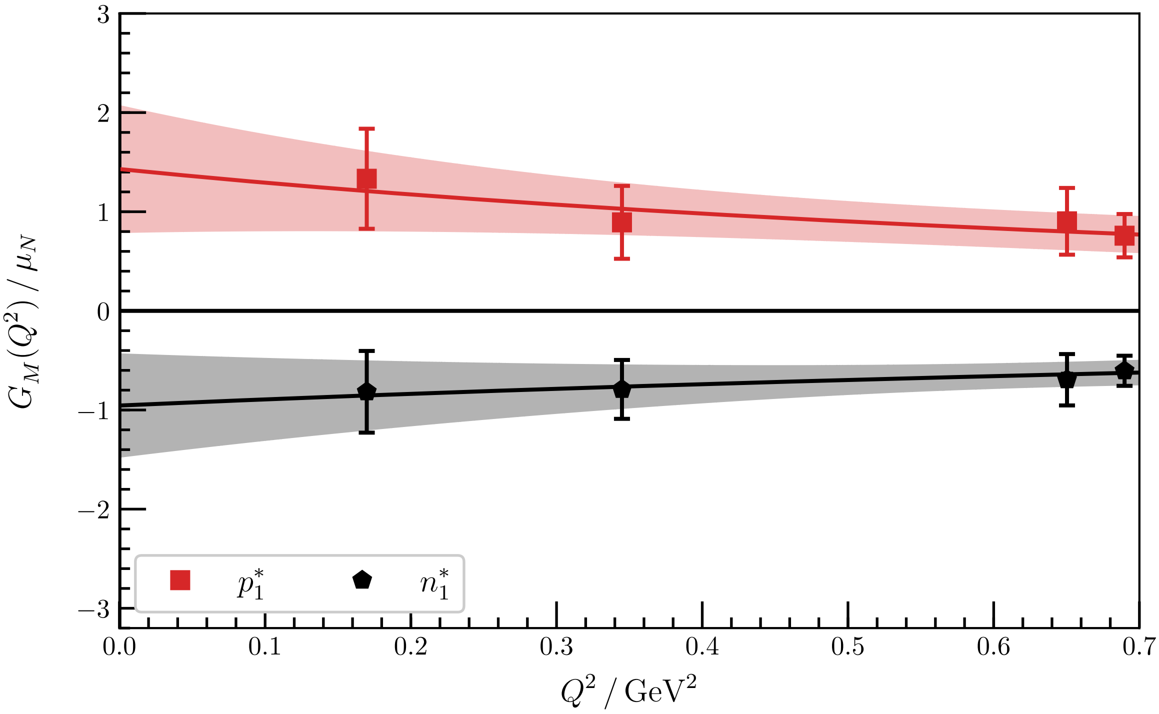

Figure D.45: $G_M(Q^2)$ for the first negative-parity excitations of the proton and neutron at $m_\pi = 156$ MeV. The shaded region corresponds to a dipole fit to the form factor, with a magnetic charge radius of 0.49(23) fm for the excited proton and 0.40(47) fm for the excited neutron.

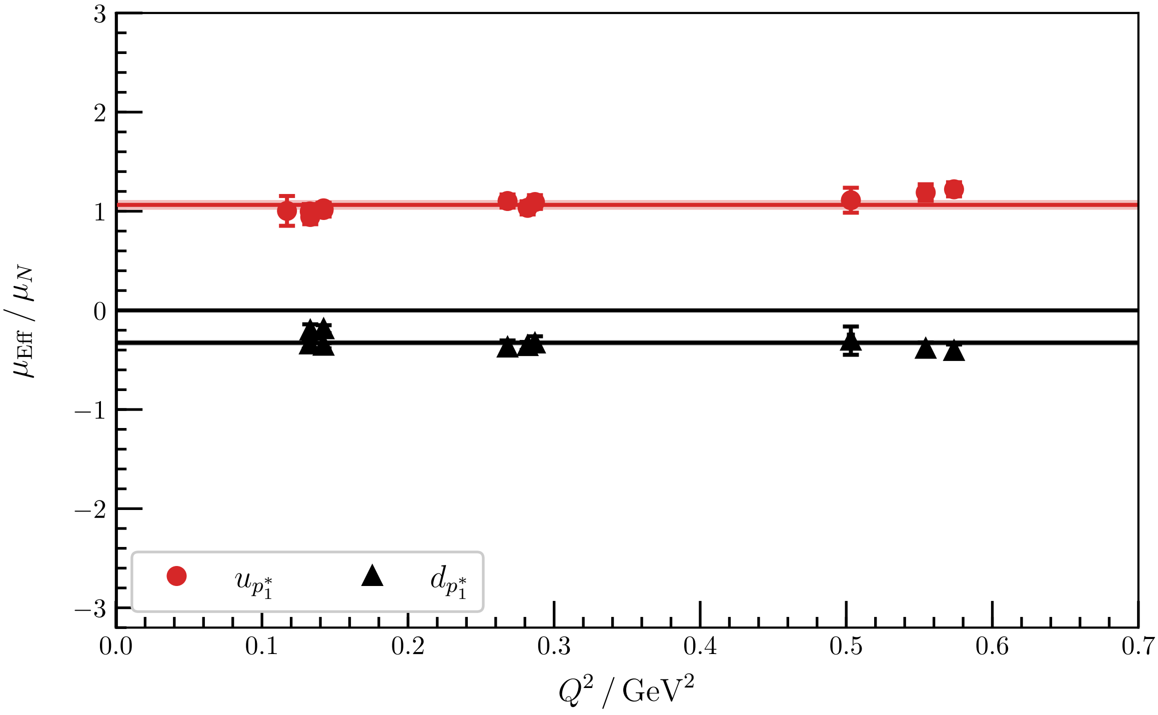

Figure D.46: $\mu_{\mathrm{Eff}}$ for the first negative-parity excitation at $m_\pi = 702$ MeV. The shaded bands are constant fits to the effective magnetic moment that have reasonable agreement with the data and correspond to magnetic moment contributions of 1.064(49) $\mu_N$ for the doubly represented quark and −0.327(28) $\mu_N$ for the singly represented quark

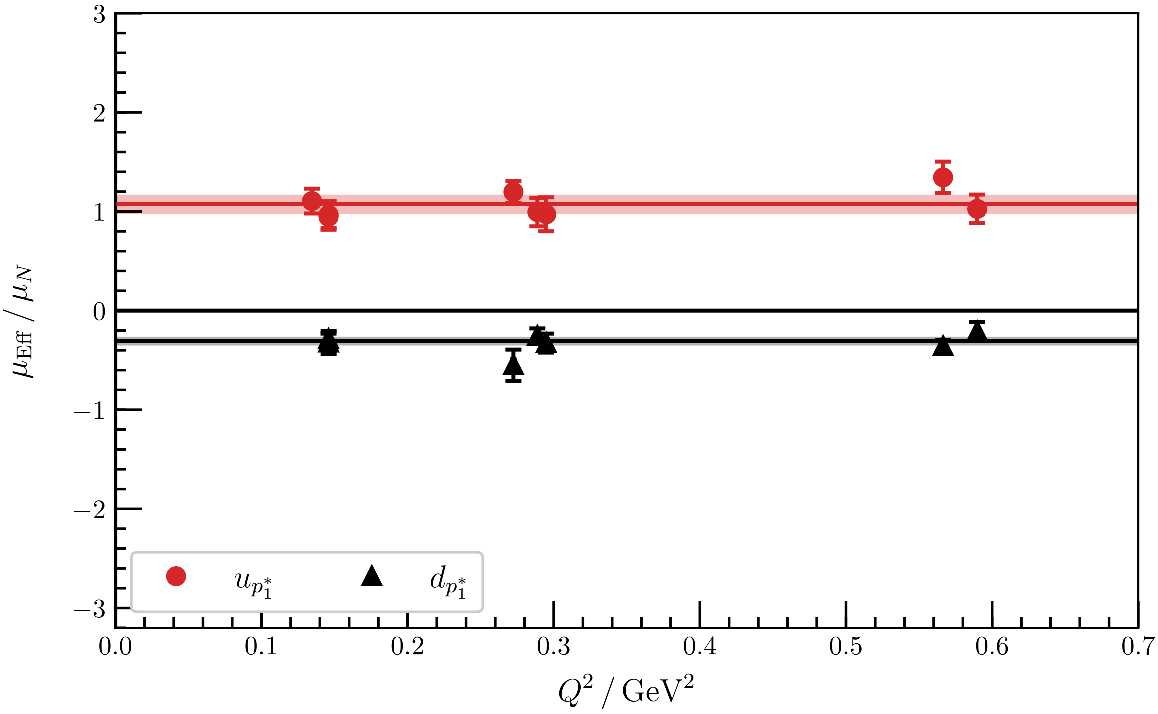

Figure D.47: $\mu_{\mathrm{Eff}}$ for the first negative-parity excitation at $m_\pi = 570\,\mathrm{MeV}$. The shaded bands are constant fits to the effective magnetic moment that have reasonable agreement with the data, and correspond to magnetic moment contributions of 1.073(97) $\mu_N$ for the doubly represented quark and −0.307(44) $\mu_N$ for the singly represented quark.

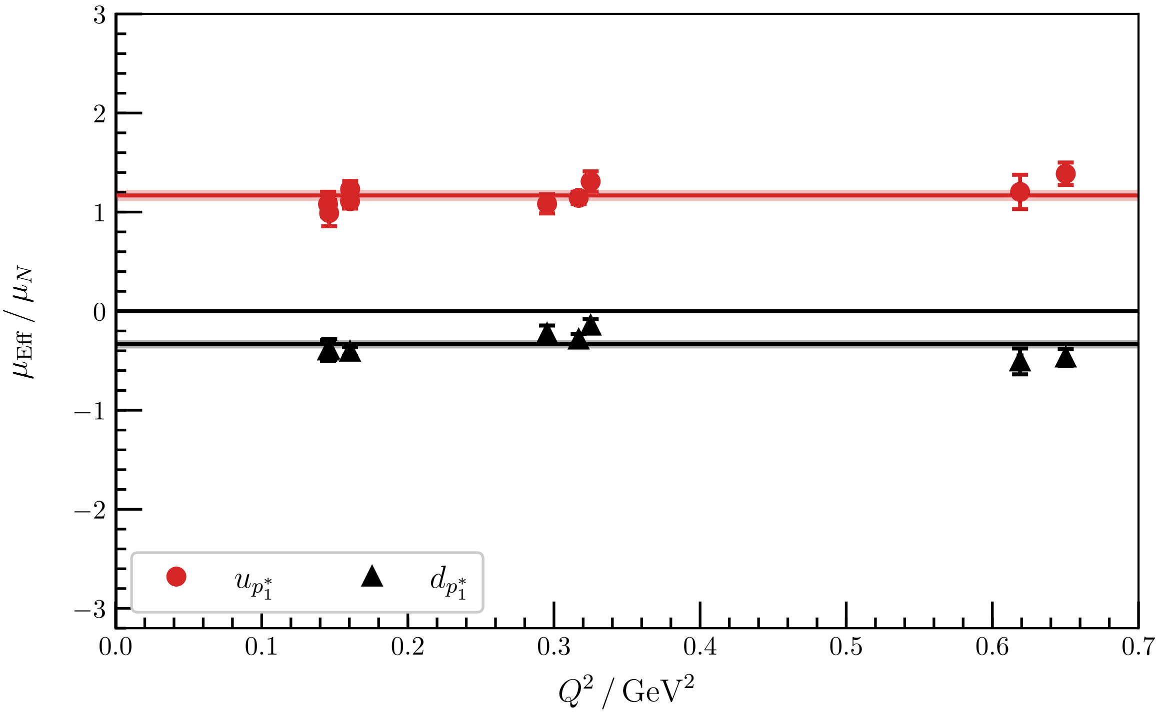

Figure D.48: $\mu_{\mathrm{Eff}}$ for the first negative-parity excitation at $m_\pi = 411\,\mathrm{MeV}$. The shaded bands are constant fits to the effective magnetic moment that have reasonable agreement with the data, and correspond to magnetic moment contributions of 1.168(57) $\mu_N$ for the doubly represented quark and −0.333(43) $\mu_N$ for the singly represented quark.

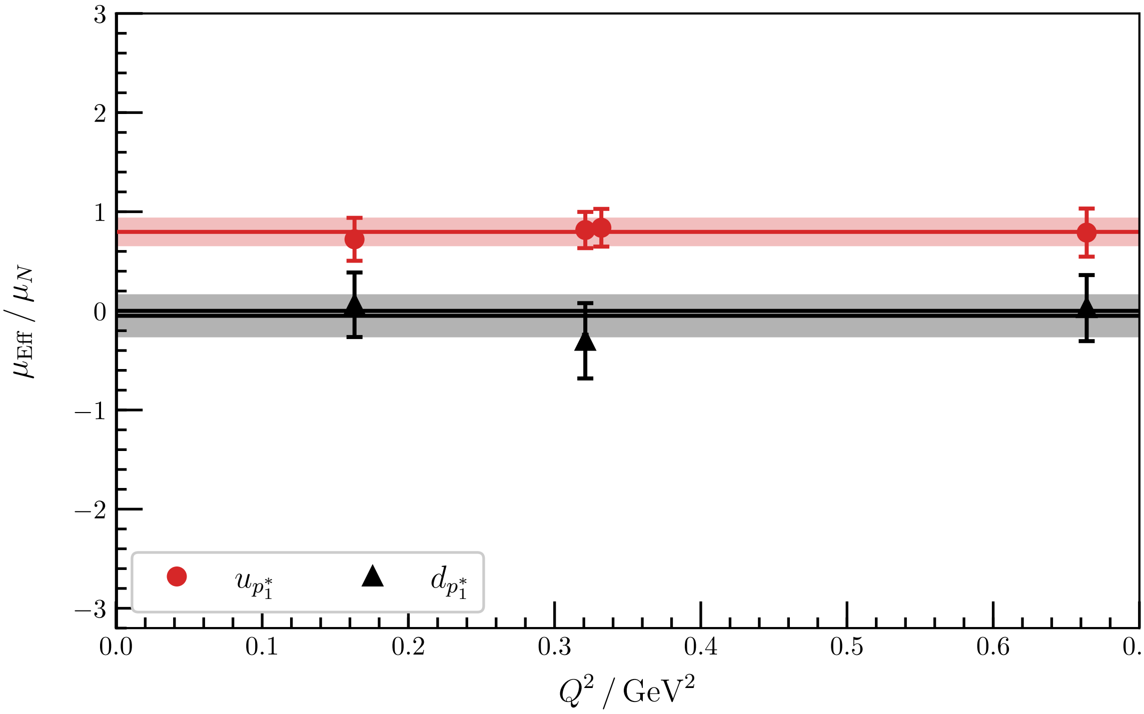

Figure D.49: $\mu_{\text{Eff}}$ for the first negative-parity excitation at $m_\pi = 296\,\text{MeV}$. The shaded bands are constant fits to the effective magnetic moment that have reasonable agreement with the data, and correspond to magnetic moment contributions of 0.80(15) $\mu_N$ for the doubly represented quark and −0.050(22) $\mu_N$ for the singly represented quark.

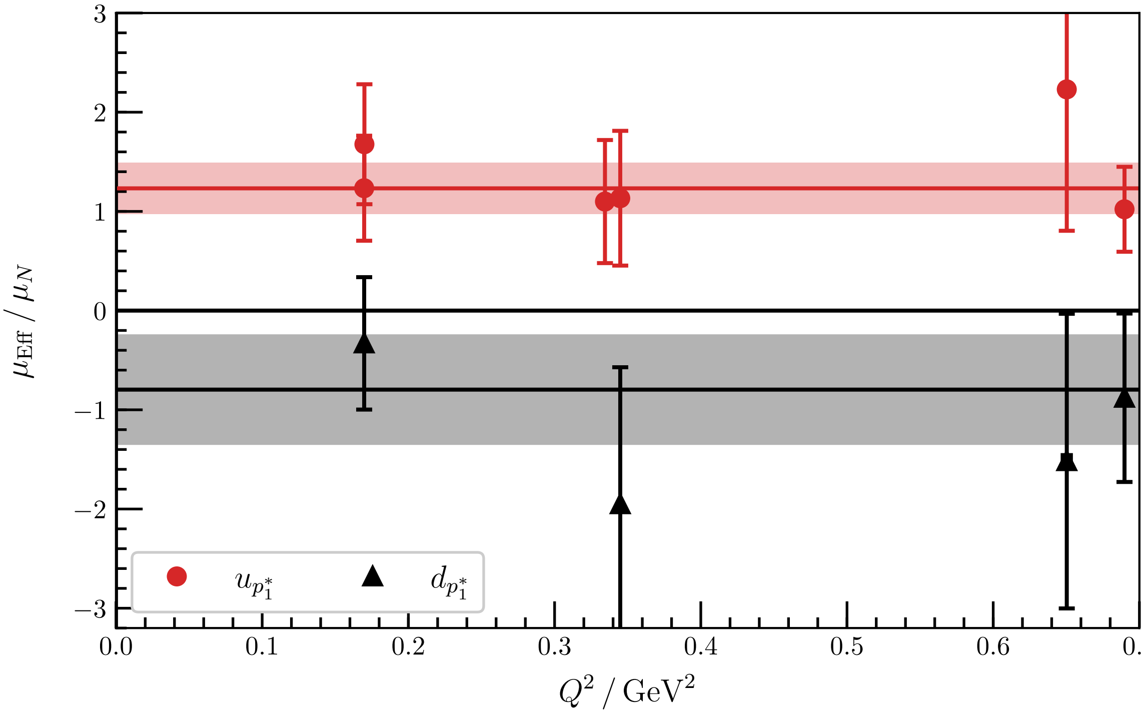

Figure D.50: $\mu_{\text{Eff}}$ for the first negative-parity excitation at $m_\pi = 156\,\text{MeV}$. The shaded bands are constant fits to the effective magnetic moment that have reasonable agreement with the data, and correspond to magnetic moment contributions of 1.23(26) $\mu_N$ for the doubly represented quark and −0.80(56) $\mu_N$ for the singly represented quark.

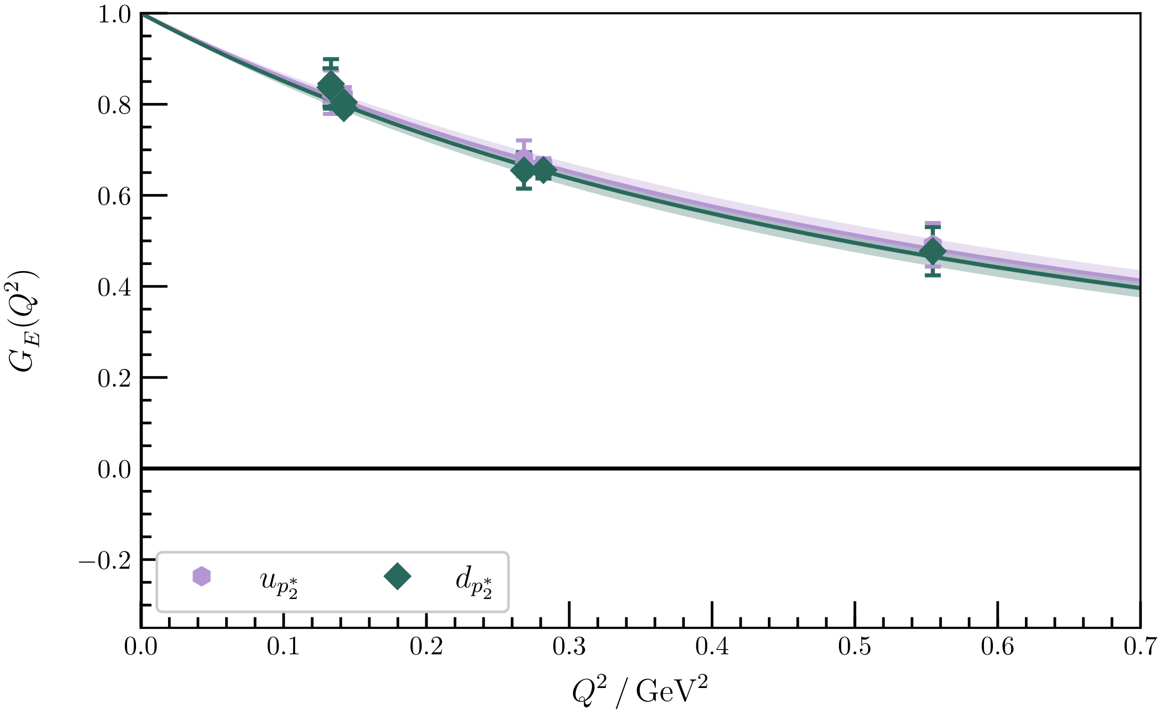

Figure D.51: Quark-flavour contributions to $G_E(Q^2)$ for second negative parity excitation at $m_\pi = 702\,\mathrm{MeV}$. The shaded regions are dipole fits to the form factor, with the y-intercept fixed to unity.

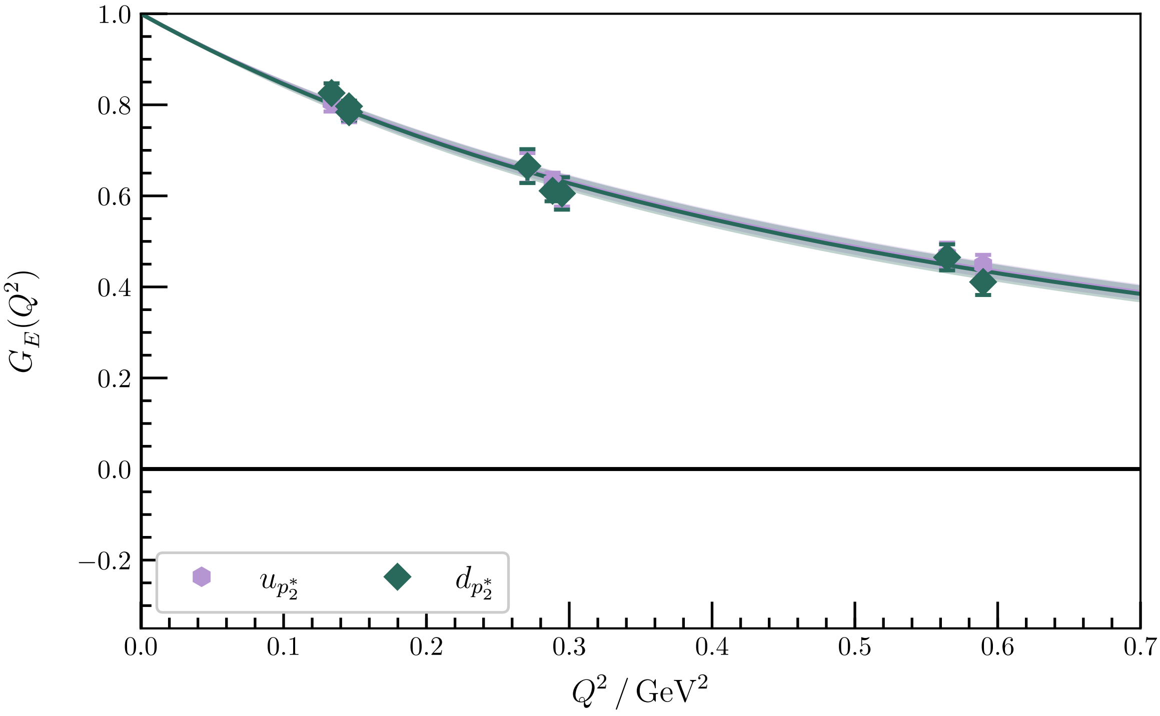

Figure D.52: Quark-flavour contributions to $G_E(Q^2)$ for second negative parity excitation at $m_\pi = 570\,\mathrm{MeV}$. The shaded regions are dipole fits to the form factor, with the y-intercept fixed to unity.

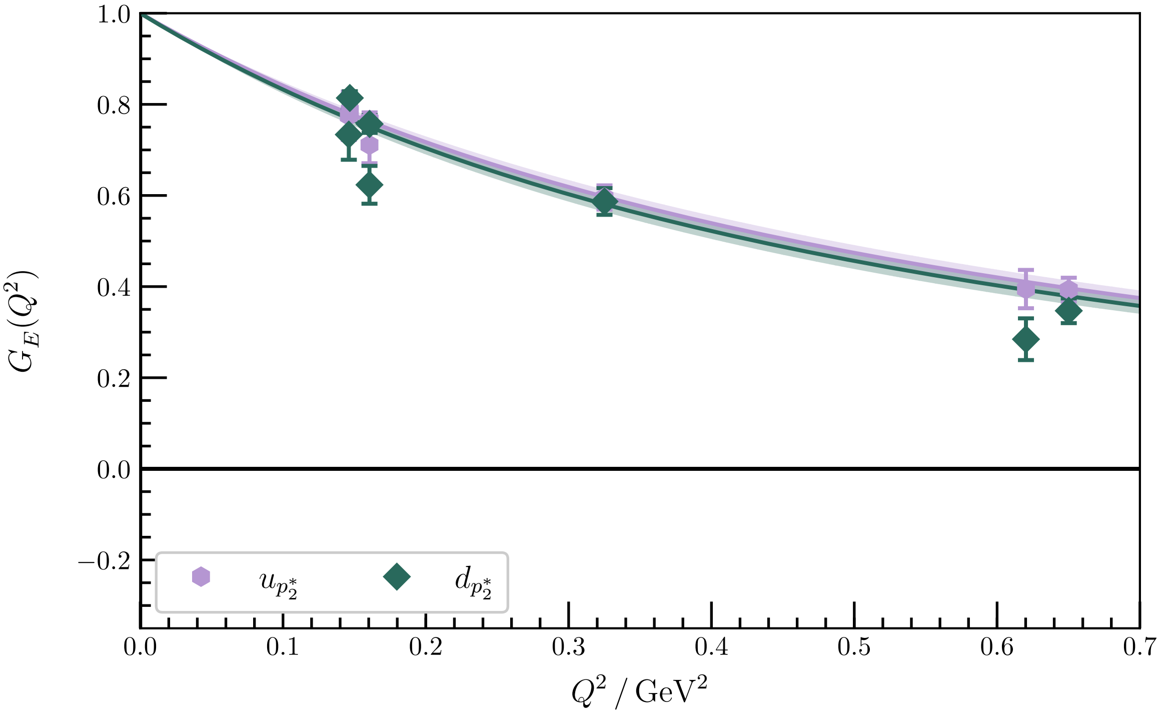

Figure D.53: Quark-flavour contributions to $G_E(Q^2)$ for second negative parity excitation at $m_\pi = 411\,\text{MeV}$. The shaded regions are dipole fits to the form factor, with the y-intercept fixed to unity.

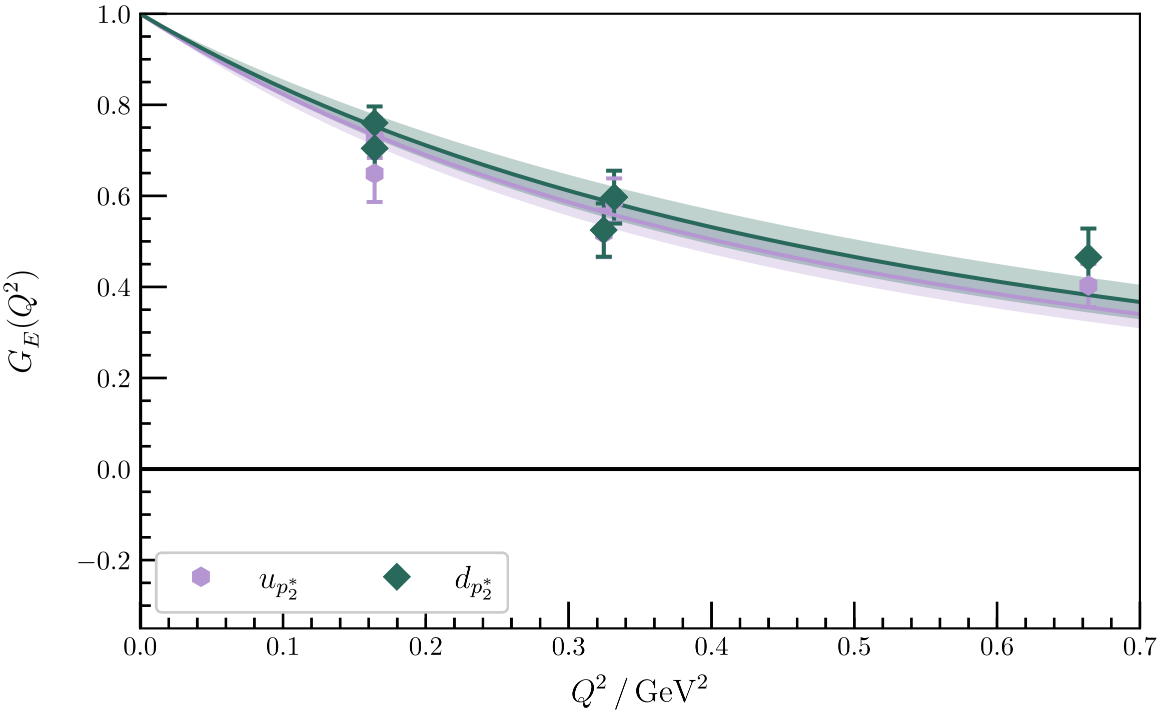

Figure D.54: Quark-flavour contributions to $G_E(Q^2)$ for second negative parity excitation at $m_\pi = 296\,\text{MeV}$. The shaded regions are dipole fits to the form factor, with the y-intercept fixed to unity.

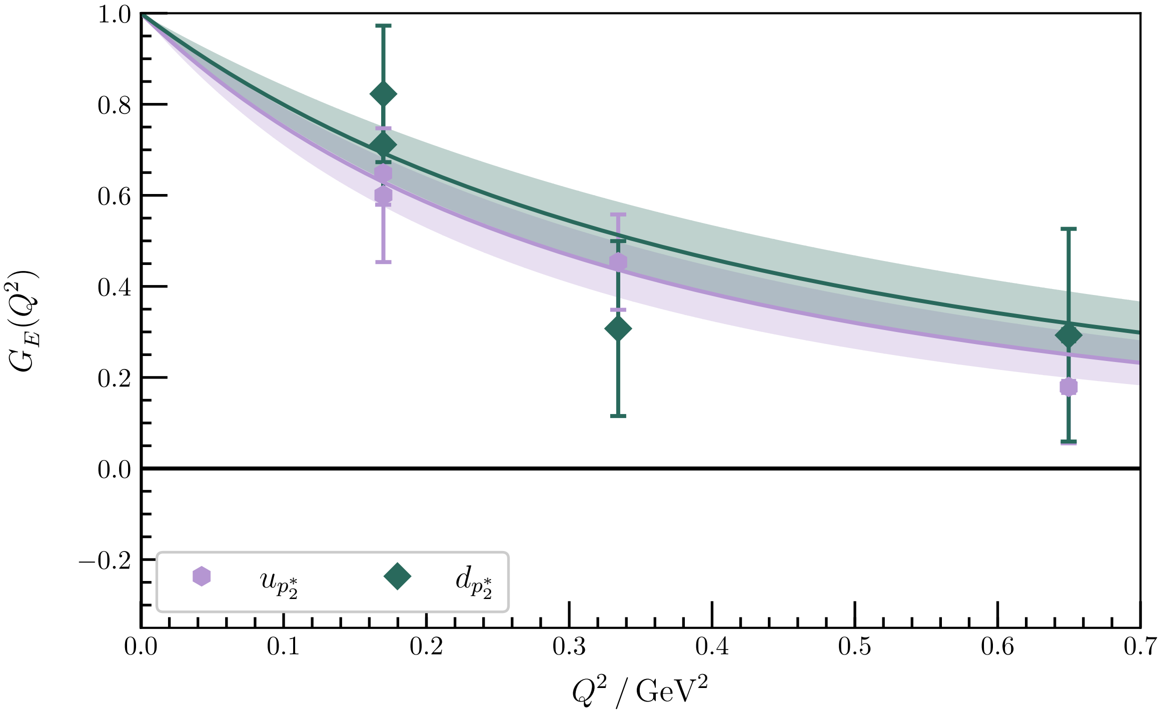

Figure D.55: Quark-flavour contributions to $G_E(Q^2)$ for second negative parity excitation at $m_\pi = 156\,\mathrm{MeV}$. The shaded regions are dipole fits to the form factor, with the y-intercept fixed to unity.

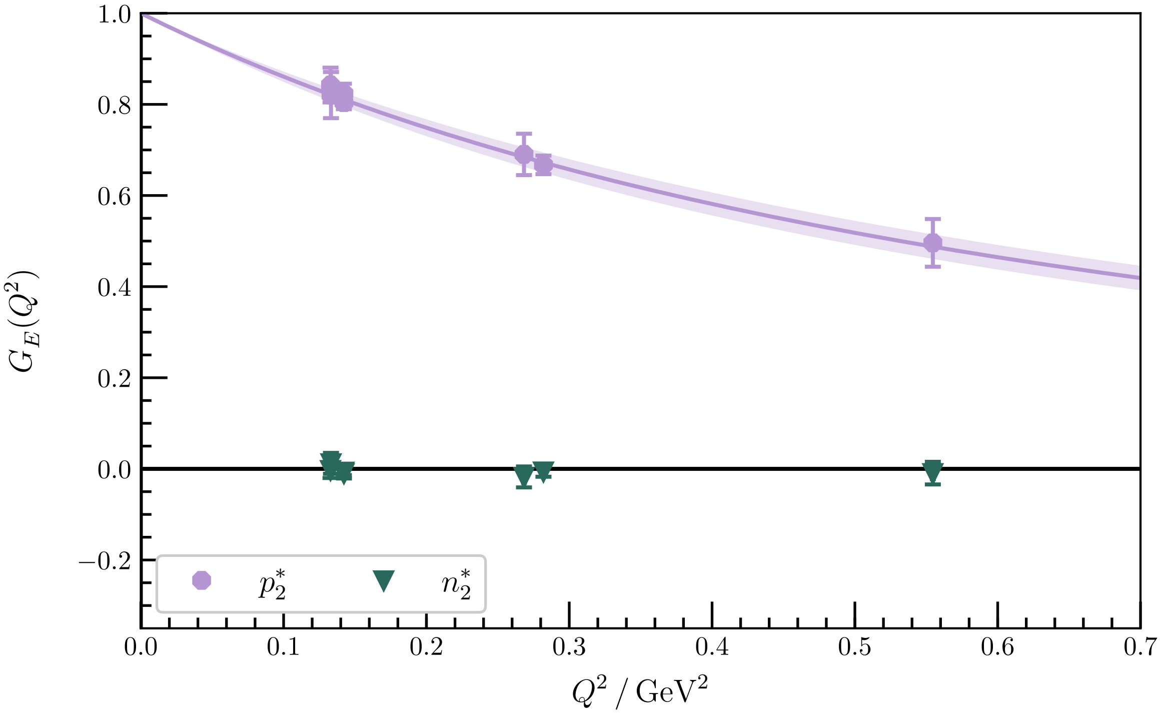

Figure D.56: $G_E(Q^2)$ for the second negative-parity excitations of the proton and neutron at $m_\pi = 702\,\mathrm{MeV}$. The shaded region corresponds to a dipole fit to the electric form factor for the excited proton, with a charge radius of 0.603(28) fm.

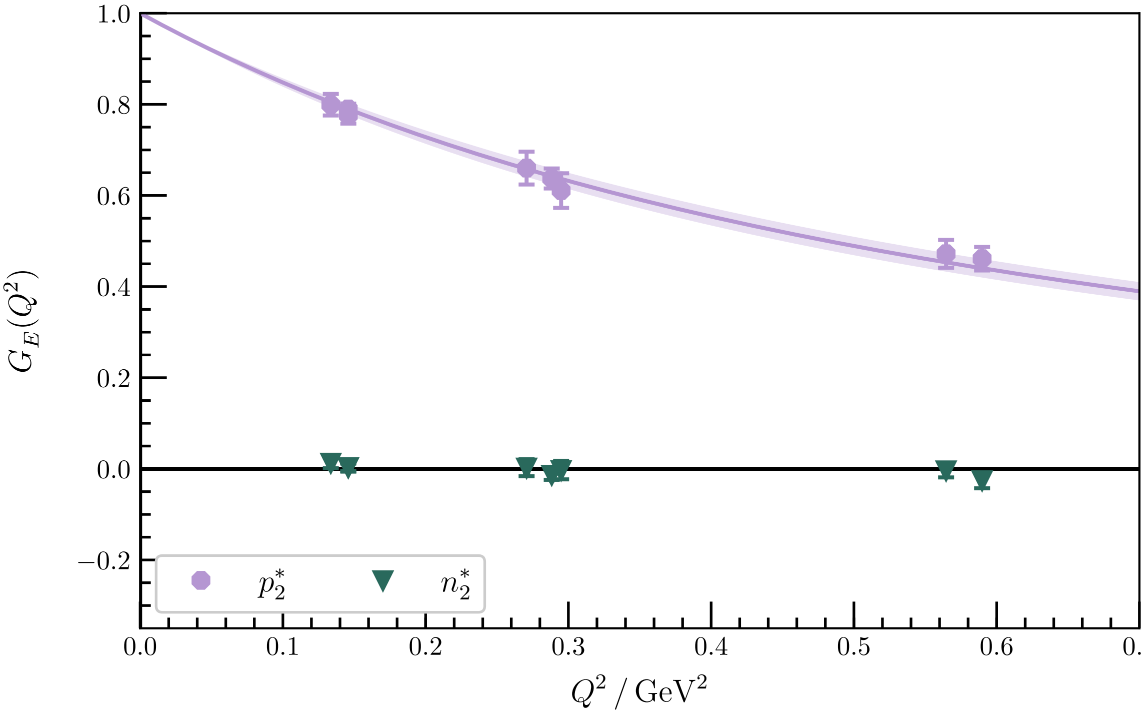

Figure D.57: $G_E(Q^2)$ for the second negative-parity excitations of the proton and neutron at $m_\pi = 570\,\mathrm{MeV}$. The shaded region corresponds to a dipole fit to the electric form factor for the excited proton, with a charge radius of 0.634(22) fm.

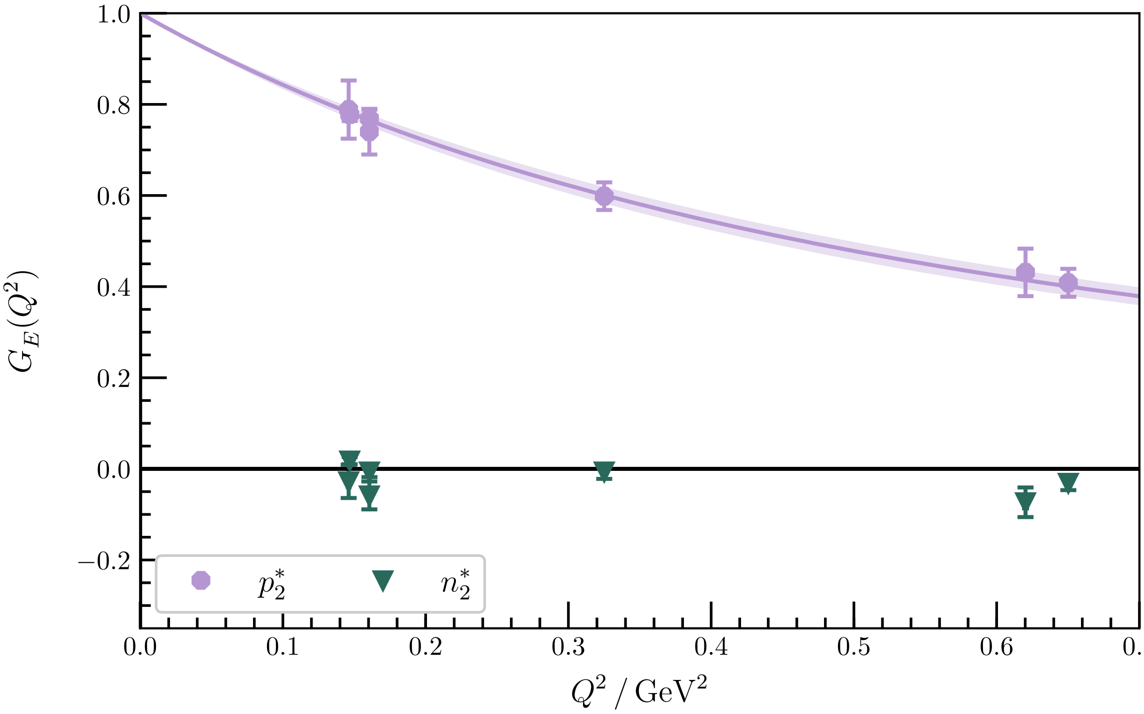

Figure D.58: $G_E(Q^2)$ for the second negative-parity excitations of the proton and neutron at $m_\pi = 411\,\mathrm{MeV}$. The shaded region corresponds to a dipole fit to the excited proton, with a charge radius of 0.646(22) fm.

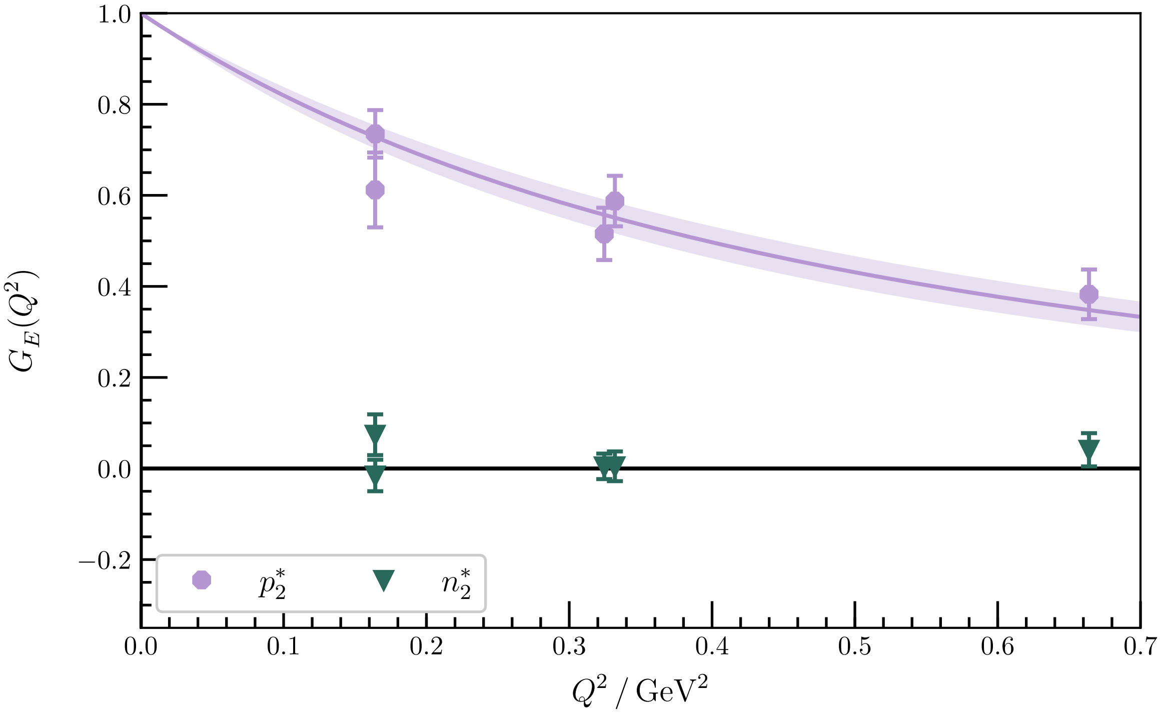

Figure D.59: $G_E(Q^2)$ for the second negative-parity excitations of the proton and neutron at $m_\pi = 296\,\text{MeV}$. The shaded region corresponds to a dipole fit to the electric form factor for the excited proton, with a charge radius of 0.699(42) fm.

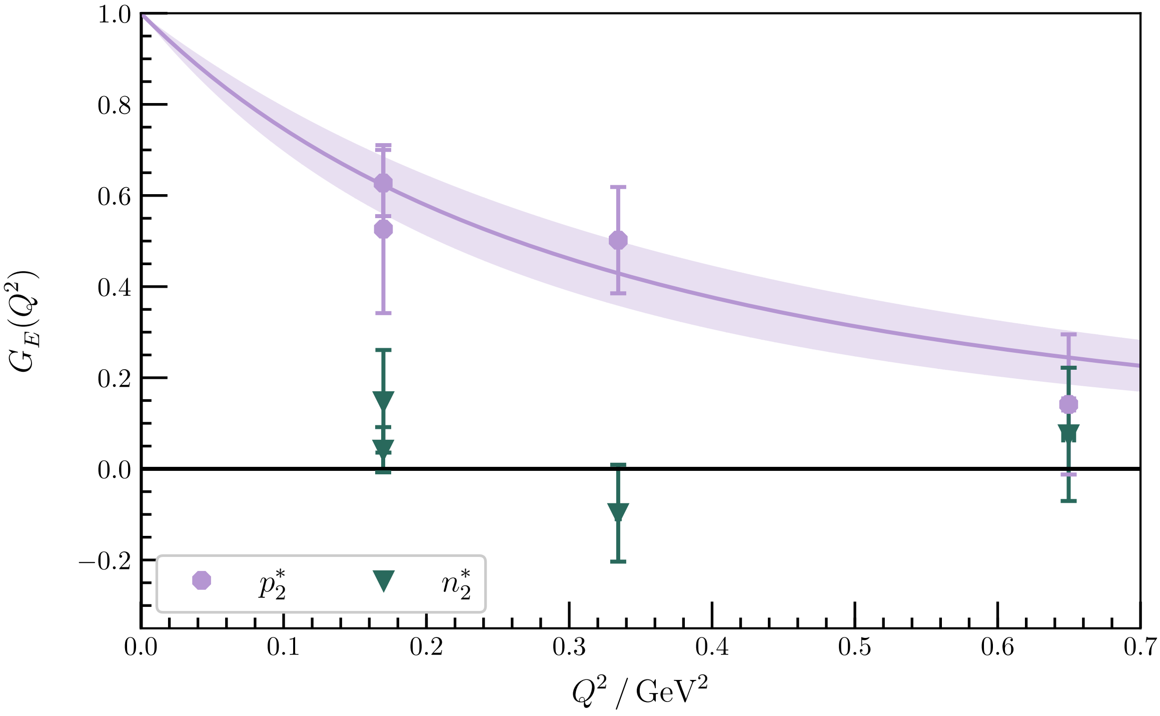

Figure D.60: $G_E(Q^2)$ for the second negative-parity excitations of the proton and neutron at $m_\pi = 156\,\text{MeV}$. The shaded region corresponds to a dipole fit to the electric form factor for the excited proton, with a charge radius of 0.797(95) fm.

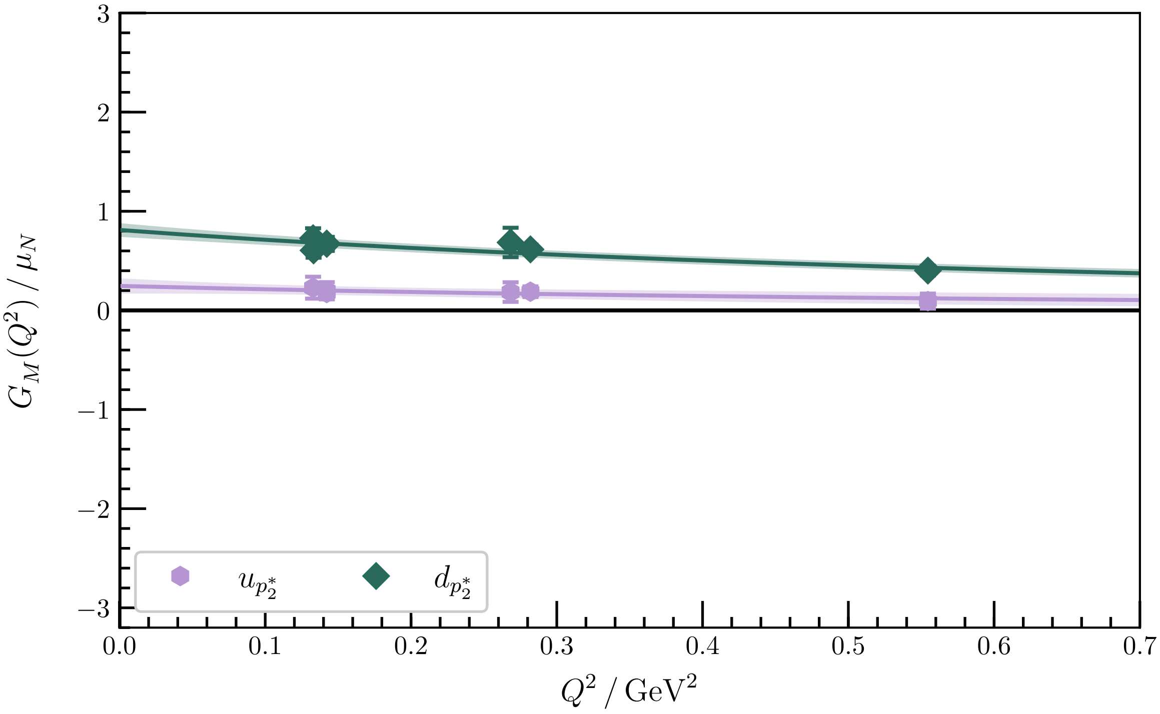

Figure D.61: Quark-flavour contributions to $G_M(Q^2)$ for the second negative-parity excitation at $m_\pi = 702\,\mathrm{MeV}$. The shaded regions are dipole fits to the form factor.

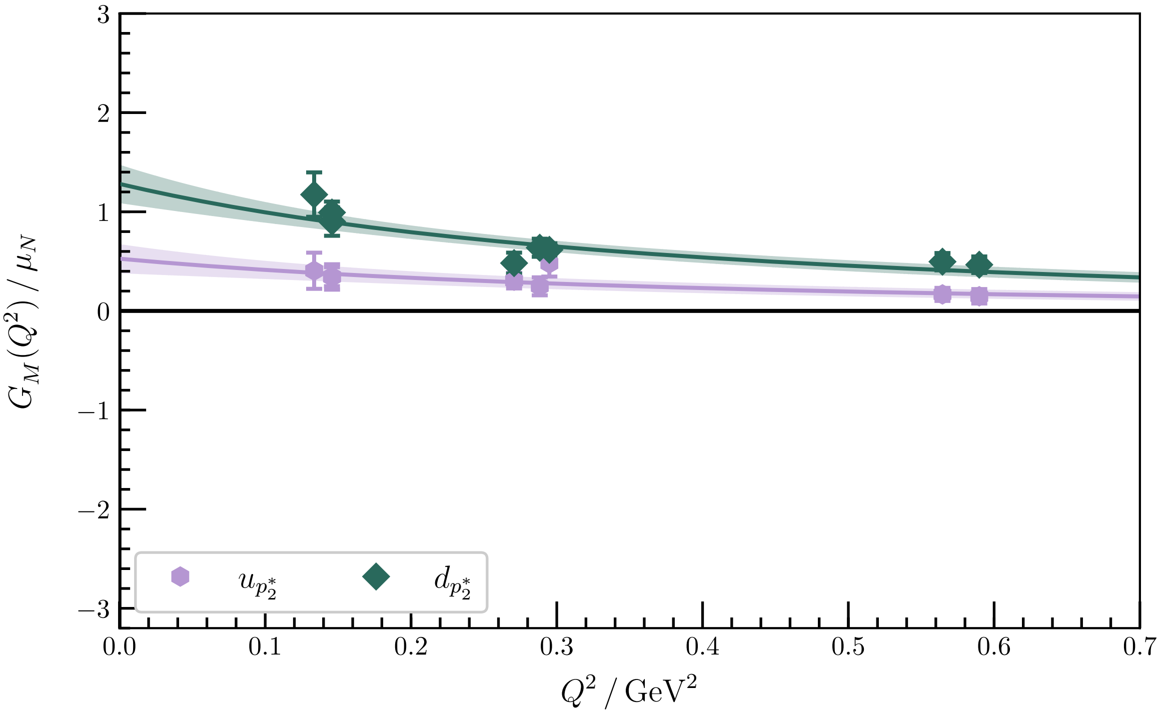

Figure D.62: Quark-flavour contributions to $G_M(Q^2)$ for the second negative-parity excitation at $m_\pi = 570\,\mathrm{MeV}$. The shaded regions are dipole fits to the form factor.

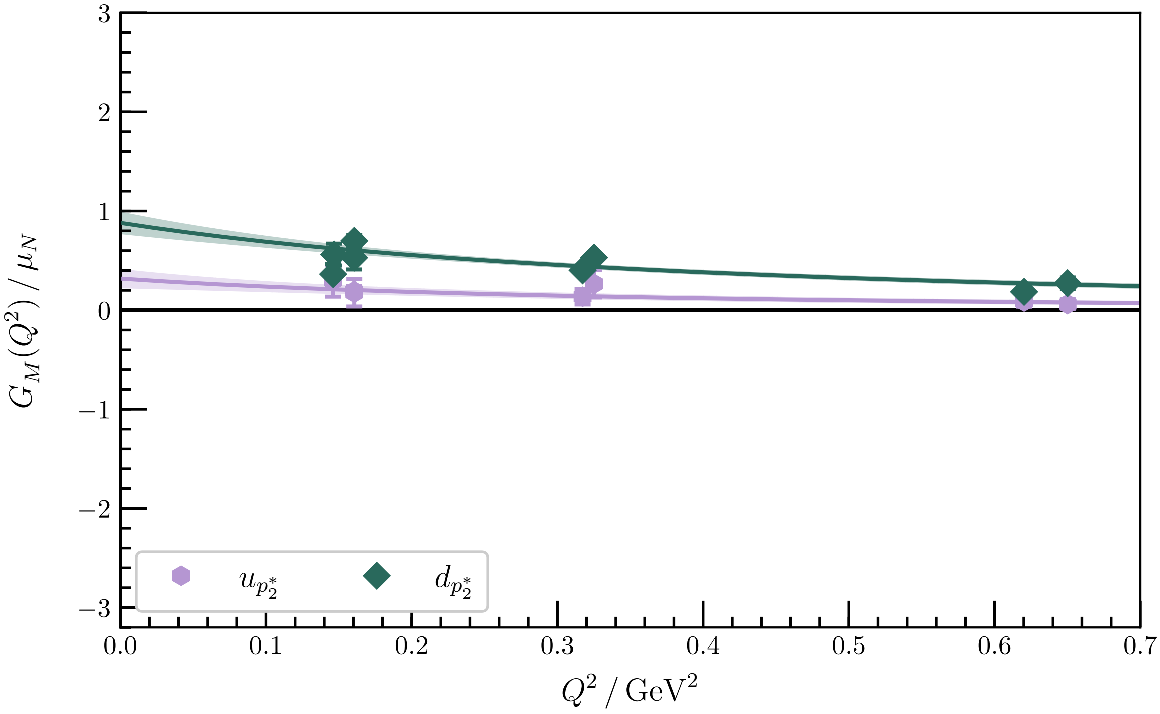

Figure D.63: Quark-flavour contributions to $G_M(Q^2)$ for the second negative-parity excitation at $m_\pi = 411\,\mathrm{MeV}$. The shaded regions are dipole fits to the form factor.

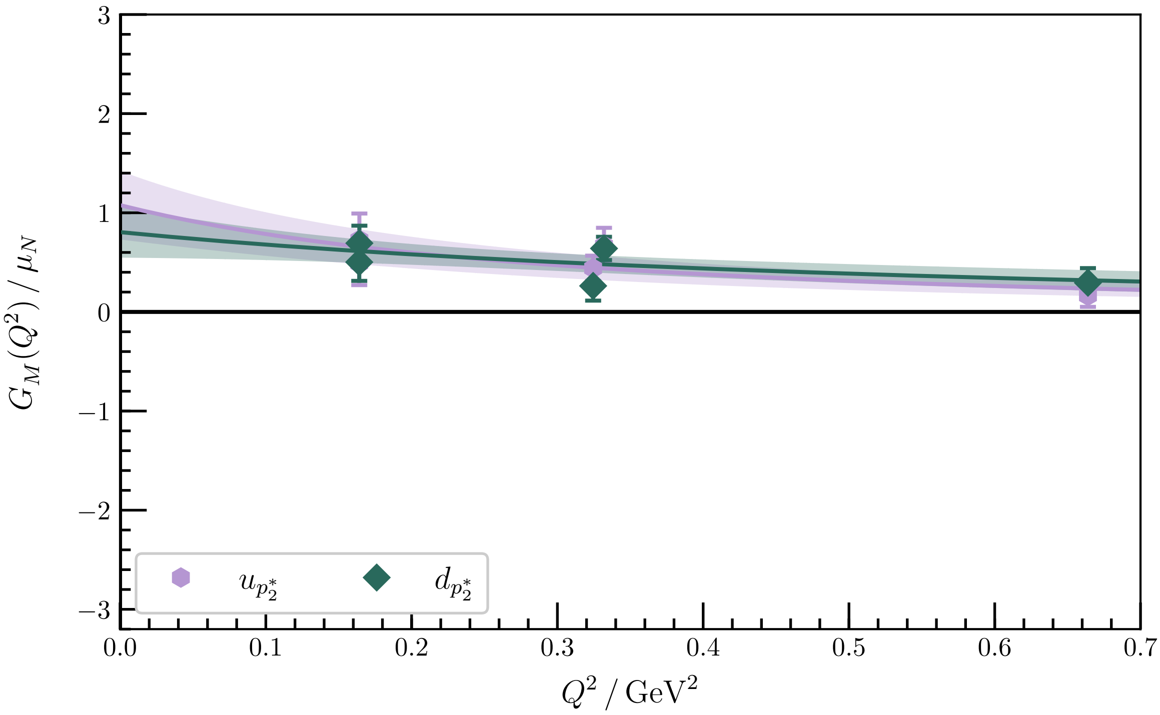

Figure D.64: Quark-flavour contributions to $G_M(Q^2)$ for the second negative-parity excitation at $m_\pi = 296\,\mathrm{MeV}$. The shaded regions are dipole fits to the form factor.

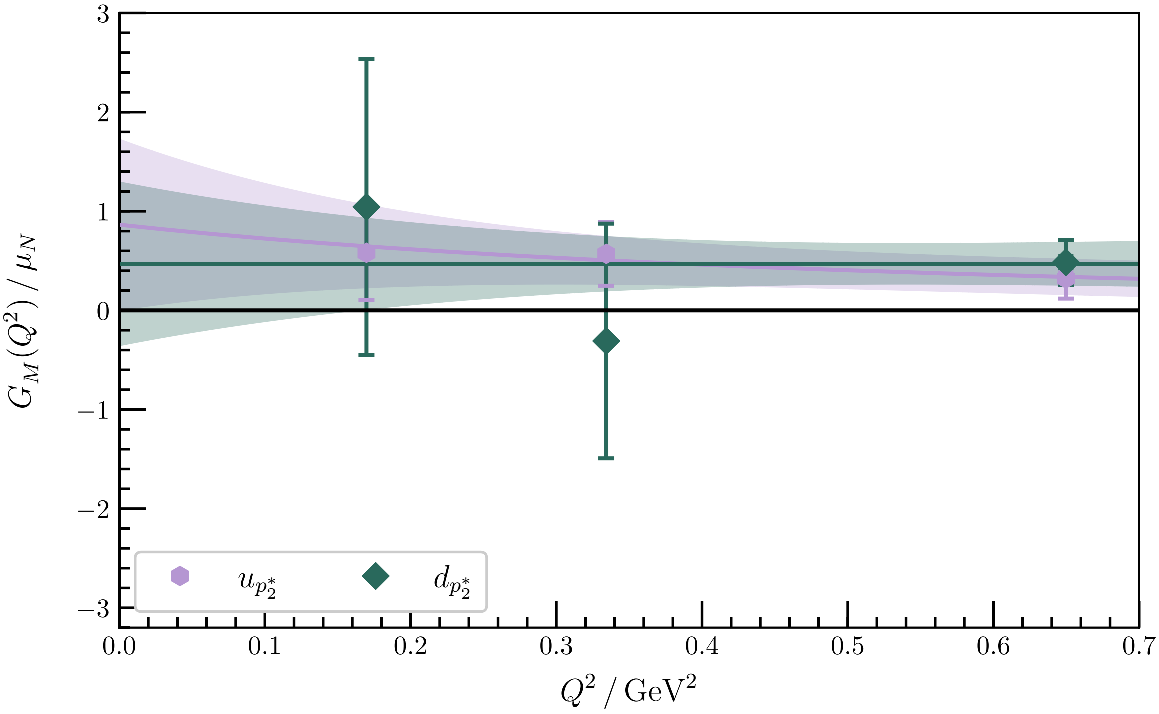

Figure D.65: Quark-flavour contributions to $G_M(Q^2)$ for the second negative-parity excitation at $m_\pi = 156\,\mathrm{MeV}$. The shaded regions are dipole fits to the form factor.

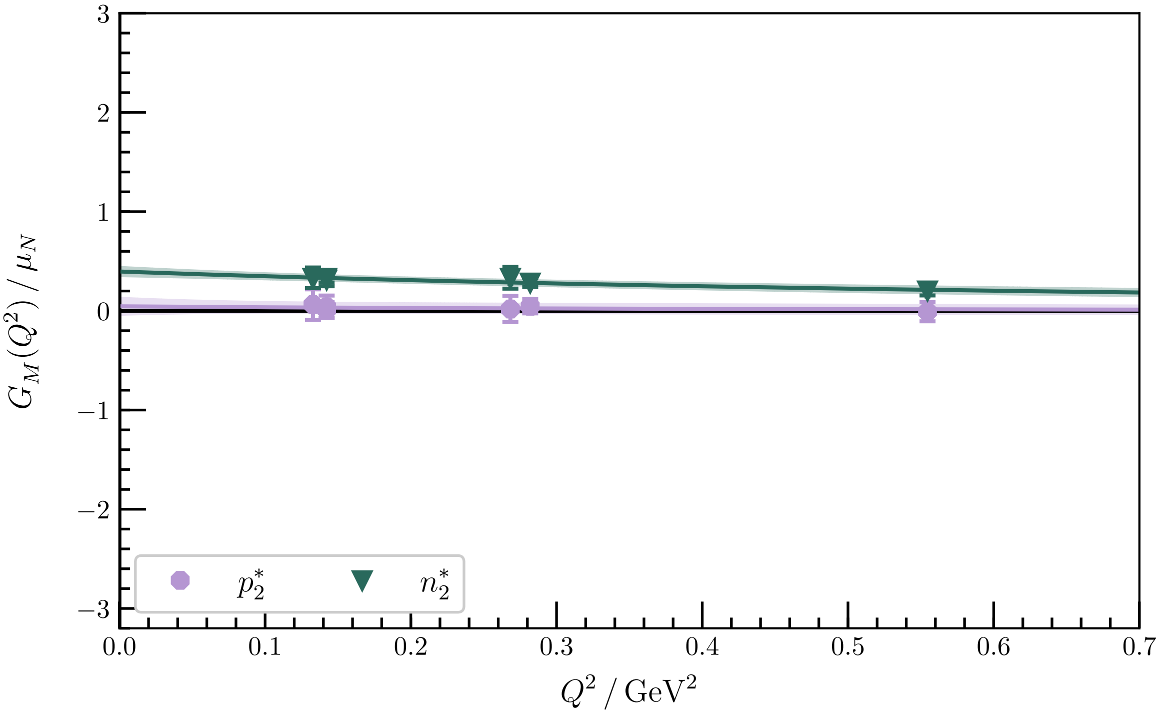

Figure D.66: $G_M(Q^2)$ for the second negative-parity excitations of the proton and neutron at $m_\pi = 702\,\mathrm{MeV}$. The shaded regions correspond to dipole fits to the form factors, with a magnetic charge radius of $0.8(20)\,\mathrm{fm}$ for the proton and $0.56(14)\,\mathrm{fm}$ for the neutron.

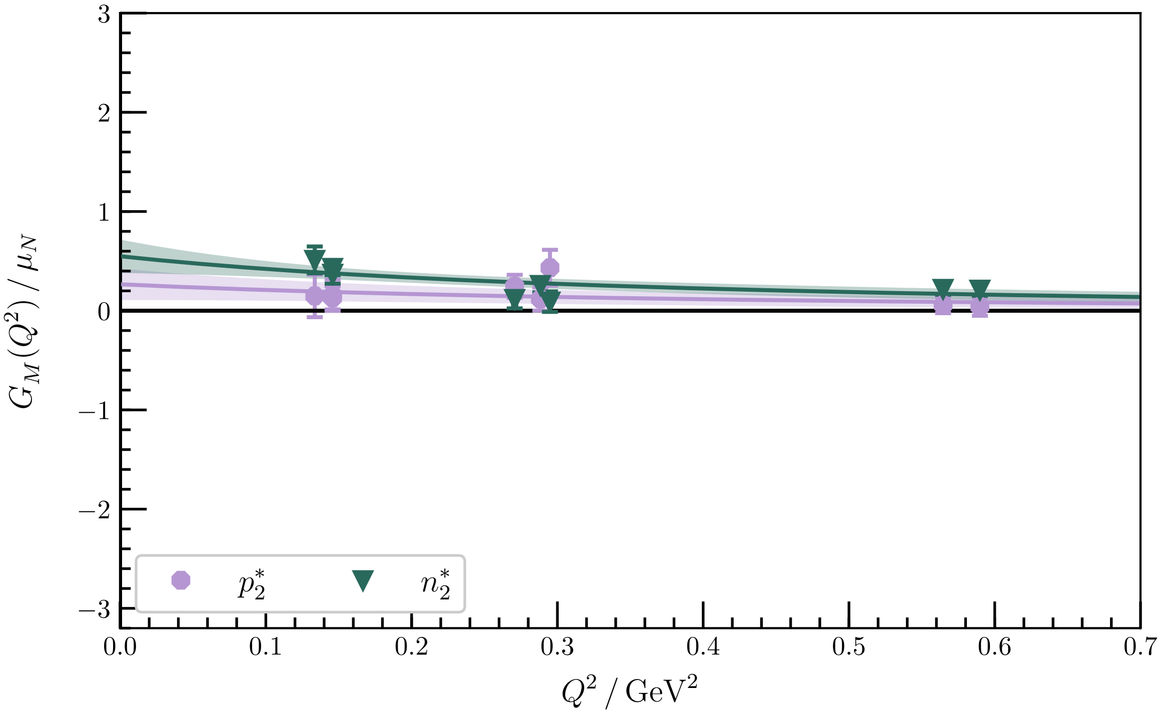

Figure D.67: $G_M(Q^2)$ for the second negative-parity excitations of the proton and neutron at $m_\pi = 570\,\text{MeV}$. The shaded regions correspond to dipole fits, with a magnetic charge radius of 0.78(32) fm for the proton and 0.81(25) fm for the neutron.

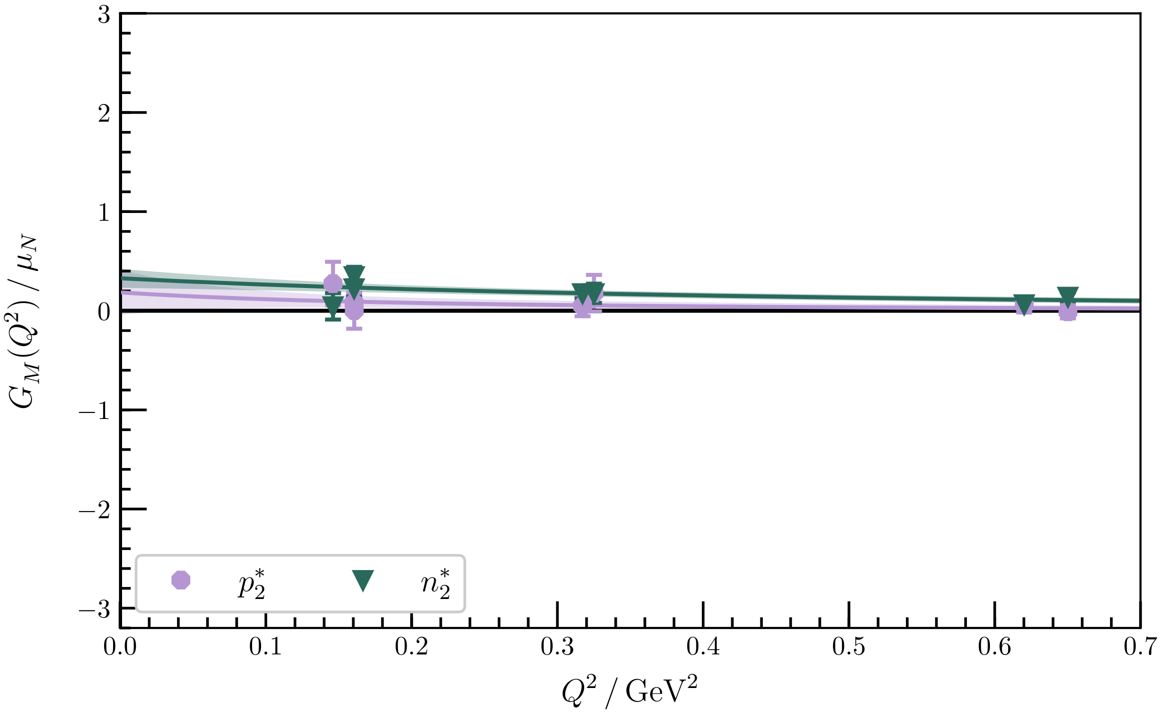

Figure D.68: $G_M(Q^2)$ for the second negative-parity excitations of the excited proton and neutron at $m_\pi = 411\,\text{MeV}$. The shaded regions correspond to dipole fits to the form factors, with a magnetic charge radius of 1.1(9) fm for the proton and 0.73(19) fm for the neutron.

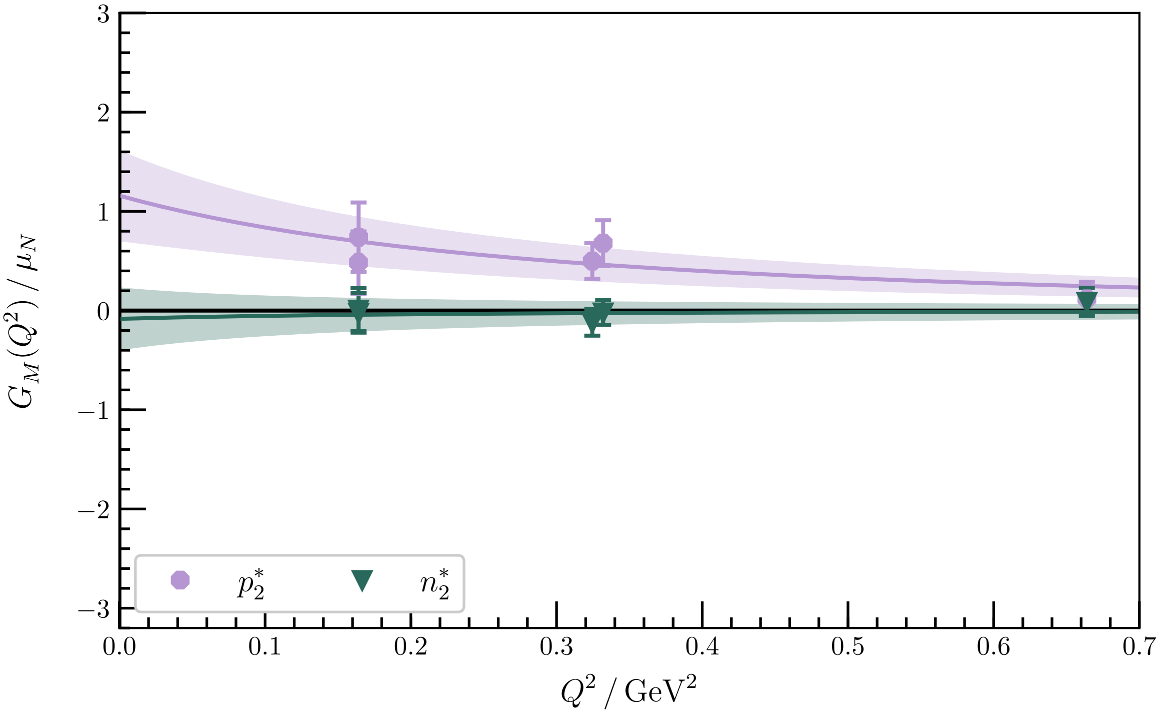

Figure D.69: $G_M(Q^2)$ for the second negative-parity excitations of the proton and neutron at $m_\pi = 296\,\mathrm{MeV}$. The shaded region corresponds to a dipole fit to the form factor, with a magnetic charge radius of 0.90(17) fm for the proton and 1.1(24) fm for the neutron.

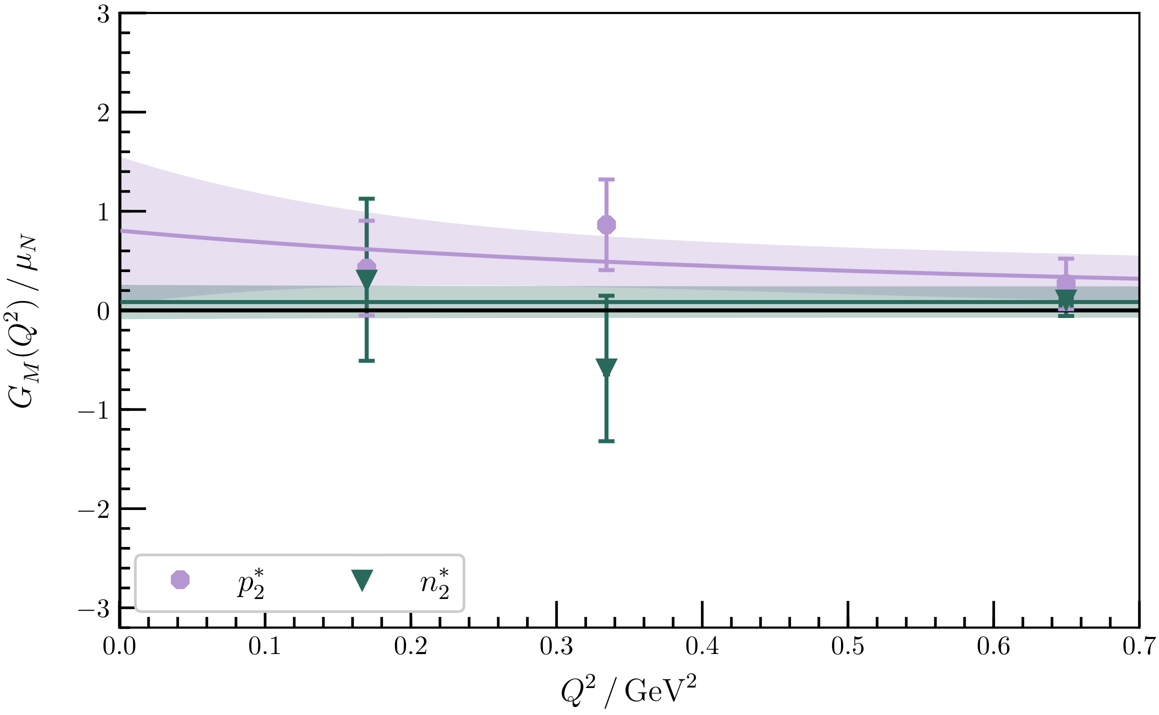

Figure D.70: $G_M(Q^2)$ for the second negative-parity excitations of the proton and neutron at $m_\pi = 156\,\mathrm{MeV}$. The shaded region corresponds to a dipole fit to the form factor, with a magnetic charge radius of 0.6(6) fm for the proton and 0.0(5) fm for the neutron.

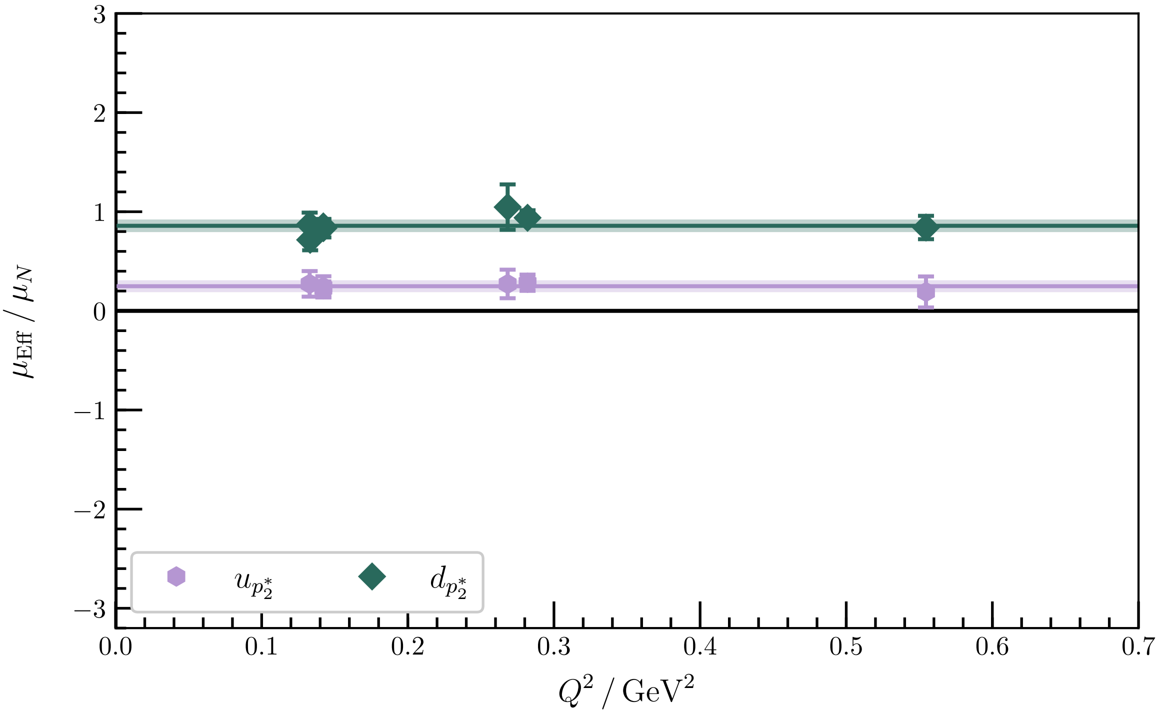

Figure D.71: $\mu_{\mathrm{Eff}}$ for the second negative-parity excitation at $m_\pi = 702\,\mathrm{MeV}$. The shaded bands are constant fits to the effective magnetic moment that have reasonable agreement with the data, and correspond to magnetic moment contributions of 0.25(6) $\mu_N$ for the doubly represented quark and 0.86(6) $\mu_N$ for the singly represented quark.

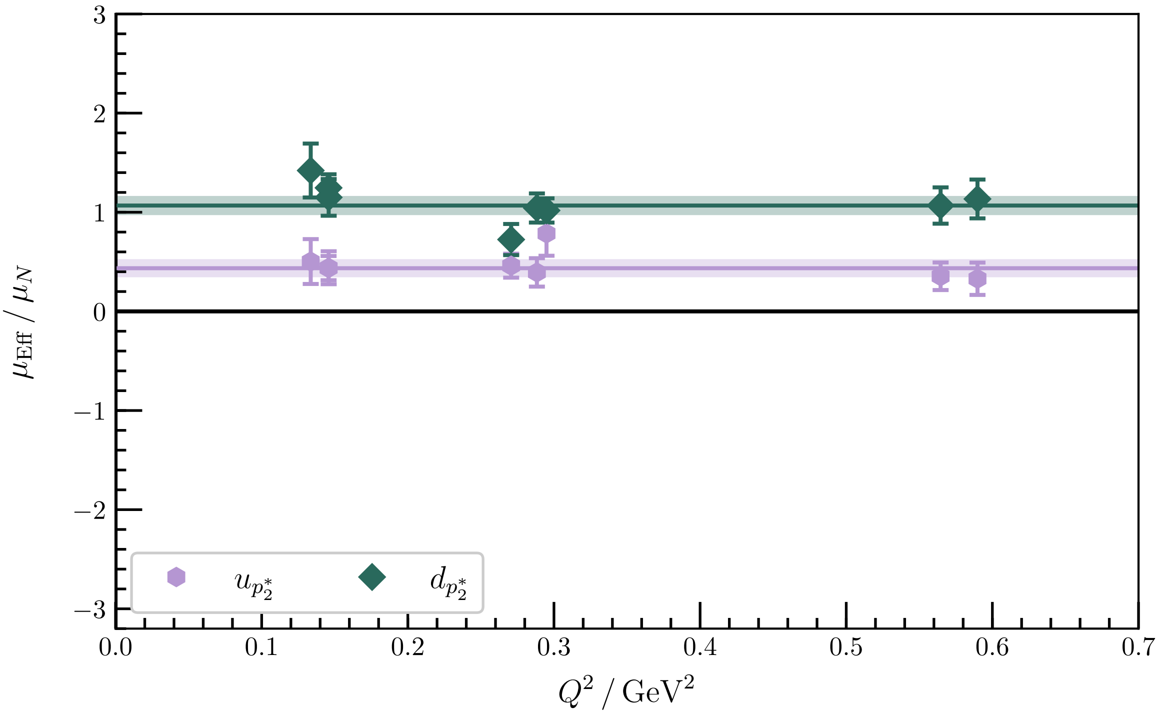

Figure D.72: $\mu_{\mathrm{Eff}}$ for the second negative-parity excitation at $m_\pi = 570\,\mathrm{MeV}$. The shaded bands are constant fits to the effective magnetic moment that have reasonable agreement with the data, and correspond to magnetic moment contributions of 0.44(9) $\mu_N$ for the doubly represented quark and 1.07(10) $\mu_N$ for the singly represented quark.

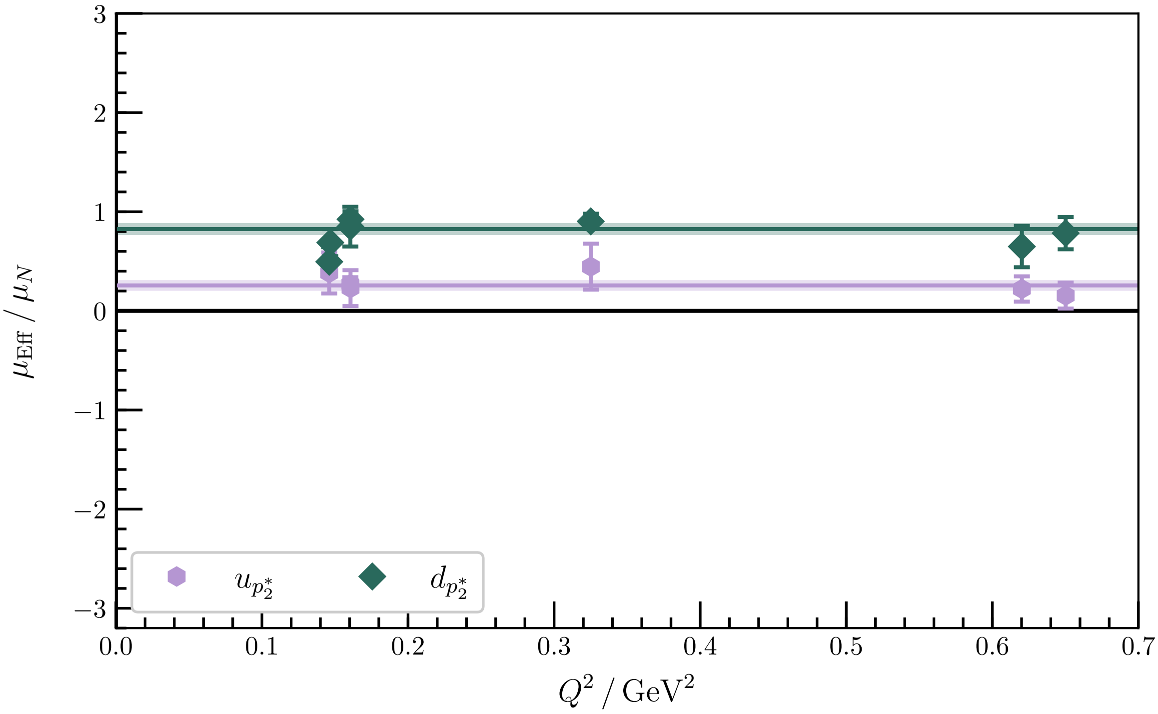

Figure D.73: $\mu_{\mathrm{Eff}}$ for the second negative-parity excitation at $m_\pi = 411\,\mathrm{MeV}$. The shaded bands are constant fits to the effective magnetic moment that have reasonable agreement with the data, and correspond to magnetic moment contributions of 0.26(5) $\mu_N$ for the doubly represented quark and 0.83(6) $\mu_N$ for the singly represented quark.

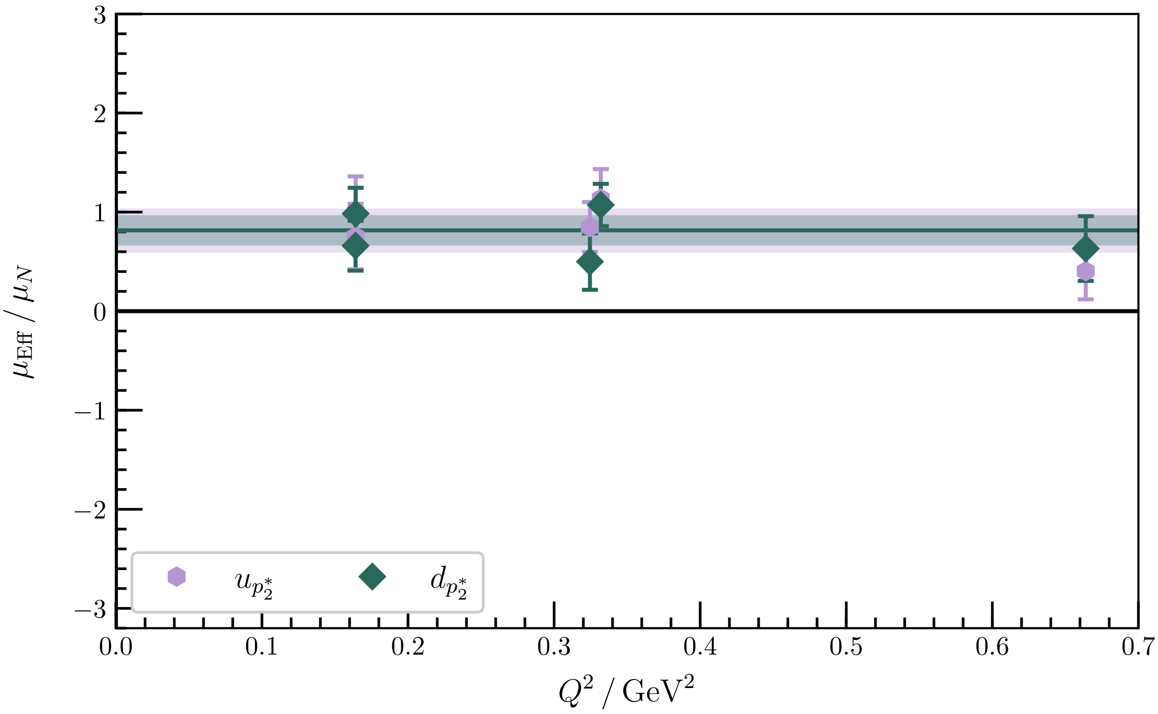

Figure D.74: $\mu_{\mathrm{Eff}}$ for the second negative-parity excitation at $m_\pi = 296\,\mathrm{MeV}$. The shaded bands are constant fits to the effective magnetic moment that have reasonable agreement with the data, and correspond to magnetic moment contributions of 0.81(22) $\mu_N$ for the doubly represented quark and 0.82(15) $\mu_N$ for the singly represented quark.

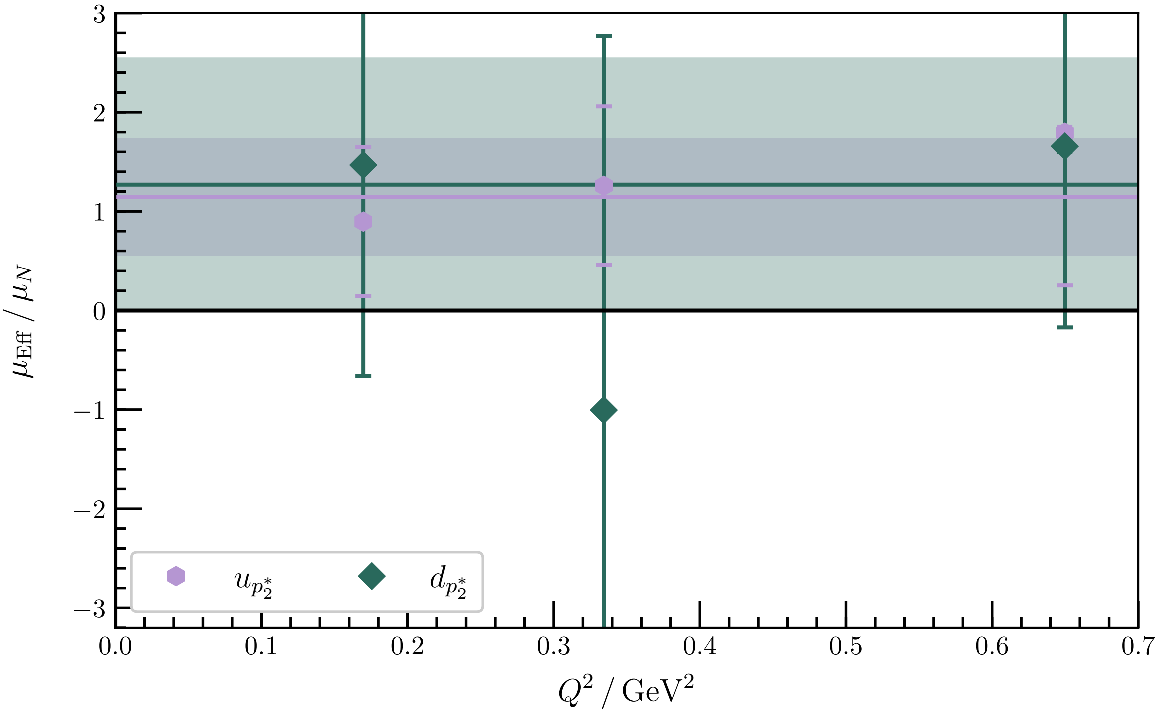

Figure D.75: $\mu_{\mathrm{Eff}}$ for the second negative-parity excitation at $m_\pi = 156\,\mathrm{MeV}$. The shaded bands are constant fits to the effective magnetic moment. These fits are poorly constrained due to the large statistical errors in the extracted values.

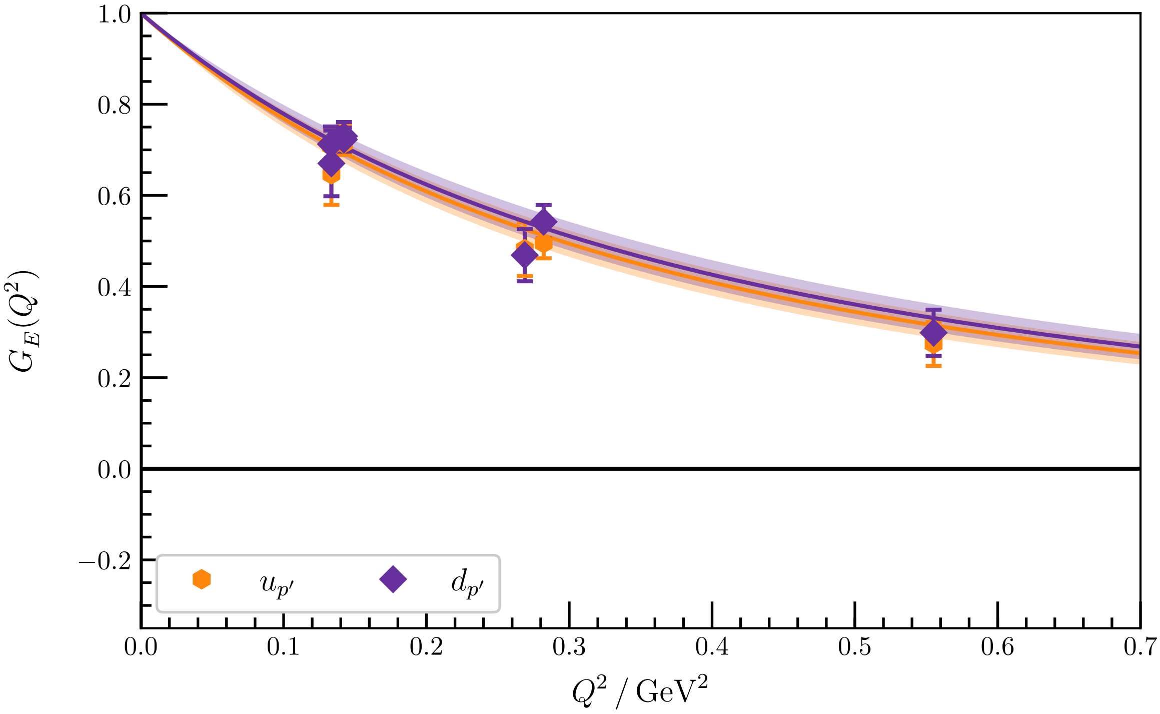

Figure D.76: $G_E(Q^2)$ for the first positive parity excitation at $m_\pi = 702\,\mathrm{MeV}$. The shaded regions are dipole fits to the form factor, with lines indicating the central values.

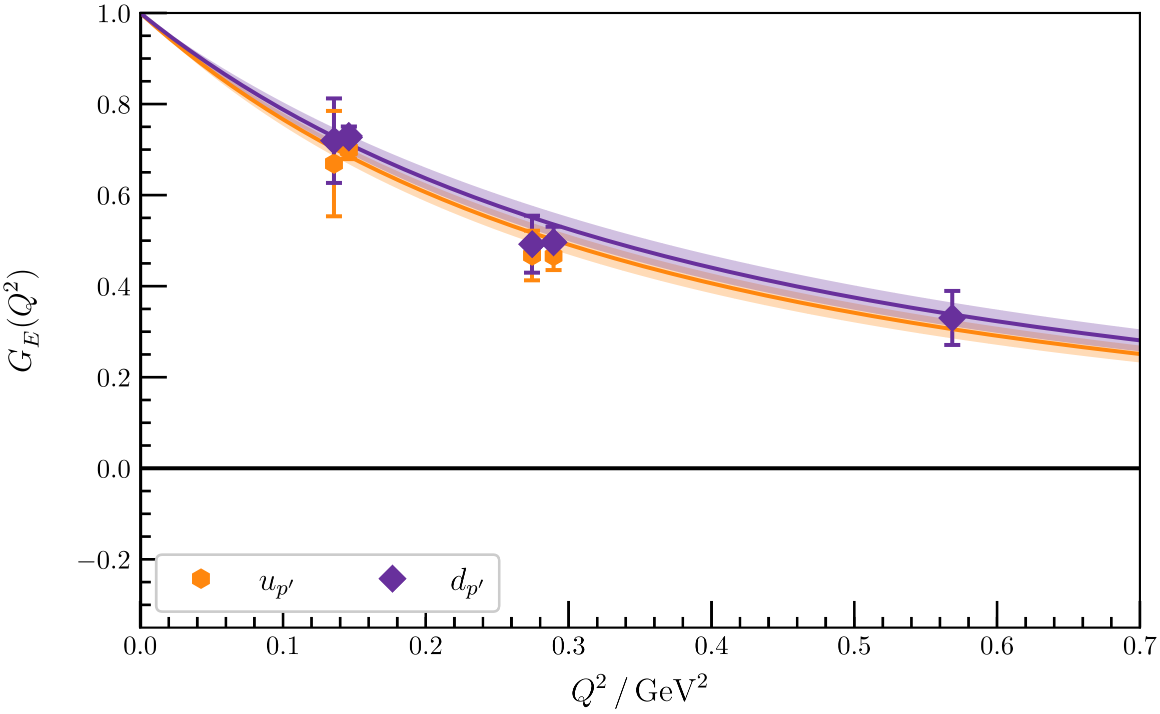

Figure D.77: $G_E(Q^2)$ for the first positive parity excitation at $m_\pi = 570\,\text{MeV}$. The shaded regions are dipole fits to the form factor, with lines indicating the central values.

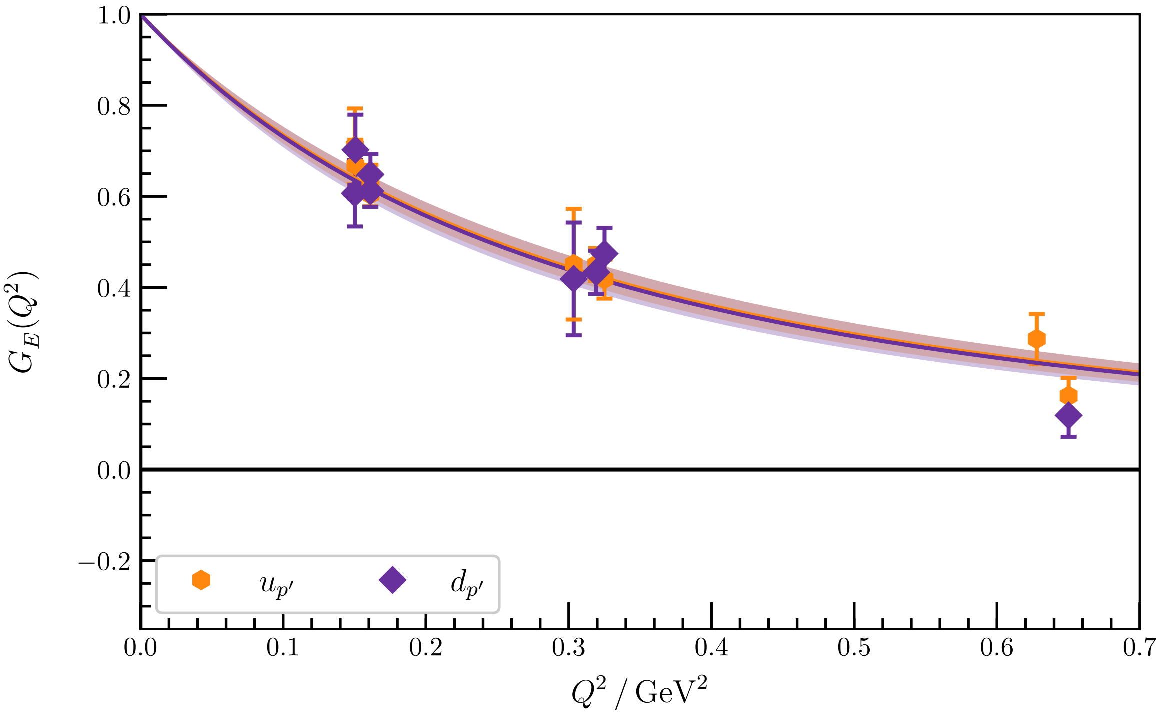

Figure D.78: $G_E(Q^2)$ for the first positive parity excitation at $m_\pi = 411\,\text{MeV}$. The shaded regions are dipole fits to the form factor, with lines indicating the central values.

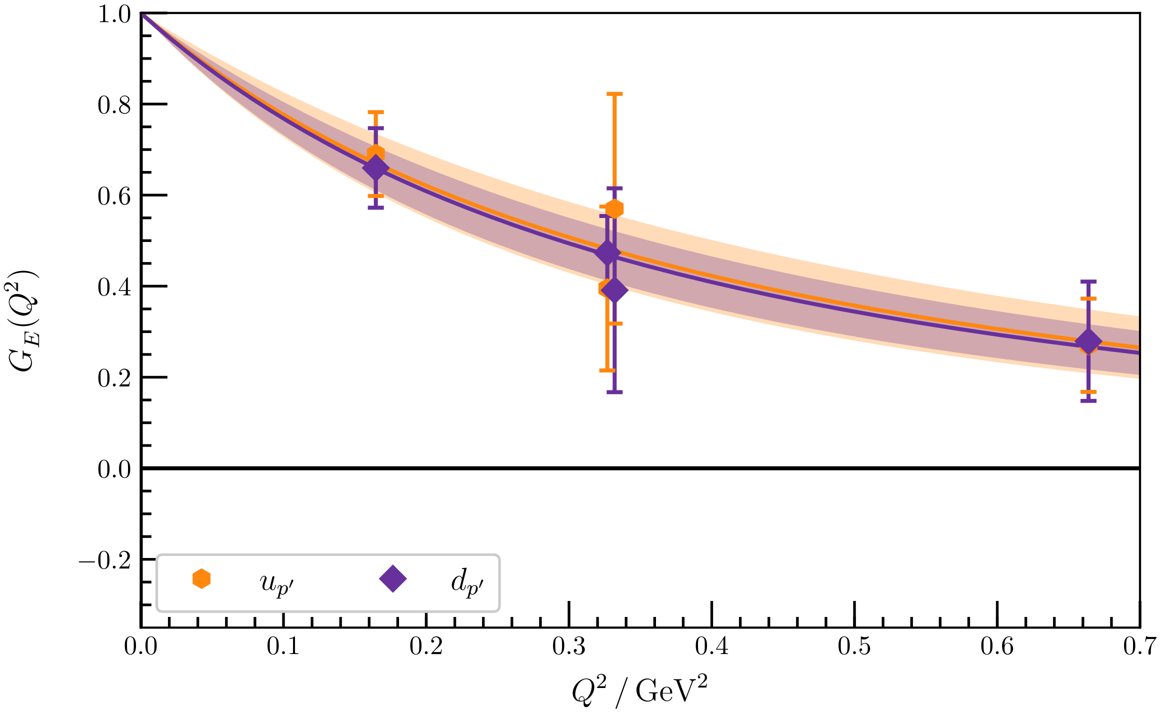

Figure D.79: $G_E(Q^2)$ for the first positive parity excitation at $m_\pi = 296\,\mathrm{MeV}$. The shaded regions are dipole fits to the form factor, with lines indicating the central values.

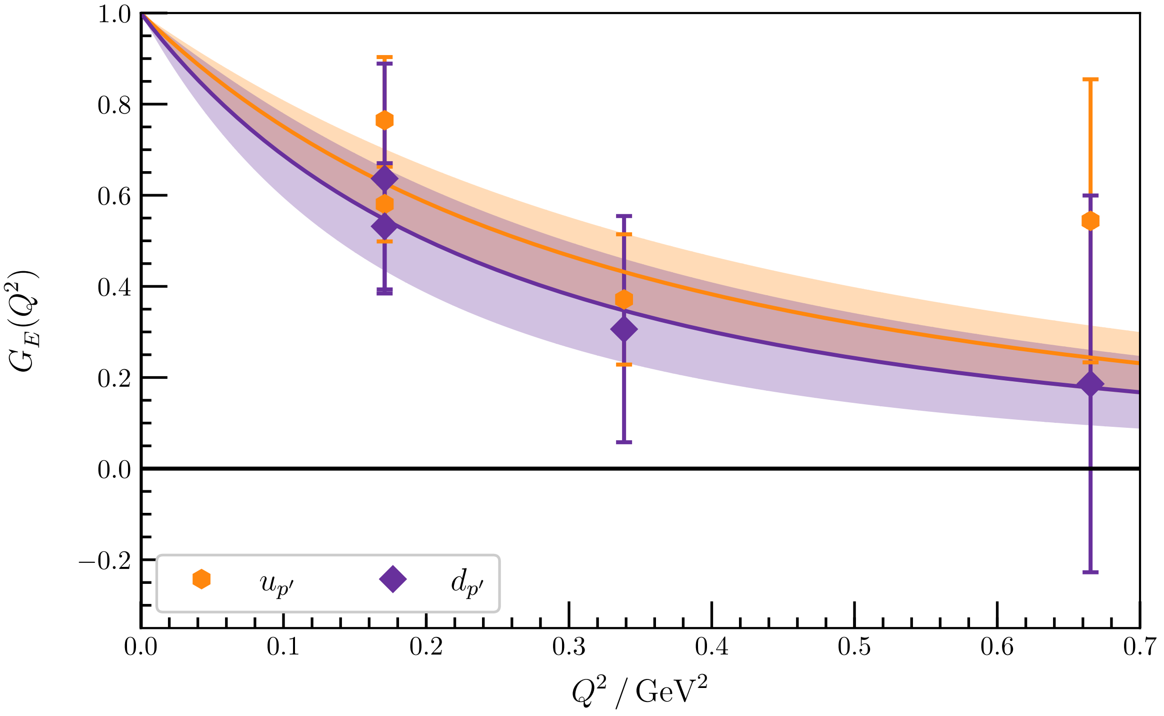

Figure D.80: $G_E(Q^2)$ for the first positive parity excitation at $m_\pi = 156\,\mathrm{MeV}$. The shaded regions are dipole fits to the form factor, with lines indicating the central values.

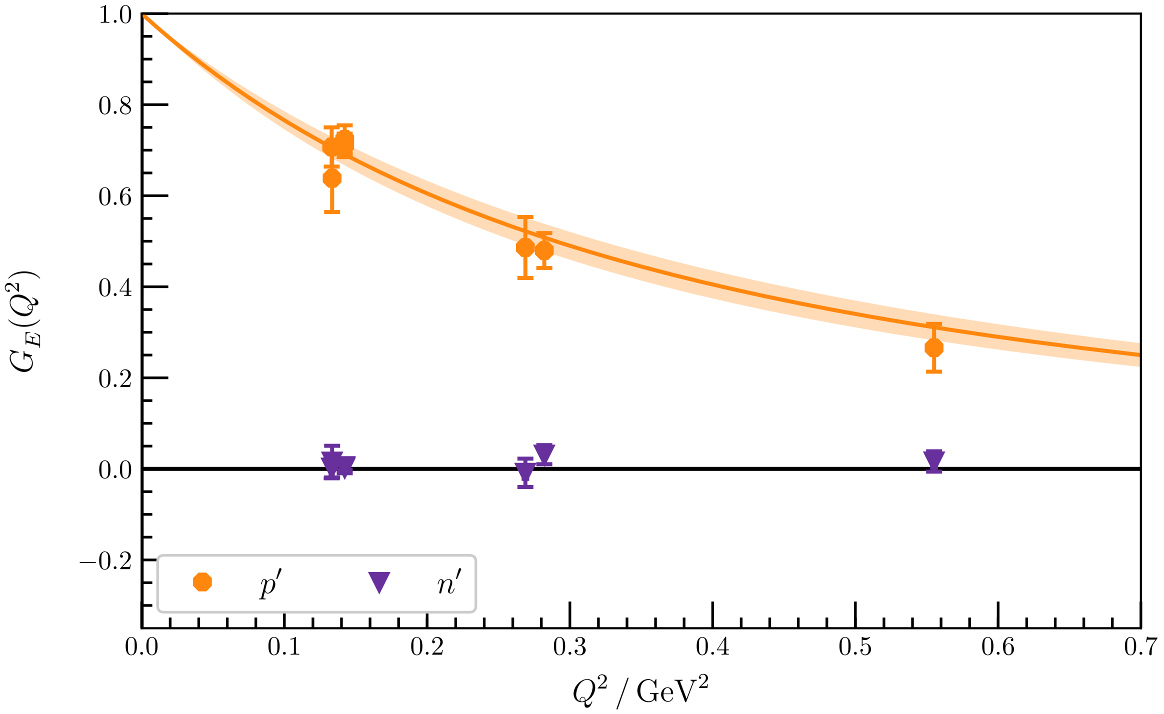

Figure D.81: $G_E(Q^2)$ for the first positive-parity excitations of the proton and neutron at $m_\pi = 702$ MeV. These are obtained by taking the appropriate linear combination of the individual quark flavour contributions. The shaded region corresponds to a dipole fit to the form factor for the proton, with a charge radius of 0.82(4) fm.

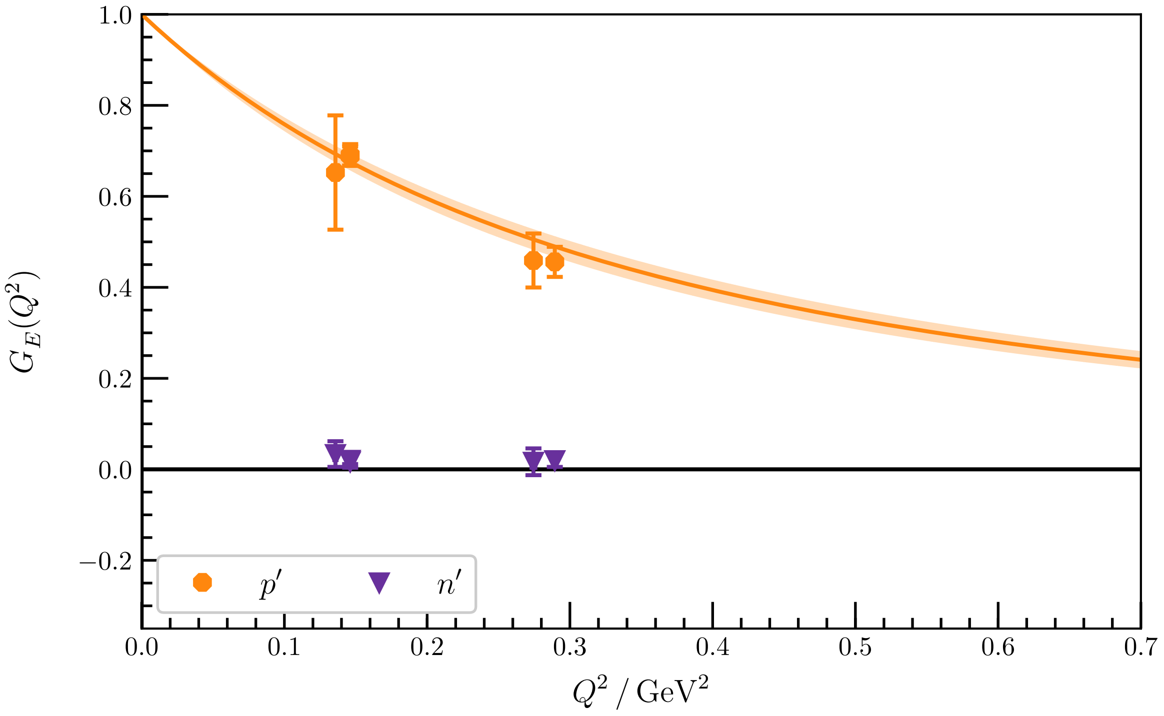

Figure D.82: $G_E(Q^2)$ for the first positive-parity excitations of the proton and neutron at $m_\pi = 570$ MeV. The shaded region corresponds to a dipole fit to the form factor for the proton, with a charge radius of 0.83(3) fm.

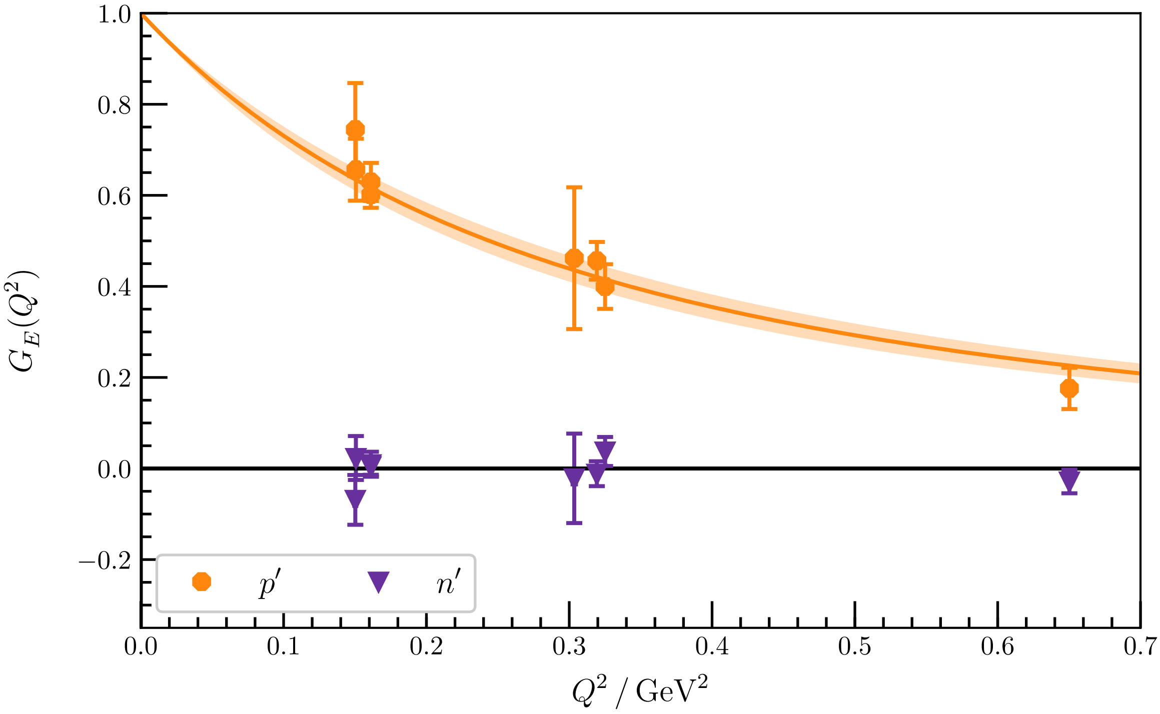

Figure D.83: $G_E(Q^2)$ for the first positive-parity excitations of the proton and neutron at $m_\pi = 411\,\mathrm{MeV}$. The shaded region corresponds to a dipole fit to the form factor for the proton, with a charge radius of 0.89(4) fm.

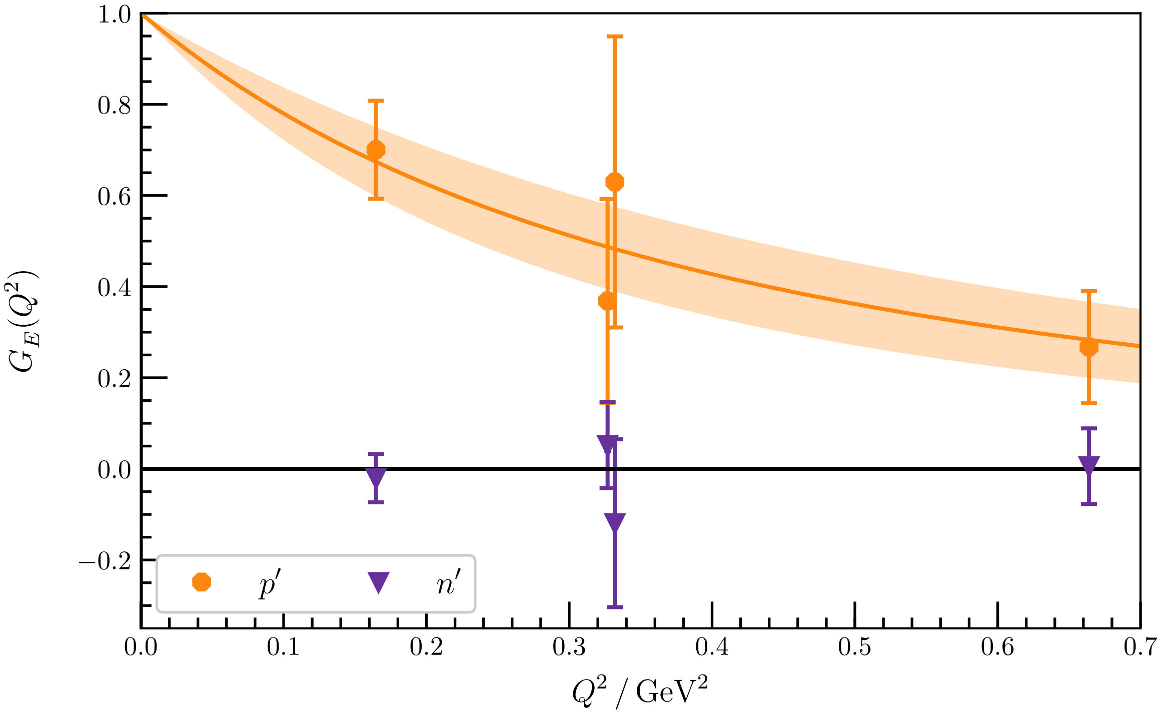

Figure D.84: $G_E(Q^2)$ for the first positive-parity excitations of the proton and neutron at $m_\pi = 296\,\mathrm{MeV}$. The shaded region corresponds to a dipole fit to the form factor, with a charge radius of 0.79(12) fm.

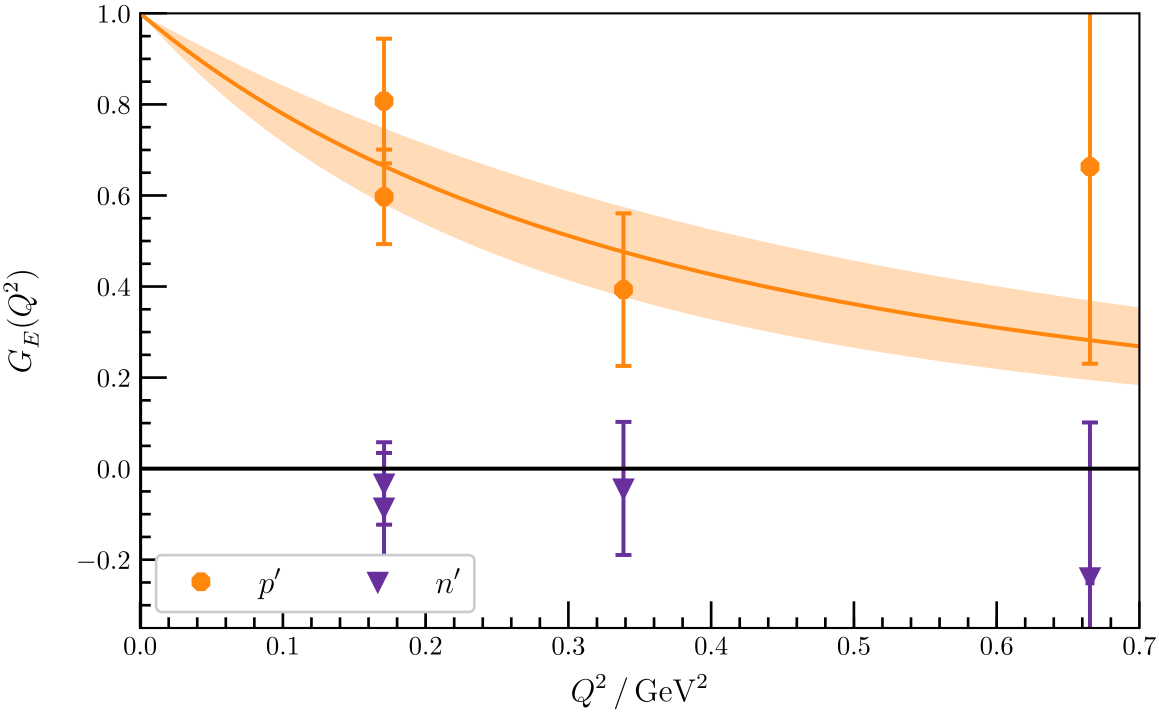

Figure D.85: $G_E(Q^2)$ for the first positive-parity excitations of the proton and neutron at $m_\pi = 156\,\text{MeV}$. The shaded region corresponds to a dipole fit to the form factor, with a charge radius of 0.79(13) fm.

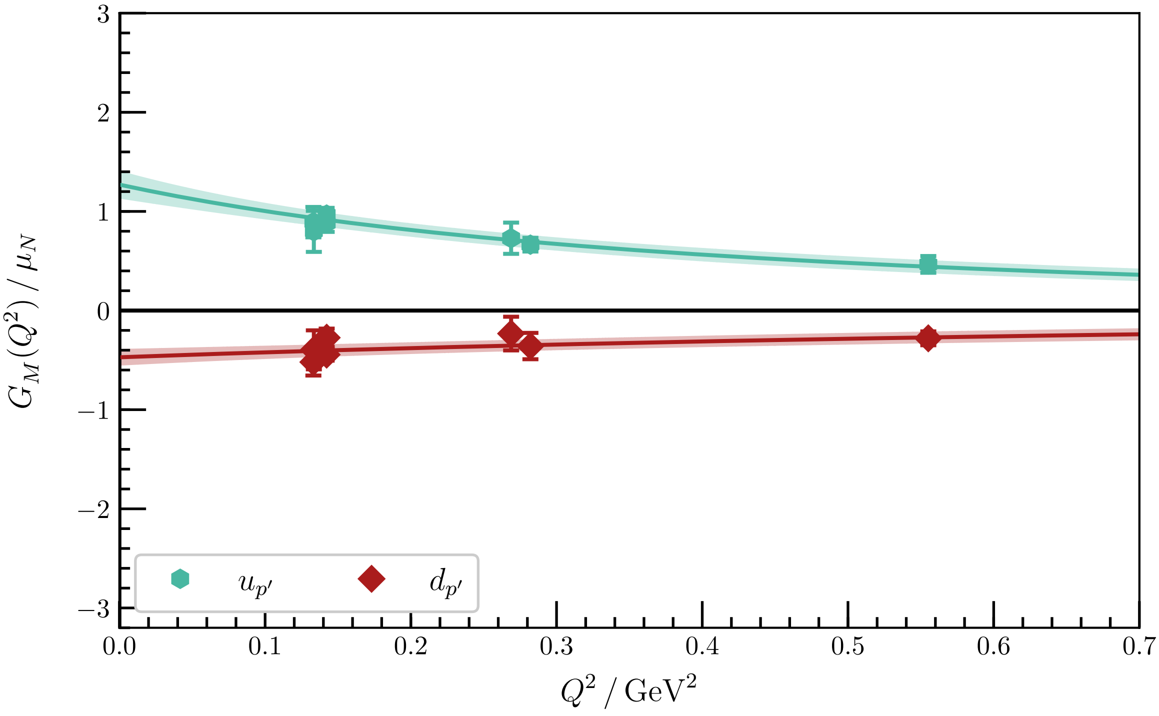

Figure D.86: Quark-flavour contributions to $G_M(Q^2)$ for the first positive-parity excitation at $m_\pi = 702\,\text{MeV}$. The shaded regions are dipole fits to the form factor.

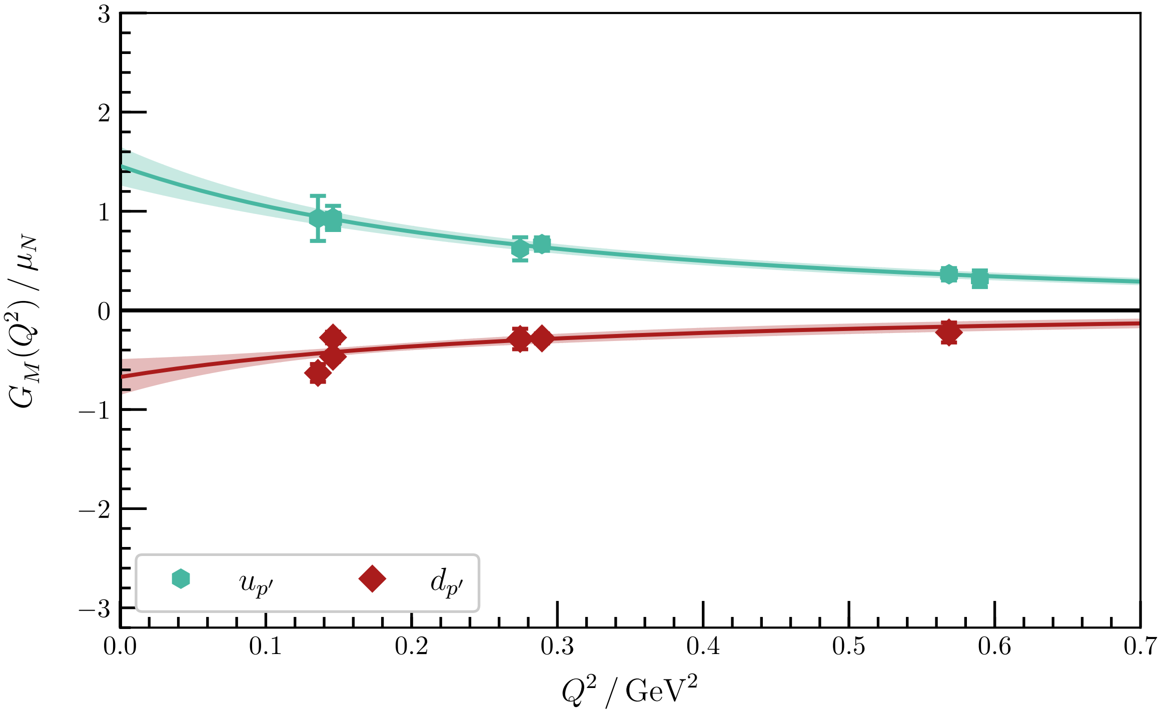

Figure D.87: Quark-flavour contributions to $G_M(Q^2)$ for the first positive-parity excitation at $m_\pi = 570\,\mathrm{MeV}$. The shaded regions are dipole fits to the form factor.

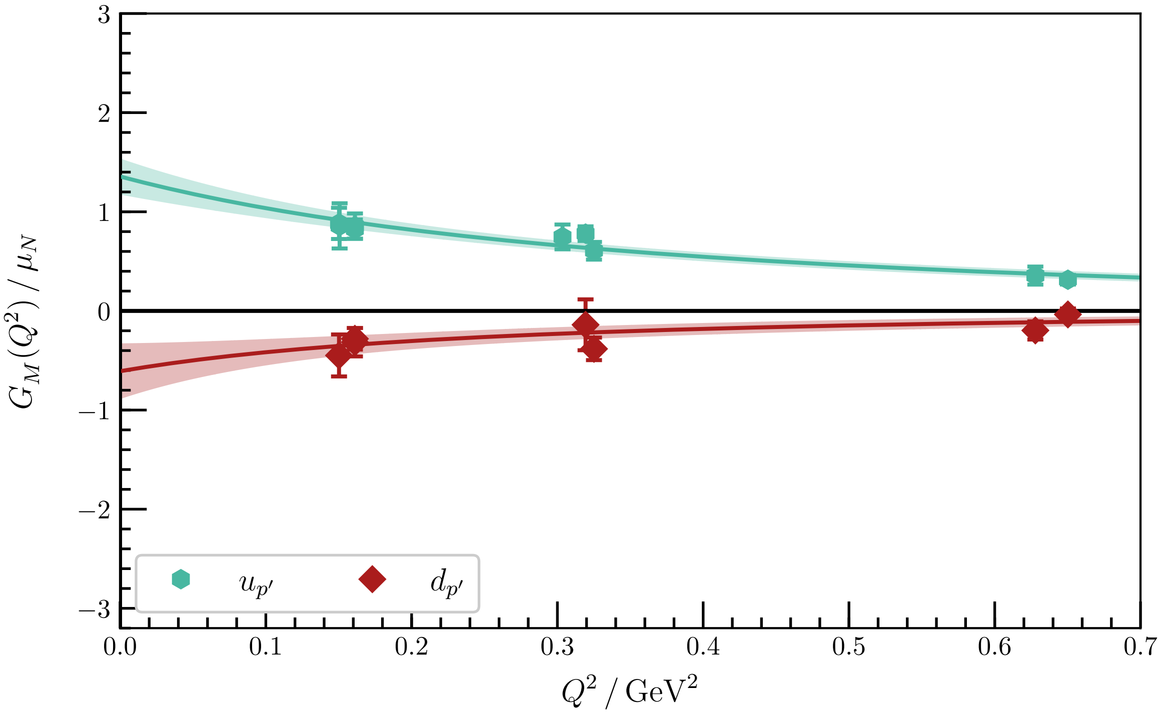

Figure D.88: Quark-flavour contributions to $G_M(Q^2)$ for the first positive-parity excitation at $m_\pi = 411\,\mathrm{MeV}$. The shaded regions are dipole fits to the form factor.

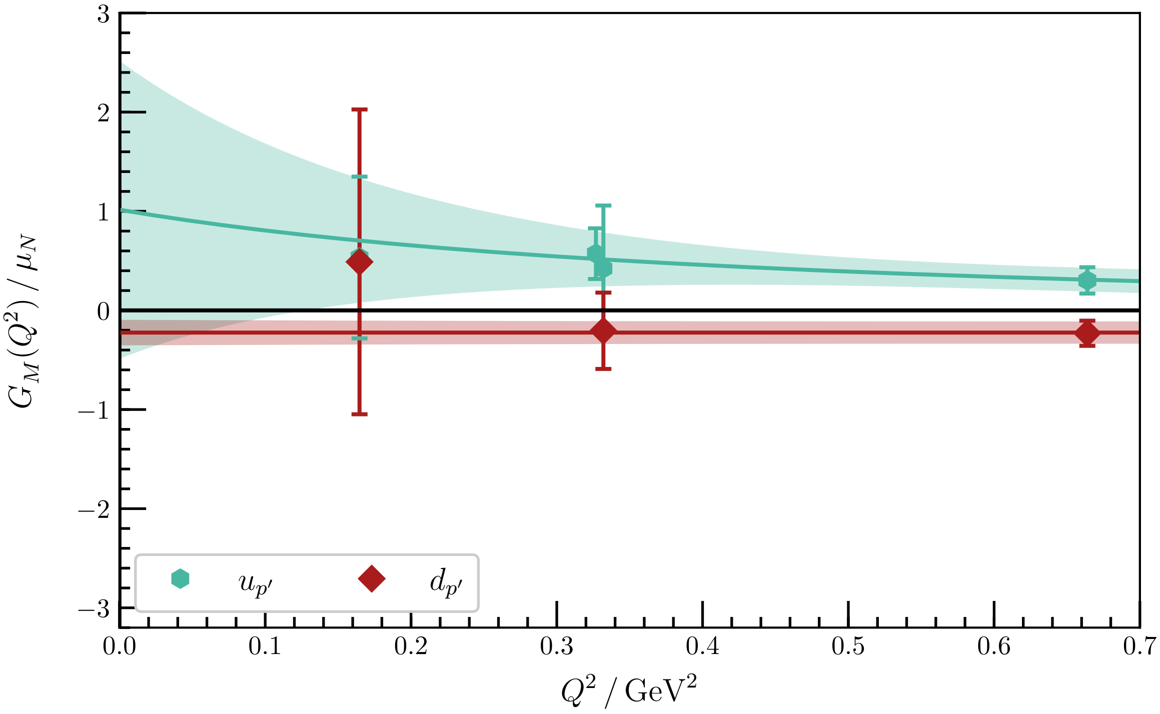

Figure D.89: Quark-flavour contributions to $G_M(Q^2)$ for the first positive-parity excitation at $m_\pi = 296\,\text{MeV}$. The shaded regions are dipole fits to the form factor.

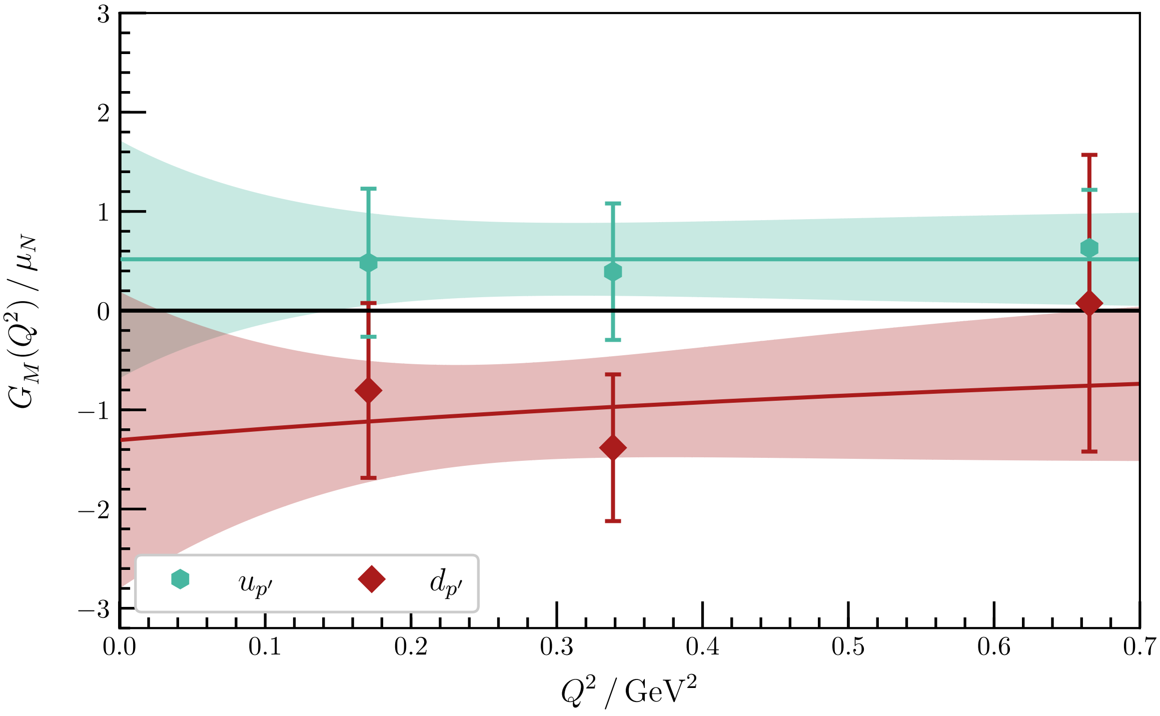

Figure D.90: Quark-flavour contributions to $G_M(Q^2)$ for the first positive-parity excitation at $m_\pi = 156\,\text{MeV}$. The shaded regions are dipole fits to the form factor.

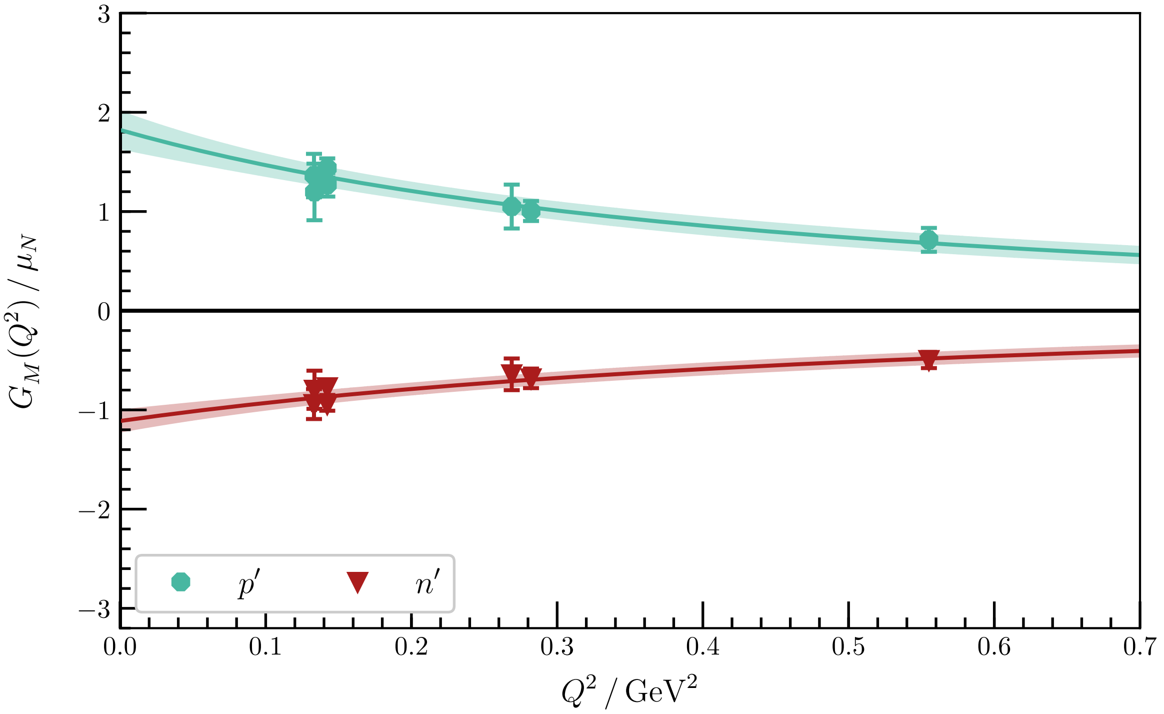

Figure D.91: $G_M(Q^2)$ for the first positive-parity excitations of the proton and neutron at $m_\pi = 702\,\mathrm{MeV}$. The shaded region corresponds to a dipole fit to the form factor, with a magnetic charge radius of 0.73(9) fm for the proton and 0.66(9) fm for the neutron.

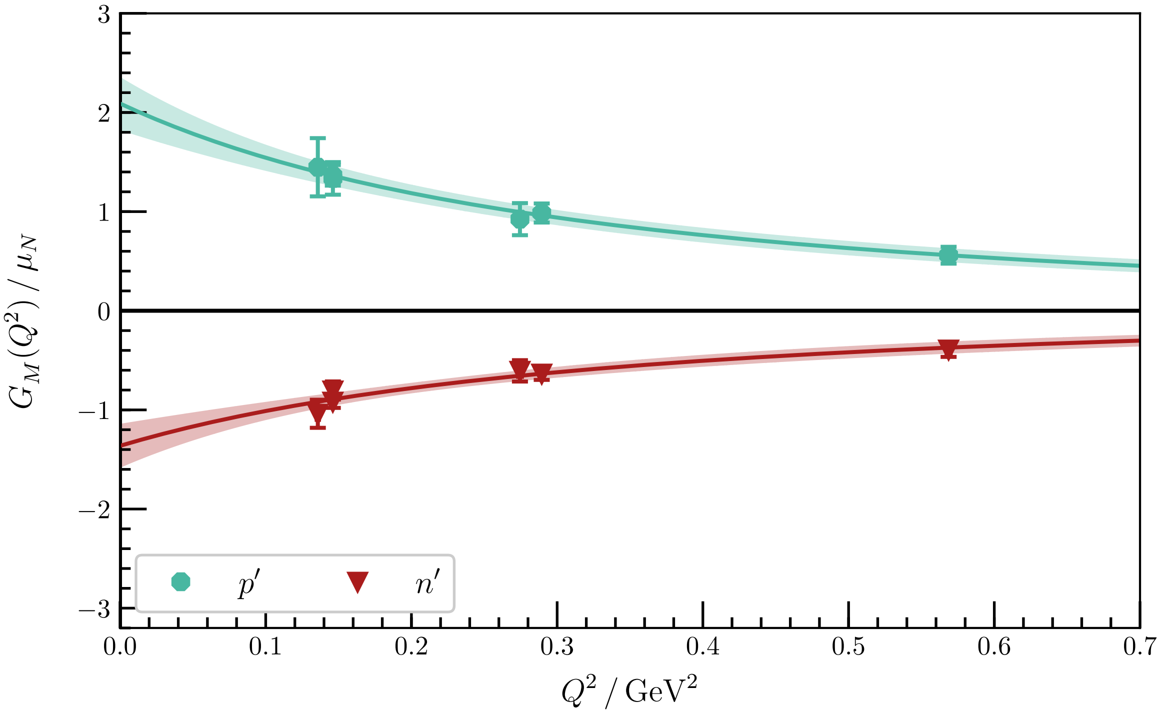

Figure D.92: $G_M(Q^2)$ for the first positive-parity excitations of the proton and neutron at $m_\pi = 570\,\mathrm{MeV}$. The shaded region corresponds to a dipole fit to the form factor, with a magnetic charge radius of 0.88(9) fm for the proton and 0.87(14) fm for the neutron.

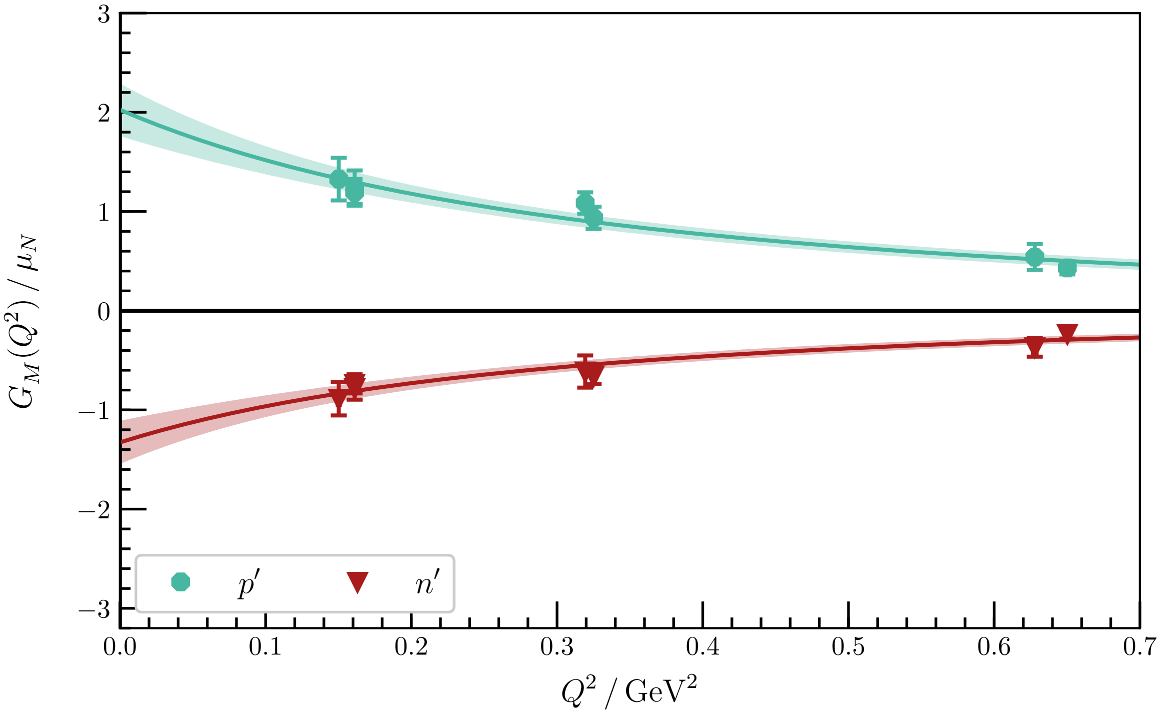

Figure D.93: $G_M(Q^2)$ for the first positive-parity excitations of the proton and neutron at $m_\pi = 411\,\mathrm{MeV}$. The shaded region corresponds to a dipole fit to the form factor, with a magnetic charge radius of 0.85(8) fm for the proton excitation and 0.90(10) fm for the neutron excitation.

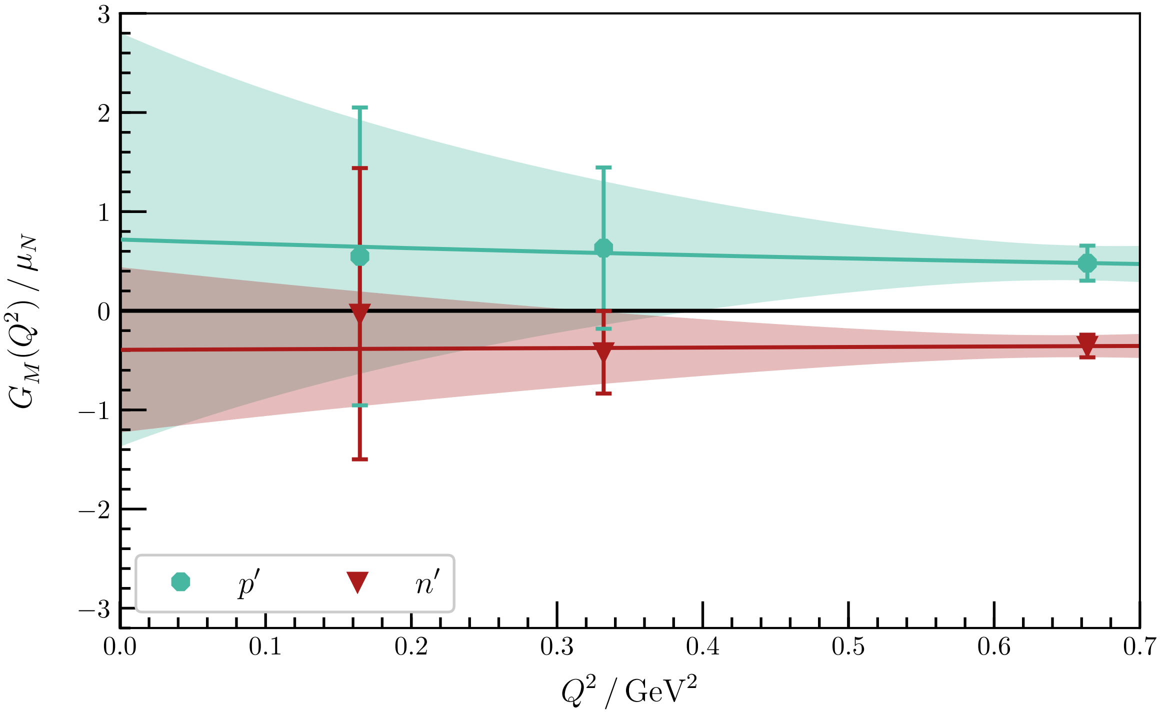

Figure D.94: $G_M(Q^2)$ for the first positive-parity excitations of the proton and neutron at $m_\pi = 296\,\mathrm{MeV}$. The shaded region corresponds to a dipole fit to the form factor. The results are too noisy to properly constrain the fit.

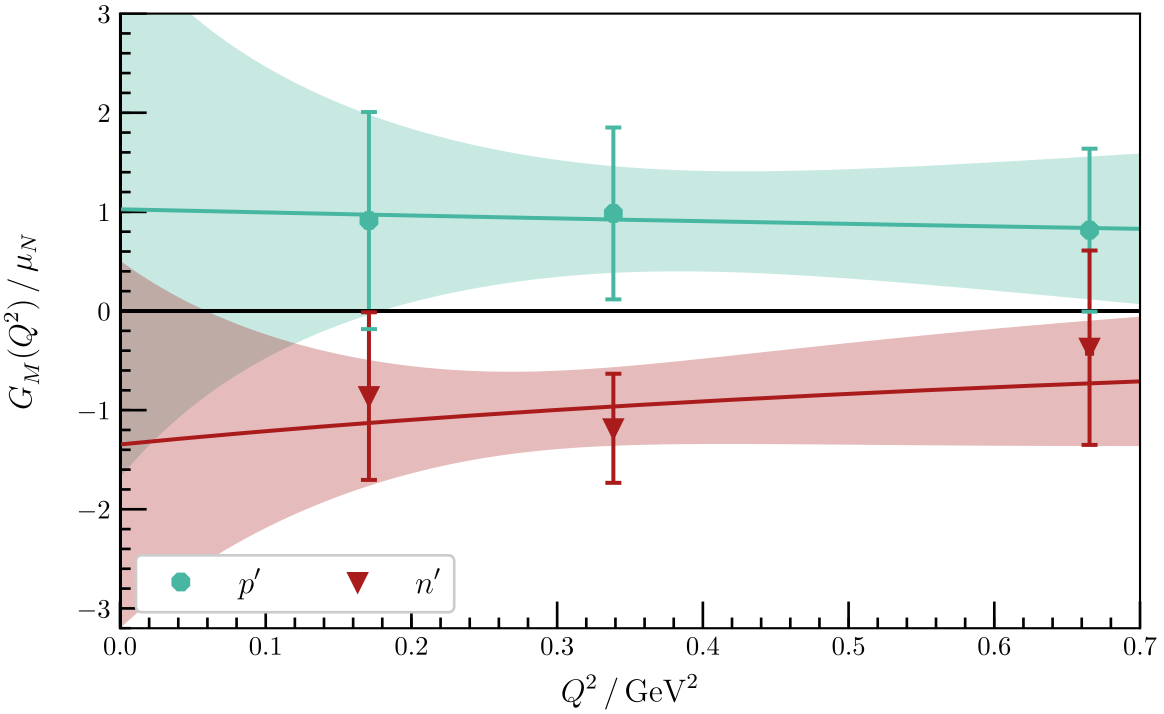

Figure D.95: $G_M(Q^2)$ for the first positive-parity excitations of the proton and neutron at $m_\pi = 156\,\mathrm{MeV}$. The shaded region corresponds to a dipole fit to the form factor. The results are too noisy to properly constrain the fit.

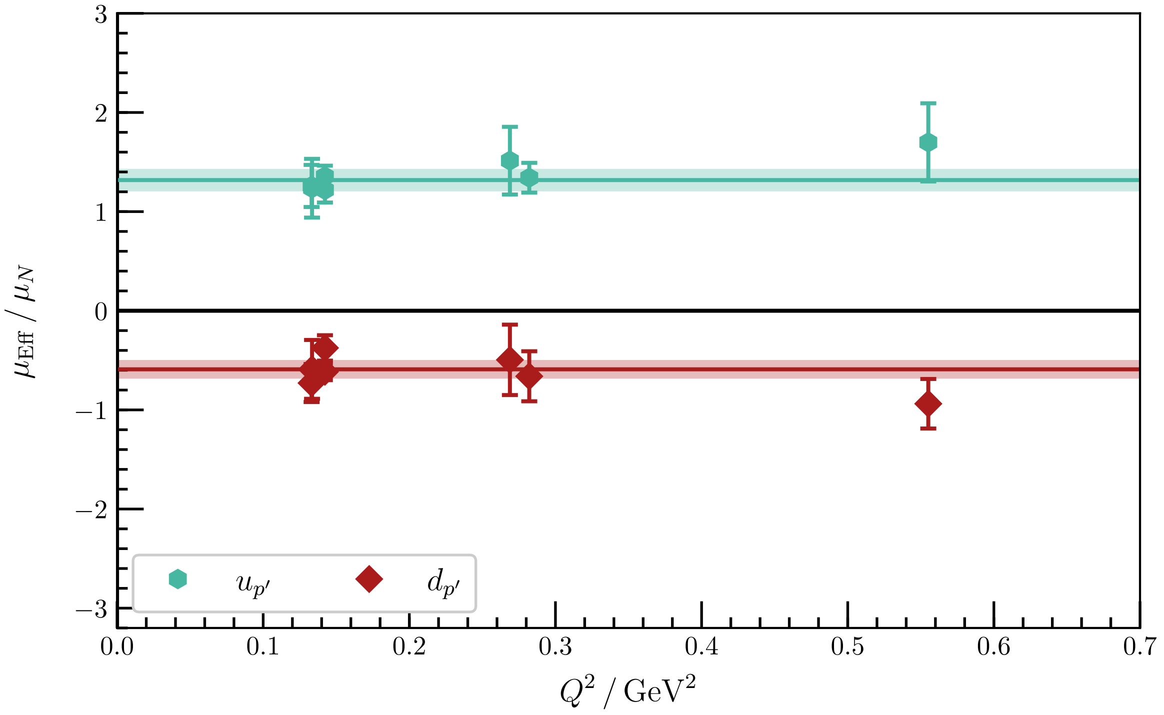

Figure D.96: $\mu_{\mathrm{Eff}}$ for the first positive-parity excitation at $m_\pi = 702\,\mathrm{MeV}$. The shaded bands are constant fits to the effective magnetic moment that have reasonable agreement with the data, and correspond to magnetic moment contributions of 1.32(11) $\mu_N$ for the doubly represented quark and $-0.59(9)$ $\mu_N$ for the singly represented quark.

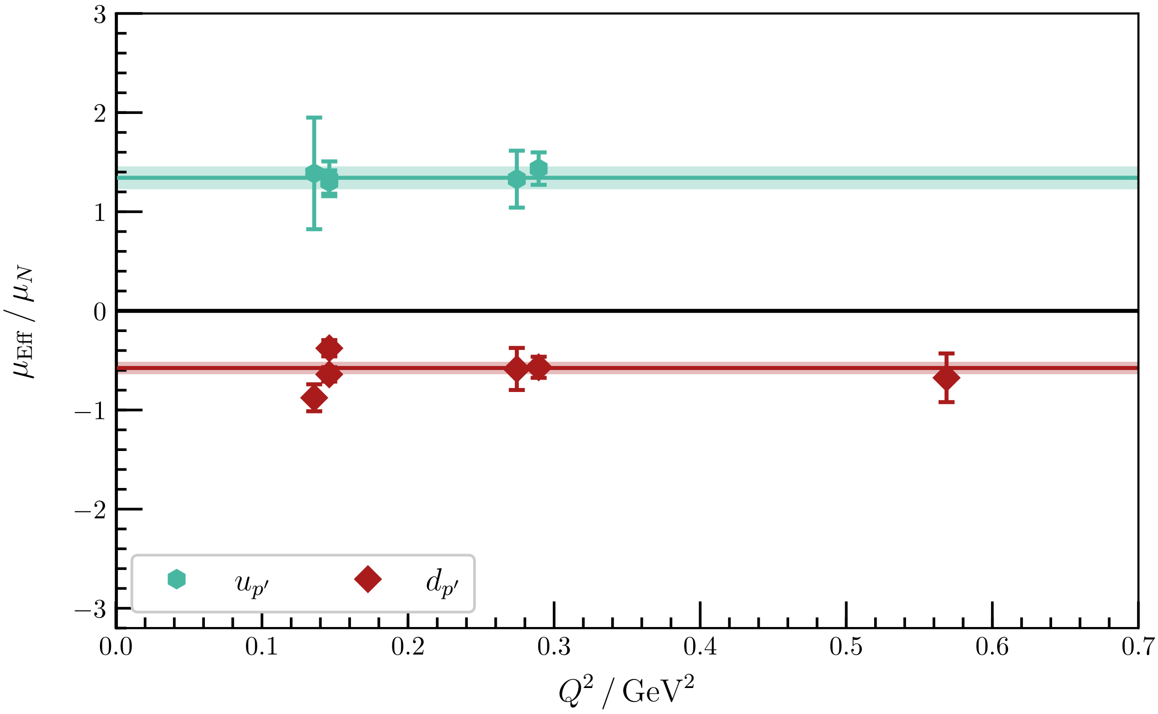

Figure D.97: $\mu_{\mathrm{Eff}}$ for the first positive-parity excitation at $m_\pi = 570\,\mathrm{MeV}$. The shaded bands are constant fits to the effective magnetic moment that have reasonable agreement with the data, and correspond to magnetic moment contributions of 1.34(12) $\mu_N$ for the doubly represented quark and $-0.58(6)$ $\mu_N$ for the singly represented quark.

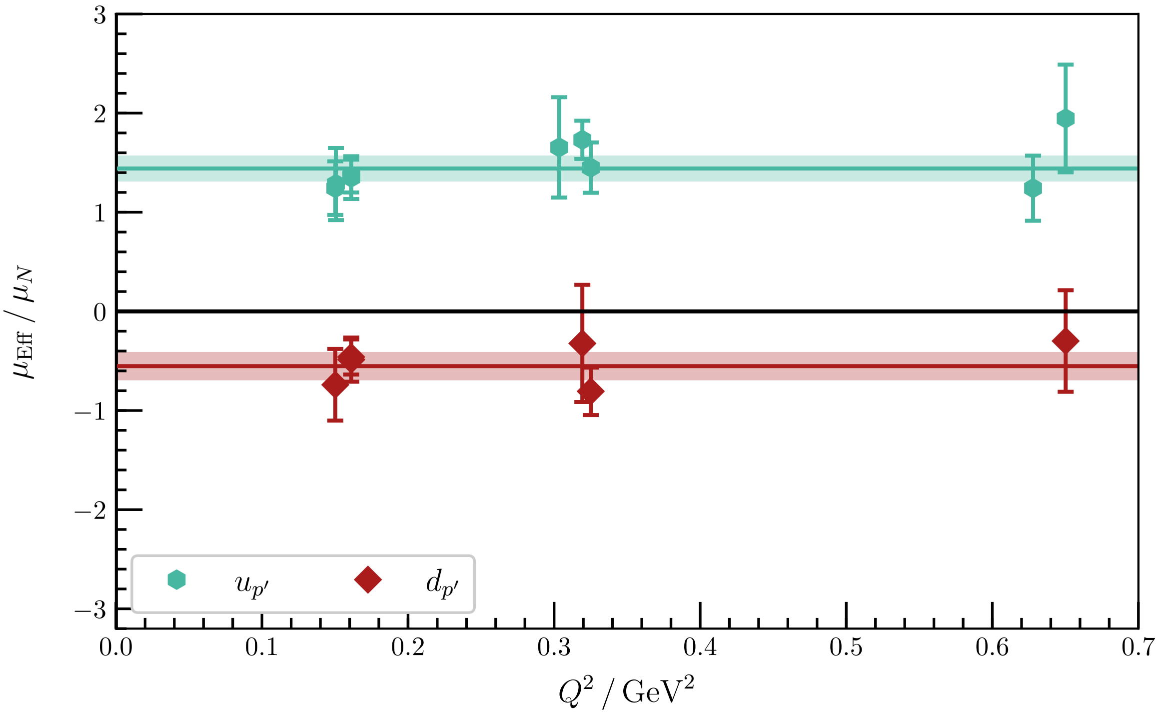

Figure D.98: $\mu_{\mathrm{Eff}}$ for the first positive-parity excitation at $m_\pi = 411\,\mathrm{MeV}$. The shaded bands are constant fits to the effective magnetic moment that have reasonable agreement with the data, and correspond to magnetic moment contributions of 1.44(13) $\mu_N$ for the doubly represented quark and $-0.55(14)$ $\mu_N$ for the singly represented quark.

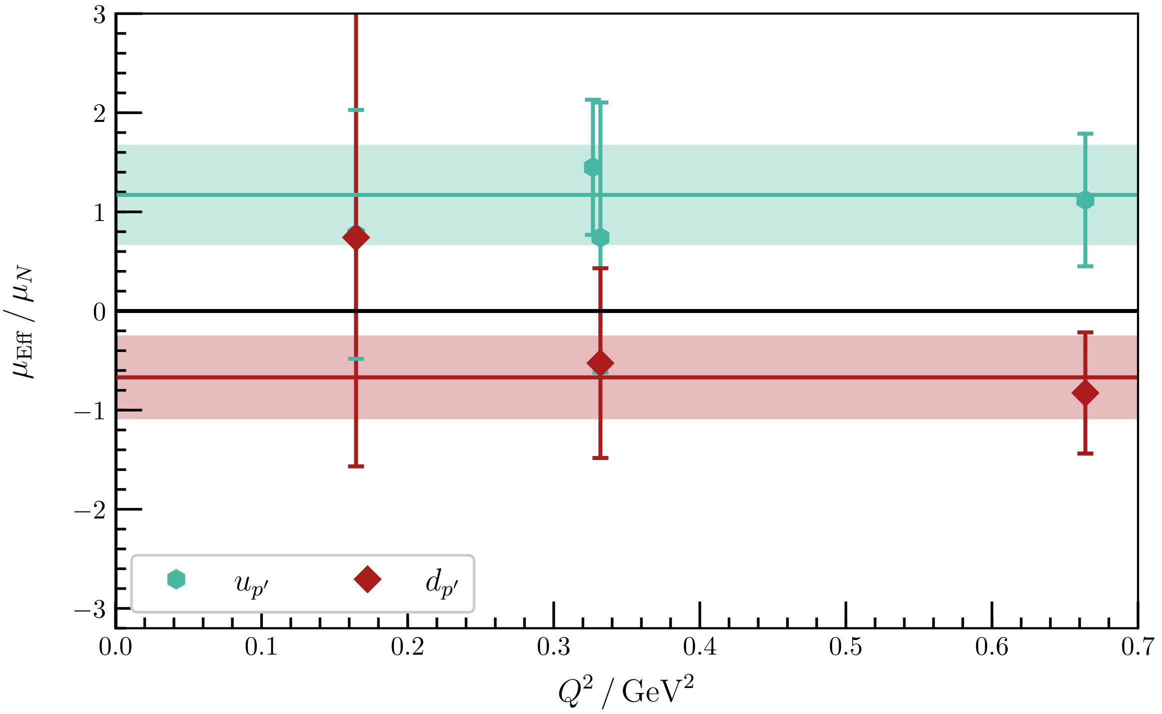

Figure D.99: $\mu_{\mathrm{Eff}}$ for the first positive-parity excitation at $m_\pi = 296\,\mathrm{MeV}$. The shaded bands are constant fits to the effective magnetic moment that have reasonable agreement with the data, and correspond to magnetic moment contributions of 1.2(5) $\mu_N$ for the doubly represented quark and $-0.7(4)$ $\mu_N$ for the singly represented quark.

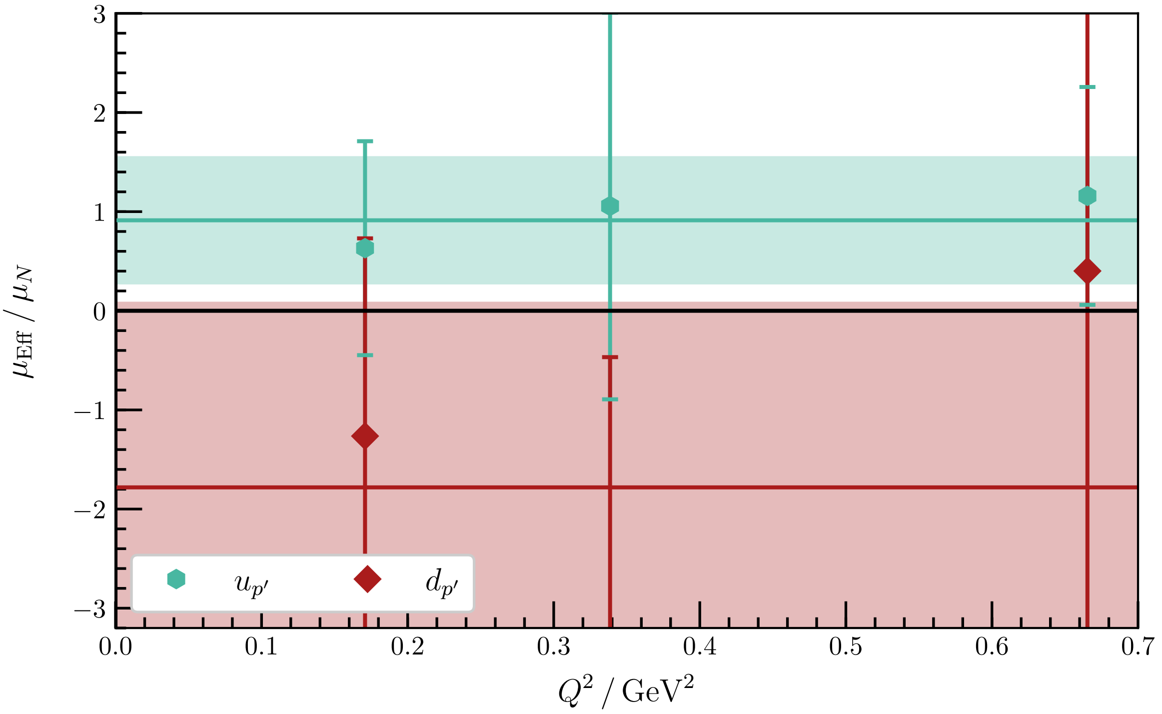

Figure D.100: $\mu_{\mathrm{Eff}}$ for the first positive-parity excitation at $m_\pi = 156\,\mathrm{MeV}$. The shaded bands are constant fits to the effective magnetic moment. These fits are poorly constrained due to the large statistical errors in the extracted values.

# Appendix E

# Papers by the Author

## Refereed Journal Publications

[1] A. L. Kiratidis, W. Kamleh, D. B. Leinweber, Z.-W. Liu, F. M. Stokes, and A. W. Thomas, *Search for low-lying lattice QCD eigenstates in the Roper regime*, Phys. Rev. D 95 (2017) 074507, [arXiv:1608.03051]

[2] Z.-W. Liu, W. Kamleh, D. B. Leinweber, F. M. Stokes, A. W. Thomas, and J.-J. Wu, *Hamiltonian effective field theory study of the* $\mathbf{N^*(1440)}$ *resonance in lattice QCD*, Phys. Rev. D 95 (2017) 034034, [arXiv:1607.04536]

[3] Z.-W. Liu, W. Kamleh, D. B. Leinweber, F. M. Stokes, A. W. Thomas, and J.-J. Wu, *Hamiltonian effective field theory study of the* $\mathbf{N^*(1535)}$ *resonance in lattice QCD*, Phys. Rev. Lett. 116 (2016) 082004, [arXiv:1512.00140]

[4] F. M. Stokes, W. Kamleh, D. B. Leinweber, M. S. Mahbub, B. J. Menadue, and B. J. Owen, *Parity-expanded variational analysis for nonzero momentum*, Phys. Rev. D 92 (2015) 114506, [arXiv:1302.4152]

[5] F. M. Stokes, W. Kamleh, and D. B. Leinweber, *Visualizations of coherent center domains in local Polyakov loops*, Annals Phys. 348 (2014) 341–361, [arXiv:1312.0991]

## Refereed Conference Proceedings

[1] A. L. Kiratidis, W. Kamleh, D. B. Leinweber, Z.-W. Liu, F. M. Stokes, and A. W. Thomas, *Spectroscopy with Local Multi-hadron Interpolators in Lattice QCD*, PoS INPC2016 (2017) 269, [arXiv:1704.08816]

[2] F. M. Stokes, W. Kamleh, D. B. Leinweber, and B. J. Owen, *Electromagnetic Form Factors of Nucleon Excitations in Lattice QCD*, PoS INPC2016 (2017) 263, [arXiv:1711.06568]

[3] Z.-W. Liu, J. M. M. Hall, W. Kamleh, D. B. Leinweber, F. M. Stokes, A. W. Thomas, and J.-J. Wu, *Study of Low-Lying Baryons with Hamiltonian Effective Field Theory*, PoS INPC2016 (2017) 288, [arXiv:1701.08582]

[4] F. M. Stokes, W. Kamleh, D. B. Leinweber, and B. J. Owen, *Electromagnetic Form Factors of Excited Nucleons via Parity-Expanded Variational Analysis*, PoS LATTICE2016 (2016) 161, [arXiv:1701.07177]

[5] D. B. Leinweber, W. Kamleh, A. L. Kiratidis, Z.-W. Liu, M. S. Mahbub, D. Roberts, F. M. Stokes, A. W. Thomas, and J.-J. Wu, *N* Spectroscopy from Lattice QCD: The Roper Explained*, JPS Conf. Proc. 10 (2016) 010011, [arXiv:1511.09146]

## In Preparation (based on thesis work)

[1] F. M. Stokes, W. Kamleh, and D. B. Leinweber, *Opposite-Parity Contaminations in Nucleon Form Factors*

[2] F. M. Stokes, W. Kamleh, and D. B. Leinweber, *Electromagnetic Structure of Nucleon Excitations in Lattice QCD*

[3] F. M. Stokes, W. Kamleh, and D. B. Leinweber, *Nucleon Excited State Transition Form Factors in Lattice QCD*

# Bibliography

[1] T. Schäfer and E. V. Shuryak, *Instantons in QCD*, *Rev. Mod. Phys.* **70** (1998) 323–426, [hep-ph/9610451].

[2] A. A. Belavin, A. M. Polyakov, A. S. Schwartz, and Yu. S. Tyupkin, *Pseudoparticle Solutions of the Yang-Mills Equations*, *Phys. Lett.* **B59** (1975) 85–87.

[3] D.-J. Kusterer, J. Hedditch, W. Kamleh, D. B. Leinweber, and A. G. Williams, *Low lying eigenmodes of the Wilson-Dirac operator and correlations with topological objects*, *Nucl. Phys.* **B628** (2002) 253–269, [hep-lat/0111029].

[4] J. Greensite, *The Confinement problem in lattice gauge theory*, *Prog. Part. Nucl. Phys.* **51** (2003) 1, [hep-lat/0301023].

[5] G. 't Hooft, *On the Phase Transition Towards Permanent Quark Confinement*, *Nucl. Phys.* **B138** (1978) 1–25.

[6] D. Trewartha, W. Kamleh, and D. Leinweber, *Evidence that centre vortices underpin dynamical chiral symmetry breaking in SU(3) gauge theory*, *Phys. Lett.* **B747** (2015) 373–377, [arXiv:1502.0675].

[7] C. Gattringer, *Coherent center domains in SU(3) gluodynamics and their percolation at $T_c$*, *Phys. Lett.* **B690** (2010) 179–182, [arXiv:1004.2200].

[8] C. Gattringer and A. Schmidt, *Center clusters in the Yang-Mills vacuum*, *JHEP* **1101** (2011) 051, [arXiv:1011.2329].

[9] F. M. Stokes, W. Kamleh, and D. B. Leinweber, *Visualizations of coherent center domains in local Polyakov loops*, *Annals Phys.* **348** (2014) 341–361, [arXiv:1312.0991].

[10] G. Endrődi, C. Gattringer, and H.-P. Schadler, *Fractality and other properties of center domains at finite temperature Part 1: SU(3) lattice gauge theory*, *Phys. Rev.* **D89** (2014), no. 5 054509, [arXiv:1401.7228].

[11] S. Durr et al., *Ab-Initio Determination of Light Hadron Masses*, *Science* **322** (2008) 1224–1227, [arXiv:0906.3599].

[12] C. Michael, *Adjoint Sources in Lattice Gauge Theory*, *Nucl. Phys.* **B259** (1985) 58–76.

[13] M. Luscher and U. Wolff, *How to Calculate the Elastic Scattering Matrix in Two-dimensional Quantum Field Theories by Numerical Simulation*, *Nucl. Phys.* **B339** (1990) 222–252.

[14] A. L. Kiratidis, W. Kamleh, D. B. Leinweber, Z.-W. Liu, F. M. Stokes, and A. W. Thomas, *Search for low-lying lattice QCD eigenstates in the Roper regime*, *Phys. Rev.* **D95** (2017), no. 7 074507, [arXiv:1608.0305].

[15] A. L. Kiratidis, W. Kamleh, D. B. Leinweber, and B. J. Owen, *Lattice baryon spectroscopy with multi-particle interpolators*, *Phys. Rev.* **D91** (2015) 094509, [arXiv:1501.0766].

[16] M. S. Mahbub, W. Kamleh, D. B. Leinweber, P. J. Moran, and A. G. Williams, *Structure and Flow of the Nucleon Eigenstates in Lattice QCD*, *Phys. Rev.* **D87** (2013), no. 9 094506, [arXiv:1302.2987].

[17] **CSSM Lattice** Collaboration, M. S. Mahbub, W. Kamleh, D. B. Leinweber, P. J. Moran, and A. G. Williams, *Roper Resonance in 2+1 Flavor QCD*, *Phys. Lett.* **B707** (2012) 389–393, [arXiv:1011.5724].

[18] **Hadron Spectrum** Collaboration, R. G. Edwards, N. Mathur, D. G. Richards, and S. J. Wallace, *Flavor structure of the excited baryon spectra from lattice QCD*, *Phys. Rev.* **D87** (2013), no. 5 054506, [arXiv:1212.5236].

[19] R. G. Edwards, J. J. Dudek, D. G. Richards, and S. J. Wallace, *Excited state baryon spectroscopy from lattice QCD*, *Phys. Rev.* **D84** (2011) 074508, [arXiv:1104.5152].

[20] C. B. Lang, L. Leskovec, M. Padmanath, and S. Prelovsek, *Pion-nucleon scattering in the Roper channel from lattice QCD*, *Phys. Rev.* **D95** (2017), no. 1 014510, [arXiv:1610.0142].

[21] C. Lang and V. Verduci, *Scattering in the $\pi N$ negative parity channel in lattice QCD*, *Phys. Rev.* **D87** (2013), no. 5 054502, [arXiv:1212.5055].

[22] P. Madanagopalan, R. G. Edwards, N. Mathur, and M. J. Peardon, *Spectroscopy of charmed baryons from lattice QCD*, *PoS* **LATTICE2014** (2015) 084, [arXiv:1410.8791].

[23] R. M. Woloshyn, *Excitations of strange bottom baryons*, *Eur. Phys. J.* **A52** (2016), no. 9 273, [arXiv:1605.0904].

[24] B. DeWitt, *Analysis over supernumbers*, p. 149. Cambridge Monographs on Mathematical Physics. Cambridge University Press, 2 ed., 1992.

[25] K. G. Wilson, *Confinement of Quarks*, *Phys. Rev.* **D10** (1974) 2445–2459.

[26] K. Symanzik, *Continuum Limit and Improved Action in Lattice Theories. 1. Principles and $\phi^4$ Theory*, *Nucl. Phys.* **B226** (1983) 187–204.

[27] K. Symanzik, *Continuum Limit and Improved Action in Lattice Theories. 2. O(N) Nonlinear Sigma Model in Perturbation Theory*, *Nucl. Phys.* **B226** (1983) 205–227.

[28] P. Weisz, *Continuum Limit Improved Lattice Action for Pure Yang-Mills Theory. 1.*, *Nucl. Phys.* **B212** (1983) 1–17.

[29] Y. Iwasaki, *Renormalization Group Analysis of Lattice Theories and Improved Lattice Action: Two-Dimensional Nonlinear O(N) Sigma Model*, *Nucl. Phys.* **B258** (1985) 141–156.

[30] S. Chandrasekharan and U. J. Wiese, *An Introduction to chiral symmetry on the lattice*, *Prog. Part. Nucl. Phys.* **53** (2004) 373–418, [hep-lat/0405024].

[31] B. Sheikholeslami and R. Wohlert, *Improved Continuum Limit Lattice Action for QCD with Wilson Fermions*, *Nucl. Phys.* **B259** (1985) 572.

[32] **JLQCD, CP-PACS** Collaboration, S. Aoki et al., *Nonperturbative O(a) improvement of the Wilson quark action with the RG-improved gauge action using the Schrodinger functional method*, *Phys. Rev.* **D73** (2006) 034501, [hep-lat/0508031].

[33] H. B. Nielsen and M. Ninomiya, *No Go Theorem for Regularizing Chiral Fermions*, *Phys. Lett.* **B105** (1981) 219–223.

[34] P. H. Ginsparg and K. G. Wilson, *A Remnant of Chiral Symmetry on the Lattice*, *Phys. Rev.* **D25** (1982) 2649.

[35] R. Narayanan and H. Neuberger, *A Construction of lattice chiral gauge theories*, *Nucl. Phys.* **B443** (1995) 305–385, [hep-th/9411108].

[36] H. Neuberger, *Exactly massless quarks on the lattice*, *Phys. Lett.* **B417** (1998) 141–144, [hep-lat/9707022].

[37] D. B. Kaplan, *A Method for simulating chiral fermions on the lattice*, *Phys. Lett.* **B288** (1992) 342–347, [hep-lat/9206013].

[38] **Fermilab Lattice, LATTICE-HPQCD, MILC** Collaboration, B. Chakraborty et al., *Strong-isospin-breaking correction to the muon anomalous magnetic moment from lattice QCD at the physical point*, *Phys. Rev. Lett.* **120** (2018), no. 15 152001, [arXiv:1710.1121].

[39] **ETM** Collaboration, C. Alexandrou et al., *Pion vector form factor from lattice QCD at the physical point*, *Phys. Rev.* **D97** (2018), no. 1 014508, [arXiv:1710.1040].

[40] **RBC, UKQCD** Collaboration, T. Blum et al., *Domain wall QCD with physical quark masses*, *Phys. Rev.* **D93** (2016), no. 7 074505, [arXiv:1411.7017].

[41] **PACS** Collaboration, K. I. Ishikawa, N. Ishizuka, Y. Kuramashi, Y. Nakamura, Y. Namekawa, Y. Taniguchi, N. Ukita, T. Yamazaki, and T. Yoshie, *2+1 Flavor QCD Simulation on a* $96^4$ *Lattice*, *PoS* **LATTICE2015** (2016) 075, [arXiv:1511.0922].

[42] H. J. Rothe, *Lattice gauge theories: An Introduction*, *World Sci. Lect. Notes Phys.* **43** (1992) 1–381. [World Sci. Lect. Notes Phys.82,1(2012)].

[43] G. C. Wick, *The Evaluation of the Collision Matrix*, *Phys. Rev.* **80** (1950) 268–272.

[44] S. Duane, A. Kennedy, B. J. Pendleton, and D. Roweth, *Hybrid monte carlo*, *Physics Letters B* **195** (1987), no. 2 216 – 222.

[45] W. Kamleh, D. B. Leinweber, and A. G. Williams, *Hybrid Monte Carlo with fat link fermion actions*, *Phys. Rev.* **D70** (2004) 014502, [hep-lat/0403019].

[46] S.-J. Dong and K.-F. Liu, *Stochastic estimation with Z(2) noise*, *Phys. Lett.* **B328** (1994) 130–136, [hep-lat/9308015].

[47] G. S. Bali, S. Collins, and A. Schafer, *Effective noise reduction techniques for disconnected loops in Lattice QCD*, *Comput. Phys. Commun.* **181** (2010) 1570–1583, [arXiv:0910.3970].

[48] **Hadron Spectrum** Collaboration, M. Peardon, J. Bulava, J. Foley, C. Morningstar, J. Dudek, R. G. Edwards, B. Joo, H.-W. Lin, D. G. Richards, and K. J. Juge, *A Novel quark-field creation operator construction for hadronic physics in lattice QCD*, *Phys. Rev.* **D80** (2009) 054506, [arXiv:0905.2160].

[49] N. Byers and C. N. Yang, *Theoretical Considerations Concerning Quantized Magnetic Flux in Superconducting Cylinders*, *Phys. Rev. Lett.* **7** (1961) 46–49.

[50] G. M. de Divitiis, R. Petronzio, and N. Tantalo, *On the discretization of physical momenta in lattice QCD*, *Phys. Lett.* **B595** (2004) 408–413, [`hep-lat/0405002`].

[51] S. Gusken, *A Study of smearing techniques for hadron correlation functions*, *Nucl. Phys. Proc. Suppl.* **17** (1990) 361–364.

[52] J. N. Hedditch, W. Kamleh, B. G. Lasscock, D. B. Leinweber, A. G. Williams, and J. M. Zanotti, *Pseudoscalar and vector meson form-factors from lattice QCD*, *Phys. Rev.* **D75** (2007) 094504, [`hep-lat/0703014`].

[53] G. Martinelli, C. T. Sachrajda, and A. Vladikas, *A Study of 'improvement' in lattice QCD*, *Nucl. Phys.* **B358** (1991) 212–227.

[54] S. Boinepalli et al., *Precision electromagnetic structure of octet baryons in the chiral regime*, *Phys. Rev.* **D74** (2006) 093005, [`hep-lat/0604022`].

[55] D. B. Leinweber, R. M. Woloshyn, and T. Draper, *Electromagnetic structure of octet baryons*, *Phys. Rev.* **D43** (1991) 1659–1678.

[56] C. W. Bernard, T. Draper, G. Hockney, and A. Soni, *Calculation of Weak Matrix Elements: Some Technical Aspects*, in *Lattice Gauge Theory: A Challenge in Large-Scale Computing*, (Wuppertal, Germany), pp. 199–207, 1985.

[57] S. Dinter, C. Alexandrou, M. Constantinou, V. Drach, K. Jansen, and D. B. Renner, *Precision Study of Excited State Effects in Nucleon Matrix Elements*, *Phys. Lett.* **B704** (2011) 89–93, [`arXiv:1108.1076`].

[58] T. Draper, R. M. Woloshyn, W. Wilcox, and K.-F. Liu, *Electromagnetic Form-factors of Hadrons*, *Nucl. Phys. Proc. Suppl.* **9** (1989) 175–180.

[59] T. Draper, R. M. Woloshyn, W. Wilcox, and K.-F. Liu, *The Pion Form-factor in Lattice QCD*, *Nucl. Phys.* **B318** (1989) 319–336.

[60] A. Bazavov, T. Bhattacharya, M. Cheng, C. DeTar, H. Ding, et al., *The chiral and deconfinement aspects of the QCD transition*, *Phys. Rev.* **D85** (2012) 054503, [`arXiv:1111.1710`].

[61] Y. Aoki, Z. Fodor, S. Katz, and K. Szabo, *The QCD transition temperature: Results with physical masses in the continuum limit*, *Phys. Lett.* **B643** (2006) 46–54, [`hep-lat/0609068`].

[62] Y. Aoki, S. Borsanyi, S. Durr, Z. Fodor, S. D. Katz, et al., *The QCD transition temperature: results with physical masses in the continuum limit II.*, *JHEP* **0906** (2009) 088, [arXiv:0903.4155].

[63] **Wuppertal-Budapest Collaboration** Collaboration, S. Borsanyi et al., *Is there still any $T_c$ mystery in lattice QCD? Results with physical masses in the continuum limit III*, *JHEP* **1009** (2010) 073, [arXiv:1005.3508].

[64] M. Asakawa, S. A. Bass, and B. Muller, *Center domains and their phenomenological consequences*, *Phys. Rev. Lett.* **110** (2013).

[65] **CMS Collaboration** Collaboration, S. Chatrchyan et al., *Observation and studies of jet quenching in PbPb collisions at nucleon-nucleon center-of-mass energy = 2.76 TeV*, *Phys. Rev.* **C84** (2011) 024906, [arXiv:1102.1957].

[66] **ATLAS Collaboration** Collaboration, G. Aad et al., *Observation of a Centrality-Dependent Dijet Asymmetry in Lead-Lead Collisions at* $\sqrt{s_{NN}} = 2.77$ *TeV with the ATLAS Detector at the LHC*, *Phys. Rev. Lett.* **105** (2010) 252303, [arXiv:1011.6182].

[67] **CMS Collaboration** Collaboration, M. B. Tonjes, *Study of jet quenching using dijets in Pb Pb collisions with CMS*, *J. Phys.* **G38** (2011) 124084.

[68] J. Danzer, C. Gattringer, S. Borsanyi, and Z. Fodor, *Center clusters and their percolation properties in lattice QCD*, *PoS* **LATTICE2010** (2010) 176, [arXiv:1010.5073].

[69] S. Borsanyi, J. Danzer, Z. Fodor, C. Gattringer, and A. Schmidt, *Coherent center domains from local Polyakov loops*, *J. Phys. Conf. Ser.* **312** (2011) 012005, [arXiv:1007.5403].

[70] H.-P. Schadler, G. Endrődi, and C. Gattringer, *Local Polyakov loop domains and their fractality*, *PoS* **LATTICE2013** (2014) 134, [arXiv:1310.8521].

[71] A. Mykkanen, M. Panero, and K. Rummukainen, *Casimir scaling and renormalization of Polyakov loops in large-N gauge theories*, *JHEP* **1205** (2012) 069, [arXiv:1202.2762].

[72] A. Schäfer, G. Endrdi, and J. Wellnhofer, *Center clusters in full QCD at finite temperature and background magnetic field*, *Phys. Rev.* **D92** (2015), no. 1 014509, [arXiv:1506.0769].

[73] F. Karsch, *Lattice QCD at finite temperature and density*, *Nucl. Phys. Proc. Suppl.* **83** (2000) 14–23, [hep-lat/9909006].

[74] B. Svetitsky and L. G. Yaffe, *Critical Behavior at Finite Temperature Confinement Transitions*, *Nucl. Phys.* **B210** (1982) 423.

[75] S. Fortunato, *Percolation and deconfinement in SU(2) gauge theory*, hep-lat/0012006.

[76] **CP-PACS Collaboration** Collaboration, T. Umeda et al., *Two flavors of dynamical quarks on anisotropic lattices*, *Phys. Rev.* **D68** (2003) 034503, [hep-lat/0302024].

[77] R. Edwards, U. M. Heller, and T. Klassen, *Accurate scale determinations for the Wilson gauge action*, *Nucl. Phys.* **B517** (1998) 377–392, [hep-lat/9711003].

[78] F. Karsch, C. Schmidt, and S. Stickan, *Common features of deconfining and chiral critical points in QCD and the three state Potts model in an external field*, *Comput. Phys. Commun.* **147** (2002) 451–454, [hep-lat/0111059].

[79] W. Janke and R. Villanova, *Three-dimensional three state Potts model revisited with new techniques*, *Nucl. Phys.* **B489** (1997) 679–696, [hep-lat/9612008].

[80] W. Hastings, *Monte carlo sampling methods using markov chains and their applications*, *Biometrika* **57** (1970), no. 1 97–109.

[81] J. Zhang, P. J. Moran, P. O. Bowman, D. B. Leinweber, and A. G. Williams, *Stout-link smearing in lattice fermion actions*, *Phys. Rev.* **D80** (2009) 074503, [arXiv:0908.3726].

[82] Advanced Visual Systems Inc., “AVS/Express.” http://www.avs.com/solutions/express/, 2014. [Online; accessed 10-March-2014].

[83] B. Muller and J. L. Nagle, *Results from the relativistic heavy ion collider*, *Ann. Rev. Nucl. Part. Sci.* **56** (2006) 93–135, [nucl-th/0602029].

[84] N. Jan and D. Stauffer, *Random site percolation in three dimensions*, *International Journal of Modern Physics C* **09** (1998), no. 02 341–347.

[85] F. M. Stokes et al., *Parity-expanded variational analysis for nonzero momentum*, *Phys. Rev.* **D92** (2015), no. 11 114506, [arXiv:1302.4152].

[86] **Budapest-Marseille-Wuppertal** Collaboration, S. Borsanyi et al., *Isospin splittings in the light baryon octet from lattice QCD and QED*, *Phys. Rev. Lett.* **111** (2013), no. 25 252001, [arXiv:1306.2287].

[87] **PACS-CS** Collaboration, S. Aoki et al., *2+1 Flavor Lattice QCD toward the Physical Point*, *Phys. Rev.* **D79** (2009) 034503, [arXiv:0807.1661].

[88] **MILC** Collaboration, A. Bazavov et al., *Nonperturbative QCD simulations with 2+1 flavors of improved staggered quarks*, *Rev. Mod. Phys.* **82** (2010) 1349–1417, [arXiv:0903.3598].

[89] Z. Fodor and C. Hoelbling, *Light Hadron Masses from Lattice QCD*, *Rev. Mod. Phys.* **84** (2012) 449, [arXiv:1203.4789].

[90] M. G. Beckett, B. Joo, C. M. Maynard, D. Pleiter, O. Tatebe, and T. Yoshie, *Building the International Lattice Data Grid*, *Comput. Phys. Commun.* **182** (2011) 1208–1214, [arXiv:0910.1692].

[91] F. X. Lee and D. B. Leinweber, *Negative parity baryon spectroscopy*, *Nucl. Phys. Proc. Suppl.* **73** (1999) 258–260, [hep-lat/9809095].

[92] V. Verduci and C. B. Lang, *Baryon resonances coupled to Pion-Nucleon states in lattice QCD*, *PoS* **LATTICE2014** (2014) 121, [arXiv:1412.0701].

[93] R. W. Schiel, *Expanding the Interpolator Basis in the Variational Method to Explicitly Account for Backward Running States*, *Phys. Rev.* **D92** (2015), no. 3 034512, [arXiv:1503.0258].

[94] C. Morningstar and M. J. Peardon, *Analytic smearing of SU(3) link variables in lattice QCD*, *Phys. Rev.* **D69** (2004) 054501, [hep-lat/0311018].

[95] Z.-W. Liu, W. Kamleh, D. B. Leinweber, F. M. Stokes, A. W. Thomas, and J.-J. Wu, *Hamiltonian effective field theory study of the* $\mathbf{N^*(1440)}$ *resonance in lattice QCD*, *Phys. Rev.* **D95** (2017), no. 3 034034, [arXiv:1607.0453].

[96] Z.-W. Liu, W. Kamleh, D. B. Leinweber, F. M. Stokes, A. W. Thomas, and J.-J. Wu, *Hamiltonian effective field theory study of the* $\mathbf{N^*(1535)}$ *resonance in lattice QCD*, *Phys. Rev. Lett.* **116** (2016), no. 8 082004, [arXiv:1512.0014].

[97] F. M. Stokes, W. Kamleh, D. B. Leinweber, and B. J. Owen, *Electromagnetic Form Factors of Excited Nucleons via Parity-Expanded Variational Analysis*, *PoS* **LATTICE2016** (2016) 161, [arXiv:1701.0717].

[98] R. Pohl, R. Gilman, G. A. Miller, and K. Pachucki, *Muonic hydrogen and the proton radius puzzle*, *Ann. Rev. Nucl. Part. Sci.* **63** (2013) 175–204, [arXiv:1301.0905].

[99] C. E. Carlson, *The Proton Radius Puzzle*, *Prog. Part. Nucl. Phys.* **82** (2015) 59–77, [arXiv:1502.0531].

[100] A. Antognini et al., *Proton Structure from the Measurement of $2S - 2P$ Transition Frequencies of Muonic Hydrogen*, *Science* **339** (2013) 417–420.

[101] P. J. Mohr, D. B. Newell, and B. N. Taylor, *CODATA Recommended Values of the Fundamental Physical Constants: 2014*, *Rev. Mod. Phys.* **88** (2016), no. 3 035009, [`arXiv:1507.0795`].

[102] A. Beyer, L. Maisenbacher, A. Matveev, R. Pohl, K. Khabarova, A. Grinin, T. Lamour, D. C. Yost, T. W. Hänsch, N. Kolachevsky, and T. Udem, *The rydberg constant and proton size from atomic hydrogen*, *Science* **358** (2017), no. 6359 79–85, [`http://science.sciencemag.org/content/358/6359/79.full.pdf`].

[103] J. Dragos et al., *Nucleon matrix elements using the variational method in lattice QCD*, *Phys. Rev.* **D94** (2016), no. 7 074505, [`arXiv:1606.0319`].

[104] B. J. Owen, J. Dragos, W. Kamleh, D. B. Leinweber, M. S. Mahbub, B. J. Menadue, and J. M. Zanotti, *Variational Approach to the Calculation of gA*, *Phys. Lett.* **B723** (2013) 217–223, [`arXiv:1212.4668`].

[105] M. J. Savage, *The Magnetic moments of the octet baryons in quenched chiral perturbation theory*, *Nucl. Phys.* **A700** (2002) 359–376, [`nucl-th/0107038`].

[106] D. B. Leinweber, *Quark contributions to baryon magnetic moments in full, quenched and partially quenched QCD*, *Phys. Rev.* **D69** (2004) 014005, [`hep-lat/0211017`].

[107] V. Punjabi et al., *Proton elastic form-factor ratios to Q**2 = 3.5-GeV**2 by polarization transfer*, *Phys. Rev.* **C71** (2005) 055202, [`nucl-ex/0501018`]. [Erratum: Phys. Rev.C71,069902(2005)].

[108] J. M. M. Hall, D. B. Leinweber, and R. D. Young, *Chiral extrapolations for nucleon magnetic moments*, *Phys. Rev.* **D85** (2012) 094502, [`arXiv:1201.6114`].

[109] C. Alexandrou, M. Constantinou, K. Hadjiyiannakou, K. Jansen, C. Kallidonis, G. Koutsou, and A. Vaquero Aviles-Casco, *Nucleon electromagnetic form factors using lattice simulations at the physical point*, *Phys. Rev.* **D96** (2017), no. 3 034503, [`arXiv:1706.0046`].

[110] R. S. Sufian, Y.-B. Yang, J. Liang, T. Draper, and K.-F. Liu, *Sea Quarks Contribution to the Nucleon Magnetic Moment and Charge Radius at the Physical Point*, *Phys. Rev.* **D96** (2017), no. 11 114504, [`arXiv:1705.0584`].

[111] D. Djukanovic, T. Harris, G. M. Von Hippel, P. M. Junnarkar, H. B. Meyer, and H. Wittig, *Electromagnetic form factors and axial charge of the nucleon from* $N_f = 2 + 1$ *Wilson fermions*, *EPJ Web Conf.* **175** (2018) 06013.

[112] Y.-C. Jang, T. Bhattacharya, R. Gupta, H.-W. Lin, and B. Yoon, *Nucleon Axial and Electromagnetic Form Factors*, *EPJ Web Conf.* **175** (2018) 06033, [arXiv:1801.0163].

[113] **PACS** Collaboration, N. Tsukamoto, K.-I. Ishikawa, Y. Kuramashi, S. Sasaki, and T. Yamazaki, *Nucleon structure from 2+1 flavor lattice QCD near the physical point*, *EPJ Web Conf.* **175** (2018) 06007, [arXiv:1710.1078].

[114] **RBC, UKQCD** Collaboration, S. Ohta and f. t. RBC, *Nucleon structure from 2+1-flavor domain-wall QCD*, *EPJ Web Conf.* **175** (2018) 06012, [arXiv:1710.0665].

[115] S. Capitani, M. Della Morte, D. Djukanovic, G. von Hippel, J. Hua, B. Jäger, B. Knippschild, H. B. Meyer, T. D. Rae, and H. Wittig, *Nucleon electromagnetic form factors in two-flavor QCD*, *Phys. Rev.* **D92** (2015), no. 5 054511, [arXiv:1504.0462].

[116] J. R. Green, J. W. Negele, A. V. Pochinsky, S. N. Syritsyn, M. Engelhardt, and S. Krieg, *Nucleon electromagnetic form factors from lattice QCD using a nearly physical pion mass*, *Phys. Rev.* **D90** (2014) 074507, [arXiv:1404.4029].

[117] T. Bhattacharya, S. D. Cohen, R. Gupta, A. Joseph, H.-W. Lin, and B. Yoon, *Nucleon Charges and Electromagnetic Form Factors from 2+1+1-Flavor Lattice QCD*, *Phys. Rev.* **D89** (2014), no. 9 094502, [arXiv:1306.5435].

[118] J.-J. Wu, T. S. H. Lee, A. W. Thomas, and R. D. Young, *Finite-volume Hamiltonian method for coupled-channels interactions in lattice QCD*, *Phys. Rev.* **C90** (2014), no. 5 055206, [arXiv:1402.4868].

[119] R. A. Briceno, J. J. Dudek, R. G. Edwards, C. J. Shultz, C. E. Thomas, and D. J. Wilson, *The resonant* $\pi^+\gamma \to \pi^+\pi^0$ *amplitude from Quantum Chromodynamics*, *Phys. Rev. Lett.* **115** (2015) 242001, [arXiv:1507.0662].

[120] B. J. Owen, W. Kamleh, D. B. Leinweber, M. S. Mahbub, and B. J. Menadue, *Transition of* $\rho \to \pi\gamma$ *in lattice QCD*, *Phys. Rev.* **D92** (2015), no. 3 034513, [arXiv:1505.0287].

[121] W.-T. Chiang, S. N. Yang, M. Vanderhaeghen, and D. Drechsel, *Magnetic dipole moment of the* $S_{11}(1535)$ *from the* $\gamma p \to \gamma\eta p$ *reaction*, *Nucl. Phys.* **A723** (2003) 205–225, [nucl-th/0211061].

[122] M. S. Mahbub, W. Kamleh, D. B. Leinweber, P. J. Moran, and A. G. Williams, *Low-lying Odd-parity States of the Nucleon in Lattice QCD*, *Phys. Rev.* **D87** (2013), no. 1 011501, [arXiv:1209.0240].

[123] J. Liu, J. He, and Y. B. Dong, *Magnetic moments of negative-parity low-lying nucleon resonances in quark models*, *Phys. Rev.* **D71** (2005) 094004.

[124] N. Sharma, A. Martinez Torres, K. P. Khemchandani, and H. Dahiya, *Magnetic moments of the low-lying* $1/2^-$ *octet baryon resonances*, *Eur. Phys. J.* **A49** (2013) 11, [arXiv:1207.3311].

[125] M. S. Mahbub, W. Kamleh, D. B. Leinweber, and A. G. Williams, *Searching for low-lying multi-particle thresholds in lattice spectroscopy*, *Annals Phys.* **342** (2014) 270–282, [arXiv:1310.6803].

[126] J. M. M. Hall, W. Kamleh, D. B. Leinweber, B. J. Menadue, B. J. Owen, A. W. Thomas, and R. D. Young, *Lattice QCD Evidence that the (1405) Resonance is an Antikaon-Nucleon Molecule*, *Phys. Rev. Lett.* **114** (2015), no. 13 132002, [arXiv:1411.3402].

[127] J. M. M. Hall, W. Kamleh, D. B. Leinweber, B. J. Menadue, B. J. Owen, and A. W. Thomas, *Light-quark contributions to the magnetic form factor of the Lambda(1405)*, *Phys. Rev.* **D95** (2017), no. 5 054510, [arXiv:1612.0747].

[128] **Particle Data Group** Collaboration, C. Patrignani et al., *Review of Particle Physics*, *Chin. Phys.* **C40** (2016), no. 10 100001.

[129] D. S. Roberts, W. Kamleh, and D. B. Leinweber, *Wave Function of the Roper from Lattice QCD*, *Phys. Lett.* **B725** (2013) 164–169, [arXiv:1304.0325].

[130] R. G. Edwards, U. M. Heller, and T. R. Klassen, *The Effectiveness of nonperturbative O(a) improvement in lattice QCD*, *Phys. Rev. Lett.* **80** (1998) 3448–3451, [hep-lat/9711052].

[131] J. M. M. Hall, D. B. Leinweber, B. J. Owen, and R. D. Young, *Finite-volume corrections to charge radii*, *Phys. Lett.* **B725** (2013) 101–105, [arXiv:1210.6124].

[132] M. Levoy, *Efficient ray tracing of volume data*, *ACM Transactions on Graphics* **9** (1990), no. 3 245–261.

[133] Khronos Consortium, “OpenGL.” http://www.opengl.org/, 2012. [Online; accessed 13-July-2012].

[134] J. Krüger and R. Westermann, *Acceleration techniques for gpu-based volume rendering*, in *Proceedings of the 14th IEEE Visualization 2003*, VIS '03, (Washington, DC, USA), IEEE Computer Society, 2003.

[135] D. Woods, N. Weber, and M. Dario, "DevIL — a full featured cross-platform image library." `http://openil.sourceforge.net/`, 2009. [Online; accessed 17-October-2012].

[136] Open source community, "FFmpeg." `http://ffmpeg.org/`, 2012. [Online; accessed 18-September-2012].

# Index